UNITED STATES DEPARTMENT OF THE INTERIOR

GEOLOGICAL SURVEY

GEOS DATA SUMMARY FOR ACTIVE AND PASSIVE SEISMIC EXPERIMENTS CONDUCTED IN SUPPORT OF NORTHERN NEVADA LITHOSPHERIC EXPERIMENTS—PASSCAL

compiled and edited by

Christopher Dietel
and
Roger D. Borcherdt

OPEN-FILE REPORT 87-326

This report is preliminary and has not been reviewed for conformity with U.S. Geological Survey editorial standards and stratigraphic nomenclature. Any use of trade names is for descriptive purposes only and does not imply endorsement by the USGS.

TABLE OF CONTENTS

FORMATS FOR ARCHIVAL AND DISTRIBUTION OF DIGITAL TIME SERIES

FIGURES

TABLES

APPENDICES

SUMMARY

The Northern Nevada Lithospheric Experiments (Thompson *et al.*, 1986) conducted in cooperation with 17 university and government organizations, were executed in northwestern Nevada from 17 July to 2 August, 1986. Controlled source experiments (chemical explosions) were executed on July 22, 25, and 28, 1986. Passive experiments to record aftershocks of the magnitude 6.1 earthquake, which occurred near Chalfant, California on July 21, 1986, were conducted during the 24–48 hour intervals prior to and after each of the controlled source experiments. This report provides a summary of the data recorded using a variable-number (16–19) of six-channel, broad-band, digital data acquisition systems (GEOS) deployed in support of both sets of experiments.

For the active experiments the instrumentation was deployed to augment the reflection and refraction data set collected to infer 1) lithospheric structures in a region of active extension, 2) anomalous upper-mantle velocity structure, and 3) characteristics of lower-crustal and upper-mantle structures. Twenty-seven chemical explosions were detonated and recorded. Data reported herein include seismograms from each of the 27 explosions. 1167 seismograms or 389 sets of three-component recordings are illustrated in record section format.

For the passive experiments the instrumentation was programmed to record other more distant seismic events to provide additional information on deeper upper-mantle structure. Fifty-one seismic events were recorded at three or more GEOS stations during the course of the passive experiments. Forty-six of these events were identified as aftershocks of the $M \sim 6.1$ Chalfant, California earthquake. One event was identified as a nuclear explosion in south-central Nevada and four events have not been identified. Of the forty-six aftershocks, 1, 2, 33, and 10 were in the magnitude ranges, respectively, of 5.5–6, 4–5, 3–4, and 2–3. The nuclear explosion was assigned a magnitude of 4.1 (M_b) by U.C. Berkeley Seismographic Station and was recorded on seven stations. Record sections displayed herein for the passive experiments include the seismograms for twenty of the events recorded on four or more stations. These seismograms are displayed at an expanded time scale, 20 seconds in duration. Record sections for nine of the events also are displayed at a reduced time scale, 60 seconds in duration.

Observed travel-times are compared with those estimated from a preliminary velocity model in order to correlate the recordings with earthquakes identified on other networks, identify location and timing errors, and to facilitate interpretation based on more detailed models. Response curves for the instrumentation computed from signals recorded *in situ* are presented for the various deployment locations.

Each of the seismograms illustrated in this report are available on nine-track magnetic tape in GEOS, cassette refraction and SEG–Y formats. Copies in SEG–Y format are available from the IRIS Data Management Center. The other formats are available from the authors on special request.

INTRODUCTION—OBJECTIVES FOR NORTHERN NEVADA LITHOSPHERIC EXPERIMENTS (NNLE)

The Basin and Range province of the western United States, characterized by north-trending ranges bounded on one or both sides by normal faults separated by alluvial valleys, represents a major continental rift zone with Cenozoic crustal extension inferred to be at least 100 km and possibly as large as 300 km or nearly one-half the present width of the province (Hamilton and Myers, 1966). Various plate tectonic models, proposed for the development of the Basin and Range province, include: continuation of the East Pacific Rise beneath the Cordillera (Menard, 1964; Cook, 1969), the development of a wide, soft transform and spreading boundary related to San Andreas transform motion (Atwater, 1970), thermal upwelling enhanced by stress relaxation upon initiation of the San Andreas transform (Smith, 1978), and asthenospheric upwelling through a subducting slab window (Dickinson and Snyder, 1979). Recent models for the structure of the mid and upper crust propose deformation of the upper crust by brittle, normal faulting, consistent with seismicity at a maximum depth of 15 km (Smith, 1978) and extension with ductile stretching below 15 km (Sibson, 1982). Interpretation of near-vertical reflection data raises questions regarding the nature of apparent upper-crustal normal faulting upon extension to depth (*e.g.,* Gans *et al.*, 1985 or Wernicke, 1981) and the nature of mid- to lower-crustal-refraction structure, especially as they relate to the nature of inferred rifting processes in the Basin and Range province. The Northern Nevada Lithospheric Experiment was conducted to provide additional insight regarding these questions and, in particular, provide estimates of the structure, physical properties, and composition of the lower crust and upper mantle as they relate to manifestations of rifting observed in the upper crust (Thompson *et al.*, 1986).

The Northern Nevada Lithospheric Experiment was conducted with the cooperative efforts of 17 government and university organizations. It consisted of active and passive experiments to record controlled sources and earthquakes. The active experiments involved a main EW profile (280 km in length) and a NS cross profile (200 km in length) together with four standard reflection spreads located near the center of the profiles. The reflection spreads were used to record seismic energy generated by both vibroseis units and chemical explosions. The passive experiments were conducted with triggered and continuous recording instruments located on the profiles so as to record aftershocks which occurred during the course of the active experiments near Chalfant, California at a distance of about 220 km from the south end of the NS profile. Instrumentation utilized for the active experiments included 120 portable vertical-component systems, 60 three-component digital systems, four standard-reflection systems, and several smoked-drum recorders. A variable number of three-component digital recorders and smoked-drum recorders were used for the passive earthquake experiments.

This report describes only the controlled source and earthquake data recorded on the GEOS systems (Borcherdt *et al.*, 1985). This report provides analog copies of these data, describes the format of magnetic tapes containing the digital time series, and provides information on instrument calibration and preliminary velocity models necessary for detailed interpretations.

The GEOS systems were requested in support of the active experiments to increase the number of recording locations for vertical-component data provided by other groups and, in particular, to augment the number of three-component recordings for inferences of shear-wave velocity structure. The fortuitous occurrence of the Chalfant earthquake sequence at the beginning of the controlled source experiments at distances of 250–320 km provided the opportunity to augment the controlled source information on lower-crust and upper-mantle structure with energy penetrating deeper upper-mantle structures. The occurrence of a nuclear explosion during the passive experiments provided recordings along the north-south profile up to distances of about 370 km.

The experiment provided an opportunity to evaluate design features of the recently-developed GEOS units in a moderately large-scale field experiment involving both controlled and earthquake sources. Although the system was designed explicitly for a variety of active and passive experiments, including the current type of experiment, these experiments provided the first opportunity to evaluate GEOS design features for both types of experiments conducted coincidently.

Deployment locations for the GEOS profiles were chosen near the center of each main profile so as to provide data focused on a number of scientific objectives, when combined with that of the other participating institutions. Objectives emphasized in the choice of locations included:

1.) crustal structure as it can be inferred from both the vertical-component reflection and refraction data,

2.) shear-wave structure as it can be inferred from the three-component reflection-refraction data for both the active and passive experiments,

3.) amplitude studies for possible inferences of Q structure and additional constraints on velocity structure as inferrable from *in situ* calibrations for each location, several of which were co-sited with instrumentation deployed by the other institutions,

4.) study of near- and post-critical reflection data for the Moho and any intermediate boundaries to provide additional insight into elastic and anelastic material properties and geometric structure as suggested might be possible by recent theoretical and laboratory results (Borcherdt *et al.*, 1985, 1986; Becker and Richardson, 1969, 1972).

5.) calibration of new types of explosives used at some of the shotpoint points using on-scale recordings of near-source ground motion with the GEOS in a six-channel configuration recording the output of both three-compoment force-balance accelerometers and velocity transducers.

INSTRUMENTATION—GENERAL DESCRIPTION OF GEOS

A detailed description of the instrumentation (GEOS; General Earthquake Observation System) used to collect the data presented in this report is provided by Borcherdt *et al.*, 1985. Only a general summary of instrumentation characteristics pertinent to this data set is provided here. Specific parameters chosen to record the data from the active and passive experiments are provided in subsequent chapters.

Recording System

The GEOS recording system was developed by the U.S. Geological Survey for use in a wide variety of active and passive seismic experiments. The digital data acquisition system operates under control of a central microcomputer, which permits simple adaptation of the system in the field to a variety of experiments; including, seismic refraction studies, near-source high-frequency studies of strong motion, teleseismic earth structure studies, studies of earth tidal strains, and free oscillation studies. Versatility in system application is achieved by isolation of the appropriate data acquisition functions on hardware modules controlled by a single microprocessor via a general computer bus. CMOS hardware components are utilized to reduce quiescent power consumption to less than two watts for use of the system as either a portable recorder in remote locations or for use in an observatory setting with inexpensive backup power sources. The GEOS together with two sets of three-component sensors (force-balance accelerometer, velocity transducer) and ferrite WWVB antenna commonly used for controlled-source, reflection-refraction experiments and local-regional earthquake experiments is shown in Figure 1 (see Borcherdt *et al.*, 1985 for hardware modules comprising the system).

The signal conditioning module for the GEOS has six input channels, selectable under software control, permitting acquisition of seismic signals ranging in amplitude from a few nanometers of seismic background noise to 2 g in acceleration for ground motions near large events. The analog-to-digital conversion module is equipped with a 16-bit CMOS analog-to-digital converter which affords 96 dB of linear dynamic range or signal resolution; this, together with two sets of sensors, implies an effective system dynamic range of about 180 dB. A data buffer with direct memory access capabilities allows for maximum throughput rates of 1200 sps. With sampling rates software selectable as any integral quotient of 1200, broad and variable system bandwidth ranging from ($10^{-5} - 6 \times 10^2$ Hz) has been achieved by using the recorders with a wide variety of sensor types (*e.g.,* Johnston, Borcherdt, and Linde, 1986).

Modern high-density (1600–6400 bpi) compact tape cartridges offer large data storage capacities (1.25–23 Mbyte) in ANSI standard format to facilitate data accessibility via minicomputer systems (1600 bpi and 1.25 Mbyte versions were used for the Nevada experiments). Read capabilities of cartridge tape recorders are utilized to allow recording parameters and system-operational software to be changed automatically. Installation of an expanded data buffer module planned for systems to be constructed will allow the system to act as a solid-state or a dual-media recorder with rapid data accessibility via microcomputer. Systems equipped with modems can be utilized to transmit data via telecommunications to a central data processing laboratory.

Microprocessor control of time-standard provides the capability to synchronize the internal clock via internal receivers (such as WWVB and satellite), external master clock, or conventional digital clocks. Microprocessor control of internal receivers permits systems on command to determine time corrections with respect to an external standard. This capability permits especially accurate correction for conventional drift of internal clocks.

Accurate *in situ* calibration of system components improves data accuracy and permits on-site evaluation of potential system performance malfunctions. The calibration module currently implemented in the GEOS permits calibration of three types of sensors and the signal-conditioning module under software control of the CPU. Calibration capabilities for sensors include velocity transducers with and without calibration coils and force-balance accelerometers. In the case of the velocity transducers, a dc voltage, derived under CPU control for appropriate gain setting from the D/A converter, is applied to either the main or calibration coil of the transducer for a software-selectable time interval. Voltage termination corresponds to an applied step function in acceleration to the sensor mass with the resultant signal determining relative calibration. In the case of force-balance accelerometers ±12 volts are applied to the damped and undamped control lines. The signal-conditioning module is calibrated using an impulse of one sample duration and an alternating dc voltage derived and applied under software control to the amplifiers while the sensors are disconnected via appropriate relays.

A 32-character alphanumeric display under control of the microcomputer, allows the system to be quickly and conveniently set up in the field and offers the operator considerable flexibility to modify the system in the field for a wide variety of applications. English-language messages to the operator, executed in an interactive mode, reduce operator field set-up errors. A complete record of recording system parameters is recorded on each tape together with calibration signals for both the sensor and the recorders. These records assure rapid and accurate interpretation via computer of signals, both in the field and in the laboratory.

Flexibility to modify the system to incorporate future improvements in technology is achieved using a structured software architecture and modular hardware components. Incorporation of new hardware modules is accomplished in a straightforward manner by replacing appropriate modules and corresponding segments of controlling software.

The system response with current velocity transducers (L–22; Mark Products) allows broad-band signals (0.5–400 Hz) to be recorded on scale with high resolution for seismic reflection-refraction studies. The amplitude response of the recording system, together with that for two types of sensors (velocity transducer, L–4; force-balance accelerometer) is shown in Figure 2. Response curves determined from signals recorded at each station location are described in a subsequent chapter.

Data Playback System

Data can be played back in either an analog or digital format in the field using the read capability of the GEOS mass-storage module. Data can also be played back using portable mini-computer systems configured with appropriate cartridge tape readers (see Borcherdt *et al.*, 1985, for details). For the experiments described herein, only the analog playback capability was utilized in the field. Analog playbacks on light-sensitive paper were utilized in the field to identify seismic events, trigger parameters, and evaluate instrument performance. Digital playback of the data was conducted with a Tanberg serpentine tape drive attached to the PDP 11/70 at the National Strong Motion Data Center in Menlo Park. Software packages, developed by G. Maxwell, E. Cranswick, and C. Mueller, were used to play back and process the data set.

FIELD SUMMARY—SOURCE, STATION, AND RECORDING SYSTEM PARAMETERS FOR ACTIVE AND PASSIVE EXPERIMENTS

The occurrence of a magnitude 5+ earthquake on July 20, 1986 near Chalfant, California stimulated the development of plans to record both aftershocks and the planned controlled sources. The instruments were transported to the field site from Menlo Park, California on July 20, with plans to deploy systems one day, early on July 21. The main shock of magnitude 6.1 occurred approximately 15 minutes prior to arrival of the instrumentation at the chosen field sites. Deployment of the systems to record aftershocks commenced about 30 minutes after the occurrence of the main shock.

Station and Shotpoint Locations

A summary of all of the GEOS locations used during the course of the experiments is shown in Figure 3 in relation to the two main deployment profiles and the shotpoints. The controlled source experiments consisted of three deployments. The first deployment was on the NS profile to provide in-line coverage of the sources detonated along the NS profile and fan coverage for one shot detonated perpendicular to the profile. The second deployment of GEOS involved extending the NS profile to provide fan coverage for each of the sources detonated along the EW profile and additional on-line aftershock data. For the second deployment, several of the locations used during the first deployment were repeated. The third deployment involved moving all of the GEOS units to locations along the EW profile to provide in-line coverage of the sources on the EW line that were detonated at the same locations used earlier for the second deployment.

The locations of the segments of the profiles to be occupied by GEOS were selected to emphasize the scientific objectives stated earlier for the controlled source experiments. In regards to the aftershocks, the same locations were used with the intent of augmenting the controlled source objectives with information on deeper upper-mantle structure as could be inferred from the more distant aftershocks. The aftershocks occurred at a distance of about 260 km from the closest GEOS instrument on the NS profile. The azimuth for the deployment profile differed from that of the in-line source direction by about 10°. Choice of the segments of the profile near the center of each of the main deployment lines permitted colocation of the instrumentation used for the reflection studies as well as the refraction studies. Data sets simultaneously recorded on each of the various types of instrumentation at these sites together with calibration curves derived *in situ* at each GEOS location (see later chapter) was obtained to facilitate calibration of the various types of instrumentation and interpretations based on all of the data sets.

Bar graphs, indicating the time intervals during which each instrument was programmed to record earthquakes and chemical explosions, are shown for each deployment (Figures 4a, 4b, and 4c). For each deployment, the chemical explosions were detonated in three preselected ten-minute time intervals. As a result of the requirement to record continuously during these intervals and the high degree of seismicity near Chalfant, CA, the GEOS units were programmed a few hours before each shot sequence to record only during the prescribed time intervals and not to trigger on earthquakes.

Timing at each of the stations was achieved using the automatic capability of the recorders to synchronize to WWVB and to record timing corrections with respect to

WWVB at programmable time intervals. Timing accuracy for the events is within the 5 ms accuracy inherent in interpretation of WWVB signals. This accuracy level has been confirmed by a number of previous experiments (Borcherdt *et al.*, 1985) and was checked during these experiments with an external master clock.

Parameters for Active Experiments

Information, regarding the identification numbers, time, location, size, and type of explosive is presented in Table 1 for each of the chemical explosions detonated during the experiments. The larger explosions were detonated for both the reflection and refraction studies. The small explosions were detonated for near-vertical reflection studies.

For the controlled source experiments, the systems were programmed to record in preset time mode for three consecutive ten-minute intervals. The two configurations of the system that were used to record the data sets are summarized in Table 2. The majority of the systems were programmed to record the three-channel output of the three-component velocity transducers at 400 samples per-second per-channel for the first two deployments and at 200 sps/channel for the third deployment. Corresponding corner frequencies for the seven-pole Butterworth anti-aliasing filters were selected at 100 Hz and 50 Hz, respectively. Gains were selected at 54 and 60 dB. For three sites used during the first deployment and one site for the second and third deployments, the systems were programmed to record signals on six-channels as detected by three-component force-balance accelerometers and three-component velocity transducers. Sampling rates for this configuration were chosen at 200 sps/channel with a 50 Hz corner for anti-aliasing filters. Gains for force-balance accelerometer channels were chosen at 6 dB. The six-channel instrument configuration was programmed for the units located near shotpoints 4, 8, and 11 during the first deployment and near shot point 4 for the second and third deployments. The on-scale recordings at shotpoints 8 and 11 were collected to compare the effectiveness of a new type of explosive. Shotpoint 4 was selected as a site for near-source on-scale recordings to assist in calibrations of the various shot points. Shotpoint 4 was selected because of its central location near the intersection of the two profiles.

Parameters for Passive Experiments

Locations of the earthquake epicenters for the events detected at 3 or more recording locations are shown on Figure 7. Locations for the aftershocks are tabulated in Table 6. The occurrence time for each aftershock, as indicated on Figures 4, 5, and 6, shows which instrument locations were occupied at the times of the events. Epicentral locations for the events were derived from CALNET.

In summary, forty-six earthquakes in the Chalfant, California area were identified as being recorded at three or more sites during the experiment. Of this number the largest event was of magnitude 5.5, three of the events were in the magnitude range 4–5, 33 of the events were in the magnitude range 3–4, and the remainder were of magnitude less than 3.0. For several of the smaller events the background noise level was sufficiently high relative to the size of this initial P-wave energy at the site, that the recording system did not trigger until the arrival of the larger-amplitude signals (S, L_g ?) later in the seismogram. Thirty events were recorded at three or more stations with triggering times occurring after the initial onset of P-wave energy. Twenty events were recorded on three or more stations with at least one station triggering at the time of the initial P-wave energy. Eight of the events were recorded simultaneously at eight or more sites. Five stations recorded the largest ($M \sim 5.5$) aftershock.

For the experiments to record the aftershocks, the instruments were programmed to record the signals from three-component velocity transducers in trigger mode. The instruments were programmed to record at 200 sps/channel, with 50 Hz corners for the anti-aliasing filter, and at gains of 48–60 dB depending on level of local background noise.

Especially high levels of background noise occurred at various locations and times during the experiment due to a large amount of vehicular traffic, compressors, vibroseis, trucks, etc. required in execution of the various experiments. The levels were especially high on the NS profile north of shotpoint 4. These high levels of noise reduced the number of earthquakes that could be recorded above background noise levels and are indicative of a significant logistic difficulty that should be considered in the execution of future experiments designed to record both natural and controlled sources.

Instrumentation Performance

In regards to an evaluation of the design goals of the GEOS for use in coincident active and passive experiments, improvements pertaining to deployment procedures were recognized, but no fundamental changes in software or hardware were found to be needed for routine use of the system for these types of experiments. A minor hardware problem discovered during the first deployment and subsequently corrected was attributable to high temperatures (>115°F) encountered during mid-afternoon in the northern Nevada alluvial basins. The high temperatures, to which the units had not been before subjected, caused the DC–DC converters on three of the units to fail during the first 24 hours due to inadequate power specification for temperatures experienced. The converters have since been replaced with converters having improved temperature specifications. During the remainder of the experiment, deployment of the systems in the shade of a bush or canopy solved the problem. Placement of the systems in styrofoam cases was found on the first deployment to only prolong the cooling-down process of the units and to be unsatisfactory. The high data return for the first test of the GEOS for coincident active and passive experiments confirms the initial design goals of the system for such applications; however, the real success of such experiments is due in large part to competent coordination and execution of a vast array of complicated logistics by experienced personnel.

Aspects of the deployment procedures found to be in need of improvement included installation of battery charging capabilities in deployment vehicles. Implementation of this capability permits internal batteries of portable recorders to be charged during transport, eliminates the need for external batteries, except for long-term deployments, and permits all record parameters to be preprogrammed at the field office. Significant reductions in size and weight of GEOS carrying cases (shipping boxes) also would facilitate frequent changes in instrument locations often required in crustal imaging studies.

The GEOS architecture represents a general framework from which a variety of special-purpose data acquisition systems can be developed. Configuration of special-purpose or limited-application systems may be practical, provided resources (financial and personnel are available for development, construction and maintenance). As the GEOS was developed for application in a variety of passive and active seismic experiments, it is of interest to consider packaging changes to the GEOS that might improve its usefulness for crustal-imaging studies, but decrease applicability for other applications.

Desirable system attributes for crustal imaging are small size and ease in operation. A configuration of GEOS currently being implemented is that of extending the data buffer module to a capacity of 2 Mbytes. This extension, which is easily implemented by adding memory to the data-buffer module and changes in corresponding software modules, would allow the system to be used without the tape cartridge and corresponding controller modules. This configuration would allow reductions in size and weight of the system. Further reductions can be achieved easily by reducing the number of input channels by simply removing corresponding signal-conditioning cards. This would allow the system to be packaged in a container not exceeding 8 x 9 x 13 inches. Weight of the system would be reduced to less than 15 lbs.

Utilization of the expanded data buffer as a memory board for mass data storage offers the advantage of increasing the operating-temperature range over that imposed by the characteristics of magnetic tape. Implementation of such a board in some systems is planned to allow use of the GEOS in cold environments, such as Alaska. However, these proposed changes cannot be implemented without sacrificing beneficial attributes of the system for other applications. Elimination of tape storage capability and exclusive utilization of the memory board reduces data capacity, data accessibility, and data transportability. Decrease in the number of channels can reduce the effective dynamic range and the usefulness of the system for studies requiring two types of three-component sensors, such as aftershock studies. Use of external batteries and external CPU for operational-parameter change eliminates the self-containment attribute of the systems and implies that full capability to reprogram the systems in the field would no longer involve merely selection of menu mode via the field-data-acquisition system. Nonetheless, repeated use of a large number of units for crustal imaging experiments could justify modifying the modules to produce a subset of the GEOS for this dedicated application. Fortunately, the microcomputer, together with modular hardware components, provides a general framework from which special application systems with emphasis on particular attributes can be easily made.

THREE-COMPONENT SEISMOGRAMS RECORDED FOR CONTROLLED SOURCES DETONATED DURING THE NORTHERN NEVADA LITHOSPHERIC EXPERIMENTS

Time histories corresponding to the three components of ground velocity recorded at each location from each of the twenty-seven explosions detonated during deployments 1, 2 and 3 are shown, respectively, in Appendicies A, B, and C. Time histories corresponding to ground acceleration recorded at three shotpoints are shown at the end of Appendix A. The velocity time histories are presented in a record-section format with each section showing one of the three components of motion recorded from each explosion. The record sections show analog traces for twelve seconds of the recordings, commencing about 1 second prior to arrival of the first energy. Continuous recordings, ten minutes in duration, are available on 9-track tape as copied from the original cartridge tapes.

The velocity record sections are arranged in chronological order according to time of the explosion and deployment interval. The record sections are identified by a capital letter, a number, and a lower-case letter in parenthesis (*e.g.,* Figure A1(a)), with exact orientation for each component of motion identified in the caption. The capital letter identifies the appendix or deployment, the number corresponds to the explosion listed in Table 1 and the lower-case letters "a, b, and c" denote respectively the vertical, radial and transverse components of motion. Exact orientations of sensors were determined, using a Brunton compass as given in the figure captions. Computed source-station azimuths and distances are given in Tables 3, 4, and 5.

Two types of record sections are presented, depending on the orientation of the deployment profile with respect to the source. For those sources located approximately in-line with the source, the traces are spaced according to distance from the source (shown on left-hand side of figure). For those sources located so that deployment profile is approximately perpendicular to in-line source direction (*i.e.,* fan profiles), the traces are equally spaced with numbers on left-hand scale referring to maximum digital counts of trace. Deployment locations (see Tables 2, 3, 4 and 5) for each trace are indicated. Amplitudes of the traces are normalized to the maximum in each trace. Those traces showing maximum digital counts can be converted to units of ground velocity (cm/sec) using the conversion factor of 6×10^{-7} (cm/sec/digital cnts.).

The time axis is shown as "reduced-time," using a velocity of six km/sec. The time of detonation for each source is shown at the top of each record-section and the origin time for the time axis is shown on the right-hand side of the figure (Greenwich mean time). A low-pass filter with corner at 30 Hz has been applied, as indicated, to improve the apparent signal-to-noise ratio for some of the analog record sections.

The record sections show each of the traces recorded at the approximate detonation times for each of the sources regardless of the signal-to-noise ratios. For some of the smallest detonations (*e.g.,* Figure C10, shotpoint 4, 30 lbs.) the seismic radiation fields generated by the source are not apparent about seismic background noise. They are shown to provide a complete visual record of recorded data.

As indicated in Table 2, the controlled sources were recorded at each location during the second and third deployment intervals at the same gain level of 60 dB. Use of this gain together with the 16-bit resolution or 96 dB dynamic range of the recorder, permitted the signals from the sources at distances greater than about 3 km to be recorded on-scale without clipping near the highest resolution permitted by seismic background noise levels. Observation of the entire data set at the same gain level facilitates interpretation especially amplitude studies, while at the same time minimizing uncertainties in relative calibrations between instruments. (Use of 12-bit recorders with gain ranging would have permitted on-scale signals for those locations close to the sources for which the sensor did not clip, but would have reduced recorded signal resolution at other locations.)

Inspection of the three-component data shows that for many of the sources the energy recorded from the horizontal sensors was comparable in amplitude to that recorded on the vertical sensors. The three-component data is expected to assist in phase identification, especially converted phases, and in inferences regarding structure and composition inferrable from shear-wave energy.

Acceleration time histories, recorded at shot points 4, 11, and 8, during the first deployment, are shown in Figures A9 through A12. The recordings at shot point 4 (Figure A9) were obtained to provide a set of on-scale recordings near the source for calibration of shot size. The recordings at shot points 11 and 8 (Figures A10–12) were obtained for purposes of comparing efficiency of two types of explosive.

THREE-COMPONENT SEISMOGRAMS RECORDED FOR EARTHQUAKES THAT OCCURRED NEAR CHALFANT, CA AND A NUCLEAR EXPLOSION IN SOUTH-CENTRAL NEVADA

Time series corresponding to the three components of ground motion recorded at GEOS stations for seismic events that occurred during the passive part of the Northern Nevada Lithospheric Experiments are shown in Appendicies D and E. To better illustrate the nature of the recorded data sets, the time histories are shown at two different time scales. The time series for twenty of the better-recorded events are shown at an expanded time scale (20 seconds in length) in Appendix D. Of this number the time series for nine of the events are shown at a reduced time scale (60 seconds in length) in Appendix E. The expanded time scale is useful for examining the nature of the body wave arrivals associated with the initial part of the seismograms. The reduced time scale is useful for examining the relative amounts of surface wave and scattered energy arriving later in the seismograms for attenuation studies.

The time series are presented in record section format similar to that discussed earlier for the controlled source data (see previous chapter for details). Each section corresponds to one of the three components of motion recorded for the earthquake and nuclear explosion whose origin time is indicated in the figure caption. A listing of the fifty events recorded on three or more stations is provided in Table 6. Of this set twenty events (listed in Table 7) were considered to be in the "best recorded" category, because the events were of sufficient size relative to the background noise level at the time of occurrence of the events that the events were recorded on at least four stations with some of the stations in general recording the onset of the initial *P*-wave motion. Record sections for the initial 20 seconds of these events are shown in Appendix D. Record sections, 60 seconds in duration, are shown for nine of the events in Appendix E.

Epicenter locations, depths, magnitudes, and quality of location were determined from CAL–NET data by R. Cockerham (pers. commun., 1987) with the exception of two events whose origin times were revised on the basis of a revised model by S. Marks (pers. commun., 1987). Epicentral distances and azimuths for each of the twenty events shown in Appendix D were computed with respect to GEOS station G69 (see Table 7). The origin times for all of the events appear consistent with travel-times for earthquakes near Chalfant, CA with the exception of event 205 15:05:51. The travel-times computed for this event are based on reported origin time and location for a nuclear explosion in south-central Nevada.

Inspection of the record sections (Appendicies D and E) shows that the level of background noise at the sites influenced both the times of onset and termination of the recordings at some of the sites. With the GEOS programmed to utilize a trigger algorithm based on the computed ratio of a short-term to long-term average, the systems did not initiate recording, until the signal strength (short-term average) exceeded the background level (long-term average) by a preselected amount. By the same token the present GEOS algorithm is programmed to terminate recording once the signal strength falls below this initial level for a preselected amount of time. This algorithm has proved especially useful for recording local, regional and in some cases large teleseisms with associated variable-signal duration chosen automatically by the recording system. Although the systems could have been programmed to record for a preselected fixed amount of time, we elected to let the systems automatically select event durations based on event size relative to background noise level resulting in the shorter and variable record length apparent at some stations.

OBSERVED AND ESTIMATED TRAVEL-TIMES FOR THE PROFILE EXTENDING FROM EPICENTRAL REGION NEAR CHALFANT, CA TO REGION NEAR FALLON, NV

Eaton (1963) developed an average one-layer velocity model using data collected on an unreversed profile extending from near Fallon, Nevada to Owens Valley (~350 km). Assuming a single layer model he deduced an average thickness along the profile of about 31 km with an average *P* velocity for the upper layer of 6.02 km/sec. As an alternative, he considered a model with an intermediate layer at 19 km depth with a velocity of 6.58 km/sec and total crustal thickness of 34.5 km. Based on data from a transverse east-west profile (Fallon–Eureka), his data indicated crustal thickening along the profile to 40 km and 44.9 km, respectively, for the one- and two-layer models in the vicinity of Owens Valley. Prodehl (1979) reinterpreted these data to infer a continuous velocity gradient model from Fallon to Mono Lake. He also provided a model based on a very limited data set (8 spreads to 160 km) reversing the profile from Mono to Fallon. His interpretations indicate crustal thickening from about 31 km south of Fallon to about 41 km near Mono Lake with relatively steep velocity gradients within a few kilometers of the surface and at the base of the crust.

In an attempt to develop an average reference model, against which the earthquake data could be checked and the events could be identified, we compared observed travel-times for the initial *P* wave arrival and the onset of a prominent secondary phase with those calculated based on models of Prodehl (1979), and preliminary models derived from the controlled source data. The calculations were made assuming flat-lying layers with linear gradients as could be specified by computer program R1D (Leutgert, 1983, pers. comm.). Both the Fallon–Mono and Mono–Fallon models interpreted by Prodehl (1979) were used, but were found to predict travel-times inconsistent with those observed. By trial and error we found that maintaining the midcrustal velocities on Prodehl's Fallon–Mono profile, extending the mid-crustal gradient, extending the thickness of the crust to an average value of 38 km, and by using a *Pn* velocity of 7.9 with a gradient of 0.01 km/sec/km for upper mantle (see Figure 9a), we obtained a trial model which seemed to be relatively consistent with the observed travel-times. This model is not proposed as a final interpretation but instead as a reference model against which to identify the events and to check for obvious errors associated with origin times, instrumental timing corrections, and event locations. The model as proposed (Figure 9a) is roughly consistent with Eaton's (1963) observations.

A ray diagram (Figure 9b), synthetic seismogram section (Figure 10a) and corresponding amplitudes (Figure 10b) were computed for this model using program RAYAMP initially developed by Spence *et al.*, 1984 and adopted for the IBM PC by Crossley (1987). For the model under consideration, the ray diagram depicts paths for P_MP, the direct wave, P_n, and the diving wave (Figure 9b). The synthetics for the model suggest at distances of about 300 km the diving wave should slightly precede P_n with larger amplitude arrivals about 6 seconds later corresponding to P_MP and the direct wave. For this model with the source at a depth of about 15 km, the ray diagram suggests that the diving rays would bottom at depths between about 45–50 km for the epicentral distance range 250–300 km over which the earthquakes were observed. For the greater distances of about 370 km, corresponding to the nuclear explosion in south-central Nevada that also was recorded during the first deployment interval, the ray diagram suggests that the diving rays bottom between 55–60 km. A more accurate model based on a thickened crust beneath Chalfant would predict somewhat deeper penetration for these rays.

The observed travel-times are plotted in Figures 11–15 for each of the events listed in Table 7. Also shown in each of the figures are the theoretical travel-times computed for the events using the depth for the event (see Table 7) and the preliminary velocity model (Figure 9a). Comparison of the observed and estimated times was helpful in identifying the events and in identifying origin time and location errors.

For several of the events the average model seems to predict the observed times relatively consistently, while for others residuals as much as 1–2 seconds are apparent. We have checked all of the event recordings for possible timing errors and have found that the largest errors (not shown) were associated with either misidentification of the event location or its origin time. We expect that complications in crustal thickening to the west beneath the epicentral region and thinning to the north are accounting for some of the apparent residuals in the Chalfant travel-times. We expect that errors in identifying a consistent secondary arrival (*e.g.*, P_MP) are accounting for some of the scatter in the secondary residuals and variations in apparent velocity for the arrivals indicted. Errors in depth determinations and station residuals associated with varying thicknesses of alluvium beneath the recording stations are also possible contributory factors. Applicability of the model to the nuclear data is also in question. We think that the events presented are correctly identified with respect to origin time and location as inferred from the referenced models, however, the high level of seismicity at the magnitude 2.5–3.5 range in the Chalfant region during the experiments allowed events in the Chalfant region to be easily confused with events in surrounding regions. Consequently, detailed studies of these events should examine carefully the identifications presented for the events.

SENSOR AND RECORDING SYSTEM RESPONSE AS CALCULATED FROM SIGNALS RECORDED *IN SITU*

Calibration signals for the sensors and the recording equipment were recorded for each deployment location with recording parameters as indicated in Table 9. These signals, automatically generated by GEOS, provide a basis for accurate inference of actual ground motion as recorded at the GEOS locations. For those sites colocated with instrumentation installed by other institutions and groups, these calibration signals together with source signals are useful for inferring response differences in the various types of instrumentation. Two signals, generated automatically by GEOS, are utilized as calibration for the data recorded on the velocity transducers. Termination of a known DC voltage applied to the main coil is used as a calibration signal for the complete sensor-recording system. An impulse voltage applied at the input of the recording system is used to provide a calibration signal for the recording system independent of the sensors. Utilization of both calibration signals allows the system response for the recording system and the transducer-recording system combination to be estimated. Fourier amplitude spectra computed for each of the two types of calibration time histories as recorded at the field locations indicated in Table 9 are shown in Appendix F.

The output signal recorded as a result of the termination in DC voltage to the sensor coil is rich in low-frequency content. This input signal simulates a step-function in ground acceleration applied to the mass of the seismometer. As the derivative of this input function can be approximated by a delta function, the unit impulse response of the complete sensor-recording system to ground velocity can be estimated from the Fourier transform of the recorded time history multiplied by the square of angular frequency. Examples of the Fourier amplitude spectra computed for each deployment location are shown for each of the velocity transducer channels in the left-hand column of each figure in Appendix F. These spectra emphasize that the recorded output signal is rich in low-frequency content and is most useful for estimating the unit impulse response to ground velocity for the sensor-recording system combination up to a high-frequency limit imposed by the corner of the selected anti-aliasing filter and seismic background noise levels. Examination of the computed spectra show that high background noise levels at the times the calibration signals were recorded indicates that the computed high-frequency response is contaminated by noise and not adequate for inferring actual instrument response.

The Fourier amplitude spectra computed from the output signal generated by the impulse in voltage applied at the input of the recording system is shown for each channel in the right-hand column of each figure in Appendix F. These spectra provide an estimate for the amplitude response of the recording system to ground velocity. As the input signal and resulting output signal are especially rich in high frequencies these spectra indicate that the high-frequency response of the recording system can be estimated for frequencies greater than some low-frequency limit imposed by the relative strength of the applied impulse voltage for the selected gain setting relative to least-count instrument noise levels.

Utilization of the information contained in each of the recorded calibration signals permits a rather detailed estimate of instrumentation response to be calculated for each deployment location. Such estimates can be used to automatically correct data recorded on GEOS for instrumentation response and to scale data recorded on colocated recording instrumentation installed by other institutions. The long-period levels of the amplitude response, computed for the GEOS, are dependent on the strength of the input signal, gain setting, sampling rate, and, of course, the response characteristics of the sensor and recording system. The amplitude responses computed for the recording system (right-hand columns; Appendix F) show a dependence on sampling rate, because the impulse applied to the input of the recording system is chosen automatically by the GEOS to be one sample in duration (*e.g.*, compare Figures F1, F3, and F6 computed at 400 sps with Figures F2 and F4 computed at 200 sps). The input signal, one sample in duration, is useful for diagnosing system noise characteristics, but a more stable input signal for routine calibration is expected to be that which might be developed using a random number algorithm. Such a calibration algorithm has been implemented on the IM–6100 by Prothero (W. Prothero, pers. commun.). Time permitting, we hope also to implement this algorithm on the GEOS.

Inspection of the amplitude response curves for the recording systems (GEOS) (right-hand column of each figure; Appendix F) shows that the curves are quite consistent with minor variations in the amplification level and the fall-off characteristics for the anti-aliasing filters apparent for some of the systems. The curves computed from the input signals recorded at 200 sps are in general more stable than those computed from signals recorded at 400 sps due to the improved stability of the input signal. The lack of stability at the higher sampling rate is not indicative of the response of the recording system but instead the characteristics of the input signal as generated by the digital-to-analog converter used for calibration purposes.

Comparison of the curves computed to estimate the sensor-recording system response (left-hand column; Appendix F) shows variations for frequencies less than the natural frequency of the sensors (nominally 2 Hz). The response of the sensor used at station G–79 (sensor #302, see Table 9) suggests that the radial component of the sensor was possibly not performing properly to high frequencies. Irregularities in the response curves near the corner frequency of the anti-aliasing filters are due to the level of seismic background noise relative to that of the input signal.

The results of checking the time stamps for each block of each recording are summarized in Table 10. These timing checks are determined by a computer program developed by G. Maxwell to compare the computed time for each corresponding sample with that recorded. The computed times are determined from the selected sample rate and WWVB times and timing corrections recorded by GEOS. The program is executed to detect missing data as might be caused by dust particles on the tape or instrument malfunction. The times for which the computed time varied by more than 0.3 percent from that recorded are summarized in Table 10. These time variations are possibly significant only for the recordings of a shot or earthquake that occurred during a time interval which includes the indicated time. The computed and recorded time differences that varied by more than 0.3% are summarized in Table 10. Timing of samples subsequent to the indicated times for only the events including the tabulated times (Table 10) should be corrected by the difference between the computed and actual differences.

FORMATS FOR ARCHIVAL AND DISTRIBUTION OF DIGITAL TIME SERIES

The digital time series described herein are available in three formats. For processing and analysis of the GEOS data at the U.S. Geological Survey, we conventionally use the data in what is termed NSMDC (National Strong Motion Data Center) format (also termed "GEOS" or "DR–100" format). For analysis of the data set in conjunction with the data collected using the analog cassette recorders developed at the U.S. Geological Survey (Healy *et al.*, 1982) the data is transferred to "Refraction" format. For distribution of the data set by the IRIS Data Management Center and to facilitate its usage by other centers, we also present the data in SEG–Y format (Barry *et al.*, 1985). This chapter describes the GEOS format and presents the mapping of the GEOS header information into the SEG–Y header. For a detailed description of SEG–Y format the reader is referred to Barry *et al.*, 1985.

Data Format for GEOS Tape Cartridges

The GEOS recording unit writes data records onto a 1/4-inch digital magnetic tape cartridge conforming to ANSI specification X3.55–1977. The tape drive writes four tracks of data, one track at a time, in a "Serpentine" manner. When one track of data has been completed, the tape drive writes the subsequent track of data in the opposite direction. The tape drives used for this study write data at a density of 1600 bits per inch.

Data on a tape cartridge are organized into events. An event is organized as one or more records of data, followed by a tape file mark. Two types of events are recognized: clock events which provide time standard information, and seismic data events, including calibrations.

Each data record is composed of 512 16-bit words, or 1024 8-bit bytes. A seismic data record contains a time stamp followed by a stream of multiplexed digitized samples from all active channels. For example, a typical seismic data record for an event with channels 4, 5, and 6 active would be organized thus:

Word 1: Year (last two digits)
Word 2: Julian day of year
Word 3: Hour of day
Word 4: Minutes
Word 5: Seconds
Word 6: Milliseconds
Word 7: Channel 4 data
Word 8: Channel 5 data
Word 9: Channel 6 data
Word 10: Channel 4 data
Word 11: Channel 5 data

.

.

.

Word 508: Channel 4 data
Word 509: Channel 5 data

Word 510: Channel 6 data

The time stamp in each data record is directly associated with the first sample in the data record. Note that some words out of a data record may not be used; such free words may be used for other purposes in future versions of the GEOS software.

The first data record of an event contains a special block of data, called an event header.* When the GEOS begins writing data to the cartridge tape, it overwrites the seismic data already sampled into the first part of the first data record with the event header. The format of a GEOS event header as presently defined is given in Table 11. With this method, the time stamp which precedes the event header applies to forty-nine data samples which have been overwritten. In the data analysis procedures, this time is adjusted to correctly reflect the time of the first sample which can be used from the first data record.

National Strong Motion Data Center Format

Data recorded by GEOS currently are read and analyzed by a Digital Equipment Corporation PDP–11/70 minicomputer which runs the RSX–11M–Plus operating system. The data is demultiplexed and stored as disk-resident time series files which conform to a data format (NSMDC format) developed initially by Jon B. Fletcher and Joanne Vinton.

Data File Organization. A single GEOS seismic event is converted to one or more files under the NSMDC format. Each NSMDC format file contains digitized data from a single motion component. Therefore, a single GEOS seismic event can generate between one and six NSMDC format files.

Each NSMDC file contains header information regarding the physical and electronic aspects of the digitized data. Although this causes some redundant information to be included with each component file from one seismic event, each component may be processed separately and independently from all other components of the same event.

A file is composed of 16-bit signed integer values and 32-bit floating point values in PDP–11 floating point format. Data may be represented in either integer or floating point format, but only one format may be used in one file. GEOS data is always stored in integer format.

Each file is organized into 512-byte records. This record size was chosen because it is the blocksize of a PDP–11 or VAX disk block. Data may then be processed by using efficient read and write requests.

Each file is organized as follows:

Record	1:	Header record (integer)
Record	2:	Header record (floating point)
Record	3:	Data record #1

---

*Event header information is subject to change in future releases of the GEOS software.

Record 4: Data record #2

.

.

.

Record 2+n: Data record #n

The ability to define extra header records has been incorporated into the data format to allow for storage of additional information. If used, these header records would follow the floating point header record.

Data file naming convention. The NSMDC file format has a very rigid file naming format. The file name is generated from the following information: the time the first data sample in the file was recorded; the particular component the file represents; and the three-character station name where the GEOS recorder or motion sensor was located.

Specifically, a NSMDC file name has the following form:

JJJHHMMSC.STA

where "JJJ" is the Julian day of the year, "HH" is the hour in 24-hour format, "MM" is the minute of the hour, "S" is a letter code from A to T which represents the three-second interval of the minute, "C" is the component number, and "STA" is the 3-letter station name.

Regarding specific fields of the file name, the following conventions have been established. The time must be normalized to Coordinated Universal Time (Greenwich Mean Time). By convention, components 1 through 3 are reserved for acceleration motion, 4 through 6 are used for velocity motion, and 7 through 9 are reserved for displacement. Components 1, 4, and 7 represent the vertical component of motion or displacement; 2, 5, and 8 represent the longitude component (typically true north); 3, 6, and 9 represent the transverse component (typically true east). The exact orientation of each component is specified within the header data for each file.

File header definitions. The header offsets which are utilized for data recorded by GEOS are presented in Tables 12 and 13. Not all of these offsets are rectified immediately when data files are created; headers are usually edited in subsequent processing. Furthermore, data recorded by other instruments may not require the use of some of these offsets in the headers. The absence of data in a particular header field is indicated by the use of the "undefined value" in such fields. The "undefined value" is usually the most negative integer which can be represented with 16 bits (−32768) or the smallest reprsentable 32-bit floating point number in PDP–11 floating point format (1.7×10^{38}).

SEG–Y Header Format for NSMDC Format Files Created from GEOS Data

This section describes the mapping used to transfer NSMDC header information into SEG–Y format. The definition of the mapping is based on definitions of the byte fields for SEG–Y headers as given by Barry *et al.*, 1985. A list of the SEG–Y byte fields together with the real (R) and integer (I) locations of corresponding information in the NSMDC header (compare definitions of Barry *et al.*, 1985 with Tables 12 and 13) is presented in Table 14. For the byte fields with identification numbers less than or equal to 180, definitions given for SEG–Y and NSMDC were interpreted to be equivalent. The SEG–Y byte fields with larger identification members are used to store NSMDC header entries for which there is no equivalent SEG–Y entry. Descriptions of the entries for the various byte fields, as given in Table 14, are presented in the context of the NSMDC format.

The magnetic tapes (nine-track; 1/2 inch) containing the digital data reported herein and submitted to the IRIS data management center are written at 1600 or 6250 bpi with header entries as identified in Table 14. Each tape contains a reel-identification header with information describing the tape and its contents. Part one of this header contains alphanumeric text in a EBCDIC card image block; part two contains additional information for various byte fields as identified in Table 14 in a binary coded block. Each digital time series presented on the tape is preceded by a trace-identification header as described in Table 14.

A difficulty encountered in presenting the GEOS data in SEG–Y format was the requirement for the digital time series to be written into a single block. Several of the earthquake recordings sampled with high resolution (400 sps) contained more digital samples than that of maximum block sizes (32,767 bytes; VAX 11/785) easily interpretable by standard computer systems. As IRIS-standard software had not been developed at this writing (J. Scheimer, oral commun.); we partially circumvented this difficulty by selecting block size of 32,256 for digital time series and 240-byte header as an upper limit to write to tape. This block size accommodates 81.24 seconds of the digital time series at 200 sps. For those events recorded at 400 samples per second the time series were filtered for anti-aliasing with a 2-pole filter applied twice to yield zero phase-shift. These traces were decimated to a standard sampling rate of 200 samples per second. Unfortunately, the sixty-second interval is not sufficient to present the recordings of some of the larger earthquakes in their entirety. Until a standard is adopted, access to the entire recording requires that the user use the tapes written in NSMDC format.

ACKNOWLEDGMENTS

The data set reported for this experiment represents the combined efforts of several institutions and individuals as indicated in part by the distributed authorship of the various sections. In particular, acknowledgment is due: 1) the principal investigators

Drs. W. Mooney, K. Priestly, R. Smith, and G. Thompson for inspiration, initiation, and coordination of the experiment, 2) graduate students at Stanford R. Catchings, and associates for major contributions in site location, surveying, and logistics coordination, and S. Larkin for his assistance in the field and the office in playing back data sets, 3) J. Van Schaack, and E. Criley, (USGS) for their guidance in preparation and detonation of shotpoints on schedule in the midst of a vast number of potentially complicating logistics, 4) members of the USGS who contributed to the development of the GEOS recording system, in addition to those listed in chapter 4, G. Jensen, J. Van Schaack, J. Fletcher, R. McClearn, 5) members of the USGS who contributed to the development of the software that facilitated the processing and analysis of the data set presented herein, in particular, G. Maxwell, E. Cranswick, and C. Mueller, with assistance in utilization of the software by L. Wennerberg, 6) L. Baker, G. Maxwell, J. Fletcher, and H. Bundock (USGS) for implementation and operation of the National Strong Motion Data Center, whose resources were utilized to process the data, 7) W. Kohler, who developed software for conversion of GEOS data format to cassette refraction format and SEG–Y format for distribution, 8) J. Luetgert and D. Crossley for their versions of programs R1D and RAYAMP, respectively, that were a pleasure to execute on an IBM PC, 9) students at University of Utah and in particular V. Heilweil, who assisted in the playback and initial processing of the data set, 10) C. Sullivan for her most helpful talents with TeX in converting a handwritten draft into discernible text.

REFERENCES CITED

Atwater, T., 1970, Implications of plate tectonics for the Cenozoic tectonic evolution of Western North America, *Geol. Soc. of America Bull.*, **81**, 3513–3536.

Barry, K. M., D. A. Cavers, and C. W. Kneale, 1975, Recommended standards for digital tape formats: *Geophysics*, **40**, 344–352.

Becker, F. L., and R. L. Richardson, 1969, Critical angle reflectivity, *J. Acous. Soc. Am.*, **45**, 793–794.

Becker, F. L., and R. L. Richardson, 1972, Influence of material properties on Rayleigh critical-angle reflectivity, *J. Acous. Soc. Am.*, **51**, 1609–1617.

Borcherdt, R. D., and L. Wennerberg, 1985, General *P*, type–I *S*, and type–II *S* waves in anelastic solids: Inhomogeneous wave fields in low-loss solids, *Bull. Seismol. Soc. Am.,* **75**, 1729–1763.

Borcherdt, R. D., Fletcher, J. B., Jensen, E. G., Maxwell, G. L., Van Schaack, J. R., Warrick, R. E., Cranswick, E., Johnston, J. J. S., and McClearn, R., A general earthquake observation system (GEOS), *Bull. Seismol. Soc. Am.,* **75**, 1783–1823.

Borcherdt, R. D., Glassmoyer, G., and Wennerberg, L., 1986, Influence of welded boundaries in anelastic media on energy flow and characteristics of *P*, *S*–I and *S*–II waves: Observational evidence for inhomogeneous body waves in low-loss solids, *J. Geophys. Res.,* **91**, 11,503–11,518.

Cook, K. C., 1969, Active rift system in the Basin and Range province: *Tectonophysics*, **8**, 469–511.

Crossley, D., 1987, RAYAMP–PC for IBM–PC and compatible microcomputers, Version 2.0, Jan. 1987, McGill University, Montreal, Canada.

Dickinson, W. R., and Snyder, W. S., 1979, Geometry of subducted slabs related to San Andreas transform, *Jour. of Geology*, **87**, 609–627.

Eaton, Jerry P., 1963, Crustal structure from San Francisco, California, to Eureka, Nevada, from seismic refraction measurements, *J. Geophys. Res.,* **68**, 5789–5806.

Gans, P. B., Miller, E. L., McCarthy, J., and Ouldcott, M. L., 1985, Tertiary extensional faulting and evolving ductile-brittle transition zones in the northern Snake Range and vicinity: New insights from seismic data, *Geology*, **13**, 189–193.

Hamilton, W., and Myers, W. B., 1966, Cenozoic tectonics of the western United States, *Rev. Geophysics*, **4**, 509–549.

Healy, J. H., Mooney, W. D., Blank, H. R., Gettings, M. E., Kohler, W. M., Lamson, R., and Leone, L. E., 1982, Saudi Arabian seismic deep-refraction profile: Final Project Report, *U.S. Geological Survey Saudi Arabian Mission Open-File Report* **02–37**, 429 p.

Menard, H. W., 1964, The East Pacific Rise, *Science*, **132**, 1737.

Prodehl, Claus, 1979, Crustal structure of the Western United States, *Geological Survey Professional Paper*, **1034**.

Sibson, R. H., 1982, Fault zone models, heat flow, and the depth distribution of earthquakes in the continental crust of the United Staes, *Bull. Seismol. Soc. Am.,* **72**, 151–163.

Smith, Robert B., 1978, Seismicity, crustal structure, and intraplate tectonics of the interior of the western Cordillera, *in Cenozoic Tectonics and Regional Geophysics of the Western Cordillera*, GSA Memoir, vol. 152, Smith R. B., and Eaton, G. P., eds., p. 111–144.

Spence, G. D., Whittall, K. P., and Clowes, R. R., 1984, Practical synthetic seismograms for laterally varying media calculated by asymptotic ray theory, *Bull. Seismol. Soc. Am.,* **74**, 1209–1223.

Thompson, George A., Smith, Robert B., Priestly, Keith F., and Mooney, Walter D., 1986, Proposal for phase I of a two-phase seismic investigation of the lithosphere in the northern Basin and Range Province, *submitted Nat'l. Science Foundation.*

Wernicke, B., 1981, Low angle normal faults in the Basin and Range province: Nappe tectonics in an extending orogen, *Nature*, **291**, 645.

Table 1: Master Shot List—Identification number, time, size and location parameters for chemical explosions detonated during Northern Nevada Lithospheric Experiments—PASSCAL.

Shot Number	Shot Point	Date Shot Time	Latitude Longitude	Elev (ft.)	Size (lbs.)
1	8	JUL 22, 1986 204 5 0 0.016	41 1.1660 117 43.0850	4300	3000
2	10	JUL 22, 1986 204 5 4 0.009	39 43.3254 118 17.6982	3950	2000
3	11	JUL 22, 1986 204 5 6 0.010	39 21.6223 118 32.8789	3930	3000
4	1	JUL 22, 1986 204 5 8 0.008	40 34.9624 119 27.5166	3900	3000
5	9	JUL 23, 1986 204 7 0 0.008	40 27.9109 117 51.7158	4920	2000
6	8	JUL 23, 1986 204 7 2 0.011	41 1.1660 117 43.0850	6860	3000
7	11	JUL 23, 1986 204 7 5 56.986	39 21.6223 118 32.8789	3930	2200
8	4	JUL 23, 1986 204 7 8 0.009	40 5.7737 117 59.4604	4120	2000
9	4	JUL 25, 1986 207 5 0 0.010	40 5.7737 117 59.4604	4120	3000
10	5	JUL 25, 1986 207 5 2 0.009	39 52.5652 117 31.8740	4550	4000
11	1	JUL 25, 1986 207 5 4 0.130	40 34.9624 119 27.5166	3900	3000
12	3	JUL 25, 1986 207 5 6 5.848	40 15.5601 118 28.4468	4300	2000
13	7	JUL 25, 1986 204 5 8 0.012	39 28.2034 116 32.5405	6340	6000
14	12	JUL 26, 1986 207 7 0 0.008	40 6.8945 118 6.2925	4130	600
15	8	JUL 26, 1986 207 7 6 0.096	41 1.1660 117 43.0850	4300	2000
16	13	JUL 26, 1986 207 9 0 0.010	40 8.8538 118 9.7485	4800	500
17	2	JUL 26, 1986 207 9 4 0.320	40 24.5386 118 54.6162	4160	2000

(Continued)

Table 1: Master Shot List—Identification number, time, size and location parameters for chemical explosions detonated during Northern Nevada Lithospheric Experiments—PASSCAL (Continued).

Shot Number	Shot Point	Date Shot Time	Latitude Longitude	Elev (ft.)	Size (lbs.)
18	7	JUL 29, 1986 211 5 0 0.008	39 28.2034 116 32.5405	6340	3000
19	8	JUL 29, 1986 211 5 2 0.012	41 1.1660 117 43.0850	4300	1500
20	14	JUL 29, 1986 211 5 4 0.012	40 2.4404 117 46.5786	3500	500
21	1	JUL 29, 1986 211 5 6 0.012	40 34.9624 119 27.5166	3900	6000
22	15	JUL 29, 1986 211 5 8 0.011	39 56.2168 117 41.2944	3760	500
23	4	JUL 30, 1986 211 7 0 0.008	40 5.7737 117 59.4604	4120	3000
24	3	JUL 30, 1986 211 7 2 0.012	40 15.5601 118 28.4468	4020	4000
25	6	JUL 30, 1986 211 7 6 0.008	39 36.4834 116 54.4380	6860	1000
26	5	JUL 30, 1986 211 7 8 0.009	39 52.5652 117 31.8740	4550	2000
27	4	JUL 30, 1986 211 9 4 0.012	40 5.7737 117 59.4604	4120	30

Table 2: Station identifications, station locations and instrument parameters used to record the controlled sources for each of the three deployment intervals used for the Northern Nevada Lithospheric Experiments.

	STATION	LATITUDE	LONGITUDE	UNIT	SAMPLE RATE/ CHANNEL (SPS)	SENSOR-L22		ANTI-ALIAS FILTER CORNER FREQ. (HZ)	COMMENTS
						NO.	GAIN		
FIRST DEPLOYMENT	G64	40 08.29	117 56.70	7	400	191	54	100	
	G65	40 07.6	117 57.49	9	400	305	54	100	
	G66	40 06.93	117 58.25	5	400	186	54	100	
	G67	40 06.29	117 59.00	33	400	197	54	100	L-22 NO. UNCERTAIN
	G68	40 05.82	117 59.35	15	200	198	54	50	FBA NO. 38; 6DB, 50HZ
	G69	40 05.05	118 00.31	36	400	304	54	100	
	G70	40 04.21	118 00.64	21	400	307	54	100	
	G71	40 03.71	118 01.66	17	400	162	54	100	
	G72	40 02.96	118 02.48	4	400	183	54	100	
	G73	40 02.02	118 02.80	8	400	184	54	100	
	G75	40 00.95	118 03.97	24	400	303	54	100	
	G77	39 59.79	118 05.35	10	400	200	54	100	
	G79	39 58.58	118 07.83	39	400	302	54	100	
	G81	39 56.67	118 08.74	12	400	160	54	100	
	G85	39 53.66	118 13.38	16	400	201	54	100	L-22 NO. UNCERTAIN
	G87	39 52.15	118 13.95	29	400	306	54	100	
	G89	39 50.63	118 14.37	22	400	308	54	100	
	G91	39 49.09	118 14.56	38	400	309	54	100	
	G93	39 47.63	118 15.13	34	400	311	54	100	
SECOND DEPLOYMENT	G59	40 11.69	117 53.0	5	400	186	60	100	
	G61	40 10.32	117 54.47	38	400	183	60	100	L-22 NO. UNCERTAIN
	G63	40 08.99	117 55.94	7	400	191	60	100	
	G65	40 07.6	117 57.49	22	400	305	60	100	
	G67	40 06.29	117 59.00	33	400	198	60	100	
	G69	40 05.05	118 00.31	4	400	307	60	100	
	G71	40 03.71	118 01.66	17	400	162	60	100	
	G73	40 02.02	118 02.80	8	400	184	60	100	
	G75	40 00.95	118 03.97	24	400	303	60	100	
	G77	39 59.79	118 05.35	10	400	200	60	100	
	G79	39 58.58	118 07.83	39	400	302	60	100	
	G81	39 56.67	118 08.74	12	400	160	60	100	
	G83	39 54.91	118 10.13	27	400	310	60	100	
	G85	39 53.66	118 13.38	16	400	201	60	100	L-22 NO. UNCERTAIN
	G87	39 52.15	118 13.95	29	400	306	60	100	
	G89	39 50.63	118 14.37	15	400	308	60	100	
	G91	39 49.09	118 14.56	34	400	309	60	100	
	G93	39 47.63	118 15.13	31	400	311	60	100	
	G95	39 46.14	118 15.94	35	400	187	60	100	L-22 NO. UNCERTAIN
THIRD DEPLOYMENT	G34	40 07.44	118 07.36	4	200	303	60	50	
	G37	40 06.78	118 05.82	21	200	304	60	50	
	G40	40 06.48	118 03.93	10	200	161	60	50	
	443	40 06.19	118 02.12	24	200	307	60	50	
	446	40 05.90	118 00.31	12	200	302	60	50	
	402	40 05.41	117 58.29	36	200	310	60	50	
	405	40 05.25	117 55.21	27	200	160	60	50	
	408	40 04.73	117 52.55	22	200	184	60	50	
	411	40 04.44	117 50.13	17	200	200	60	50	
	414	40 04.55	117 47.96	15	200	306	60	50	
	417	40 02.83	117 47.19	7	200	191	60	50	L-22 NO. UNCERTAIN
	420	40 01.56	117 45.86	34	200	198	60	50	L-22 NO. UNCERTAIN
	423	40 00.41	117 44.73	31	200	159	60	50	
	426	39 58.75	117 43.19	33	200	311	60	50	
	428	39 57.32	117 42.56	35	200	305	60	50	
	431	39 56.15	117 40.81	38	200	187	60	50	
	434	39 55.67	117 39.10	16	200	186	60	50	
	437	39 55.04	117 37.55	9	200	201	60	50	
	440	39 54.25	117 35.80	29	200	183	60	50	

Table 3: Source-station azimuths and distances for each shotpoint detonated during the first deployment interval of the Northern Nevada Lithospheric Experiments.

SHOT NUMBER 1   SHOT POINT 8

Time=22-JUL-86(204) 05:00:00.02 Lat=41.020N Long=117.718W

Station	Radial Azimuth	Epi-Dist(km)
G64	191	99.84
G65	191	101.27
G66	192	102.76
G67	192	104.14
G68	193	105.24
G69	193	106.79
G70	193	108.41
G71	194	109.65
G72	194	111.28
G73	194	113.08
G75	195	115.41
G77	195	117.99
G79	197	121.12
G81	197	124.88
G85	199	132.20
G87	199	135.11
G89	198	137.97
G91	198	140.76
G93	198	143.58

SHOT NUMBER 2   SHOT POINT 10

Time=22-JUL-86(204) 05:04:00.01 Lat=39.722N Long=118.295W

Station	Radial Azimuth	Epi-Dist(km)
G64	33	55.08
G65	33	53.41
G66	32	51.74
G67	32	50.17
G68	32	48.96
G69	32	47.24
G70	32	45.67
G71	31	44.12
G72	31	42.33
G73	32	40.60
G75	31	38.05
G77	30	35.20
G79	26	31.56
G81	27	27.82
G85	18	20.11
G87	18	17.19
G89	19	14.34
G91	23	11.57
G93	25	8.77

SHOT NUMBER 3   SHOT POINT 11

Time=22-JUL-86(204) 05:06:00.01 Lat=39.360N Long=118.548W

Station	Radial Azimuth	Epi-Dist(km)
G64	31	100.71
G65	31	99.06
G66	31	97.39
G67	30	95.83
G68	30	94.63
G69	30	92.92
G70	30	91.33
G71	30	89.80
G72	30	88.02
G73	30	86.28
G75	30	83.74
G77	29	80.90
G79	28	77.25
G81	28	73.52
G85	25	65.58
G87	26	62.70
G89	26	59.91
G91	27	57.24
G93	28	54.46

SHOT NUMBER 4   SHOT POINT 1

Time=22-JUL-86(204) 05:08:00.01 Lat=40.583N Long=119.459W

Station	Radial Azimuth	Epi-Dist(km)
G64	112	137.49
G65	112	136.85
G66	113	136.36
G67	113	135.85
G68	114	135.56
G69	115	135.10
G70	115	135.32
G71	116	134.42
G72	117	134.00
G73	117	134.39
G75	119	133.85
G77	120	133.19
G79	121	131.29
G81	123	132.08
G85	127	129.84
G87	128	130.88
G89	129	132.15
G91	130	133.75
G93	131	134.89

SHOT NUMBER 5   SHOT POINT 9

Time=23-JUL-86(204) 07:00:00.01 Lat=40.465N Long=117.862W

Station	Radial Azimuth	Epi-Dist(km)
G64	191	37.02
G65	192	38.46
G66	193	39.96
G67	194	41.37
G68	195	42.49
G69	196	44.07
G70	196	45.70
G71	197	47.00
G72	198	48.68
G73	198	50.47
G75	199	52.88
G77	200	55.56
G79	203	58.94
G81	203	62.70
G85	206	70.49
G87	205	73.37
G89	205	76.17
G91	204	78.88
G93	204	81.68

SHOT NUMBER 6   SHOT POINT 8

Time=23-JUL-86(204) 07:02:00.01 Lat=41.020N Long=117.718W

Station	Radial Azimuth	Epi-Dist(km)
G64	191	99.84
G65	191	101.27
G66	192	102.76
G67	192	104.14
G68	193	105.24
G69	193	106.79
G70	193	108.41
G71	194	109.65
G72	194	111.28
G73	194	113.08
G75	195	115.41
G77	195	117.99
G79	197	121.12
G81	197	124.88
G85	199	132.20
G87	199	135.11
G89	198	137.97
G91	198	140.76
G93	198	143.58

SHOT NUMBER 7   SHOT POINT 11

Time=23-JUL-86(204) 07:05:56.99 Lat=39.360N Long=118.548W

Station	Radial Azimuth	Epi-Dist(km)
G64	31	100.71
G65	31	99.06
G66	31	97.39
G67	30	95.83
G68	30	94.63
G69	30	92.92
G70	30	91.33
G71	30	89.80
G72	30	88.02
G73	30	86.28
G75	30	83.74
G77	29	80.90
G79	28	77.25
G81	28	73.52
G85	25	65.58
G87	26	62.70
G89	26	59.91
G91	27	57.24
G93	28	54.46

SHOT NUMBER 8   SHOT POINT 4

Time=23-JUL-86(204) 07:08:00.01 Lat=40.096N Long=117.991W

Station	Radial Azimuth	Epi-Dist(km)
G64	40	6.13
G65	39	4.44
G66	39	2.75
G67	34	1.16
G68	270	0.09
G69	222	1.79
G70	210	3.34
G71	219	4.93
G72	219	6.74
G73	214	8.41
G75	216	10.99
G77	217	13.88
G79	222	17.85
G81	218	21.40
G85	221	29.90
G87	219	32.56
G89	217	35.15
G91	215	37.62
G93	213	40.32

Table 4: Source-station azimuths and distances for each shotpoint detonated during the second deployment interval of the Northern Nevada Lithospheric Experiments.

SHOT NUMBER 9 SHOT POINT 4

Time=25-JUL-86(207) 05:00:00.01 Lat=40.096N Long=117.991W

Station	Radial Azimuth	Epi-Dist(km)
G59	40	14.23
G61	40	11.00
G63	40	7.78
G65	39	4.44
G67	34	1.16
G69	222	1.79
G71	219	4.93
G73	214	8.41
G75	216	10.99
G77	217	13.88
G79	222	17.85
G81	218	21.40
G83	217	25.23
G85	221	29.90
G87	219	32.56
G89	217	35.15
G91	215	37.62
G93	213	40.32
G95	213	43.26

SHOT NUMBER 10 SHOT POINT 5

Time=25-JUL-86(207) 05:02:00.01 Lat=39.876N Long=117.531W

Station	Radial Azimuth	Epi-Dist(km)
G59	320	46.47
G61	316	45.94
G63	312	45.75
G65	307	45.84
G67	303	46.15
G69	300	46.53
G71	296	47.08
G73	292	47.30
G75	289	48.18
G77	286	49.42
G79	282	52.30
G81	278	52.96
G83	274	54.61
G85	272	59.06
G87	269	59.85
G89	266	60.56
G91	264	61.08
G93	261	62.24
G95	259	63.85

SHOT NUMBER 11 SHOT POINT 1

Time=25-JUL-86(207) 05:04:00.13 Lat=40.583N Long=119.459W

Station	Radial Azimuth	Epi-Dist(km)
G59	108	140.13
G61	110	139.07
G63	111	137.97
G65	112	136.85
G67	113	135.85
G69	115	135.10
G71	116	134.42
G73	117	134.39
G75	119	133.85
G77	120	133.19
G79	121	131.29
G81	123	132.08
G83	125	132.22
G85	127	129.84
G87	128	130.88
G89	129	132.15
G91	130	133.75
G93	131	134.89
G95	132	135.86

SHOT NUMBER 12 SHOT POINT 3

Time=25-JUL-86(207) 05:06:05.85 Lat=40.259N Long=118.474W

Station	Radial Azimuth	Epi-Dist(km)
G59	98	50.58
G61	102	49.06
G63	105	47.60
G65	109	46.22
G67	113	45.10
G69	116	44.37
G71	120	43.84
G73	125	44.16
G75	128	44.00
G77	132	43.88
G79	137	42.94
G81	142	44.79
G83	146	46.24
G85	152	45.87
G87	155	48.01
G89	157	50.33
G91	158	52.86
G93	160	55.10
G95	162	57.34

SHOT NUMBER 13 SHOT POINT 7

Time=25-JUL-86(207) 05:08:00.01 Lat=39.470N Long=116.542W

Station	Radial Azimuth	Epi-Dist(km)
G59	305	140.09
G61	303	140.32
G63	302	140.74
G65	301	141.31
G67	299	141.92
G69	298	142.43
G71	297	142.99
G73	296	143.05
G75	294	143.72
G77	293	144.64
G79	292	147.02
G81	291	146.94
G83	289	147.73
G85	288	151.36
G87	287	151.31
G89	285	151.11
G91	284	150.64
G93	283	150.78
G95	282	151.30

SHOT NUMBER 14 SHOT POINT 12

Time=26-JUL-86(207) 07:00:00.01 Lat=40.115N Long=118.105W

Station	Radial Azimuth	Epi-Dist(km)
G59	65	20.74
G61	69	17.91
G63	75	15.17
G65	84	12.55
G67	96	10.39
G69	112	9.15
G71	132	8.82
G73	151	10.29
G75	163	11.49
G77	174	13.22
G79	188	15.55
G81	190	19.26
G83	194	22.89
G85	202	26.50
G87	202	29.40
G89	201	32.24
G91	200	35.02
G93	199	37.84
G95	200	40.82

SHOT NUMBER 15 SHOT POINT 8

Time=26-JUL-86(207) 07:06:00.10 Lat=41.020N Long=117.718W

Station	Radial Azimuth	Epi-Dist(km)
G59	189	92.76
G61	190	95.58
G63	191	98.37
G65	191	101.27
G67	192	104.14
G69	193	106.79
G71	194	109.65
G73	194	113.08
G75	195	115.41
G77	195	117.99
G79	197	121.12
G81	197	124.88
G83	197	128.60
G85	199	132.20
G87	199	135.11
G89	198	137.97
G91	198	140.76
G93	198	143.58
G95	198	146.57

SHOT NUMBER 16 SHOT POINT 13

Time=26-JUL-86(207) 09:00:00.01 Lat=40.147N Long=118.162W

Station	Radial Azimuth	Epi-Dist(km)
G59	78	24.21
G61	83	21.81
G63	89	19.56
G65	97	17.52
G67	107	15.95
G69	118	15.13
G71	130	14.91
G73	142	16.04
G75	151	16.78
G77	160	17.91
G79	172	19.23
G81	176	22.62
G83	181	25.86
G85	190	28.62
G87	191	31.52
G89	191	34.40
G91	191	37.25
G93	191	40.06
G95	192	42.99

SHOT NUMBER 17 SHOT POINT 2

Time=26-JUL-86(207) 09:04:00.32 Lat=40.409N Long=118.910W

Station	Radial Azimuth	Epi-Dist(km)
G59	106	90.20
G61	108	89.01
G63	109	87.82
G65	112	86.65
G67	114	85.62
G69	115	84.90
G71	118	84.28
G73	120	84.37
G75	122	83.96
G77	124	83.47
G79	126	81.86
G81	129	82.99
G83	131	83.56
G85	135	81.77
G87	136	83.20
G89	138	84.86
G91	139	86.83
G93	141	88.39
G95	143	89.84

Table 5: Source-station azimuths and distances for each shotpoint detonated during the third deployment interval of the Northern Nevada Lithospheric Experiments.

SHOT NUMBER 18 SHOT POINT 7

Time=29-JUL-86(211) 05:00:00.01 Lat=39.470N Long=116.542W

Station	Radial Azimuth	Epi-Dist(km)
G34	298	153.34
G37	298	150.84
G40	298	148.21
443	298	145.70
446	299	143.19
402	299	140.24
405	300	136.29
408	300	132.55
411	301	129.32
414	302	126.79
417	301	124.11
420	300	121.55
423	300	118.93
426	299	115.52
428	298	113.47
431	298	110.26
434	298	107.69
437	298	105.20
440	298	102.32

SHOT NUMBER 19 SHOT POINT 8

Time=29-JUL-86(211) 05:02:00.01 Lat=41.020N Long=117.718W

Station	Radial Azimuth	Epi-Dist(km)
G34	199	105.27
G37	197	105.75
G40	196	105.51
443	195	105.35
446	193	105.25
402	192	105.53
405	189	105.02
408	187	105.44
411	185	105.60
414	184	105.15
417	183	108.28
420	182	110.54
423	181	112.62
426	180	115.67
428	180	118.33
431	178	120.54
434	177	121.51
437	176	122.80
440	175	124.44

SHOT NUMBER 20 SHOT POINT 14

Time=29-JUL-86(211) 05:04:00.01 Lat=40.041N Long=117.776W

Station	Radial Azimuth	Epi-Dist(km)
G34	287	30.89
G37	286	28.44
G40	287	25.72
443	287	23.11
446	288	20.50
402	288	17.50
405	293	13.30
408	297	9.47
411	306	6.25
414	333	4.37
417	313	1.04
420	153	1.83
423	145	4.59
426	145	8.36
428	149	11.07
431	145	14.25
434	140	16.44
437	137	18.77
440	135	21.56

SHOT NUMBER 21 SHOT POINT 1

Time=29-JUL-86(211) 05:06:00.01 Lat=40.583N Long=119.459W

Station	Radial Azimuth	Epi-Dist(km)
G34	115	124.16
G37	115	126.65
G40	115	129.32
443	114	131.88
446	114	134.44
402	114	137.42
405	113	141.54
408	113	145.39
411	113	148.76
414	112	151.52
417	113	153.86
420	114	156.27
423	114	158.77
426	115	162.04
428	116	163.98
431	116	167.17
434	116	169.74
437	116	172.23
440	116	175.11

SHOT NUMBER 22 SHOT POINT 15

Time=29-JUL-86(211) 05:08:00.01 Lat=39.937N Long=117.688W

Station	Radial Azimuth	Epi-Dist(km)
G34	299	42.44
G37	299	39.93
G40	300	37.33
443	302	34.86
446	304	32.41
402	305	29.53
405	310	25.89
408	315	22.45
411	320	19.74
414	328	18.11
417	326	14.77
420	326	11.94
423	328	9.17
426	330	5.41
428	318	2.72
431	101	0.69
434	108	3.27
437	112	5.75
440	115	8.61

SHOT NUMBER 23 SHOT POINT 4

Time=30-JUL-86(211) 07:00:00.01 Lat=40.096N Long=117.991W

Station	Radial Azimuth	Epi-Dist(km)
G34	285	11.62
G37	282	9.21
G40	282	6.47
443	282	3.85
446	281	1.23
402	112	1.79
405	99	6.10
408	101	9.98
411	101	13.46
414	98	16.46
417	107	18.33
420	112	20.64
423	116	23.14
426	119	26.50
428	123	28.64
431	124	31.91
434	123	34.43
437	123	36.91
440	123	39.80

SHOT NUMBER 24 SHOT POINT 3

Time=30-JUL-86(211) 07:02:00.01 Lat=40.259N Long=118.474W

Station	Radial Azimuth	Epi-Dist(km)
G34	117	33.43
G37	117	35.93
G40	116	38.58
443	115	41.12
446	114	43.68
402	114	46.66
405	112	50.80
408	112	54.66
411	111	58.05
414	110	60.86
417	112	63.12
420	114	65.51
423	115	68.01
426	116	71.30
428	118	73.30
431	118	76.51
434	118	79.08
437	118	81.57
440	118	84.45

SHOT NUMBER 25 SHOT POINT 6

Time=30-JUL-86(211) 07:06:00.01 Lat=39.608N Long=116.907W

Station	Radial Azimuth	Epi-Dist(km)
G34	299	118.53
G37	299	116.03
G40	299	113.41
443	299	110.91
446	300	108.41
402	300	105.48
405	301	101.58
408	302	97.86
411	303	94.68
414	304	92.22
417	303	89.46
420	302	86.86
423	302	84.21
426	300	80.76
428	299	78.66
431	299	75.44
434	299	72.88
437	299	70.39
440	299	67.50

SHOT NUMBER 26 SHOT POINT 5

Time=30-JUL-86(211) 07:08:00.01 Lat=39.876N Long=117.531W

Station	Radial Azimuth	Epi-Dist(km)
G34	298	57.43
G37	298	54.92
G40	299	52.31
443	300	49.82
446	301	47.34
402	302	44.42
405	305	40.63
408	307	37.02
411	310	34.00
414	314	31.86
417	311	28.81
420	310	26.08
423	308	23.34
426	305	19.75
428	300	17.56
431	298	14.34
434	299	11.77
437	300	9.28
440	299	6.40

Table 5(continued): Source-station azimuths and distances for each shotpoint detonated during the third deployment interval of the Northern Nevada Lithospheric Experiments.

SHOT NUMBER 27   SHOT POINT 4

Time=30-JUL-86(211) 09:04:00.01 Lat=40.096N Long=117.991W

Station	Radial Azimuth	Epi-Dist (km)
C34	285	11.62
C37	282	9.21
C40	282	6.47
443	282	3.85
446	281	1.23
402	112	1.79
405	99	6.10
408	101	9.98
411	101	13.46
414	98	16.46
417	107	18.33
420	112	20.64
423	116	23.14
426	119	26.50
428	123	28.64
431	124	31.91
434	123	34.43
437	123	36.91
440	123	39.80

Table 6: Origin time, location, depth, and size for earthquakes near Chalfant, CA, recorded at three or more GEOS stations. (see text)

CHALFANT EARTHQUAKES RECORDED AT THREE OR MORE GEOS STATIONS

TIME (GMT)	LAT. (degrees)	LONG.	DEP. (km)	MAG.	RATING
202 20:36:04.54	37-31.69	118-26.42	11.0	3.7	BR|AC
202 21:08:41.21	37-35.09	118-27.36	8.3	3.4	CR|AD
202 21:51:44.35	37-36.12	118-25.79	5.2	3.2	BR|AB
*202 22:07:16.70	37-29.40	118-25.74	19.5	5.5?	-D-
202 22:39:17.94	37-36.67	118-34.48	0.1	2.7	DR|DC
202 23:43:05.93	37-35.83	118-28.14	9.4	3.2	BR|BA
(203 00:09:53.21	37-36.70	118-25.64	3.8	3.5	DR|DD)
203 00:09:53.23	37-36.53	118-25.77	4.8	-?-	BC|AB
203 02:21:31.02	37-36.06	118-28.77	8.7	3.0	BR|BA
203 03:02:10.26	37-35.04	118-28.40	8.3	3.5	BR|BA
203 03:17:41.84	37-36.82	118-29.61	8.7	2.8	DR|DC
203 03:18:47.63	37-31.89	118-26.12	10.1	3.2	CR|AD
203 03:47:09.53	37-33.32	118-26.53	11.2	2.9	AR|AA
203 03:51:04.16	37-28.27	118-22.25	11.7	3.0	CR|BD
203 04:11:34.53	37-34.81	118-28.00	8.8	2.8	AR|AA
203 04:22:46.99	37-34.33	118-29.17	12.8	2.8	CR|AD
203 05:05:20.68	37-35.59	118-25.49	5.6	3.2	BR|BB
(203 05:24:04.76	37-33.06	118-18.11	0.8	3.2	DR|DD)
203 05:24:07.42	37-33.22	118-25.12	6.9	?	BC|AB
203 05:40:43.79	37-32.21	118-28.61	0.9	3.5	CR|DB
203 06:21:52.32	37-27.00	118-23.10	13.3	3.7	AR|AA
203 06:33:38.68	37-32.00	118-25.96	12.0	3.2	BR|CA
203 06:43:26.43	37-32.00	118-26.03	12.6	2.9	AR|AA
(203 06:57:59.89	37-29.26	118-21.88	6.1	3.6	CR|AD)
203 06:58:10.64	37-36.65	118-28.13	9.2	?	AC|AA
203 07:55:28.78	37-35.59	118-27.04	8.9	2.6	CR|AD
203 08:29:15.22	37-31.99	118-24.86	4.2	3.4	CR|BC
203 09:34:15.65	37-27.21	118-22.60	10.0	3.3	AR|AA
203 12:15:47.03	37-36.57	118-28.08	10.6	2.9	BR|CA
203 12:24:49.57	37-31.60	118-28.36	11.8	3.9	BR|BA
203 13:33:59.35	37-32.03	118-28.36	11.3	3.7	BR|BA
(203 13:48:44.21	37-26.29	118-24.40	11.3	4.0	DR|DD)
(203 13:48:46.29	37-34.59	118-33.19	9.6	4.1	DR|DC)
203 13:48:59.21	37-31.82	118-28.47	11.5	-?-	AC|AA
203 13:57:34.23	37-31.83	118-28.46	12.6	3.2	CR|AD
203 17:12:00.55	37-30.22	118-28.35	5.3	3.2	BR|AB
203 17:17:20.92	37-30.94	118-25.94	11.4	3.6	CR|AD
*203 18:29:43.13	37-29.58	118-22.98	8.7	4.1	-C-
205 01:17:09.22	37-34.61	118-28.39	9.8	3.2	AR|AA
205 02:43:10.35	37-36.16	118-28.06	4.0	3.5	BR|AB
205 06:10:04.67	37-27.71	118-21.50	9.3	3.5	CR|AD
205 09:22:30.19	37-33.99	118-25.57	6.1	3.0	DR|DD
205 11:34:50.82	37-32.73	118-25.79	13.3	3.1	BR|AB
205 14:58:44.34	37-29.35	118-22.60	8.6	3.3	CR|AD
n205 15:05:00.09	37-08.56	116-04.27	0.4	4.4	-
205 16:44:39.77	37-33.64	118-24.83	11.6	3.3	CR|BC
205 19:03:25.25	37-28.30	118-21.76	10.0	3.5	CR|AD
206 06:10:30.40	37-31.45	118-28.60	13.4	3.1	BR|AB
206 09:31:38.37	37-31.62	118-26.09	10.5	2.8	AR|AA
206 10:11:03.94	37-34.88	118-28.76	9.0	3.0	BR|CA
210 07:11:58.18	37-32.88	118-26.26	10.1	3.6	BR|AB
210 09:57:56.47	37-35.76	118-27.45	12.1	3.9	CR|AD

* = earthquakes timed and located from a different listing
( ) = origin times and locations that are uncertain

Table 7: Twenty of the better recorded events, with seismograms shown for 20 second duration in Appendix D, with distances and azimuths computed with respect to station G69.

	TIME (GMT)	LAT. (degrees)	LONG. (degrees)	DEP. (km)	MAG.	AZIM. (deg.)	EPI/HYPO-DIST. (km)		RATING
202	21:51:44.35	37-36.12	118-25.79	5.2	3.2	8	278.43	278.37	BR|AB
*202	22:07:16.70	37-29.40	118 25.74	19.5	5.5?	7	290.78	290.71	-D-
203	00:09:53.23	37-36.53	118-25.77	4.8	-?-	8	277.68	277.61	BC|AB
203	02:21:31.02	37-36.06	118-28.77	8.7	3.0	9	279.14	279.08	BR|BA
203	03:02:10.26	37-35.04	118-28.40	8.3	3.5	8	280.94	280.87	BR|BA
203	05:05:20.68	37-35.59	118-25.49	5.6	3.2	8	279.35	279.20	BR|BB
203	05:40:43.79	37-32.21	118-28.61	0.9	3.5	8	286.17	286.10	CR|DB
203	06:21:52.32	37-27.00	118-23.10	13.3	3.7	7	294.74	294.67	AR|AA
203	06:33:38.68	37-32.00	118-25.96	12.0	3.2	8	286.04	285.97	BR|CA
203	08:29:15.22	37-31.99	118-24.86	4.2	3.4	7	285.85	285.79	CR|BC
203	12:24:49.57	37-31.60	118-28.36	11.8	3.9	8	287.24	287.17	BR|BA
203	13:33:59.35	37-32.03	118-28.36	11.3	3.7	8	286.45	286.38	BR|BA
203	13:48:59.21	37-31.82	118-28.47	11.5	-?-	8	286.86	286.79	DR|CD
*203	18:29:43.13	37-29.58	118-22.98	8.7	4.1	7	289.92	289.90	-C-
205	02:43:10.35	37-36.16	118-28.06	4.0	3.5	8	278.81	278.75	BR|AB
n205	15:05:00.09	37-08.56	116-04.27	0.4	4.4	332	367.67	367.57	-
205	19:03:25.25	37-28.30	118-21.76	10.0	3.5	6	292.13	292.06	CR|AD
206	10:11:03.94	37-34.88	118-28.76	9.0	3.0	9	281.30	281.24	BR|CA
210	07:11:58.18	37-32.88	118-26.26	10.1	3.6	8	284.48	284.41	BR|AB
210	09:57:56.47	37-35.76	118-27.45	12.1	3.9	8	279.42	279.35	CR|AD

* = earthquakes timed and located from a different listing
n = NTS shot

Table 8: Nine of the better recorded events, with seismograms shown for 60 second duration in Appendix E, with distances and azimuths computed with respect to station G69.

CHALFANT EARTHQUAKES (60 SECOND TIME SERIES)

	TIME (GMT)	LAT. (degrees)	LONG. (degrees)	DEP. (km)	MAG.	AZIM. (deg.)	EPI/HYPO-DIST. (km)		RATING
202	21:51:44.35	37-36.12	118-25.79	5.2	3.2	8	278.43	278.37	BR|AB
*202	22:07:16.70	37-29.40	118 25.74	19.5	5.5?	7	290.78	290.71	-D-
203	02:21:31.02	37-36.06	118-28.77	8.7	3.0	9	279.14	279.08	BR|BA
203	03:02:10.26	37-35.04	118-28.40	8.3	3.5	8	280.94	280.87	BR|BA
203	06:21:52.32	37-27.00	118-23.10	13.3	3.7	7	294.74	294.67	AR|AA
203	12:24:49.57	37-31.60	118-28.36	11.8	3.9	8	287.24	287.17	BR|BA
203	13:48:59.21	37-31.82	118-28.47	11.5	-?-	8	286.86	286.79	DR|CD
n205	15:05:00.09	37-08.56	116-04.27	0.4	4.4	332	367.67	367.57	-
210	09:57:56.47	37-35.76	118-27.45	12.1	3.9	8	279.42	279.35	CR|AD

* = earthquakes timed and located from a different listing
n = NTS shot

Table 9: GEOS recording parameters used to record in-situ calibration signals.

CALIBRATIONS WITH SPECTRA IN APPENDIX E

STATION	LATITUDE	LONGITUDE	UNIT	SAMPLE RATE/ CHANNEL (SPS)	SENSOR-L22		ANTI-ALIAS FILTER CORNER FREQ. (HZ)
					NO.	GAIN	
G61	40 10.32	117 54.47	36	400	183	60	100
G63	40 08.99	117 55.94	7	200	191	54	50
G64	40 08.29	117 56.70	7	400	191	54	100
G65	40 07.6	117 57.49	22	200	305	54	50
G67	40 06.29	117 59.00	33	400	197	54	100
G68	40 05.82	117 59.35	15	400	198	54	100
G69	40 05.05	118 00.31	36	400	304	54	100
G70	40 04.21	118 00.64	21	400	307	54	100
G71	40 03.71	118 01.66	17	400	162	54	100
G73	40 02.02	118 02.80	8	400	184	54	100
G75	40 00.95	118 03.97	24	400	303	54	100
G79	39 58.58	118 07.83	39	400	302	54	100
G81	39 56.67	118 08.74	12	400	160	54	100
G83	39 54.91	118 10.13	27	200	310	54	50
G85	39 53.66	118 13.38	16	400	201	54	100
G87	39 52.15	118 13.95	29	200	306	54	50
G89	39 50.63	118 14.37	22	400	308	54	100
G91	39 49.09	118 14.56	38	400	309	54	100
G93	39 47.63	118 15.13	31	200	311	54	50
G95	39 46.14	118 15.94	35	200	187	54	50
402	40 05.41	117 58.29	38	200	310	60	50
405	40 05.25	117 55.21	27	200	160	60	50
414	40 04.55	117 47.96	15	200	306	54	50
417	40 02.83	117 47.19	7	200	191	54	50
420	40 01.56	117 45.86	39	200	198	54	50
423	40 00.41	117 44.73	31	200	159	54	50
426	39 58.75	117 43.19	33	200	311	54	50
431	39 56.15	117 40.81	36	200	187	60	50
440	39 54.25	117 35.80	29	200	183	60	50
443	40 06.19	118 02.12	24	200	307	60	50
446	40 05.90	118 00.31	12	200	302	60	50
G37	40 06.78	118 05.82	21	200	304	60	50

Table 10: Summary of timing checks with differences greater than 0.3%

CHEMICAL EXPLOSIONS

Station	Time at error	Exp. Diff	Actual Diff
G67	204:05:04:24.804000	0.310000	0.420000
G71	204:07:08:09.730000	0.352500	0.420000
G81	204:07:01:41.873000	0.107500	0.420000
G69	207:05:06:10.783000	0.420000	0.000000
G79	207:05:04:38.093000	0.420000	0.840000
G89	207:05:06:45.012000	0.420000	0.840000
G91	207:05:01:18.635000	0.420000	0.840000
G65	207:07:07:25.676000	0.267500	0.420000
G73	207:07:00:10.008000	0.420000	0.422000
G77	207:07:09:43.357000	0.420000	0.840000
G79	207:07:06:22.850000	0.157500	0.420000
G85	207:07:01:12.793000	0.107500	0.420000
G91	207:07:00:53.570000	0.420000	0.840000
G59	207:09:05:19.142000	0.420000	0.840000
	207:09:05:19.562000	0.840000	0.420000
G89	207:08:59:59.008000	0.420000	0.422000
	207:09:00:20.009000	0.420000	0.422000
G93	207:08:59:53.129000	0.382500	0.381000
	207:09:00:00.689000	0.420000	0.840000
	207:09:00:01.109000	0.840000	0.420000
G37	211:05:00:11.912000	0.840000	2.520000
	211:05:00:12.752000	2.520000	0.840000
423	211:07:08:08.026000	0.840000	1.680000
	211:07:08:08.866000	1.680000	0.840000
G34	211:07:01:25.468000	0.840000	2.520000
	211:07:01:26.308000	2.520000	0.840000
	EARTHQUAKES		
G72	0:00:00:00.000000	0.420000	********
	202:22:08:40.812000	0.000000	********
G65	203:00:11:51.263000	0.420000	1.260000
	203:00:11:51.683000	1.265000	0.420000
G67	203:02:22:14.015000	0.115000	0.420000
G71	203:03:03:21.652000	0.302500	0.420000
	203:03:03:29.632000	0.420000	0.840000
G72	203:05:41:48.284000	0.420000	1.260000
	203:05:41:48.704000	1.265000	0.420000
G79	203:05:41:53.763000	0.090000	0.420000
G81	203:06:23:24.712000	0.392500	0.421000
G73	203:13:36:17.298000	0.420000	0.840000
	203:13:36:17.718000	0.842500	0.420000
423	210:07:12:57.634000	0.840000	1.680000
	210:07:12:58.474000	1.680000	0.840000
420	210:07:13:49.389000	0.840000	1.680000
	210:07:13:50.229000	1.680000	0.840000

Table 11: GEOS seismic event header description.

Word 1:	Year (last two digits)
Word 2:	Julian day of year
Word 3:	Hour of day
Word 4:	Minutes
Word 5:	Seconds
Word 6:	Milliseconds
Word 7:	Station number
Word 8:	Experiment number
Word 9:	GEOS serial number
Word 10:	Event sequence number
Word 11:	Event type code
Word 12:	Lowest active channel no.
Word 13:	Highest active channel no.
Word 14:	Channel 1 sensor type
Word 15:	Channel 1 amplifier gain (db)
Word 16:	Channel 1 anti-alias filter (Hz)
Word 17:	Channel 2 sensor type
Word 18:	Channel 2 amplifier gain (db)
Word 19:	Channel 2 anti-alias filter (Hz)
Word 20:	Channel 3 sensor type
Word 21:	Channel 3 amplifier gain (db)
Word 22:	Channel 3 anti-alias filter (Hz)
Word 23:	Channel 4 sensor type
Word 24:	Channel 4 amplifier gain (db)
Word 25:	Channel 4 anti-alias filter (Hz)
Word 26:	Channel 5 sensor type
Word 27:	Channel 5 amplifier gain (db)
Word 28:	Channel 5 anti-alias filter (Hz)
Word 29:	Channel 6 sensor type
Word 30:	Channel 6 amplifier gain (db)
Word 31:	Channel 6 anti-alias filter (Hz)
Word 32:	Aggregate sample rate (Hz)
Word 33:	Number of pre-event records
Word 34:	Number of samples per record
Word 35:	Time standard code
Word 36:	Clock correction block (8 words)
Word 44:	- (Remaining free correction words)
Word 45:	Trigger channel number
Word 46:	Trigger short term average interval
Word 47:	Trigger long term average interval
Word 48:	Trigger short term/long term ratio
Word 49:	Battery voltage (encoded)

Table 12: Definition of GEOS header offsets for first header record.

	First Header Record: 256 16–Bit Integers
(1)	Number of optional integer header records in use
(2)	Number of optional ASCII header records in use
(3)	"Undefined value" used to flag unused offsets
(4)	Data type flag: if positive, data are in floating point format; if negative, data are in integer format. The absolute value of this offset specified the number of bytes per data point. Special cases: if 1, then 32-bit floating point format; if "undefined," then 16-bit integer format.
(10)	Year of the event
(11)	Julian day
(12)	Hours
(13)	Minutes
(14)	Seconds
(15)	Milliseconds
(16)	Microseconds
(17)	Sample number of first time mark
(18)	Detection amplitude of tickmark
(19)	Number of tickmarks detected
(20)	Serial number of recording unit
(21)	Event sequence number
(27)	Number of first active channel recorded by unit
(28)	Recorder channel number used for this component
(29)	Number of active channels recorded by unit
(30)	Number of components recorded under this component's station name
(31)	Number of data records (excluding headers)
(32)	Index of the last sample in the last data record
(33)	Total samples per data record recorded by unit
(34)	Playback program identification code
(35)	Playback program major version number
(36)	Playback program minor version number
(37)	Recording unit type identification code
(38)	Major version number of recording unit software
(39)	Minor version number of recording unit software
(40)	Sensor serial number
(41)	Vertical orientation, in degrees
(42)	Horizontal orientation, in degrees
(43–49)	Sensor model ID (14 ASCII characters)
(50)	Station location number
(51)	Experiment or tape number

(52)	Trigger algorithm identification code
(53)	Trigger short-term average interval (tenths of seconds)
(54)	Trigger long-term average interval (seconds)
(55)	Trigger STA/LTA ratio (powers of 2)
(56)	Trigger channel number
(57)	Pre-event memory size (tenths of seconds)
(58)	Post-trigger record duration (seconds)
(101–200)	Processing history (ASCII)
(208)	Data file directory I.D.
(209)	Data file sub-directory I.D.
(210–216)	ASCII filename
(217–219)	ASCII study name

Notes:

The GEOS does not record tickmarks.

Header record 1, offset 41: vertical orientation is expressed as a number from 0 to 90, with 0 representing true vertical and 90 representing true horizontal.

Header record 1, offset 42: horizontal orientation is expressed as a number from 0 to 359, with 0 representing true north, and 90 representing true east.

Table 13: Definition of GEOS header offsets for second header record.

Second Header Record: 128 32–Bit Floating Point Values

(1)	Number of optional reel header blocks in use
(2)	"Undefined value" to flag unused offsets
(5)	Component sampling rate, in samples per second
(6)	Component sample lag, in seconds
(39)	Transducer type (four ASCII characters)
(40)	Sensor latitude (decimal degrees)
(41)	Sensor local x-coordinate (meters)
(42)	Sensor longitude (decimal degrees)
(43)	Sensor local y-coordinate (meters)
(44)	Sensor elevation (meters)
(45)	Sensor local z-coordinate (meters)
(46)	Digitizing constant, digital counts per volt
(47)	Anti-alias corner frequency
(48)	Poles of anti-alias filter
(49)	Sensor natural frequency (hertz)
(50)	Sensor damping coefficient
(51)	Sensor motion constant (volts per motion-unit)
(52)	Amplifier gain
(60)	Clock correction
(61)	Seconds since last clock correction
(62)	Instrument battery voltage
(63)	Desired trigger algorithm STA/LTA ratio
(64)	Actual STA value at trigger moment
(65)	Actual LTA value at trigger moment
(66)	Maximum value of STA/LTA ratio during event

Notes:

Header record 2, offset 48: filter roll-off equals 6 db per pole indicated.
Header record 2, offset 52: gain expressed in dB if Header record 1, offset 5 is equal to one (1); otherwise, gain expressed as an algebraic factor.
Header record 2, offset 60: the clock correction is subtracted from the time specified in Header record 1 to generate the corrected time.

Table 14: SEG–Y Header format for including NSMDC Header entries created for GEOS data.

Reel Identification Header, Part 2

SEG–Y Byte No.	NSMDC Header	Description
3205–3208	–	Line number
3209–3212	–	Reel number
3213–3214	–	Number of data traces per record (always 1)
3215–3216	–	Number of auxiliary traces per record (always 0)
3217–3218	R(5)	Sample interval, microseconds
3221–3222	I (31,32)	Maximum number of samples in a data trace on this reel ((I(31)*256)+I(32))
3225–3226	–	Data format (always 3, fixed 2-byte format)
3227–3228	–	CDP fold
3255–3256	–	Measurement system (always 1, meters)

Trace Identification Header

SEG–Y Byte No.	NSMDC Header	Description
1– 4	–	Trace sequence number
9– 12	I(50)	Original field location number
13– 16	I(28)	GEOS channel number
26– 30	I(255)	Trace identification code (I(255)*10) (stored as component number times 10)
35– 35	–	Data use (always 1, production)
41– 44	R(44)	Receiver Surface elevation
69– 70	–	Elevation scaler (always −100, elevation in centimeters)
71– 72	–	Coordinates scaler (always −100, hundredths of seconds)
81– 84	R(42)	Group coordinate X
85– 88	R(40)	Group coordinate Y
89– 90	–	Coordinate units (always 2, seconds of arc)
115–116	I(31,32)	Number of samples in this trace ((I(31)*256)+I(32)(10^6/R(5))
117–118	R(5)	Sample interval (microseconds)
119–120	–	Gain type (always 1, fixed)

Trace Identification Header (Continued)

SEG–Y Byte No.	NSMDC Header	Description
121–122	R(52)	Amplifier gain
141–142	R(47)	Anti-alias corner frequency
143–144	R(48)	Alias filter slope (R(48)*6)
157–158	I(10)	Year data recorded
159–160	I(11)	Day of year
161–162	I(12)	Hour of day
163–164	I(13)	Minute of hour
165–166	I(14)	Second of minute
167–168	I(14)	Time basis (always 2, GMT)
181–184	I(15),I(16)	Milliseconds, microseconds, and sample lag time (in microseconds) $(I(15)*1000+I(16)+R(6)*10^6)$
185–186	R(60)	Clock correction in milliseconds (subtract from recording time) (R(60)*1000)
187–188	I(20)	GEOS serial number
189–190	I(21)	GEOS event sequence number
191–192	I(29)	No. channels recorded by GEOS
193–194	I(30)	No. channels in this component group
195–196	I(38),I(39)	Recorder version number
197–198	I(41)	Sensor vertical orientation (degrees from vertical up)
199–200	I(42)	Sensor horizontal orientation (degrees from north)
201–202	I(43)	Sensor type (1 = FBA, 2 = L–22, 3 = L–4, 4 = Dilatometer, 5 = other)
203–204	I(51)	Experiment or tape number
205–206	R(49)	Sensor natural frequency
207–208	R(50)	Sensor damping coefficient (times 100) (R(50)*100)
209–212	R(51)	Sensor motion constant (microvolts per motion-unit)
213–216	R(46)	Digitizing constant (counts per volt times 1000)
217–218	I(53)	Trigger algorithm short-term-average interval (tenths of seconds)
219–220	I(54)	Trigger algorithm long-term-average interval (seconds)
221–222	I(55)	Trigger threshold, STA to LTA ratio
223–224	I(56)	Trigger component number

Figure 1. Side and front panel view of the General Earthquake Observation System (GEOS) together with a WWVB antenna and two sets of three-component sensors commonly used to provide more than 180 dB of linear, dynamic range.

Figure 1

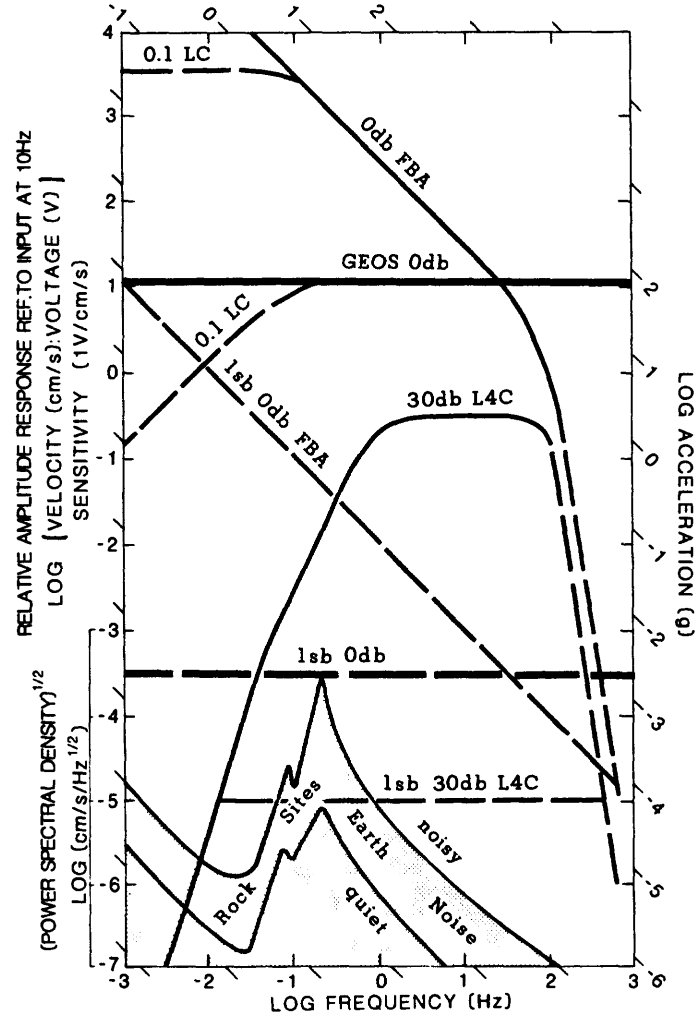

Figure 2. The unit-impulse response designed for the GEOS recorder, spectra for Earth noise (Aki and Richards, 1980), and complete system response with two types of sensors (force-balance accelerometer at 0 dB gain and L4–C velocity transducer at 30 dB gain).

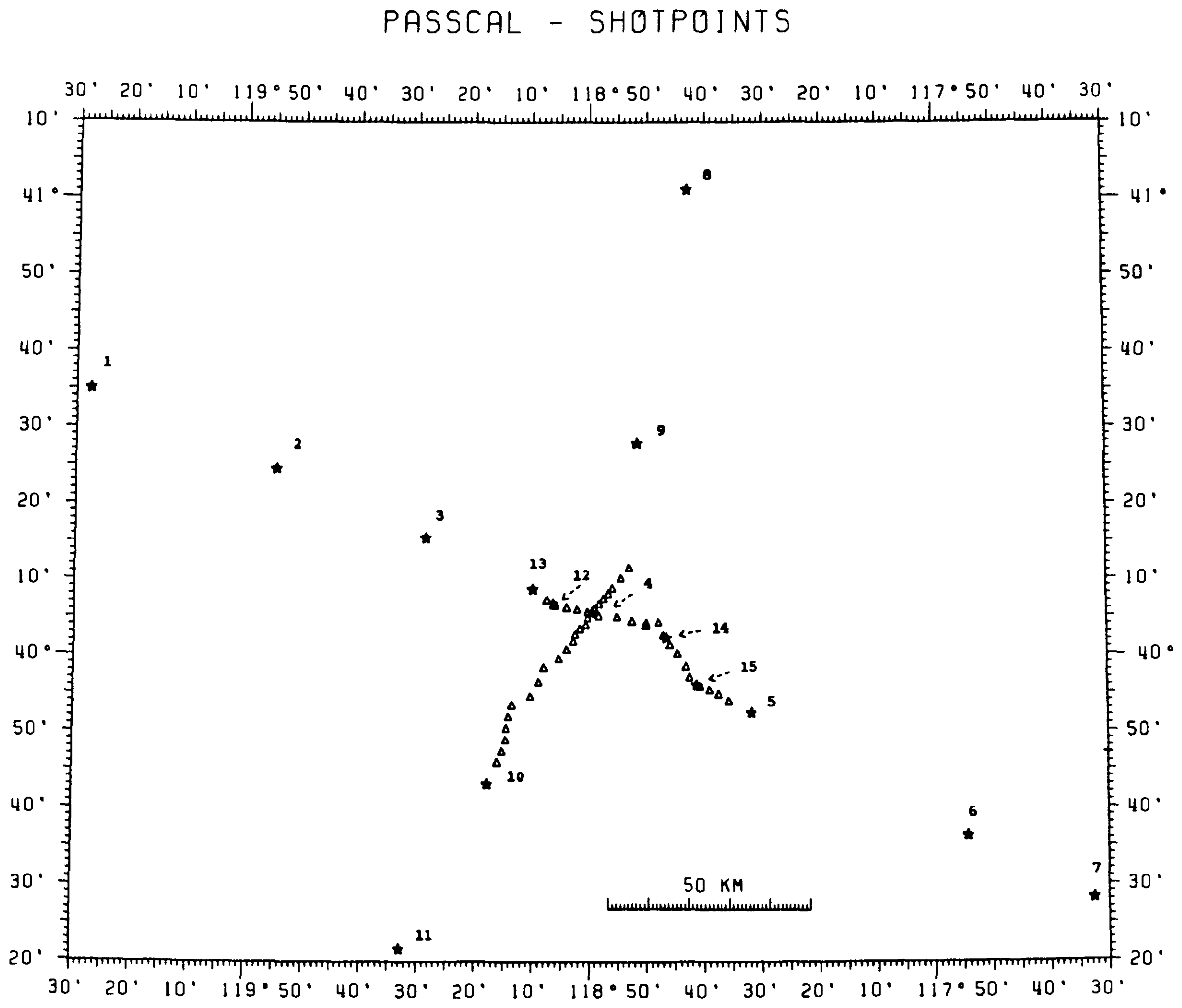

Figure 3(a): Map showing station locations for GEOS (triangles) relative to shot points (numbers) detonated during Northern Nevada Lithospheric Experiments.

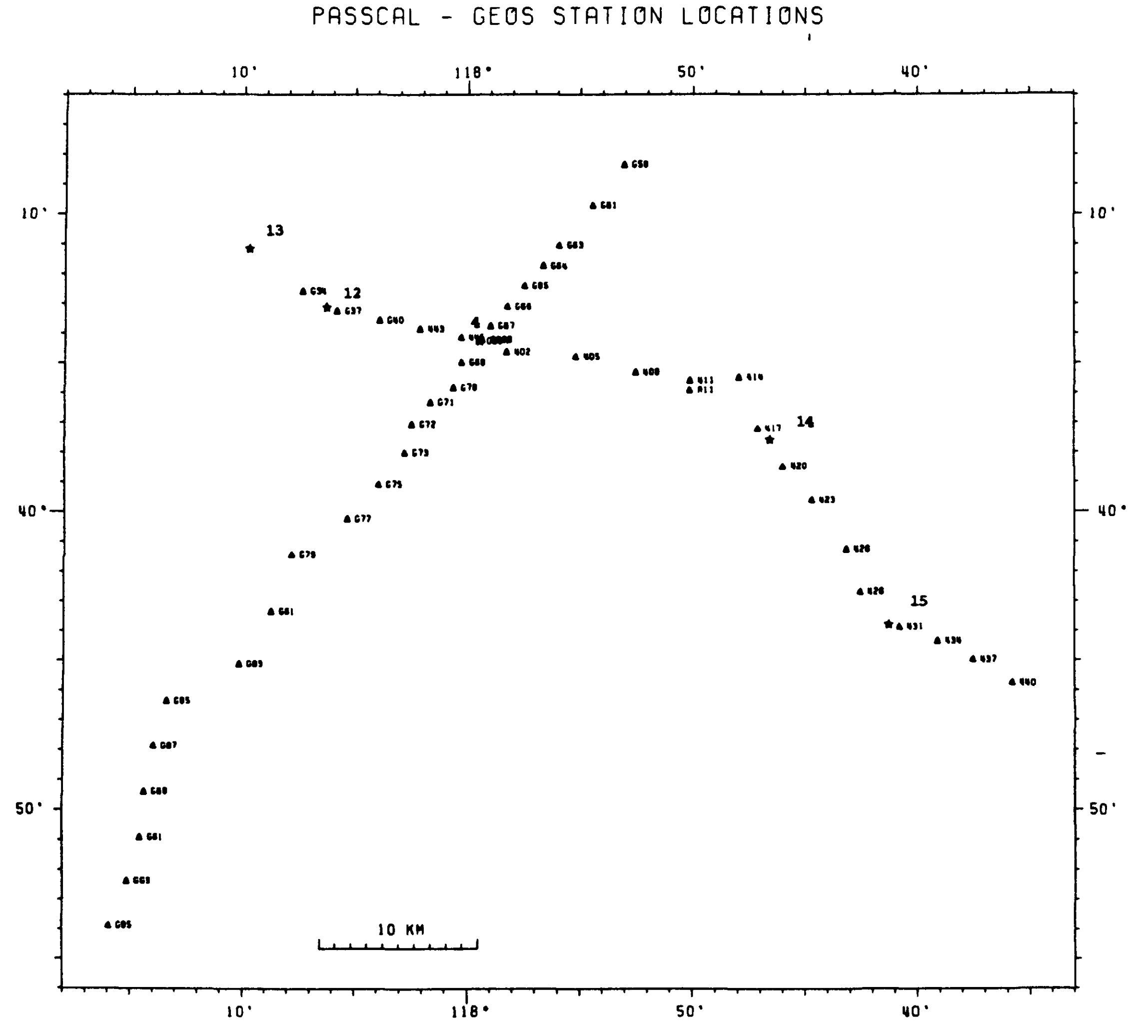

Figure 3(b): Map with expanded scale (see fig. 3(a)) showing station locations as identified by three digit station names relative to closest shot points (numbers).

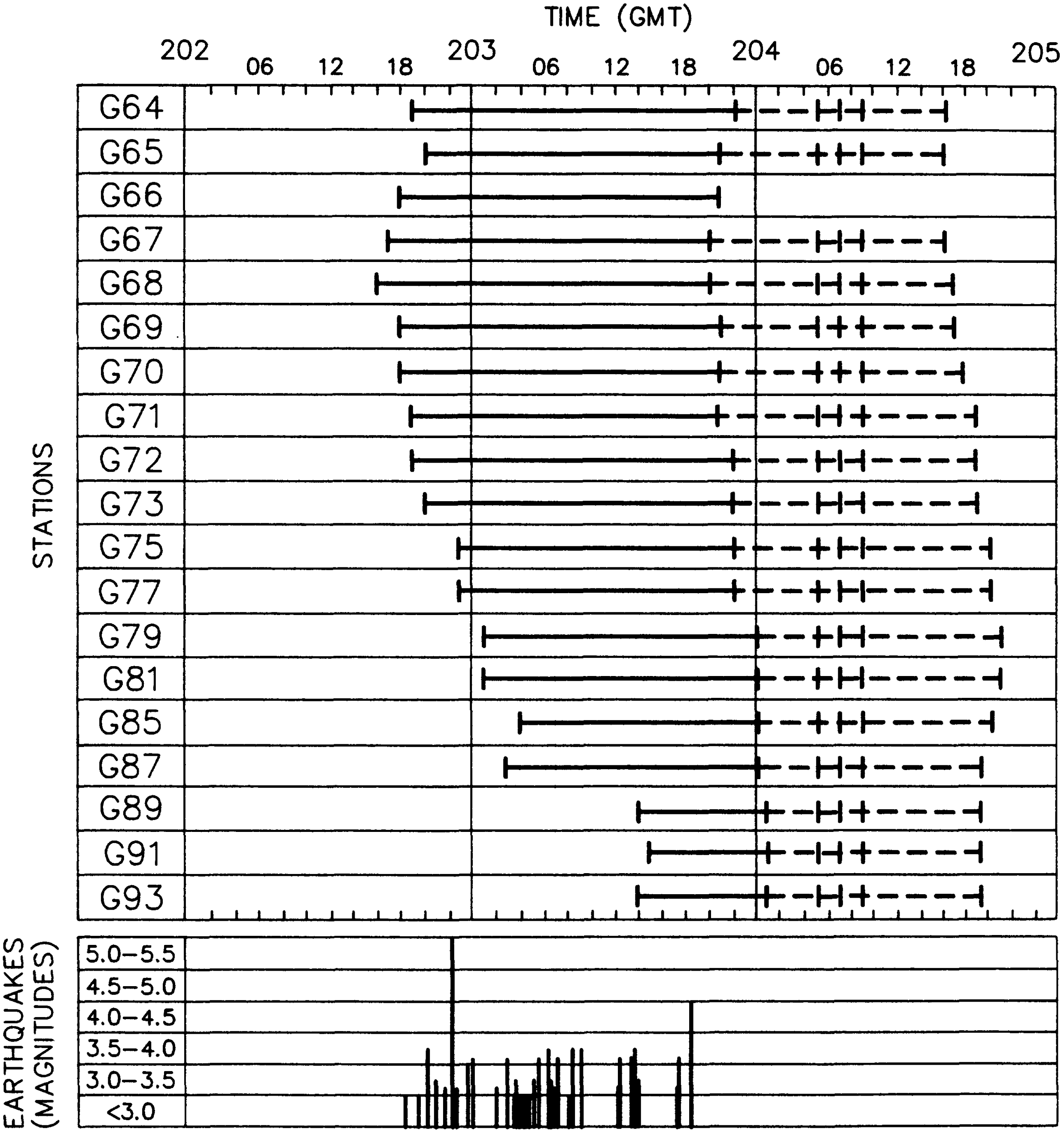

Figure 4(a): Bar graphs indicating deployment intervals for GEOS station locations together with the occurrence times and magnitudes for Chalfant earthquakes recorded at three or more stations for the first part of the first deployment interval. Time intervals for GEOS recorders programmed to record earthquakes in " trigger mode" and to record shots in " preset time mode" are indicated by solid and dashed lines, respectively.

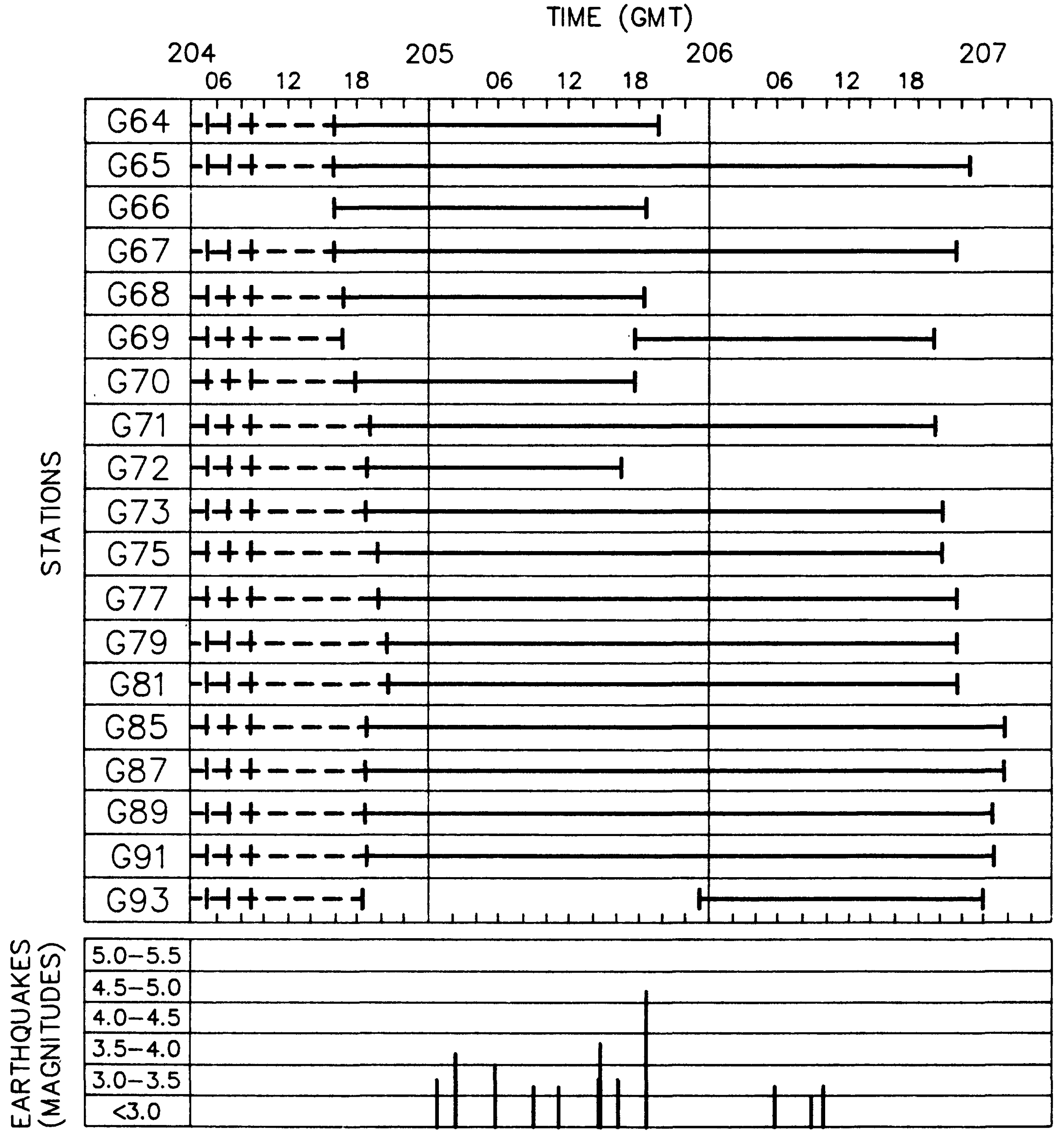

Figure 4(b): Bar graphs indicating deployment intervals for GEOS station locations together with the occurrence times and magnitudes for Chalfant earthquakes recorded at three or more stations during the second part of deployment interval 1. Time intervals for GEOS recorders programmed to record earthquakes in "trigger mode" and to record shots in "preset time mode" are indicated by solid and dashed lines, respectively.

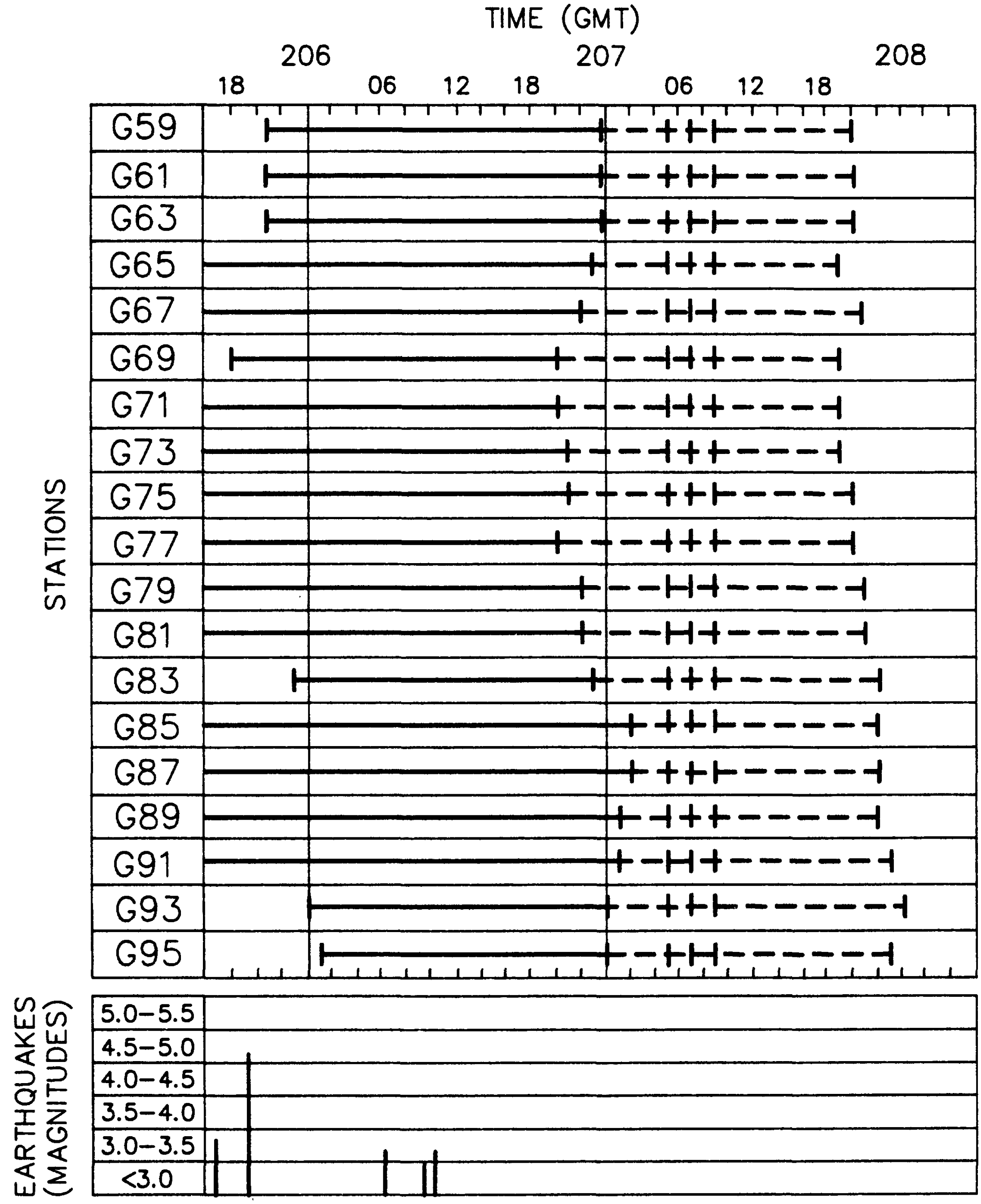

Figure 5: Bar graphs indicating deployment intervals for GEOS station locations together with the occurrence times and magnitudes for Chalfant earthquakes recorded at three or more stations during the second deployment interval. Time intervals for GEOS recorders programmed to record earthquakes in "trigger mode" and to record shots in "pre-set time mode" are indicated by solid and dashed lines, respectively.

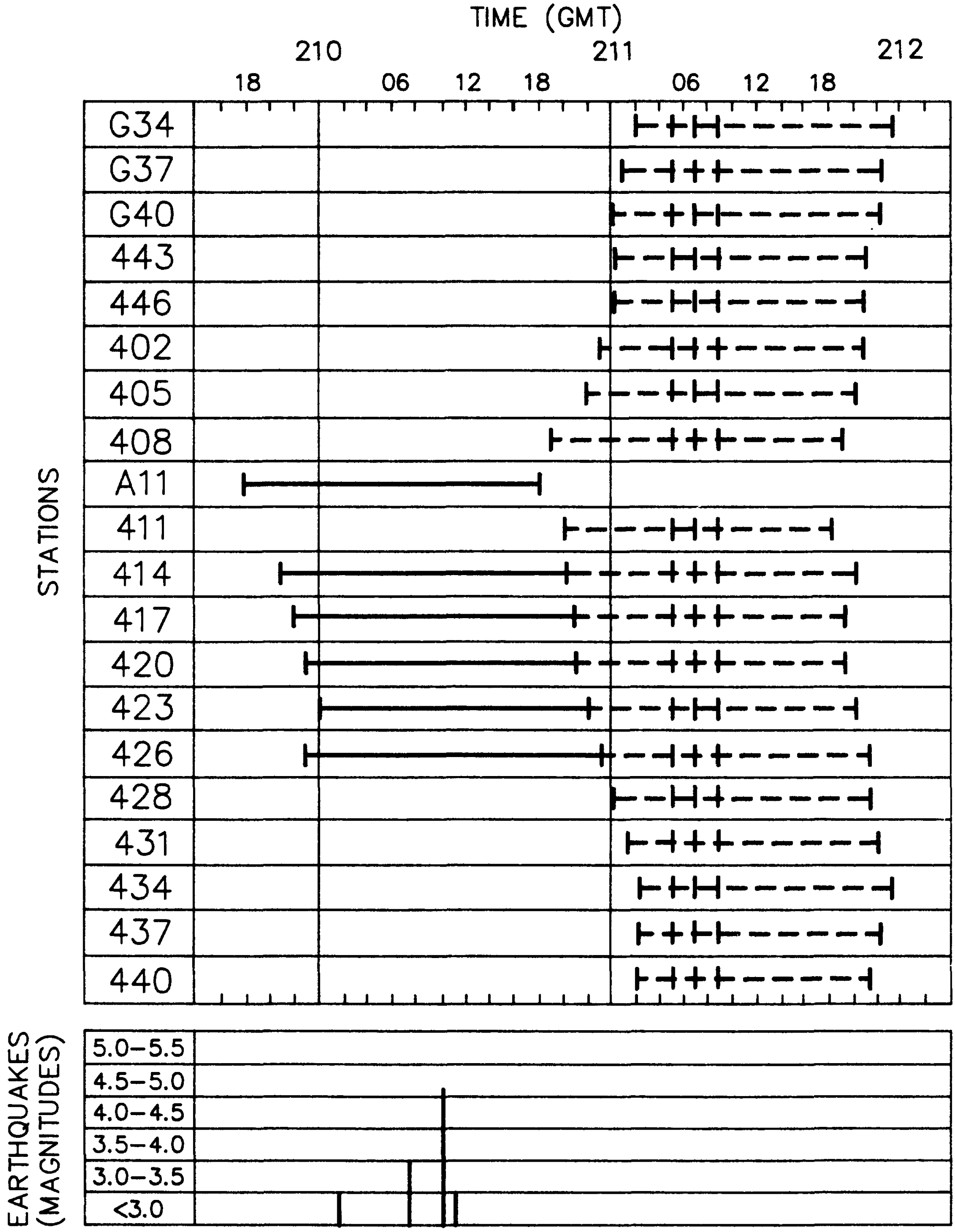

Figure 6: Bar graphs indicating deployment intervals for GEOS station locations together with the occurrence times and magnitudes for Chalfant earthquakes recorded at three or more stations during the third deployment interval. Time intervals for GEOS recorders programmed to record earthquakes in "trigger mode" and to record shots in "pre-set time mode" are indicated by solid and dashed lines, respectively.

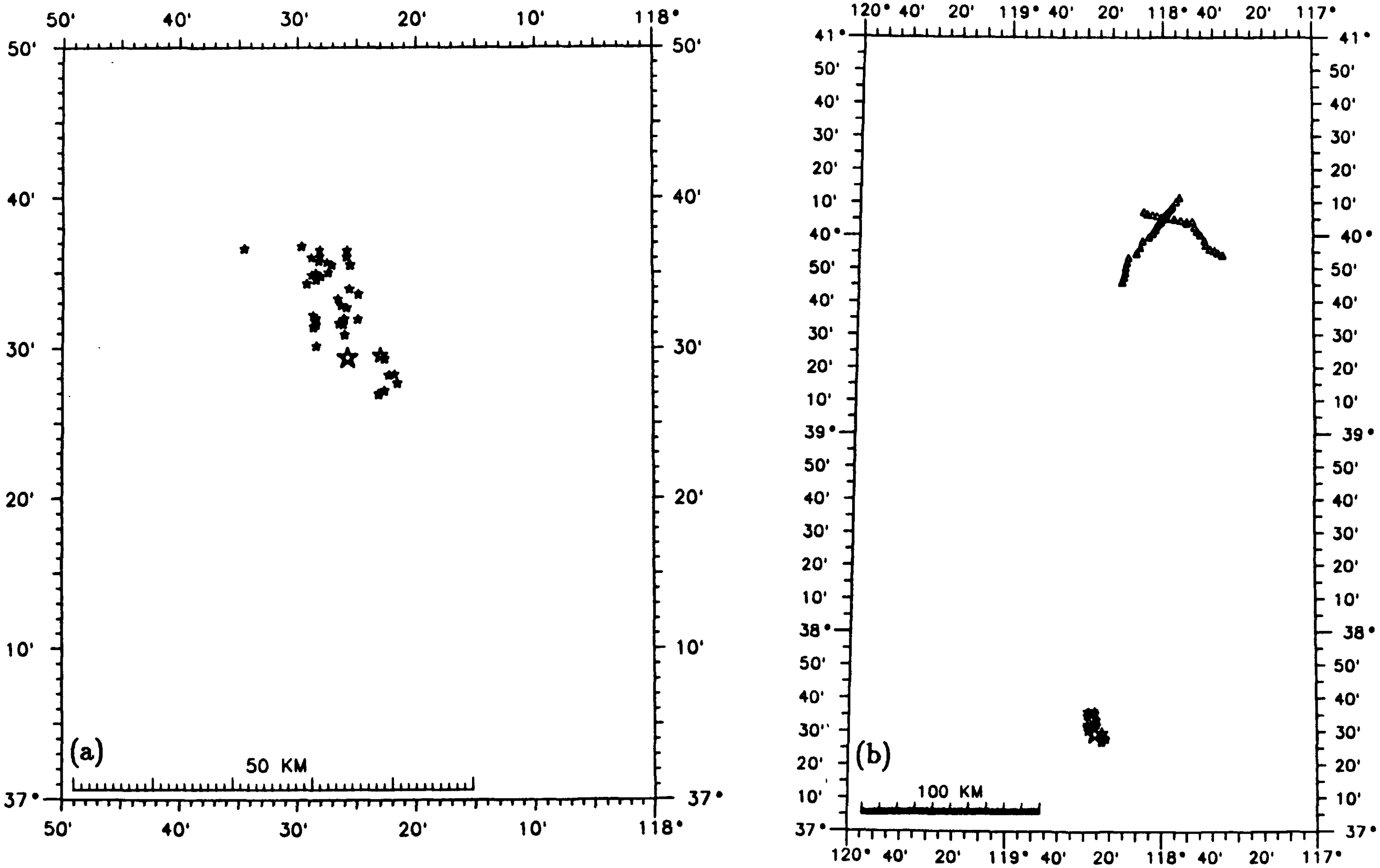

Figure 7: Map showing epicenter locations for 46 earthquakes near Chalfant, CA, as identified in table 6 (a) and map showing epicenter locations in relation to locations of GEOS stations (b).

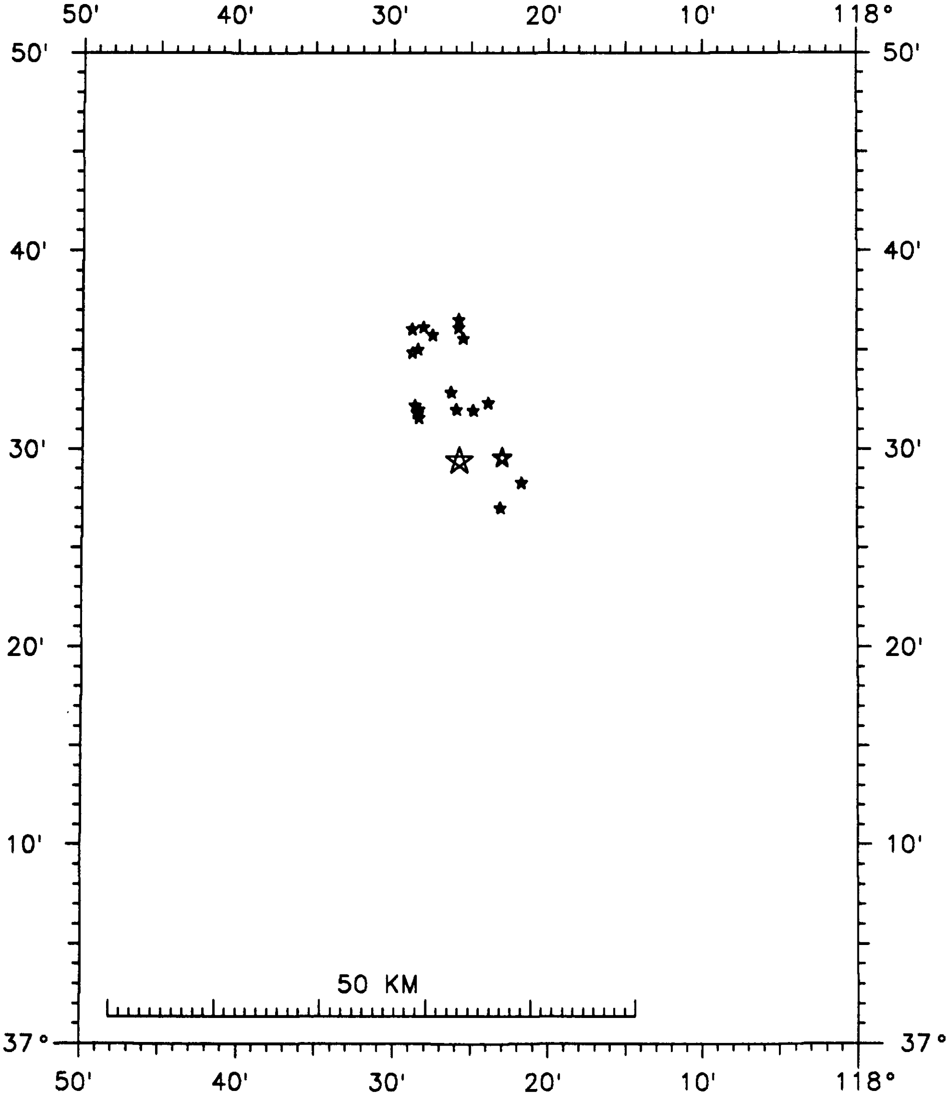

Figure 8: Map showing epicenter locations corresponding to Chalfant earthquakes for which three component seismograms are presented in Appendix D.

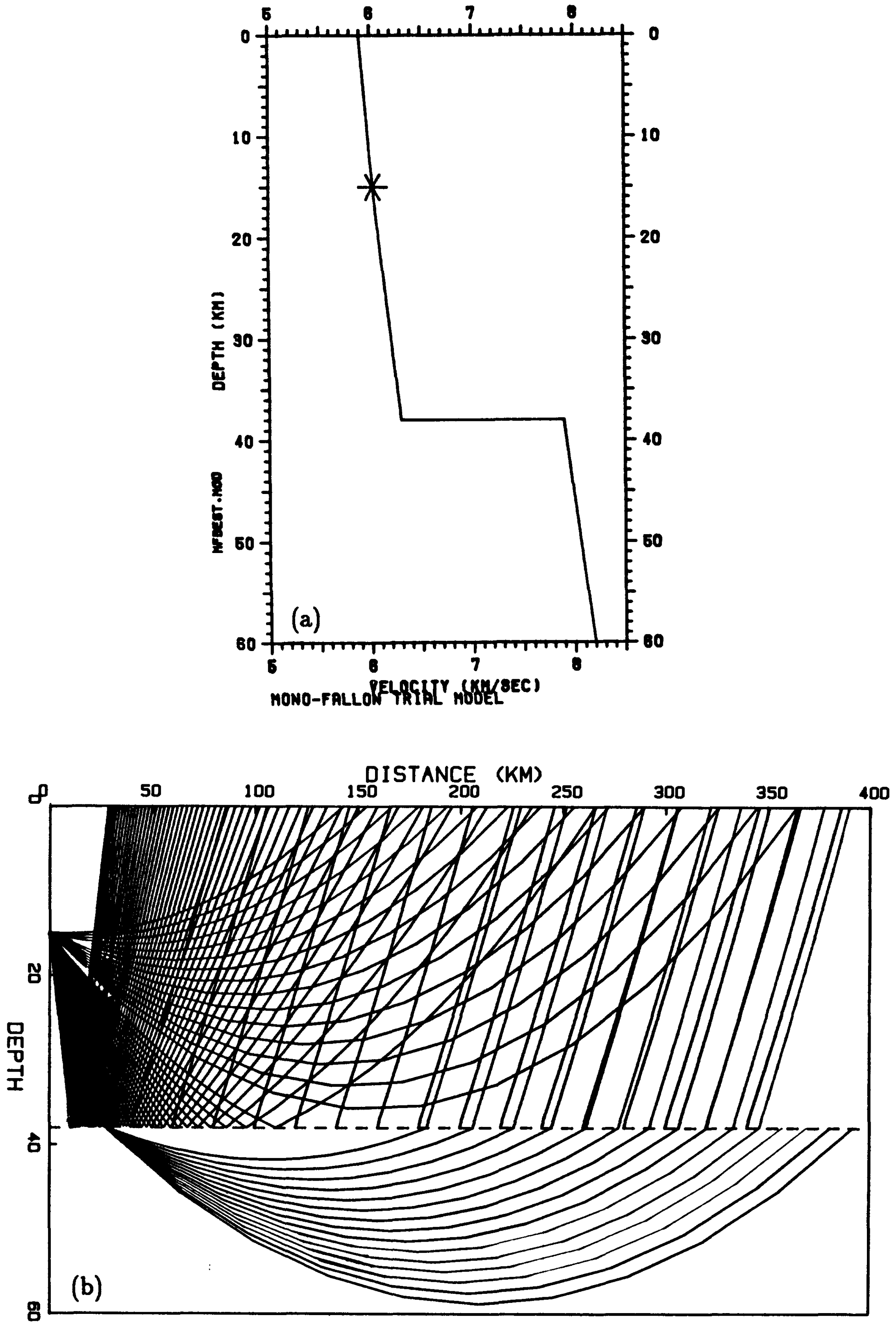

Figure 9: Average velocity model (a) and ray diagram (b) for profile extending from Chalfant, CA to Fallon, NV.

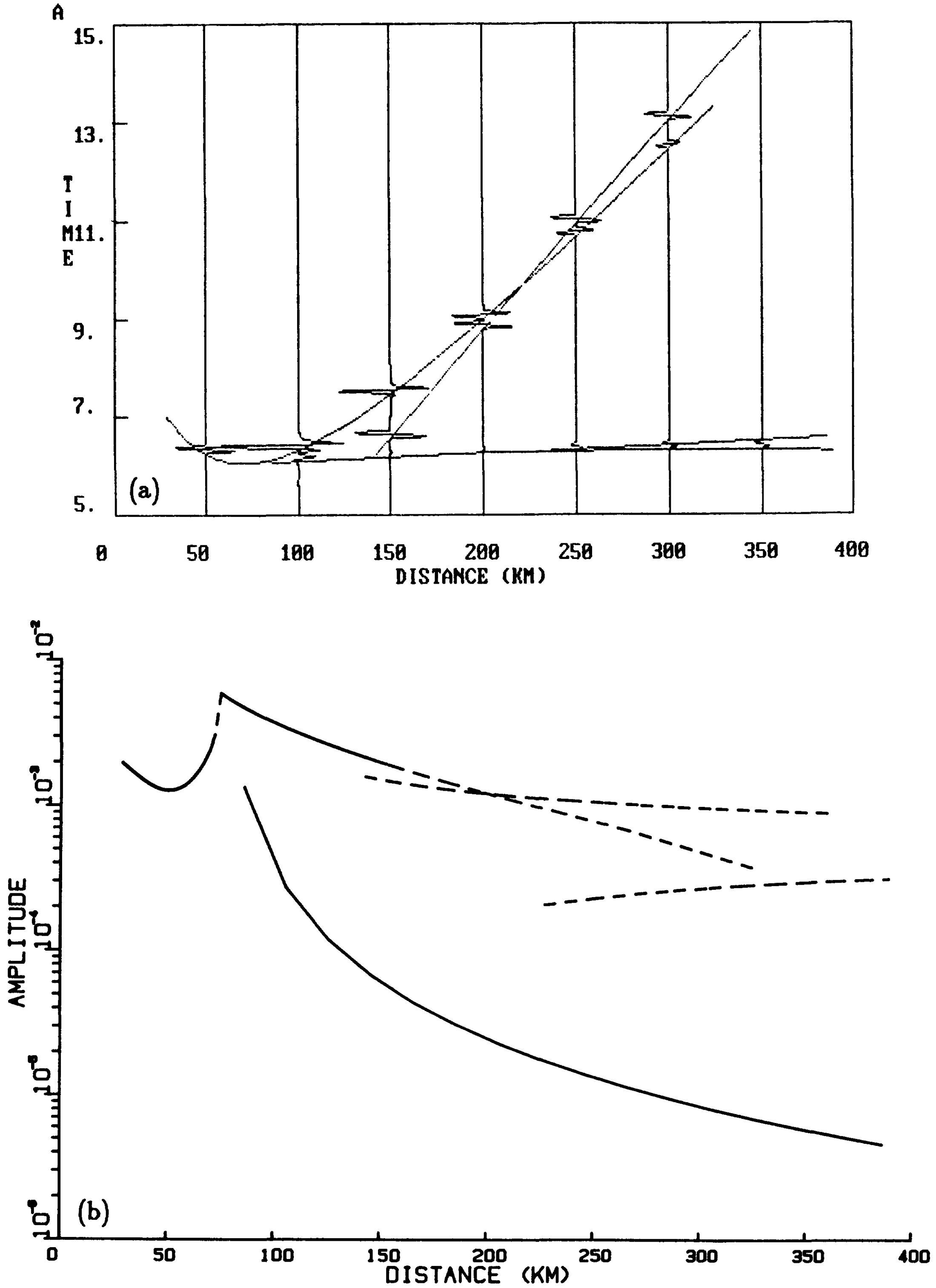

Figure 10: Synthetic record section (a) and amplitudes (b) estimated for average velocity model shown in Figure 7.

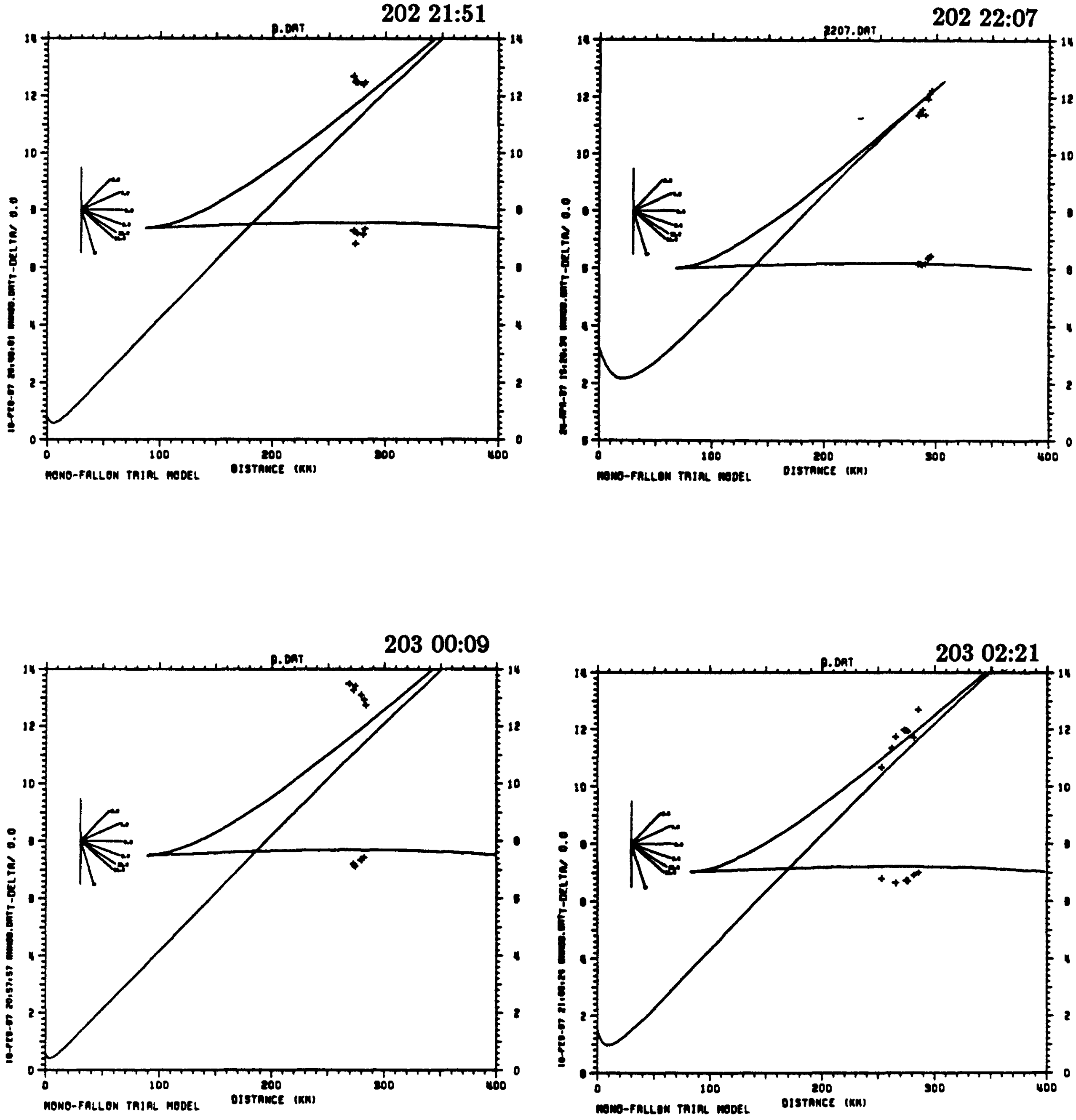

Figure 11: Observed travel-times for earthquakes identified by origin time (see Table 7) and travel-times estimated using an average velocity model (Fig. 9(a)) for the Chalfant-Fallon profile.

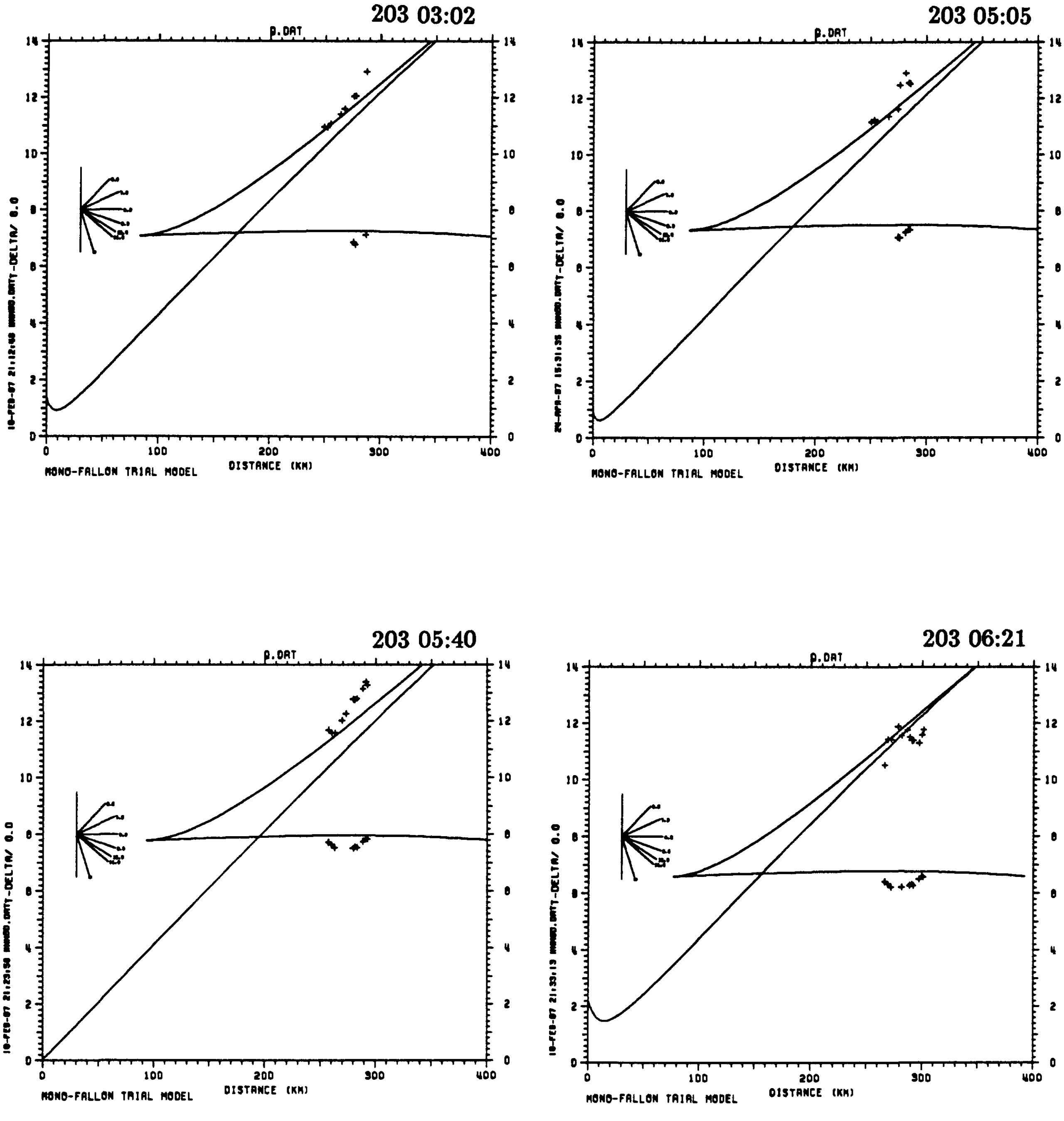
203 03:02

203 05:05

203 05:40

203 06:21

Figure 12: Observed travel-times for earthquakes identified by origin time (see Table 7) and travel-times estimated using an average velocity model (Fig. 9(a)) for the Chalfant-Fallon profile.

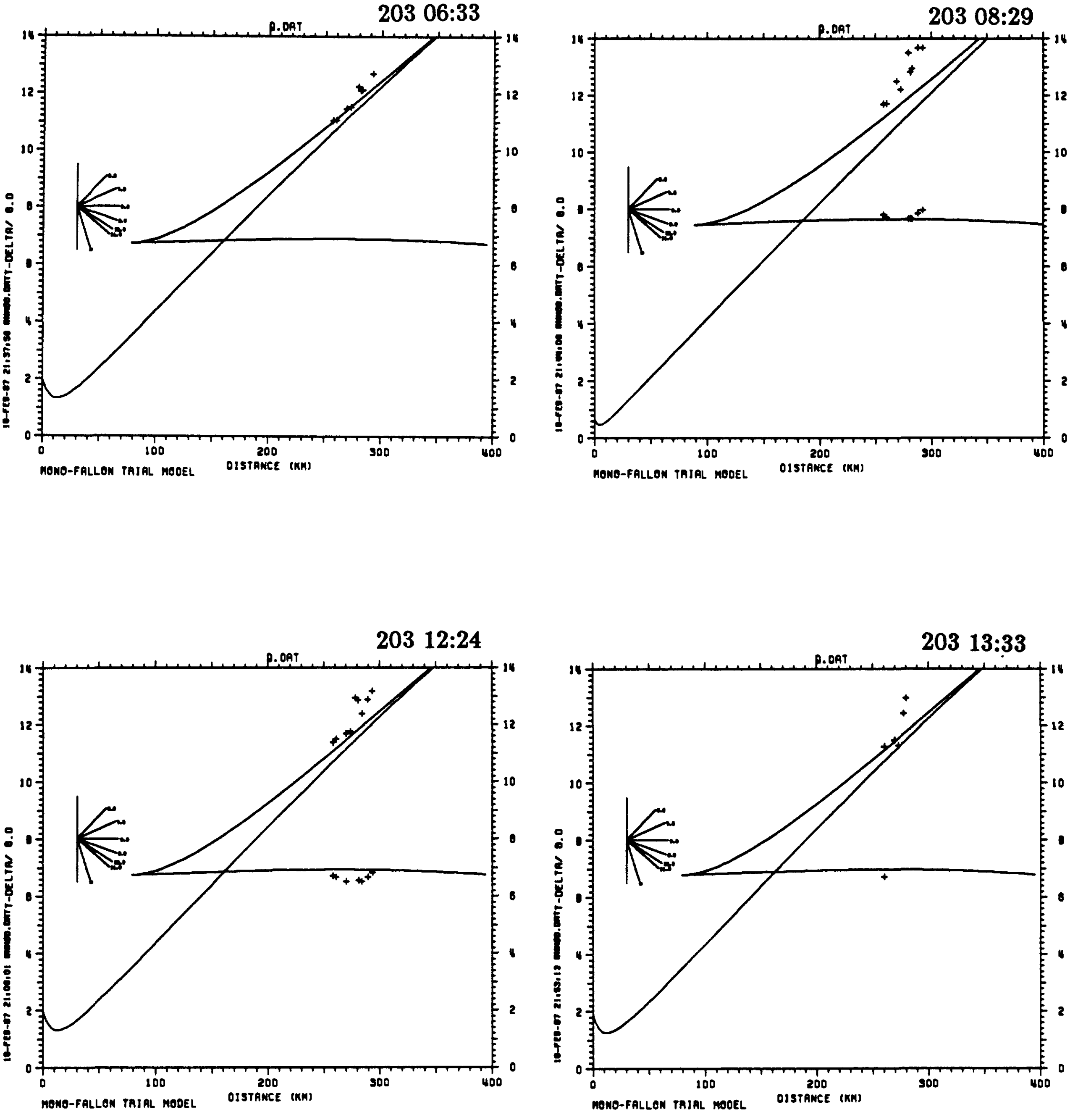

Figure 13: Observed travel-times for earthquakes identified by origin time (see Table 7) and travel-times estimated using an average velocity model (Fig. 9(a)) for the Chalfant-Fallon profile.

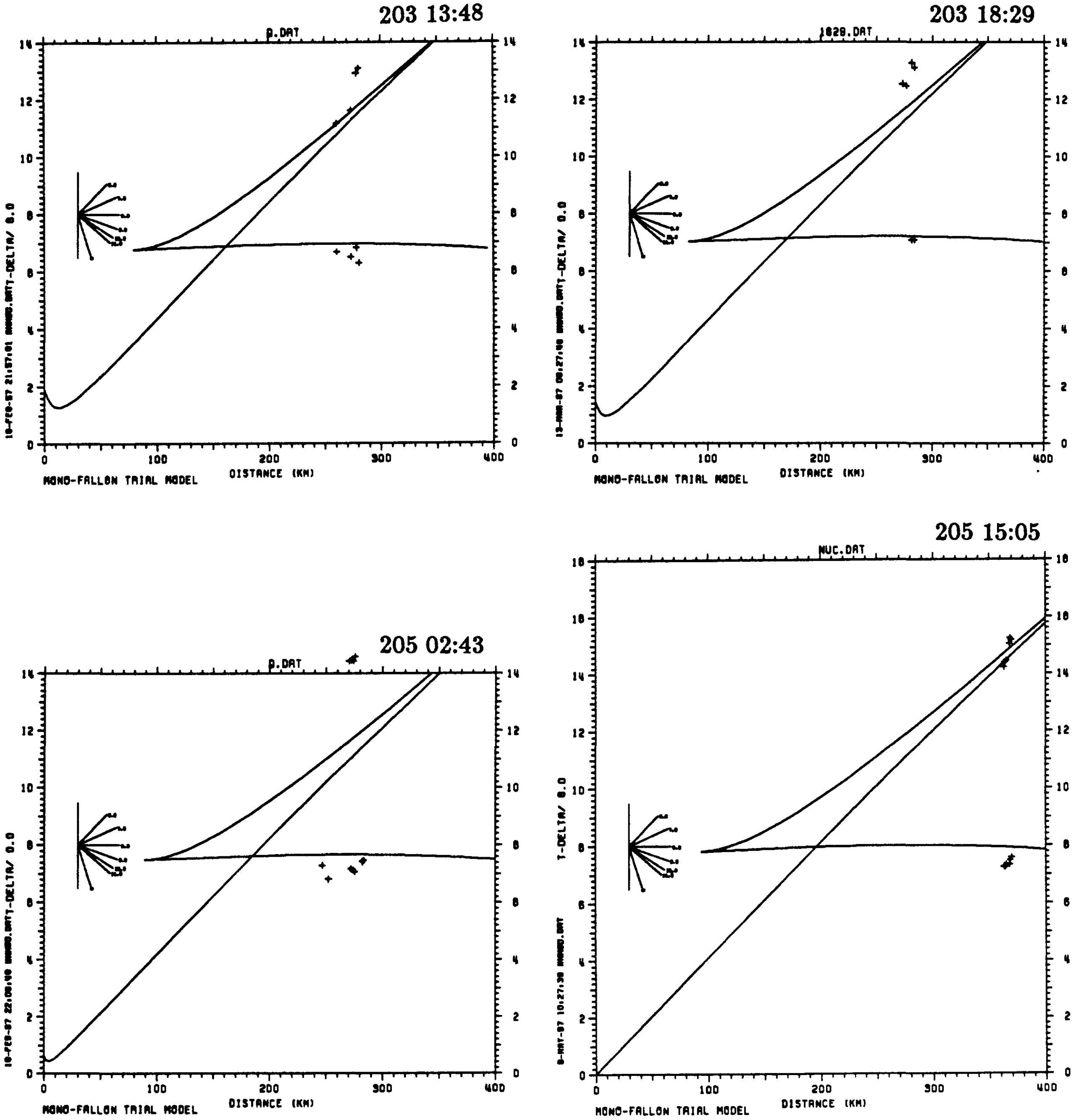

Figure 14: Observed travel-times for earthquakes identified by origin time (see Table 7) and travel-times estimated using an average velocity model (Fig. 9(a)) for the Chalfant-Fallon profile. Travel-times for event 205 15:05 correspond to those for a nuclear explosion detonated in south-central Nevada.

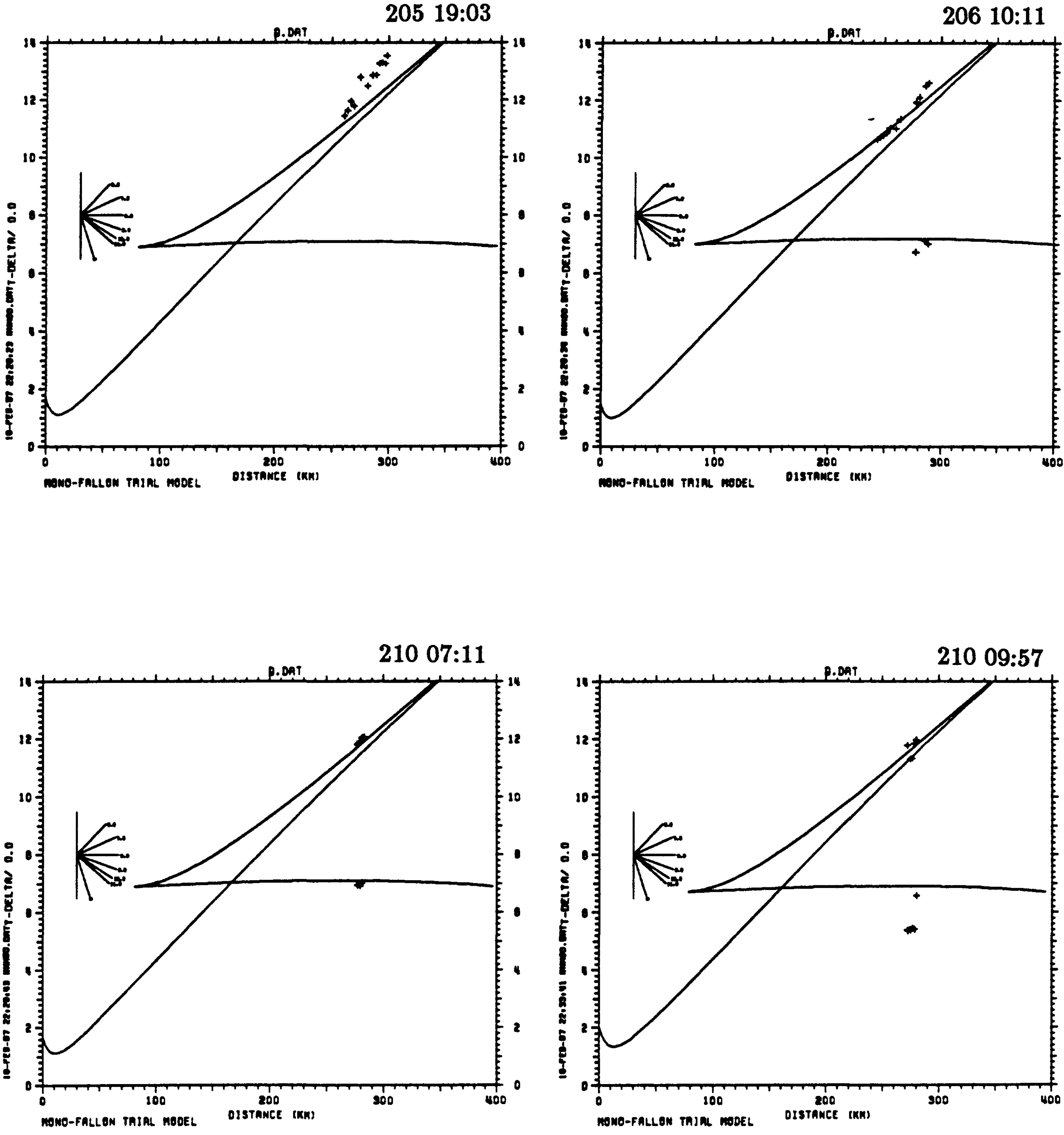

205 19:03

206 10:11

210 07:11

210 09:57

Figure 15: Observed travel-times for earthquakes identified by origin time (see Table 7) and travel-times estimated using an average velocity model (Fig. 9(a)) for the Chalfant-Fallon profile.

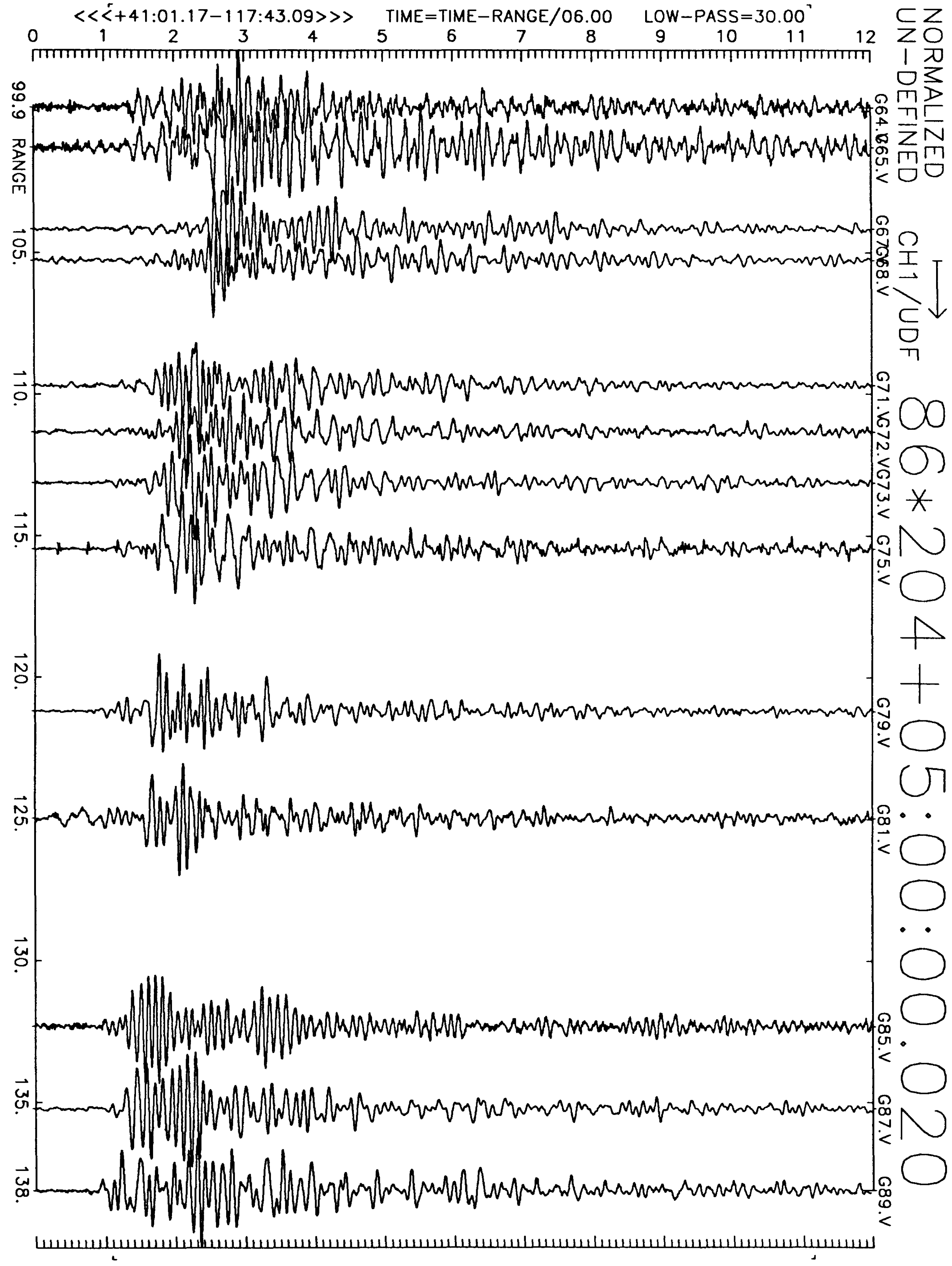

Figure A1(a), shot point 8: 12 second velocity record. Positive vertical motion is to right. Abscissa is distance to shot point. Top of trace is labeled with station number. Times are reduced by 6 km/sec. Shot time is indicated.

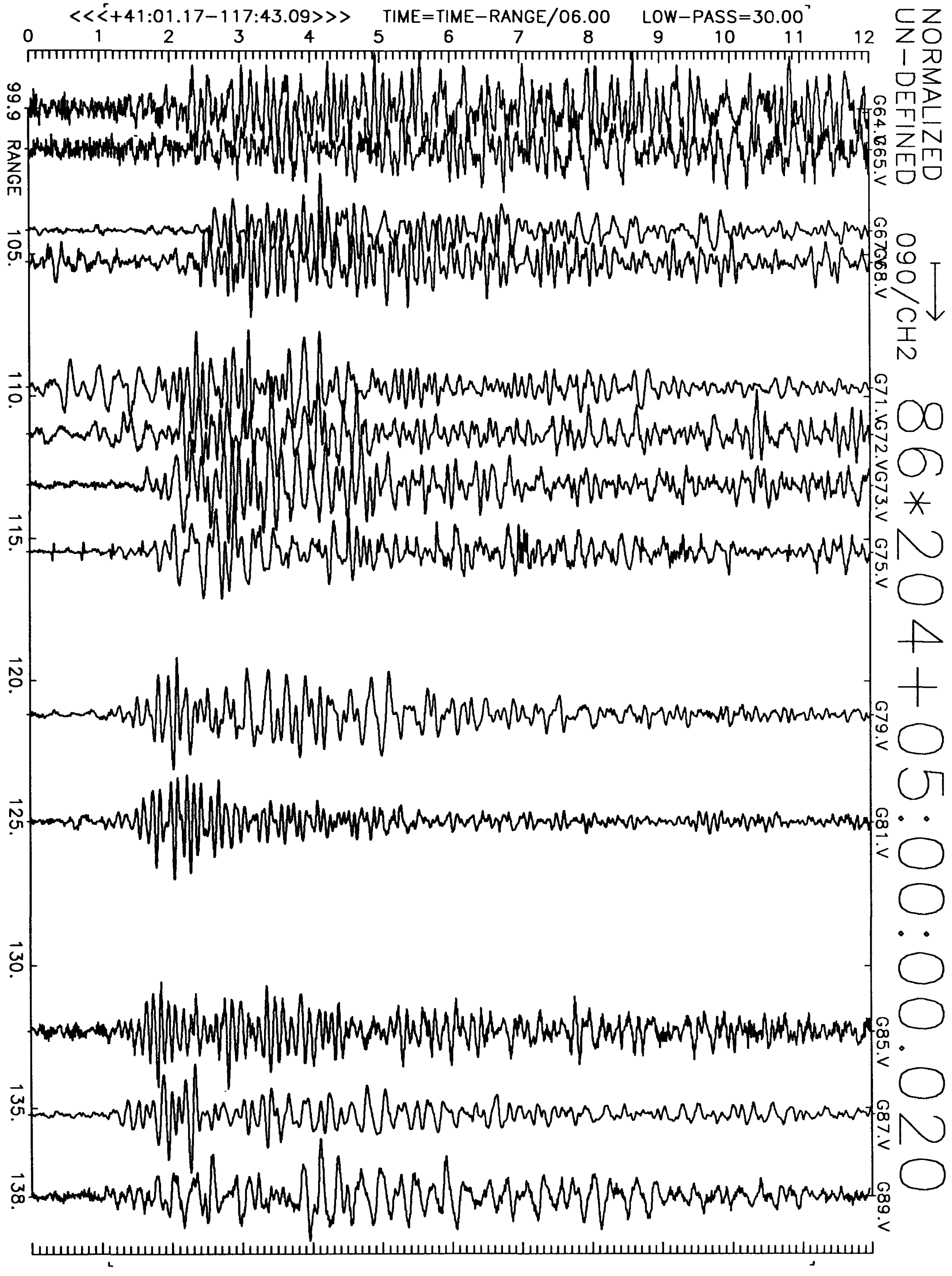

Figure A1(b), shot point 8: 12 second velocity record. Positive N16E motion is to right. Abscissa is distance to shot point. Top of trace is labeled with station number. Times are reduced by 6 km/sec. Shot time is indicated.

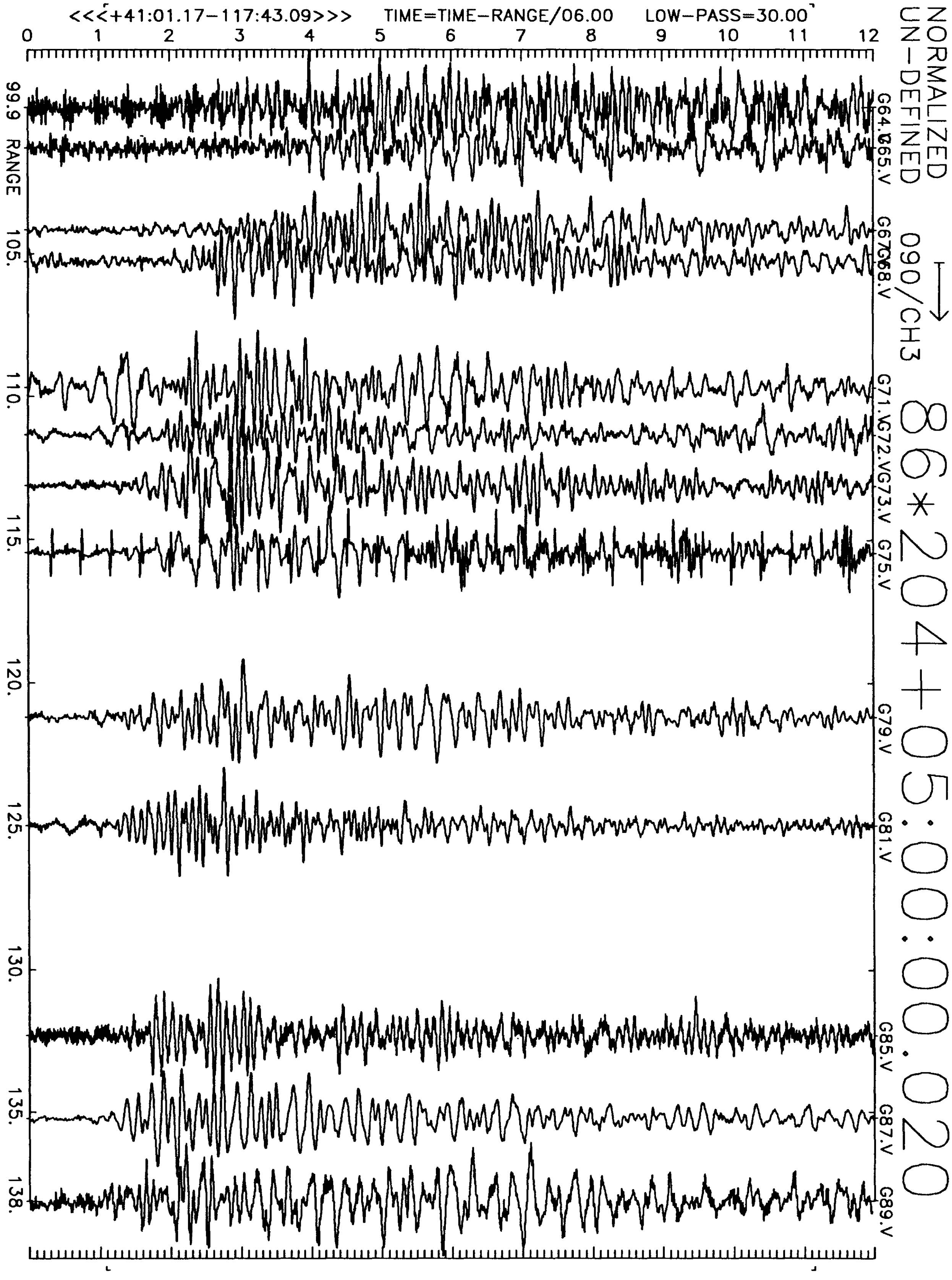

Figure A1(c), shot point 8: 12 second velocity record. Positive N106E motion is to right. Abscissa is distance to shot point. Top of trace is labeled with station number. Times are reduced by 6 km/sec. Shot time is indicated.

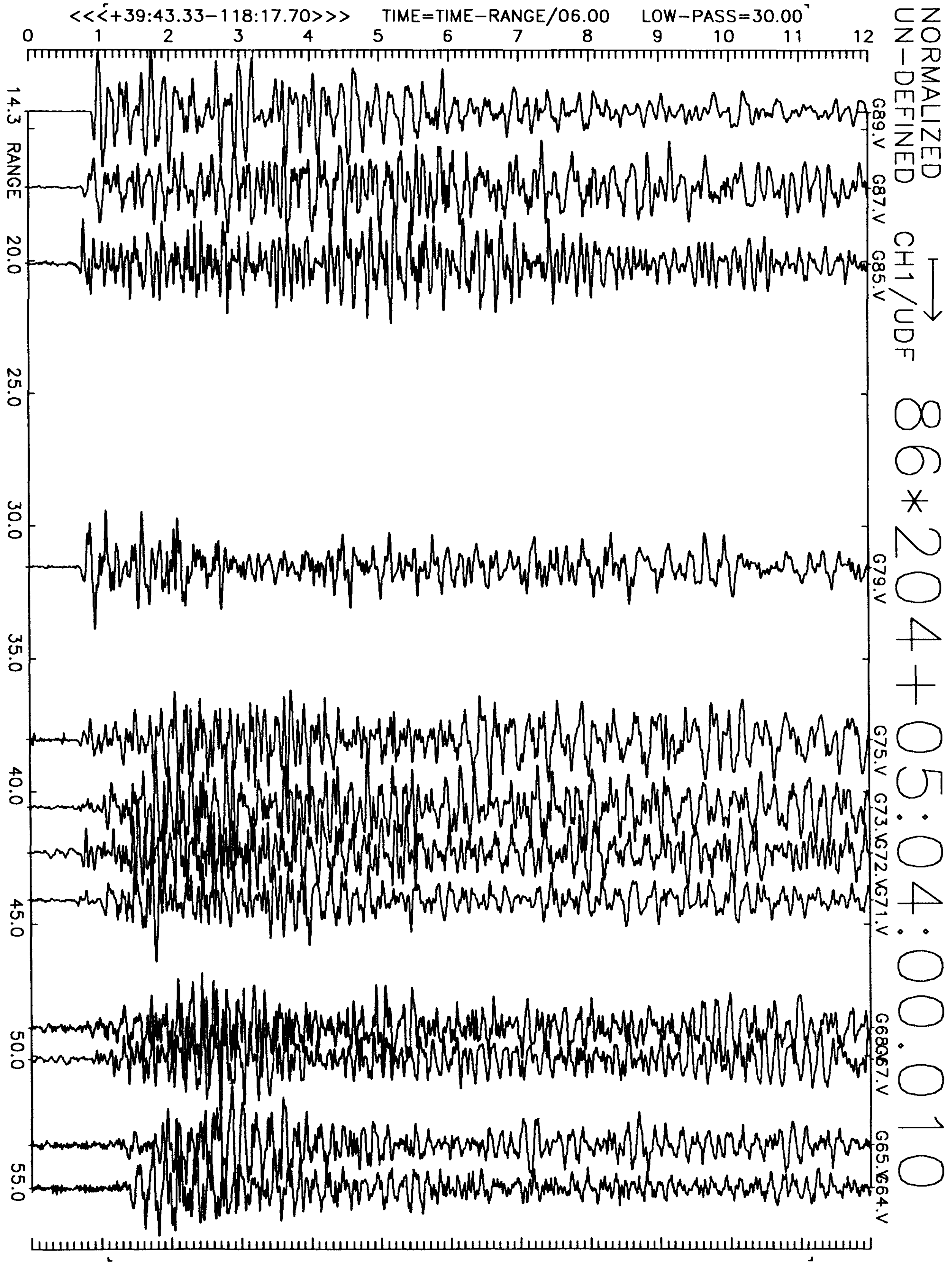

Figure A2(a), shot point 10: 12 second velocity record. Positive vertical motion is to right. Abscissa is distance to shot point. Top of trace is labeled with station number. Times are reduced by 6 km/sec. Shot time is indicated.

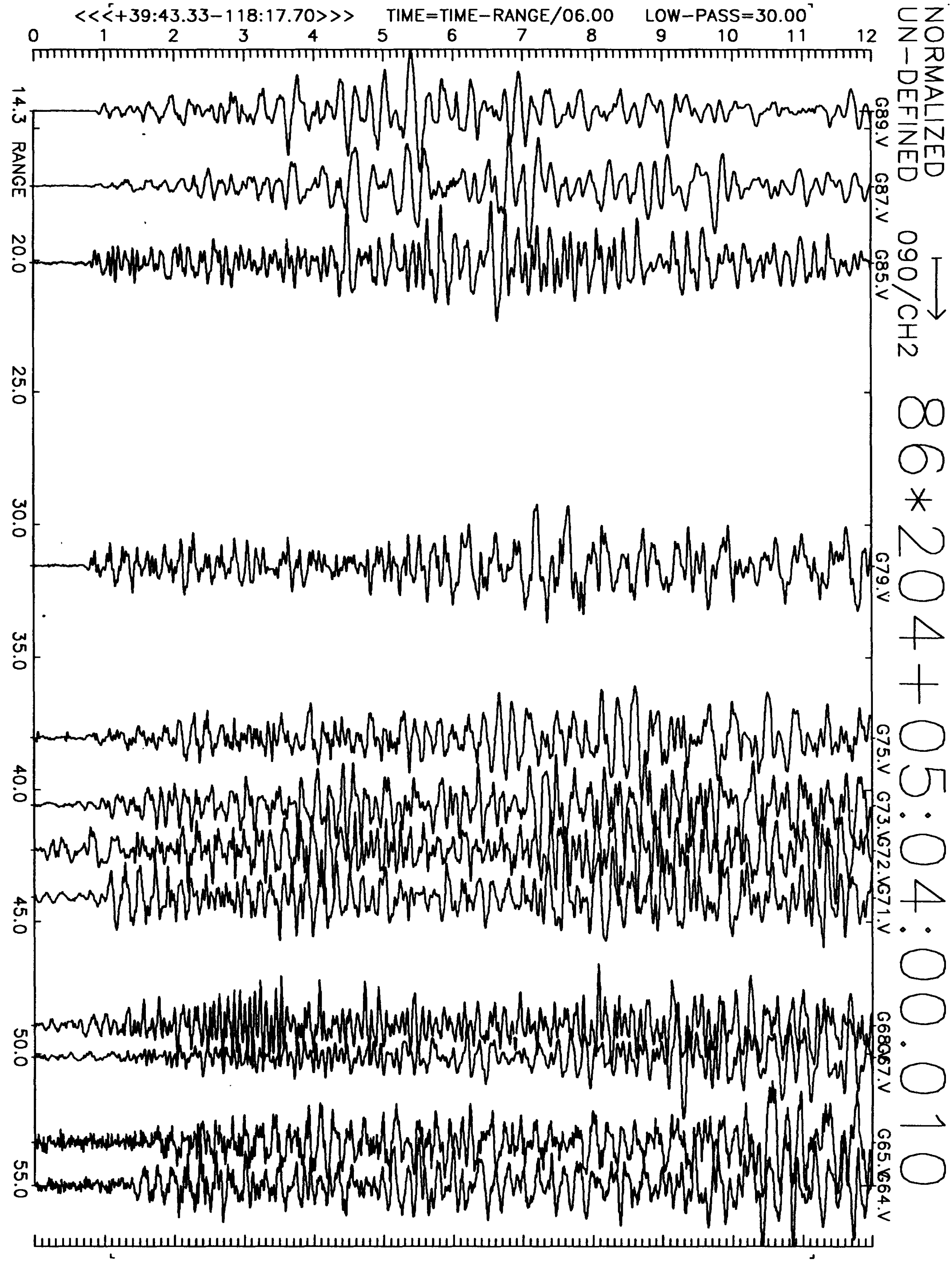

Figure A2(b), shot point 10: 12 second velocity record. Positive N16E motion is to right. Abscissa is distance to shot point. Top of trace is labeled with station number. Times are reduced by 6 km/sec. Shot time is indicated.

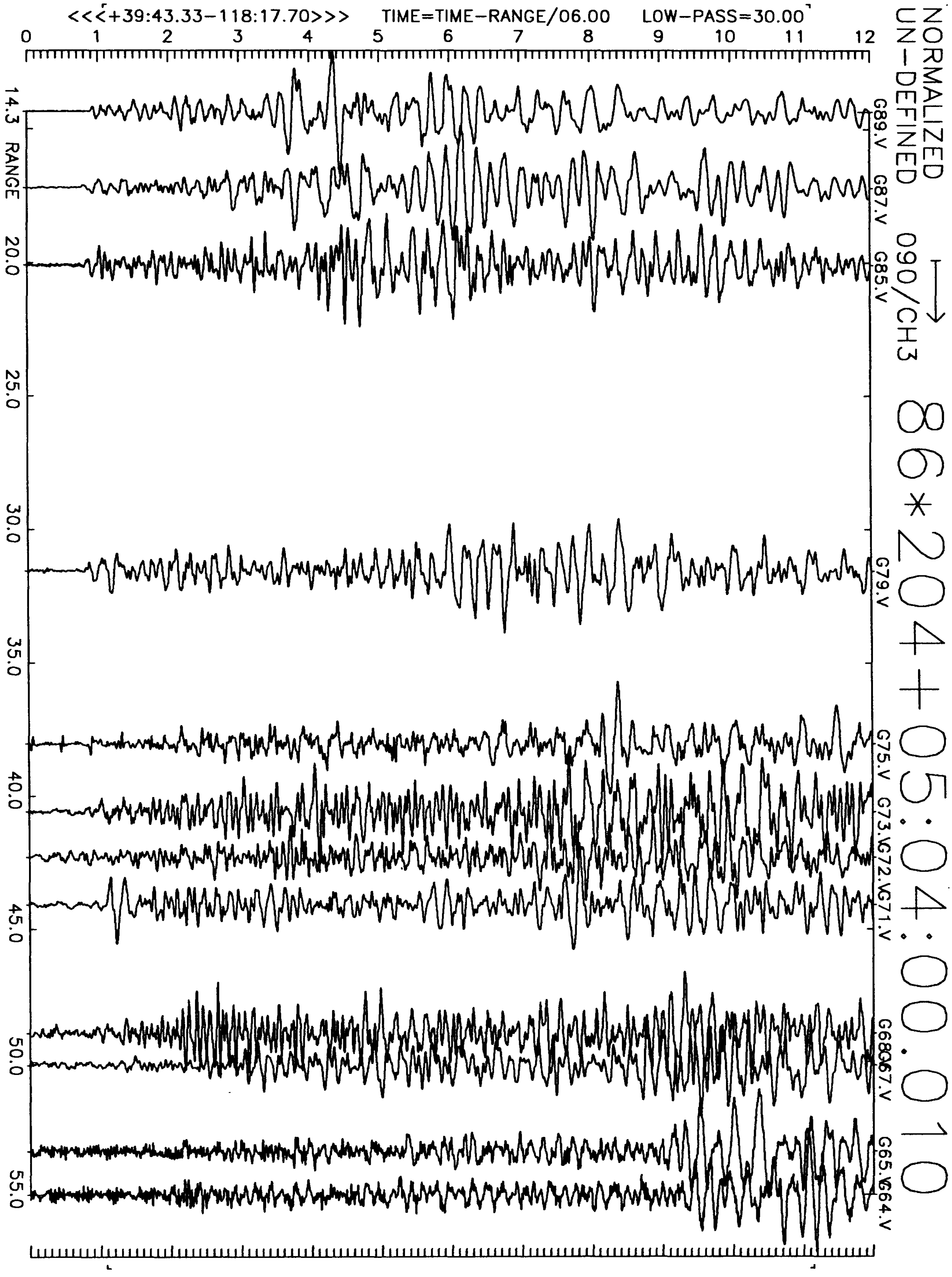

Figure A2(c), shot point 10: 12 second velocity record. Positive N106E motion is to right. Abscissa is distance to shot point. Top of trace is labeled with station number. Times are reduced by 6 km/sec. Shot time is indicated.

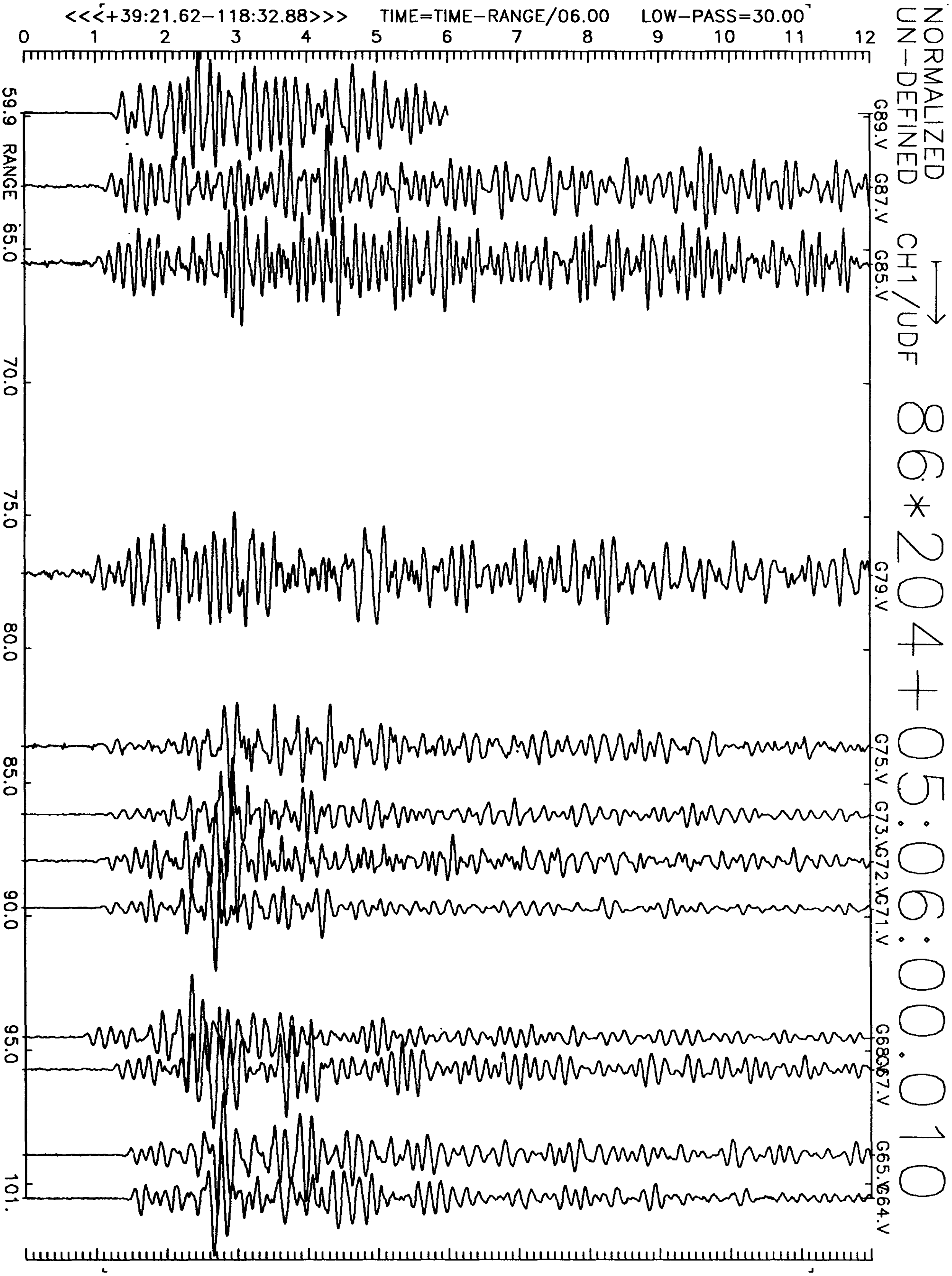

Figure A3(a), shot point 11: 12 second velocity record. Positive vertical motion is to right. Abscissa is distance to shot point. Top of trace is labeled with station number. Times are reduced by 6 km/sec. Shot time is indicated.

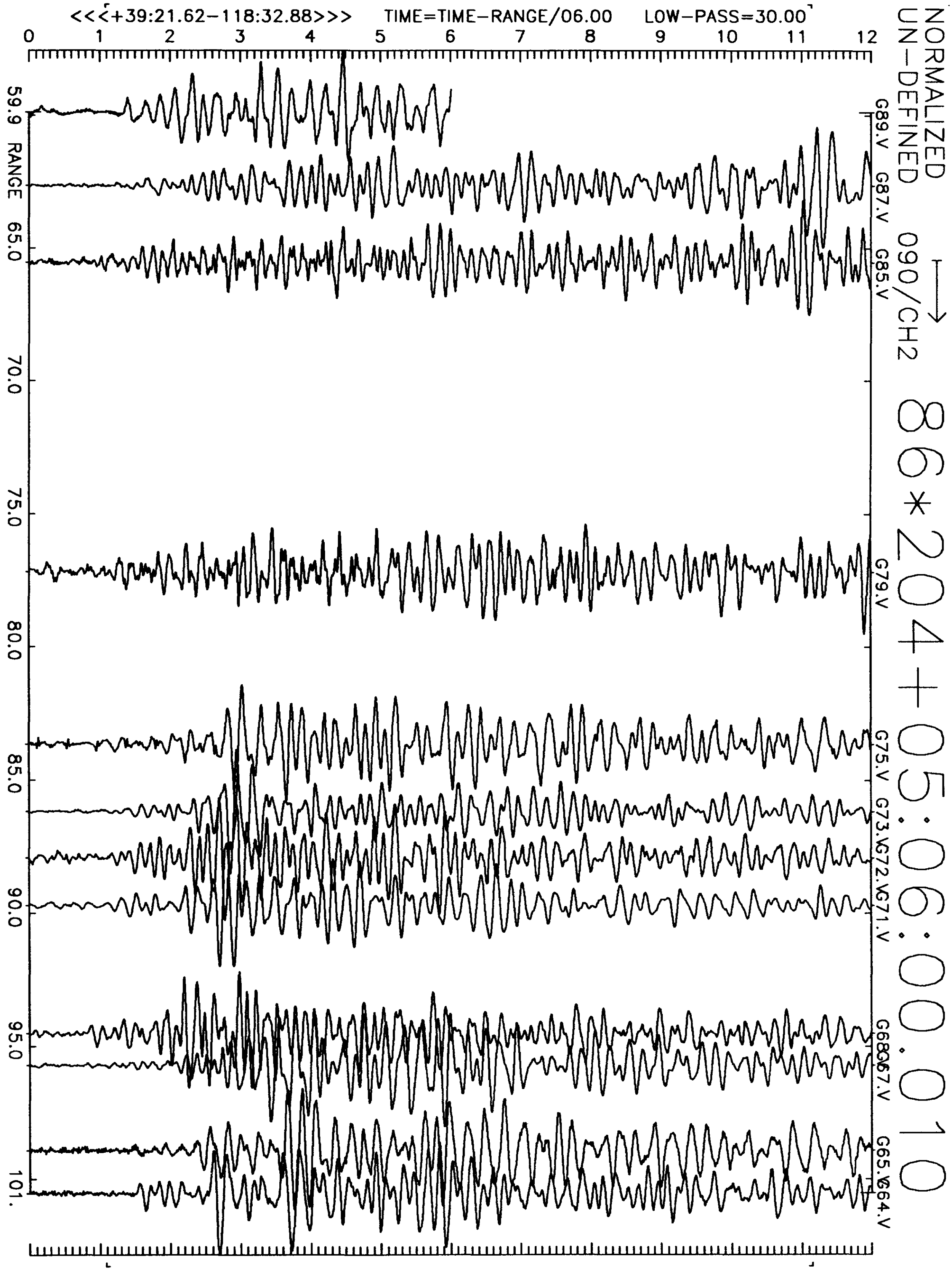

Figure A3(b), shot point 11: 12 second velocity record. Positive N16E motion is to right. Abscissa is distance to shot point. Top of trace is labeled with station number. Times are reduced by 6 km/sec. Shot time is indicated.

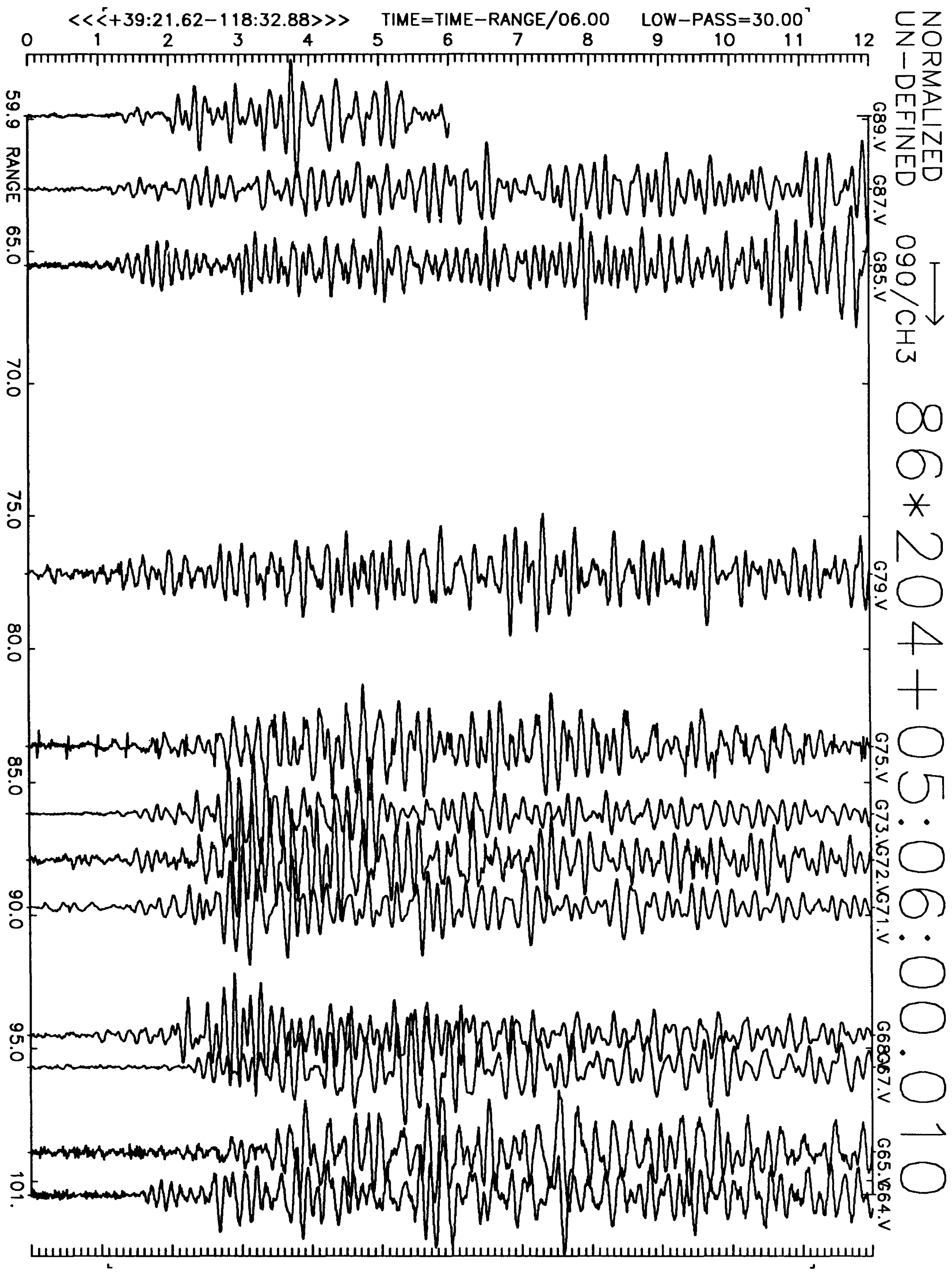

Figure A3(c), shot point 11: 12 second velocity record. Positive N106E motion is to right. Abscissa is distance to shot point. Top of trace is labeled with station number. Times are reduced by 6 km/sec. Shot time is indicated.

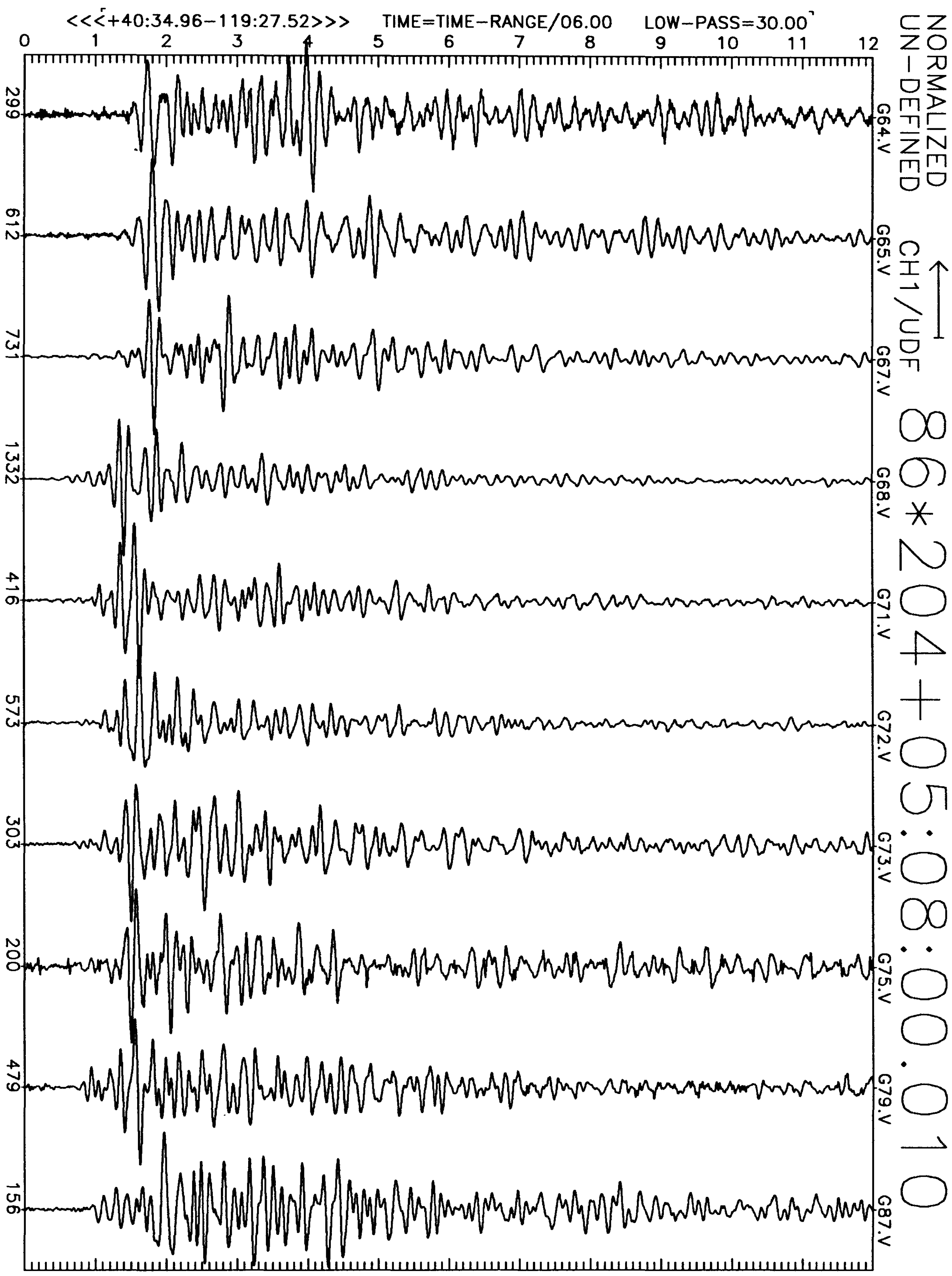

Figure A4(a), shot point 1: 12 second vertical velocity record. Abscissa is labeled with maximum counts in record (multiply by $\frac{10}{2^{24}-2^{5}} \approx 6 \times 10^{-7}$ to get cm/sec). Times are reduced by 6 km/sec. Shot time is indicated.

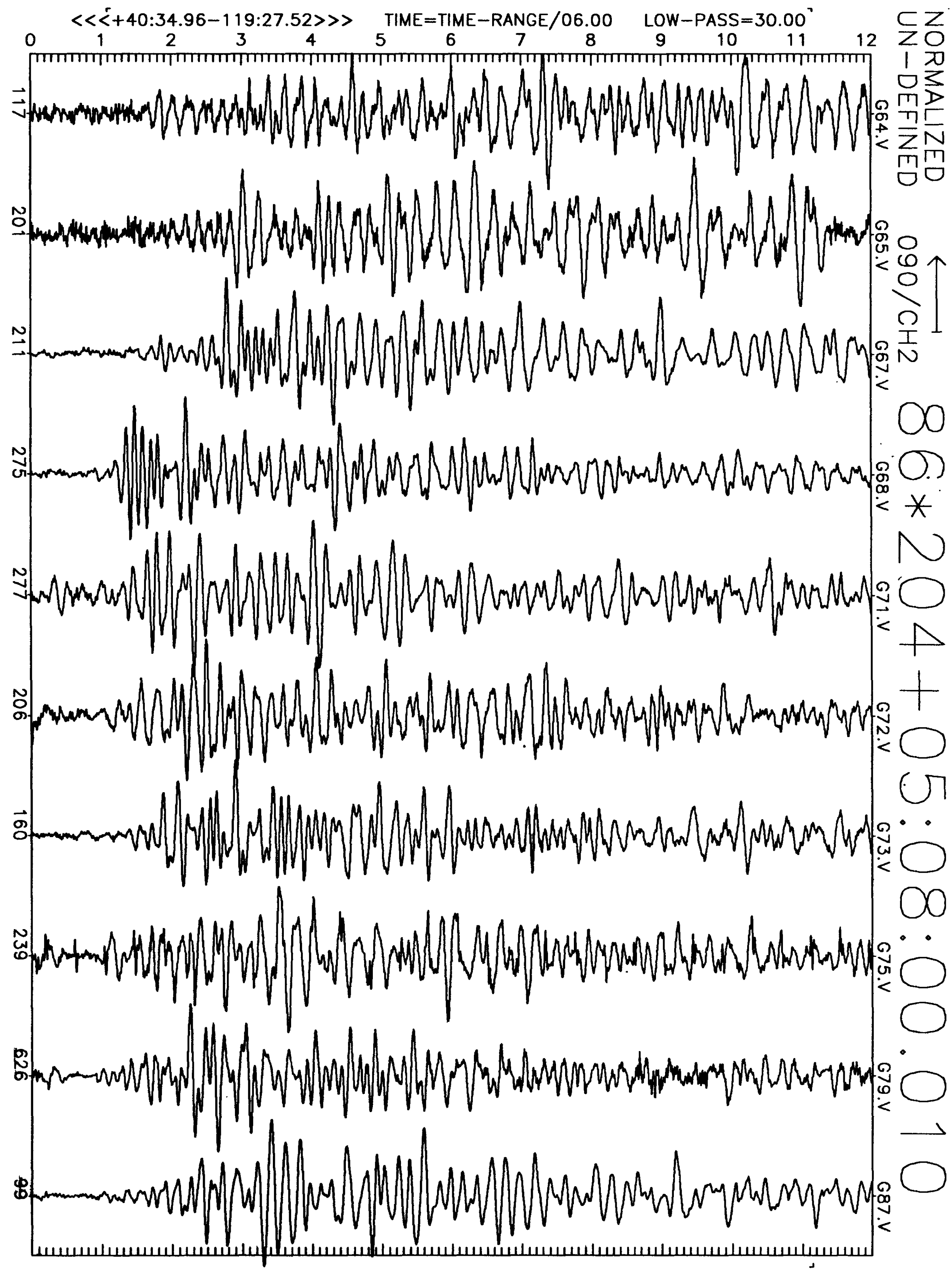

Figure A4(b), shot point 1: 12 second N16E velocity record. Abscissa is labeled with maximum counts in record (multiply by $\frac{10}{2^{24}-2^{9}} \approx 6 \times 10^{-7}$ to get cm/sec). Times are reduced by 6 km/sec. Shot time is indicated.

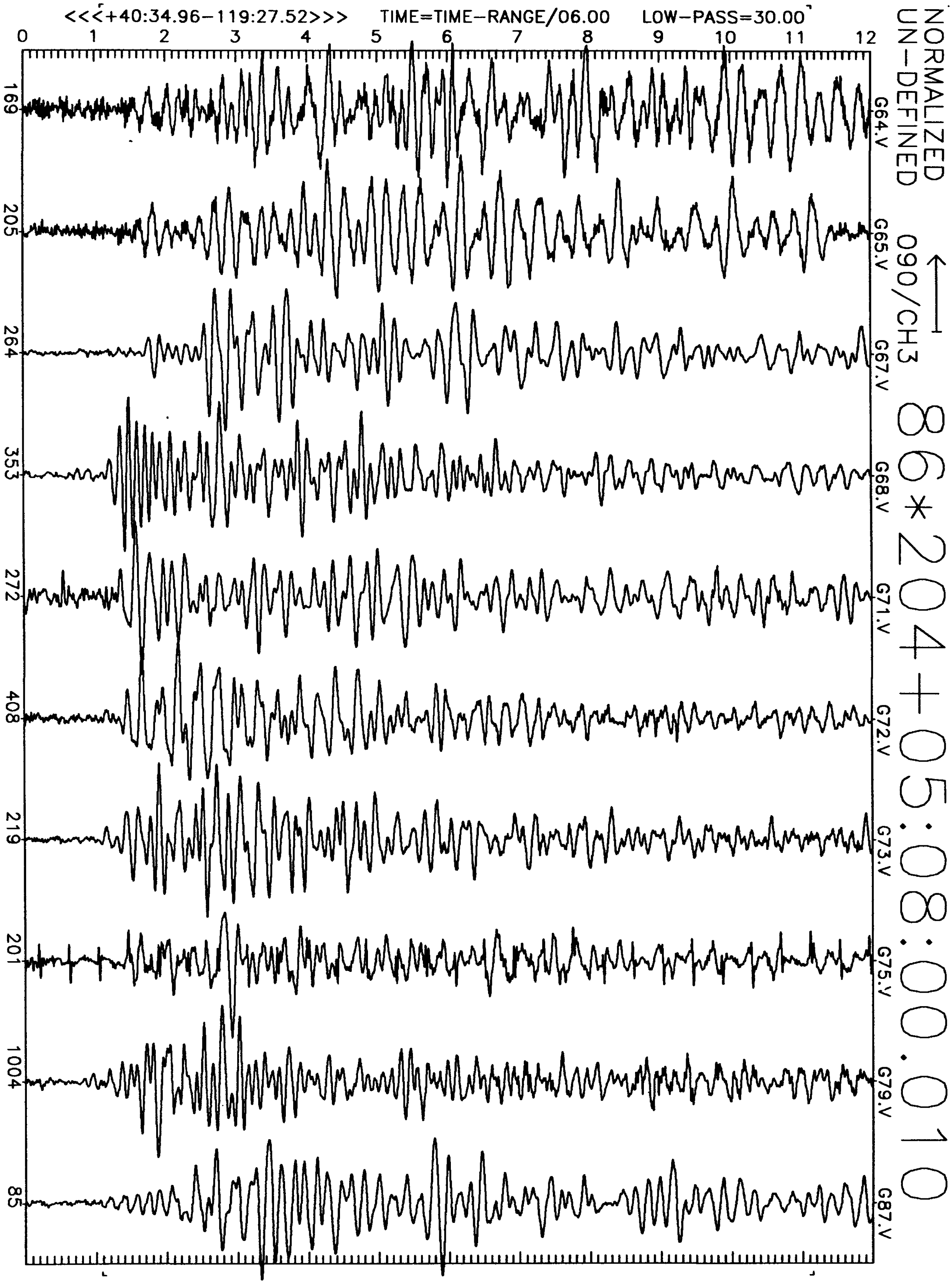

Figure A4(c), shot point 1: 12 second N106E velocity record. Abscissa is labeled with maximum counts in record (multiply by $\frac{10}{2^{24}-2^{9}} \approx 6 \times 10^{-7}$ to get cm/sec). Times are reduced by 6 km/sec. Shot time is indicated.

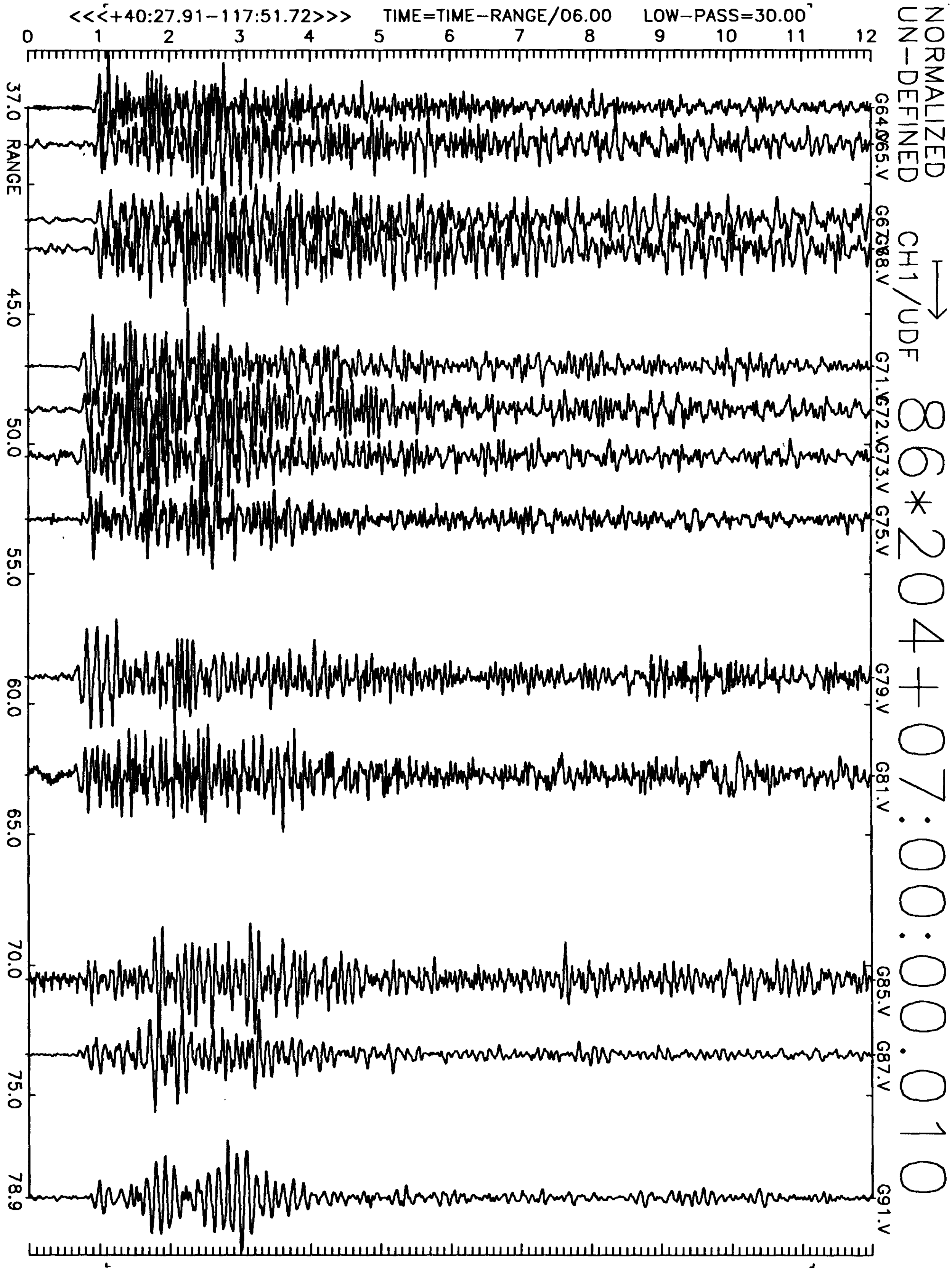

Figure A5(a), shot point 9: 12 second velocity record. Positive vertical motion is to right. Abscissa is distance to shot point. Top of trace is labeled with station number. Times are reduced by 6 km/sec. Shot time is indicated.

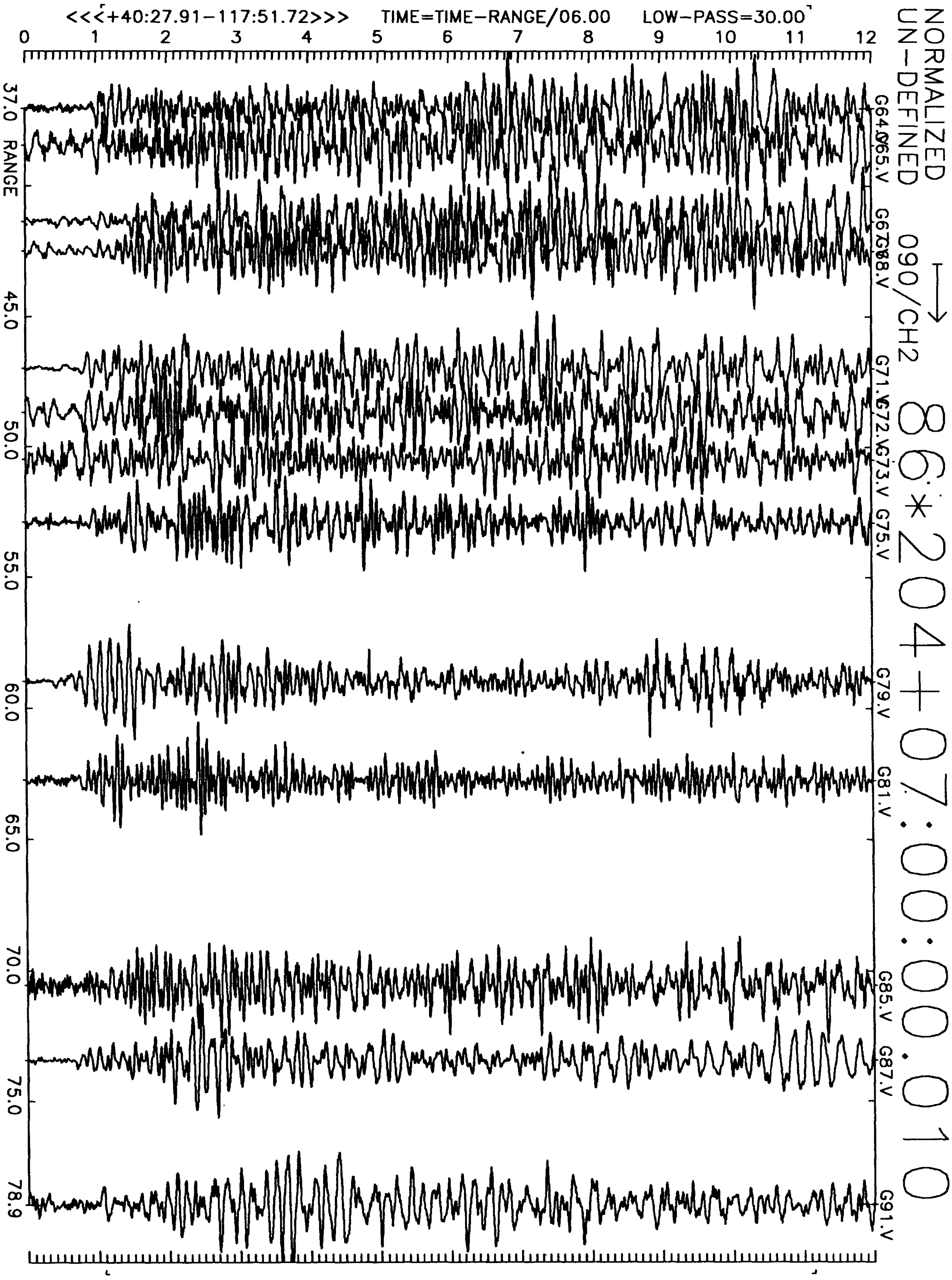

Figure A5(b), shot point 9: 12 second velocity record. Positive N16E motion is to right. Abscissa is distance to shot point. Top of trace is labeled with station number. Times are reduced by 6 km/sec. Shot time is indicated.

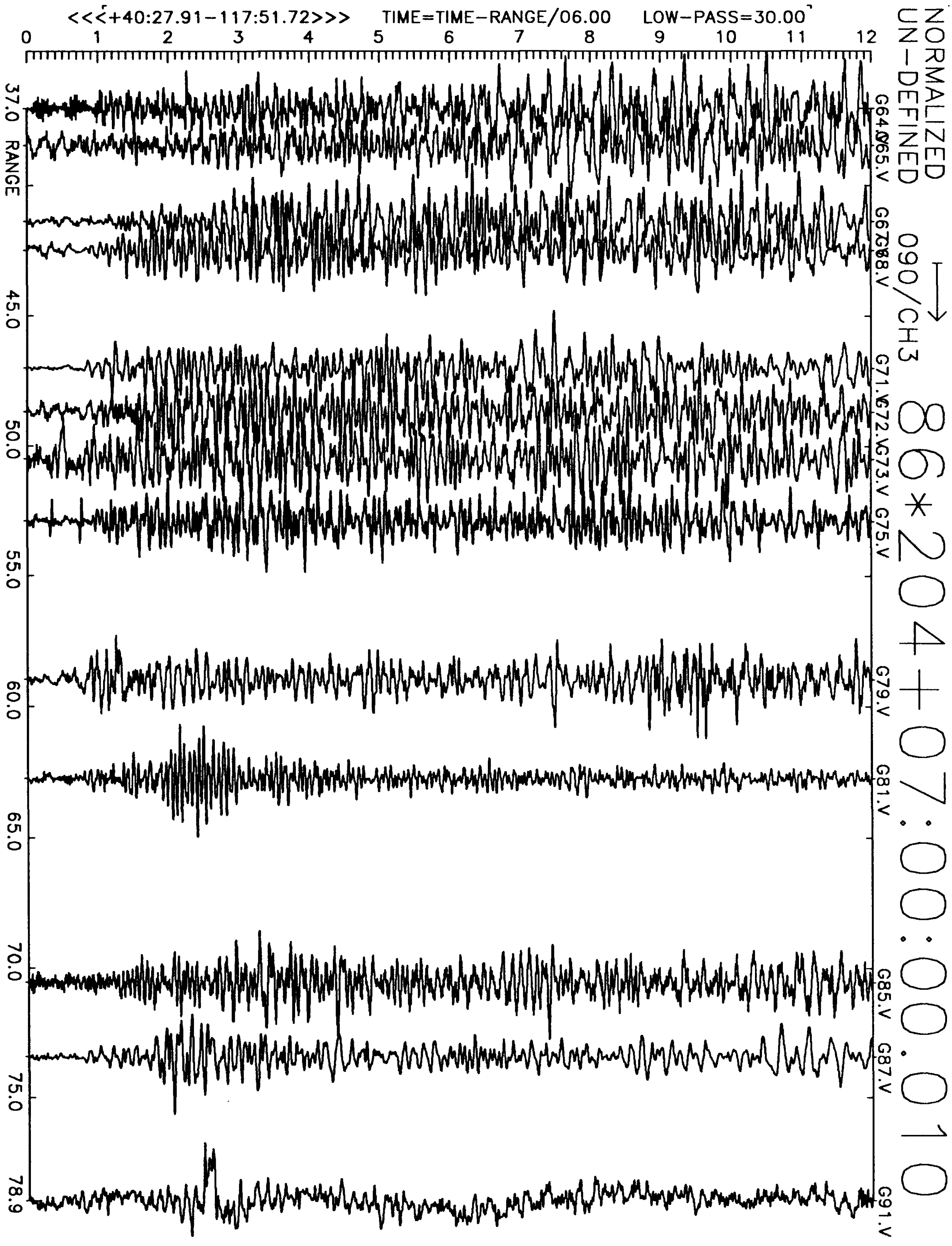

Figure A5(c), shot point 9: 12 second velocity record. Positive N106E motion is to right. Abscissa is distance to shot point. Top of trace is labeled with station number. Times are reduced by 6 km/sec. Shot time is indicated.

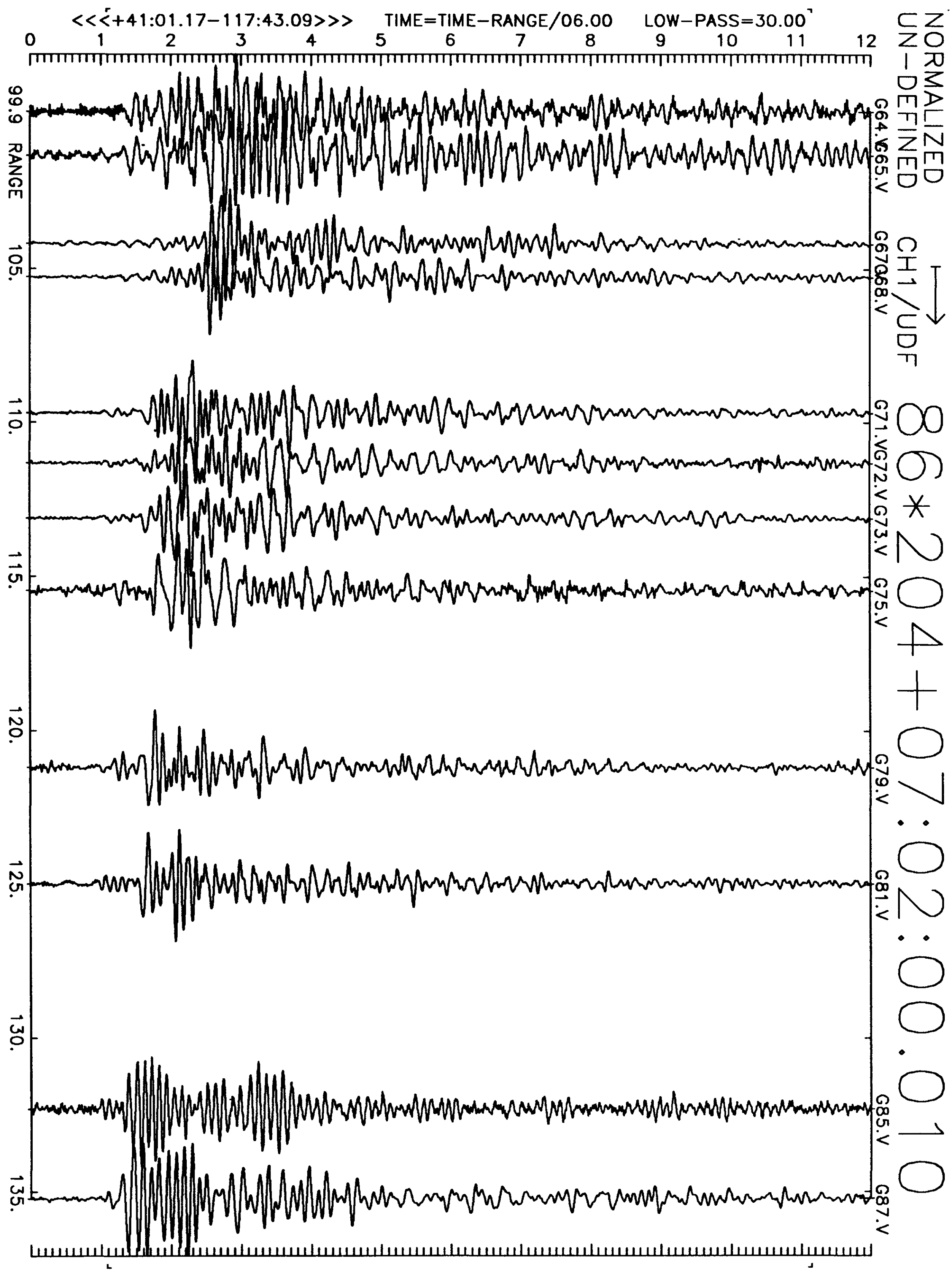

Figure A6(a), shot point 8: 12 second velocity record. Positive vertical motion is to right. Abscissa is distance to shot point. Top of trace is labeled with station number. Times are reduced by 6 km/sec. Shot time is indicated.

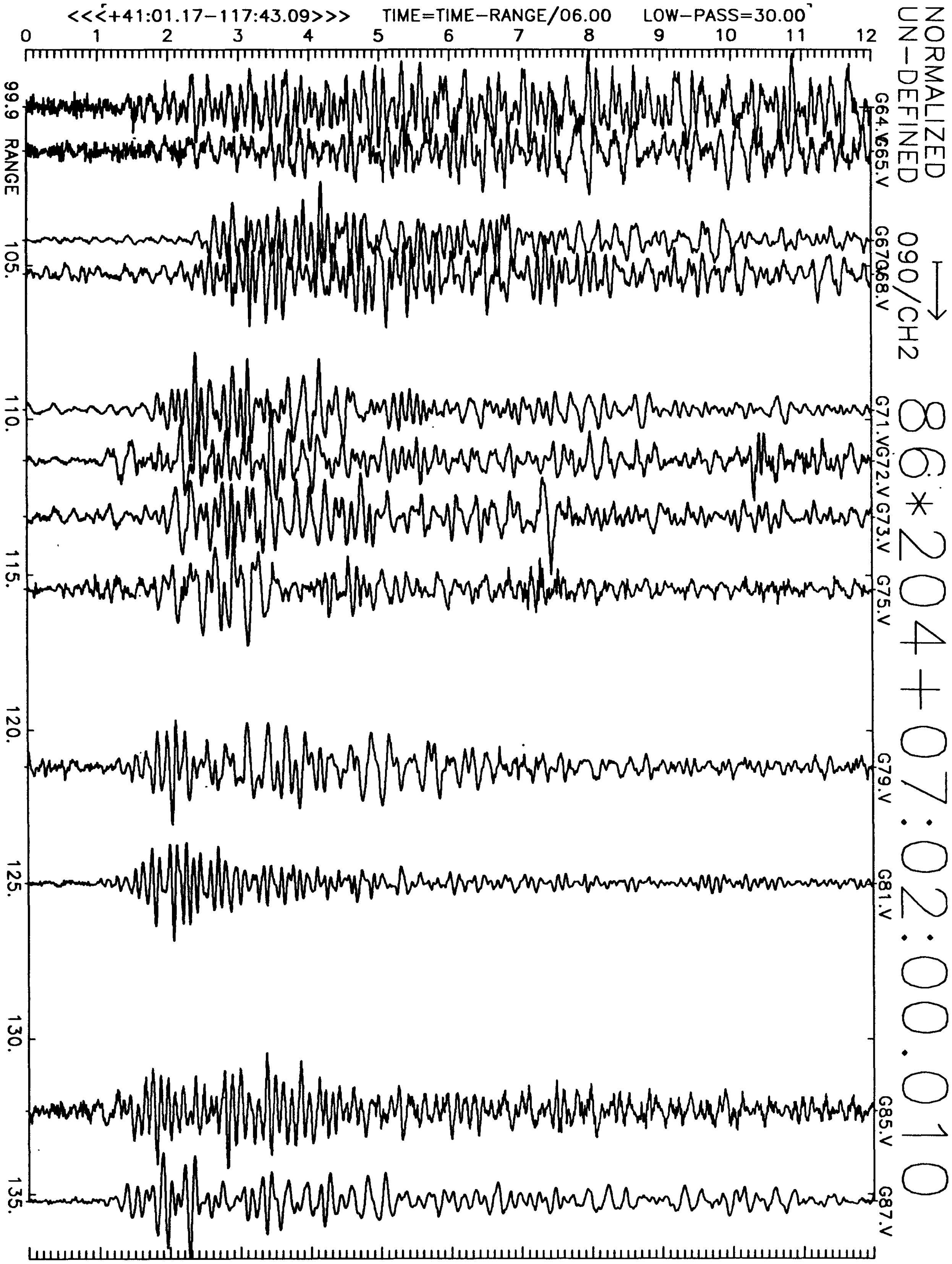

Figure A6(b), shot point 8: 12 second velocity record. Positive N16E motion is to right. Abscissa is distance to shot point. Top of trace is labeled with station number. Times are reduced by 6 km/sec. Shot time is indicated.

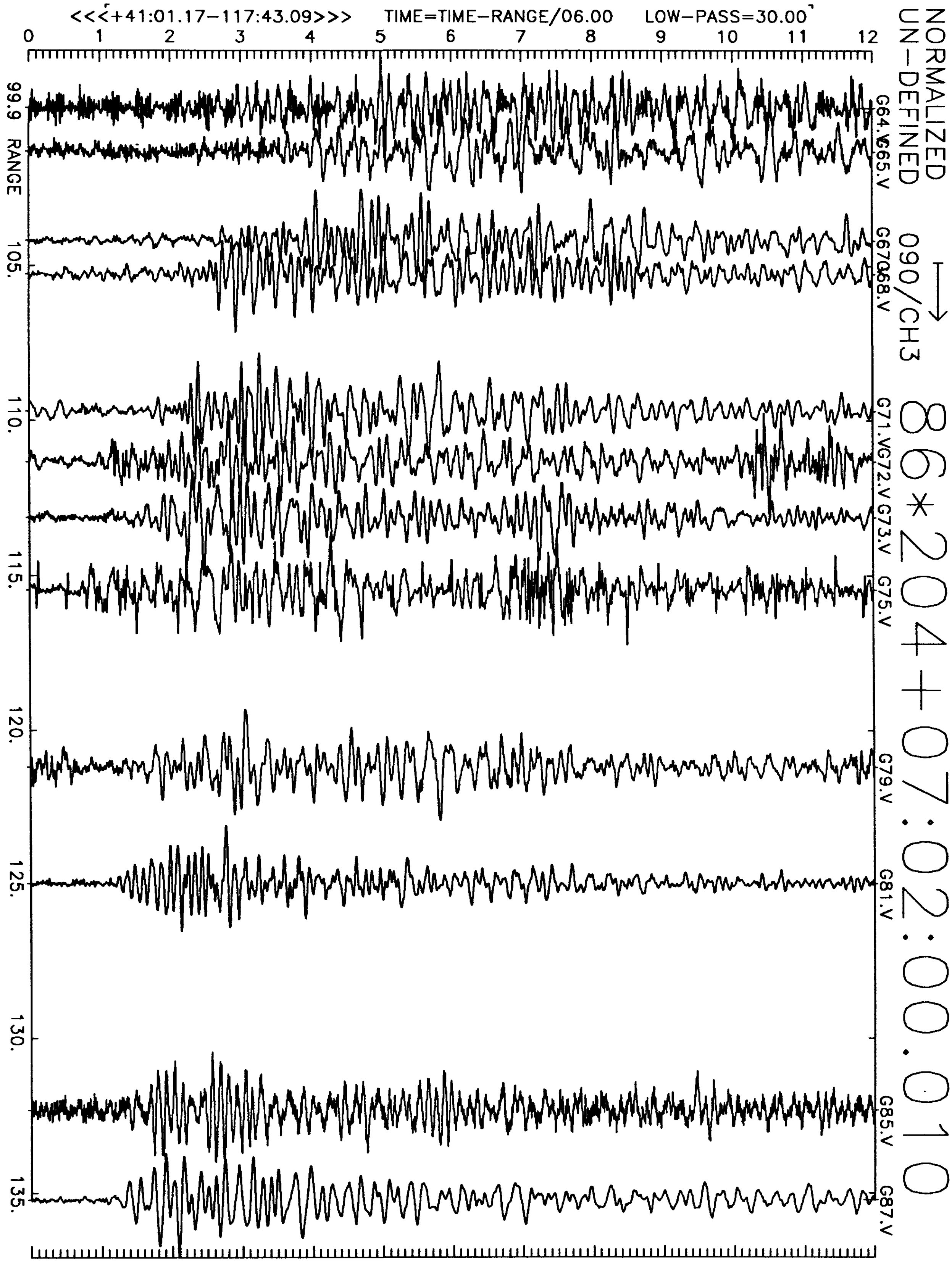

Figure A6(c), shot point 8: 12 second velocity record. Positive N106E motion is to right. Abscissa is distance to shot point. Top of trace is labeled with station number. Times are reduced by 6 km/sec. Shot time is indicated.

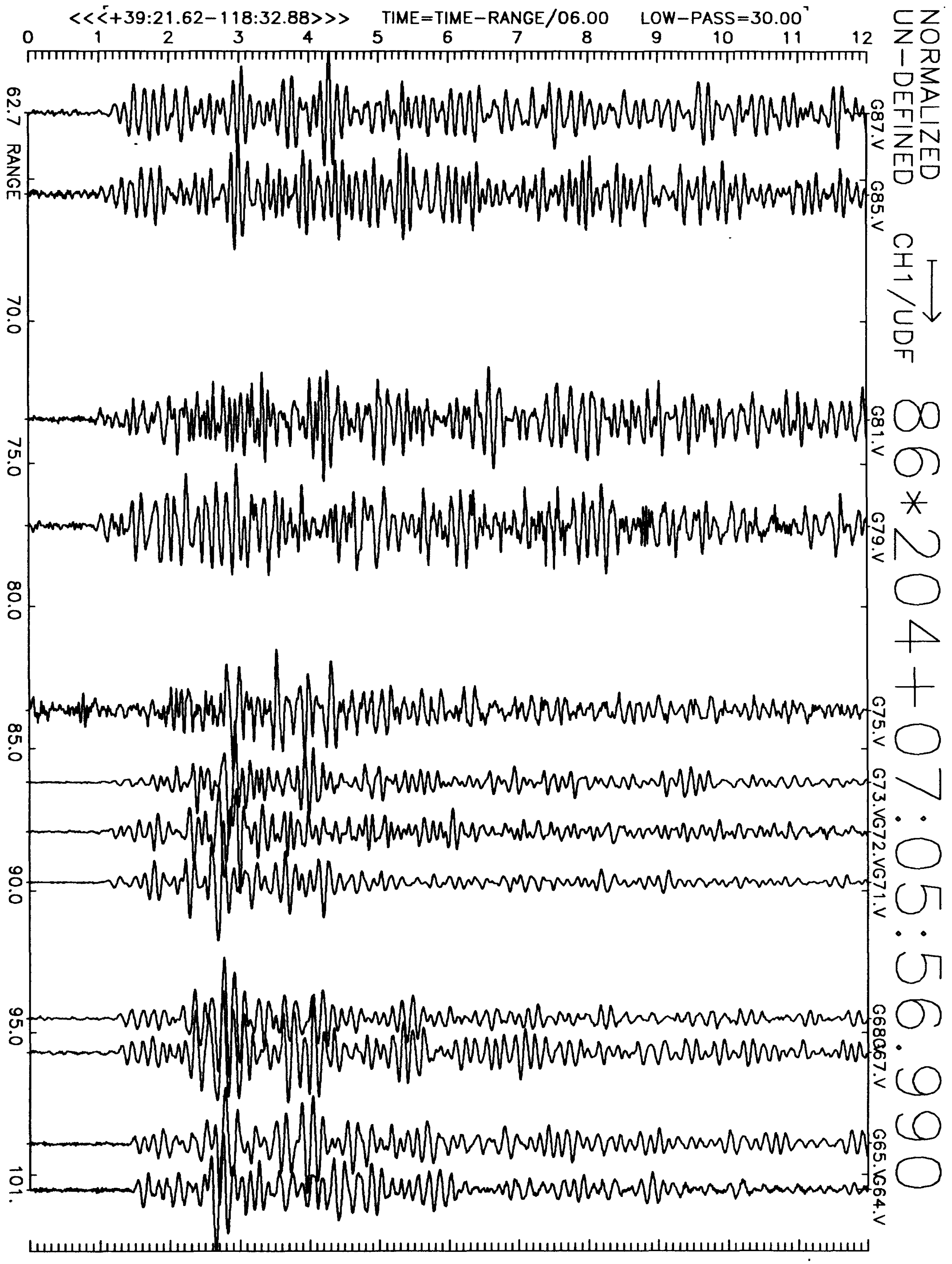

Figure A7(a), shot point 11: 12 second velocity record. Positive vertical motion is to right. Abscissa is distance to shot point. Top of trace is labeled with station number. Times are reduced by 6 km/sec. Shot time is indicated.

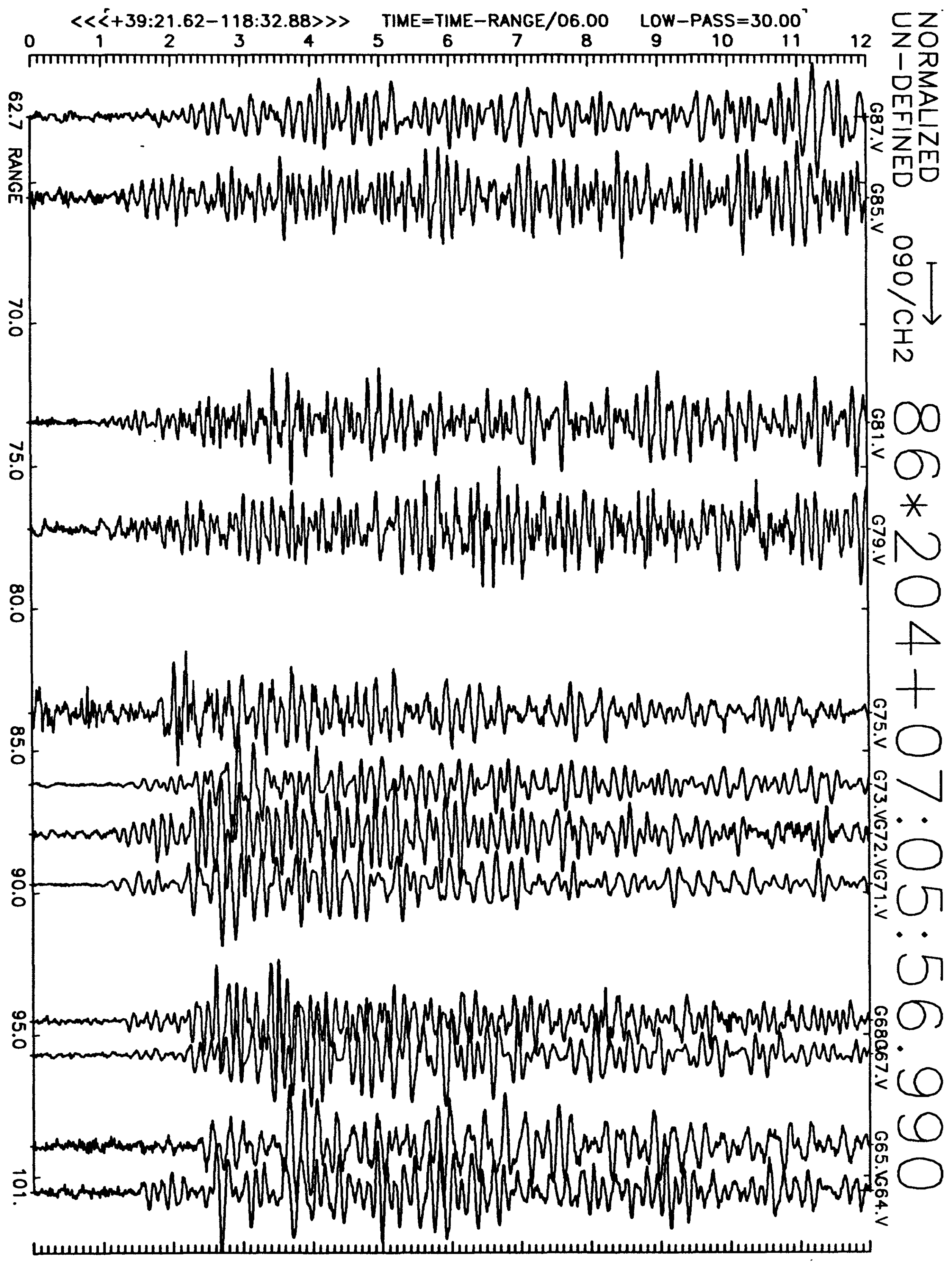

Figure A7(b), shot point 11: 12 second velocity record. Positive N16E motion is to right. Abscissa is distance to shot point. Top of trace is labeled with station number. Times are reduced by 6 km/sec. Shot time is indicated.

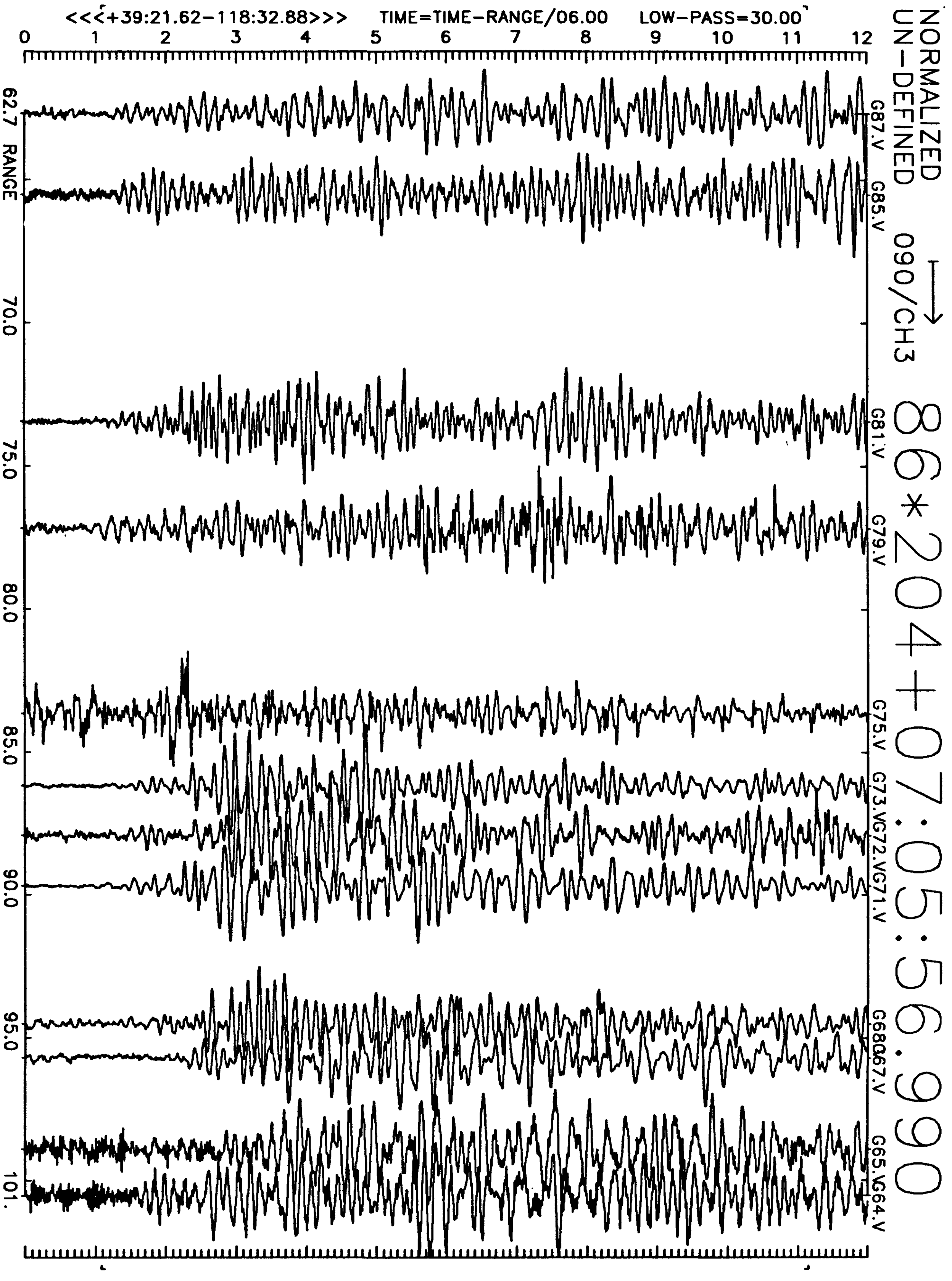

Figure A7(c), shot point 11: 12 second velocity record. Positive N106E motion is to right. Abscissa is distance to shot point. Top of trace is labeled with station number. Times are reduced by 6 km/sec. Shot time is indicated.

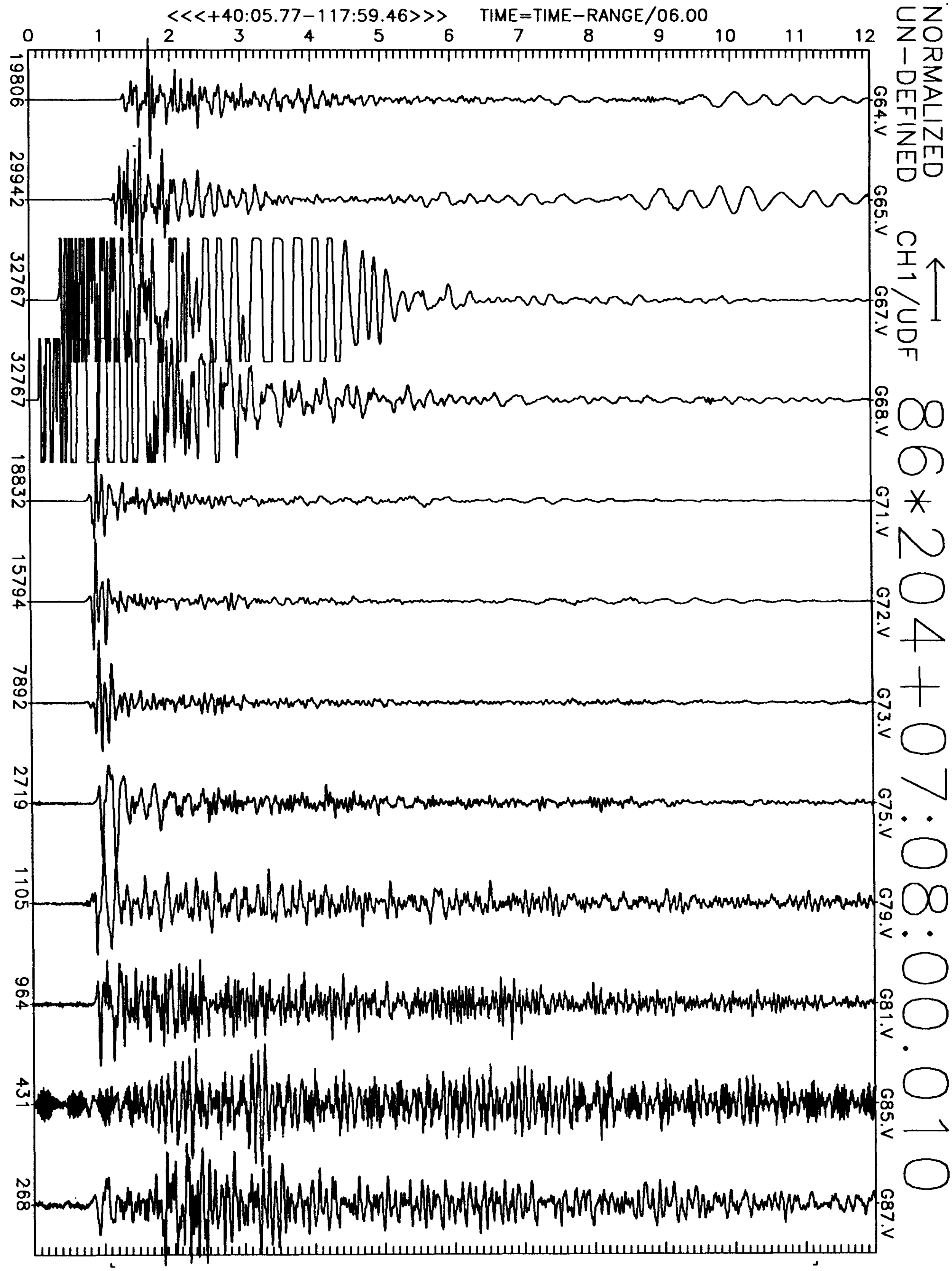

Figure A8(a), shot point 4: 12 second vertical velocity record. Abscissa is labeled with maximum counts in record (multiply by $\frac{10}{2^{24}-2^{8}}$ ≈ 6×10^{-7} to get cm/sec). Times are reduced by 6 km/sec. Shot time is indicated.

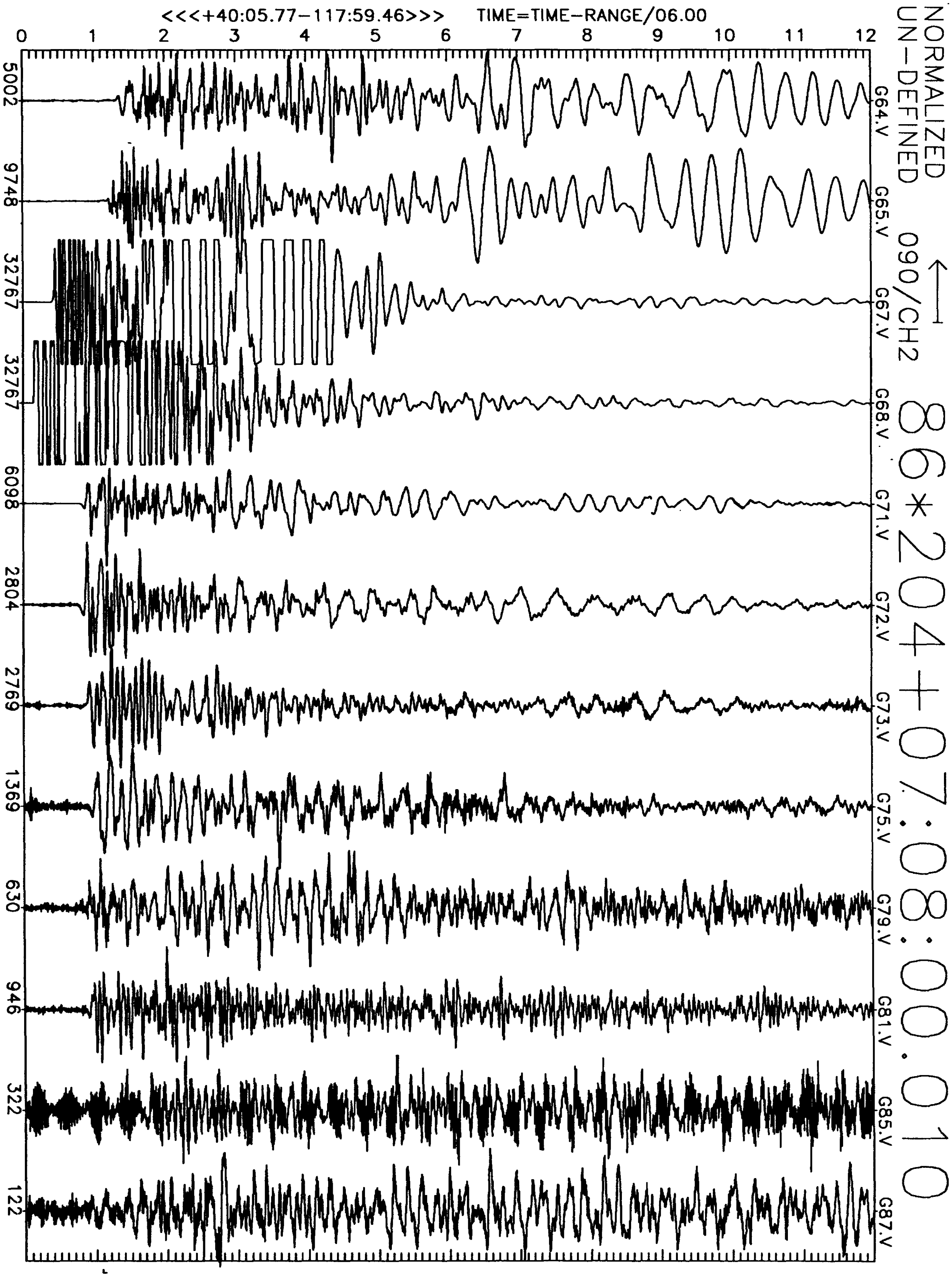

Figure A8(b), shot point 4: 12 second N16E velocity record. Abscissa is labeled with maximum counts in record (multiply by $\frac{10}{2^{24}-2^{9}} \approx 6 \times 10^{-7}$ to get cm/sec). Times are reduced by 6 km/sec. Shot time is indicated.

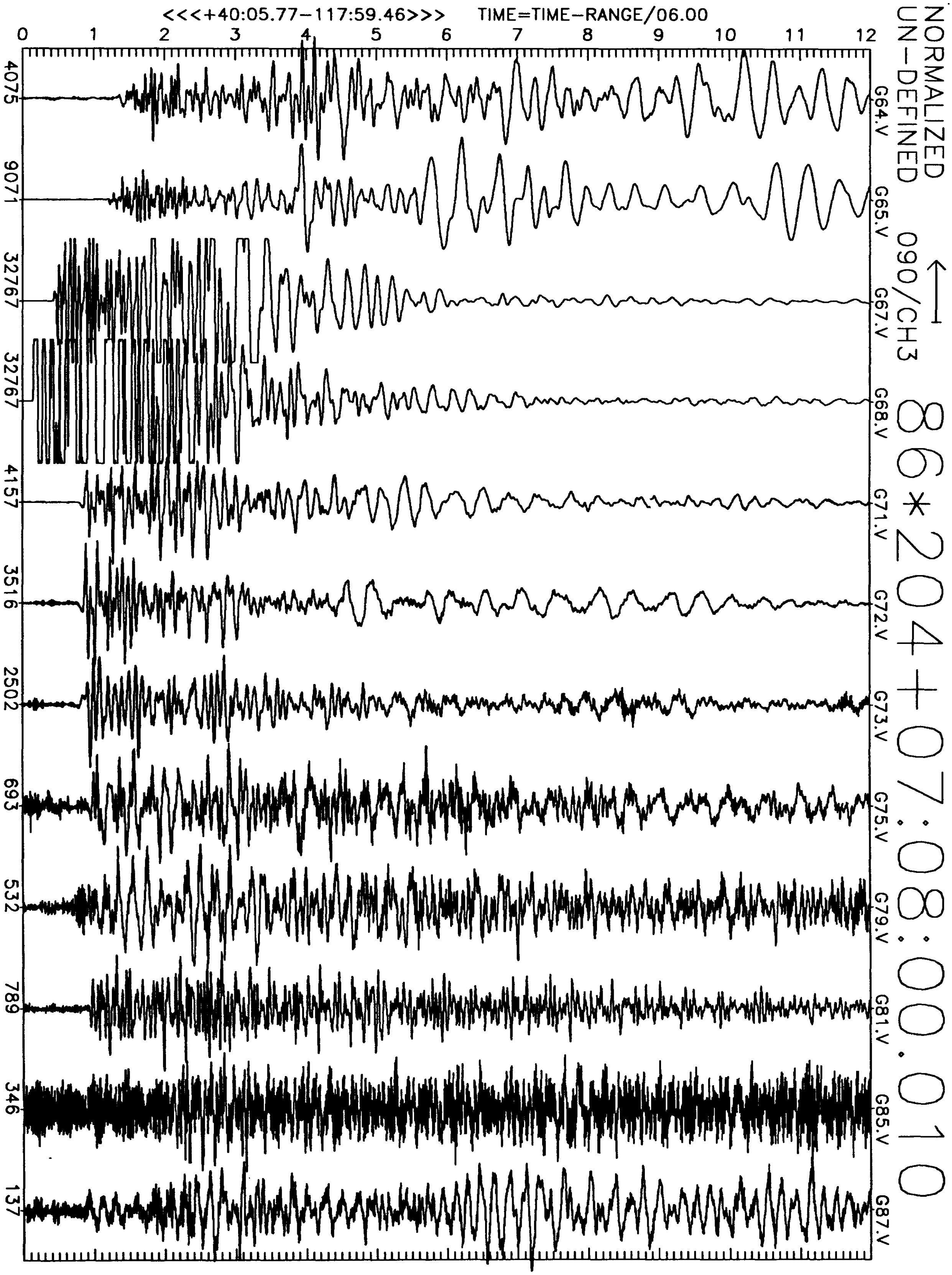

Figure A8(c), shot point 4: 12 second N106E velocity record. Abscissa is labeled with maximum counts in record (multiply by $\frac{10}{2^{24}-2^{8}} \approx 6 \times 10^{-7}$ to get cm/sec). Times are reduced by 6 km/sec. Shot time is indicated.

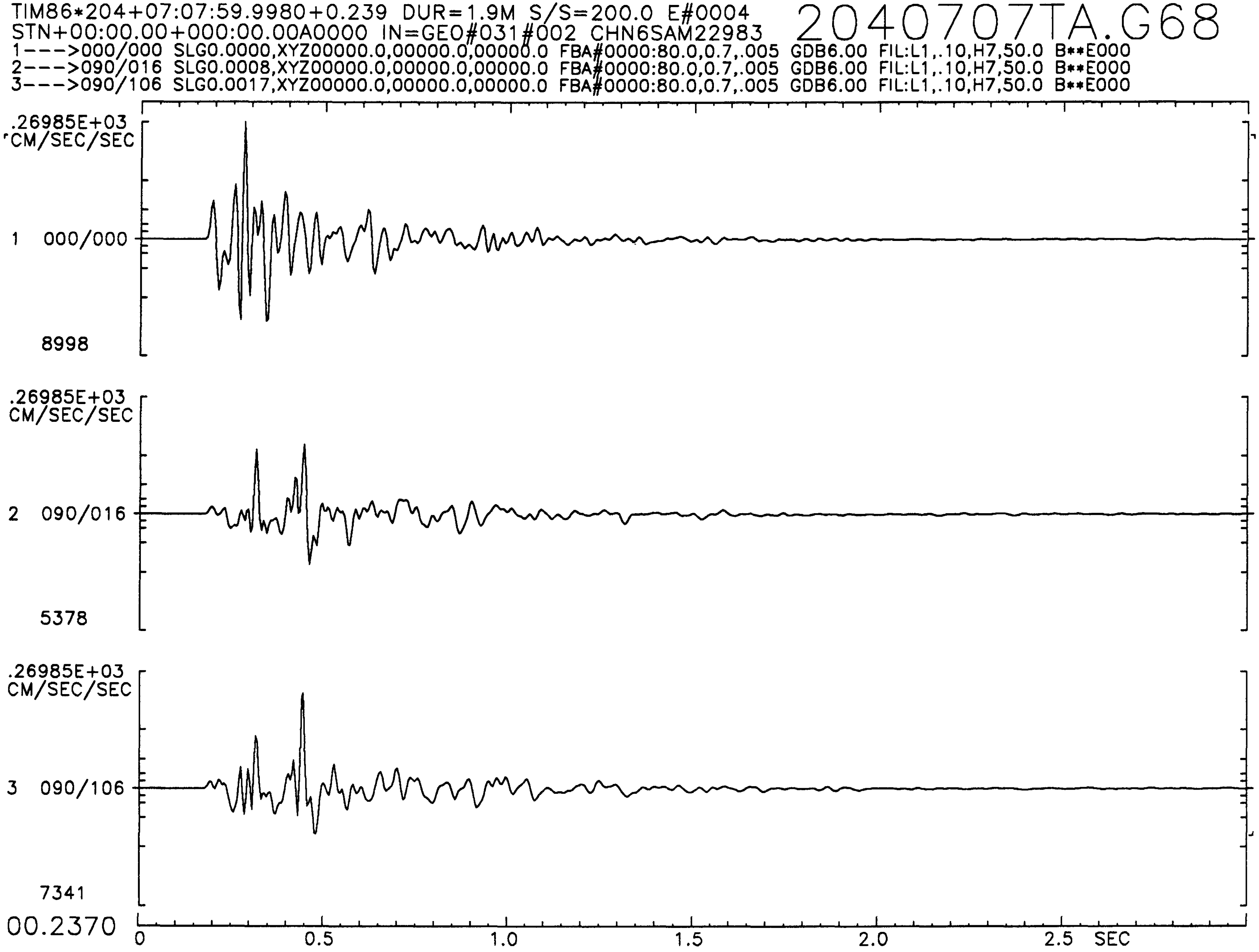

Figure A–9: Three-component acceleration time histories recorded at shotpoint 4.

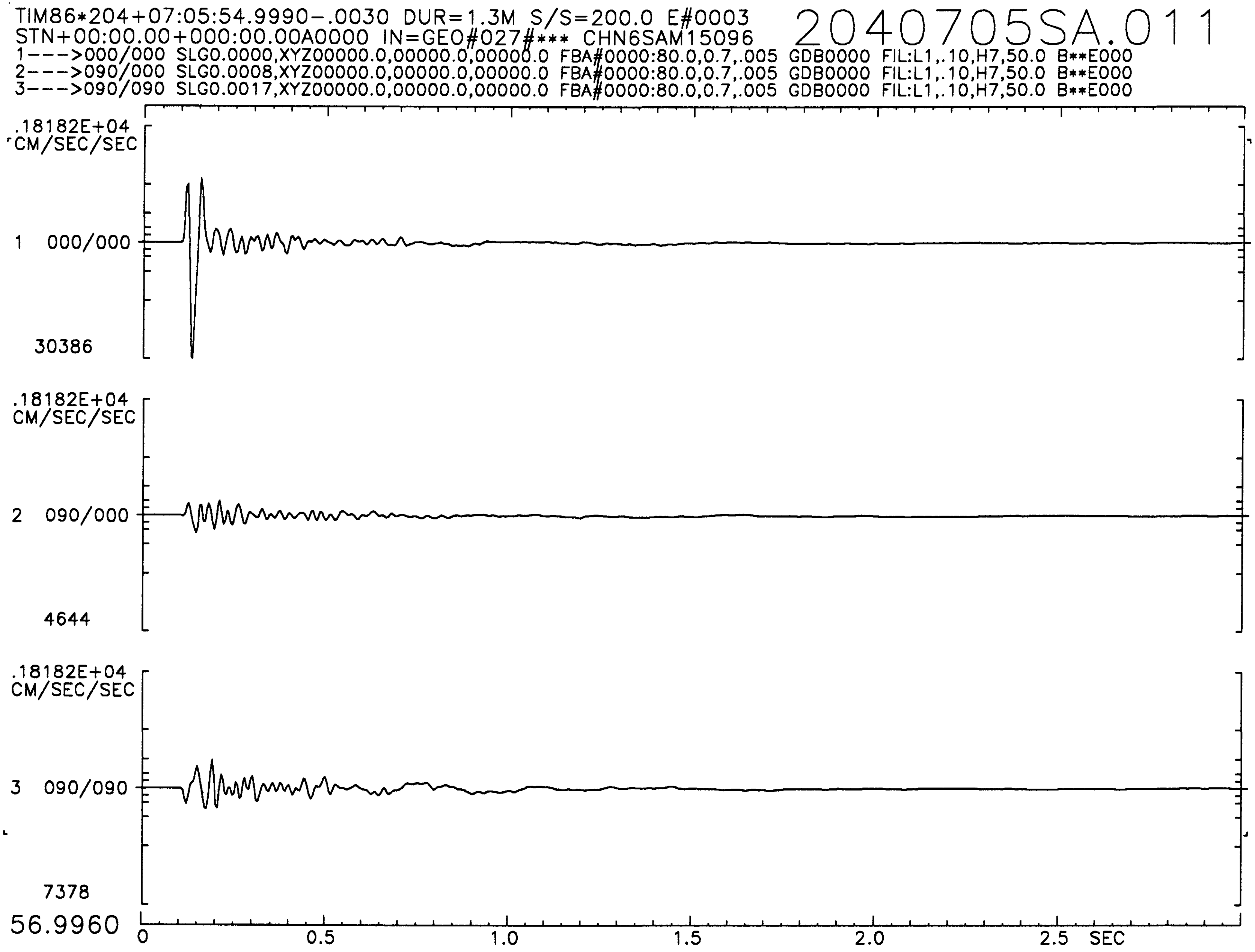

Figure A–10: Three-component acceleration time histories recorded at shotpoint 11.

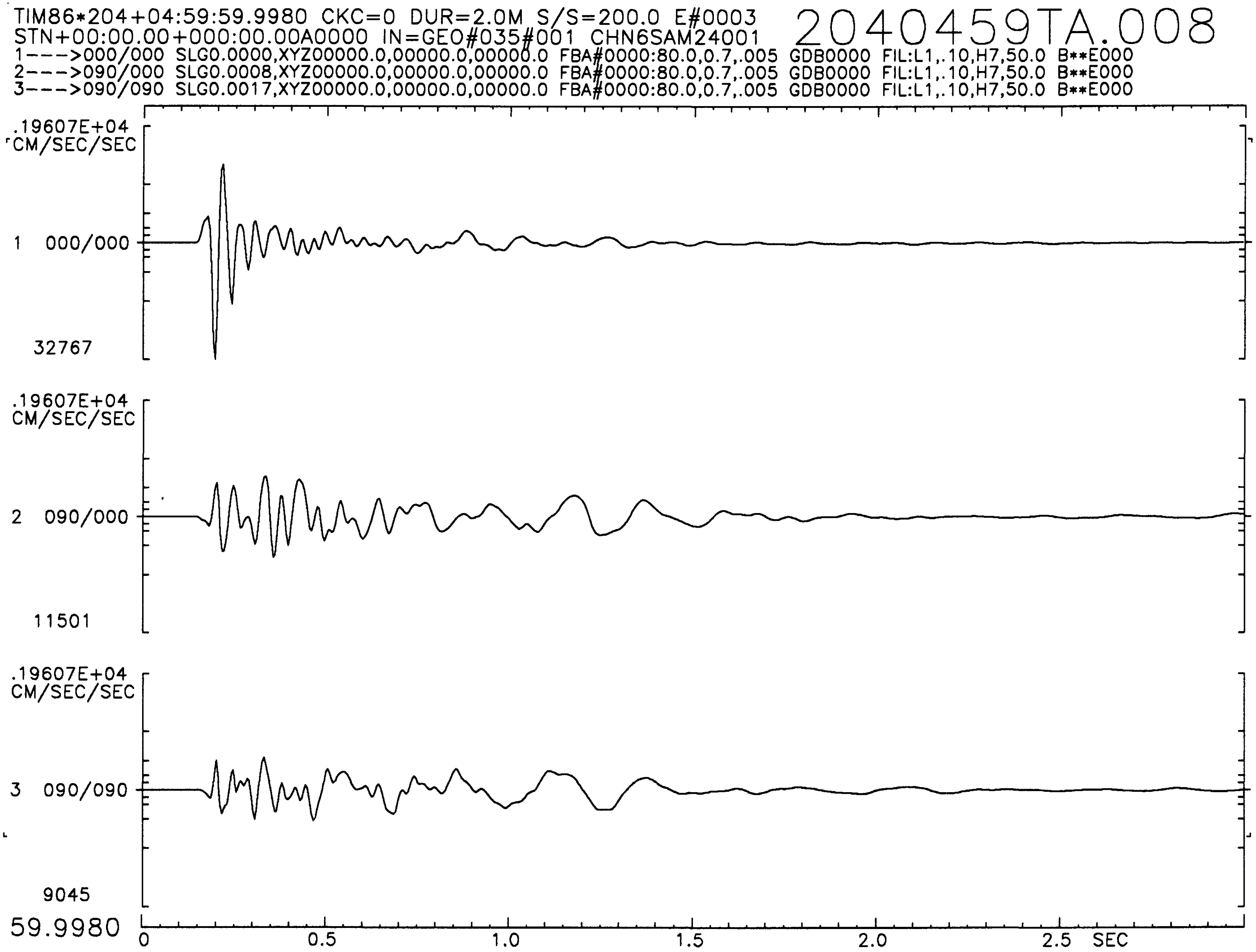

Figure A–11: Three-component acceleration time histories recorded at shotpoint 8.

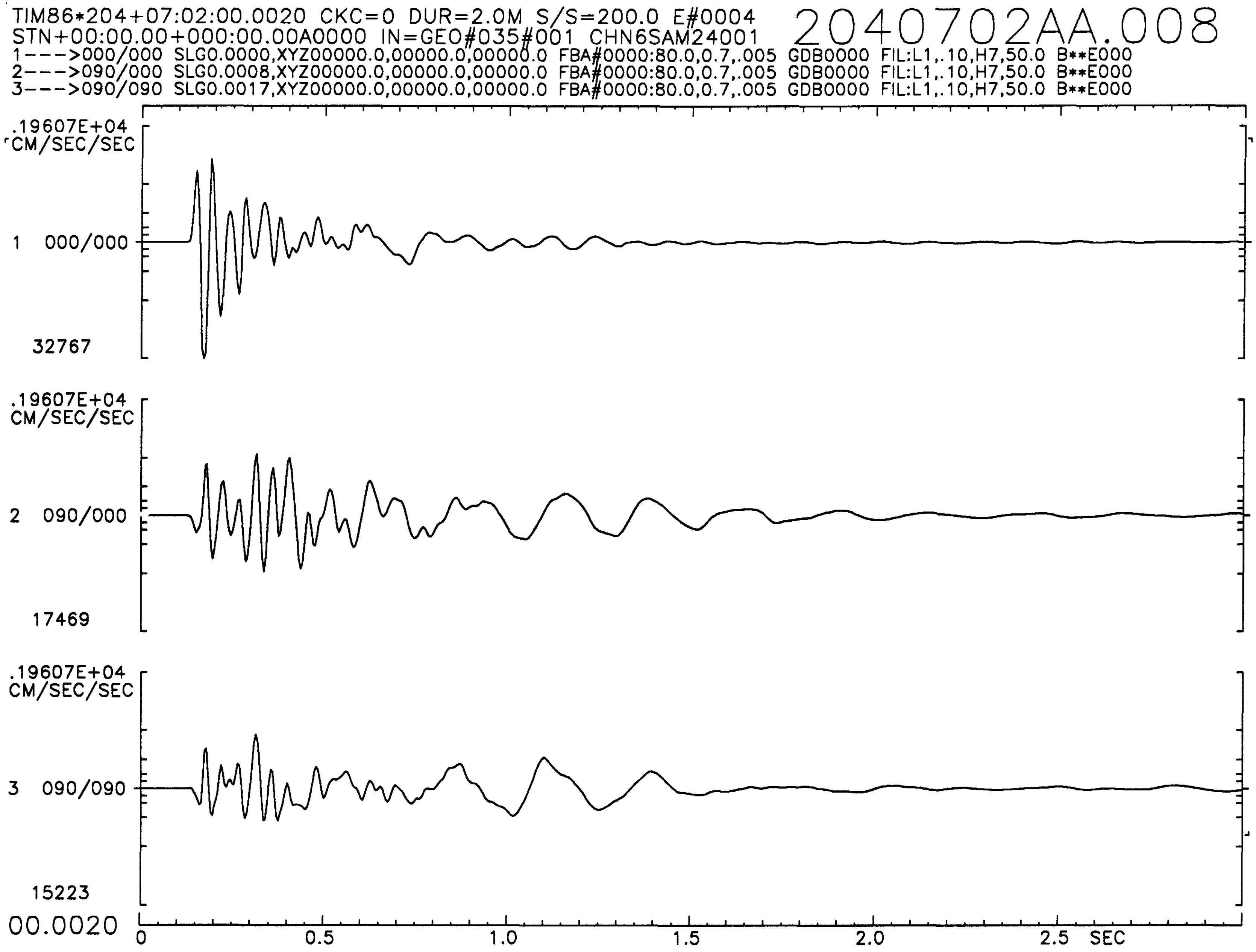

Figure A–12: Three-component acceleration time histories recorded at shotpoint 8.

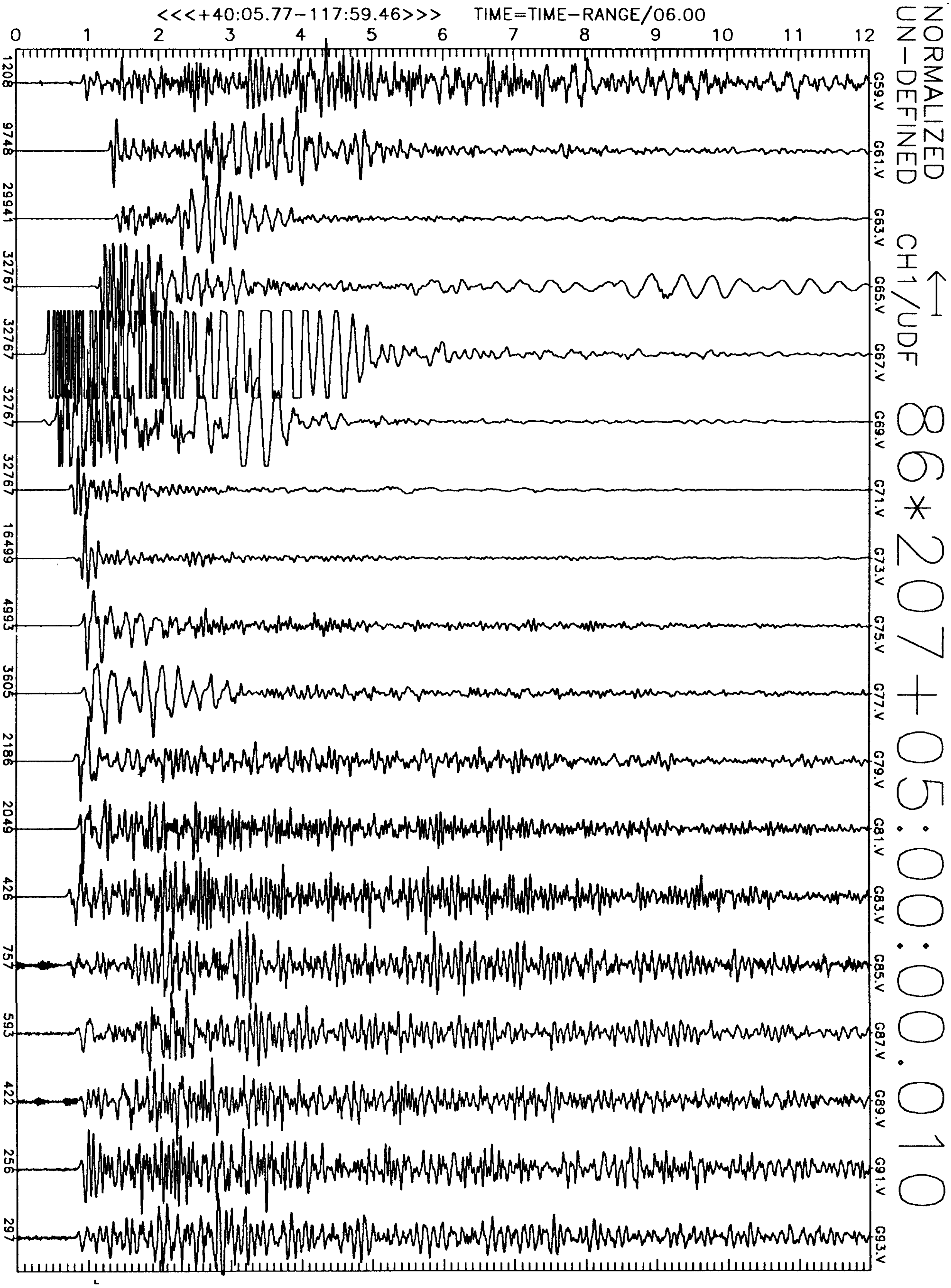

Figure B1(a), shot point 4: 12 second vertical velocity record. Abscissa is labeled with maximum counts in record (multiply by $\frac{10}{2^{24}-2^{5}} \approx 6 \times 10^{-7}$ to get cm/sec). Times are reduced by 6 km/sec. Shot time is indicated.

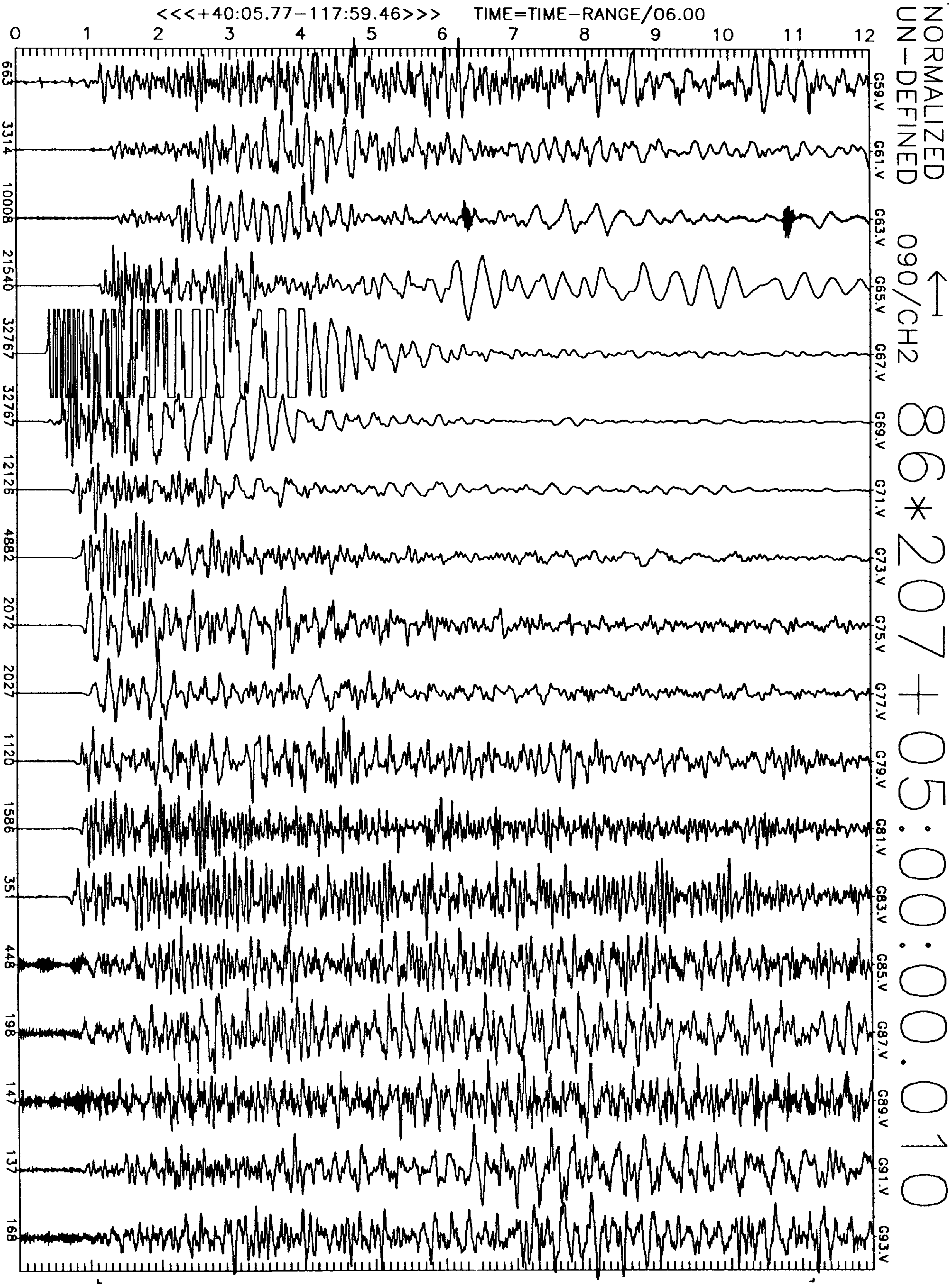

Figure B1(b), shot point 4: 12 second N16E velocity record. Abscissa is labeled with maximum counts in record (multiply by $\frac{10}{2^{24}-2^{9}} \approx 6 \times 10^{-7}$ to get cm/sec). Times are reduced by 6 km/sec. Shot time is indicated.

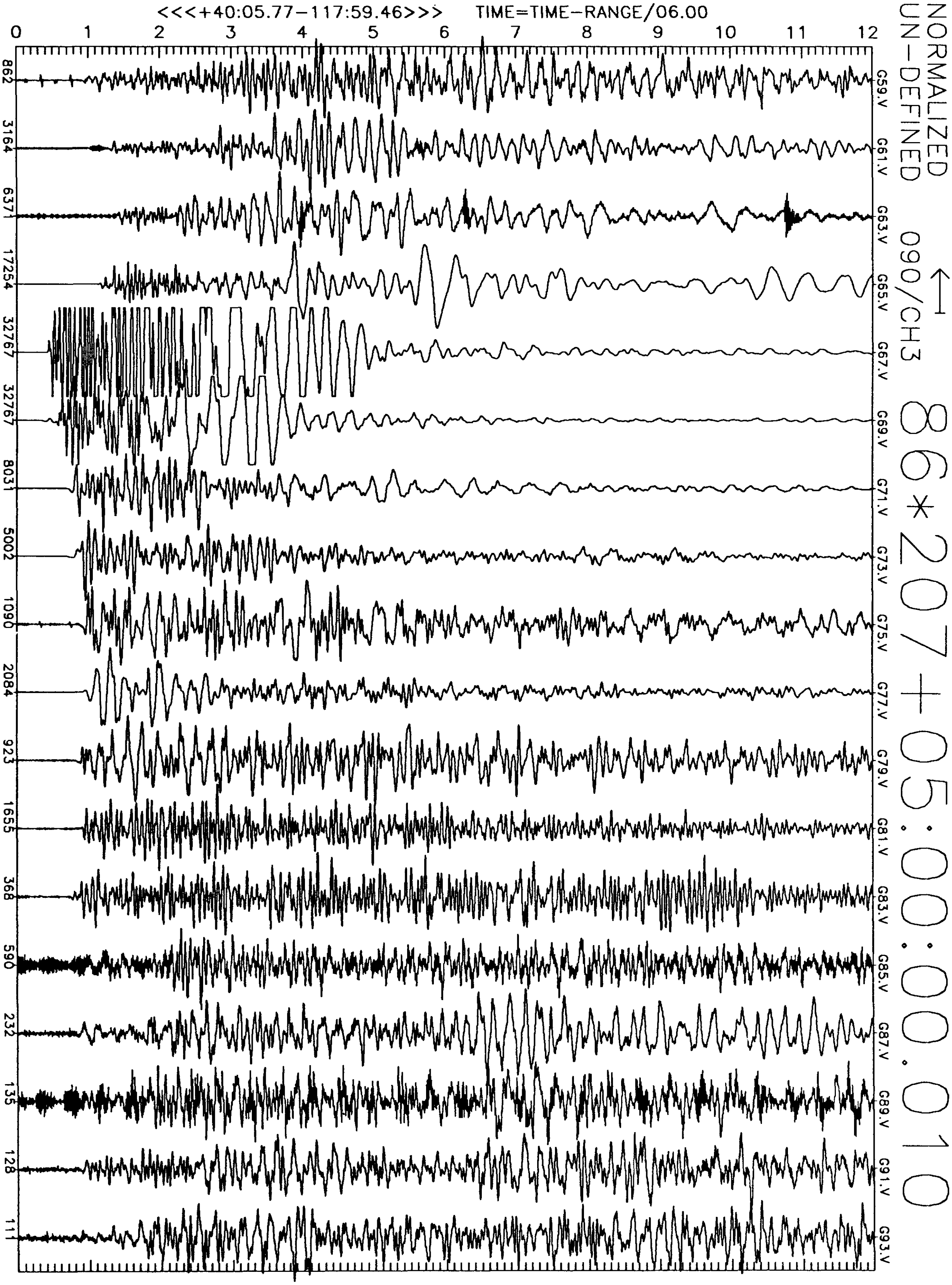

Figure B1(c), shot point 4: 12 second N106E velocity record. Abscissa is labeled with maximum counts in record (multiply by $\frac{10}{2^{24}-2^{5}} \approx 6 \times 10^{-7}$ to get cm/sec). Times are reduced by 6 km/sec. Shot time is indicated.

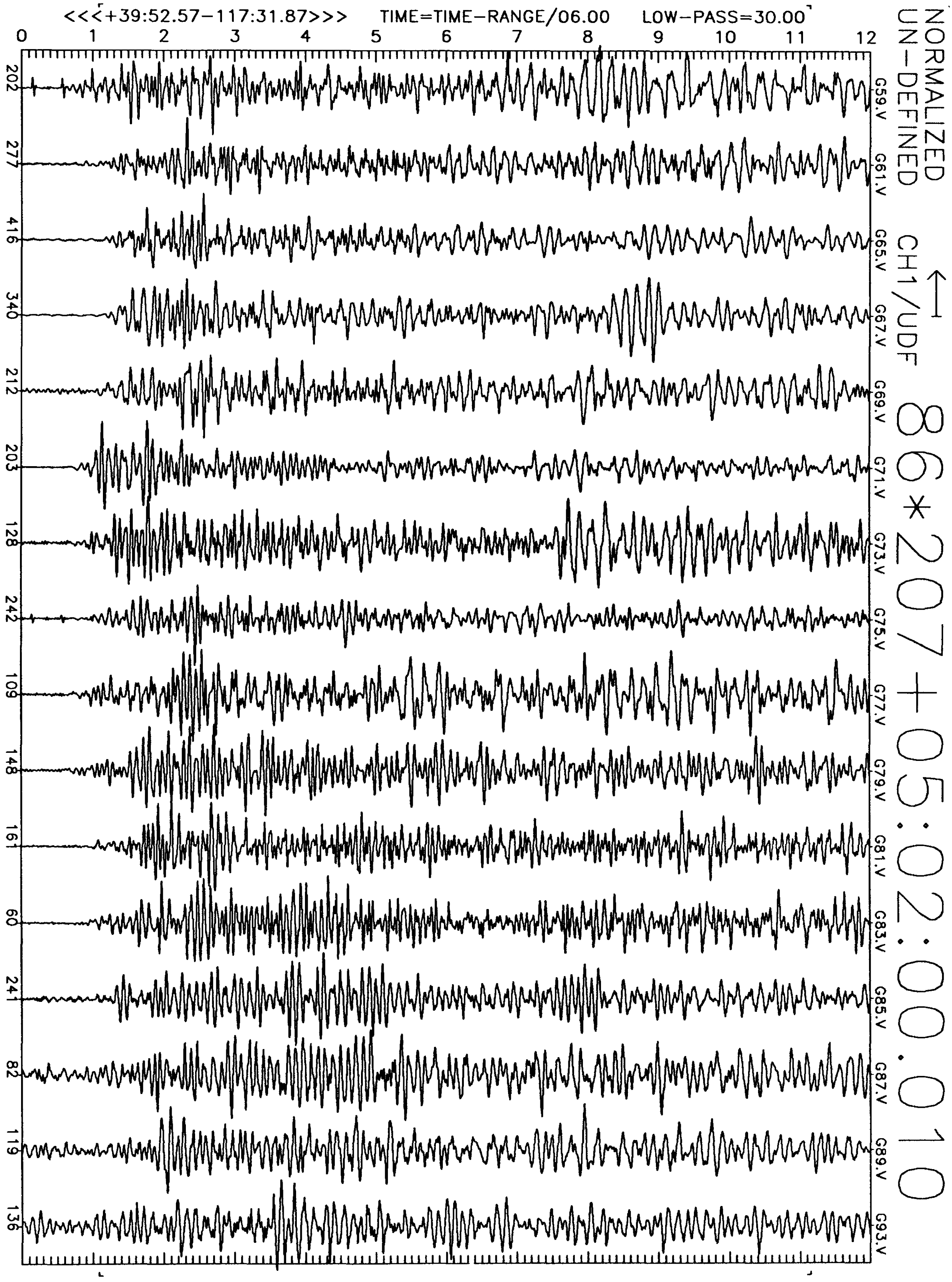

Figure B2(a), shot point 5: 12 second vertical velocity record. Abscissa is labeled with maximum counts in record (multiply by $\frac{10}{2^{24}-2^{9}} \approx 6 \times 10^{-7}$ to get cm/sec). Times are reduced by 6 km/sec. Shot time is indicated.

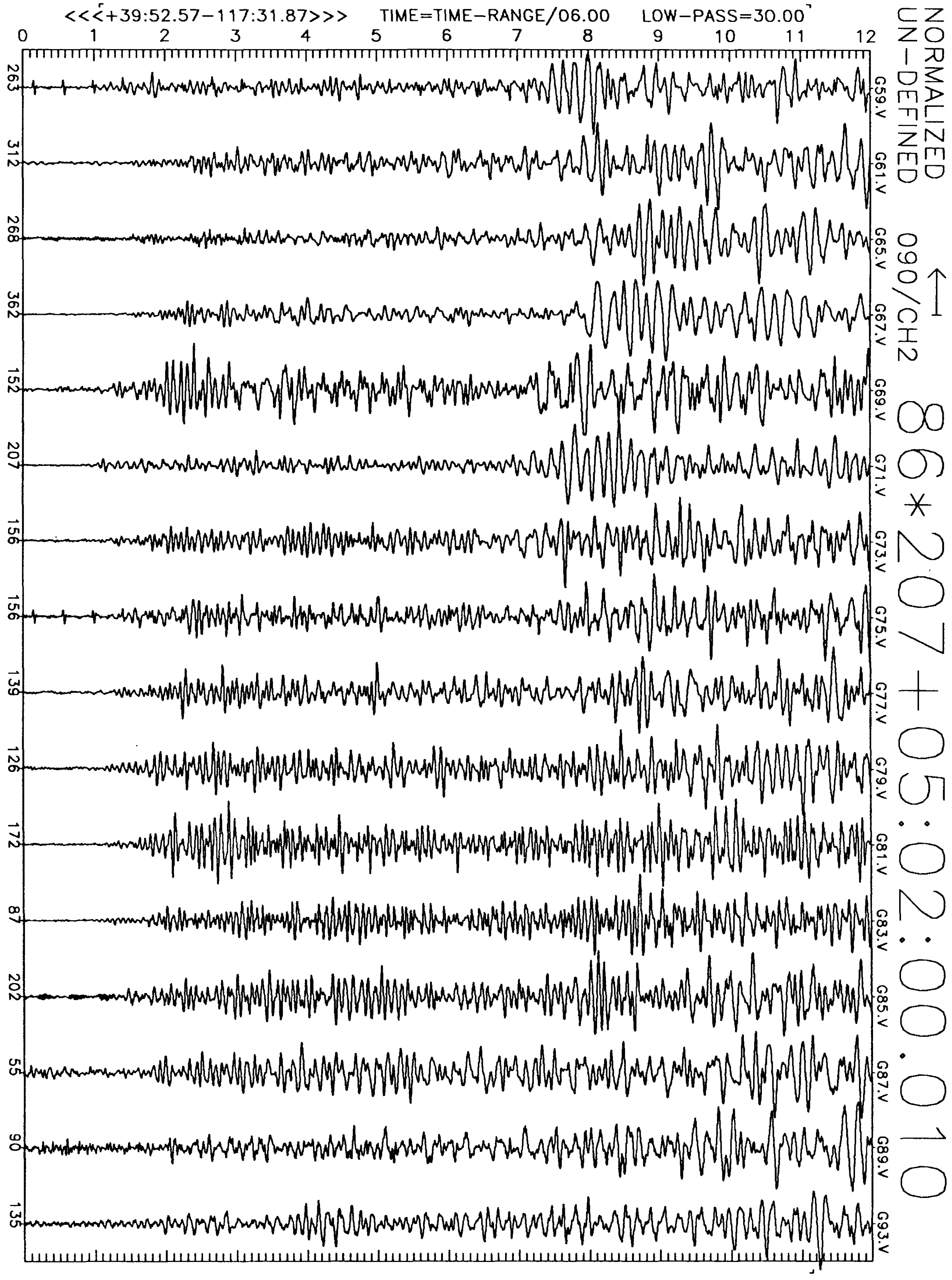

Figure B2(b), shot point 5: 12 second N16E velocity record. Abscissa is labeled with maximum counts in record (multiply by $\frac{10}{2^{24}-2^{9}} \approx 6 \times 10^{-7}$ to get cm/sec). Times are reduced by 6 km/sec. Shot time is indicated.

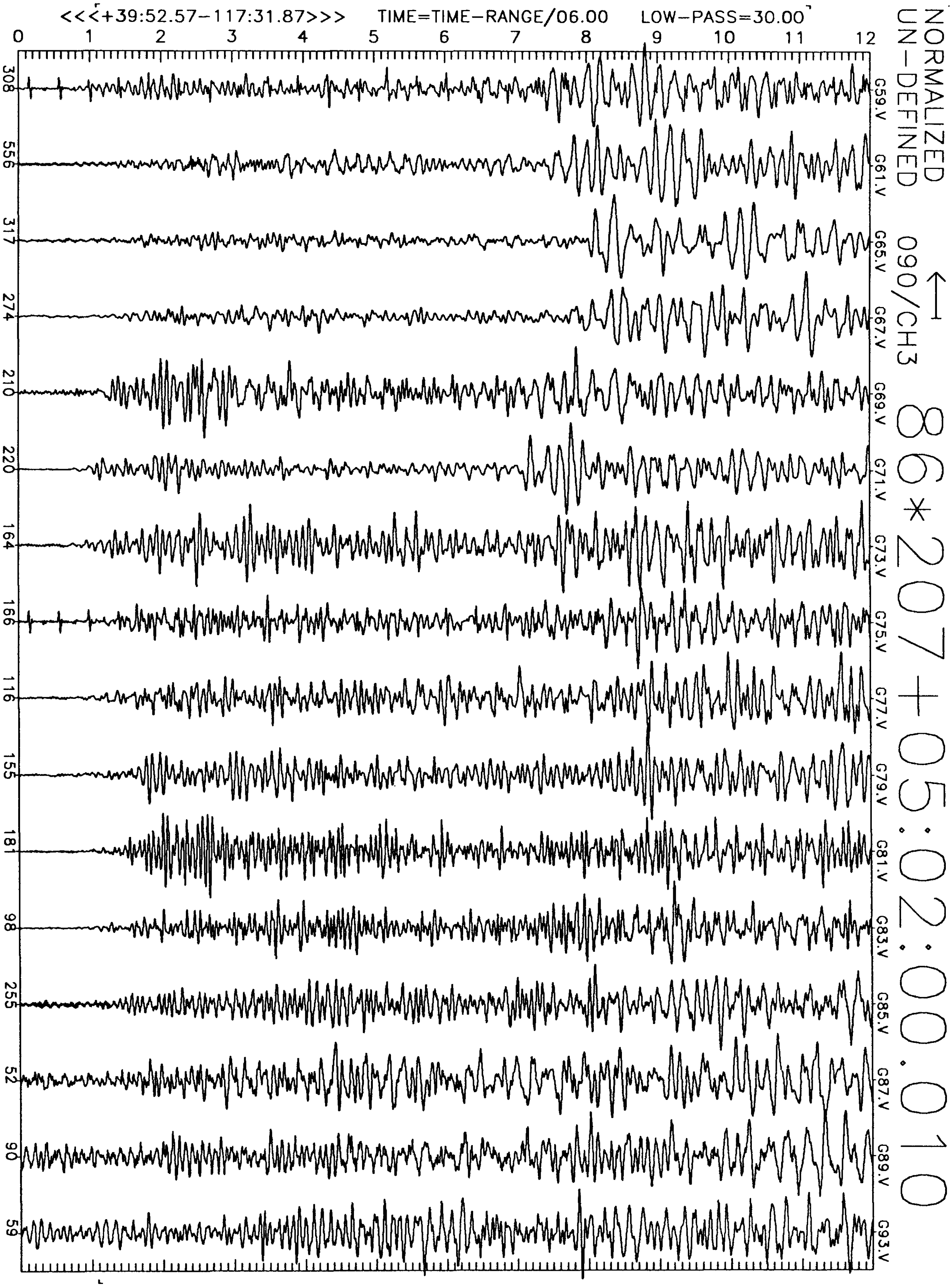

Figure B2(c), shot point 5: 12 second N106E velocity record. Abscissa is labeled with maximum counts in record (multiply by $\frac{10}{2^{24}-2^{9}} \approx 6 \times 10^{-7}$ to get cm/sec). Times are reduced by 6 km/sec. Shot time is indicated.

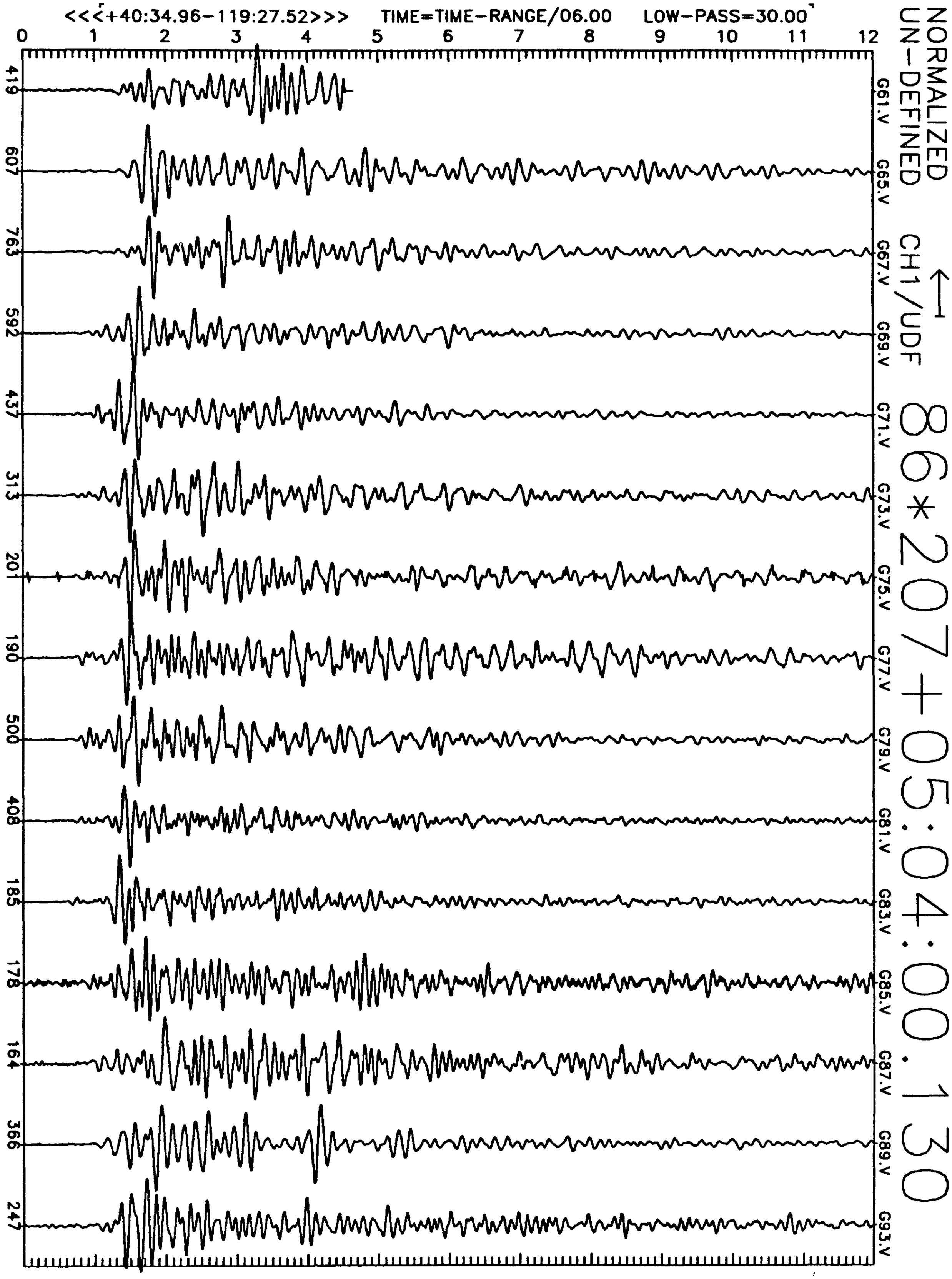

Figure B3(a), shot point 1: 12 second vertical velocity record. Abscissa is labeled with maximum counts in record (multiply by $\frac{10}{2^{24}-2^{9}}$ ≈ 6 × 10^{-7} to get cm/sec). Times are reduced by 6 km/sec. Shot time is indicated.

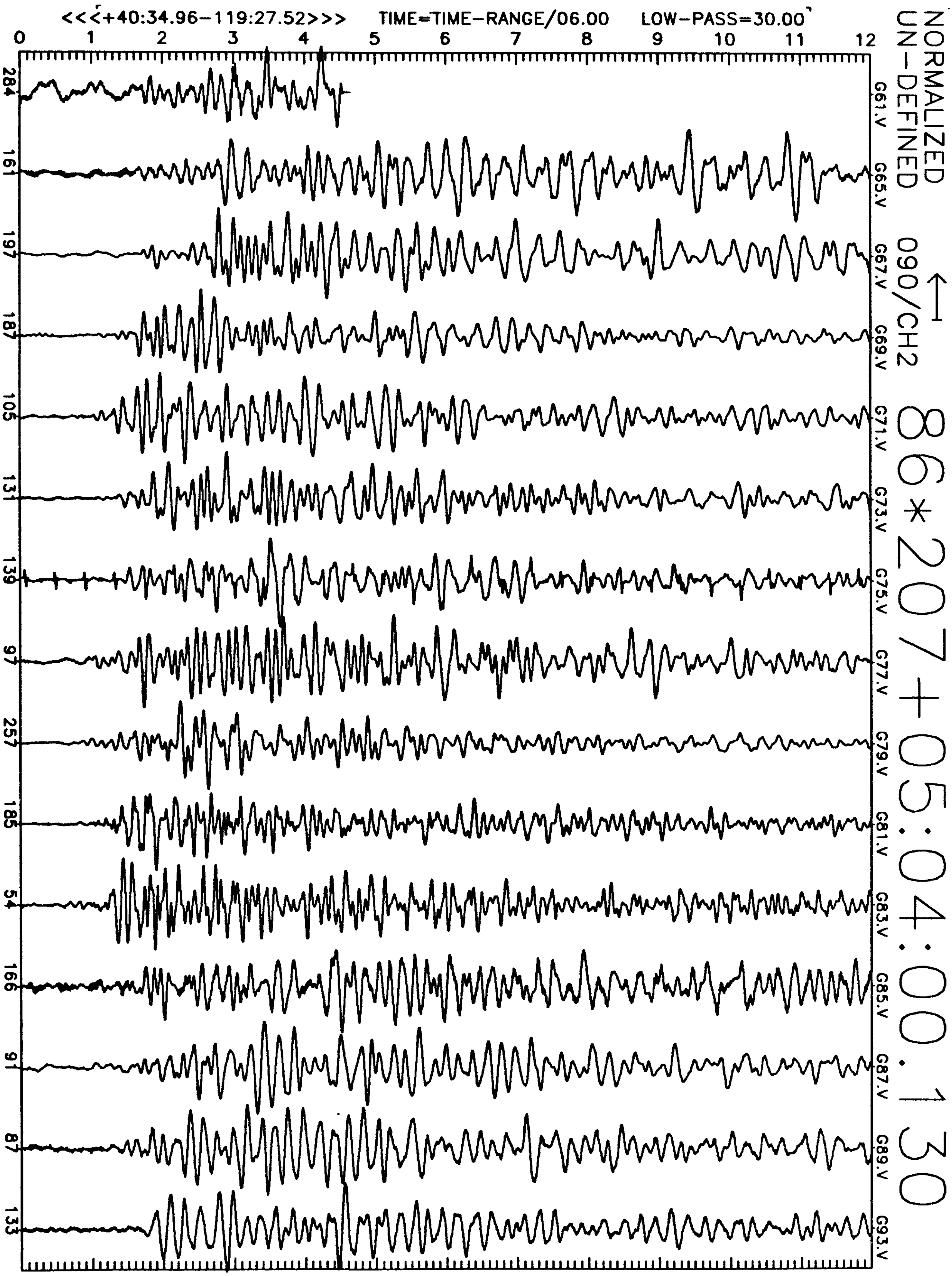

Figure B3(b), shot point 1: 12 second N16E velocity record. Abscissa is labeled with maximum counts in record (multiply by $\frac{10}{2^{24}-2^{9}} \approx 6 \times 10^{-7}$ to get cm/sec). Times are reduced by 6 km/sec. Shot time is indicated.

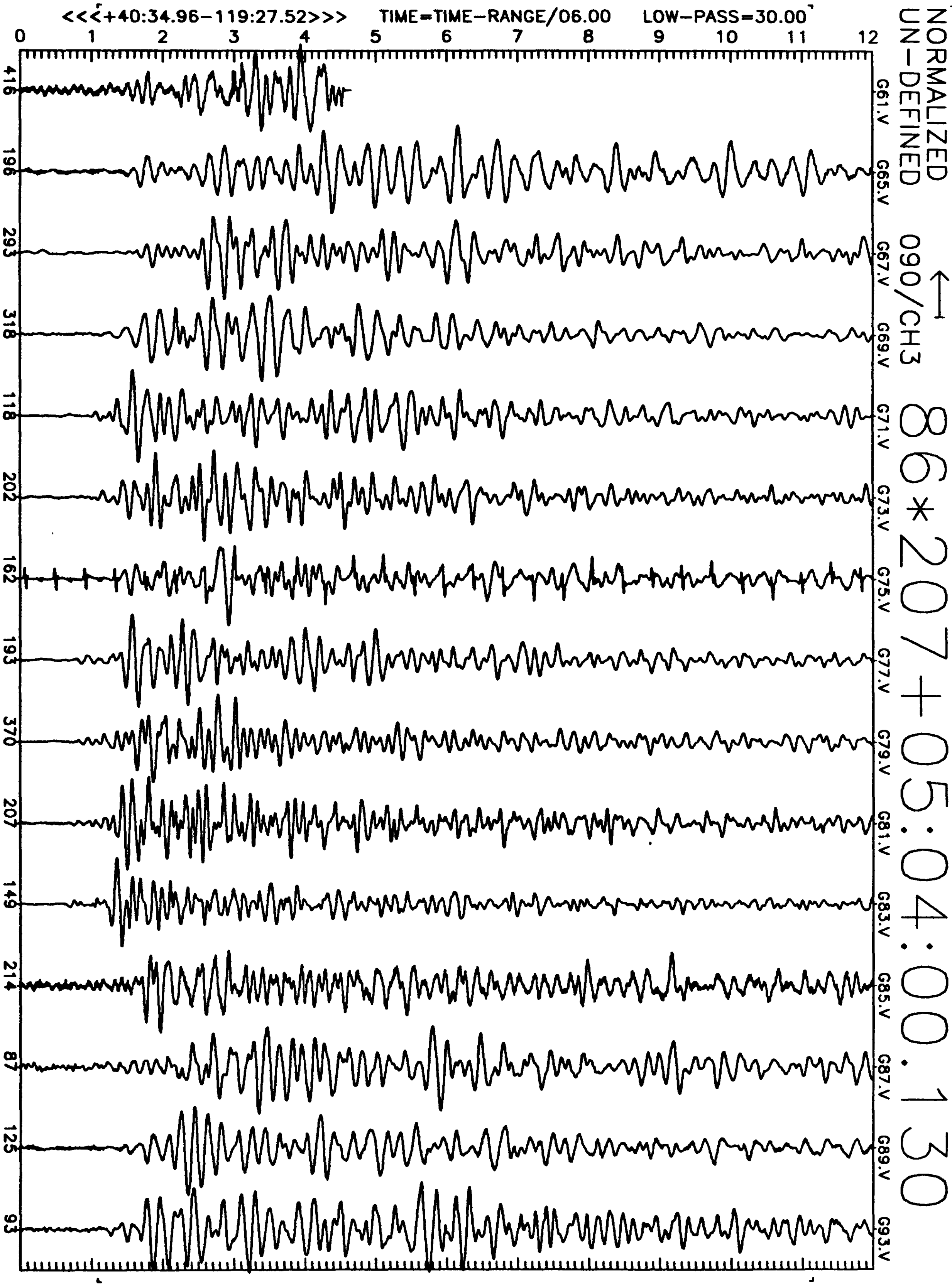

Figure B3(c), shot point 1: 12 second N106E velocity record. Abscissa is labeled with maximum counts in record (multiply by $\frac{10}{2^{24}-2^{9}} \approx 6 \times 10^{-7}$ to get cm/sec). Times are reduced by 6 km/sec. Shot time is indicated.

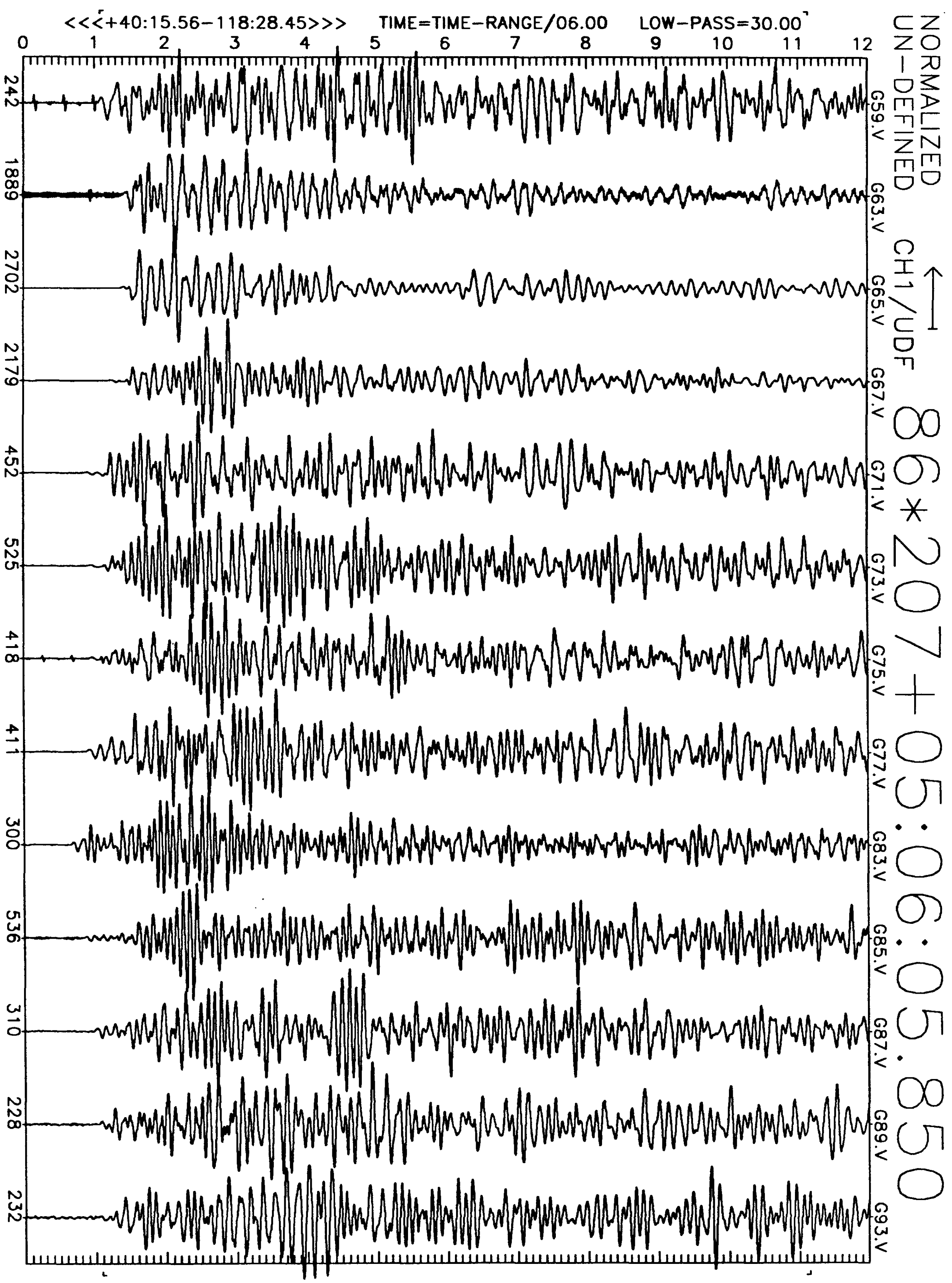

Figure B4(a), shot point 3: 12 second vertical velocity record. Abscissa is labeled with maximum counts in record (multiply by $\frac{10}{2^{24}-2^{9}} \approx 6 \times 10^{-7}$ to get cm/sec). Times are reduced by 6 km/sec. Shot time is indicated.

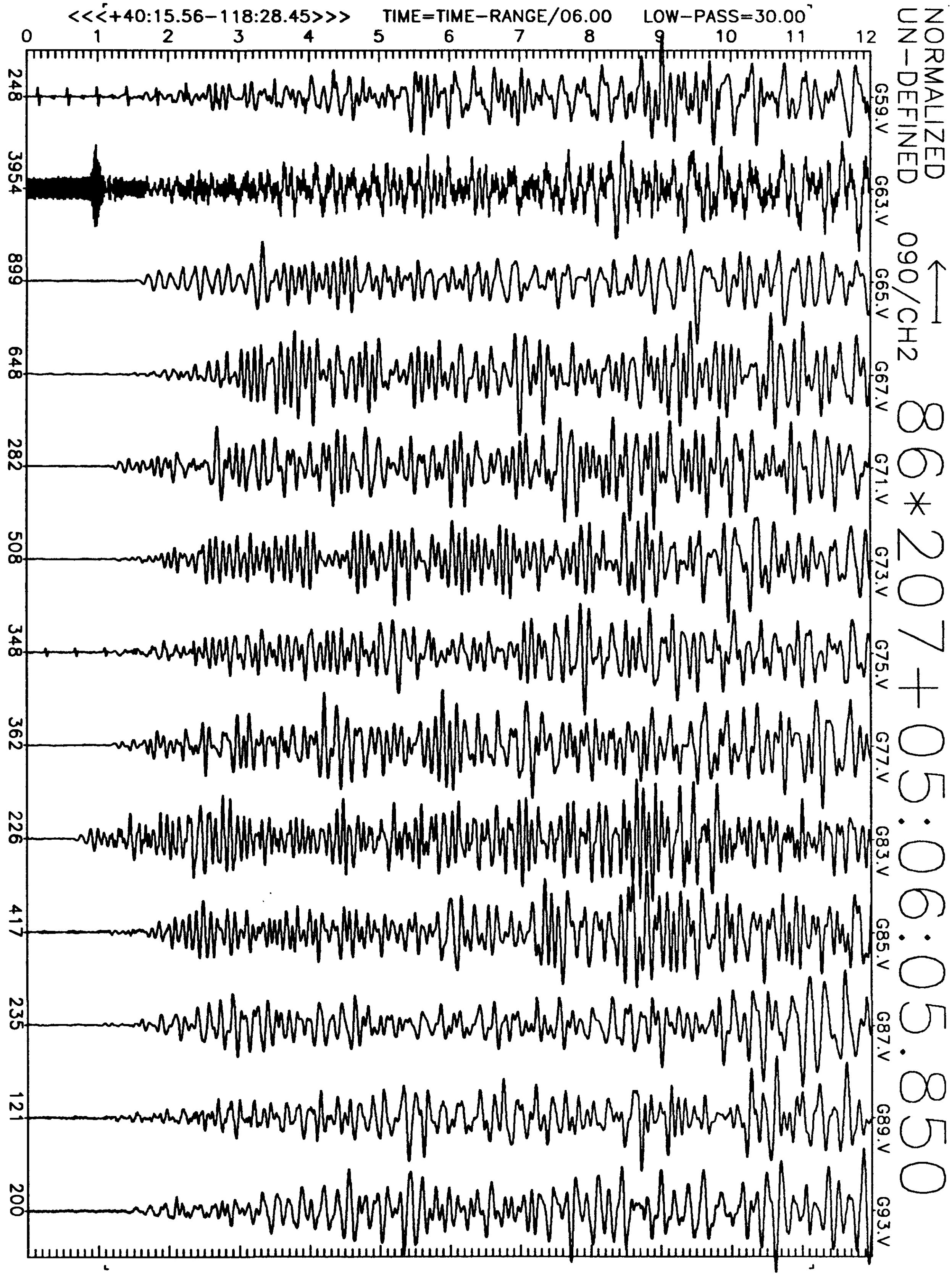

Figure B4(b), shot point 3: 12 second N16E velocity record. Abscissa is labeled with maximum counts in record (multiply by $\frac{10}{2^{24}-2^{9}} \approx 6 \times 10^{-7}$ to get cm/sec). Times are reduced by 6 km/sec. Shot time is indicated.

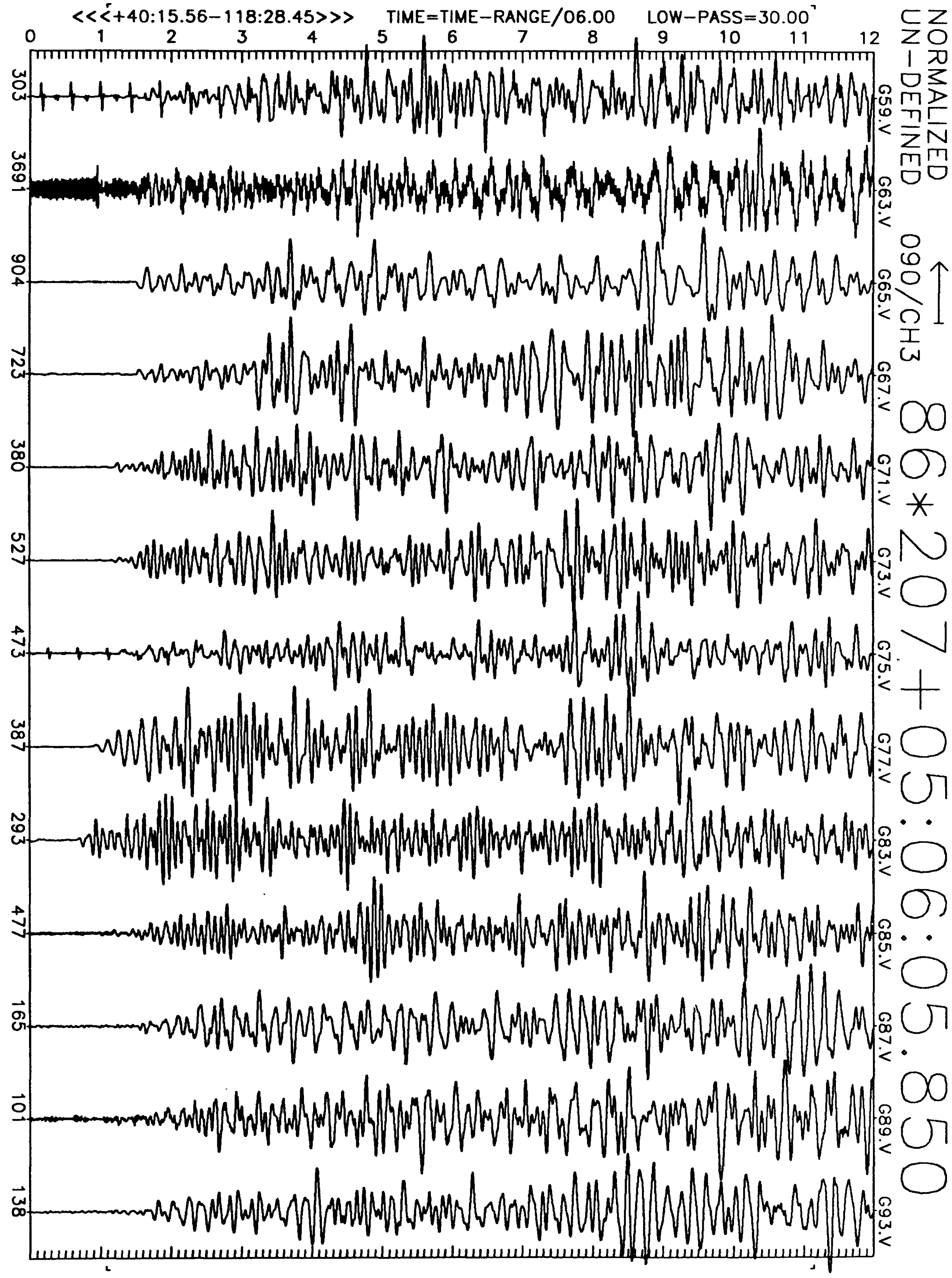

Figure B4(c), shot point 3: 12 second N106E velocity record. Abscissa is labeled with maximum counts in record (multiply by $\frac{10}{2^{24}-2^{9}} \approx 6 \times 10^{-7}$ to get cm/sec). Times are reduced by 6 km/sec. Shot time is indicated.

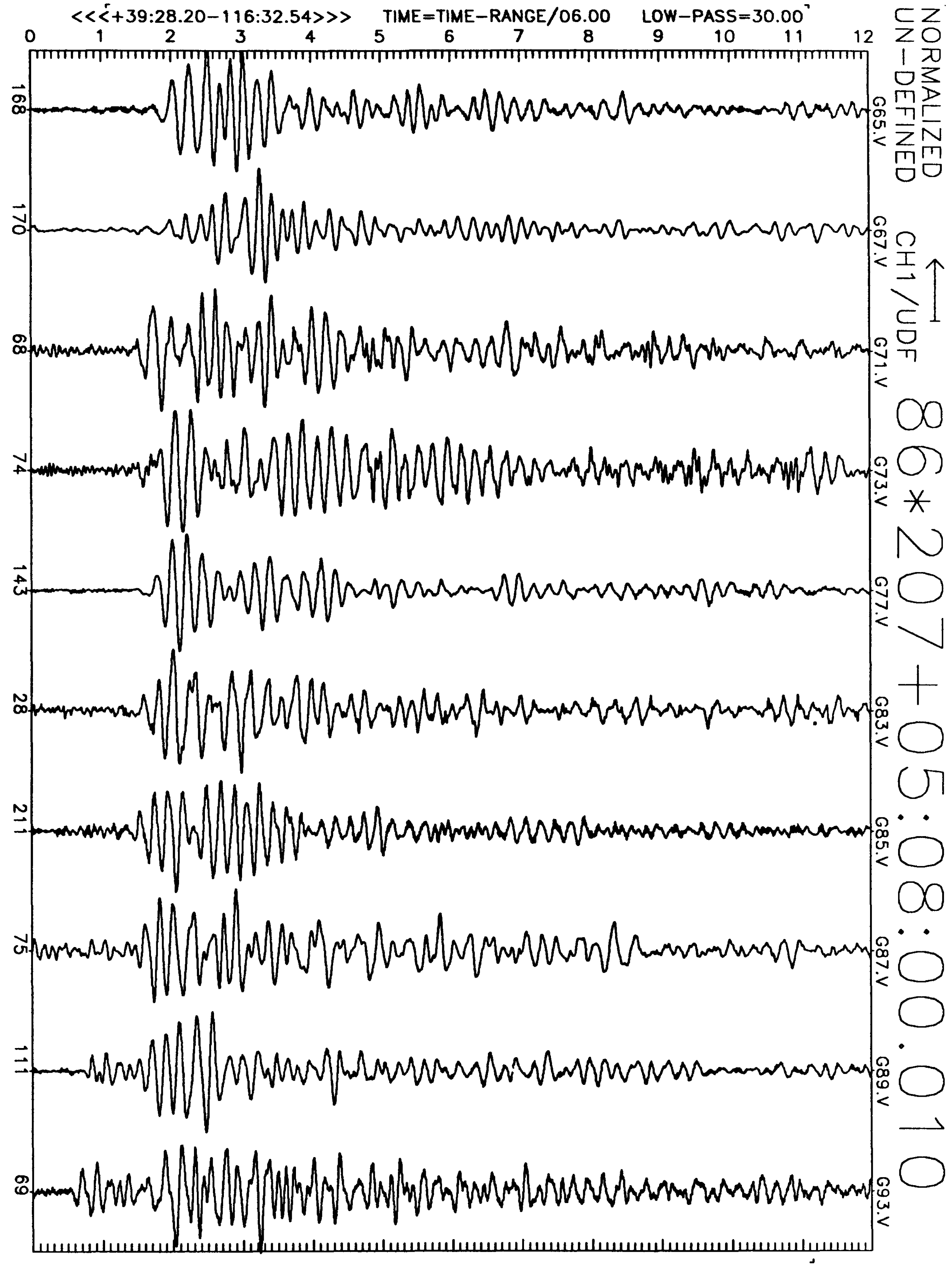

Figure B5(a), shot point 7: 12 second vertical velocity record. Abscissa is labeled with maximum counts in record (multiply by $\frac{10}{2^{24}-2^{9}} \approx 6 \times 10^{-7}$ to get cm/sec). Times are reduced by 6 km/sec. Shot time is indicated.

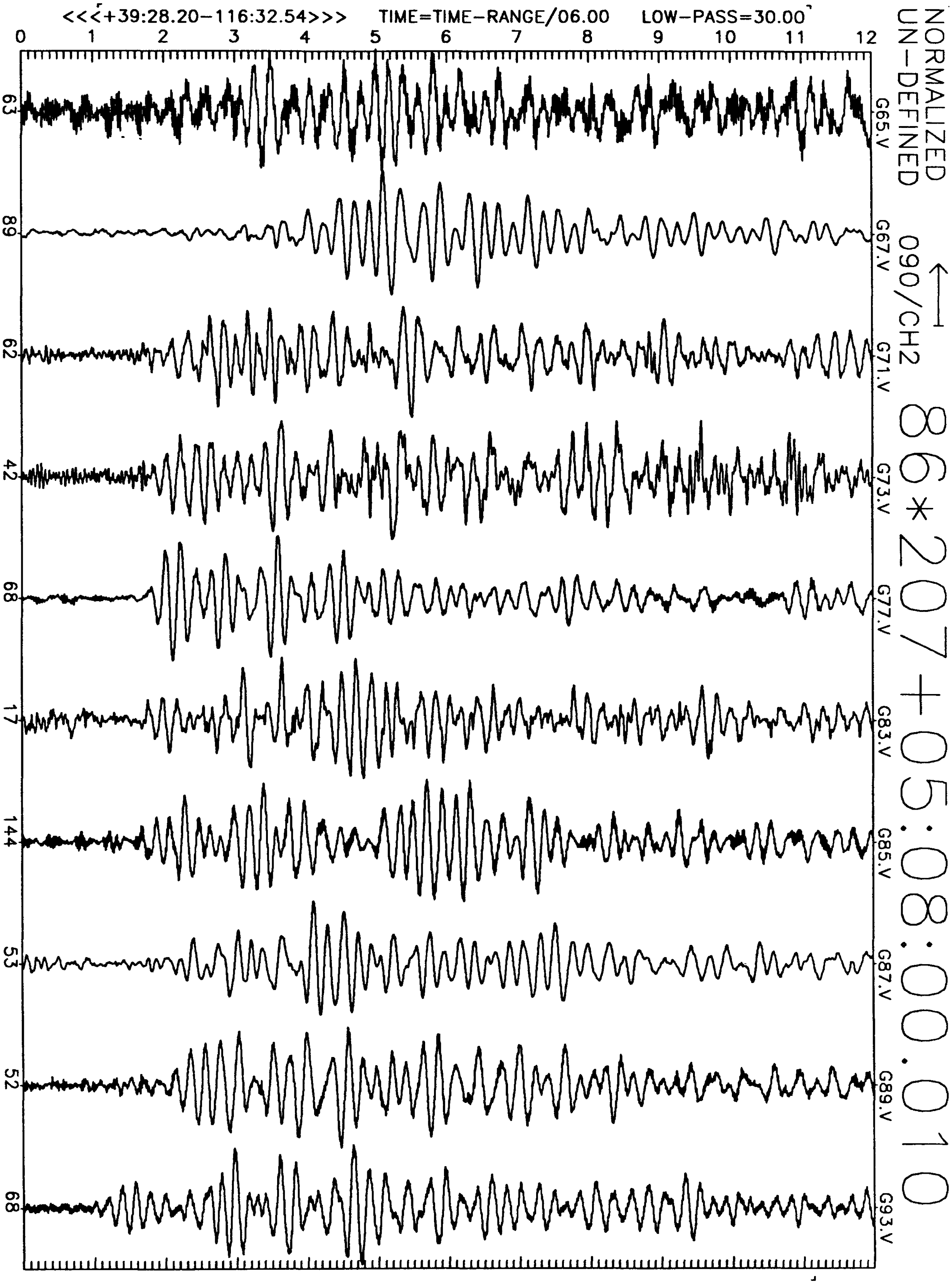

Figure B5(b), shot point 7: 12 second N16E velocity record. Abscissa is labeled with maximum counts in record (multiply by $\frac{10}{2^{24}-2^{9}}$ ≈ 6 × 10^{-7} to get cm/sec). Times are reduced by 6 km/sec. Shot time is indicated.

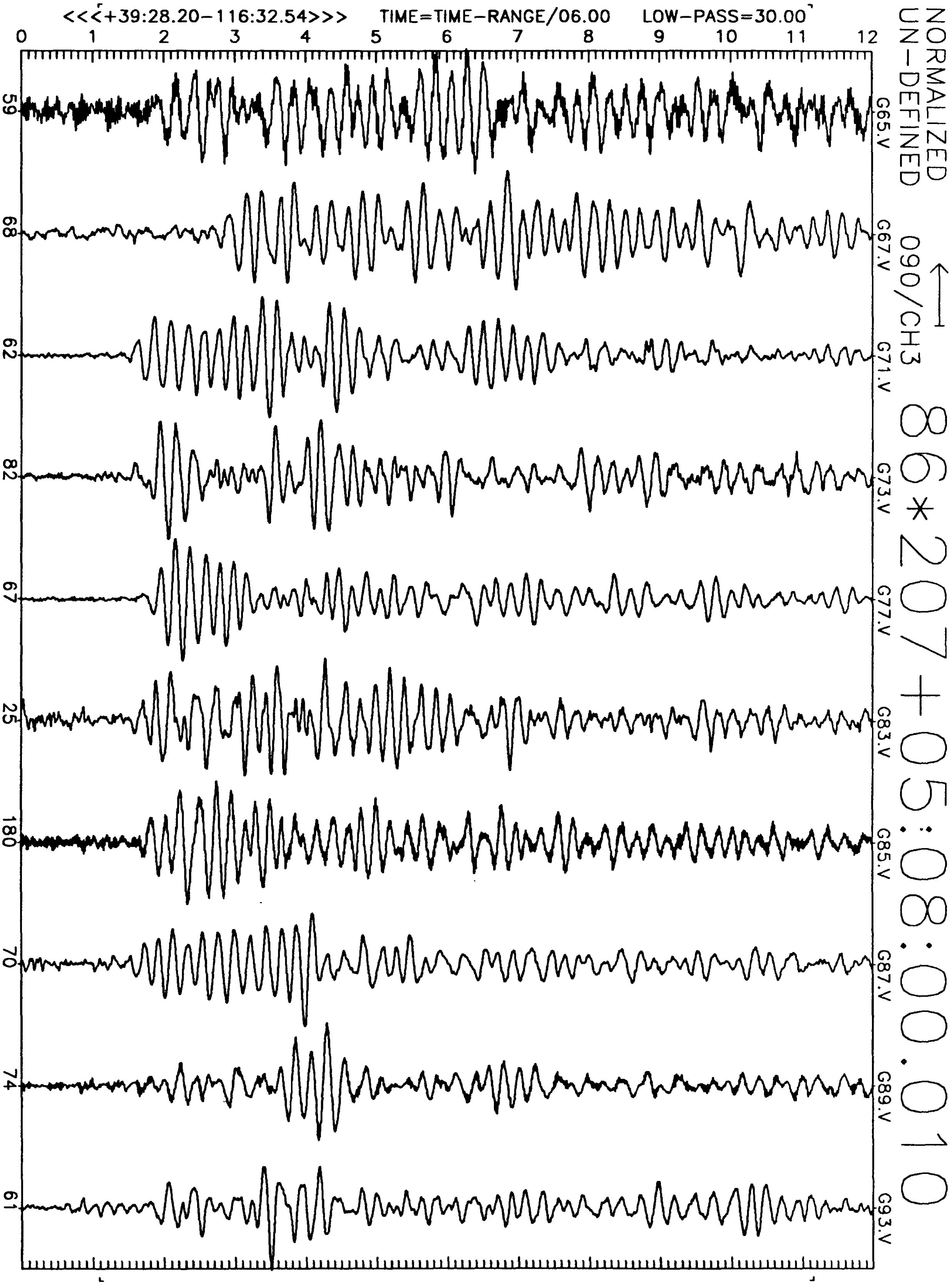

Figure B5(c), shot point 7: 12 second N106E velocity record. Abscissa is labeled with maximum counts in record (multiply by $\frac{10}{2^{24}-2^{9}} \approx 6 \times 10^{-7}$ to get cm/sec). Times are reduced by 6 km/sec. Shot time is indicated.

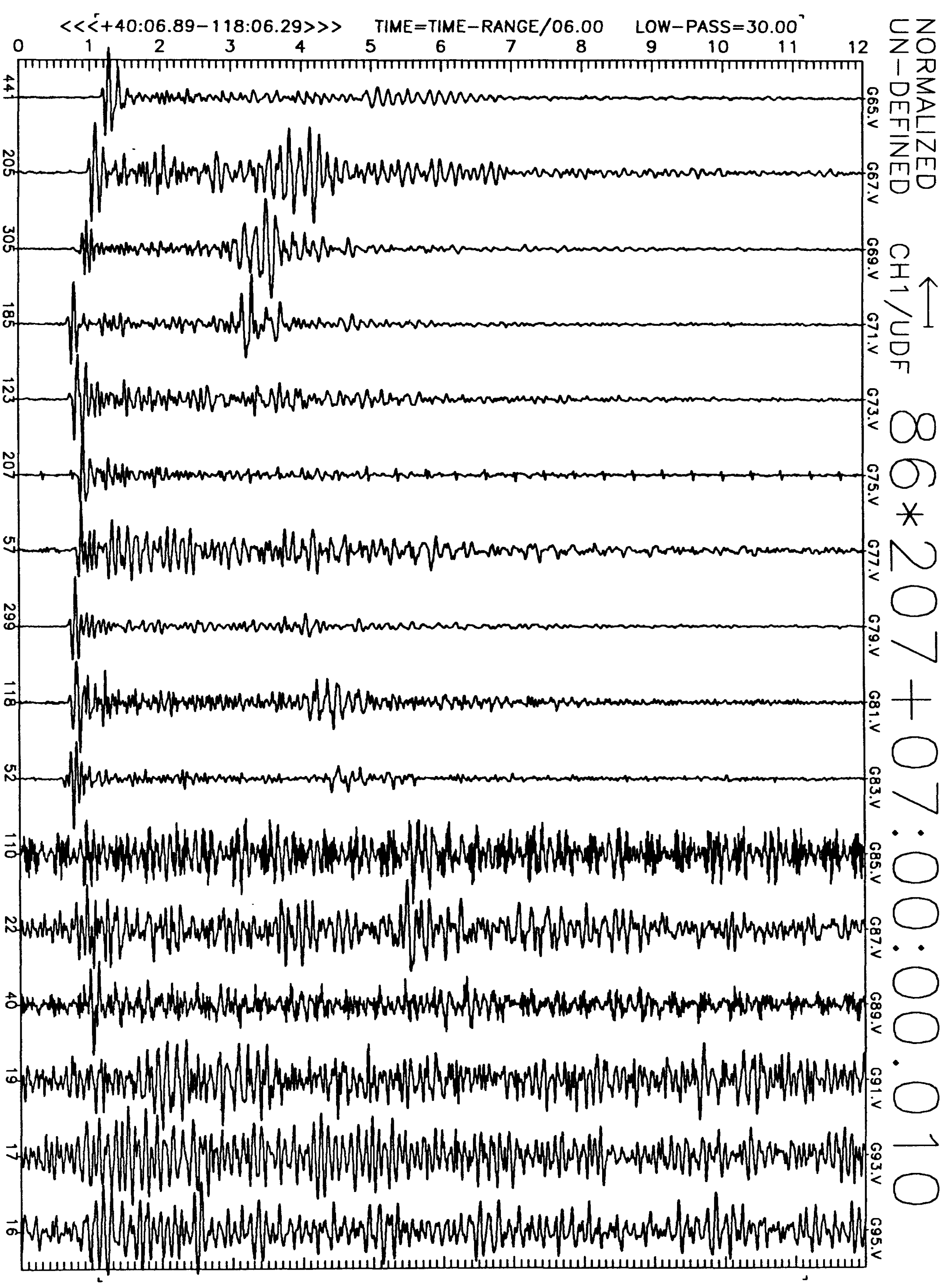

Figure B6(a), shot point 12: 12 second vertical velocity record. Abscissa is labeled with maximum counts in record (multiply by $\frac{10}{2^{24}-2^{5}} \approx 6 \times 10^{-7}$ to get cm/sec). Times are reduced by 6 km/sec. Shot time is indicated.

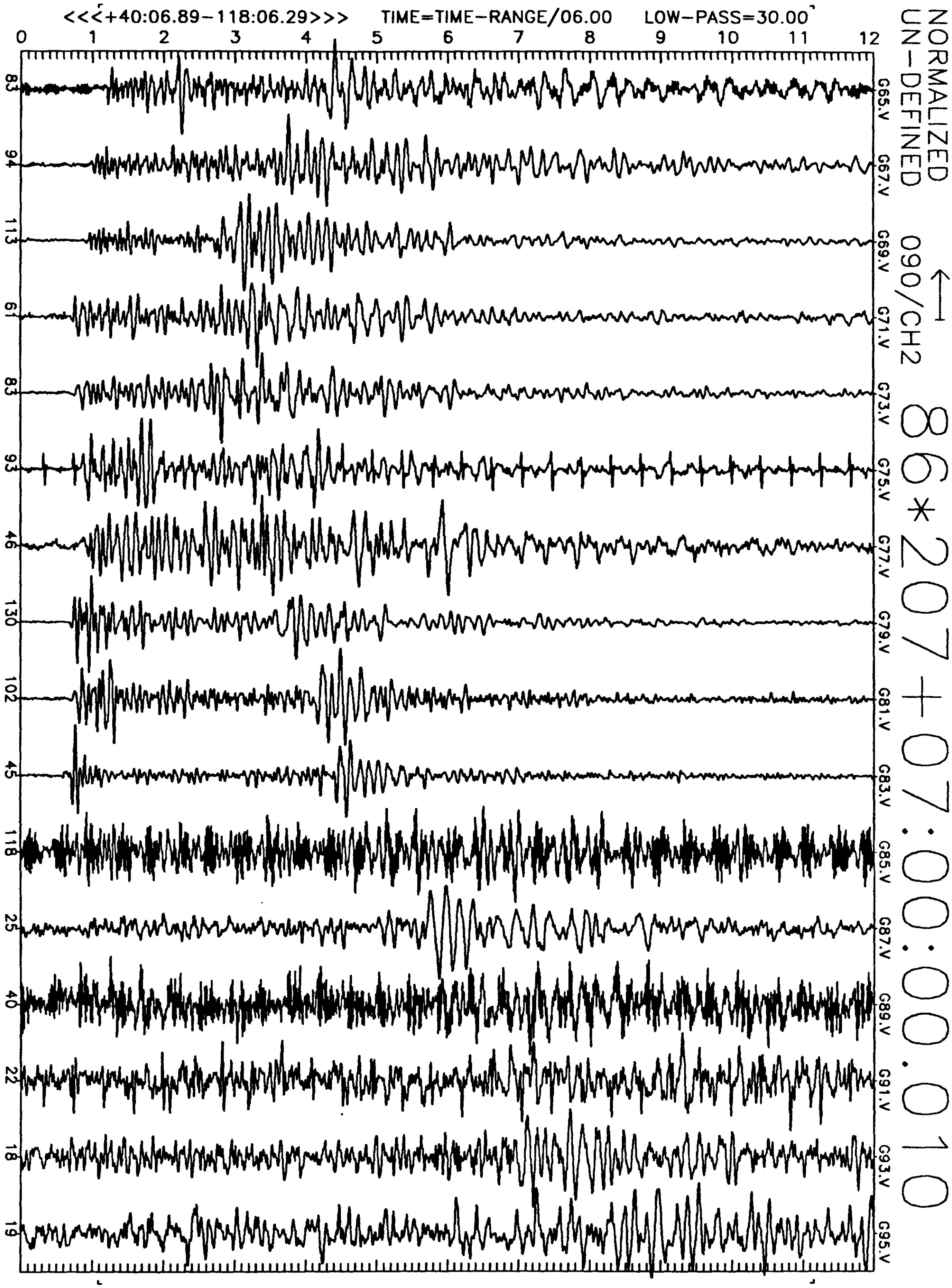

Figure B6(b), shot point 12: 12 second N16E velocity record. Abscissa is labeled with maximum counts in record (multiply by $\frac{10}{2^{24}-2^{9}} \approx 6 \times 10^{-7}$ to get cm/sec). Times are reduced by 6 km/sec. Shot time is indicated.

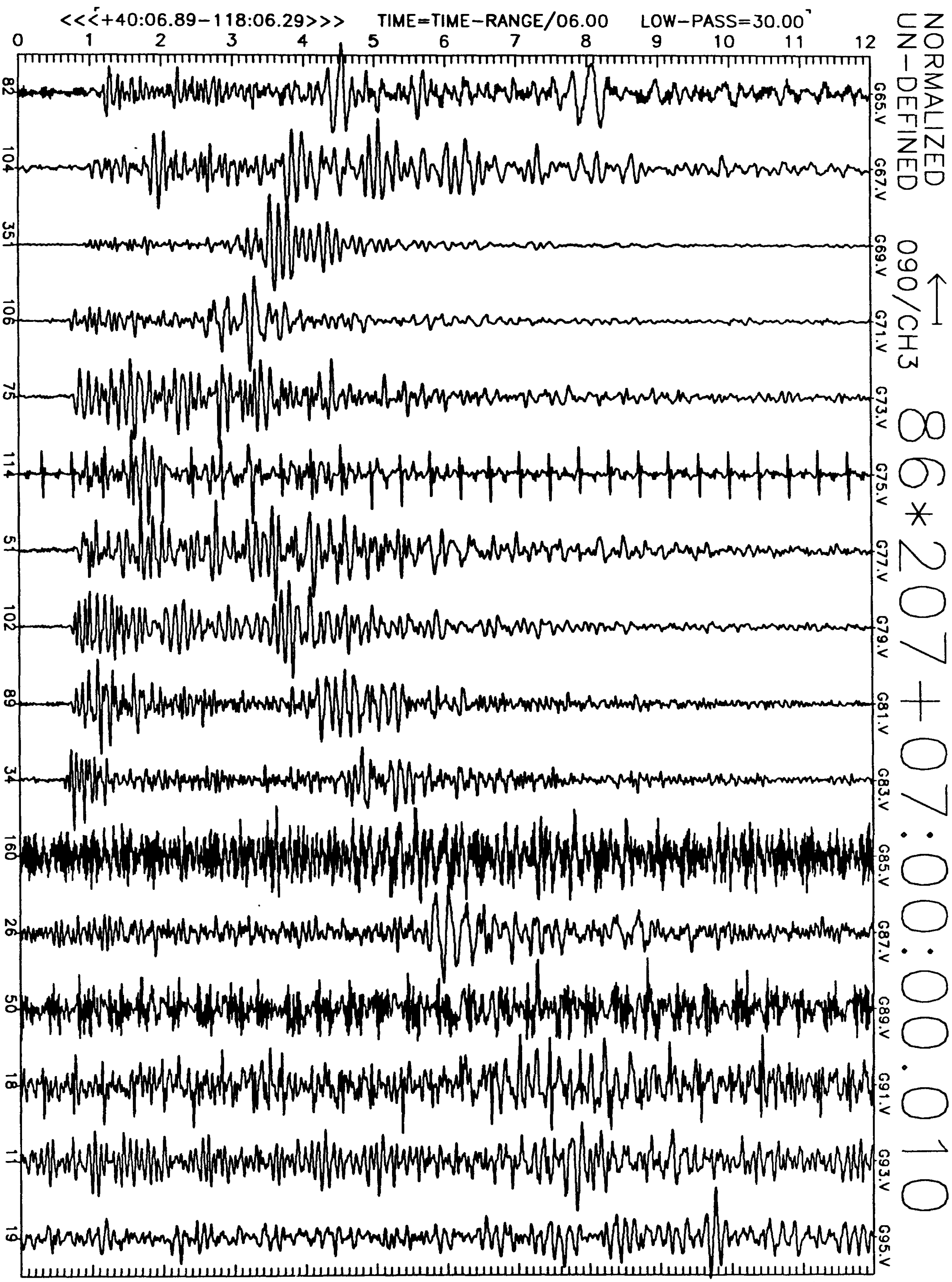

Figure B6(c), shot point 12: 12 second N106E velocity record. Abscissa is labeled with maximum counts in record (multiply by $\frac{10}{2^{24}-2^{9}}$ ≈ 6×10^{-7} to get cm/sec). Times are reduced by 6 km/sec. Shot time is indicated.

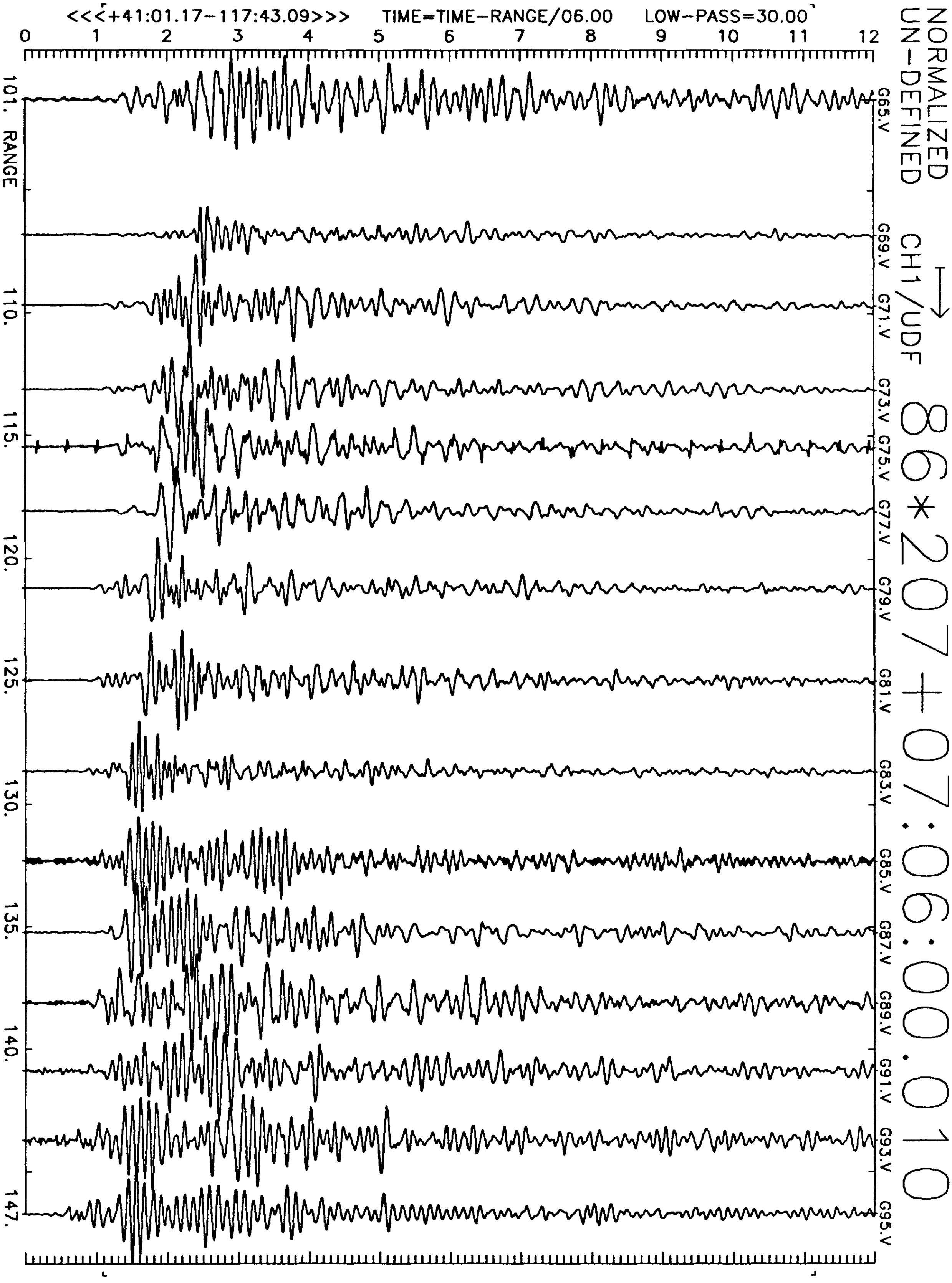

Figure B7(a), shot point 8: 12 second velocity record. Positive vertical motion is to right. Abscissa is distance to shot point. Top of trace is labeled with station number. Times are reduced by 6 km/sec. Shot time is indicated.

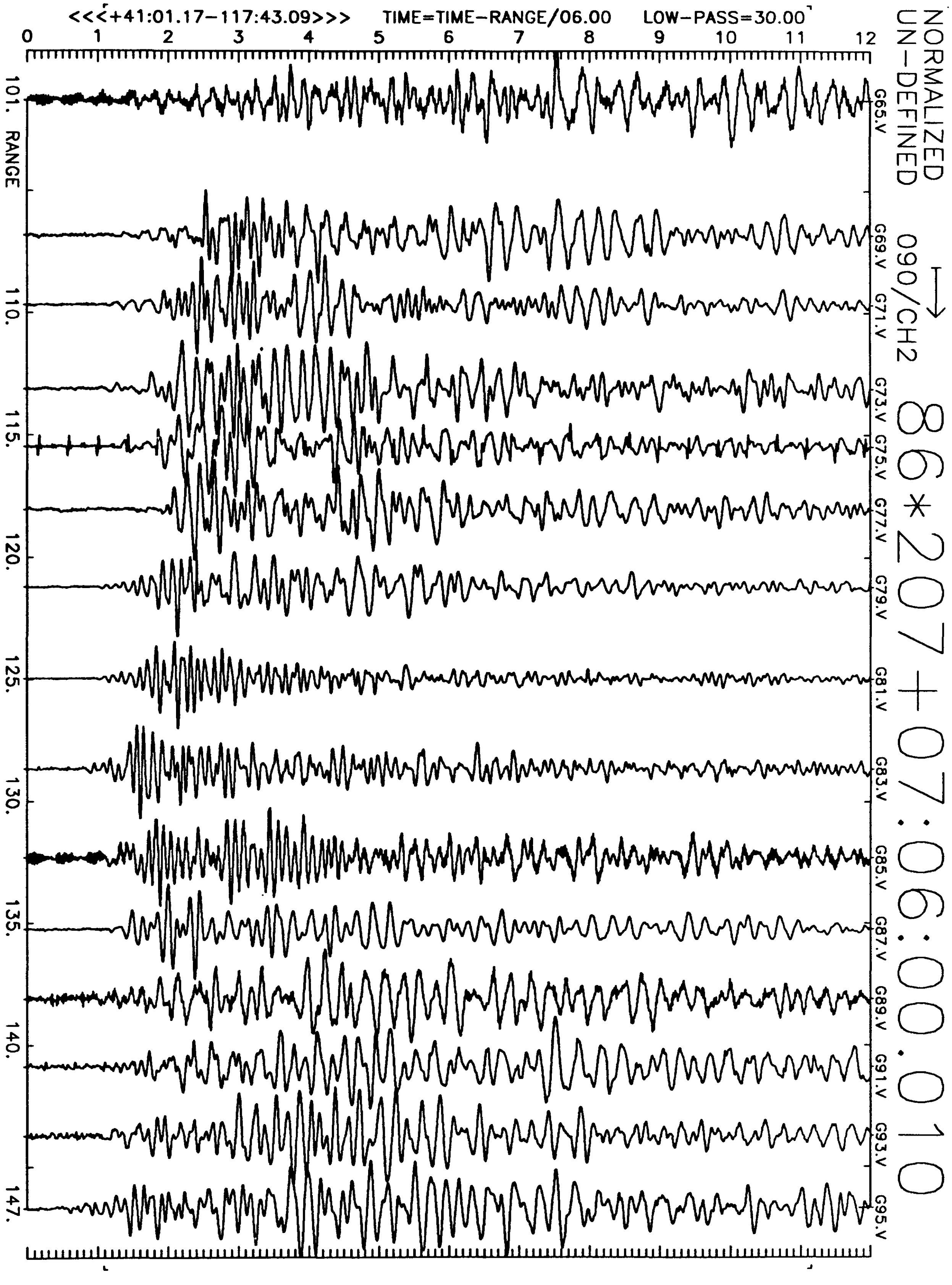

Figure B7(b), shot point 8: 12 second velocity record. Positive N16E motion is to right. Abscissa is distance to shot point. Top of trace is labeled with station number. Times are reduced by 6 km/sec. Shot time is indicated.

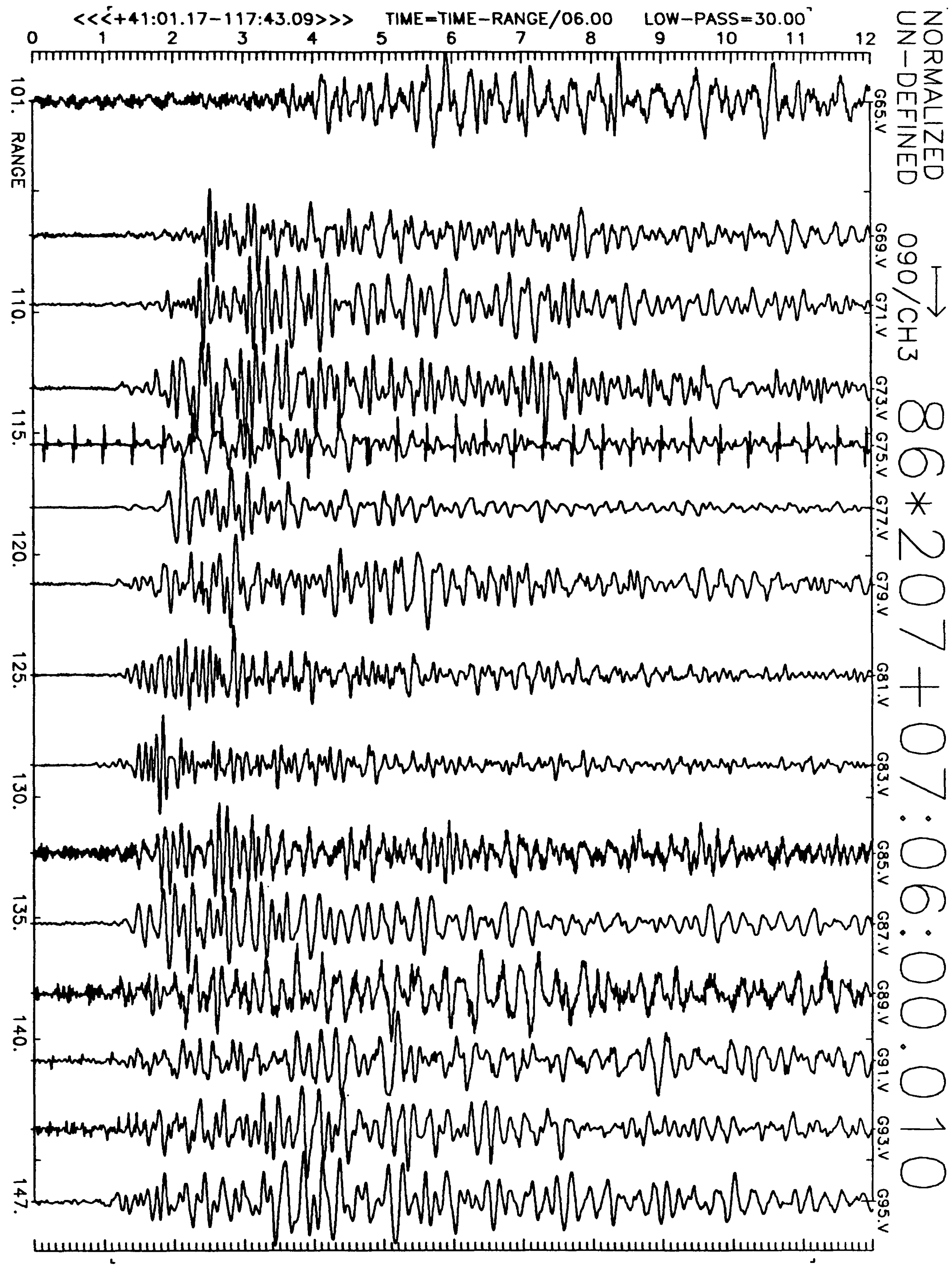

Figure B7(c), shot point 8: 12 second velocity record. Positive N106E motion is to right. Abscissa is distance to shot point. Top of trace is labeled with station number. Times are reduced by 6 km/sec. Shot time is indicated.

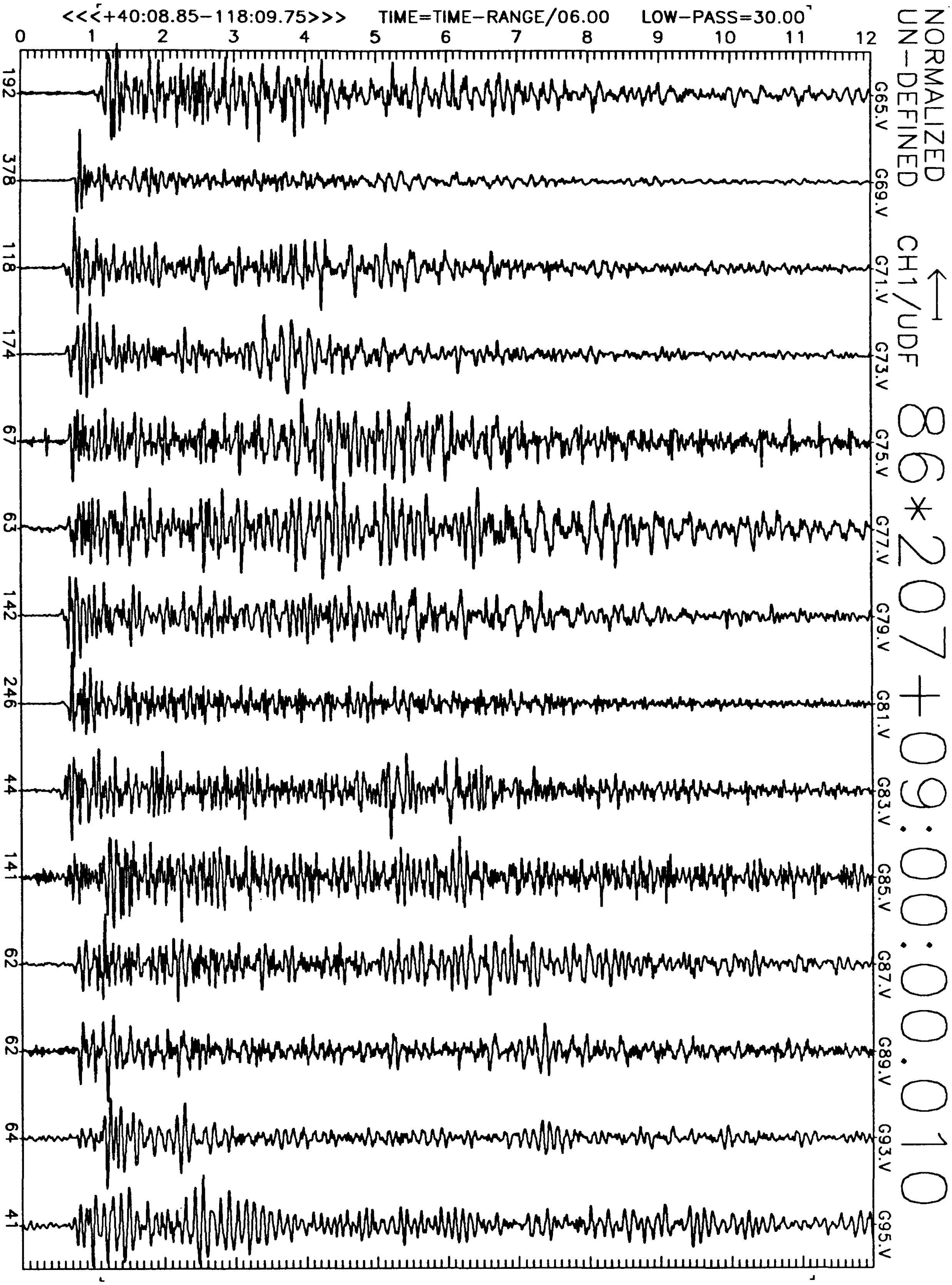

Figure B8(a), shot point 13: 12 second vertical velocity record. Abscissa is labeled with maximum counts in record (multiply by $\frac{10}{2^{24}-2^{5}}$ $\approx 6 \times 10^{-7}$ to get cm/sec). Times are reduced by 6 km/sec. Shot time is indicated.

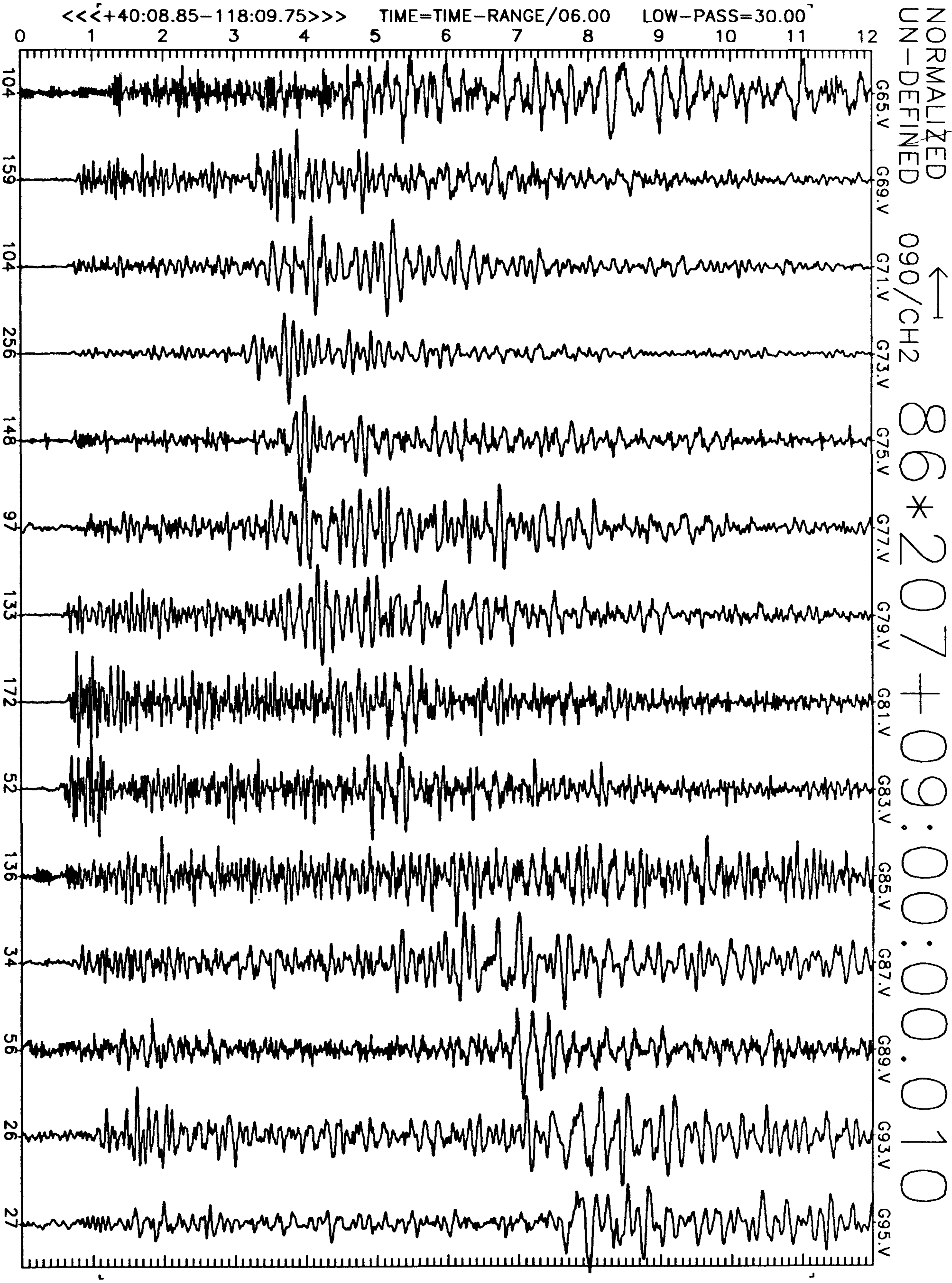

Figure B8(b), shot point 13: 12 second N16E velocity record. Abscissa is labeled with maximum counts in record (multiply by $\frac{10}{2^{24}-2^{9}}$ ≈ 6 × 10^{-7} to get cm/sec). Times are reduced by 6 km/sec. Shot time is indicated.

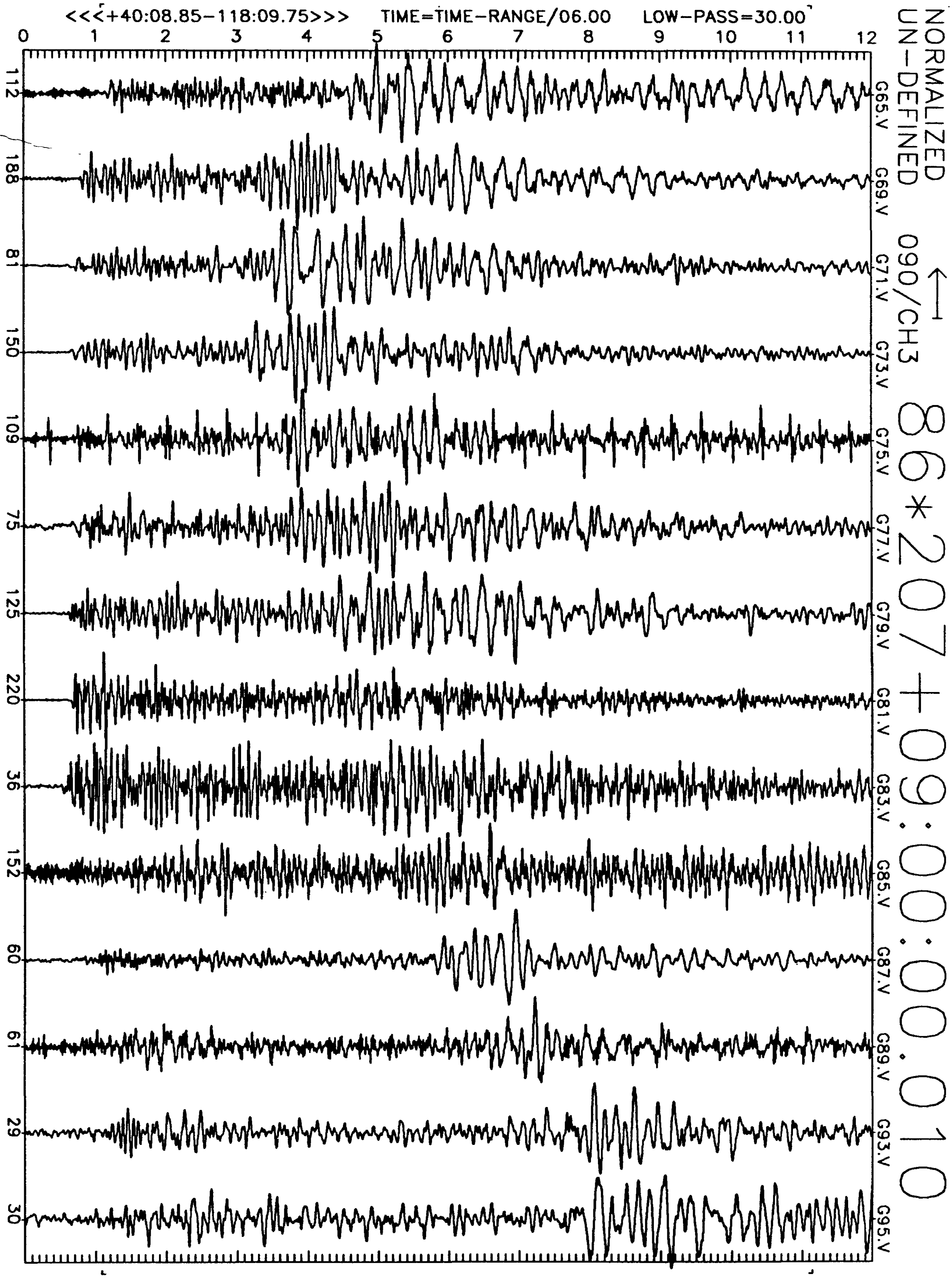

Figure B8(c), shot point 13: 12 second N106E velocity record. Abscissa is labeled with maximum counts in record (multiply by $\frac{10}{2^{24}-2^{9}} \approx 6 \times 10^{-7}$ to get cm/sec). Times are reduced by 6 km/sec. Shot time is indicated.

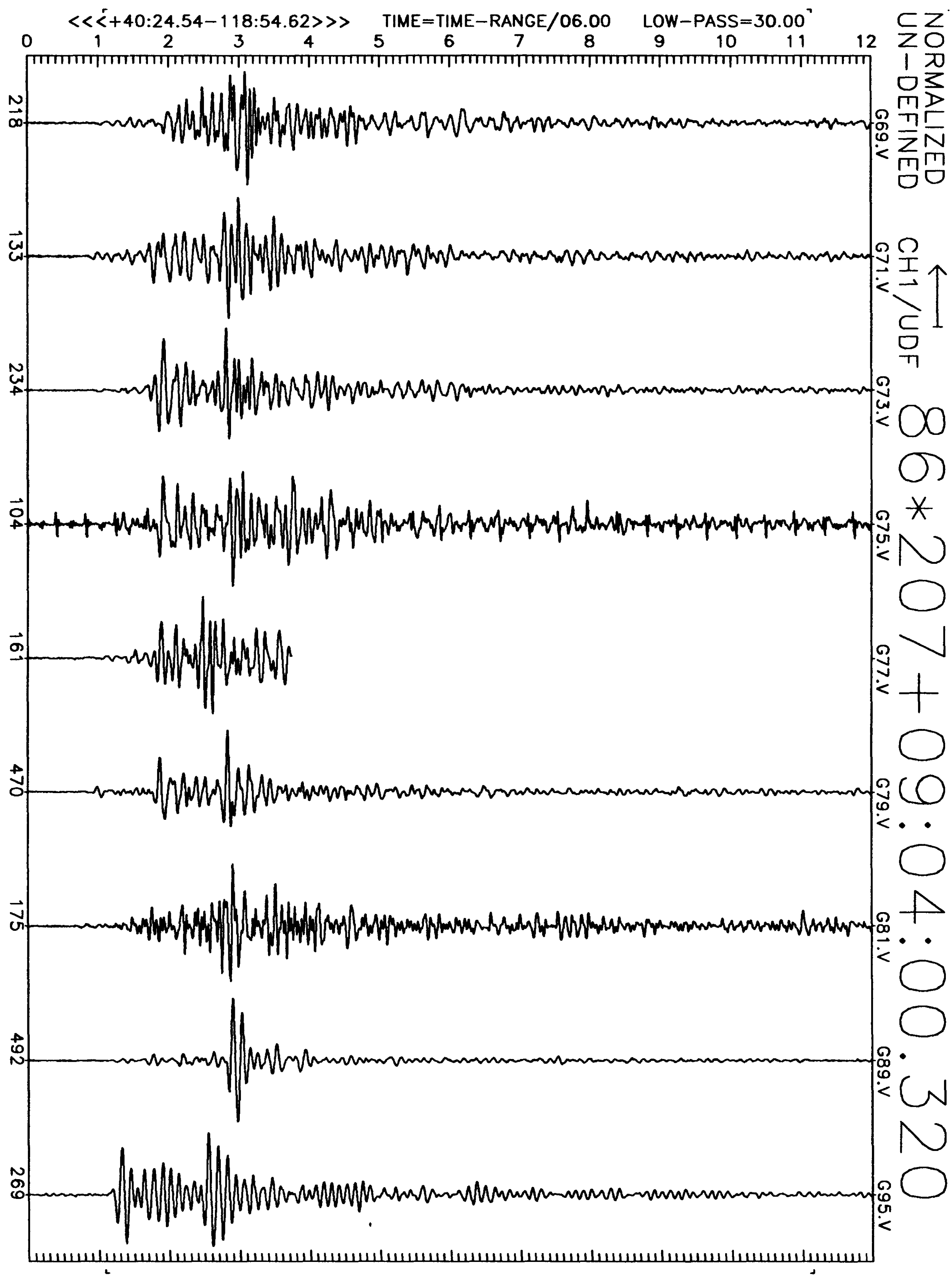

Figure B9(a), shot point 2: 12 second vertical velocity record. Abscissa is labeled with maximum counts in record (multiply by $\frac{10}{2^{24}-2^{5}} \approx 6 \times 10^{-7}$ to get cm/sec). Times are reduced by 6 km/sec. Shot time is indicated.

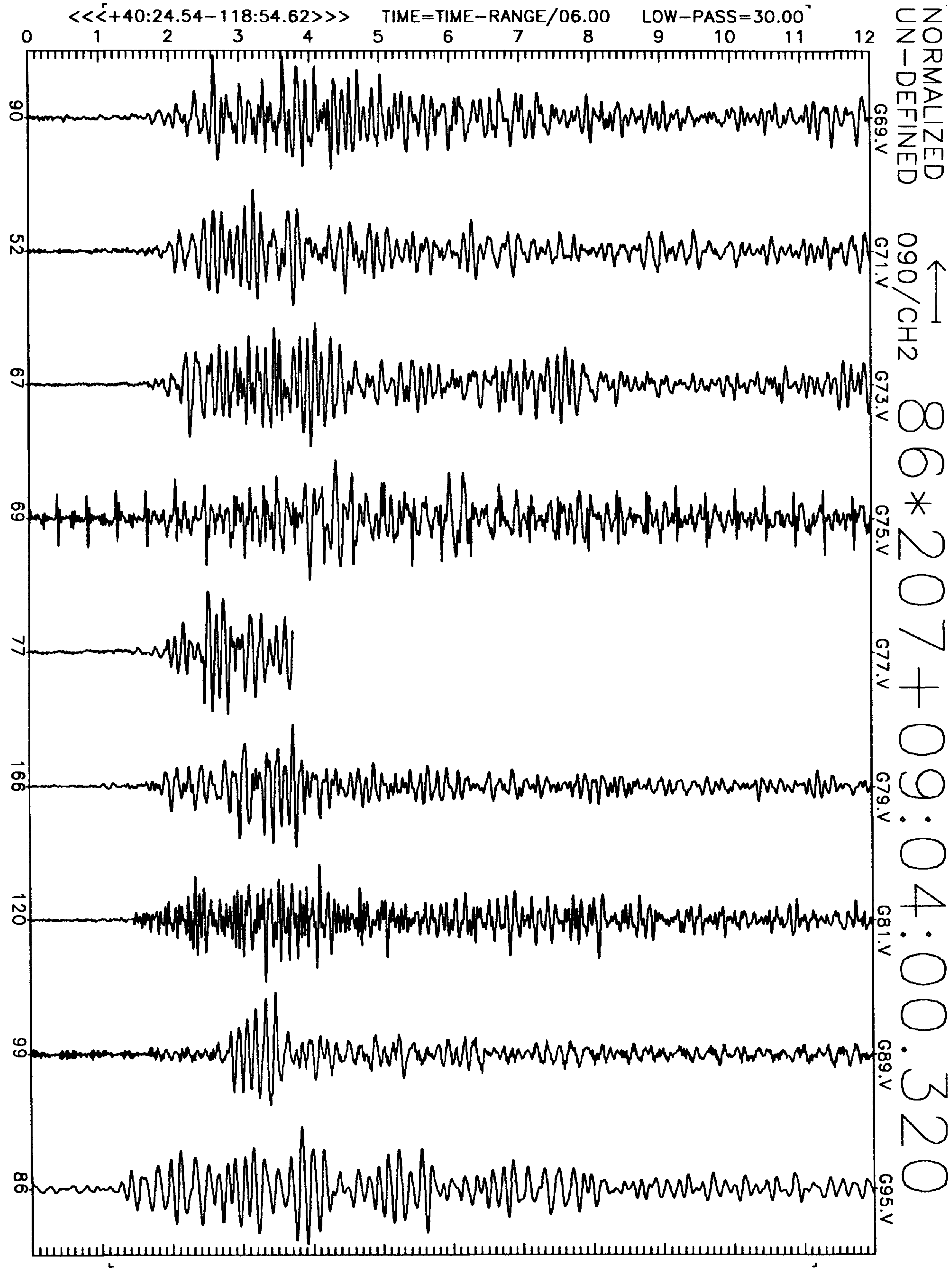

Figure B9(b), shot point 2: 12 second N16E velocity record. Abscissa is labeled with maximum counts in record (multiply by $\frac{10}{2^{24}-2^{9}} \approx 6 \times 10^{-7}$ to get cm/sec). Times are reduced by 6 km/sec. Shot time is indicated.

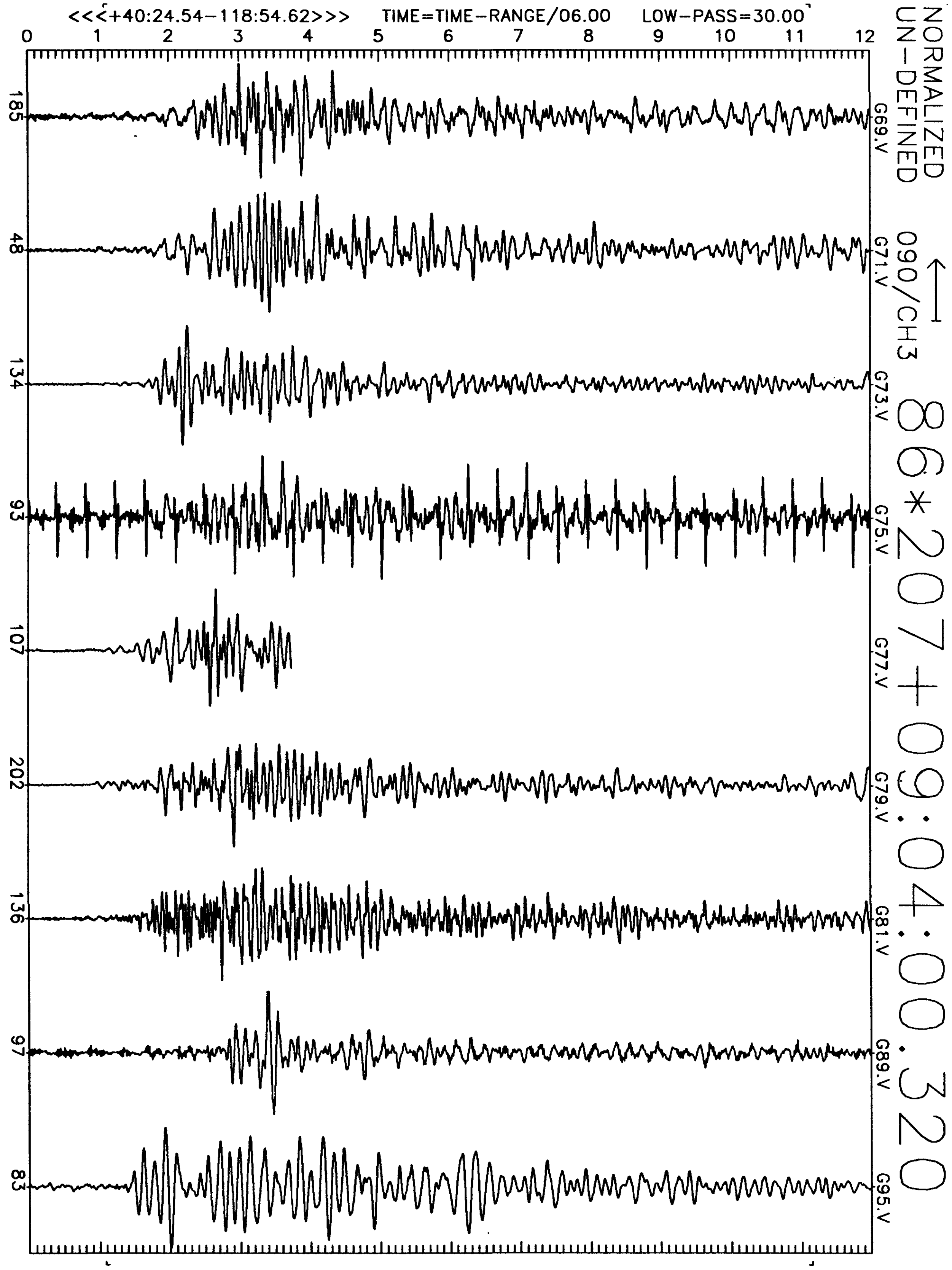

Figure B9(c), shot point 2: 12 second N106E velocity record. Abscissa is labeled with maximum counts in record (multiply by $\frac{10}{2^{24}-2^{9}} \approx 6 \times 10^{-7}$ to get cm/sec). Times are reduced by 6 km/sec. Shot time is indicated.

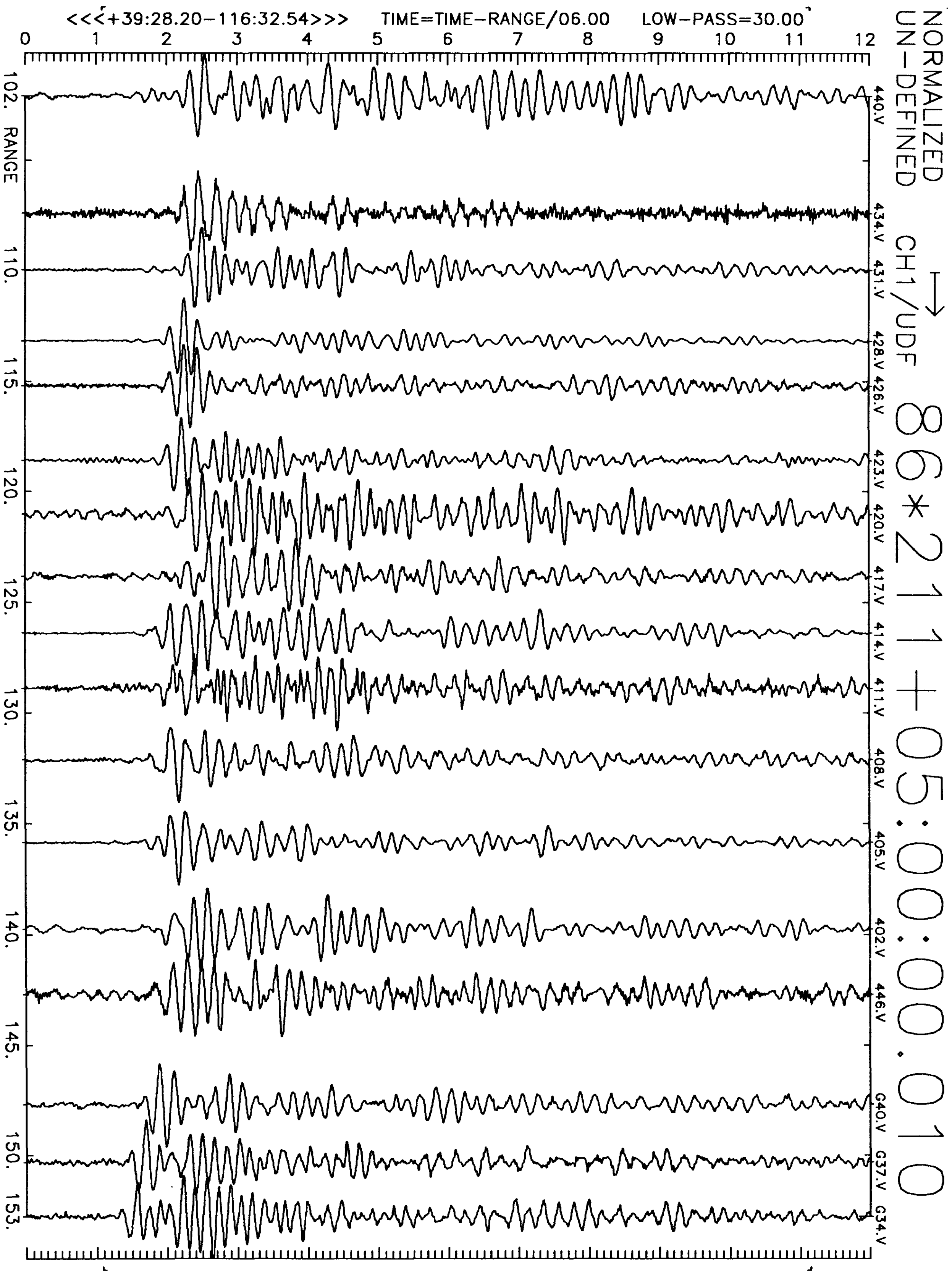

Figure C1(a), shot point 7: 12 second velocity record. Positive vertical motion is to right. Abscissa is distance to shot point. Top of trace is labeled with station number. Times are reduced by 6 km/sec. Shot time is indicated.

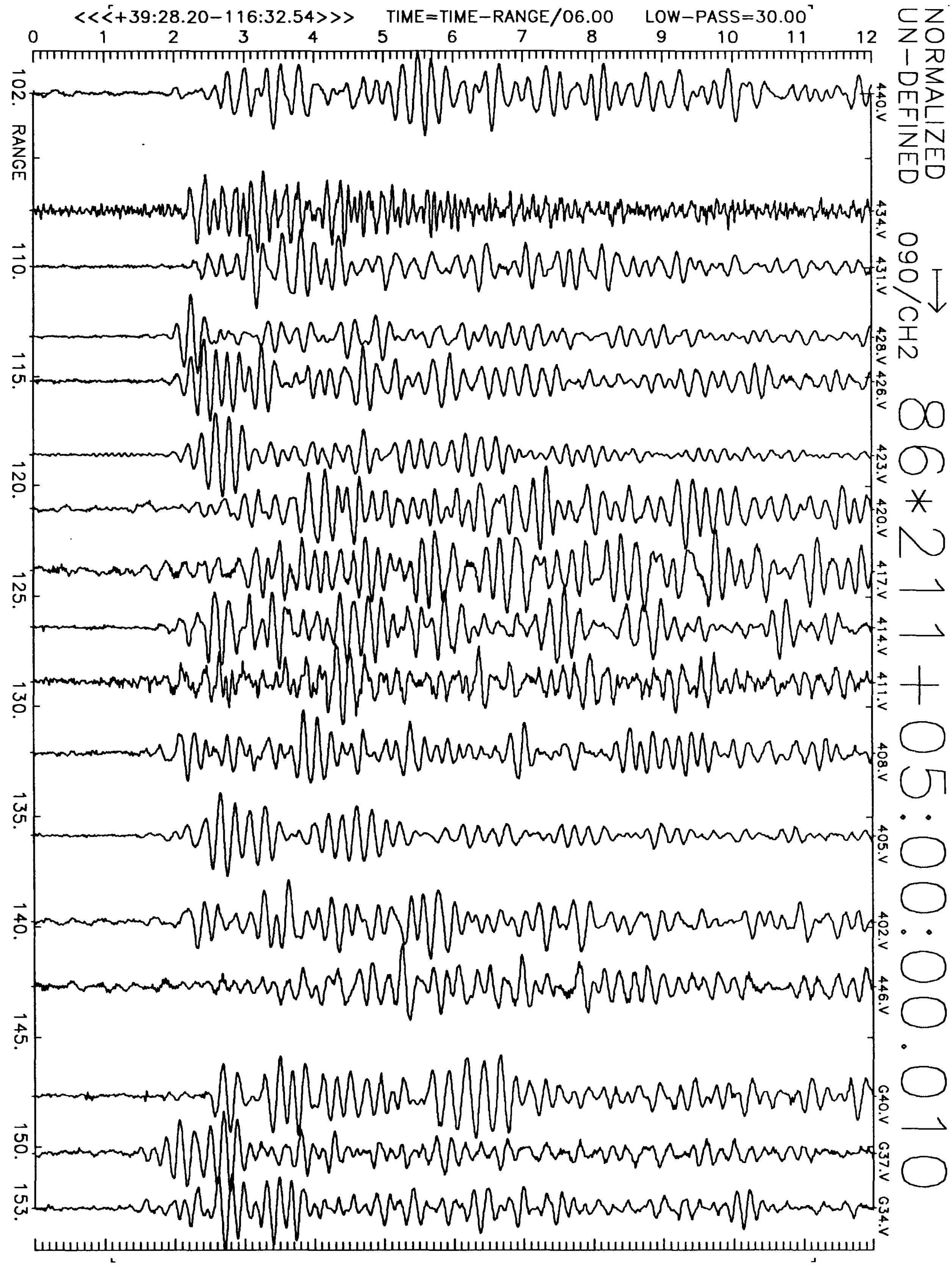

Figure C1(b), shot point 7: 12 second velocity record. Positive N16E motion is to right. Abscissa is distance to shot point. Top of trace is labeled with station number. Times are reduced by 6 km/sec. Shot time is indicated.

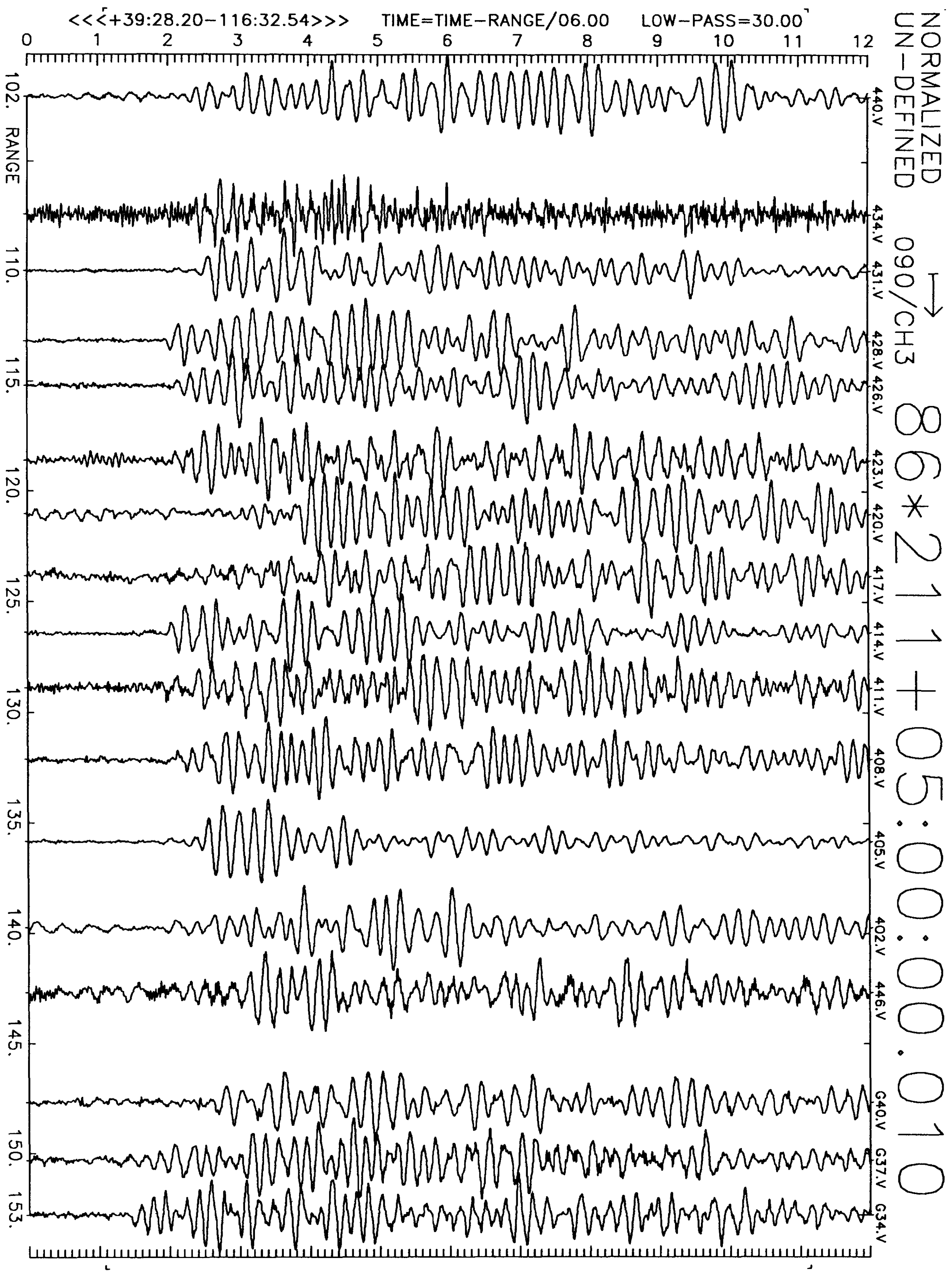

Figure C1(c), shot point 7: 12 second velocity record. Positive N106E motion is to right. Abscissa is distance to shot point. Top of trace is labeled with station number. Times are reduced by 6 km/sec. Shot time is indicated.

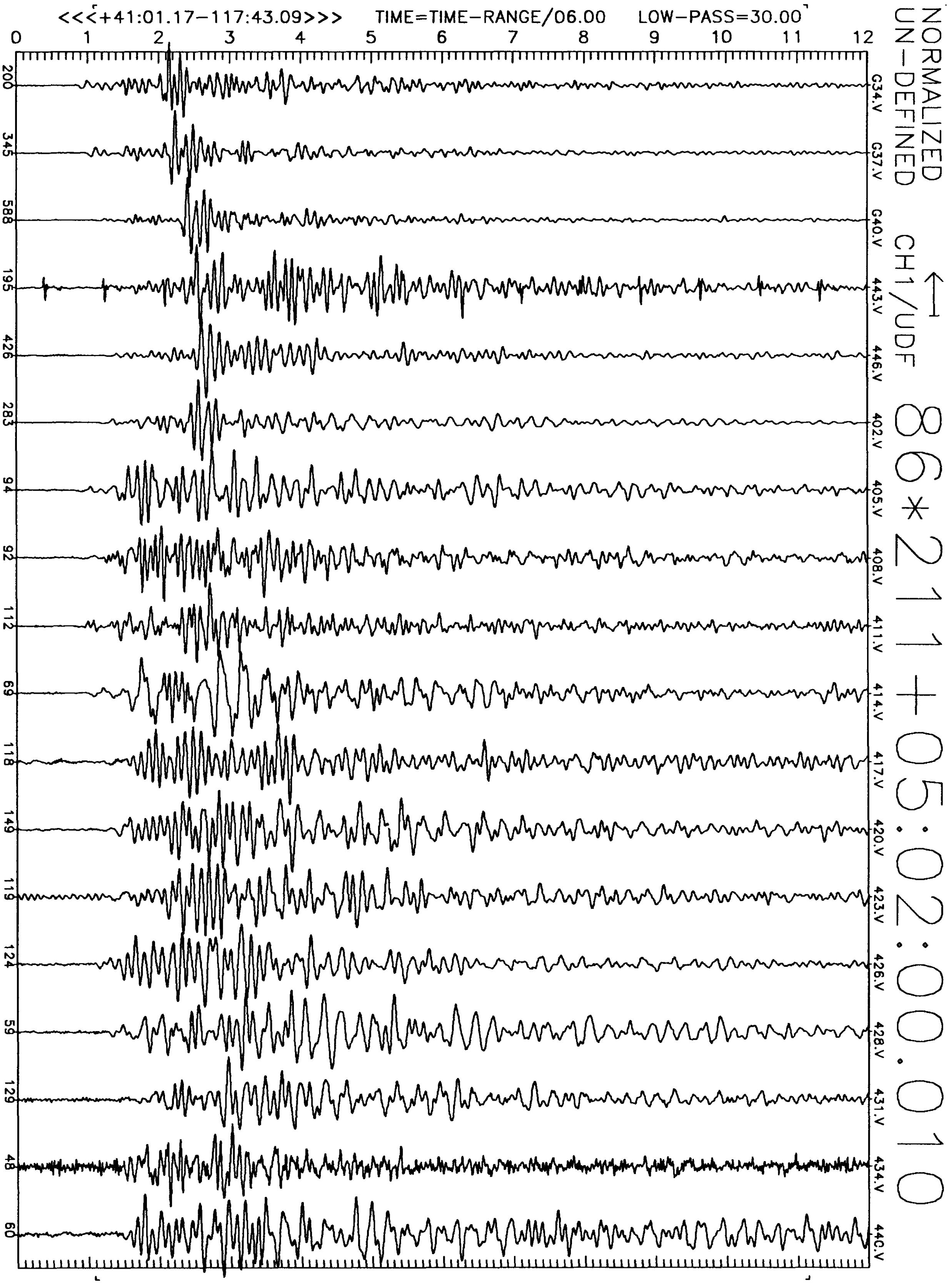

Figure C2(a), shot point 8: 12 second vertical velocity record. Abscissa is labeled with maximum counts in record (multiply by $\frac{10}{2^{24}-2^{9}} \approx 6 \times 10^{-7}$ to get cm/sec). Times are reduced by 6 km/sec. Shot time is indicated.

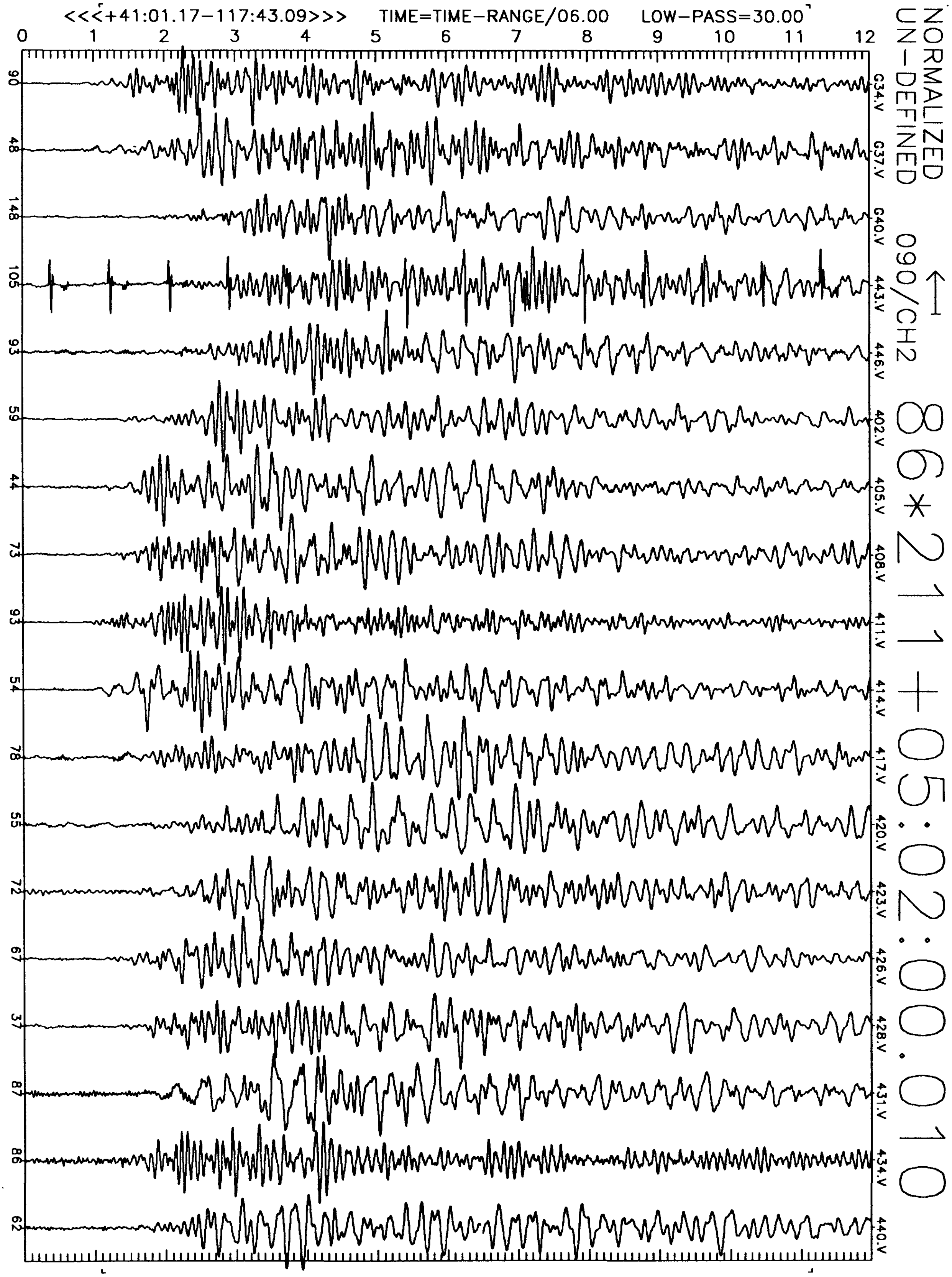

Figure C2(b), shot point 8: 12 second N16E velocity record. Abscissa is labeled with maximum counts in record (multiply by $\frac{10}{2^{24}-2^{5}} \approx 6 \times 10^{-7}$ to get cm/sec). Times are reduced by 6 km/sec. Shot time is indicated.

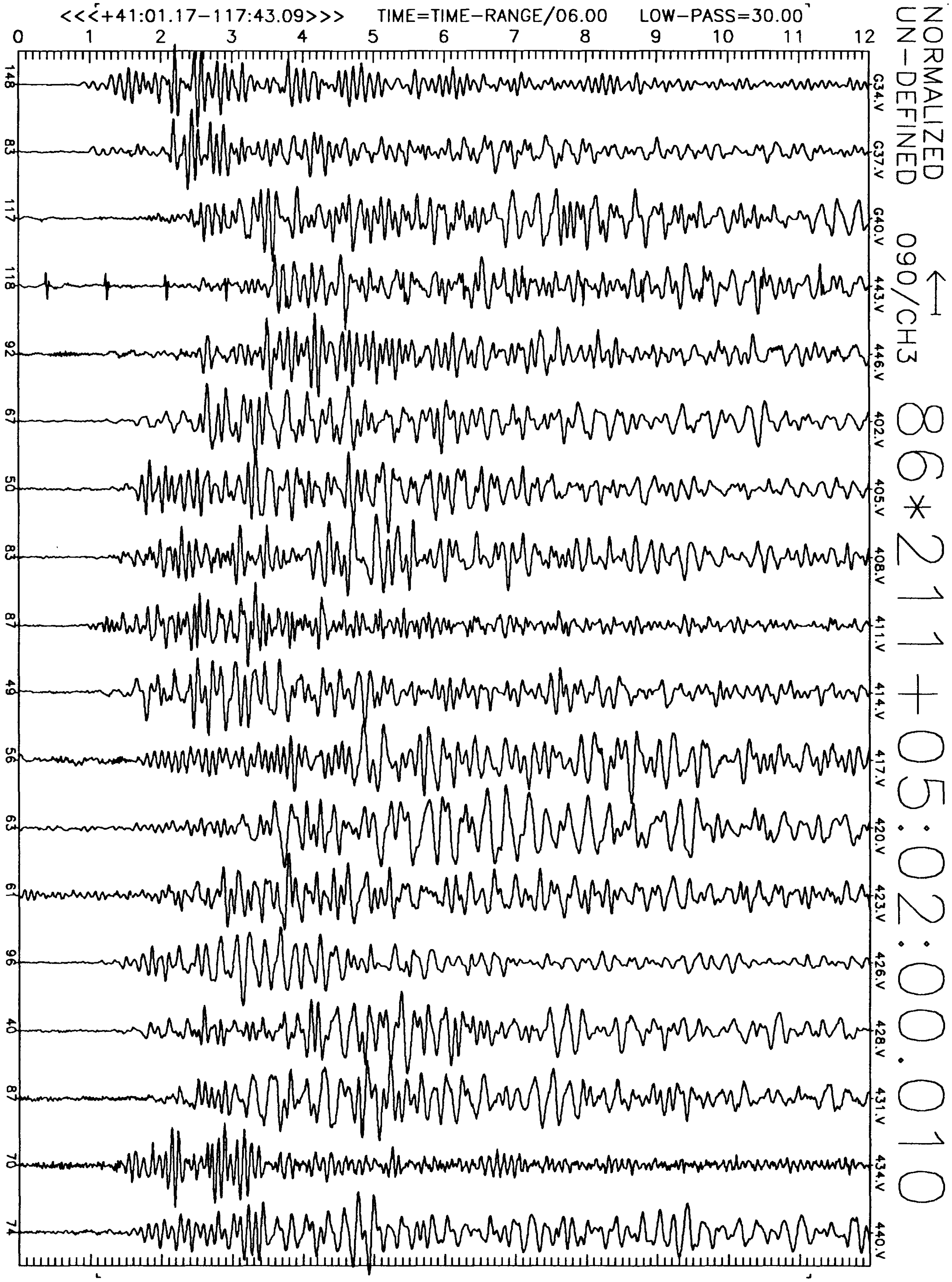

Figure C2(c), shot point 8: 12 second N106E velocity record. Abscissa is labeled with maximum counts in record (multiply by $\frac{10}{2^{24}-2^{5}} \approx 6 \times 10^{-7}$ to get cm/sec). Times are reduced by 6 km/sec. Shot time is indicated.

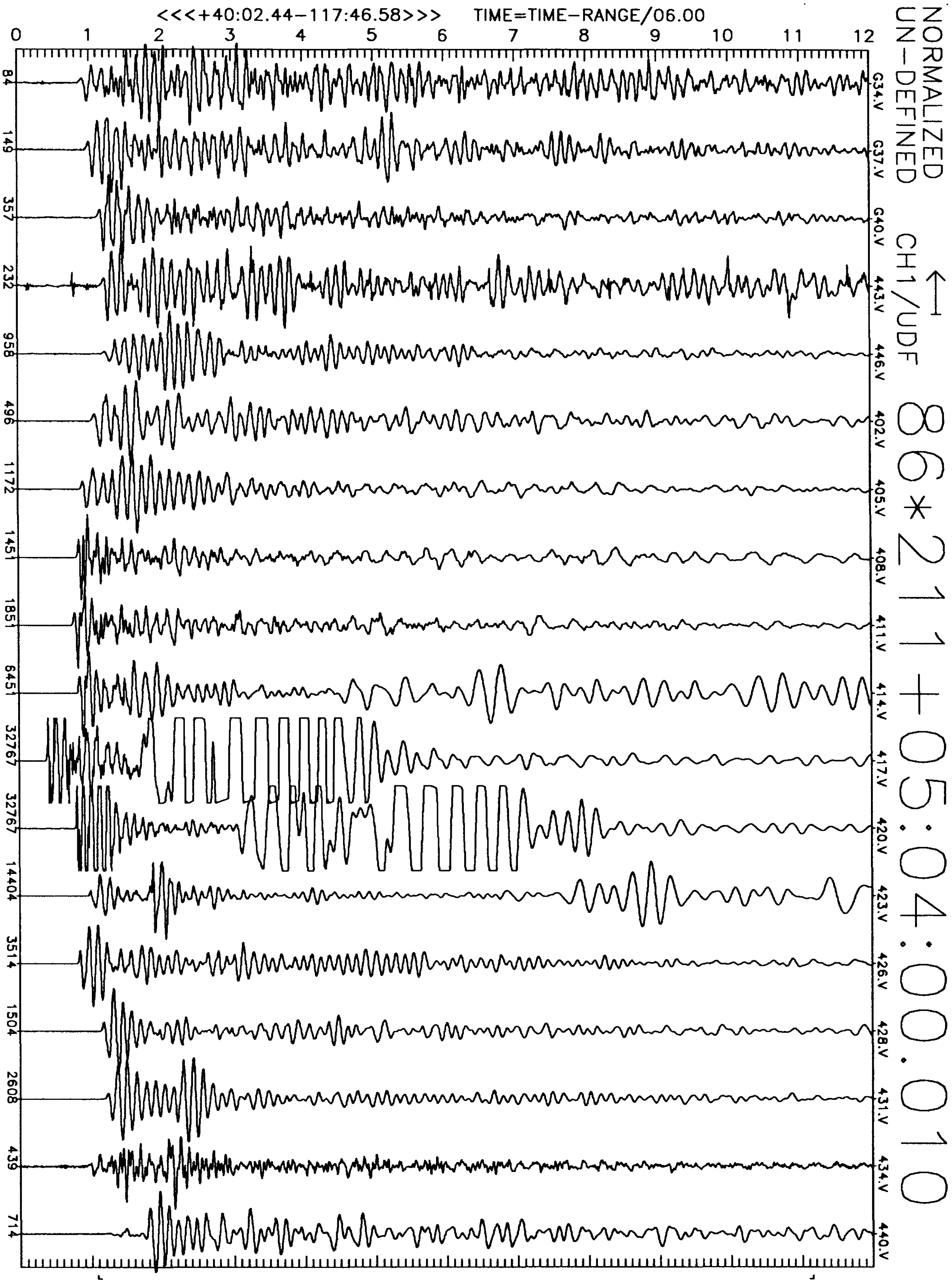

Figure C3(a), shot point 14: 12 second vertical velocity record. Abscissa is labeled with maximum counts in record (multiply by $\frac{10}{2^{24}-2^{5}} \approx 6 \times 10^{-7}$ to get cm/sec). Times are reduced by 6 km/sec. Shot time is indicated.

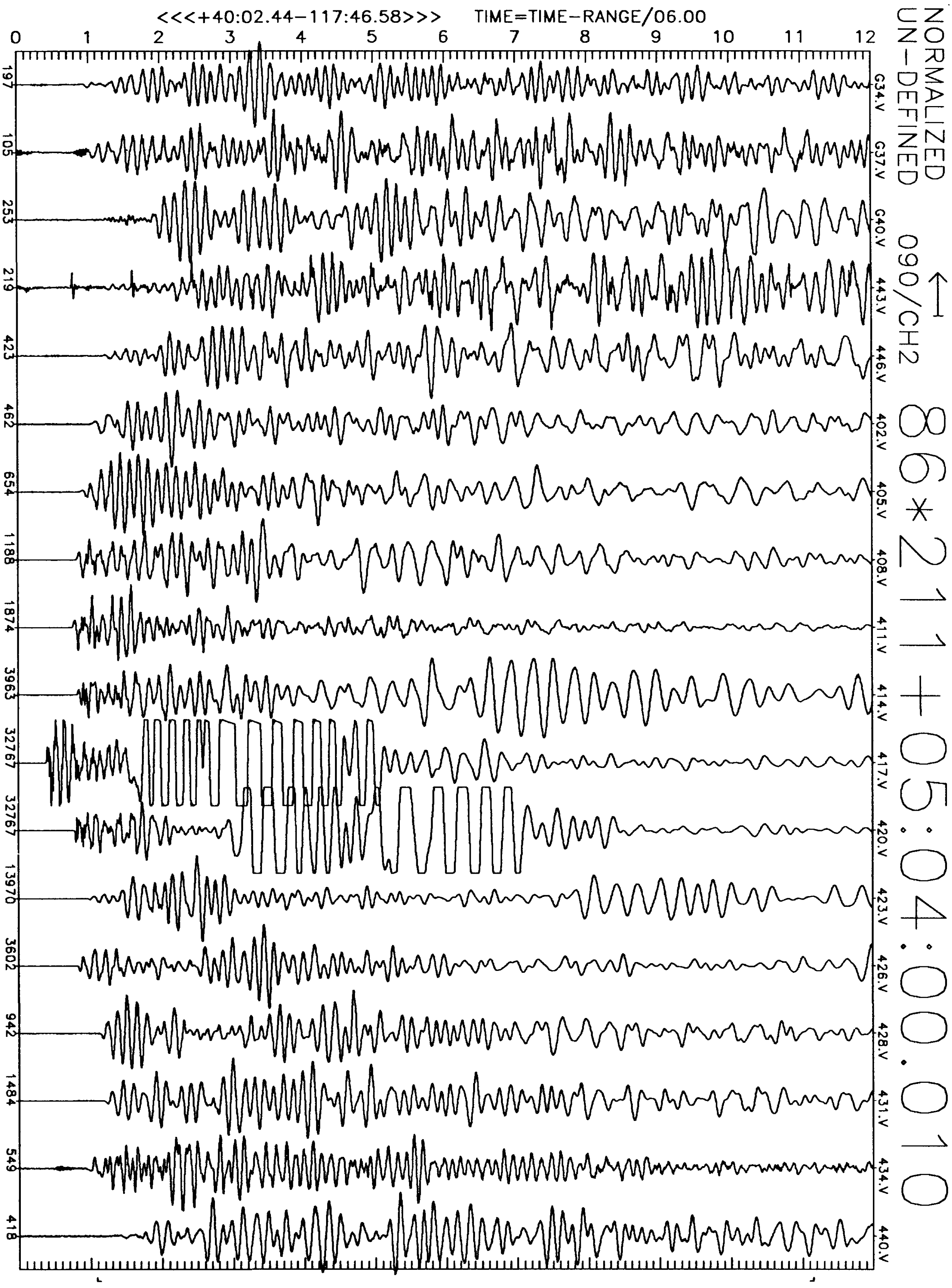

Figure C3(b), shot point 14: 12 second N16E velocity record. Abscissa is labeled with maximum counts in record (multiply by $\frac{10}{2^{24}-2^{9}} \approx 6 \times 10^{-7}$ to get cm/sec). Times are reduced by 6 km/sec. Shot time is indicated.

]

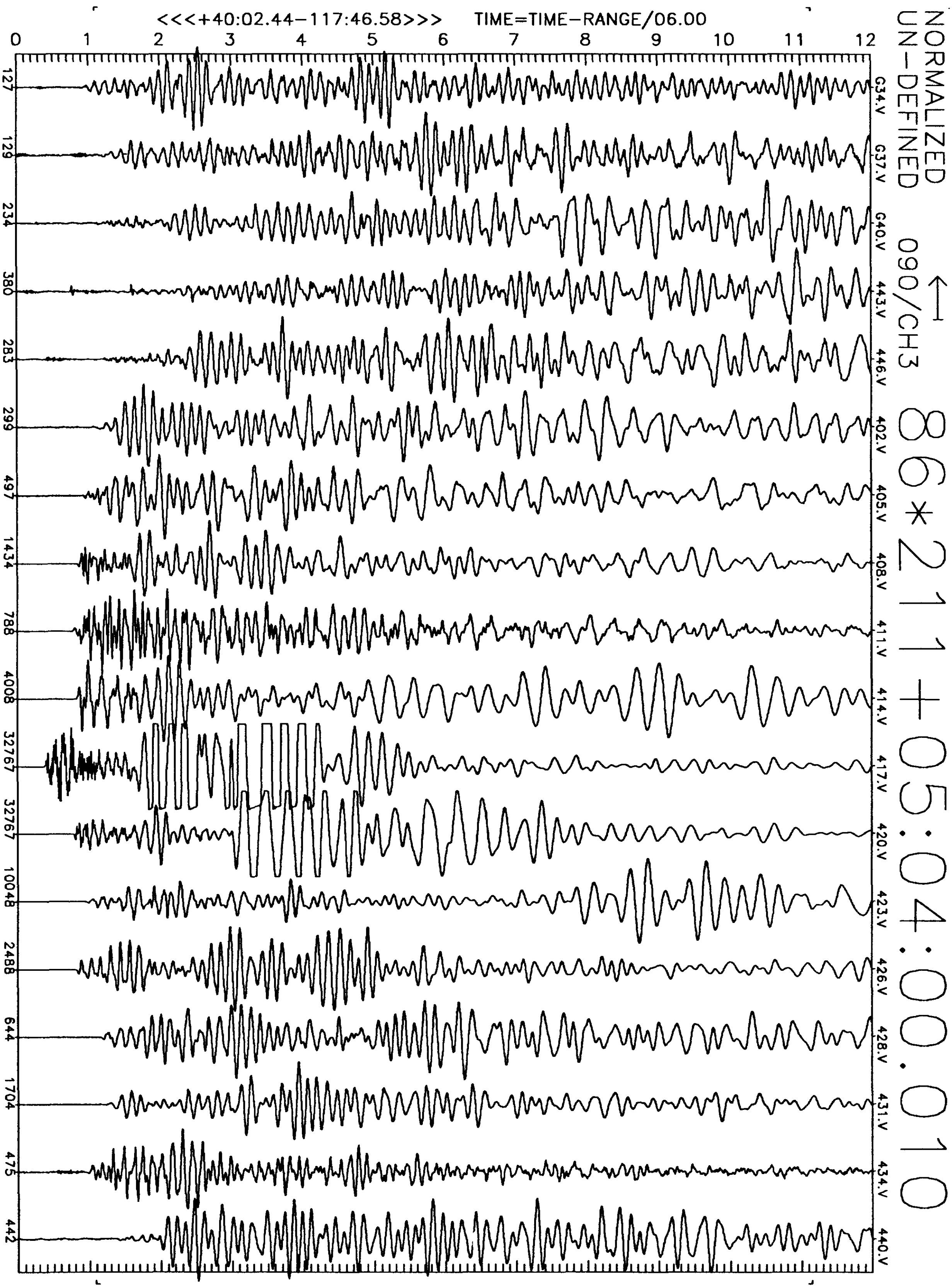

Figure C3(c), shot point 14: 12 second N106E velocity record. Abscissa is labeled with maximum counts in record (multiply by $\frac{10}{2^{24}-2^{5}} \approx 6 \times 10^{-7}$ to get cm/sec). Times are reduced by 6 km/sec. Shot time is indicated.

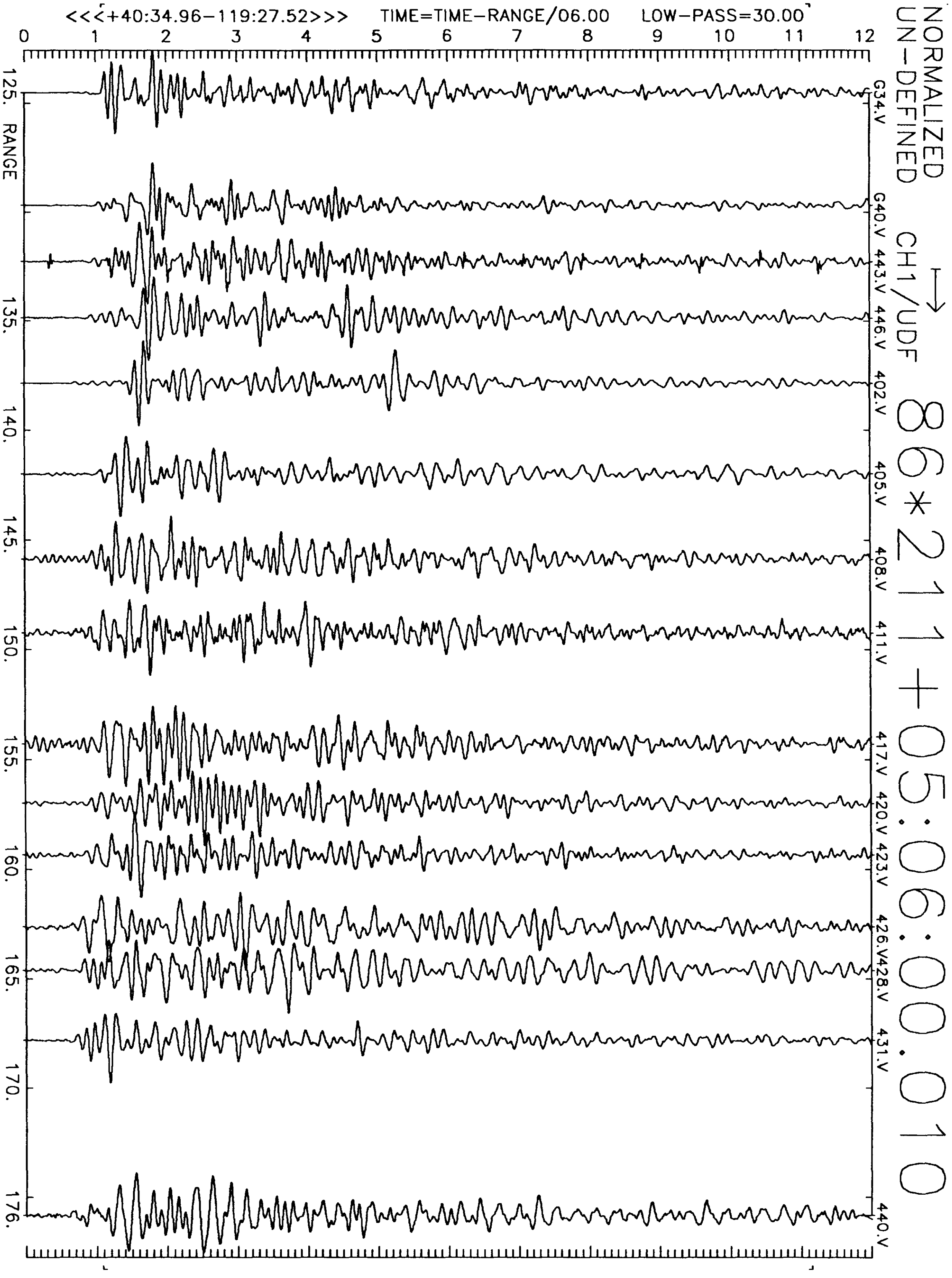

Figure C4(a), shot point 1: 12 second velocity record. Positive vertical motion is to right. Abscissa is distance to shot point. Top of trace is labeled with station number. Times are reduced by 6 km/sec. Shot time is indicated.

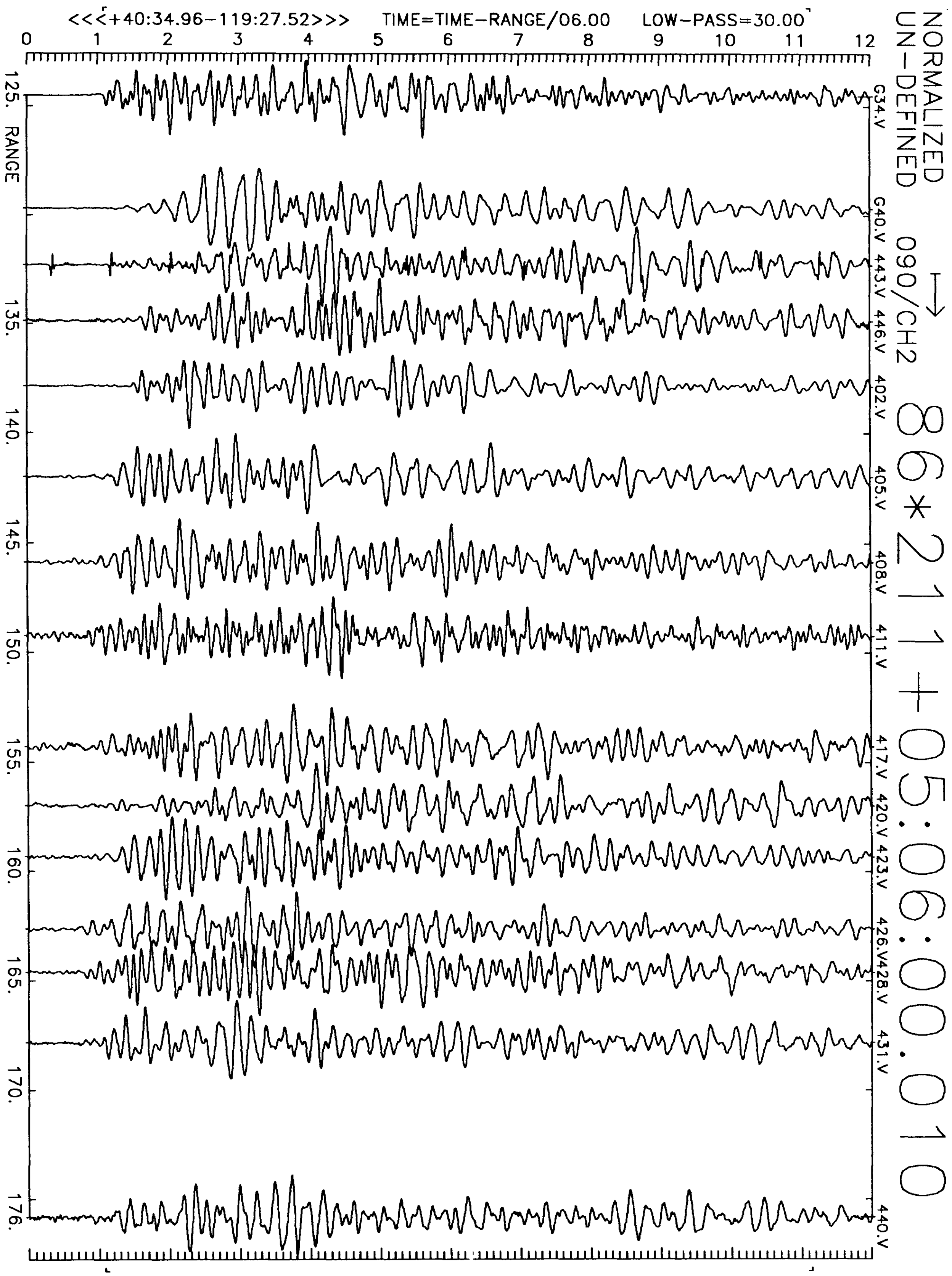

Figure C4(b), shot point 1: 12 second velocity record. Positive N16E motion is to right. Abscissa is distance to shot point. Top of trace is labeled with station number. Times are reduced by 6 km/sec. Shot time is indicated.

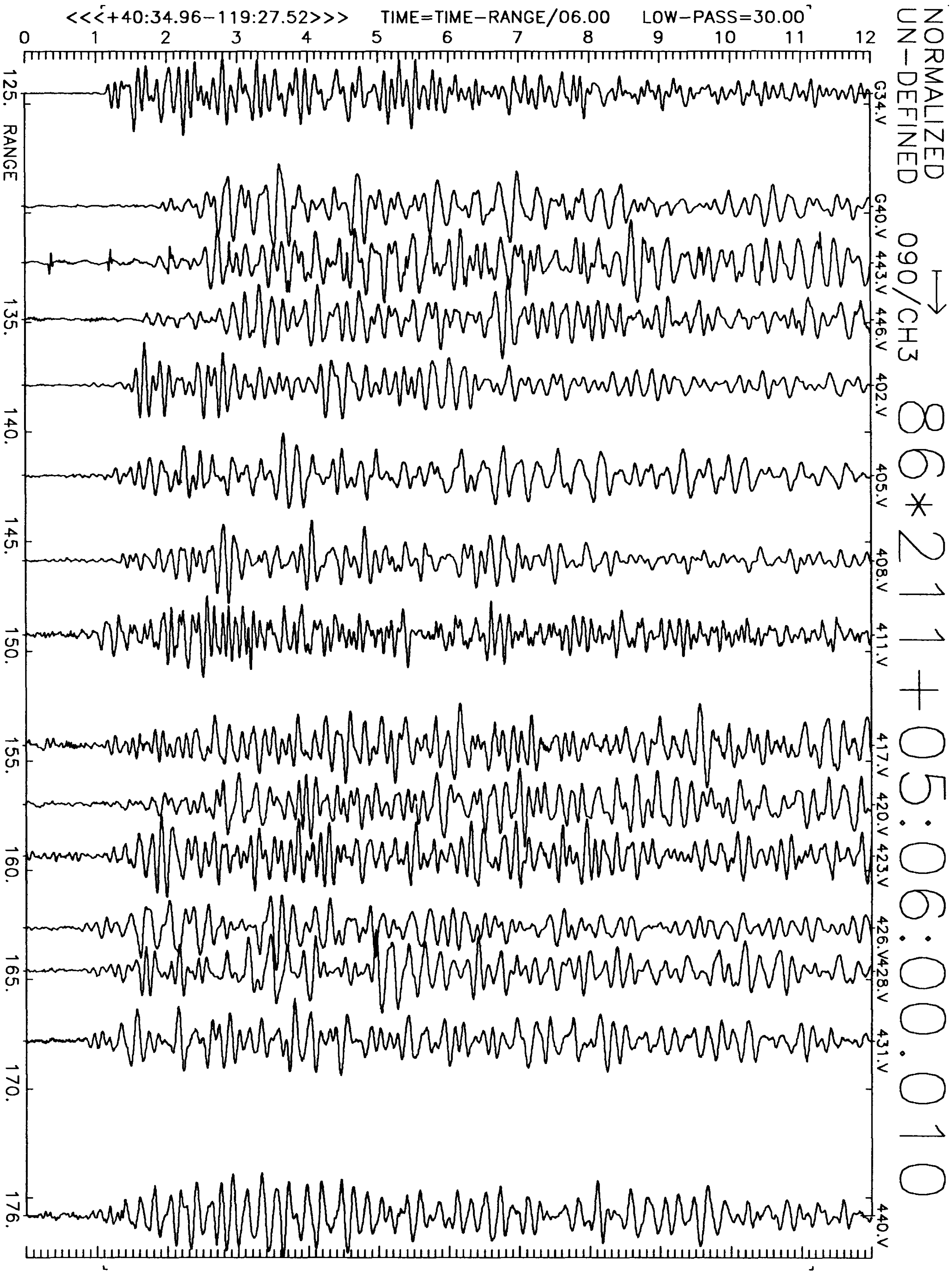

Figure C4(c), shot point 1: 12 second velocity record. Positive N106E motion is to right. Abscissa is distance to shot point. Top of trace is labeled with station number. Times are reduced by 6 km/sec. Shot time is indicated.

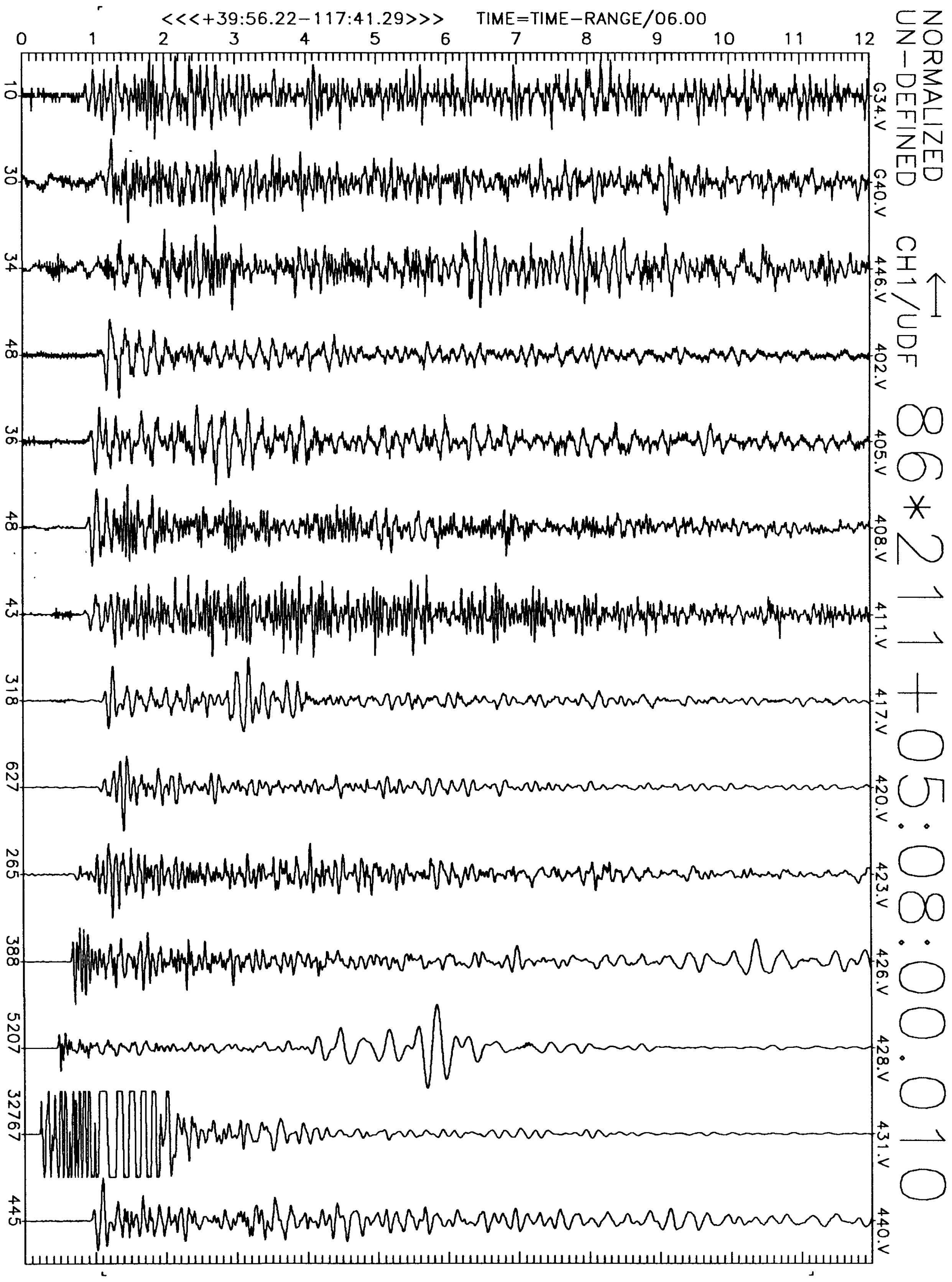

Figure C5(a), shot point 15: 12 second vertical velocity record. Abscissa is labeled with maximum counts in record (multiply by $\frac{10}{2^{24}-2^{5}} \approx 6 \times 10^{-7}$ to get cm/sec). Times are reduced by 6 km/sec. Shot time is indicated.

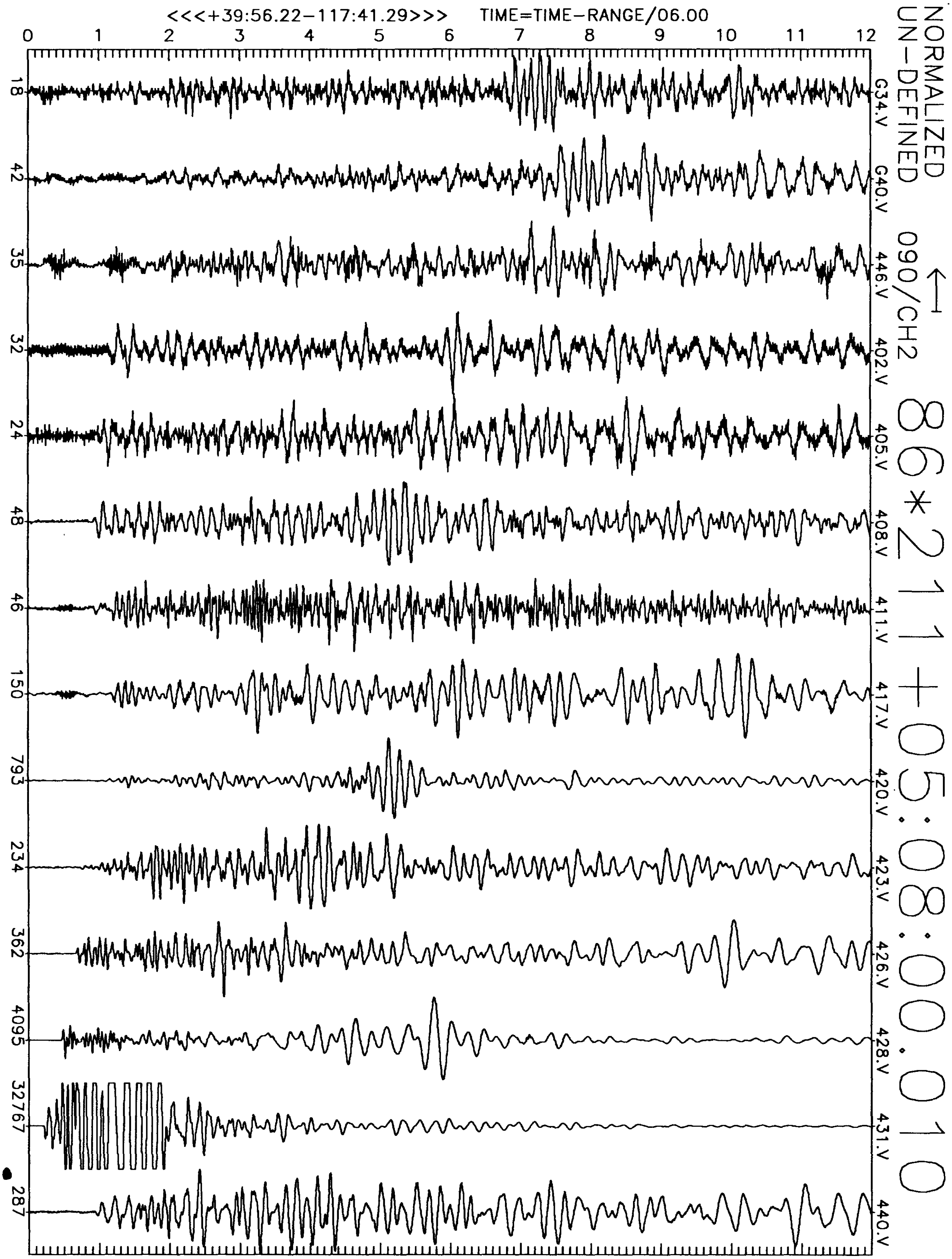

Figure C5(b), shot point 15: 12 second N16E velocity record. Abscissa is labeled with maximum counts in record (multiply by $\frac{10}{2^{24}-2^{5}} \approx 6 \times 10^{-7}$ to get cm/sec). Times are reduced by 6 km/sec. Shot time is indicated.

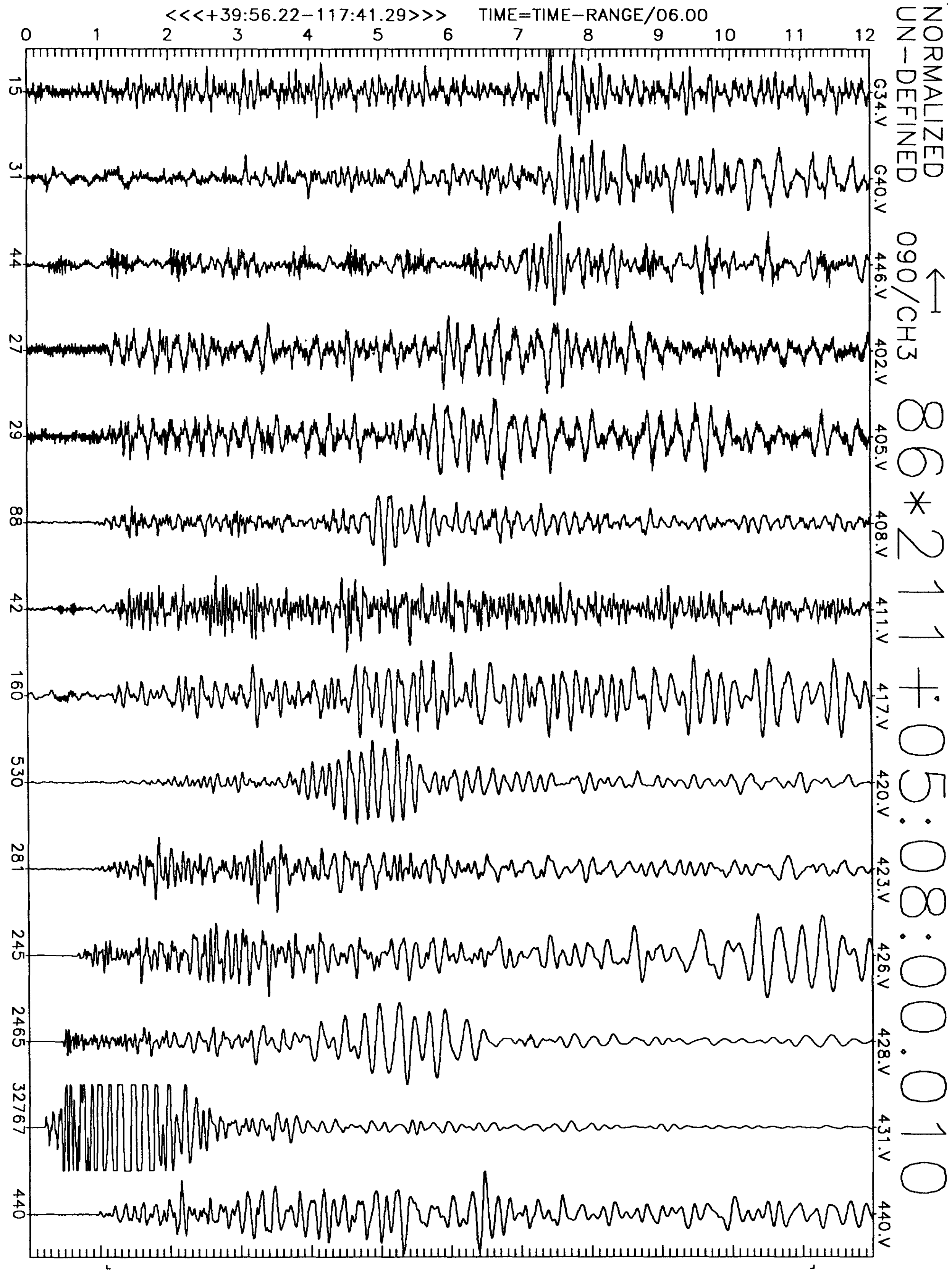

Figure C5(c), shot point 15: 12 second N106E velocity record. Abscissa is labeled with maximum counts in record (multiply by $\frac{10}{2^{24}-2^{5}} \approx 6 \times 10^{-7}$ to get cm/sec). Times are reduced by 6 km/sec. Shot time is indicated.

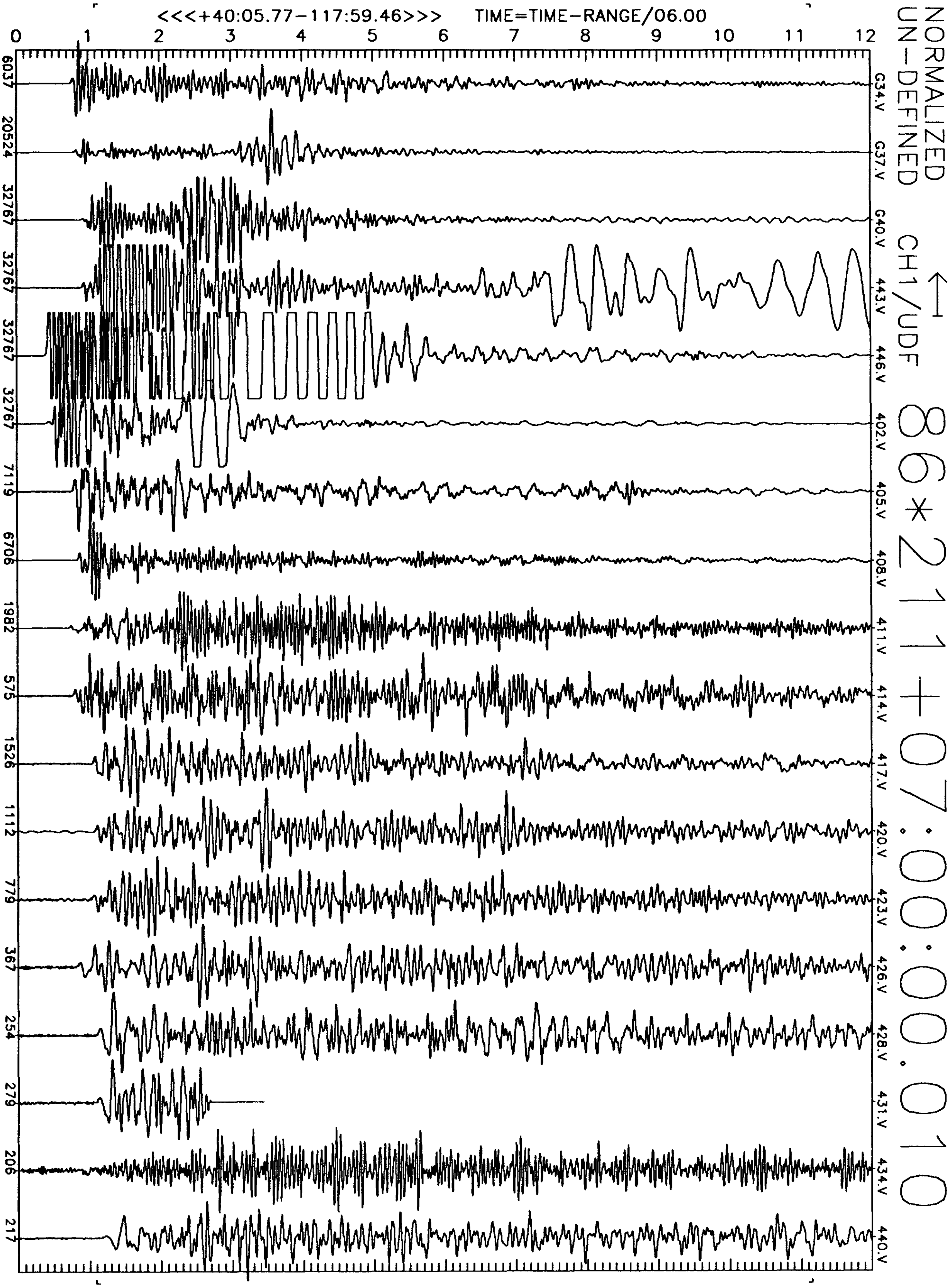

Figure C6(a), shot point 4: 12 second vertical velocity record. Abscissa is labeled with maximum counts in record (multiply by $\frac{10}{2^{24}-2^{9}} \approx 6 \times 10^{-7}$ to get cm/sec). Times are reduced by 6 km/sec. Shot time is indicated.

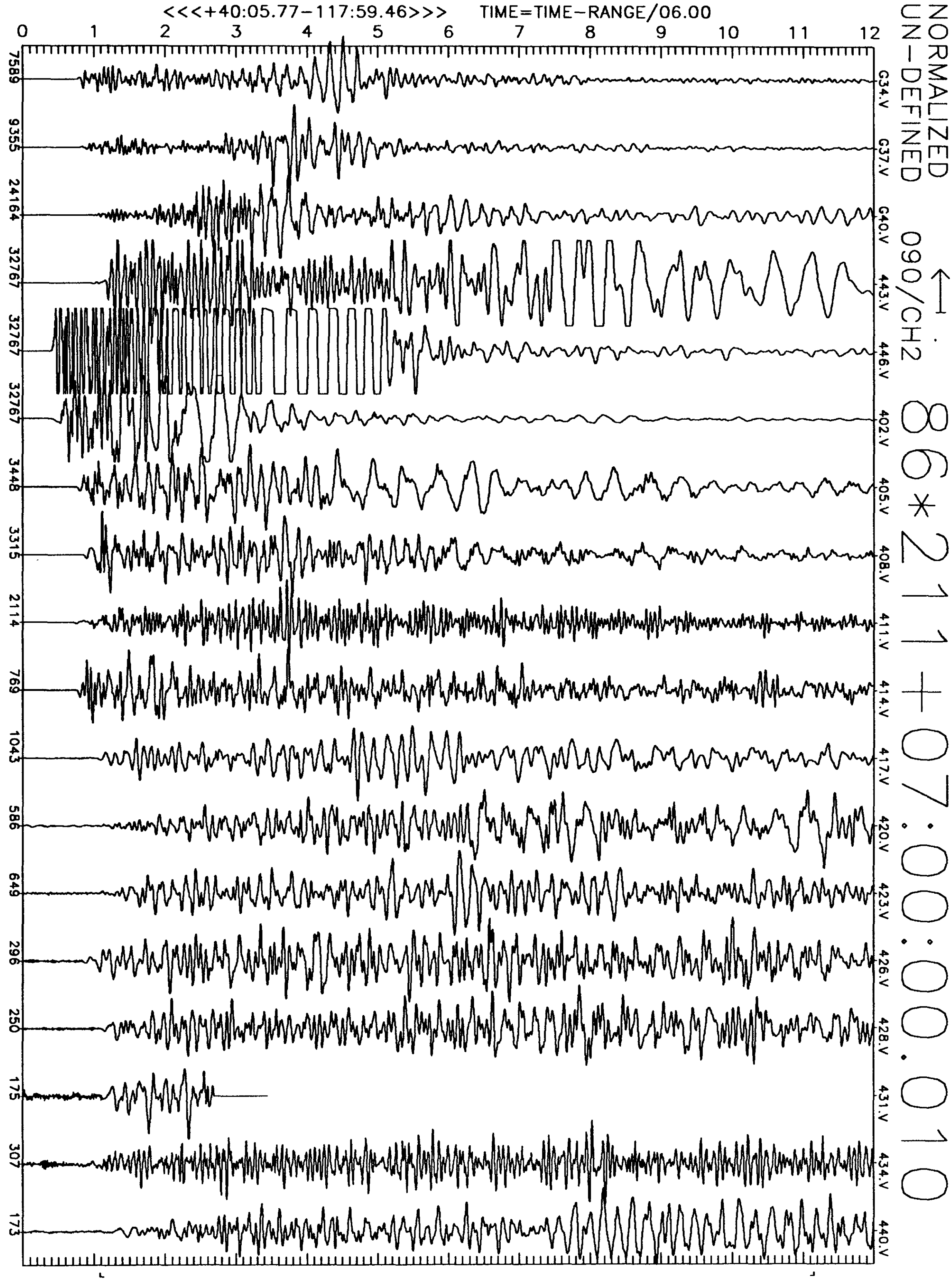

Figure C6(b), shot point 4: 12 second N305E velocity record. Abscissa is labeled with maximum counts in record (multiply by $\frac{10}{2^{24}-2^{9}} \approx 6 \times 10^{-7}$ to get cm/sec). Times are reduced by 6 km/sec. Shot time is indicated.

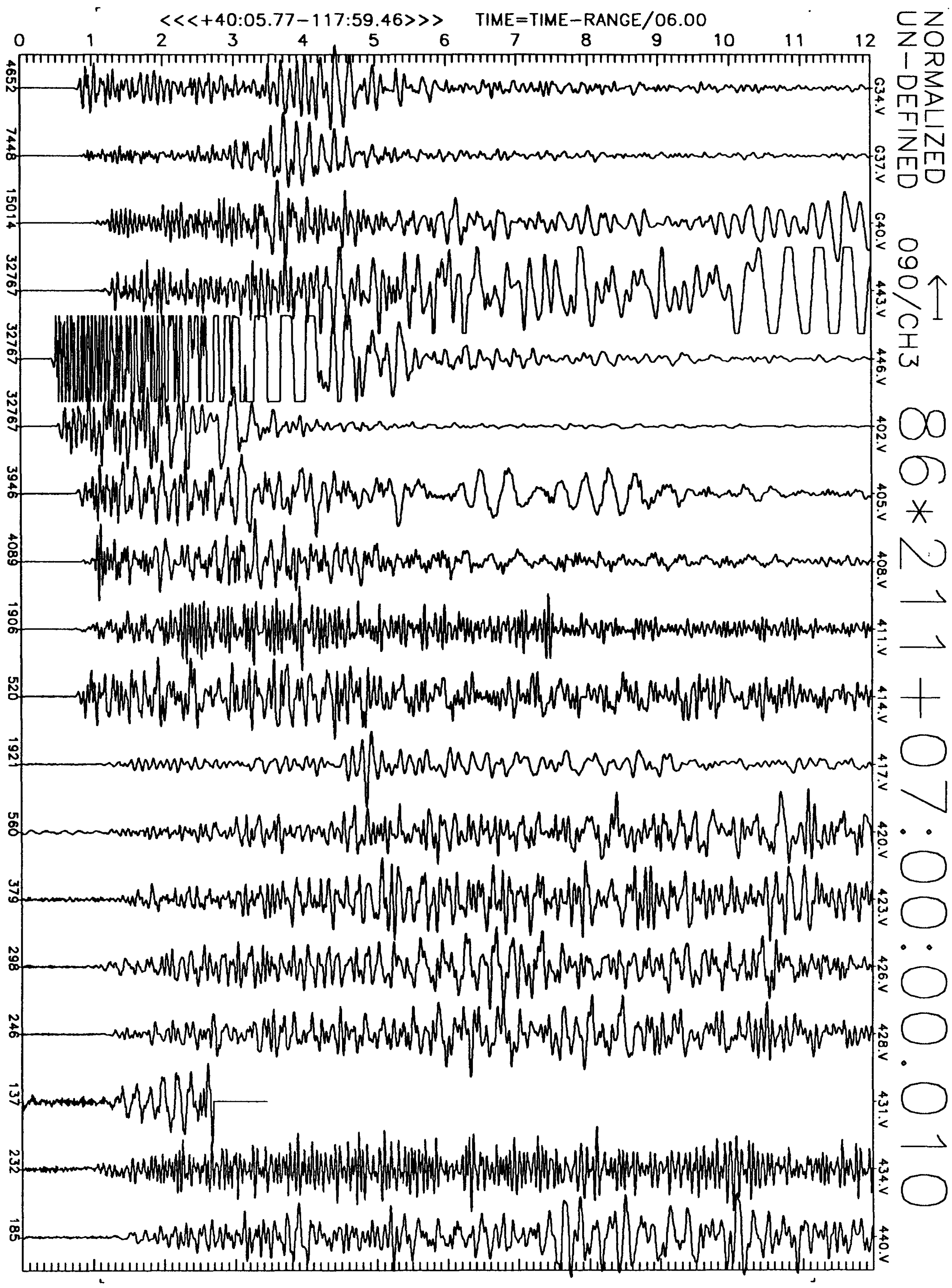

Figure C6(c), shot point 4: 12 second N35E velocity record. Abscissa is labeled with maximum counts in record (multiply by $\frac{10}{2^{24}-2^{9}} \approx 6 \times 10^{-7}$ to get cm/sec). Times are reduced by 6 km/sec. Shot time is indicated.

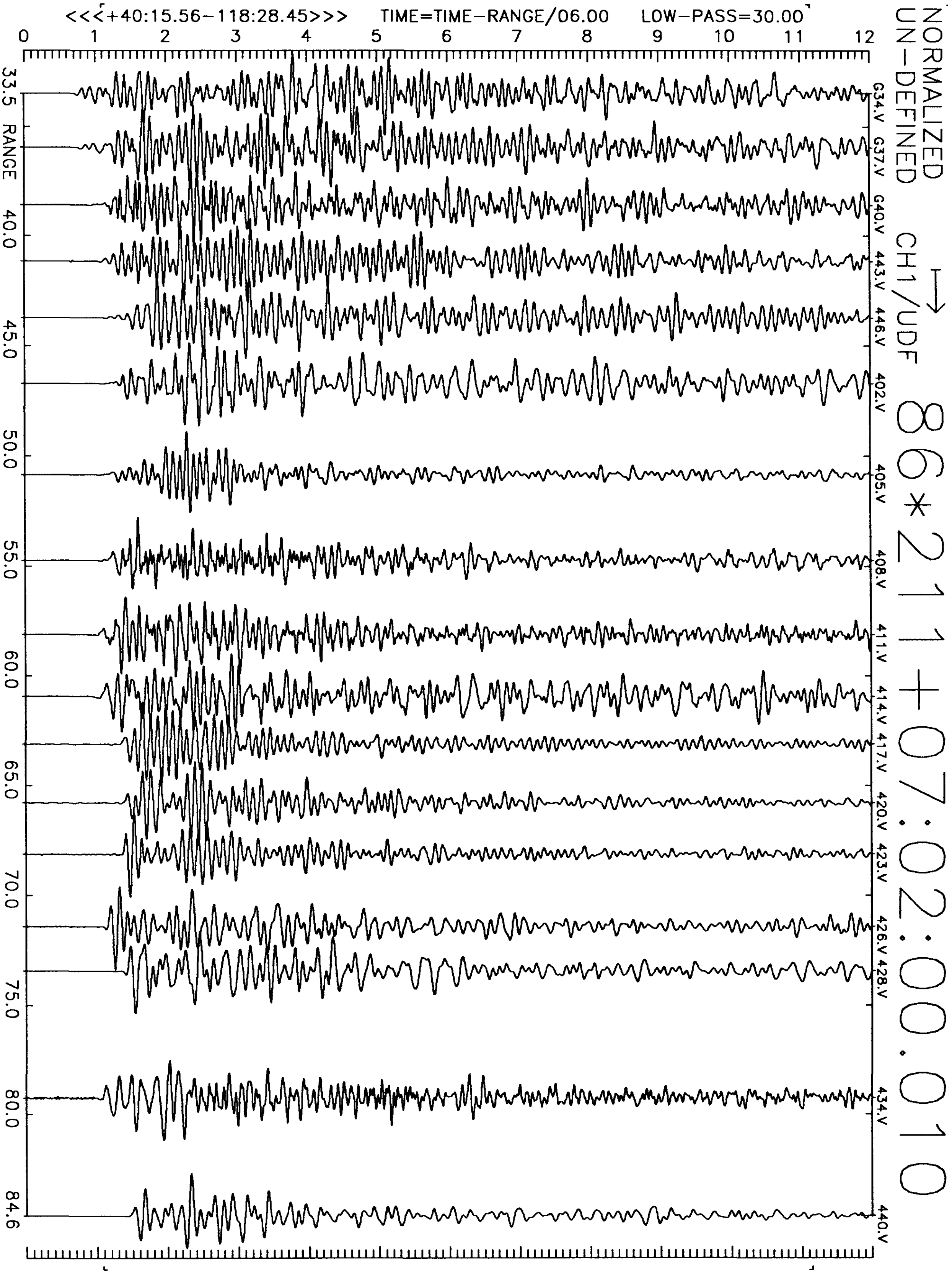

Figure C7(a), shot point 3: 12 second velocity record. Positive vertical motion is to right. Abscissa is distance to shot point. Top of trace is labeled with station number. Times are reduced by 6 km/sec. Shot time is indicated.

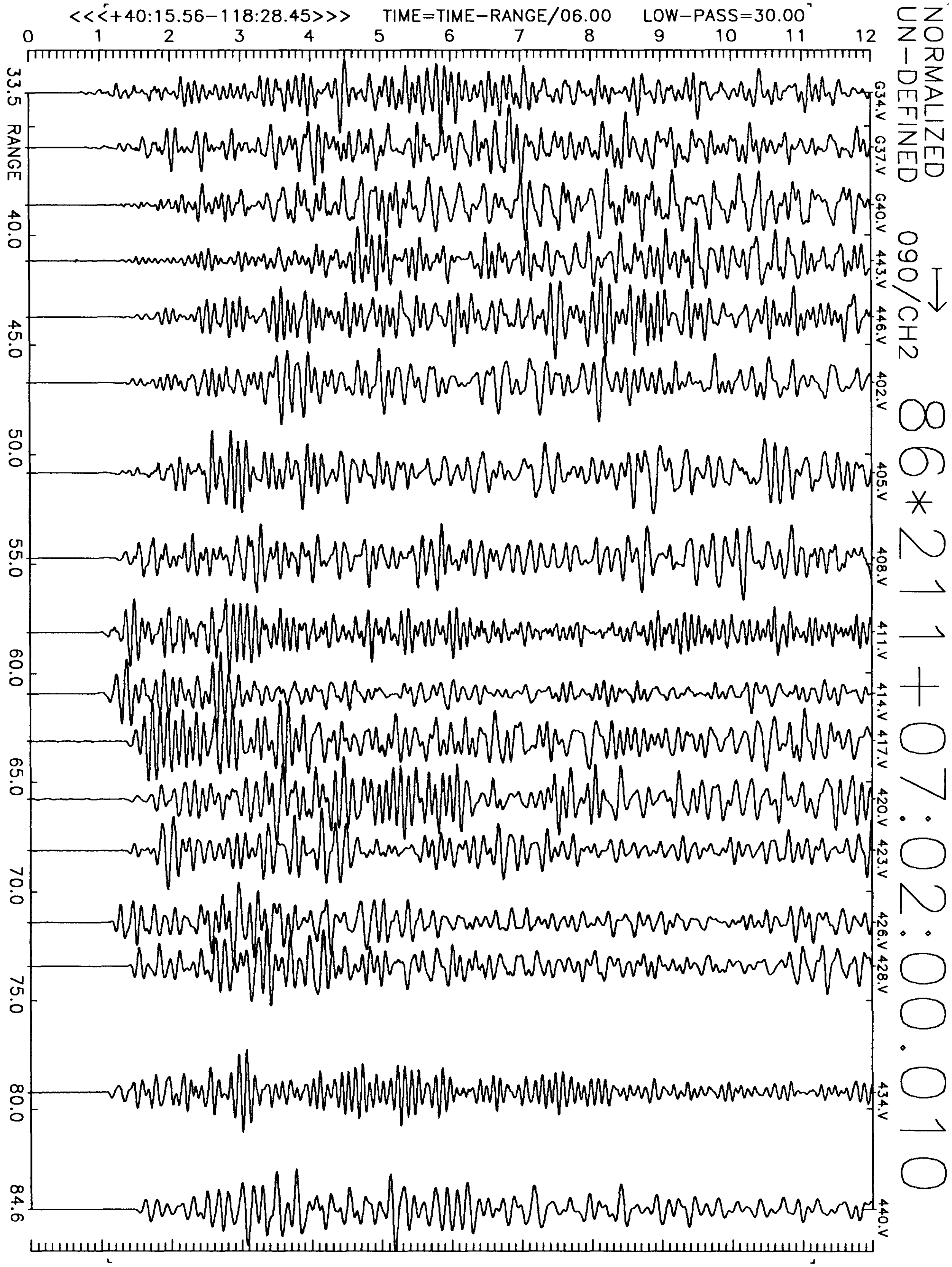

Figure C7(b), shot point 3: 12 second velocity record. Positive N16E motion is to right. Abscissa is distance to shot point. Top of trace is labeled with station number. Times are reduced by 6 km/sec. Shot time is indicated.

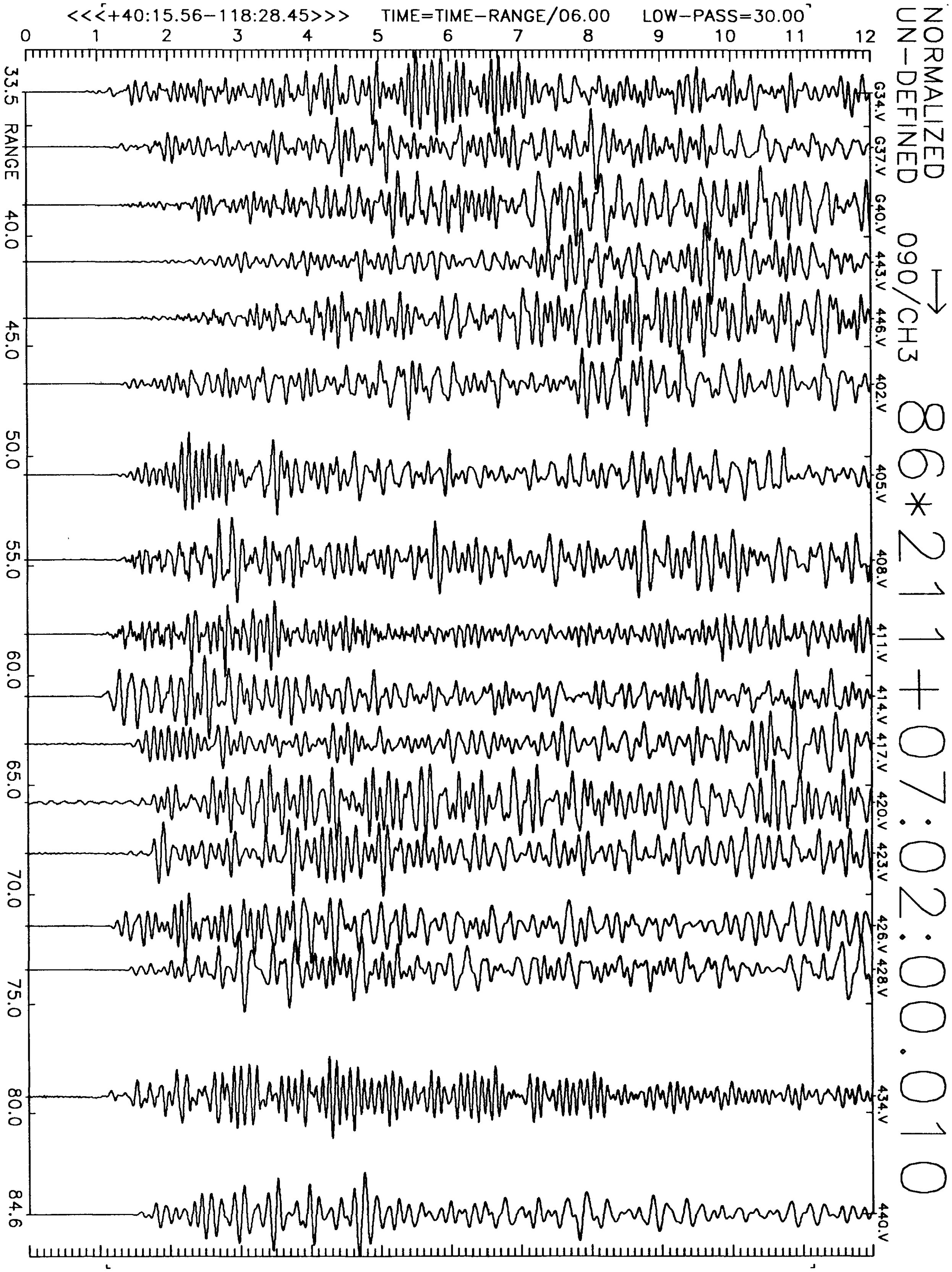

Figure C7(c), shot point 3: 12 second velocity record. Positive N106E motion is to right. Abscissa is distance to shot point. Top of trace is labeled with station number. Times are reduced by 6 km/sec. Shot time is indicated.

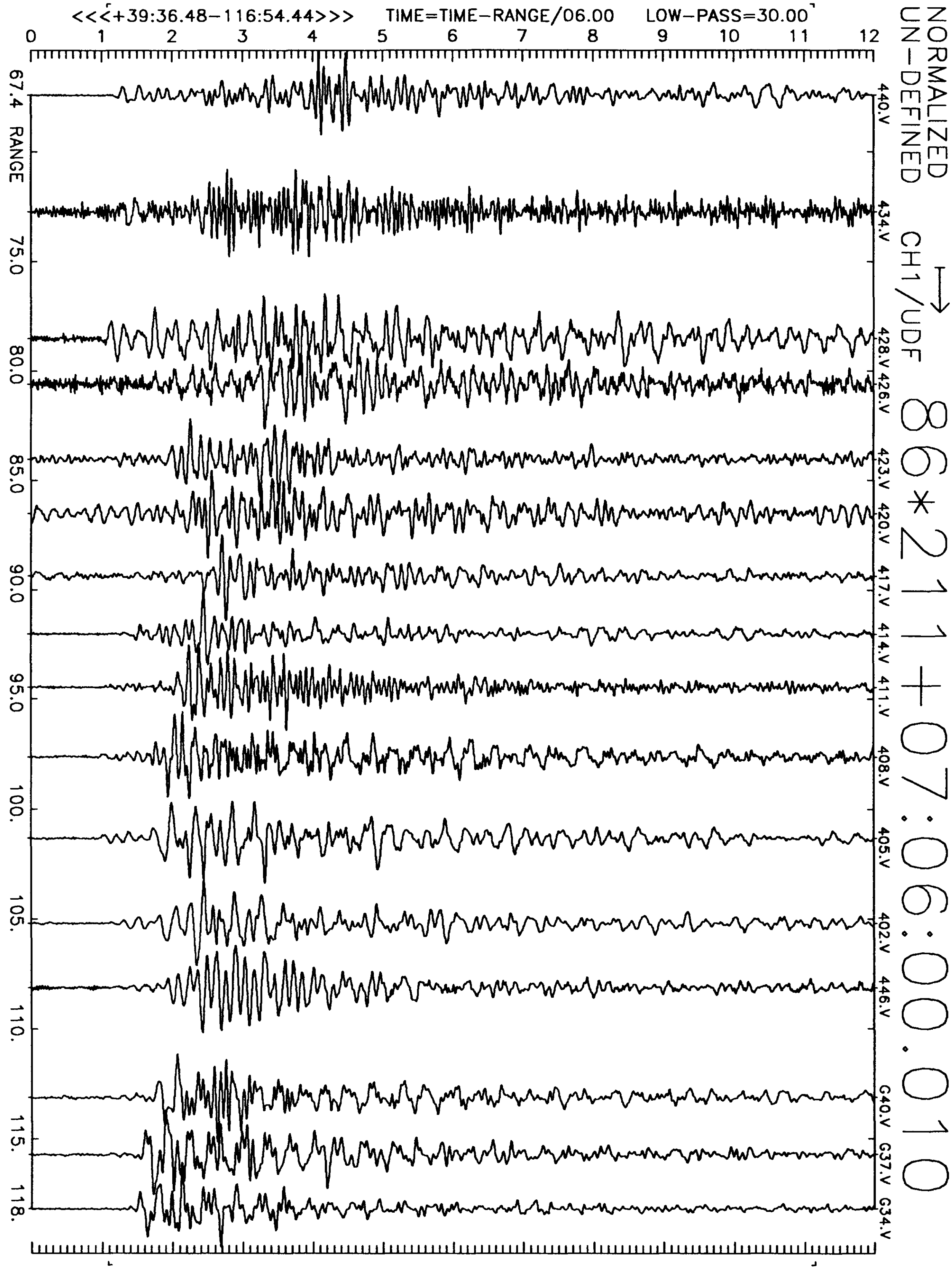

Figure C8(a), shot point 6: 12 second velocity record. Positive vertical motion is to right. Abscissa is distance to shot point. Top of trace is labeled with station number. Times are reduced by 6 km/sec. Shot time is indicated.

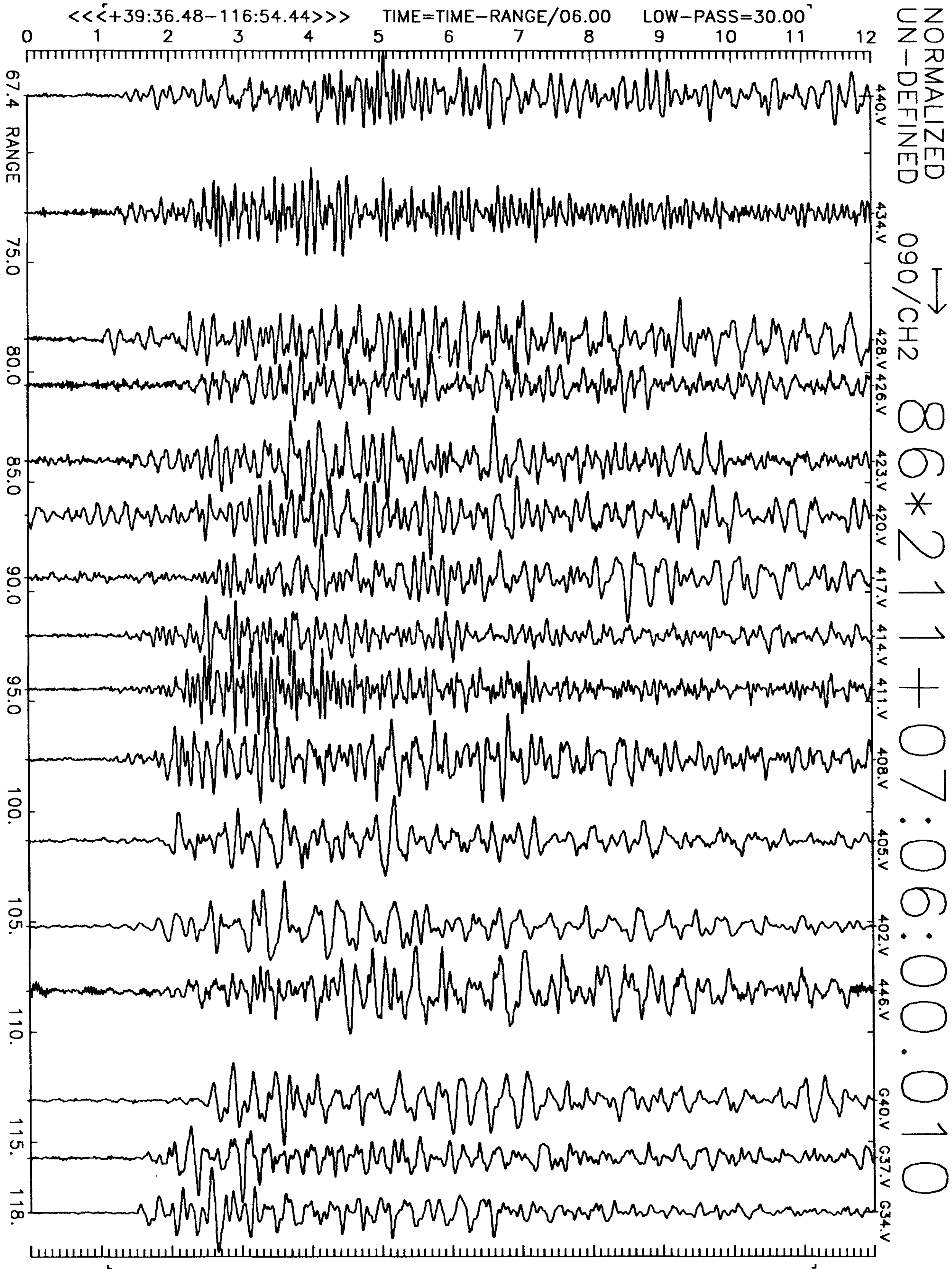

Figure C8(b), shot point 6: 12 second velocity record. Positive N16E motion is to right. Abscissa is distance to shot point. Top of trace is labeled with station number. Times are reduced by 6 km/sec. Shot time is indicated.

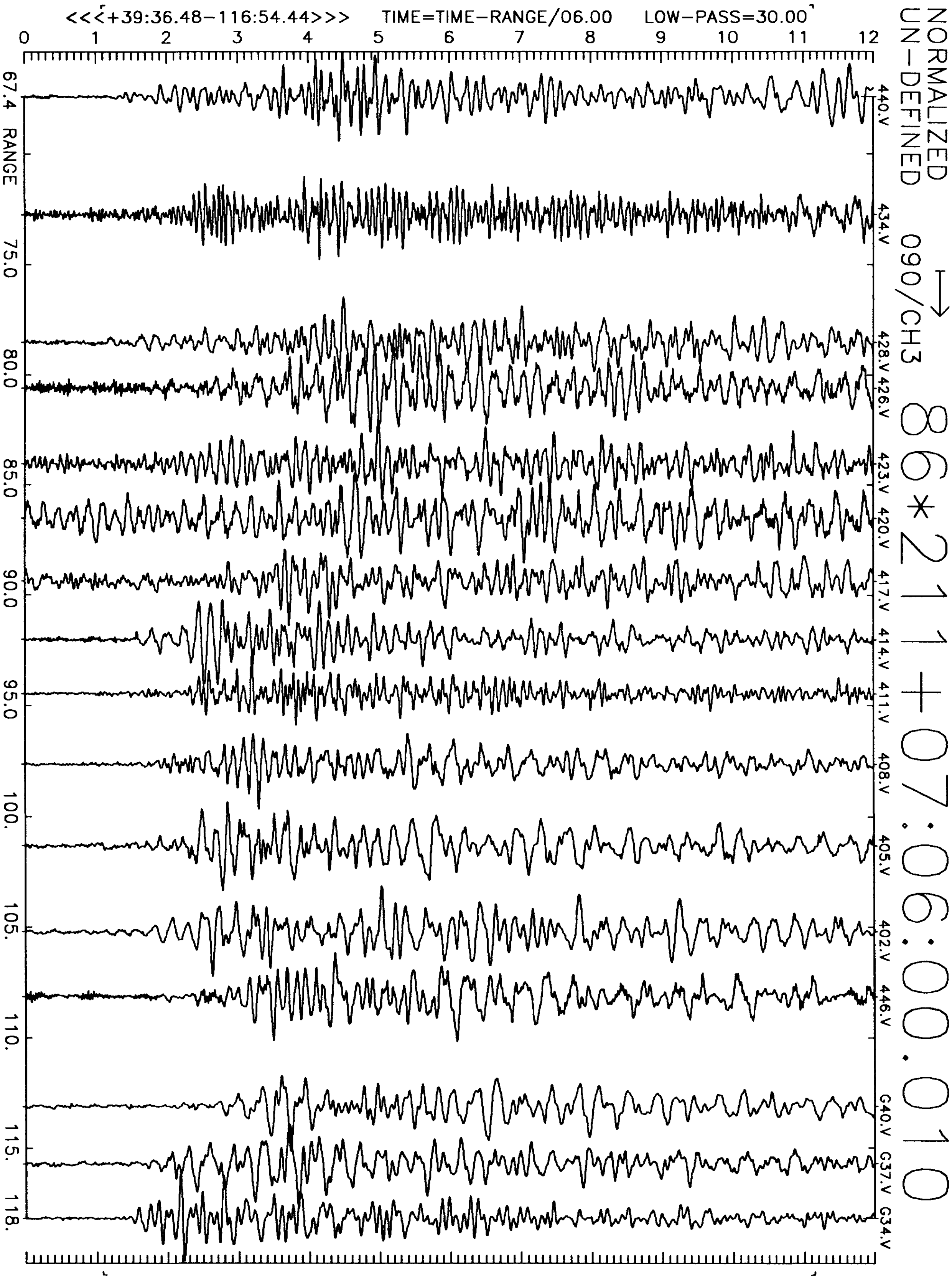

Figure C8(c), shot point 6: 12 second velocity record. Positive N106E motion is to right. Abscissa is distance to shot point. Top of trace is labeled with station number. Times are reduced by 6 km/sec. Shot time is indicated.

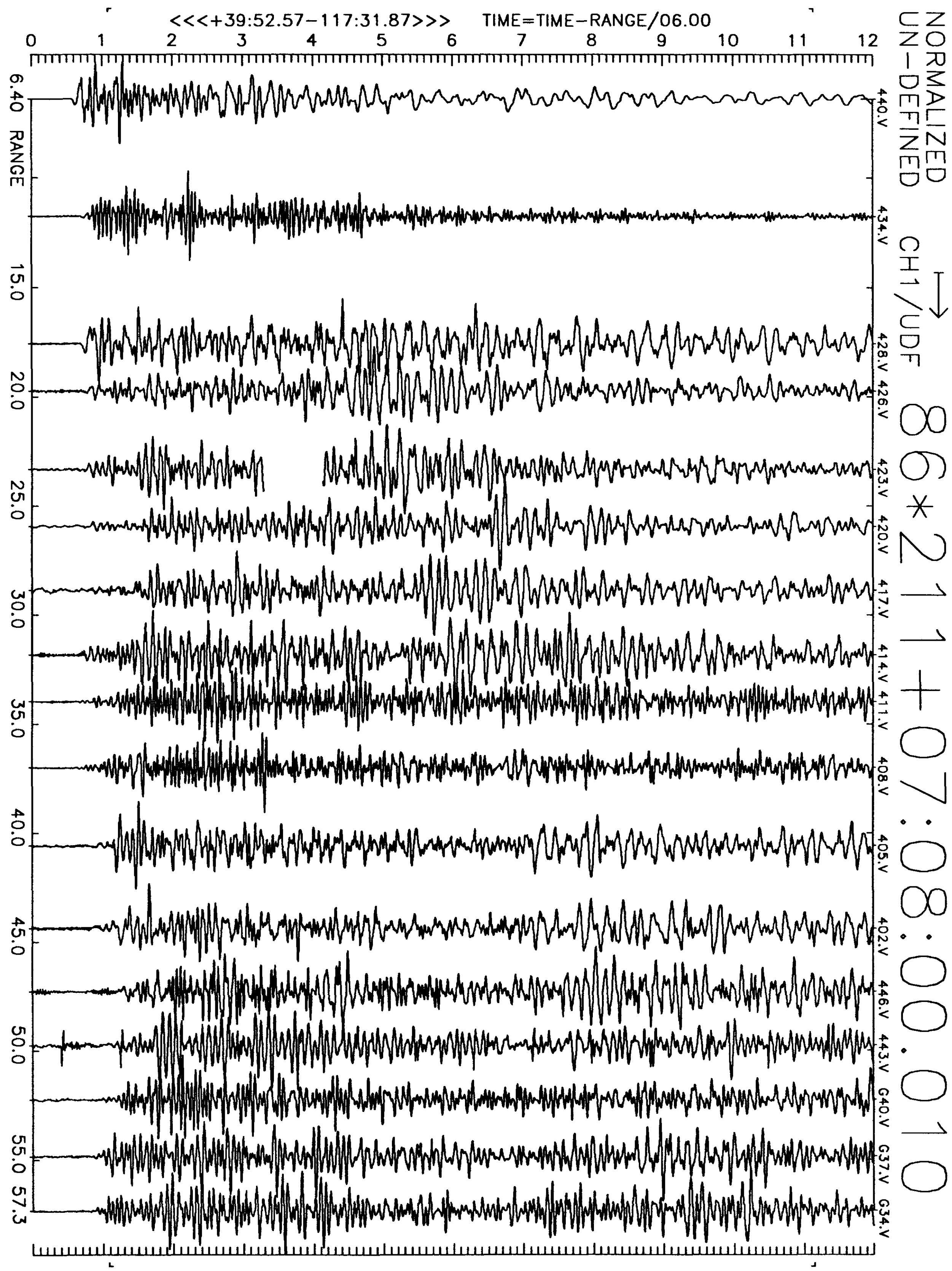

Figure C9(a), shot point 5: 12 second velocity record. Positive vertical motion is to right. Abscissa is distance to shot point. Top of trace is labeled with station number. Times are reduced by 6 km/sec. Shot time is indicated.

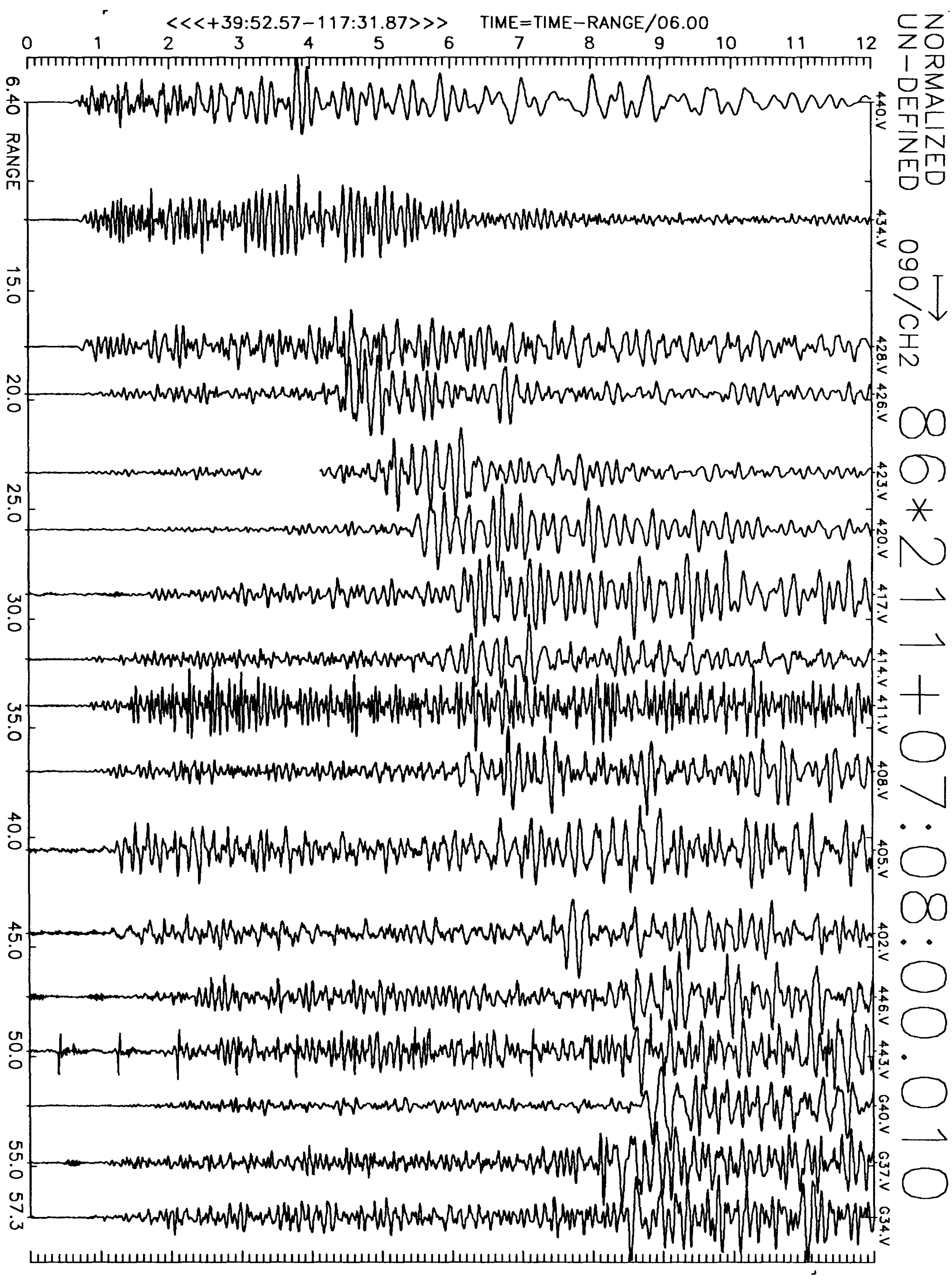

Figure C9(b), shot point 5: 12 second velocity record. Positive N16E motion is to right. Abscissa is distance to shot point. Top of trace is labeled with station number. Times are reduced by 6 km/sec. Shot time is indicated.

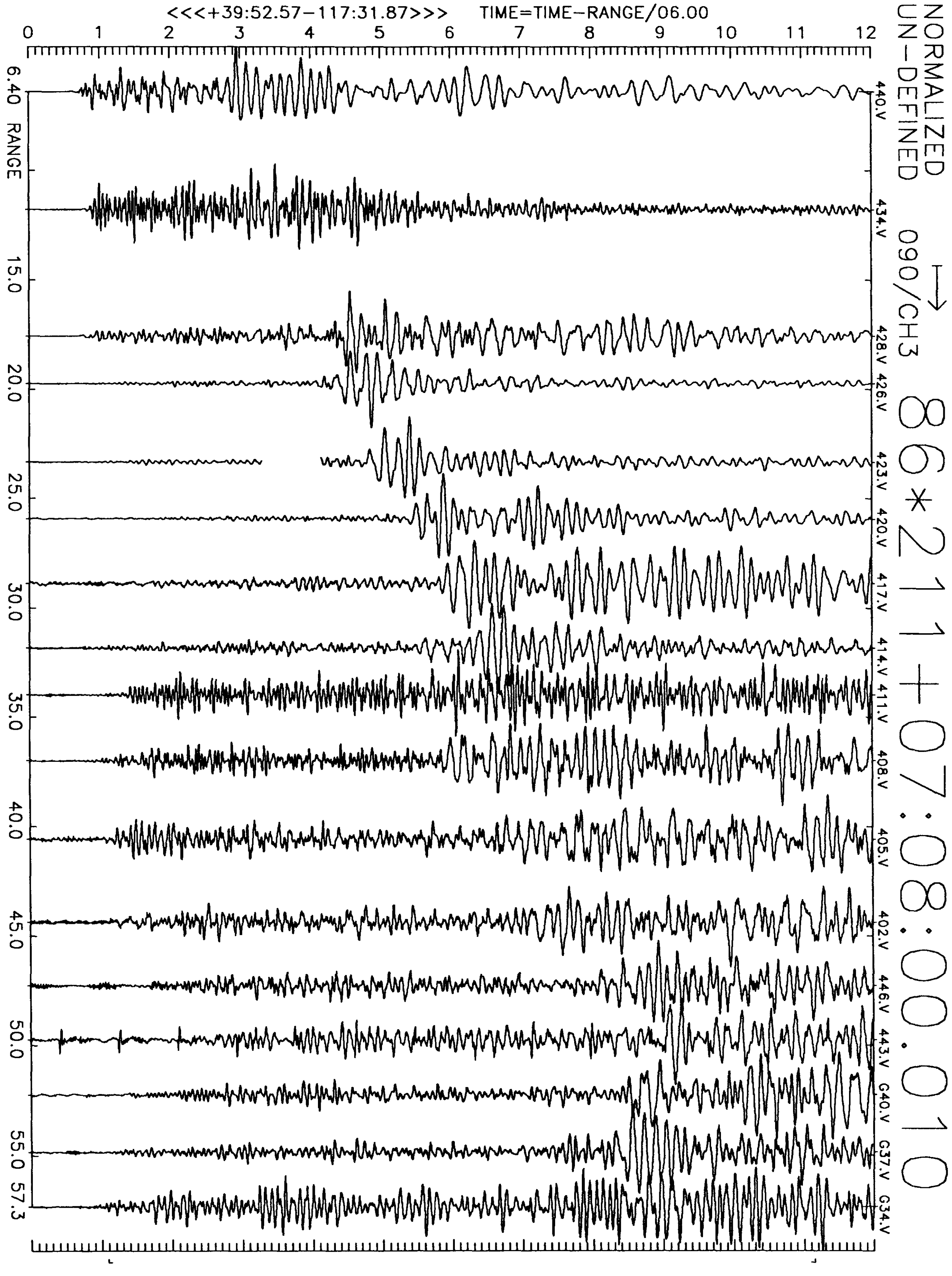

Figure C9(c), shot point 5: 12 second velocity record. Positive N106E motion is to right. Abscissa is distance to shot point. Top of trace is labeled with station number. Times are reduced by 6 km/sec. Shot time is indicated.

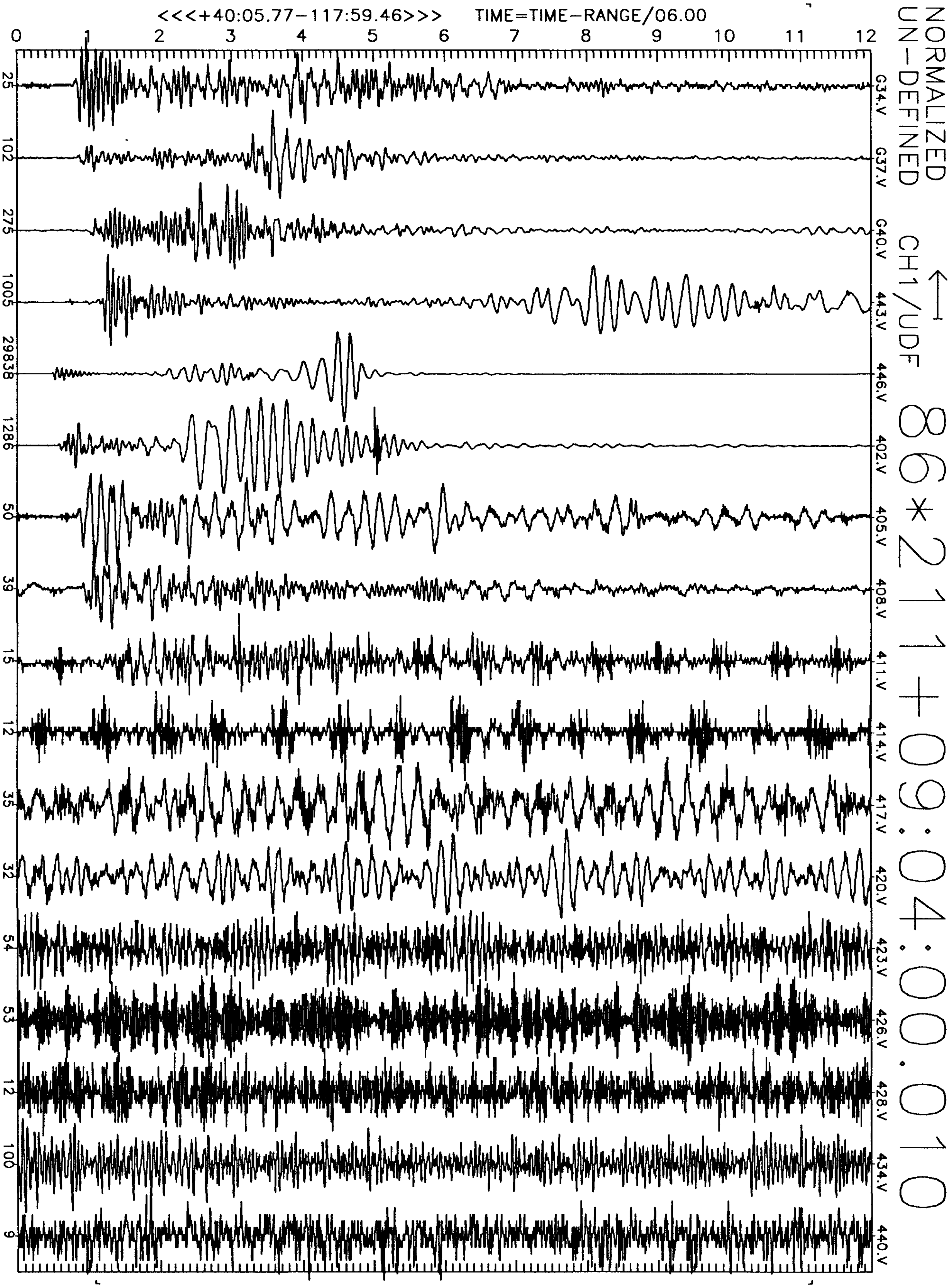

Figure C10(a), shot point 4: 12 second vertical velocity record. Abscissa is labeled with maximum counts in record (multiply by $\frac{10}{2^{24}-2^{5}} \approx 6 \times 10^{-7}$ to get cm/sec). Times are reduced by 6 km/sec. Shot time is indicated.

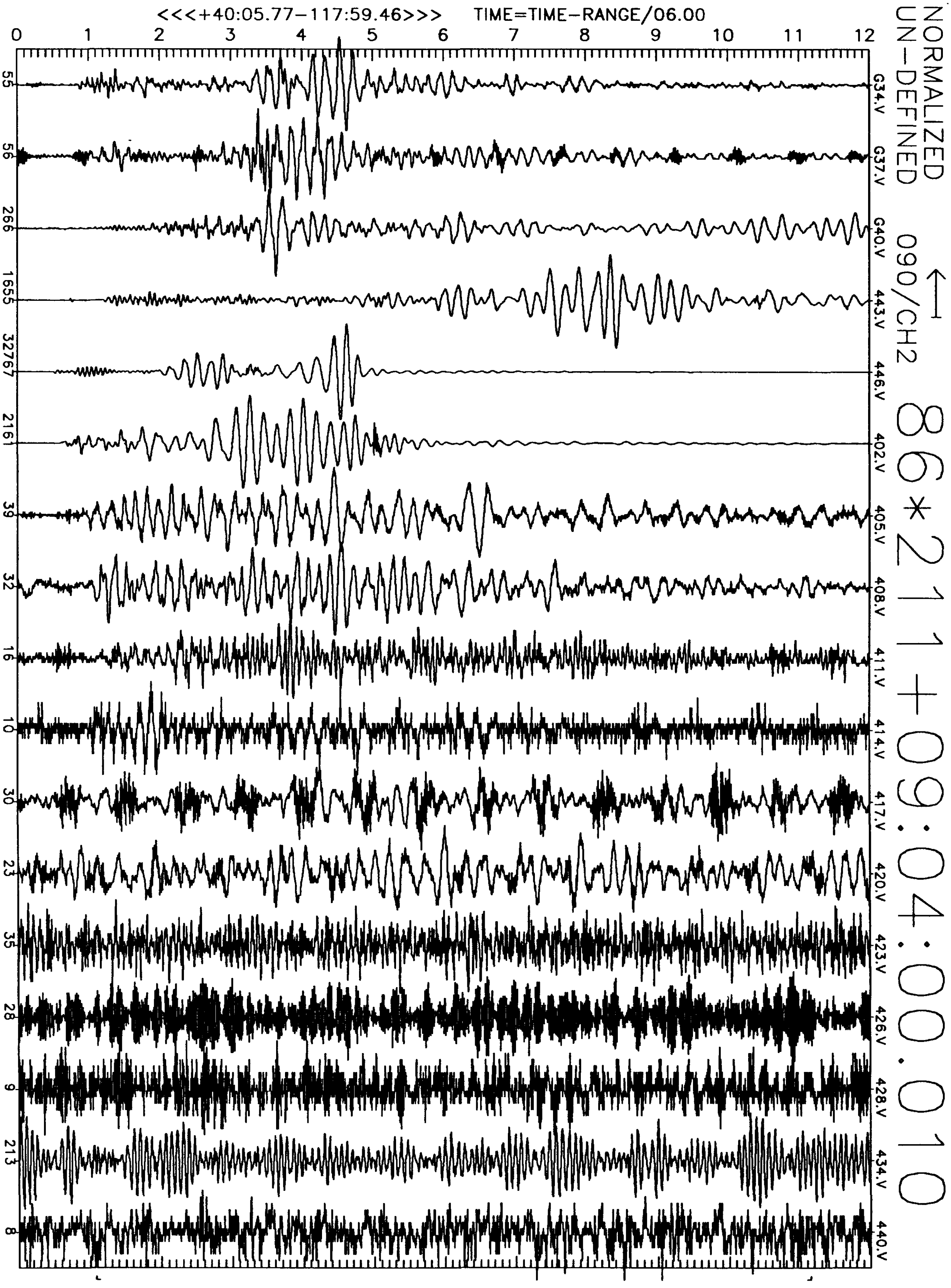

Figure C10(b), shot point 4: 12 second N16E velocity record. Abscissa is labeled with maximum counts in record (multiply by $\frac{10}{2^{24}-2^{9}} \approx 6 \times 10^{-7}$ to get cm/sec). Times are reduced by 6 km/sec. Shot time is indicated.

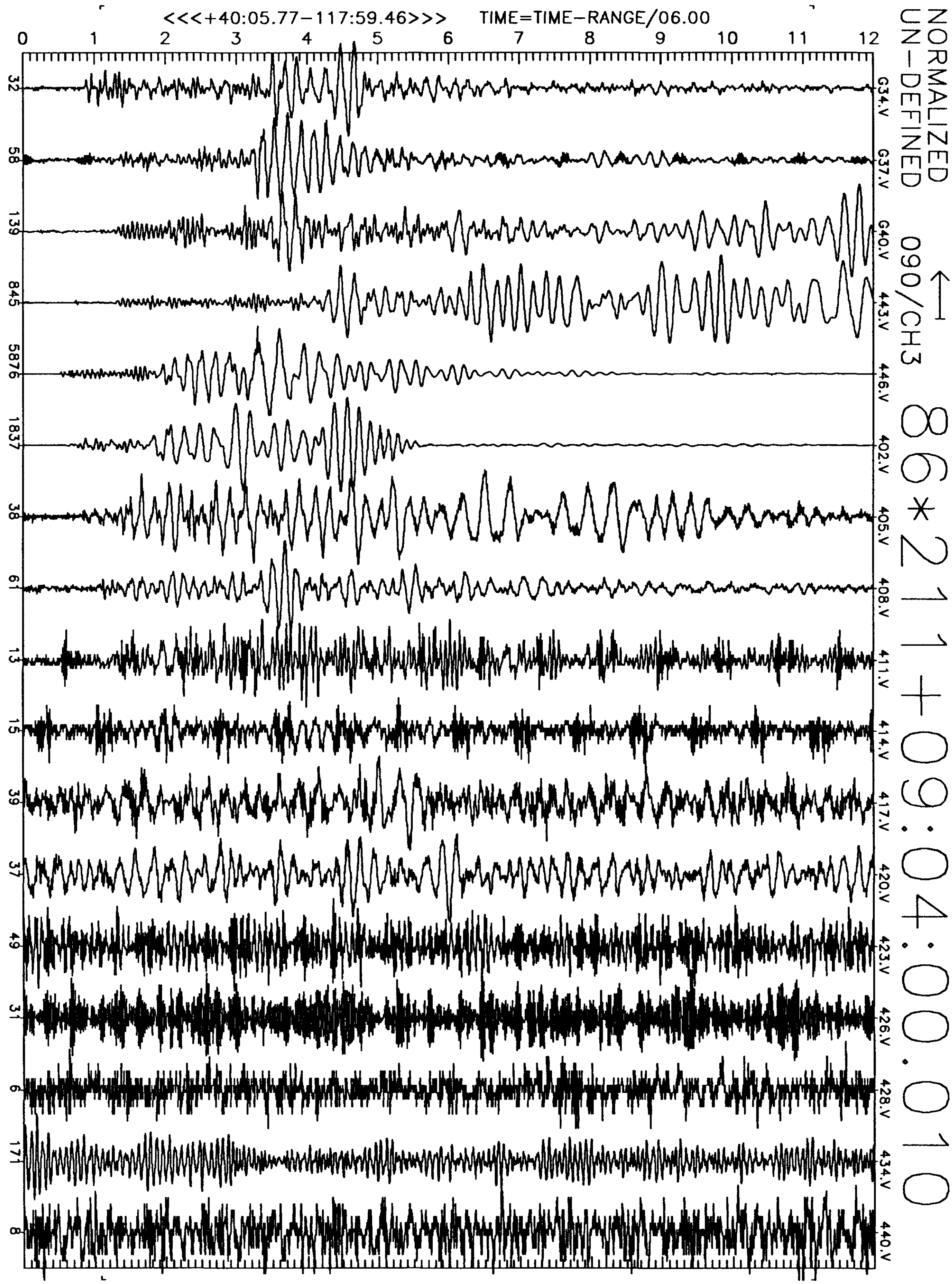

Figure C10(c), shot point 4: 12 second N106E velocity record. Abscissa is labeled with maximum counts in record (multiply by $\frac{10}{2^{24}-2^{9}} \approx 6 \times 10^{-7}$ to get cm/sec). Times are reduced by 6 km/sec. Shot time is indicated.

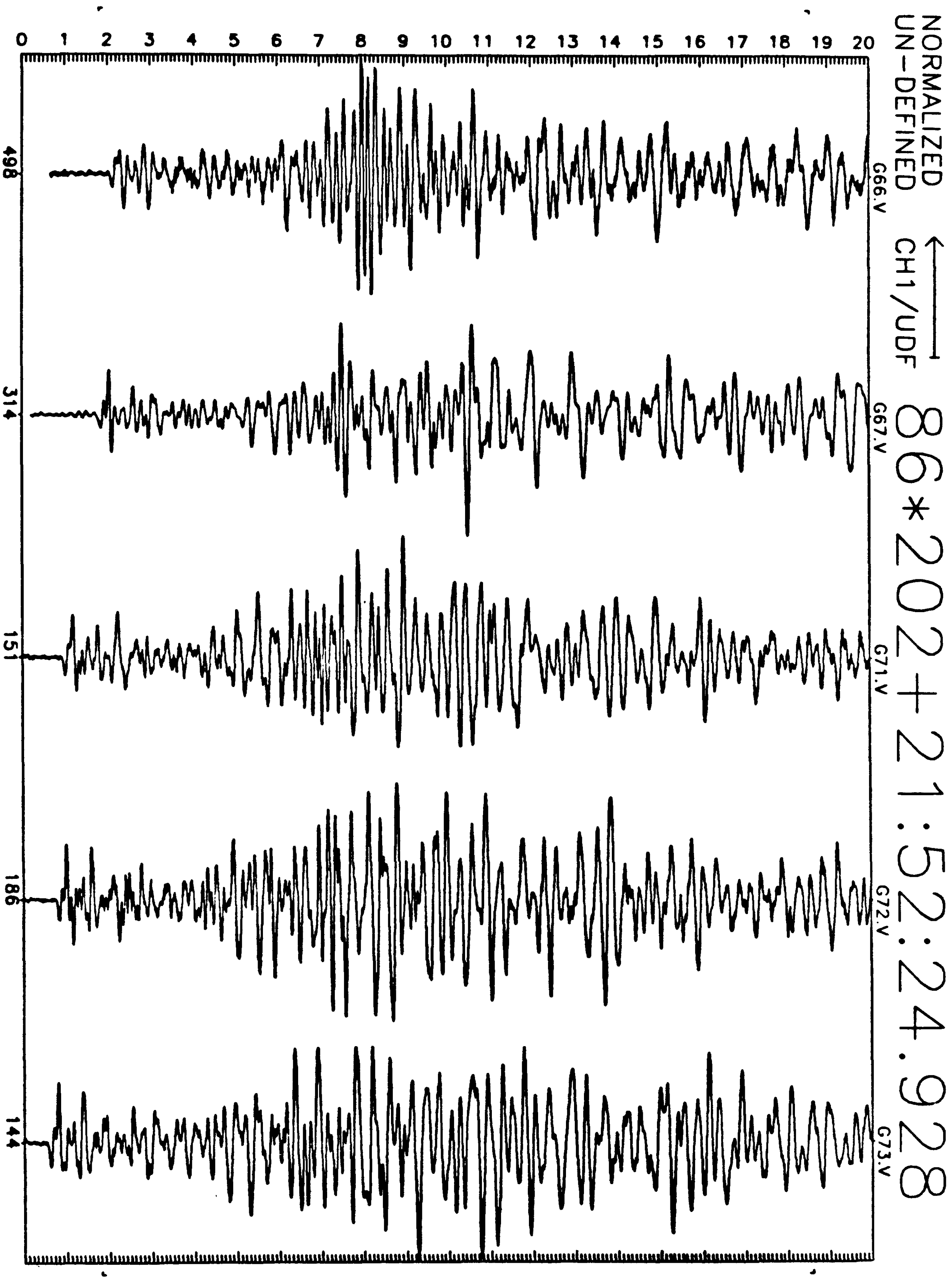

Figure D1(a): Earthquake record section for 20 seconds of vertical motion recorded at GEOS stations. Origin time for record section, station ID, and maximum digital counts (6×10^{-7} cm/sec/digital count) are indicated along abscissa.

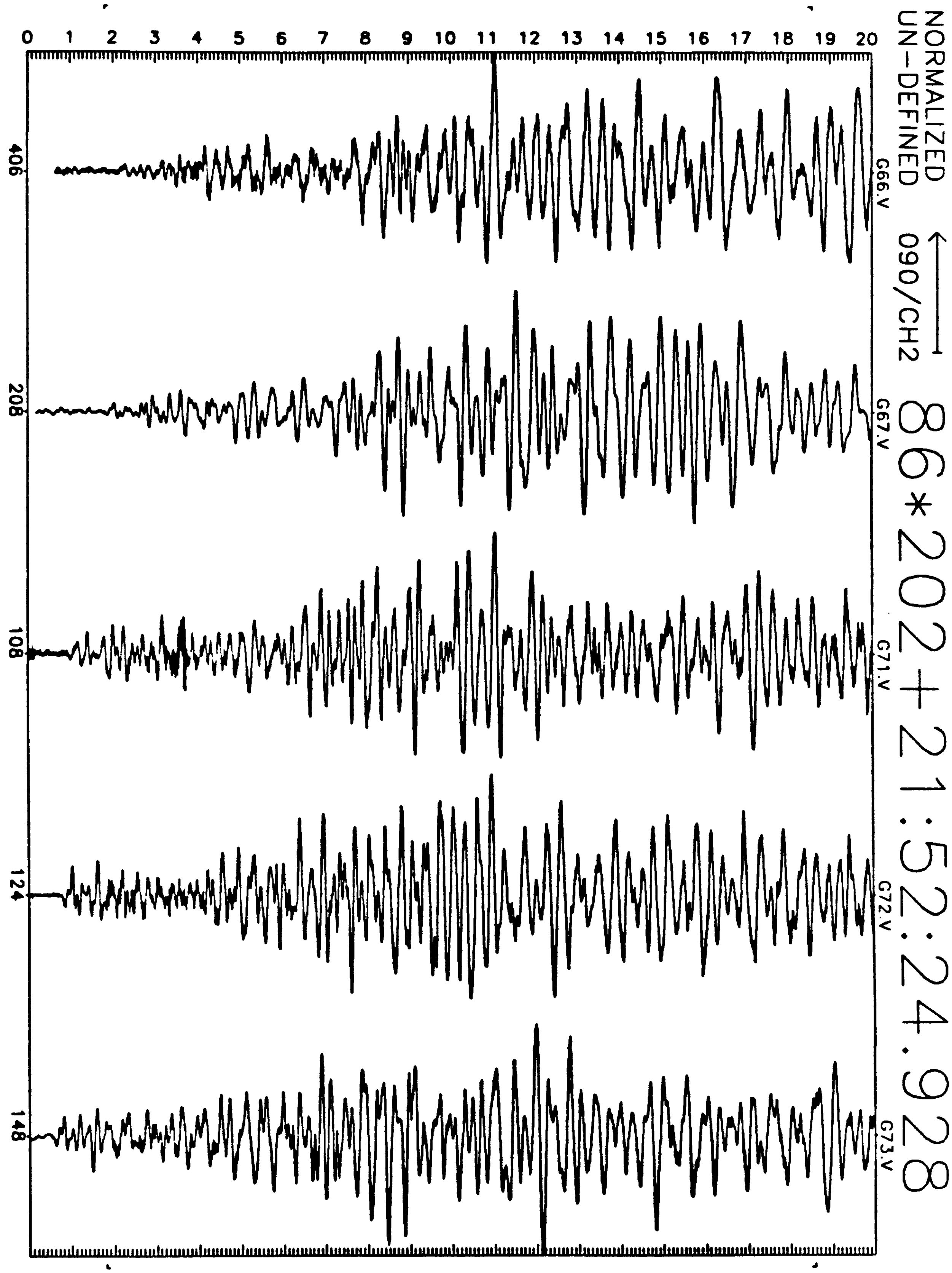

Figure D1(b): Earthquake record section for 20 seconds of N16E motion recorded at GEOS stations. Origin time for record section, station ID, and maximum digital counts (6×10^{-7} cm/sec/digital count) are indicated along abscissa.

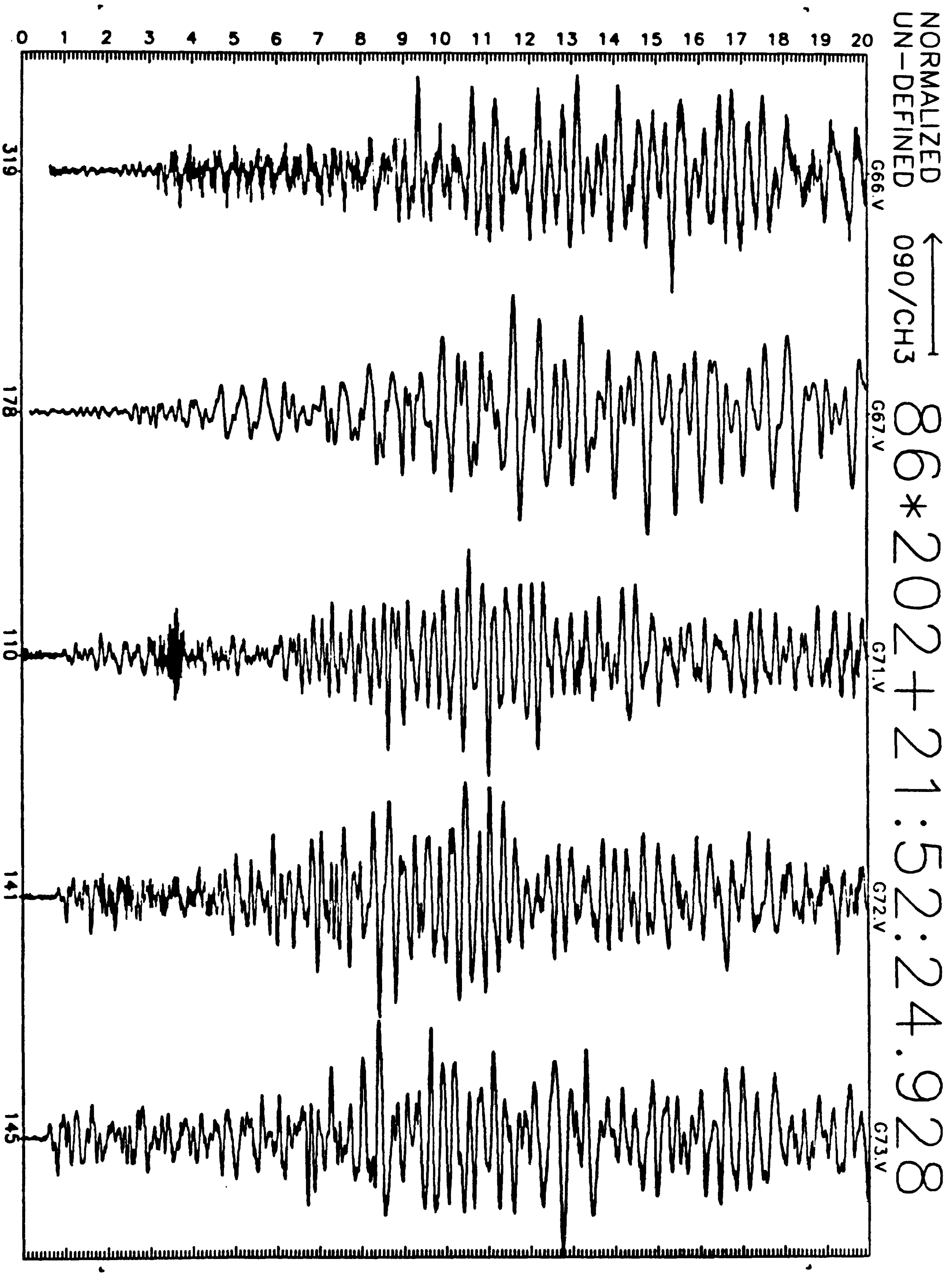

Figure D1(c): Earthquake record section for 20 seconds of N106E motion recorded at GEOS stations. Origin time for record section, station ID, and maximum digital counts (6×10^{-7} cm/sec/digital count) are indicated along abscissa.

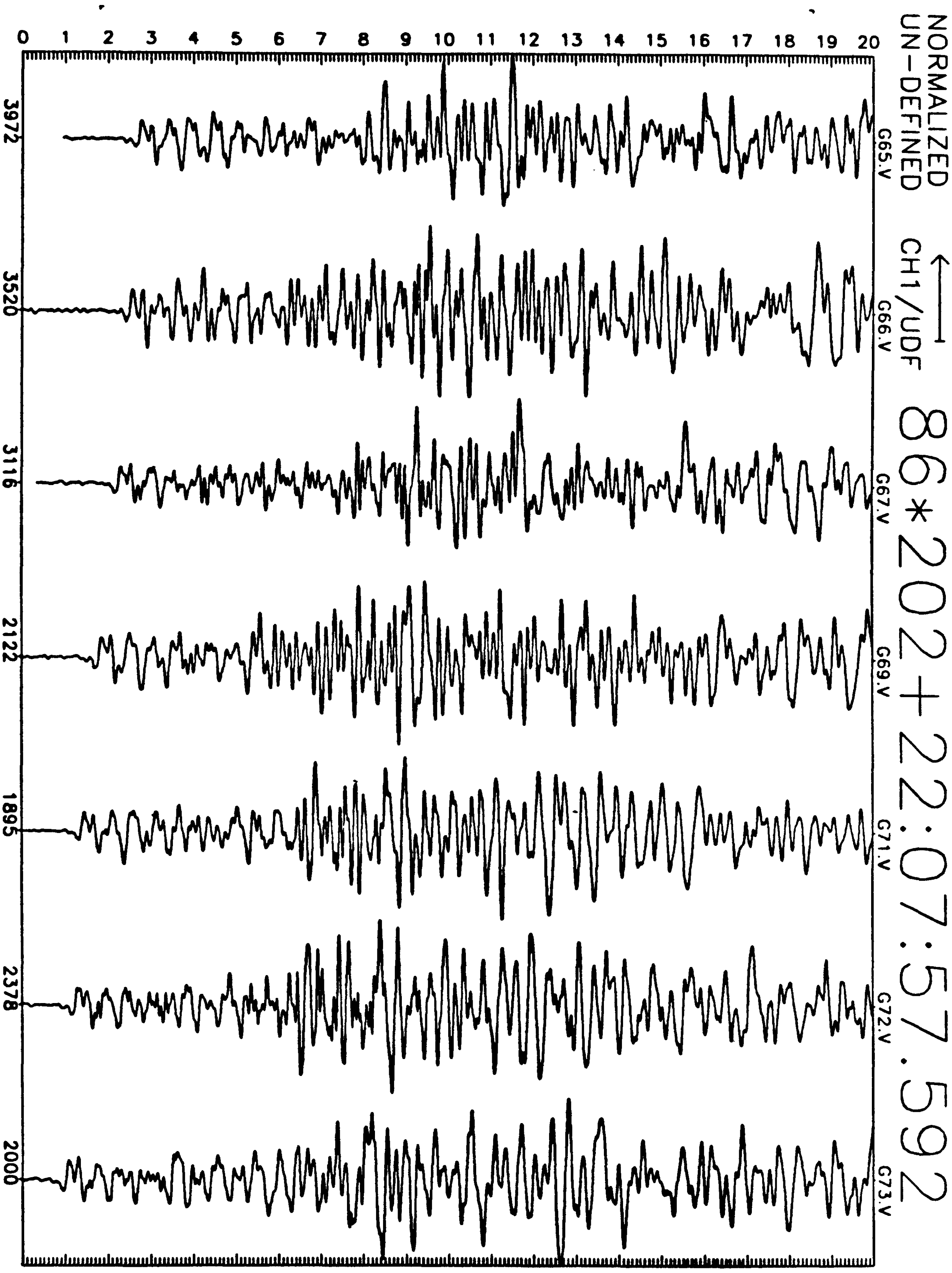

Figure D2(a): Earthquake record section for 20 seconds of vertical motion recorded at GEOS stations. Origin time for record section, station ID, and maximum digital counts (6×10^{-7} cm/sec/digital count) are indicated along abscissa.

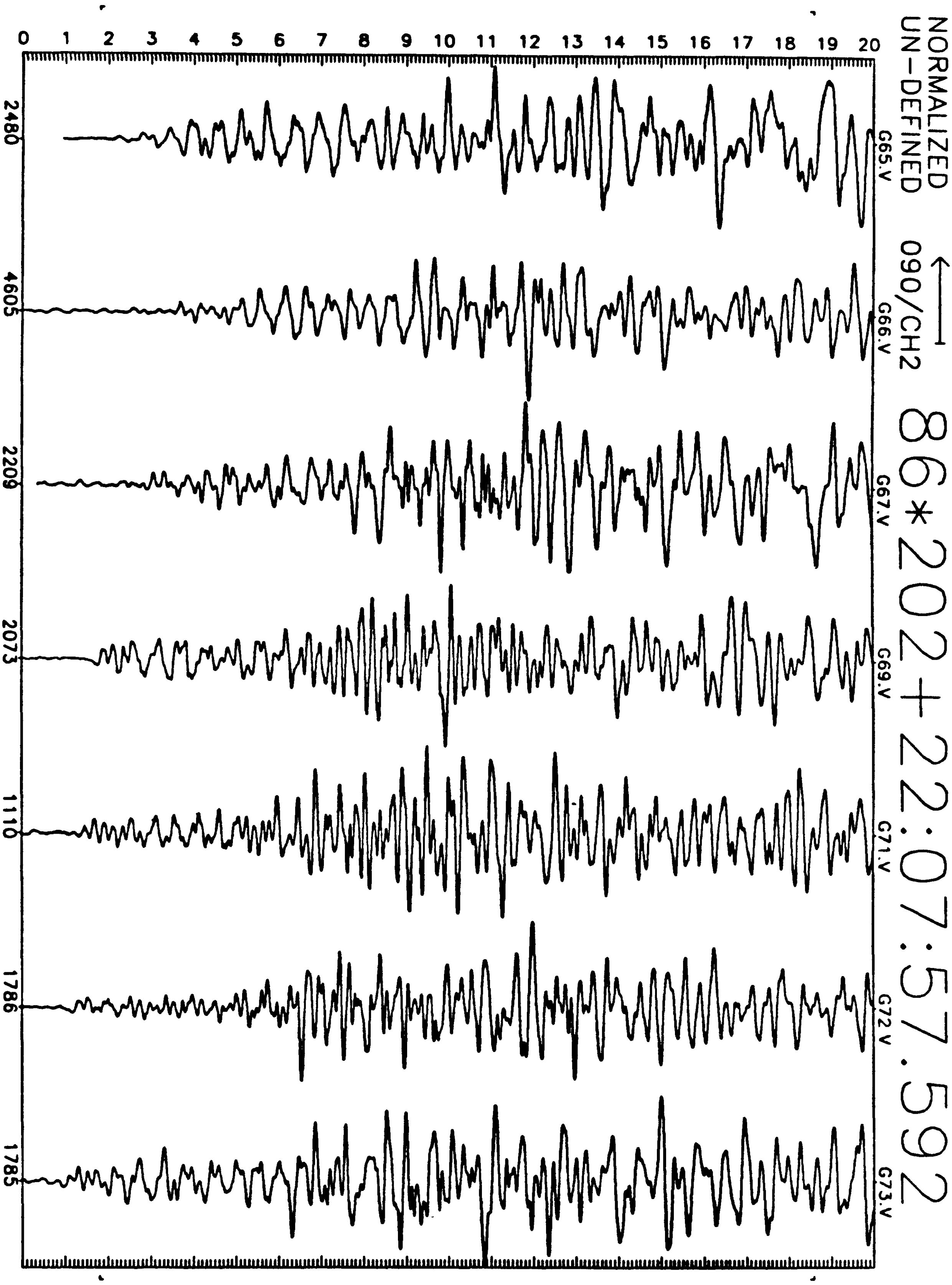

Figure D2(b): Earthquake record section for 20 seconds of N16E motion recorded at GEOS stations. Origin time for record section, station ID, and maximum digital counts (6×10^{-7} cm/sec/digital count) are indicated along abscissa.

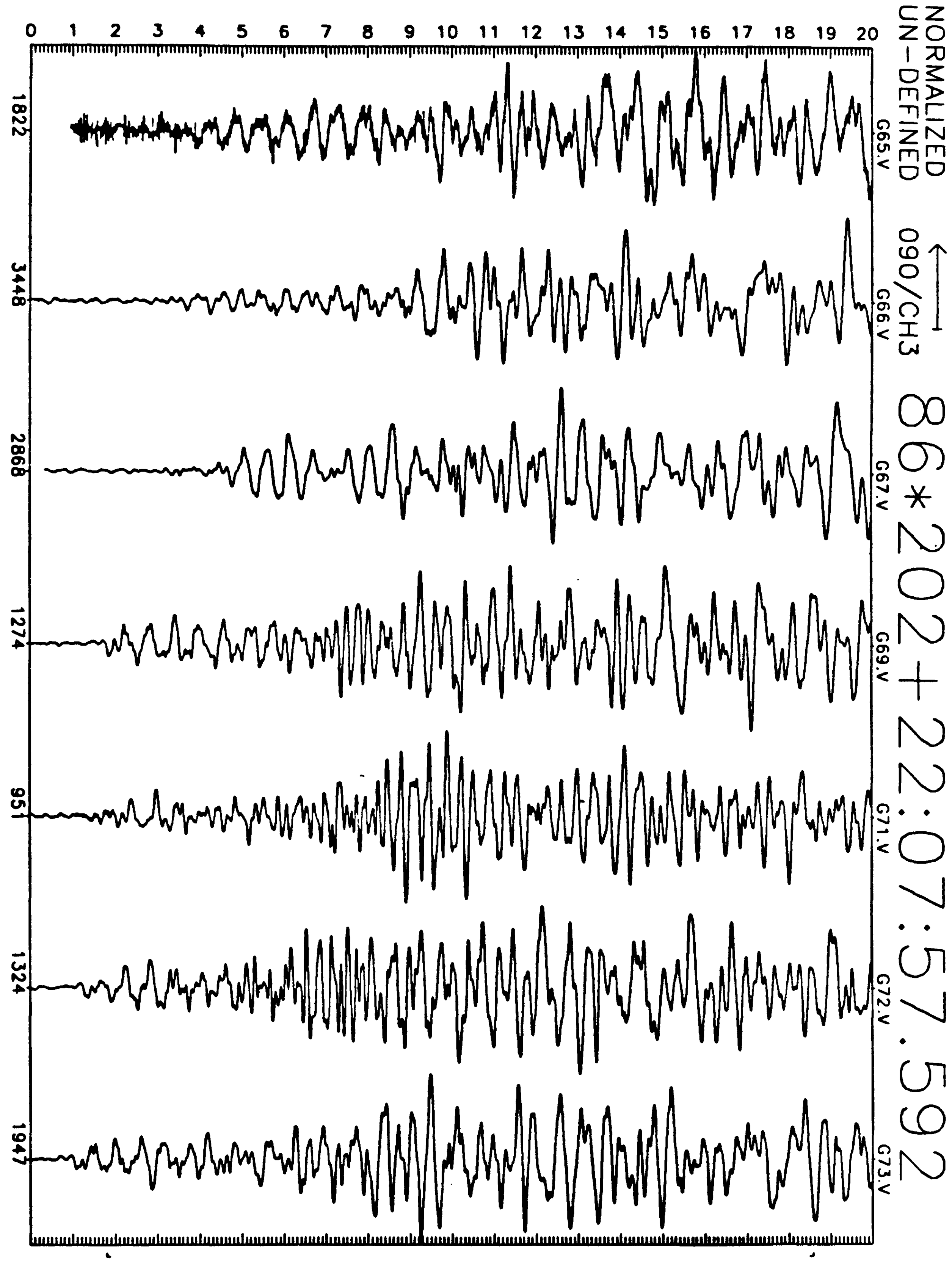

Figure D2(c): Earthquake record section for 20 seconds of N106E motion recorded at GEOS stations. Origin time for record section, station ID, and maximum digital counts (6×10^{-7} cm/sec/digital count) are indicated along abscissa.

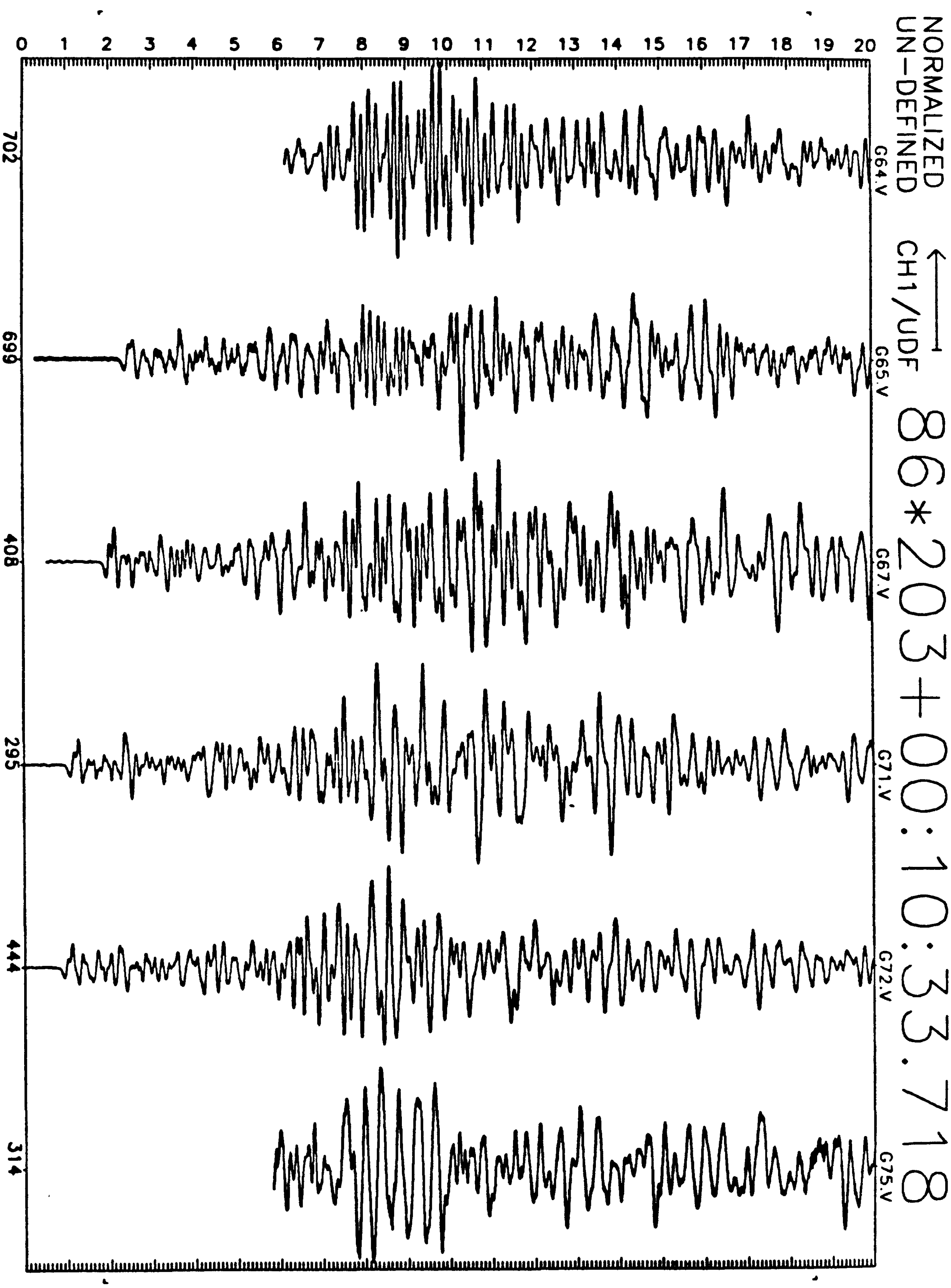

Figure D3(a): Earthquake record section for 20 seconds of vertical motion recorded at GEOS stations. Origin time for record section, station ID, and maximum digital counts (6×10^{-7} cm/sec/digital count) are indicated along abscissa.

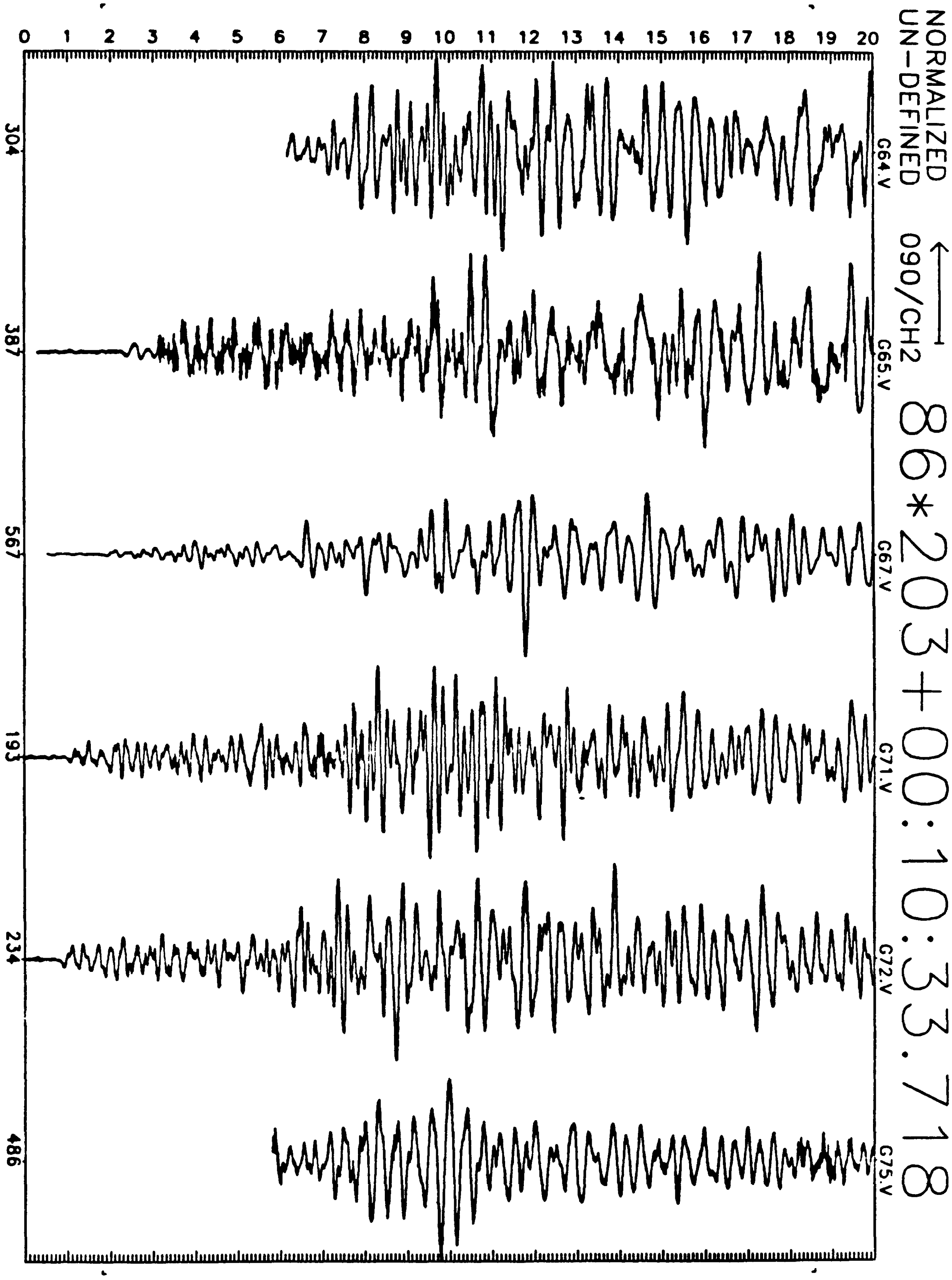

Figure D3(b): Earthquake record section for 20 seconds of N16E motion recorded at GEOS stations. Origin time for record section, station ID, and maximum digital counts (6×10^{-7} cm/sec/digital count) are indicated along abscissa.

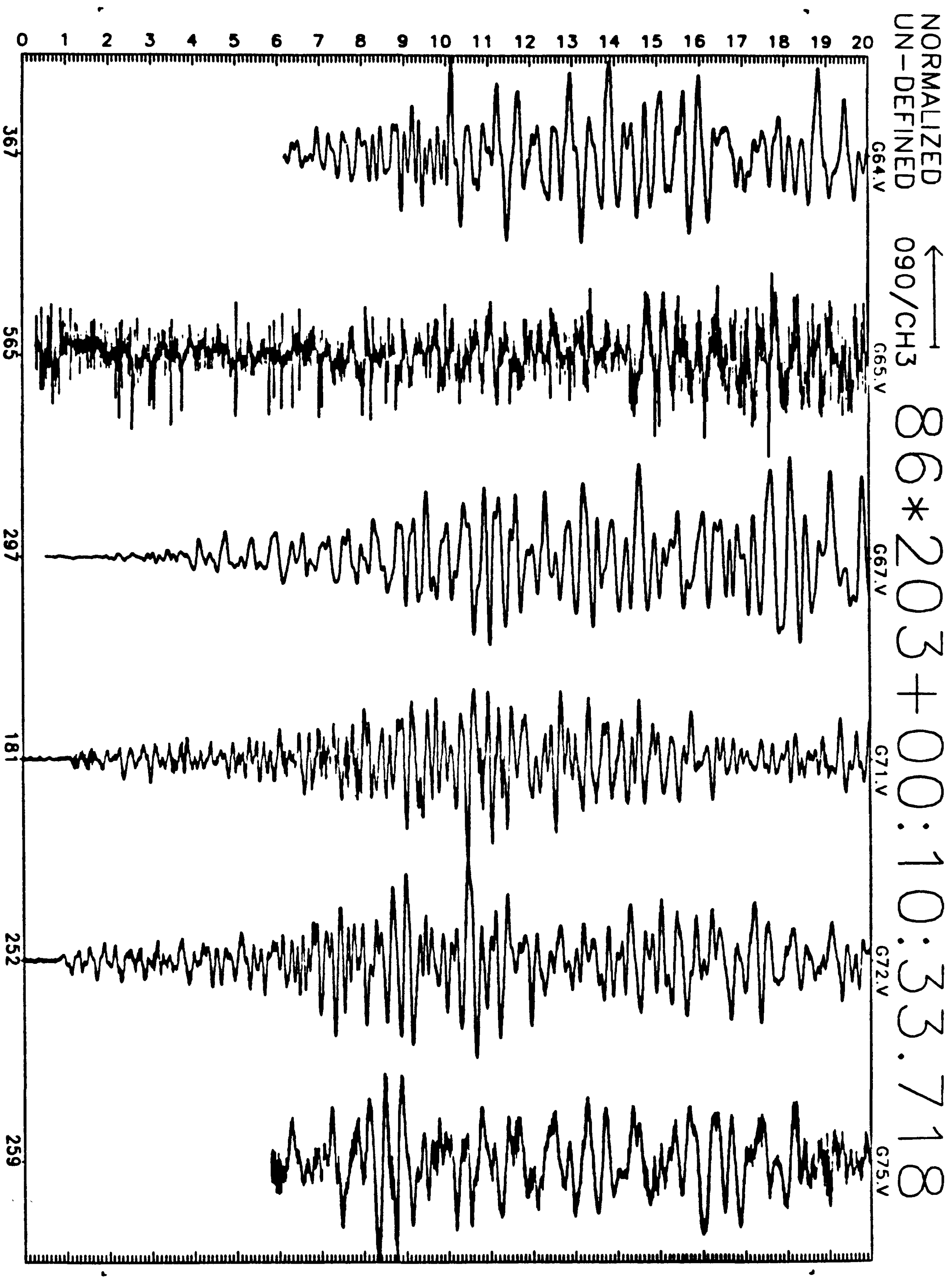

Figure D3(c): Earthquake record section for 20 seconds of N106E motion recorded at GEOS stations. Origin time for record section, station ID, and maximum digital counts (6×10^{-7} cm/sec/digital count) are indicated along abscissa.

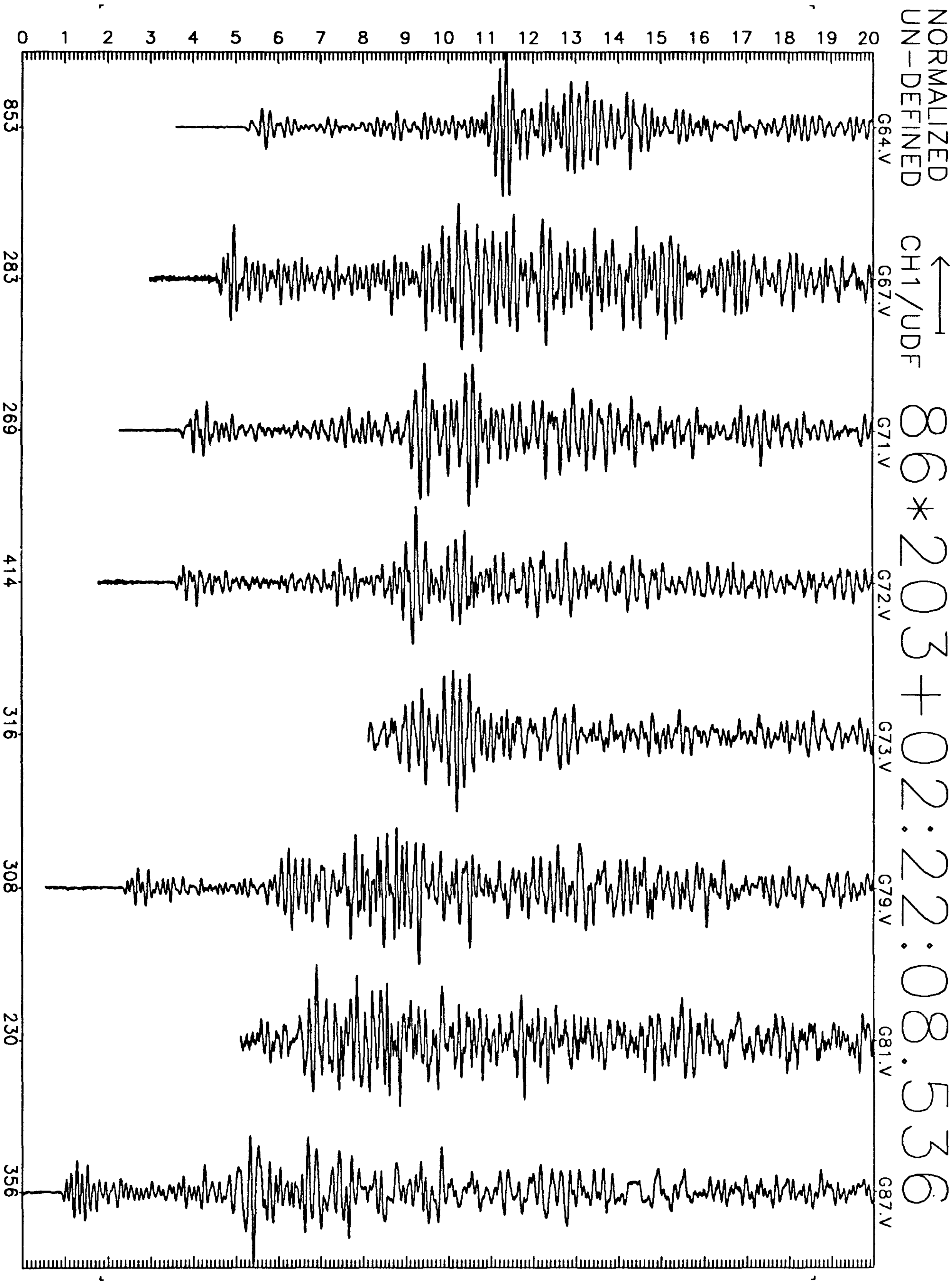

Figure D4(a): Earthquake record section for 20 seconds of vertical motion recorded at GEOS stations. Origin time for record section, station ID, and maximum digital counts (6×10^{-7} cm/sec/digital count) are indicated along abscissa.

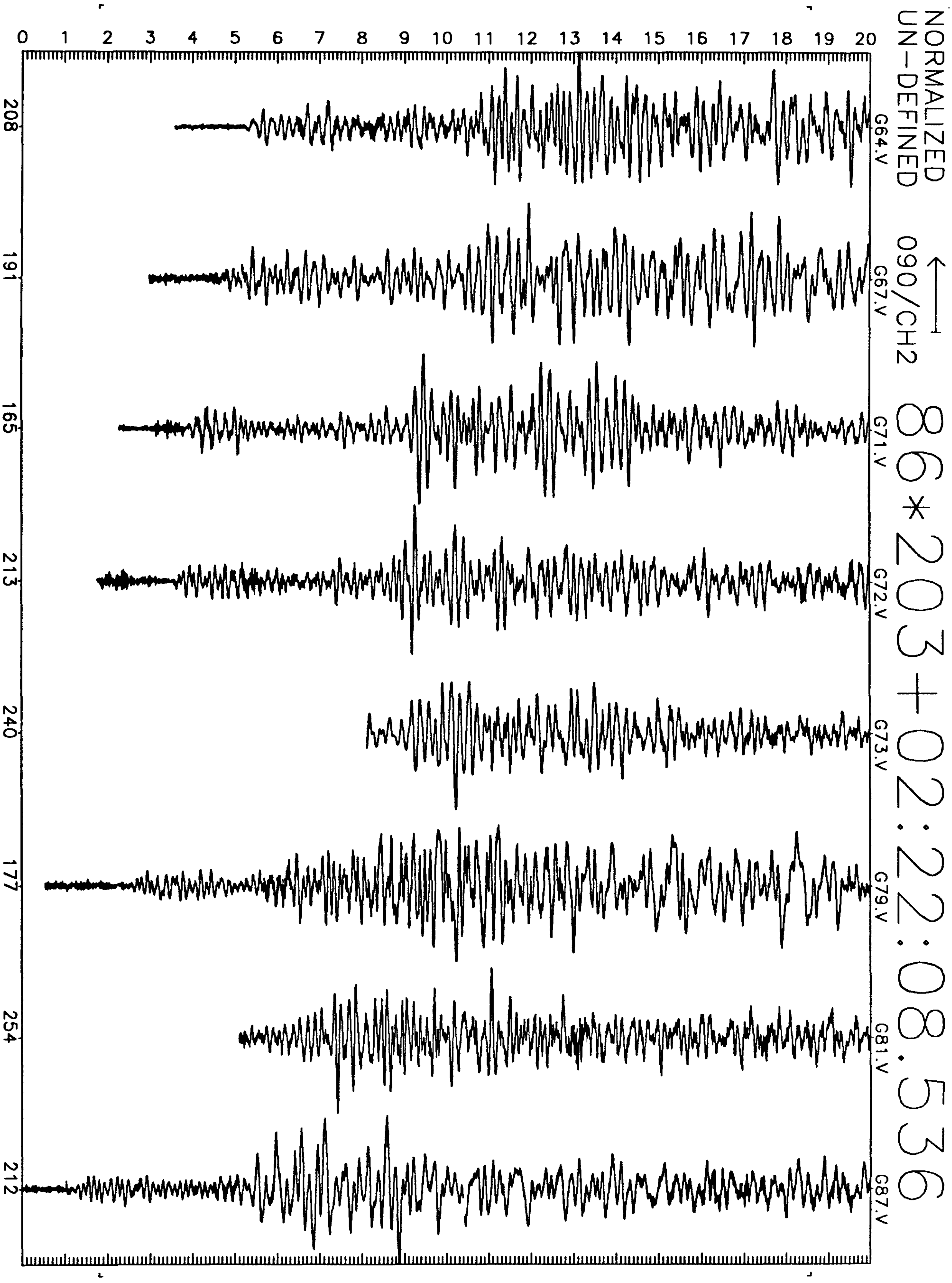

Figure D4(b): Earthquake record section for 20 seconds of N16E motion recorded at GEOS stations. Origin time for record section, station ID, and maximum digital counts (6×10^{-7} cm/sec/digital count) are indicated along abscissa.

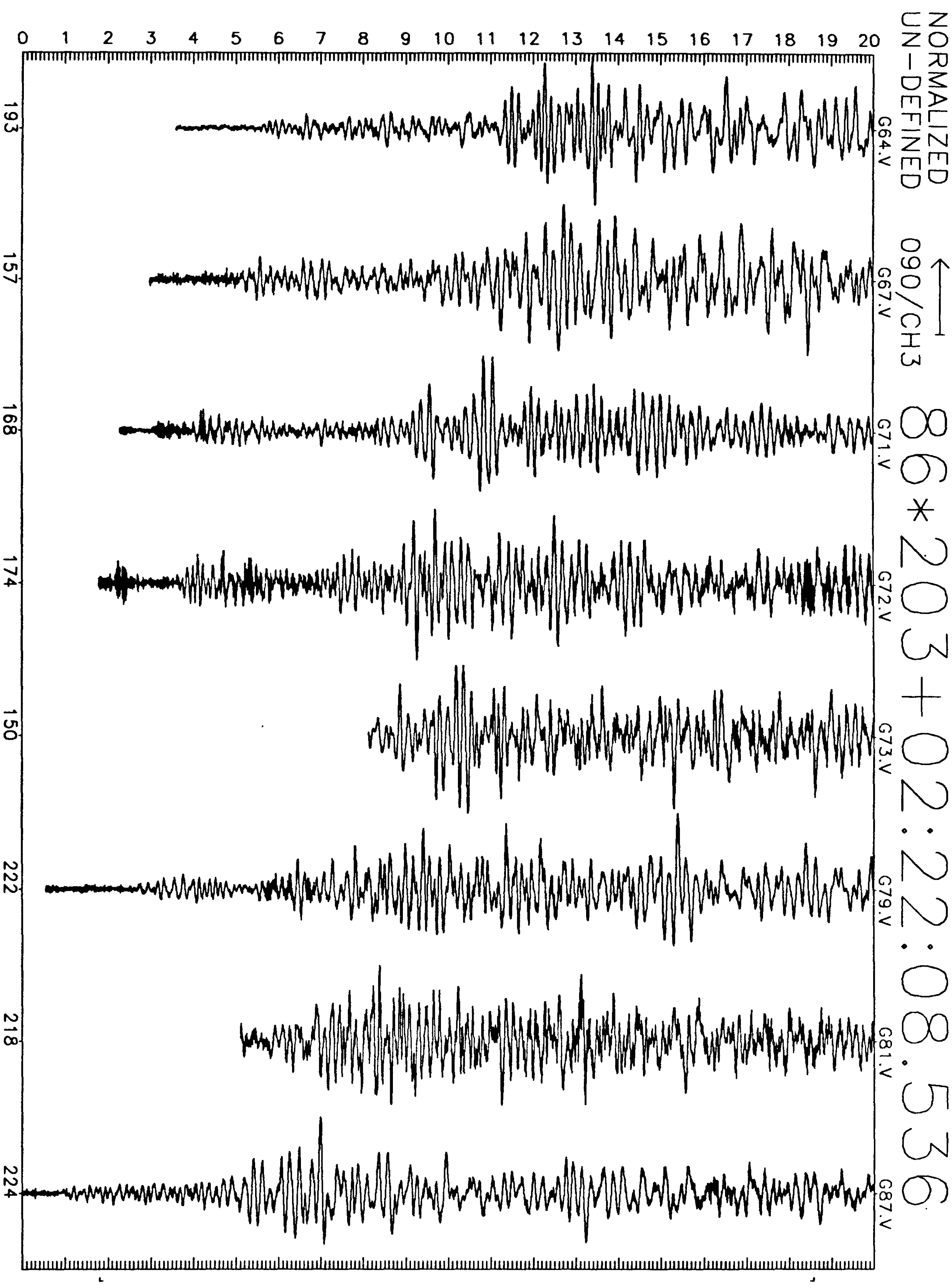

Figure D4(c): Earthquake record section for 20 seconds of N106E motion recorded at GEOS stations. Origin time for record section, station ID, and maximum digital counts (6×10^{-7} cm/sec/digital count) are indicated along abscissa.

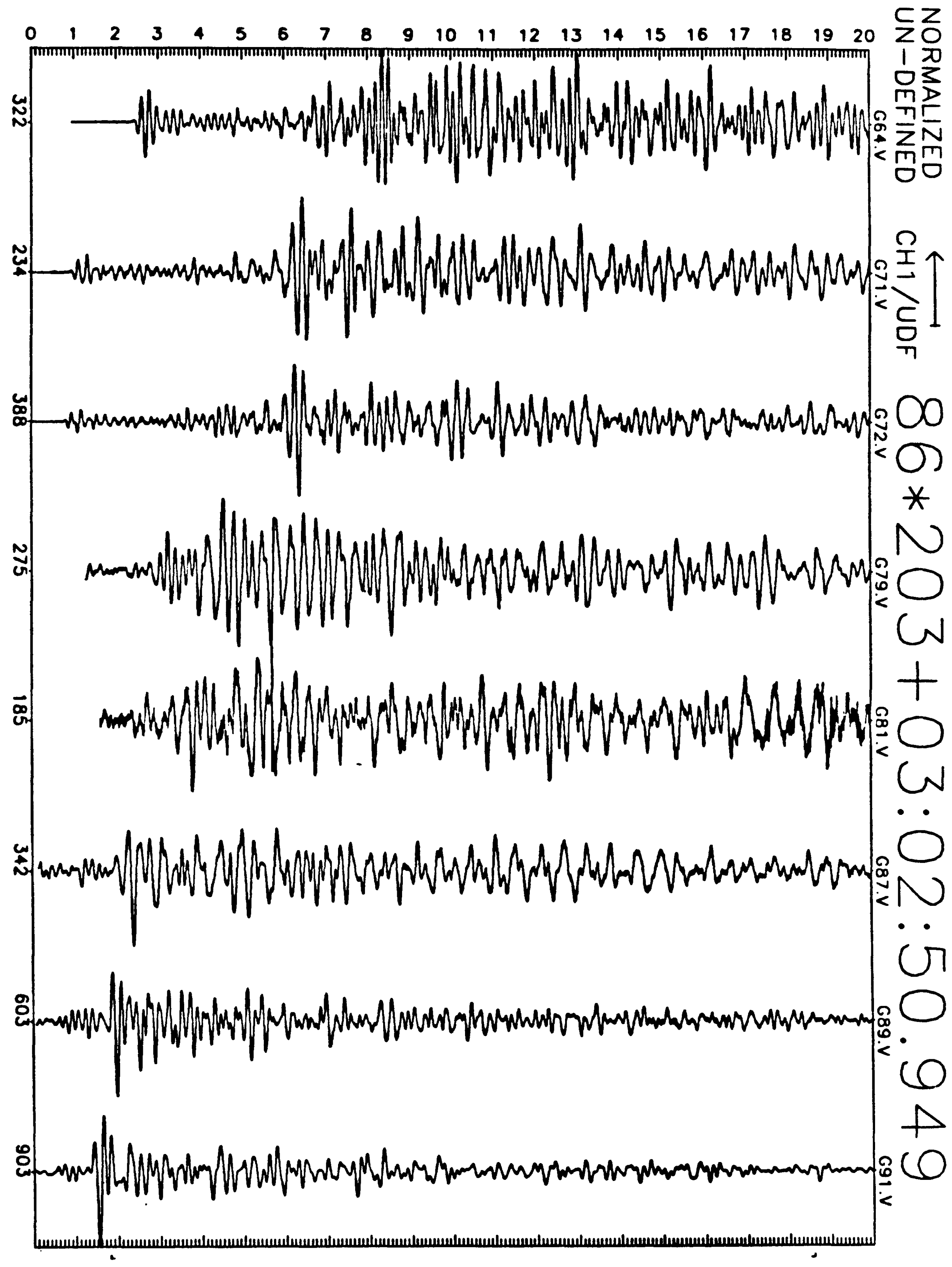

Figure D5(a): Earthquake record section for 20 seconds of vertical motion recorded at GEOS stations. Origin time for record section, station ID, and maximum digital counts (6×10^{-7} cm/sec/digital count) are indicated along abscissa.

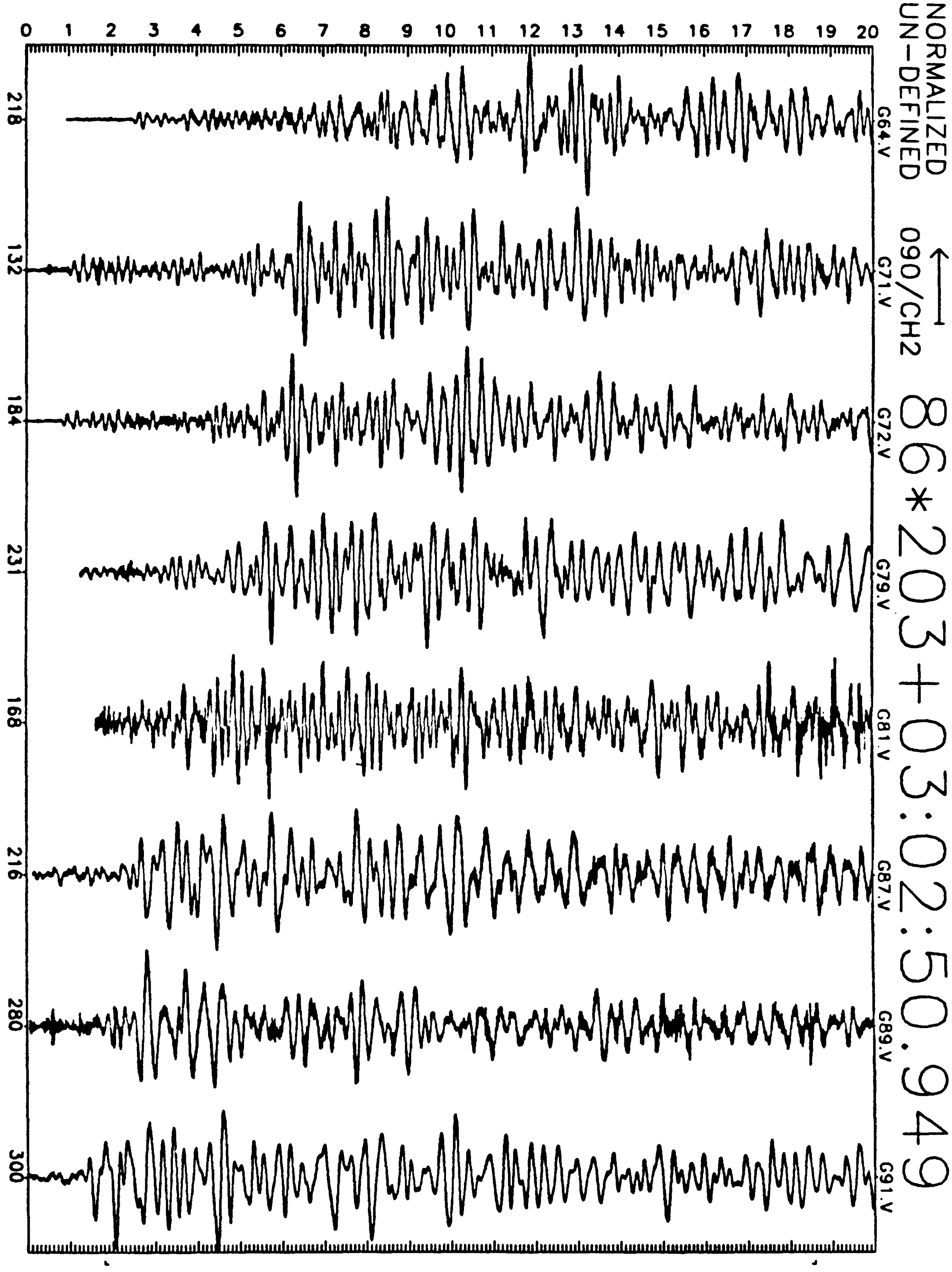

Figure D5(b): Earthquake record section for 20 seconds of N16E motion recorded at GEOS stations. Origin time for record section, station ID, and maximum digital counts (6×10^{-7} cm/sec/digital count) are indicated along abscissa.

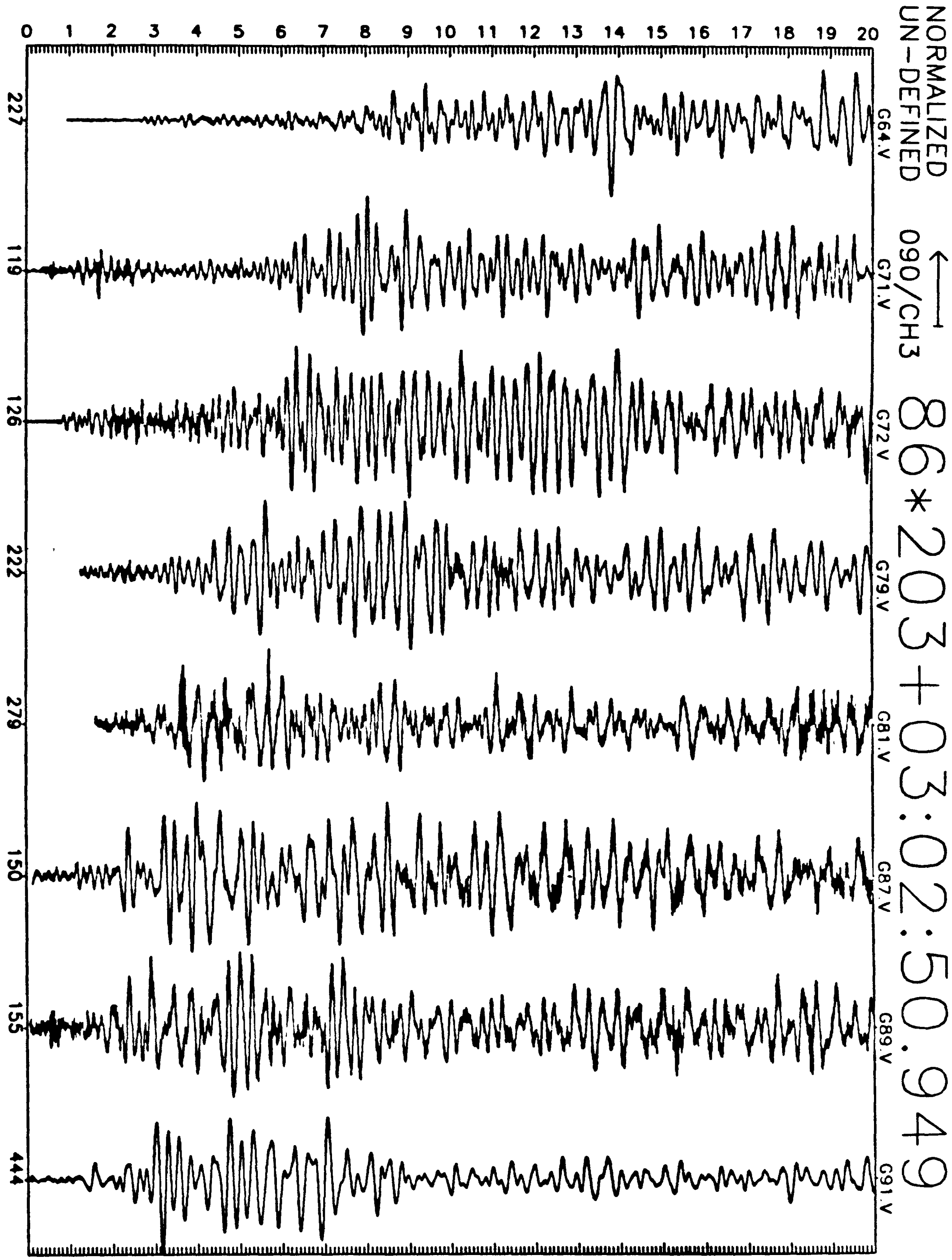

Figure D5(c): Earthquake record section for 20 seconds of N106E motion recorded at GEOS stations. Origin time for record section, station ID, and maximum digital counts (6×10^{-7} cm/sec/digital count) are indicated along abscissa.

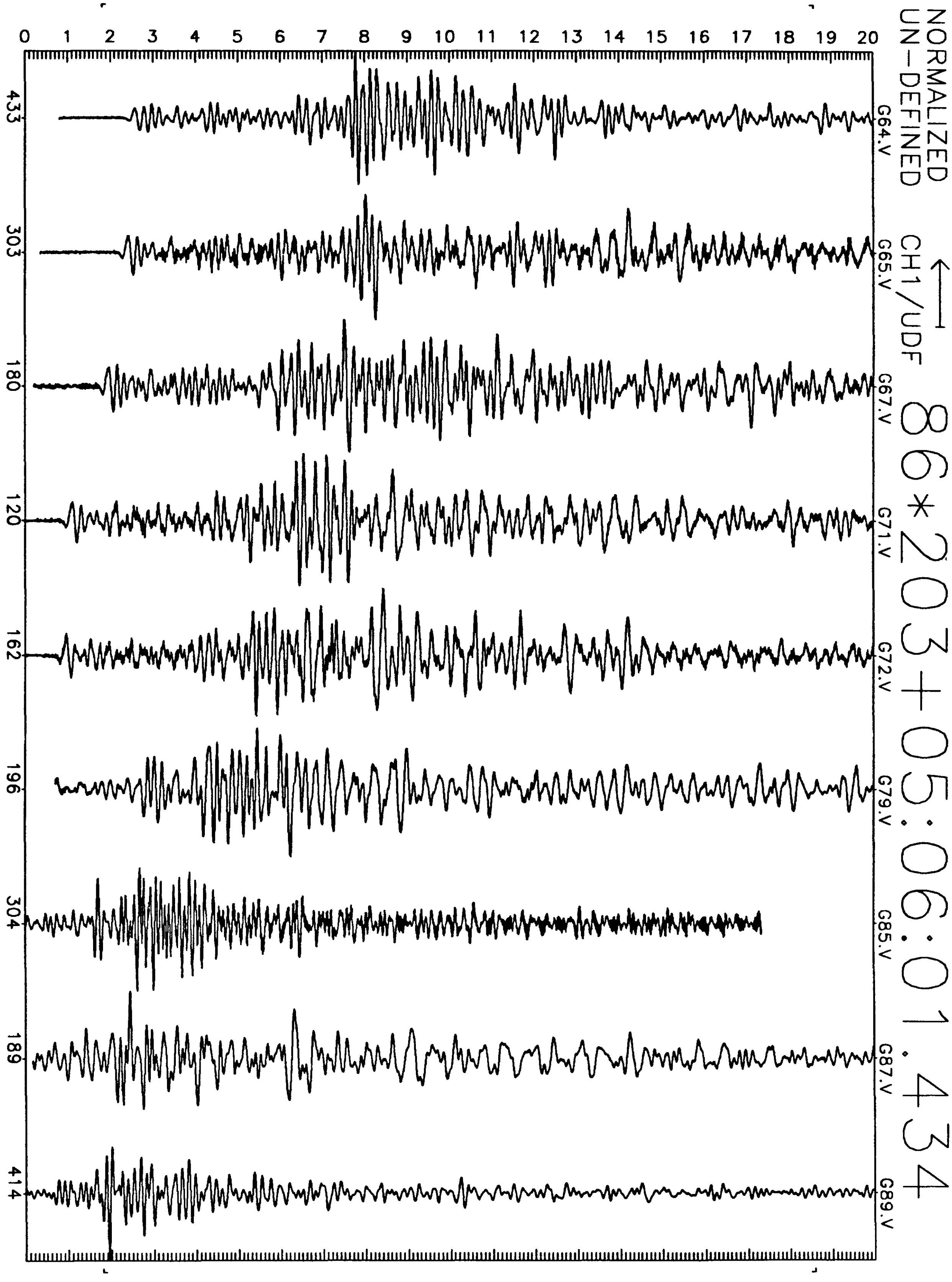

Figure D6(a): Earthquake record section for 20 seconds of vertical motion recorded at GEOS stations. Origin time for record section, station ID, and maximum digital counts (6×10^{-7} cm/sec/digital count) are indicated along abscissa.

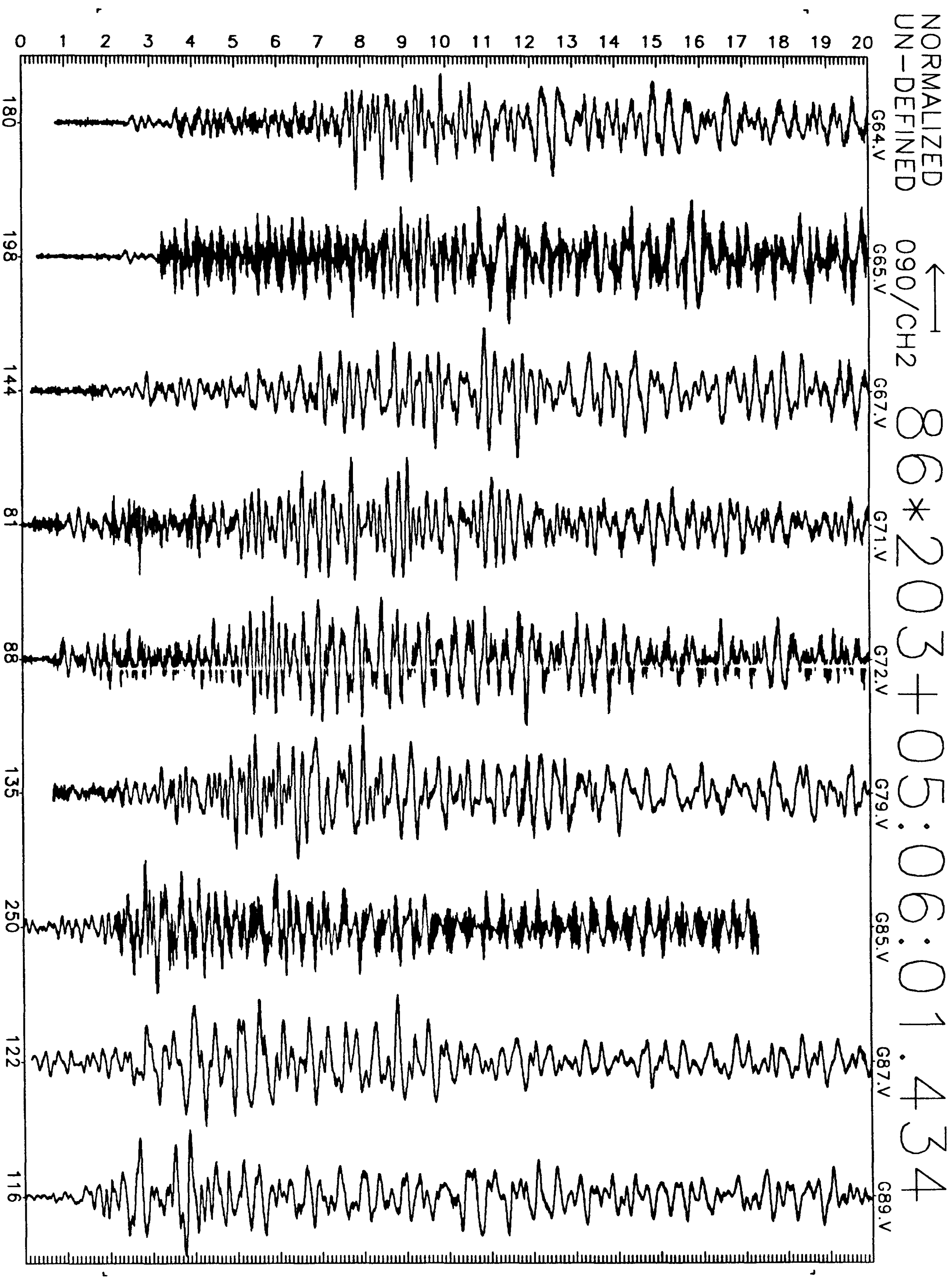

Figure D6(b): Earthquake record section for 20 seconds of N16E motion recorded at GEOS stations. Origin time for record section, station ID, and maximum digital counts (6×10^{-7} cm/sec/digital count) are indicated along abscissa.

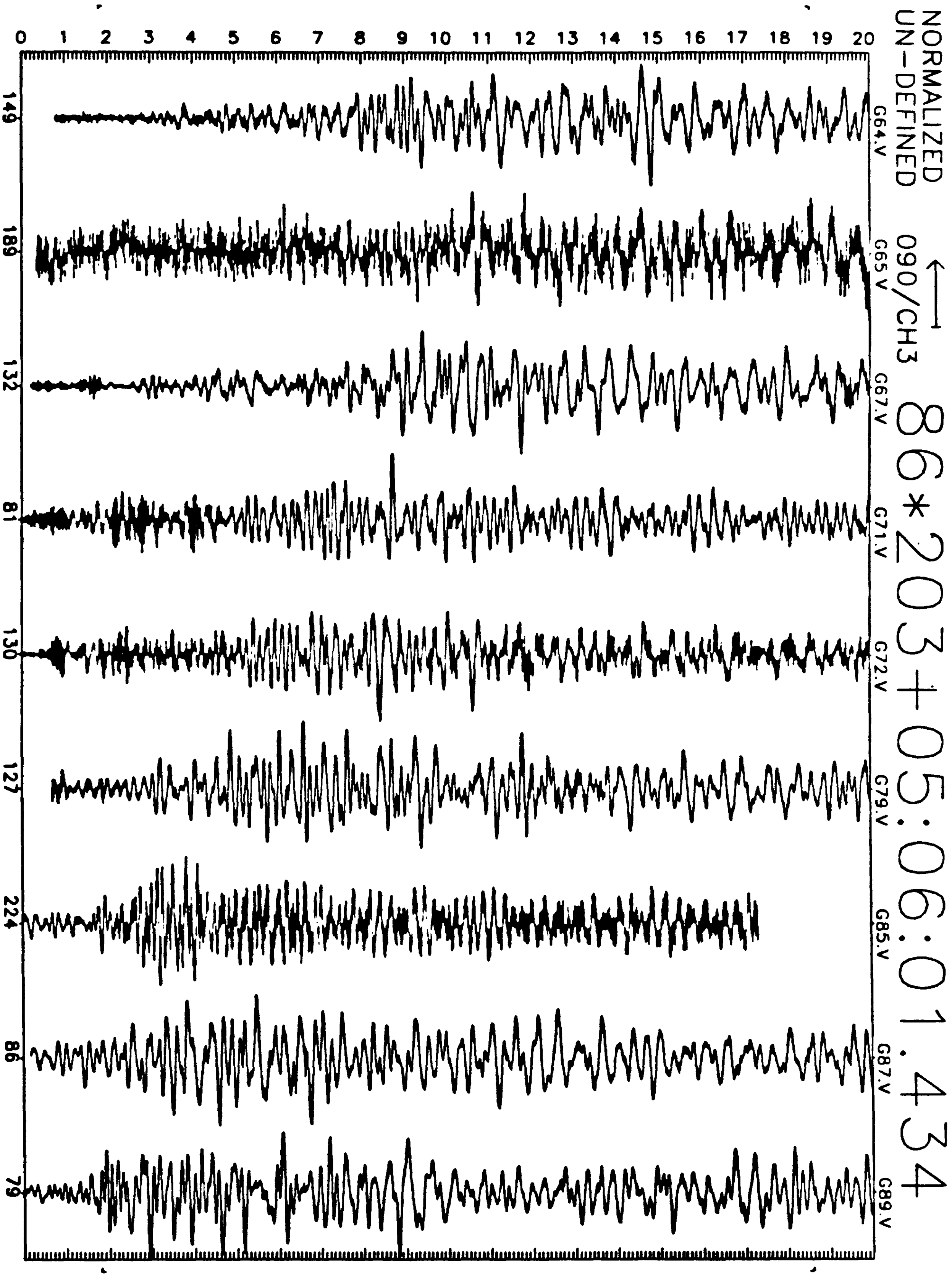

Figure D6(c): Earthquake record section for 20 seconds of N106E motion recorded at GEOS stations. Origin time for record section, station ID, and maximum digital counts (6×10^{-7} cm/sec/digital count) are indicated along abecissa.

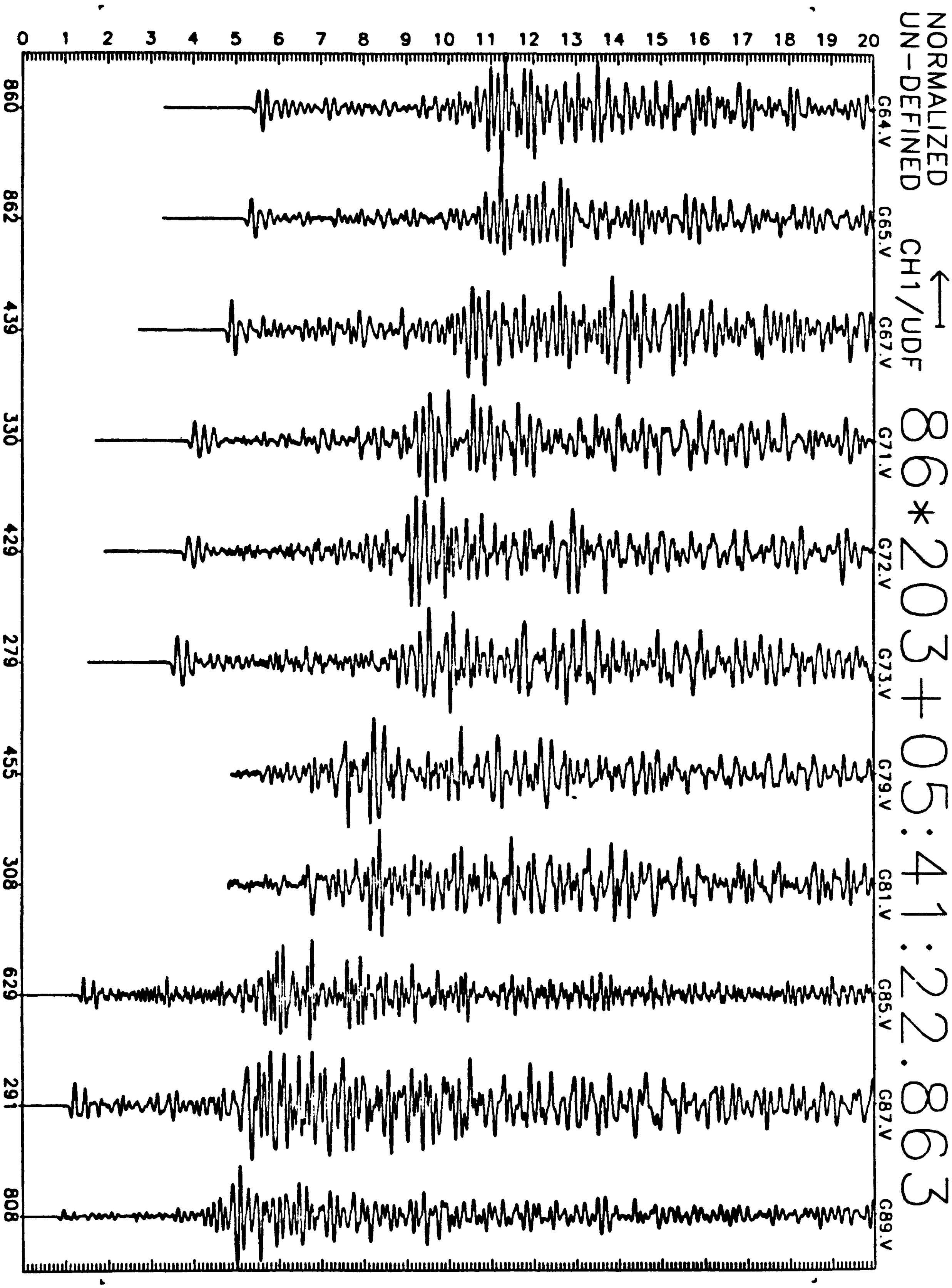

Figure D7(a): Earthquake record section for 20 seconds of vertical motion recorded at GEOS stations. Origin time for record section, station ID, and maximum digital counts (6×10^{-7} cm/sec/digital count) are indicated along abscissa.

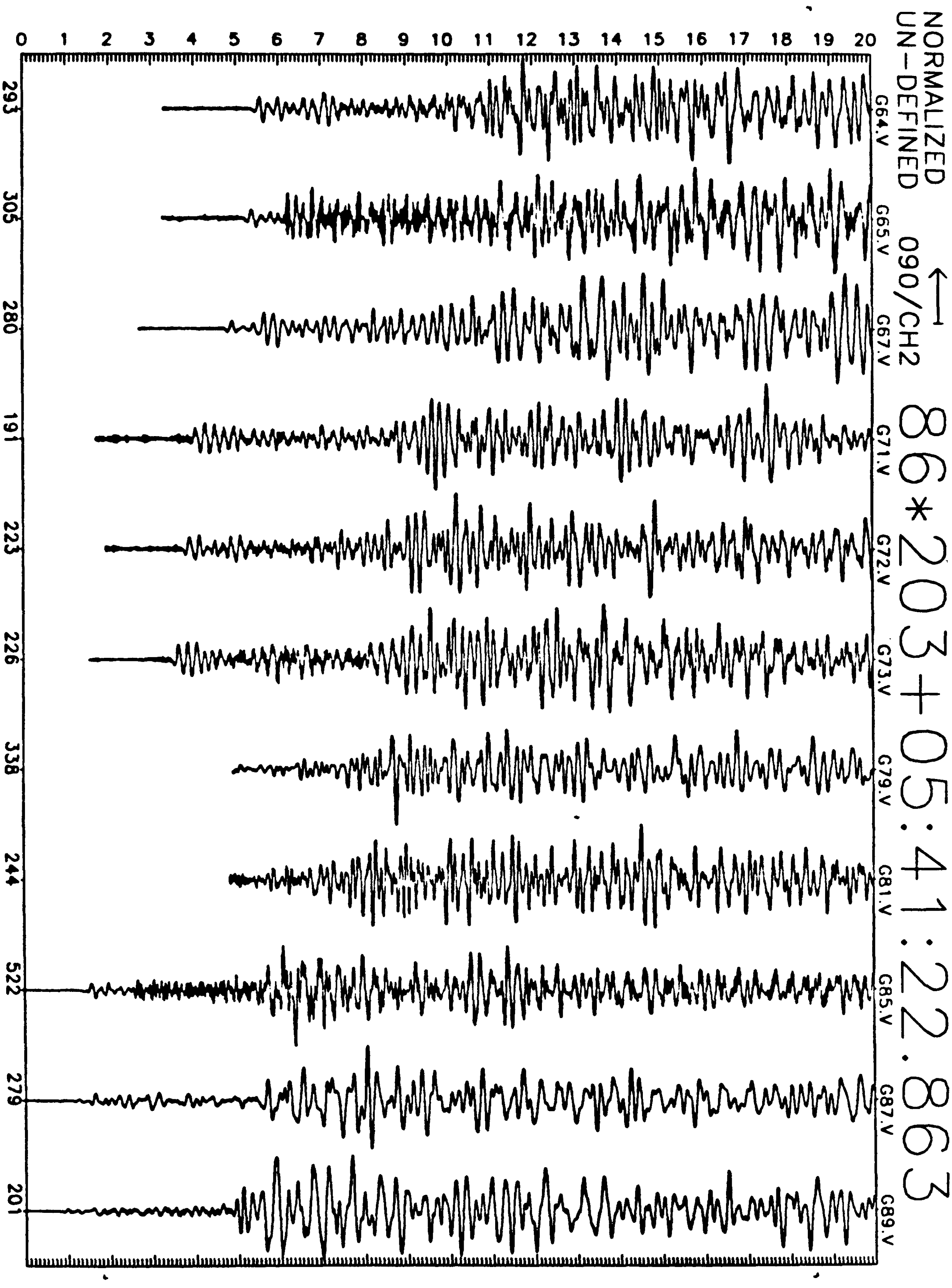

Figure D7(b): Earthquake record section for 20 seconds of N16E motion recorded at GEOS stations. Origin time for record section, station ID, and maximum digital counts (6×10^{-7} cm/sec/digital count) are indicated along abscissa.

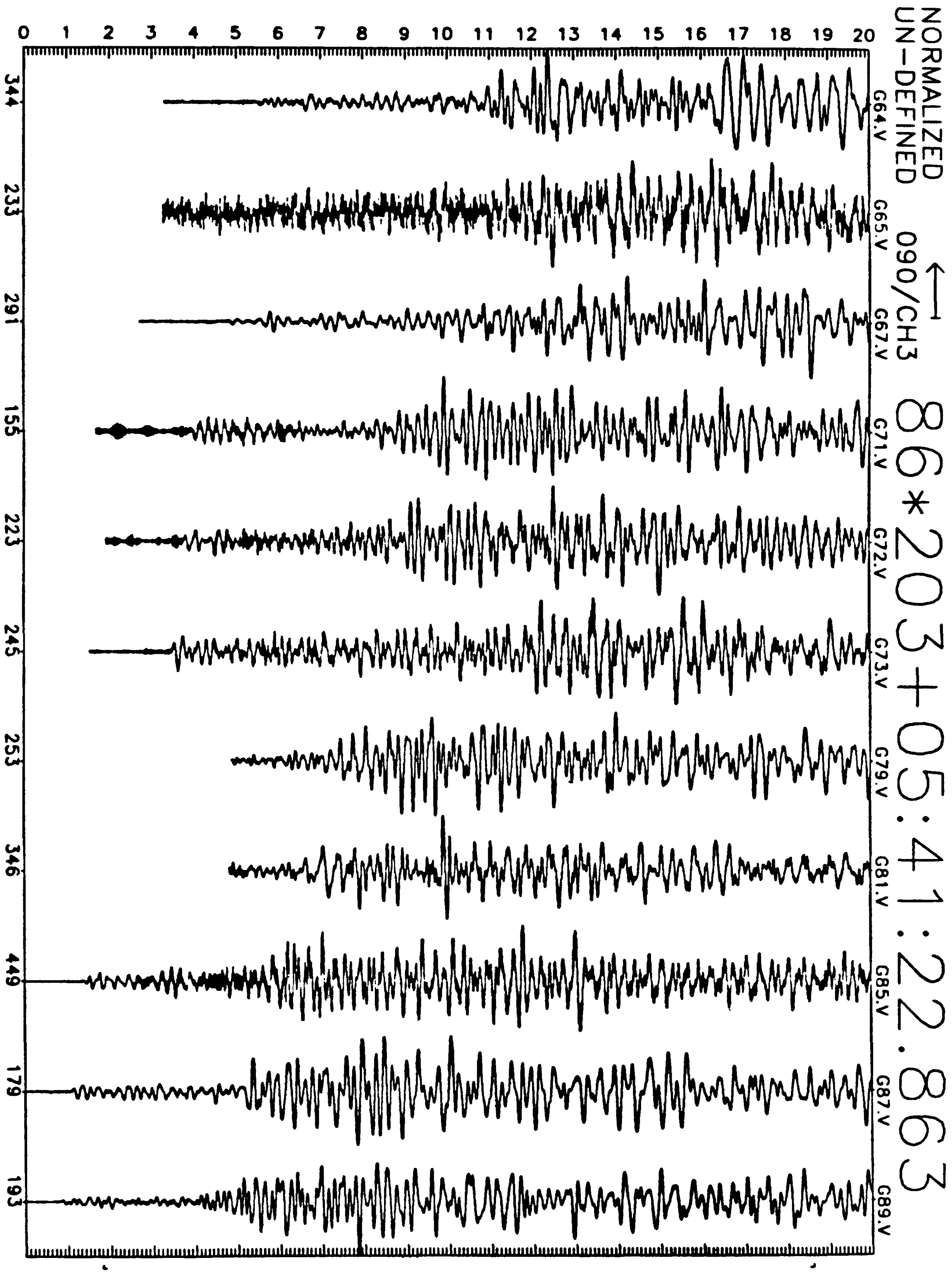

Figure D7(c): Earthquake record section for 20 seconds of N106E motion recorded at GEOS stations. Origin time for record section, station ID, and maximum digital counts (6×10^{-7} cm/sec/digital count) are indicated along abscissa.

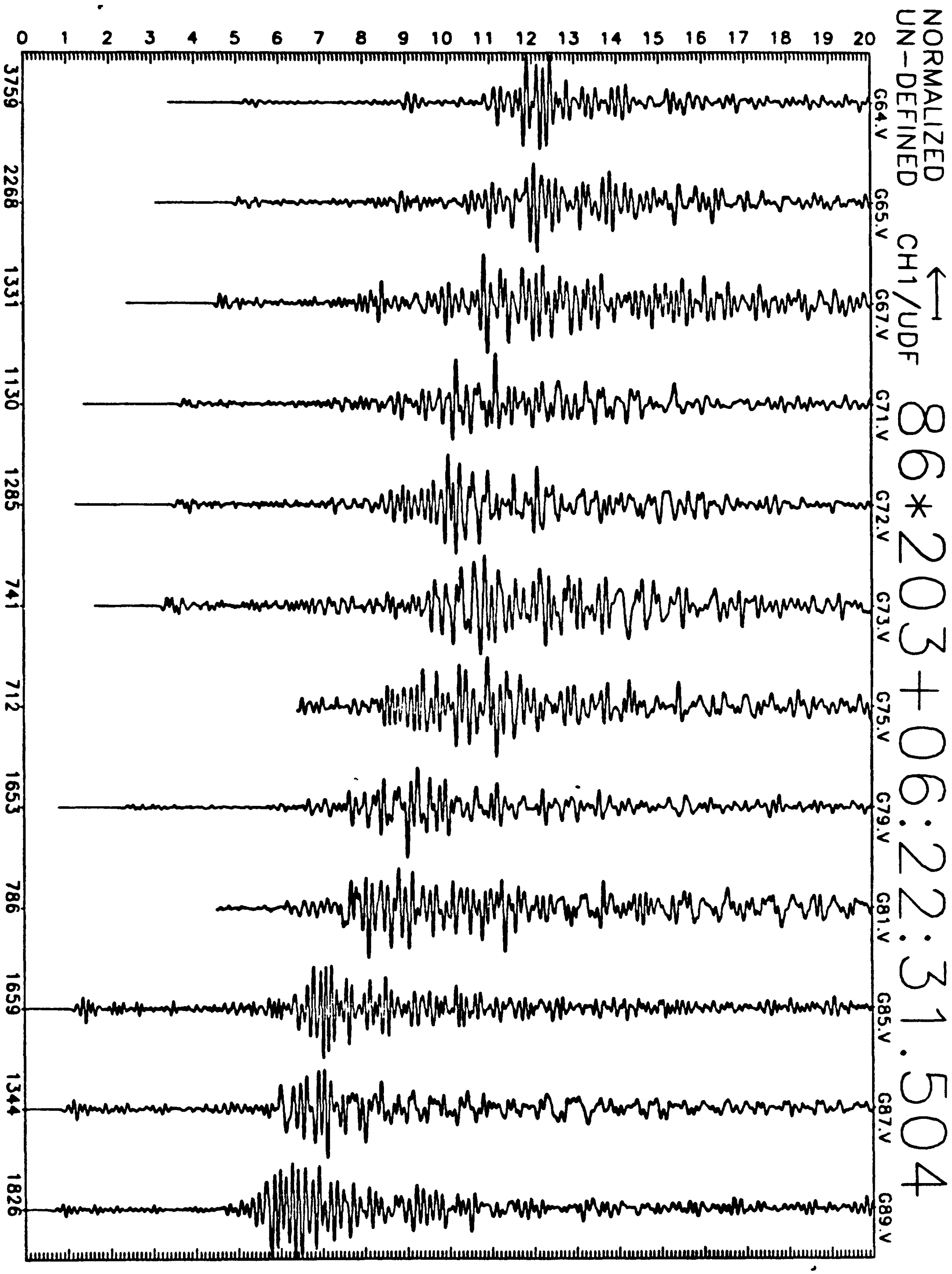

Figure D8(a): Earthquake record section for 20 seconds of vertical motion recorded at GEOS stations. Origin time for record section, station ID, and maximum digital counts (6×10^{-7} cm/sec/digital count) are indicated along abscissa.

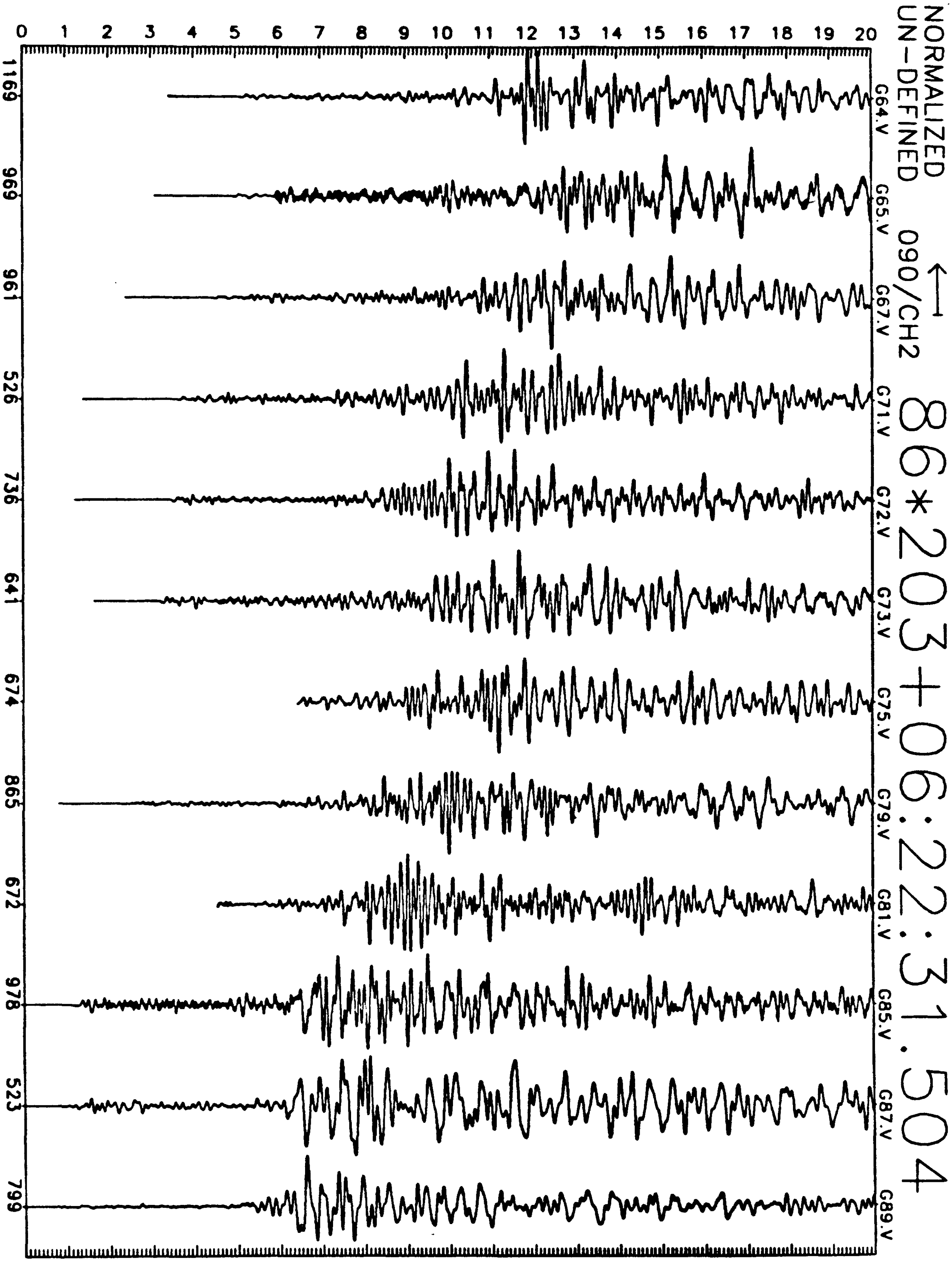

Figure D8(b): Earthquake record section for 20 seconds of N16E motion recorded at GEOS stations. Origin time for record section, station ID, and maximum digital counts (6×10^{-7} cm/sec/digital count) are indicated along abscissa.

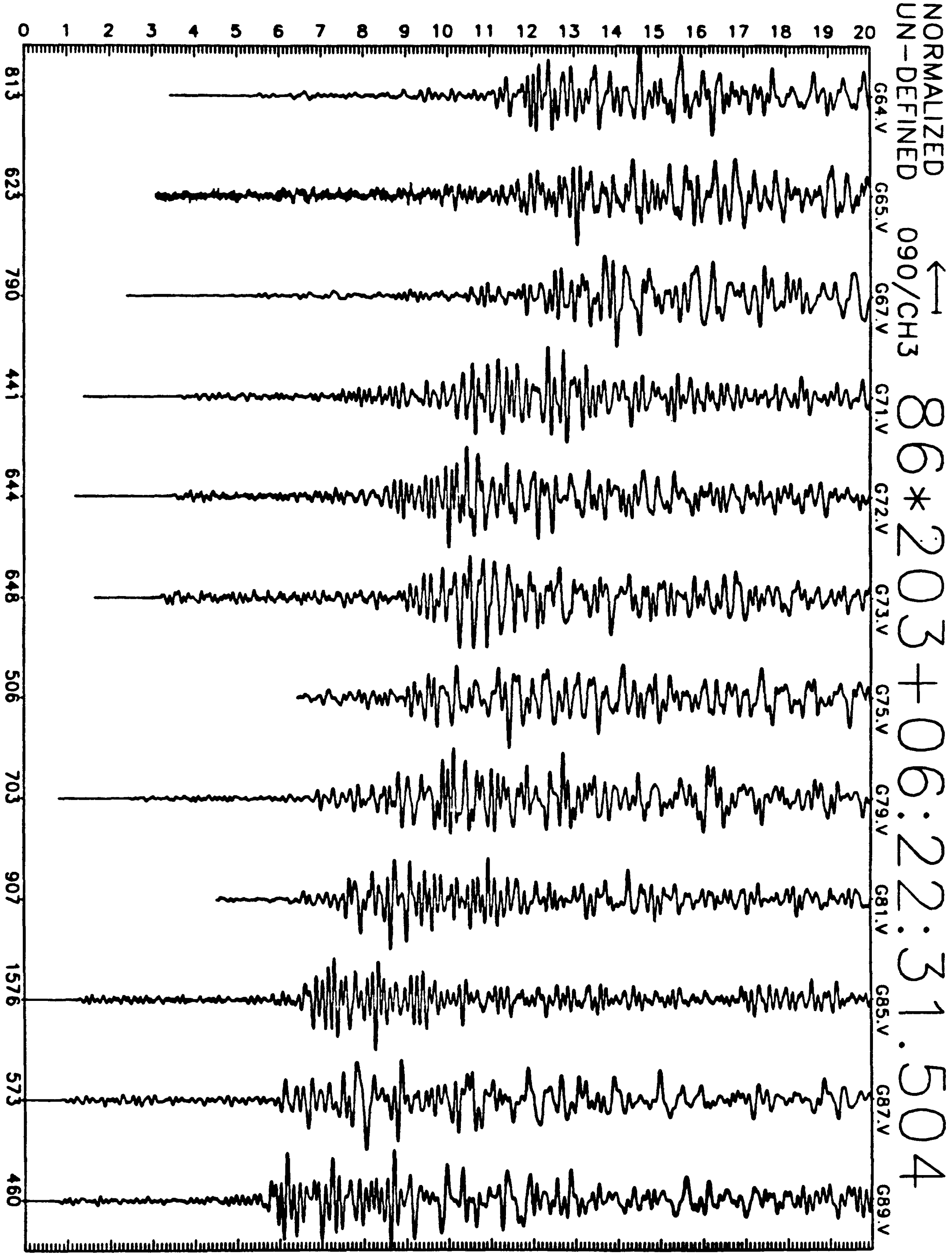

Figure D8(c): Earthquake record section for 20 seconds of N106E motion recorded at GEOS stations. Origin time for record section, station ID, and maximum digital counts (6×10^{-7} cm/sec/digital count) are indicated along abscissa.

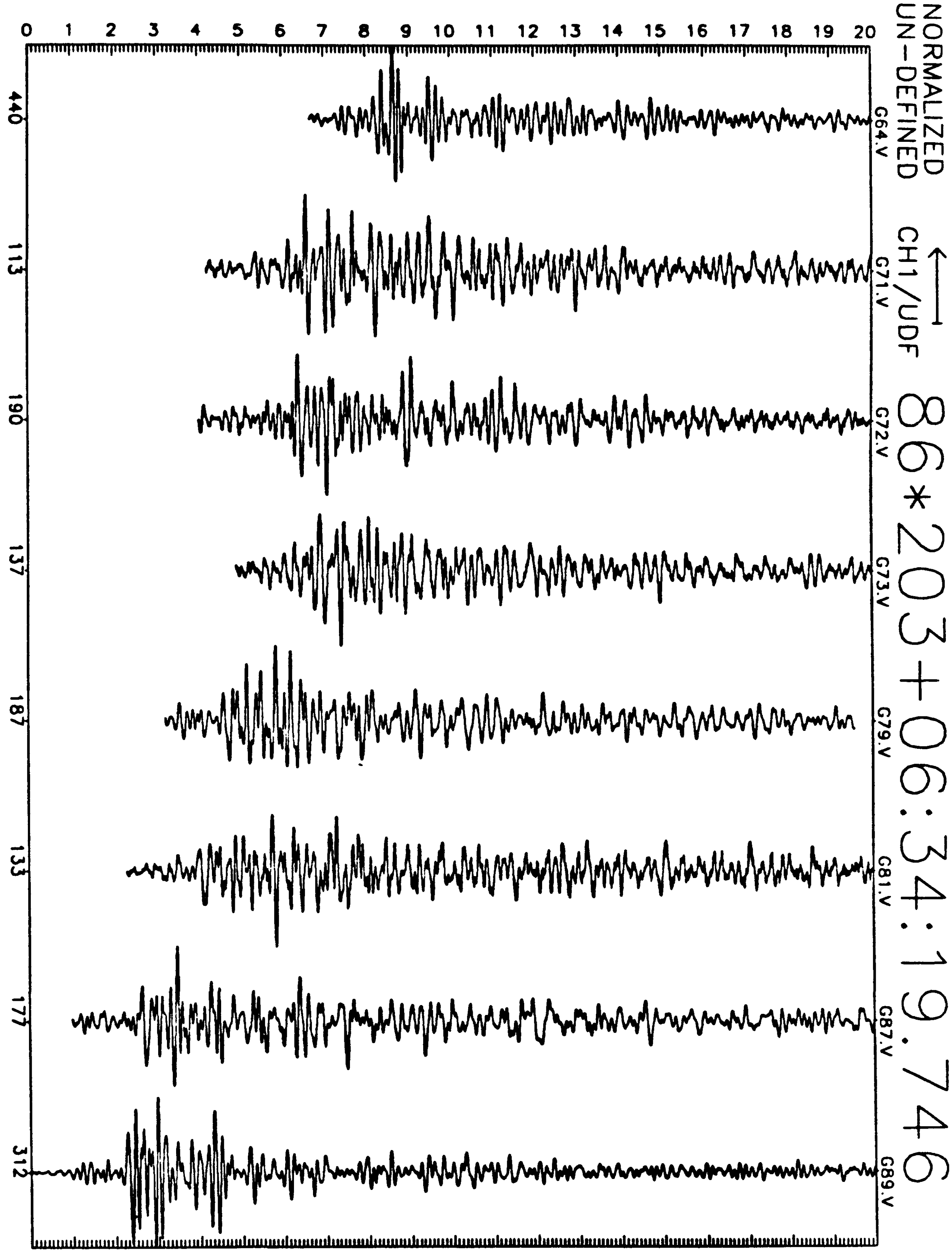

Figure D9(a): Earthquake record section for 20 seconds of vertical motion recorded at GEOS stations. Origin time for record section, station ID, and maximum digital counts (6×10^{-7} cm/sec/digital count) are indicated along abscissa.

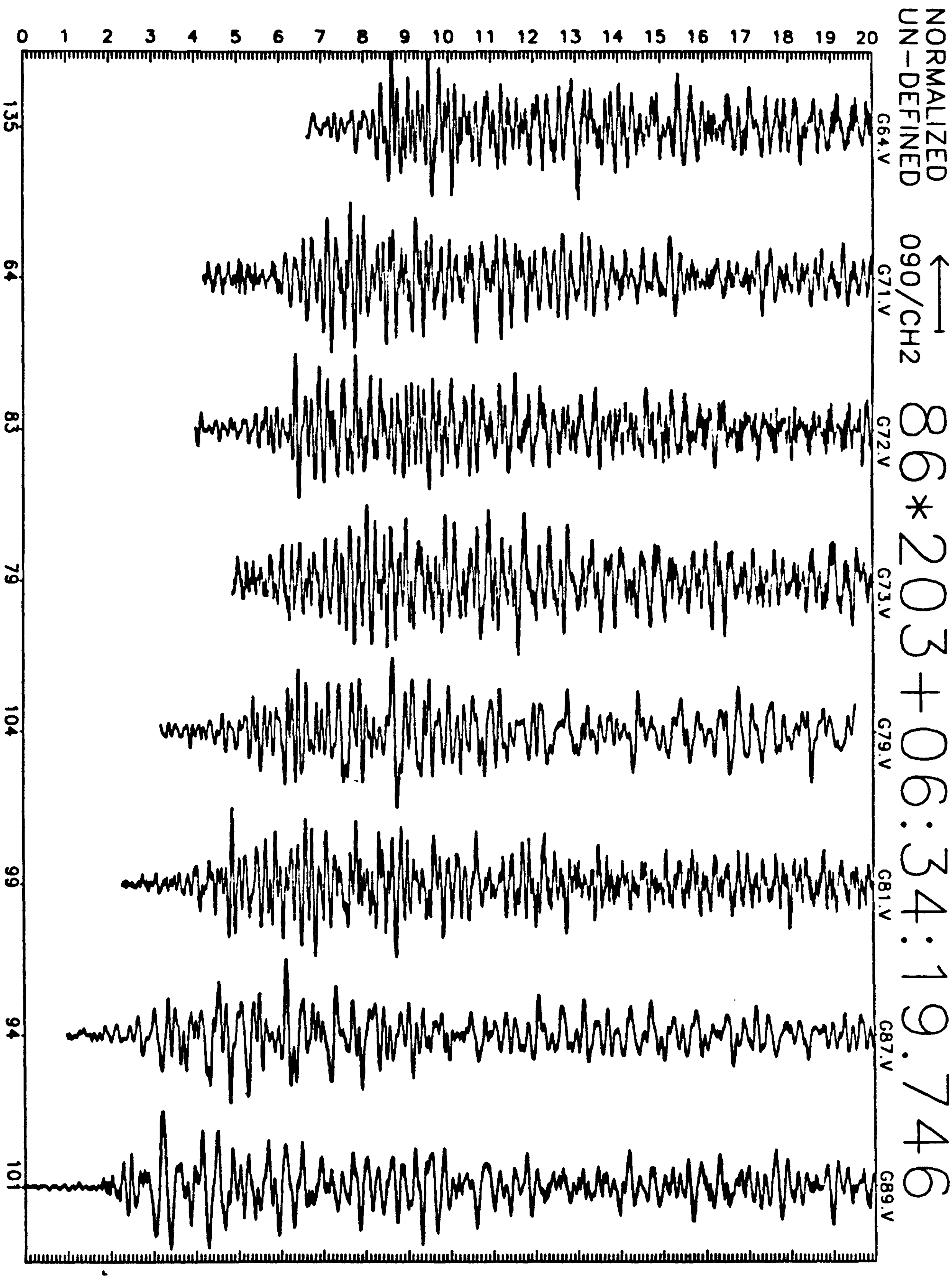

Figure D9(b): Earthquake record section for 20 seconds of N16E motion recorded at GEOS stations. Origin time for record section, station ID, and maximum digital counts (6×10^{-7} cm/sec/digital count) are indicated along abscissa.

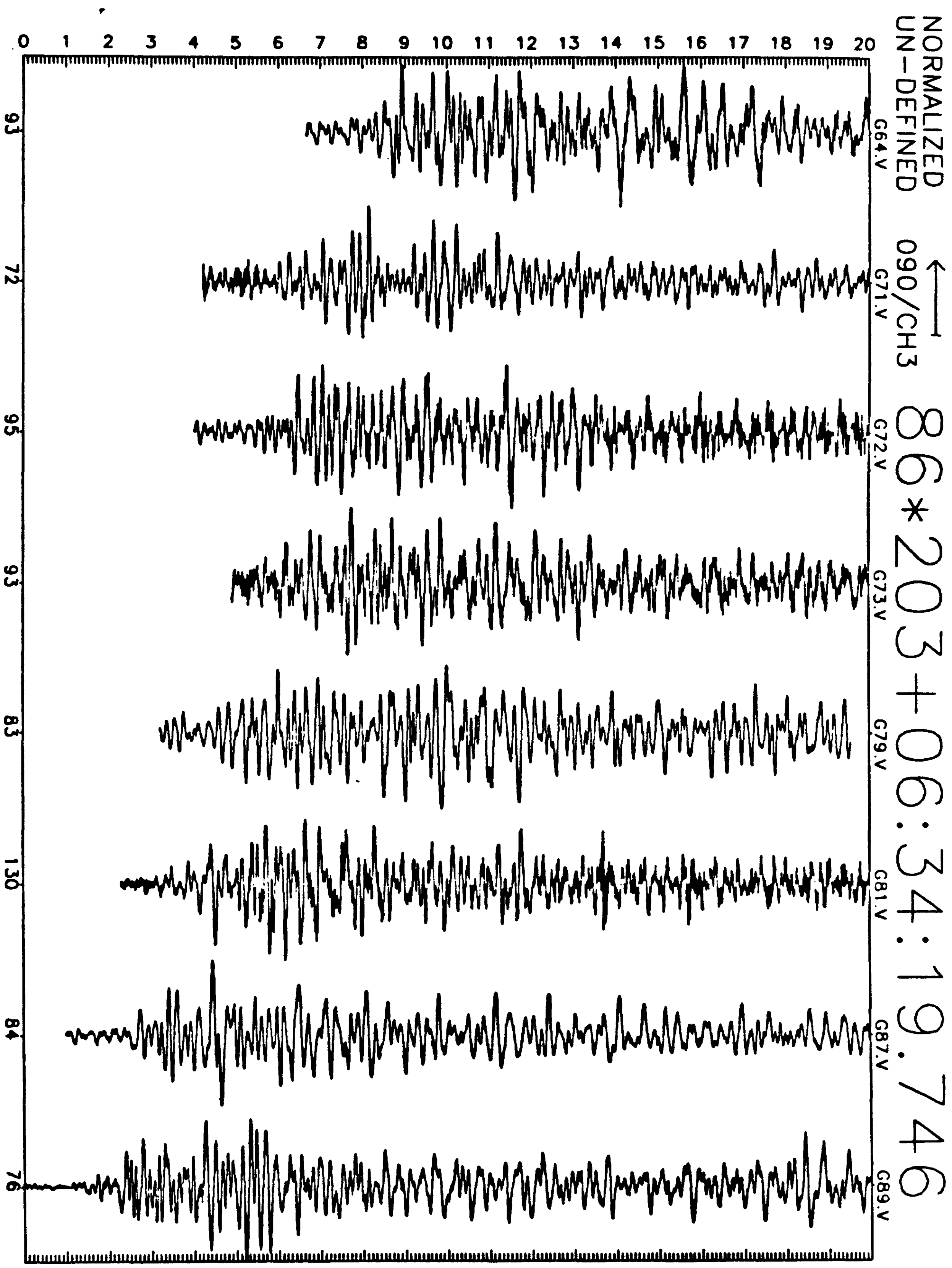

Figure D9(c): Earthquake record section for 20 seconds of N106E motion recorded at GEOS stations. Origin time for record section, station ID, and maximum digital counts (6×10^{-7} cm/sec/digital count) are indicated along abscissa.

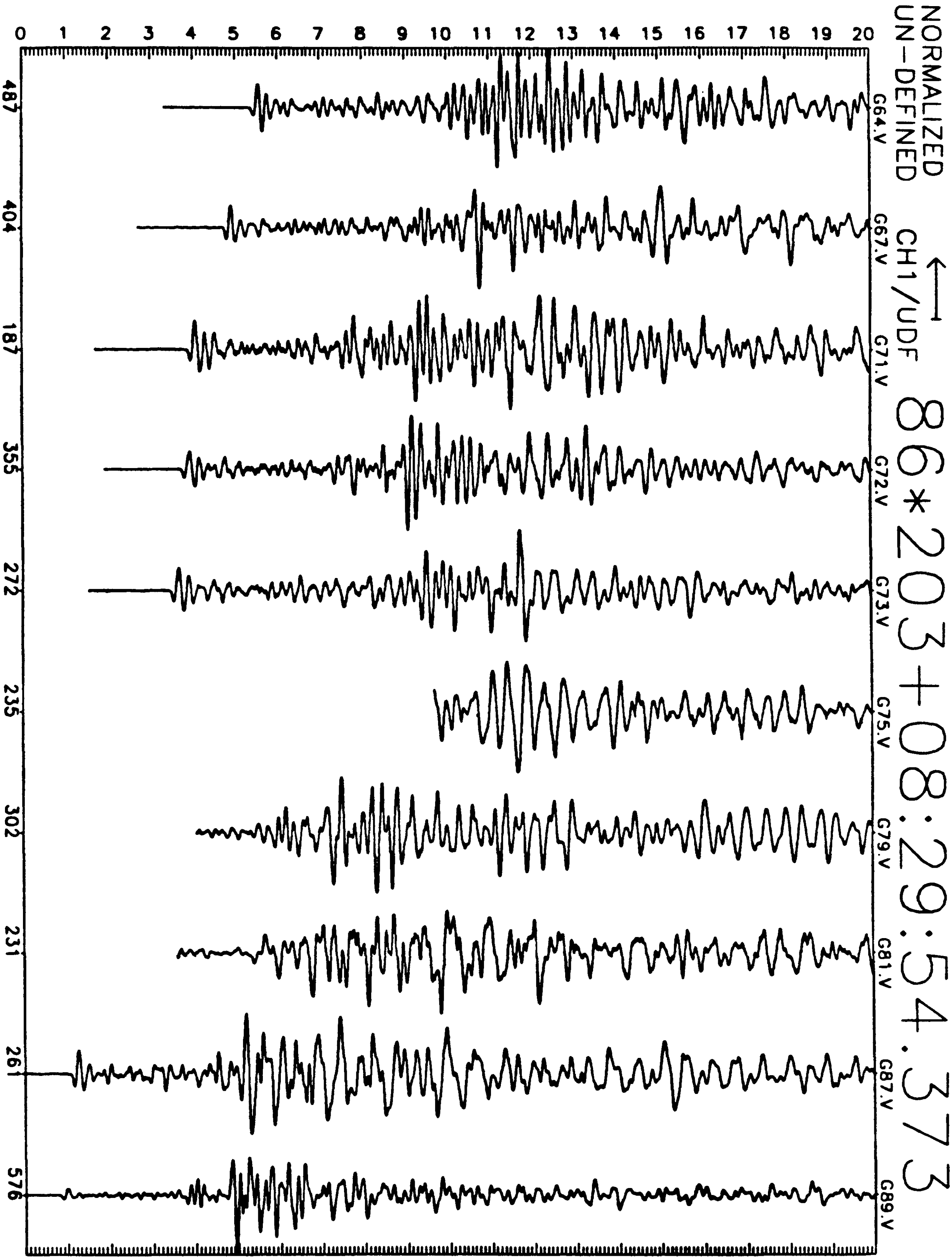

Figure D10(a): Earthquake record section for 20 seconds of vertical motion recorded at GEOS stations. Origin time for record section, station ID, and maximum digital counts (6×10^{-7} cm/sec/digital count) are indicated along abscissa.

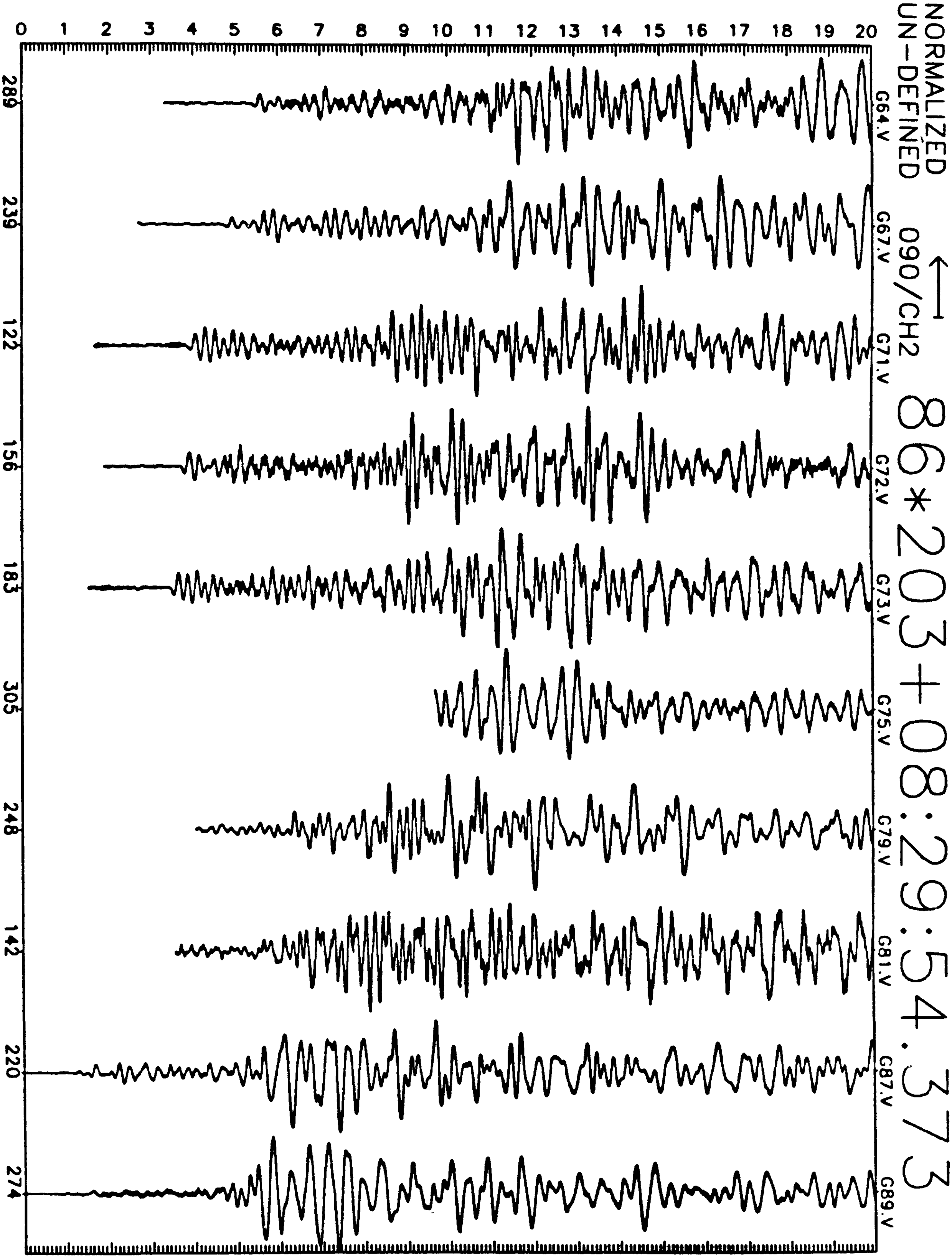

Figure D10(b): Earthquake record section for 20 seconds of N16E motion recorded at GEOS stations. Origin time for record section, station ID, and maximum digital counts (6×10^{-7} cm/sec/digital count) are indicated along abscissa.

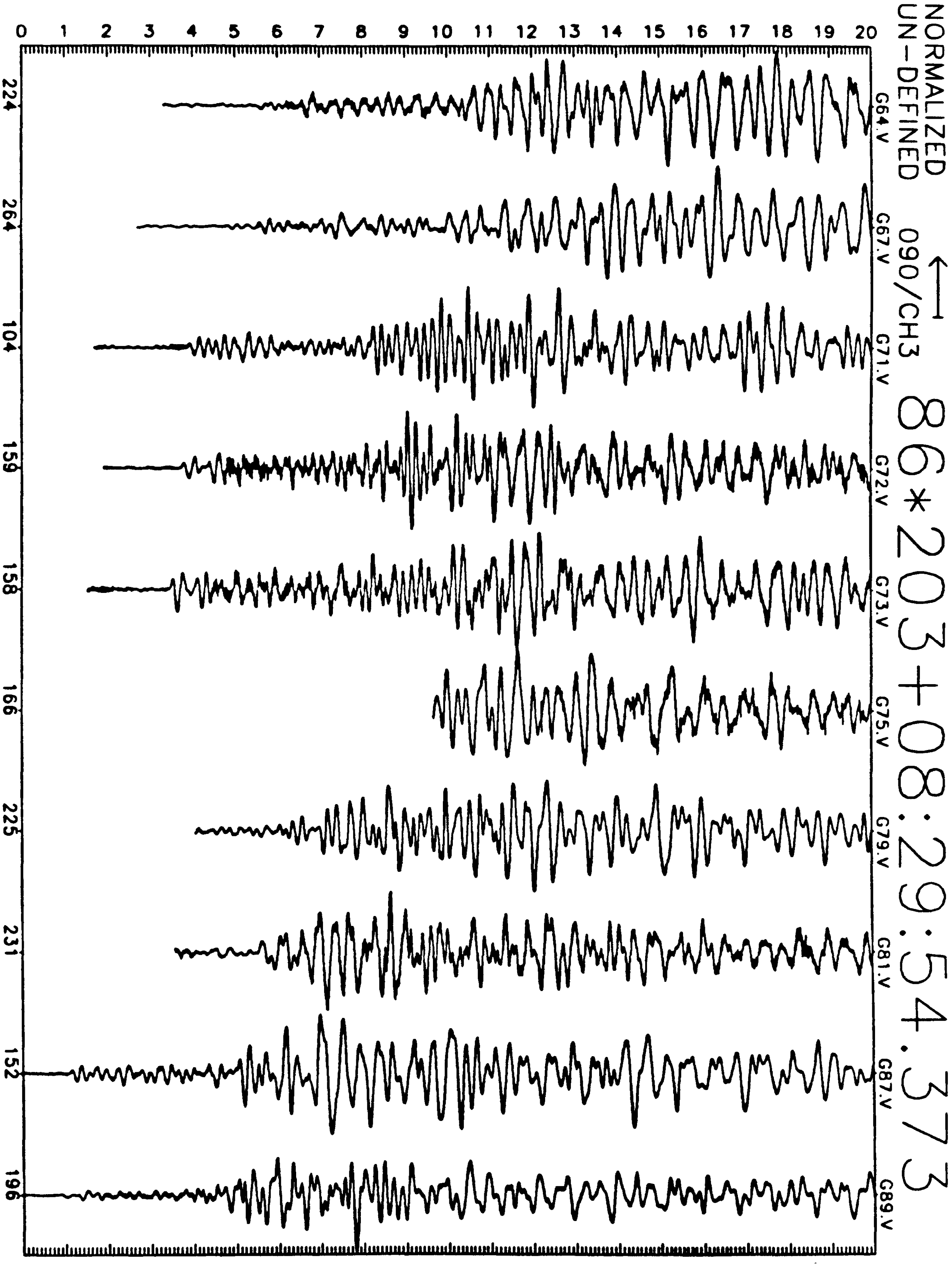

Figure D10(c): Earthquake record section for 20 seconds of N106E motion recorded at GEOS stations. Origin time for record section, station ID, and maximum digital counts (6×10^{-7} cm/sec/digital count) are indicated along abscissa.

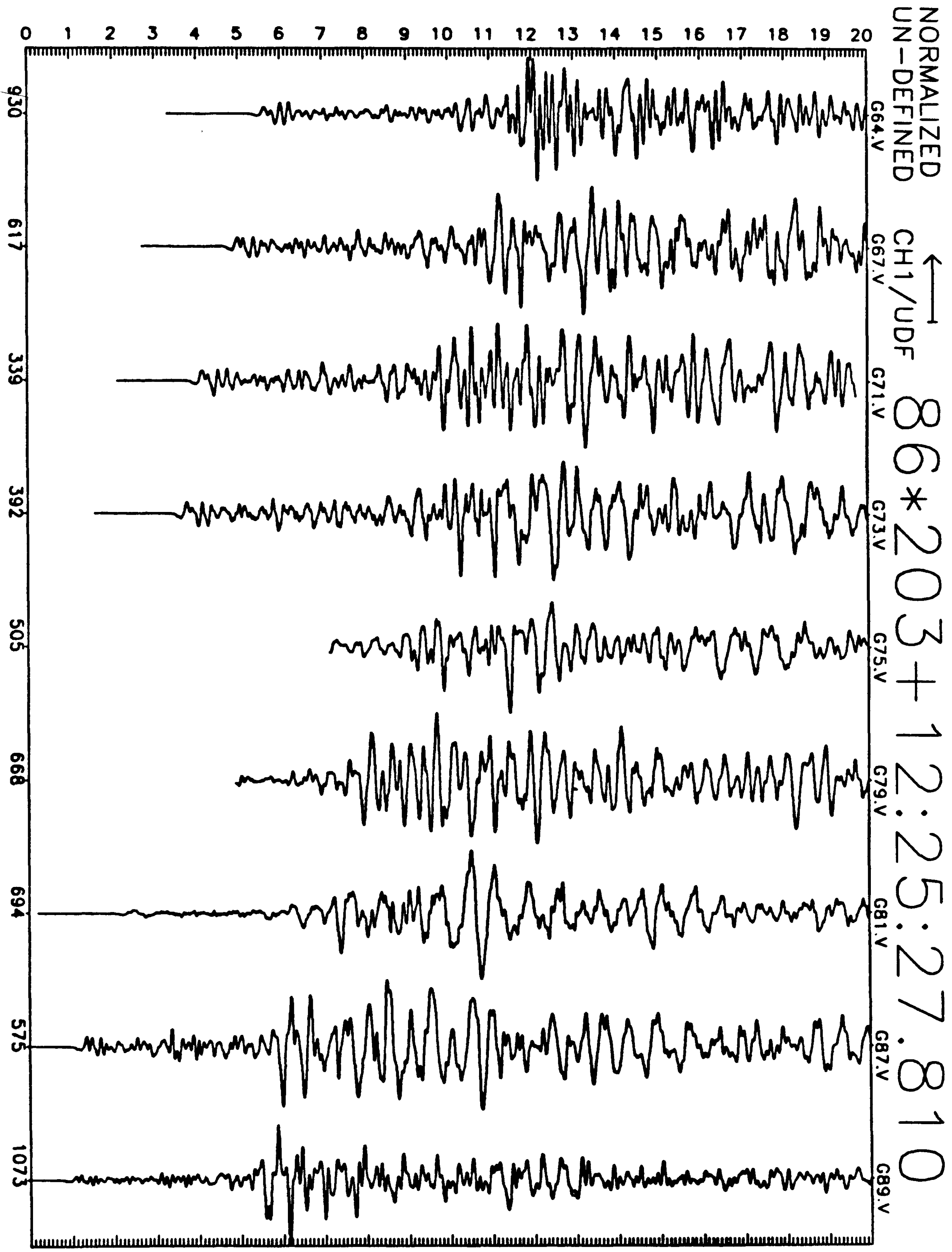

Figure D11(a): Earthquake record section for 20 seconds of vertical motion recorded at GEOS stations. Origin time for record section, station ID, and maximum digital counts (6×10^{-7} cm/sec/digital count) are indicated along abscissa.

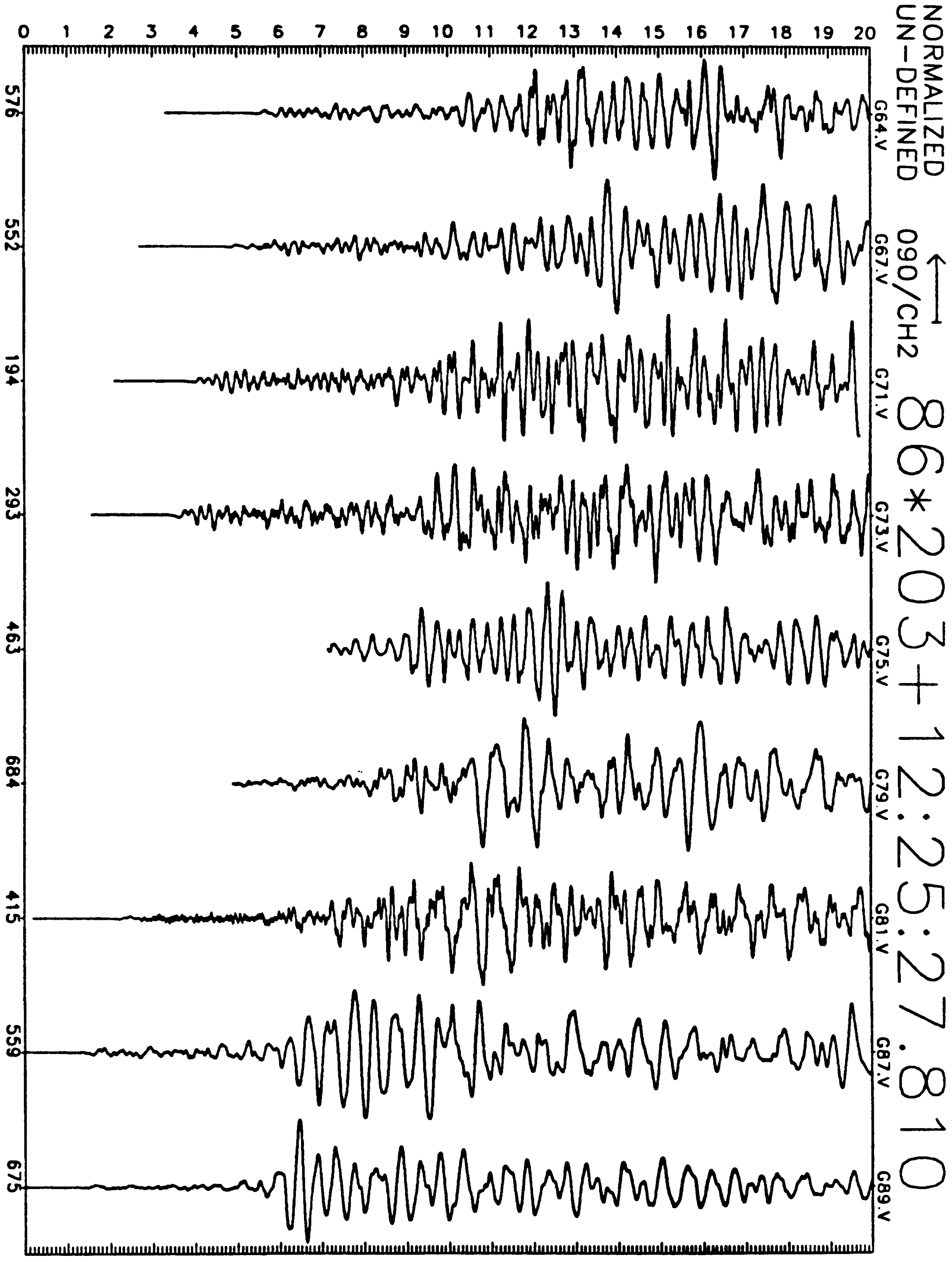

Figure D11(b): Earthquake record section for 20 seconds of N16E motion recorded at GEOS stations. Origin time for record section, station ID, and maximum digital counts (6×10^{-7} cm/sec/digital count) are indicated along abscissa.

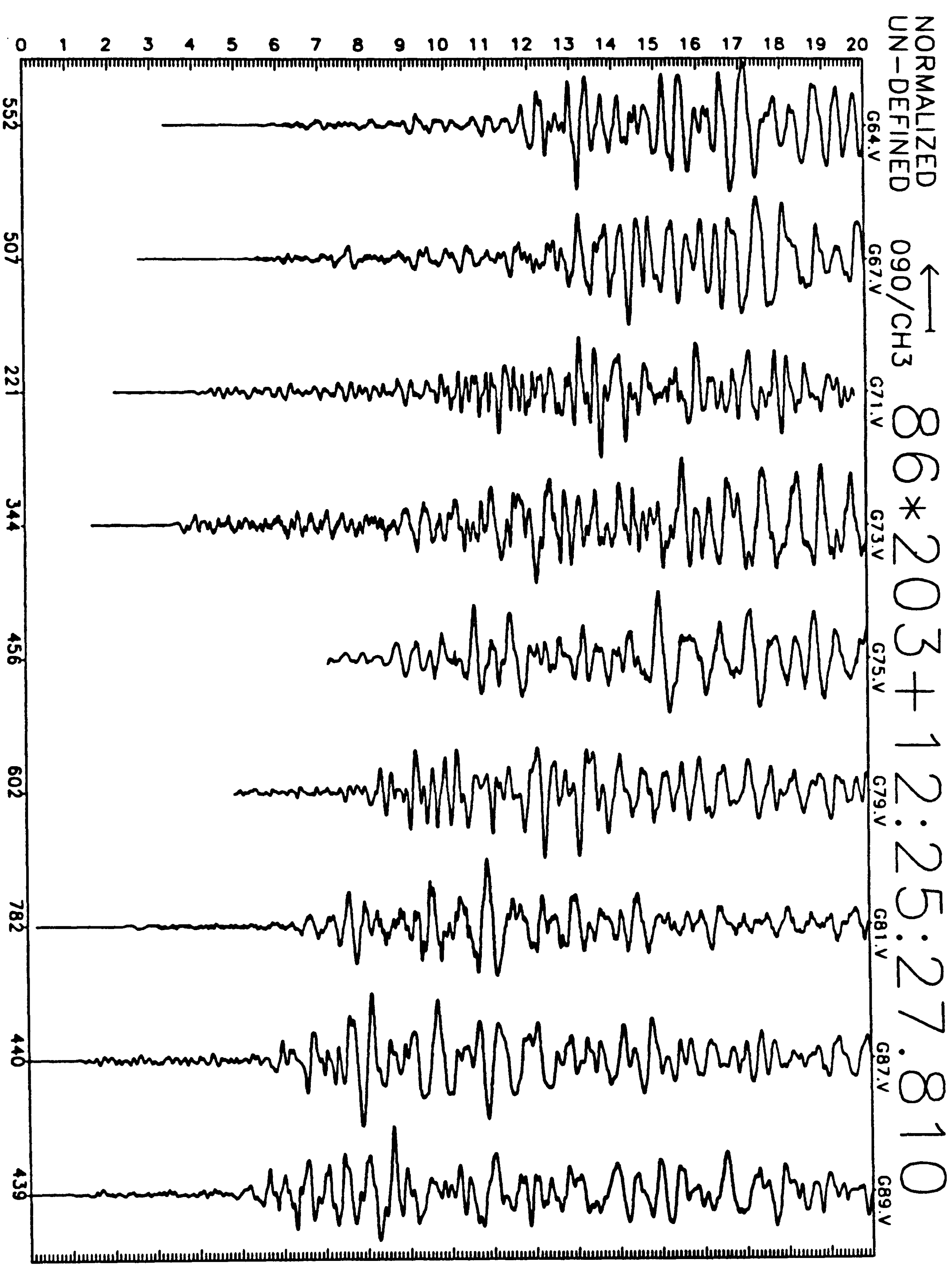

Figure D11(c): Earthquake record section for 20 seconds of N106E motion recorded at GEOS stations. Origin time for record section, station ID, and maximum digital counts (6×10^{-7} cm/sec/digital count) are indicated along abscissa.

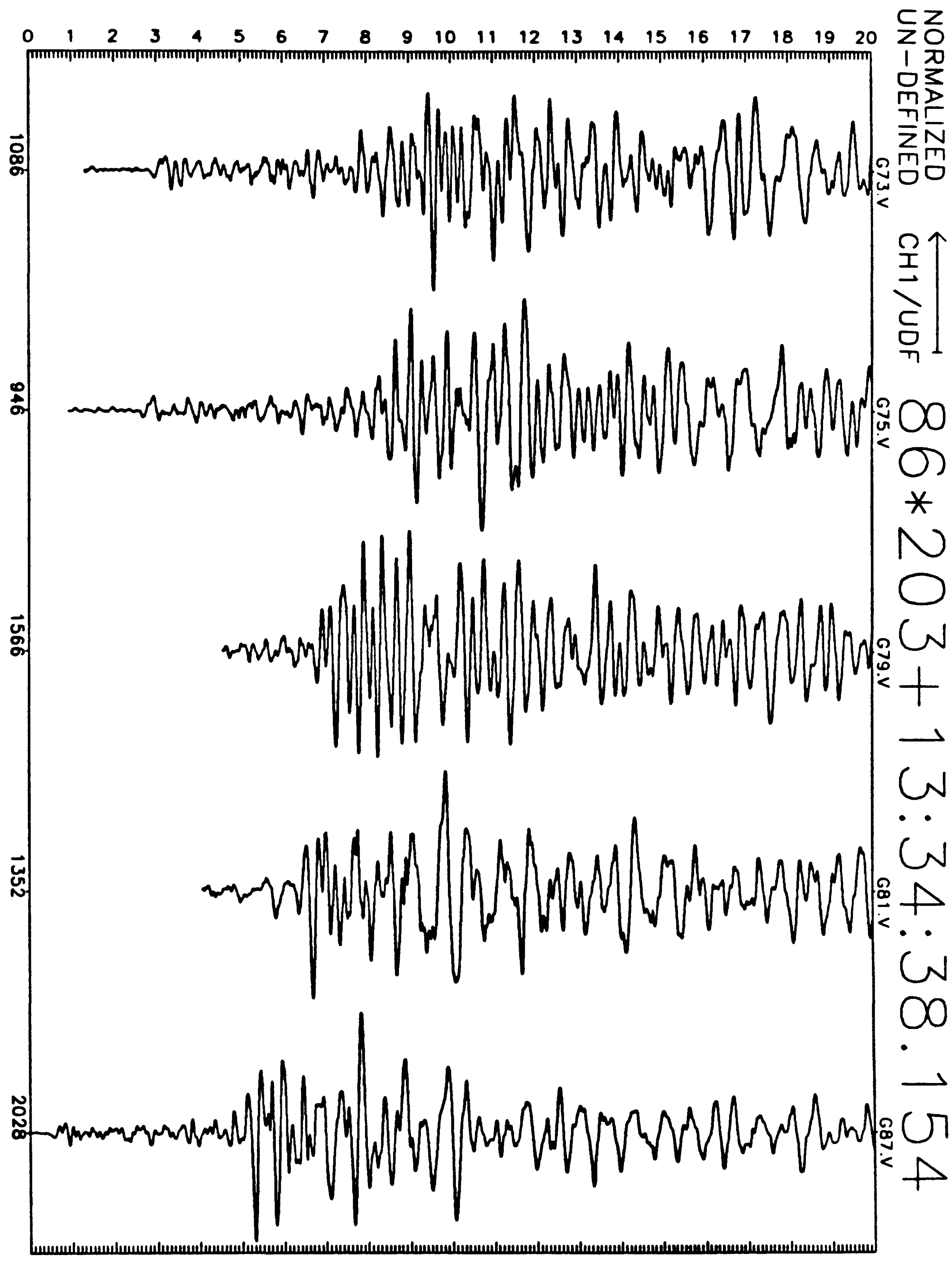

Figure D12(a): Earthquake record section for 20 seconds of vertical motion recorded at GEOS stations. Origin time for record section, station ID, and maximum digital counts (6×10^{-7} cm/sec/digital count) are indicated along abscissa.

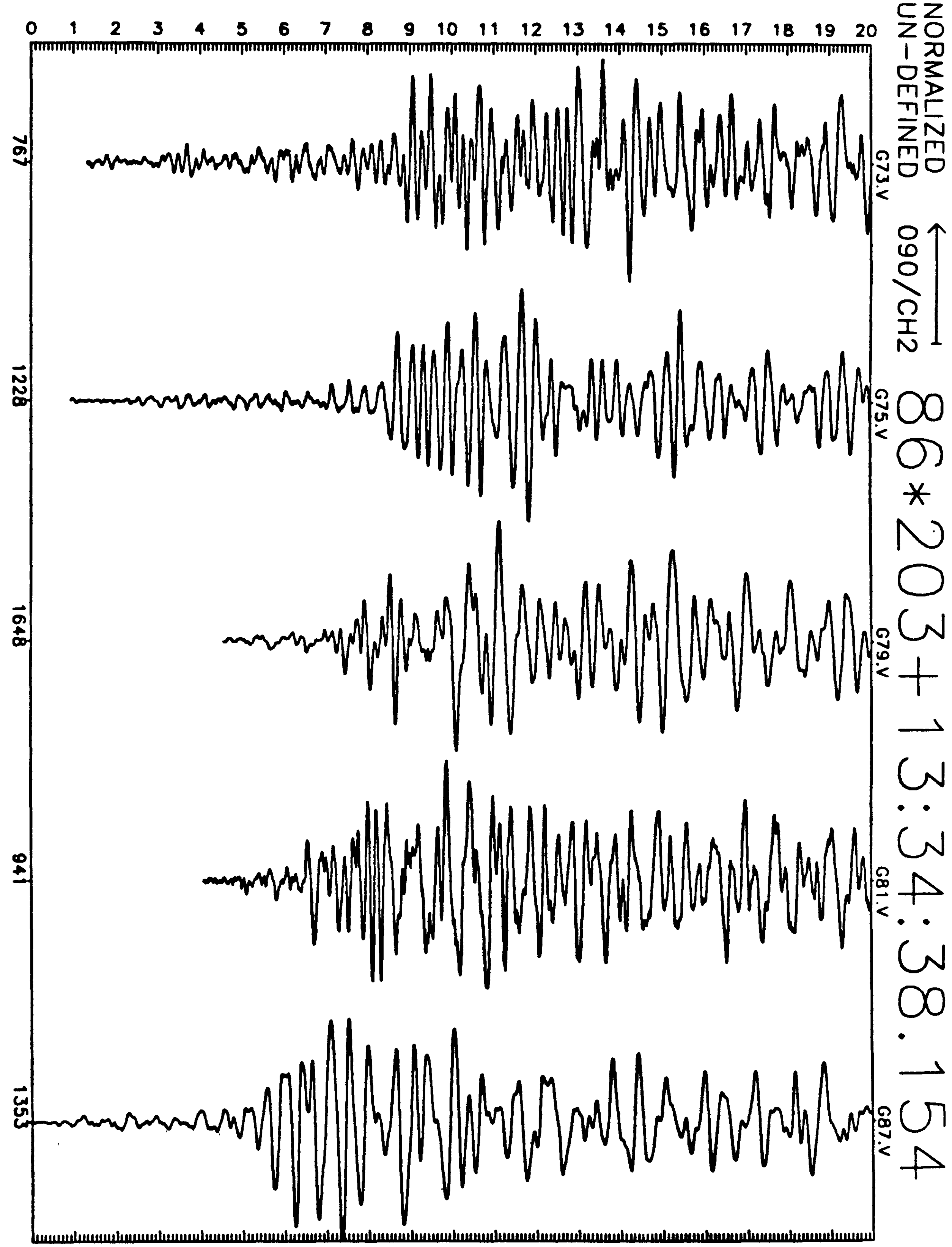

Figure D12(b): Earthquake record section for 20 seconds of N16E motion recorded at GEOS stations. Origin time for record section, station ID, and maximum digital counts (6×10^{-7} cm/sec/digital count) are indicated along abscissa.

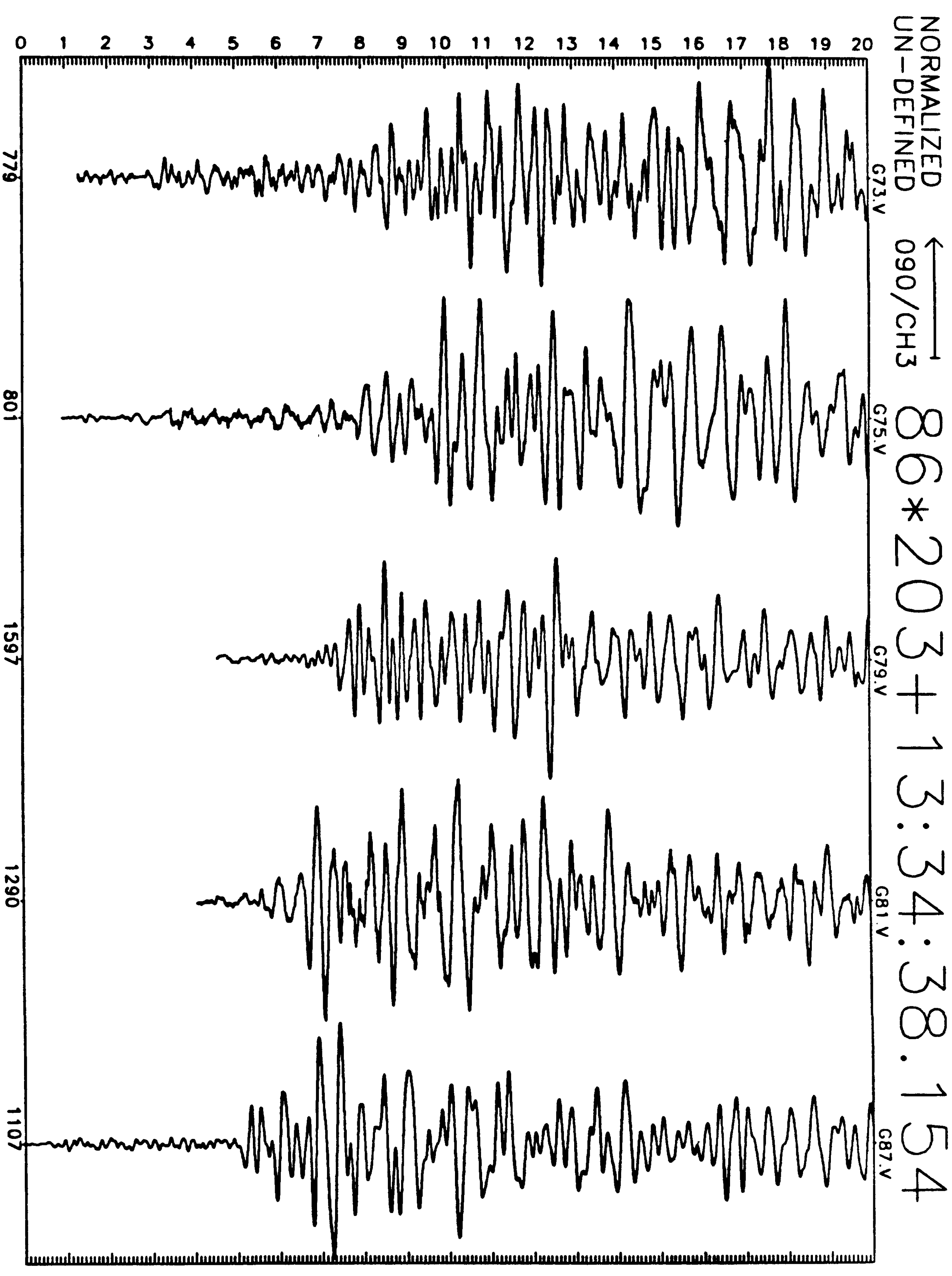

Figure D12(c): Earthquake record section for 20 seconds of N106E motion recorded at GEOS stations. Origin time for record section, station ID, and maximum digital counts (6×10^{-7} cm/sec/digital count) are indicated along abscissa.

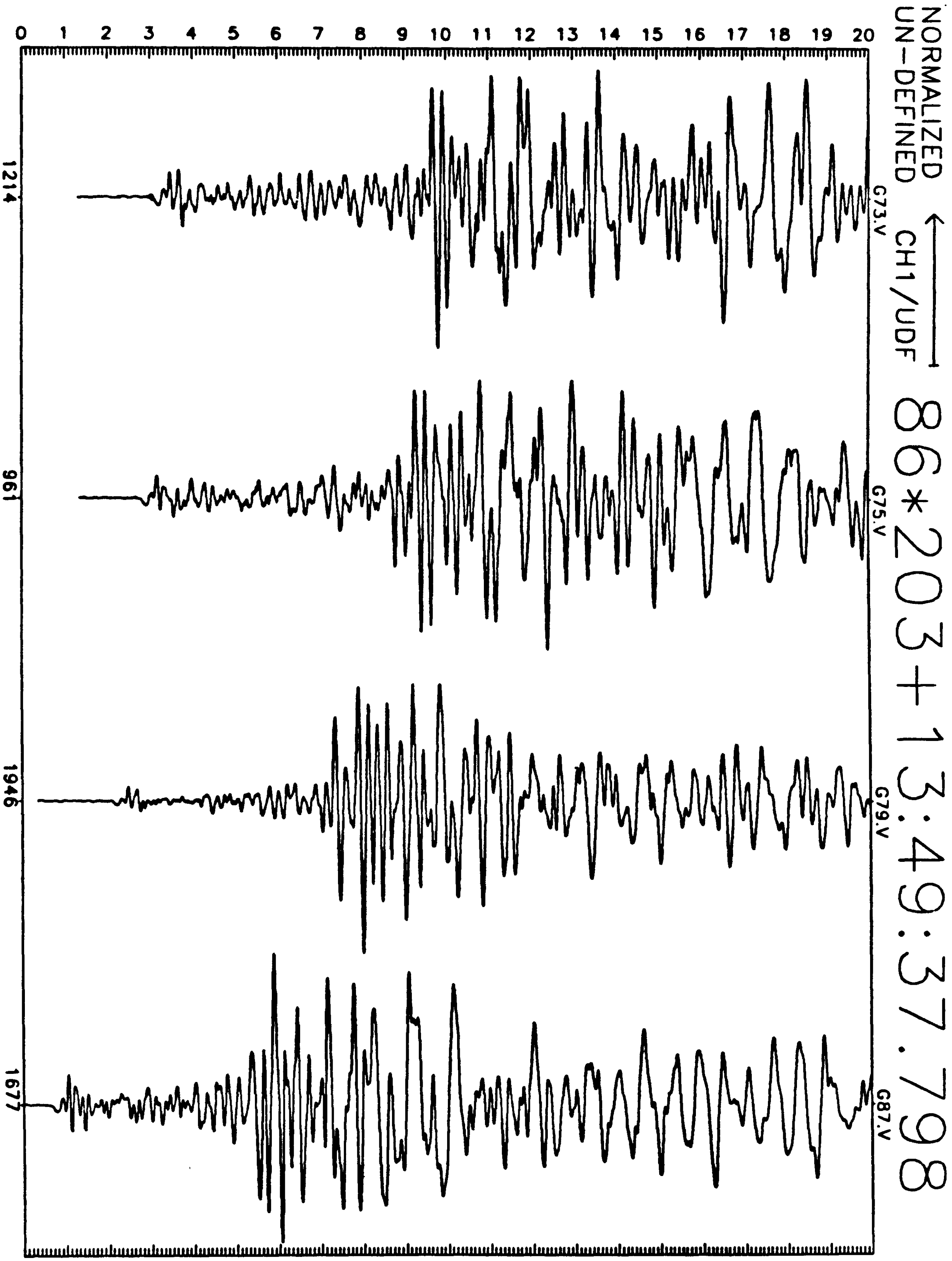

Figure D13(a): Earthquake record section for 20 seconds of vertical motion recorded at GEOS stations. Origin time for record section, station ID, and maximum digital counts (6×10^{-7} cm/sec/digital count) are indicated along abscissa.

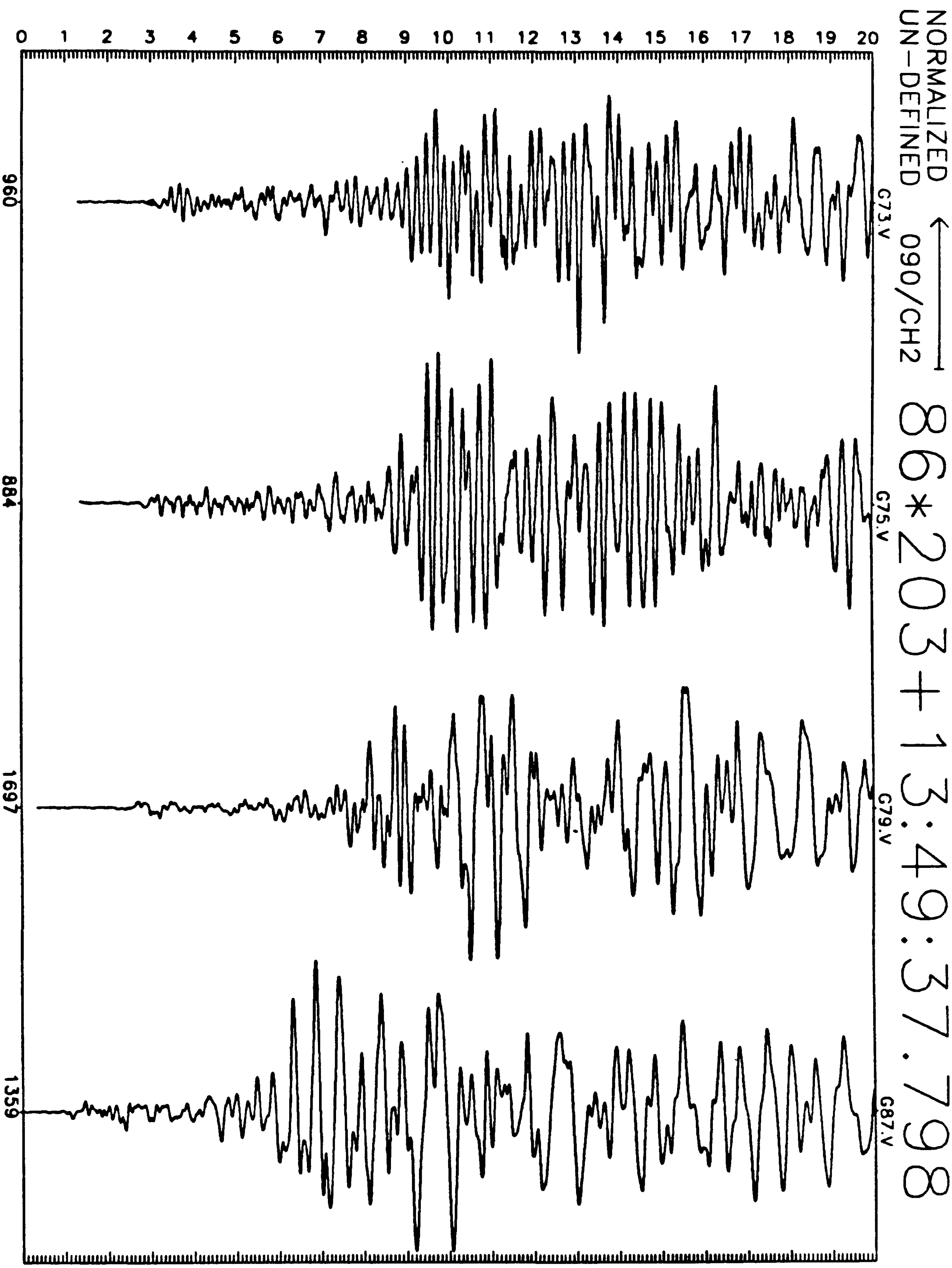

Figure D13(b): Earthquake record section for 20 seconds of N16E motion recorded at GEOS stations. Origin time for record section, station ID, and maximum digital counts (6×10^{-7} cm/sec/digital count) are indicated along abscissa.

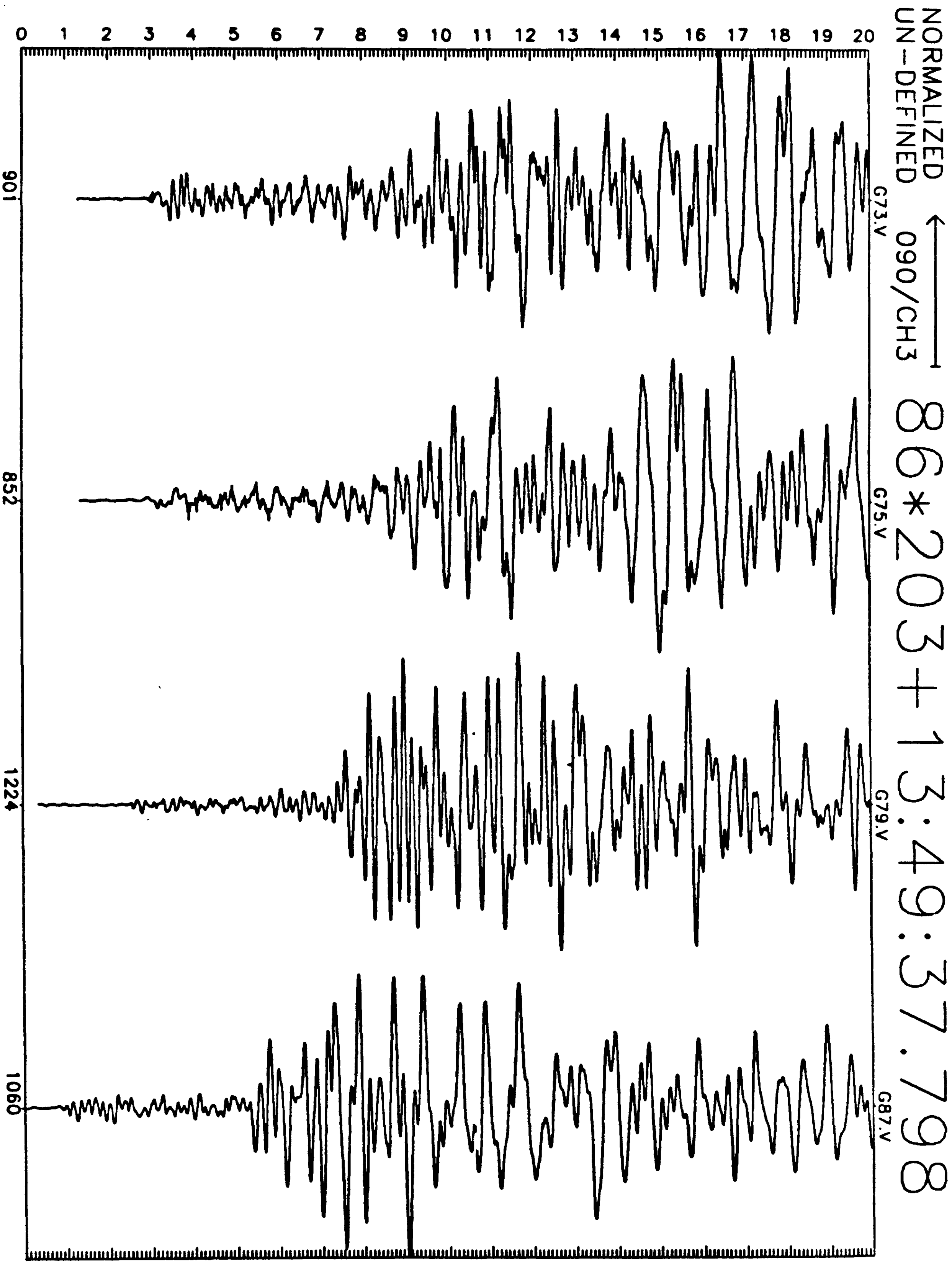

Figure D13(c): Earthquake record section for 20 seconds of N106E motion recorded at GEOS stations. Origin time for record section, station ID, and maximum digital counts (6×10^{-7} cm/sec/digital count) are indicated along abscissa.

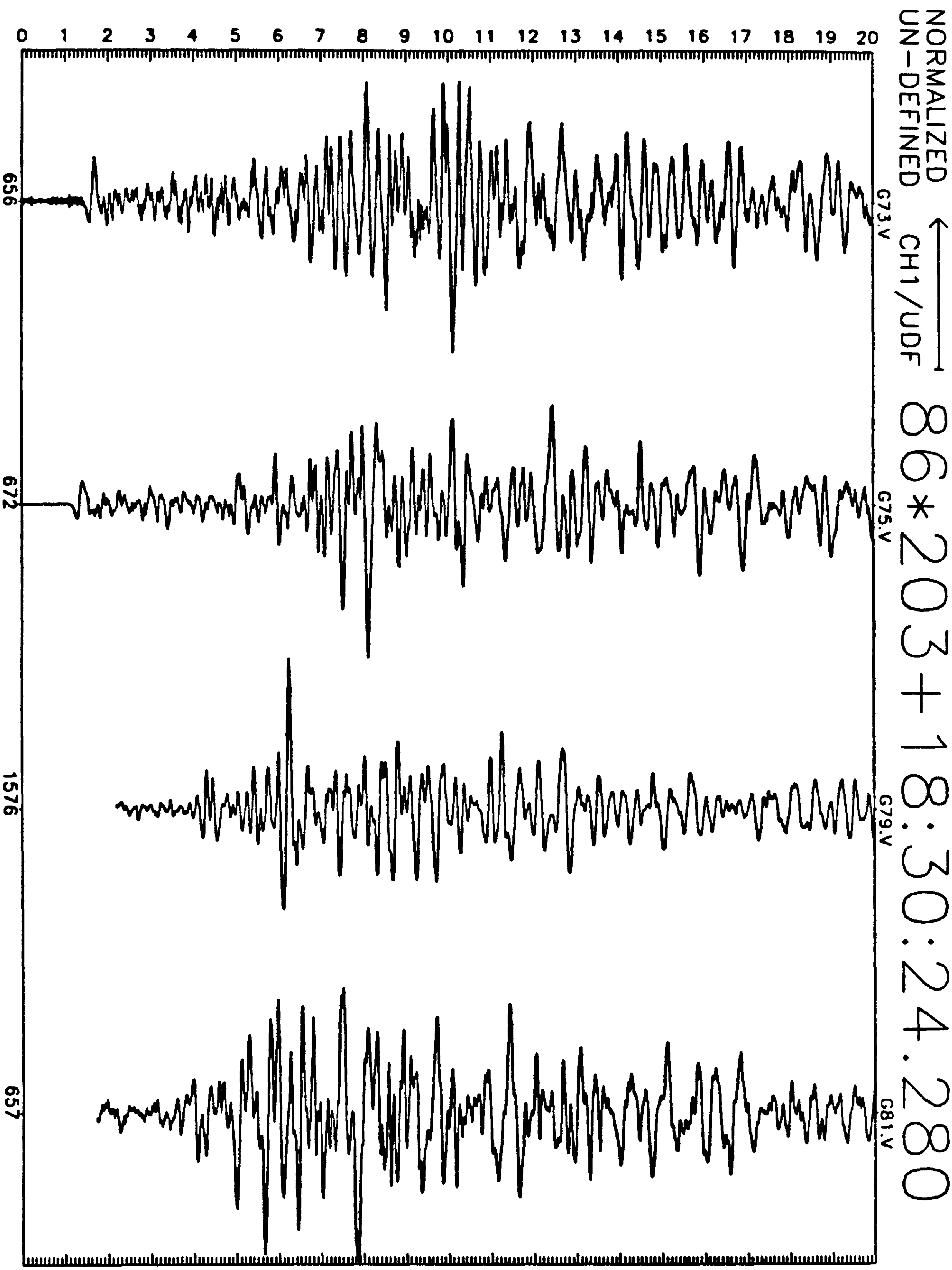

Figure D14(a): Earthquake record section for 20 seconds of vertical motion recorded at GEOS stations. Origin time for record section, station ID, and maximum digital counts (6×10^{-7} cm/sec/digital count) are indicated along abscissa.

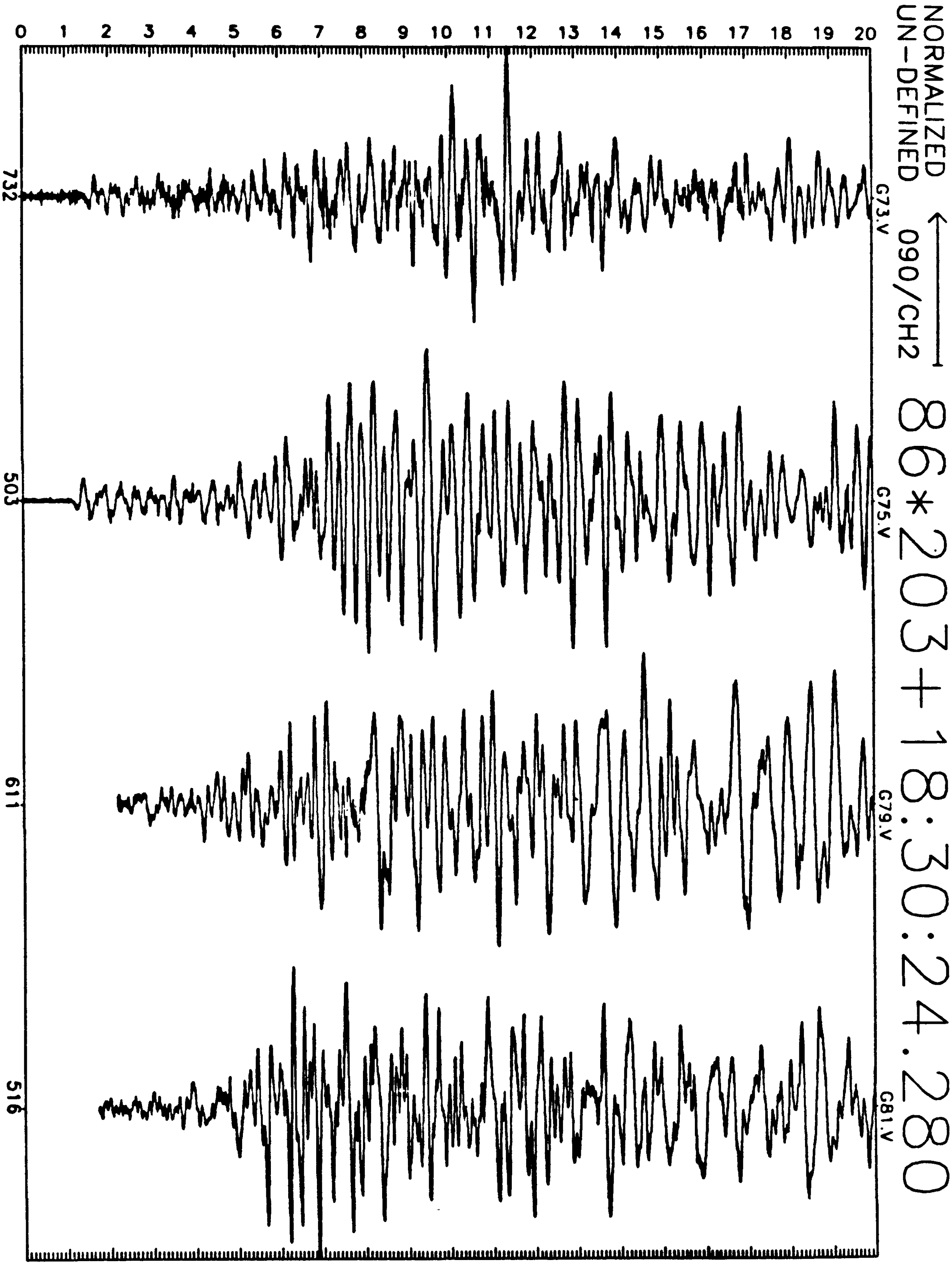

Figure D14(b): Earthquake record section for 20 seconds of N16E motion recorded at GEOS stations. Origin time for record section, station ID, and maximum digital counts (6×10^{-7} cm/sec/digital count) are indicated along abscissa.

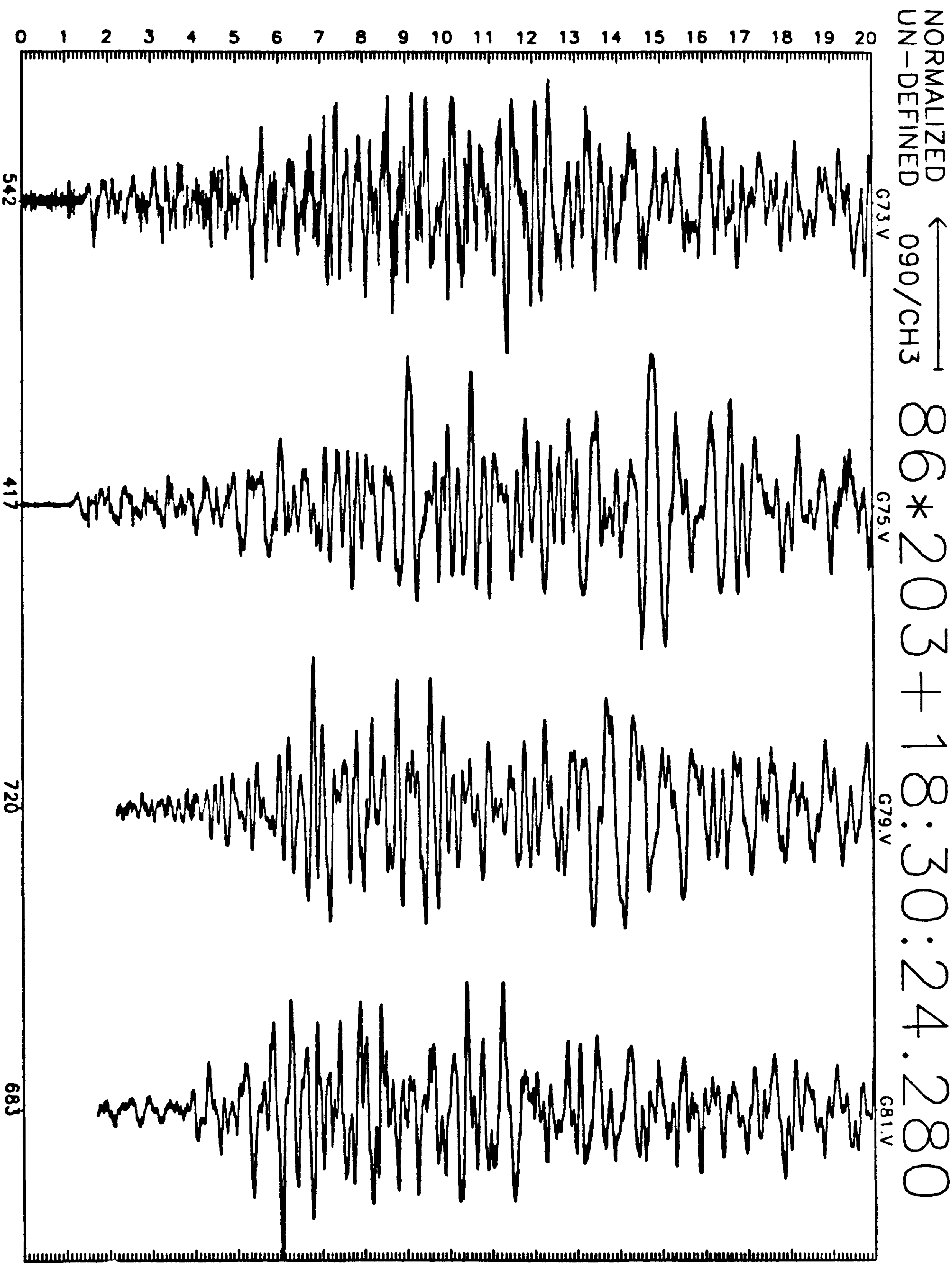

Figure D14(c): Earthquake record section for 20 seconds of N106E motion recorded at GEOS stations. Origin time for record section, station ID, and maximum digital counts (6×10^{-7} cm/sec/digital count) are indicated along abscissa.

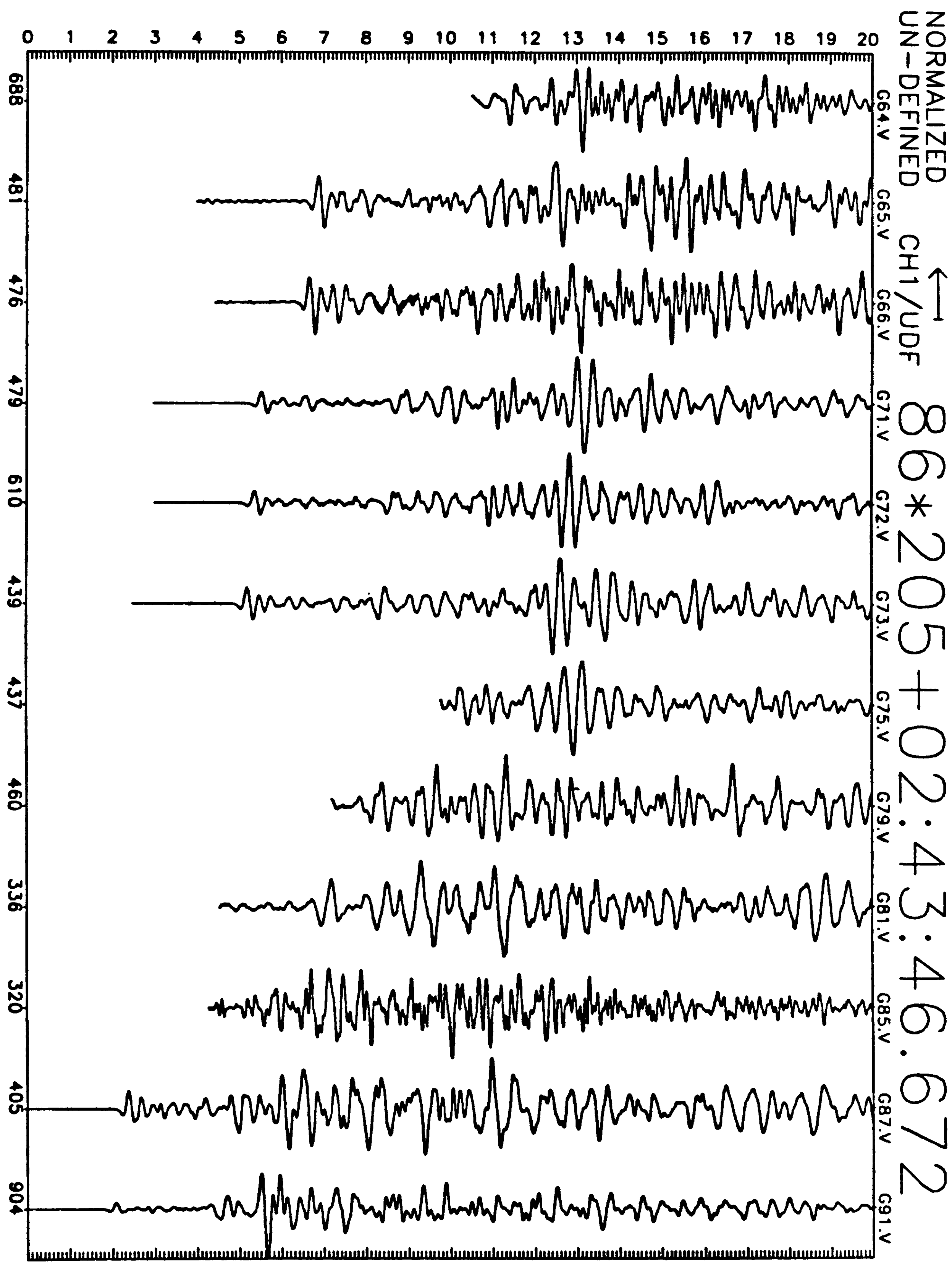

Figure D15(a): Earthquake record section for 20 seconds of vertical motion recorded at GEOS stations. Origin time for record section, station ID, and maximum digital counts (6×10^{-7} cm/sec/digital count) are indicated along abscissa.

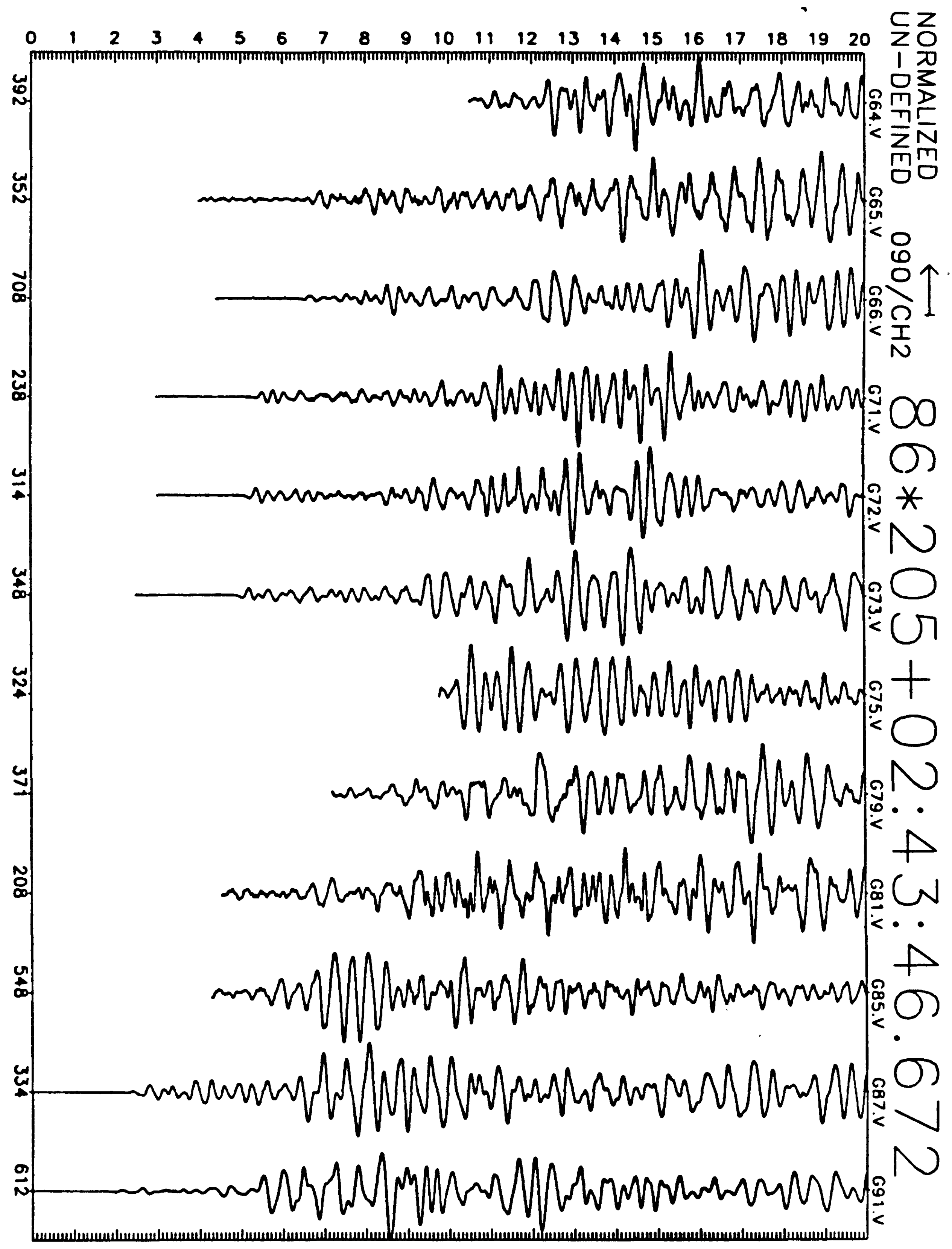

Figure D15(b): Earthquake record section for 20 seconds of N16E motion recorded at GEOS stations. Origin time for record section, station ID, and maximum digital counts (6×10^{-7} cm/sec/digital count) are indicated along abscissa.

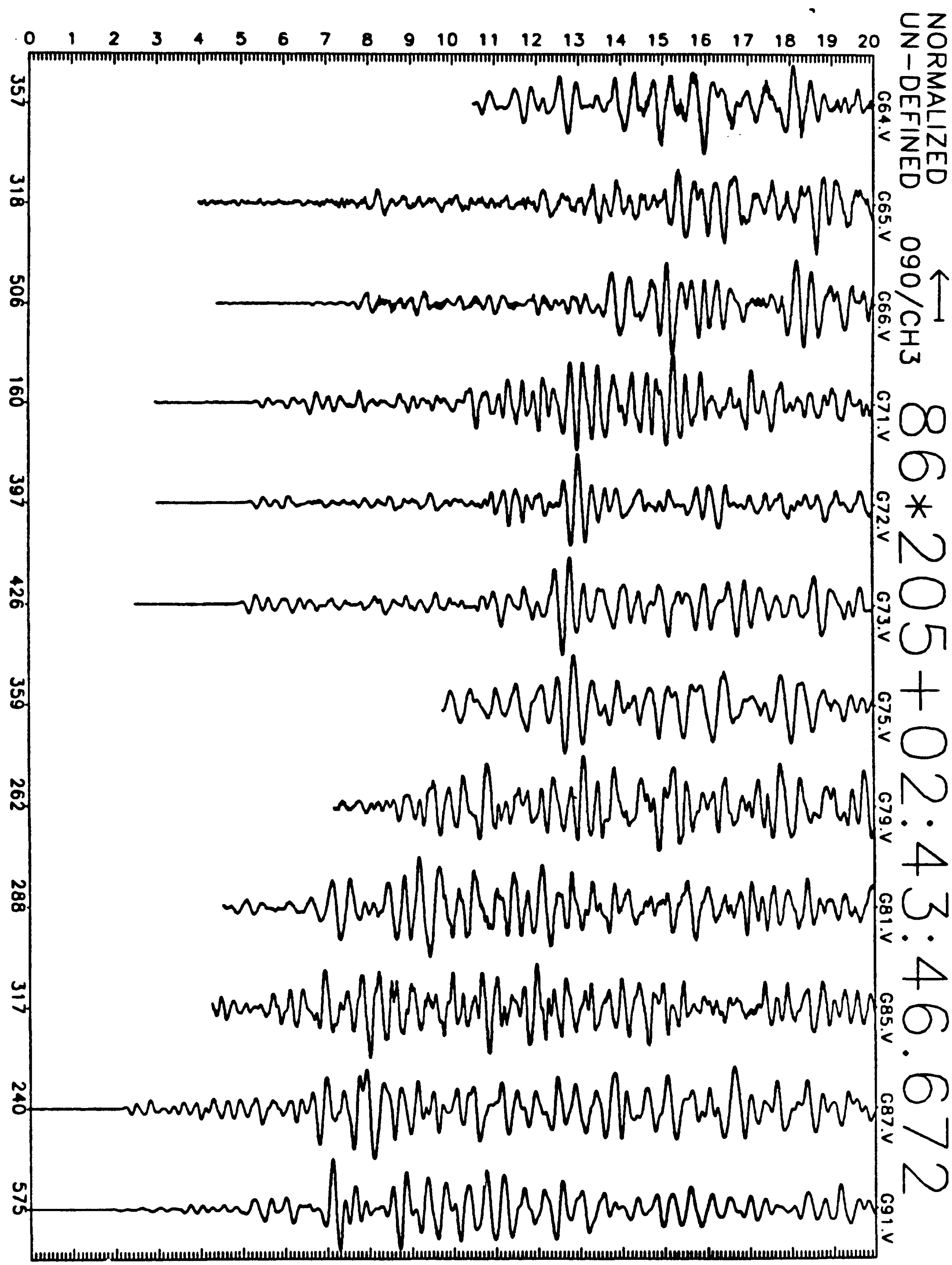

Figure D15(c): Earthquake record section for 20 seconds of N106E motion recorded at GEOS stations. Origin time for record section, station ID, and maximum digital counts (6×10^{-7} cm/sec/digital count) are indicated along abscissa.

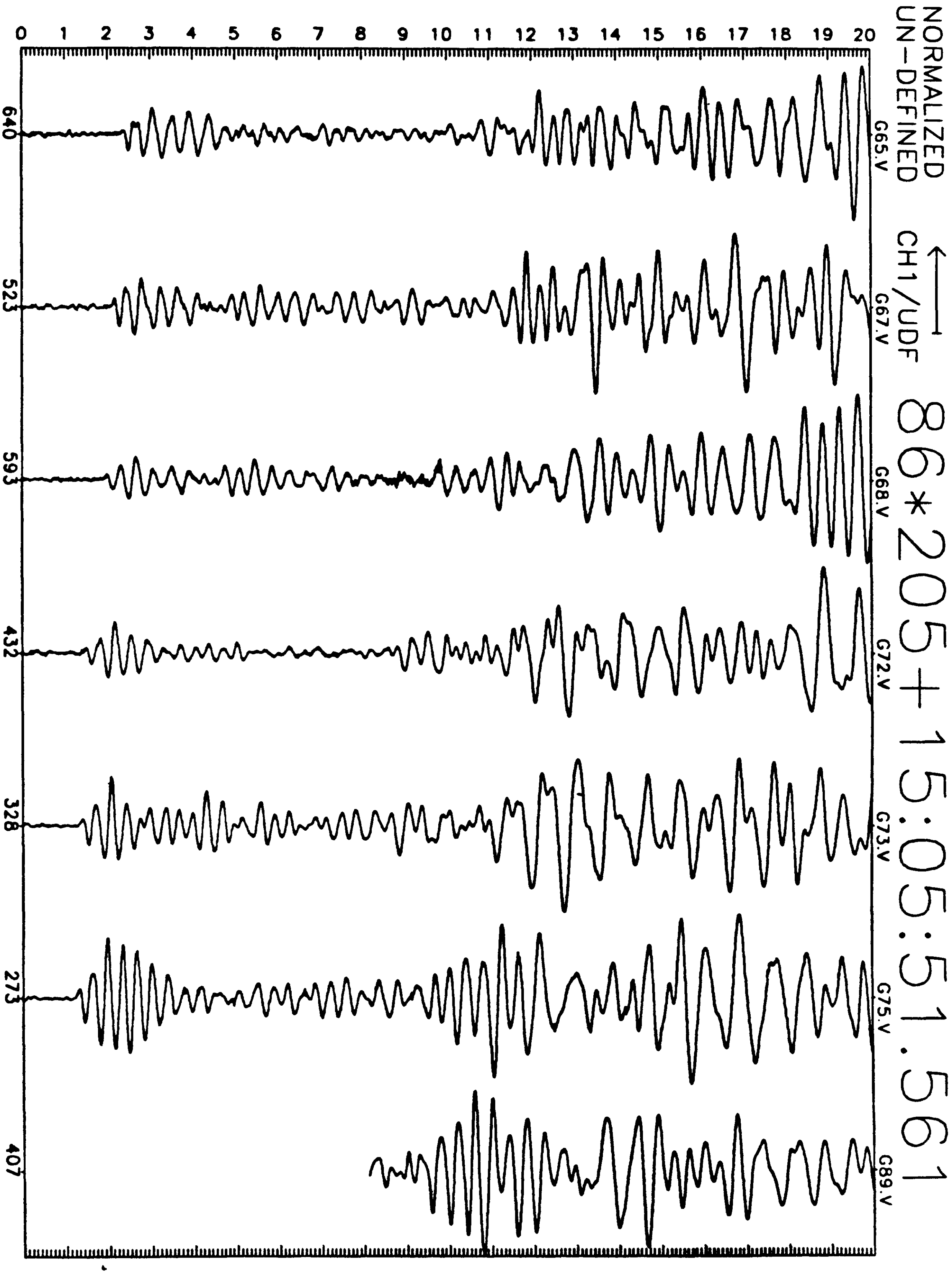

Figure D16(a): Earthquake record section for 20 seconds of vertical motion recorded at GEOS stations. Origin time for record section, station ID, and maximum digital counts (6×10^{-7} cm/sec/digital count) are indicated along abscissa.

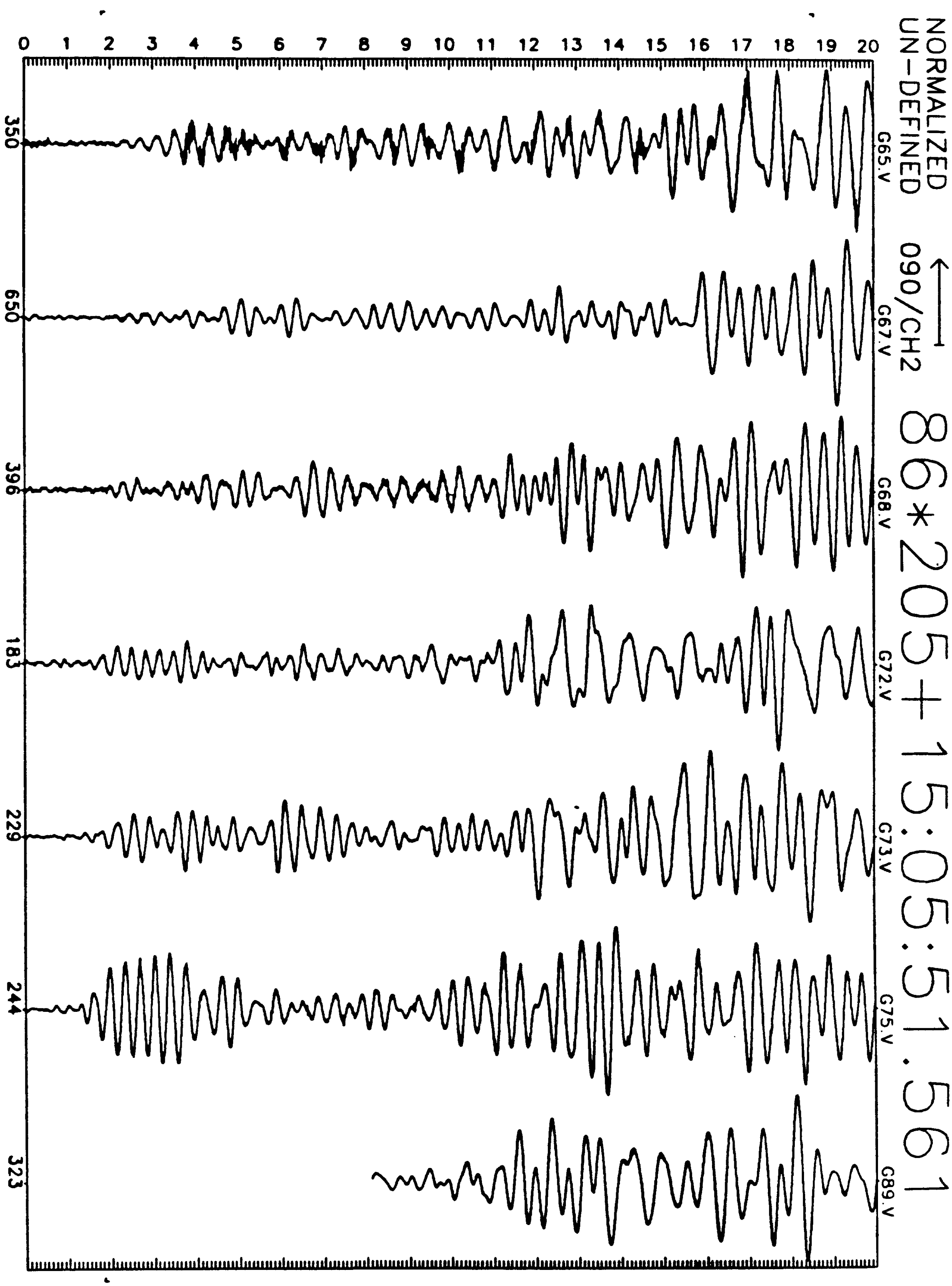

Figure D16(b): Earthquake record section for 20 seconds of N16E motion recorded at GEOS stations. Origin time for record section, station ID, and maximum digital counts (6×10^{-7} cm/sec/digital count) are indicated along abscissa.

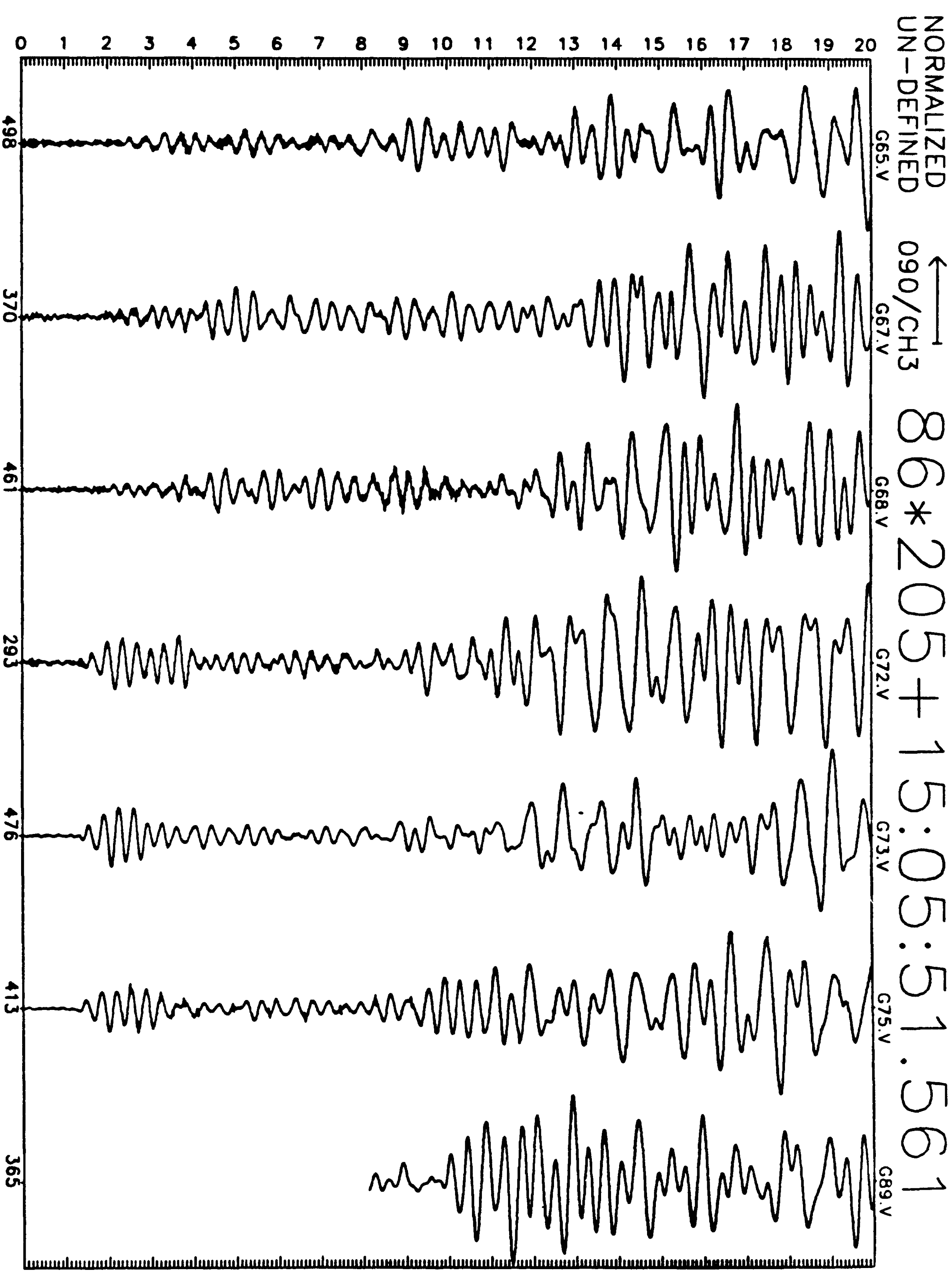

Figure D16(c): Earthquake record section for 20 seconds of N106E motion recorded at GEOS stations. Origin time for record section, station ID, and maximum digital counts (6×10^{-7} cm/sec/digital count) are indicated along abscissa.

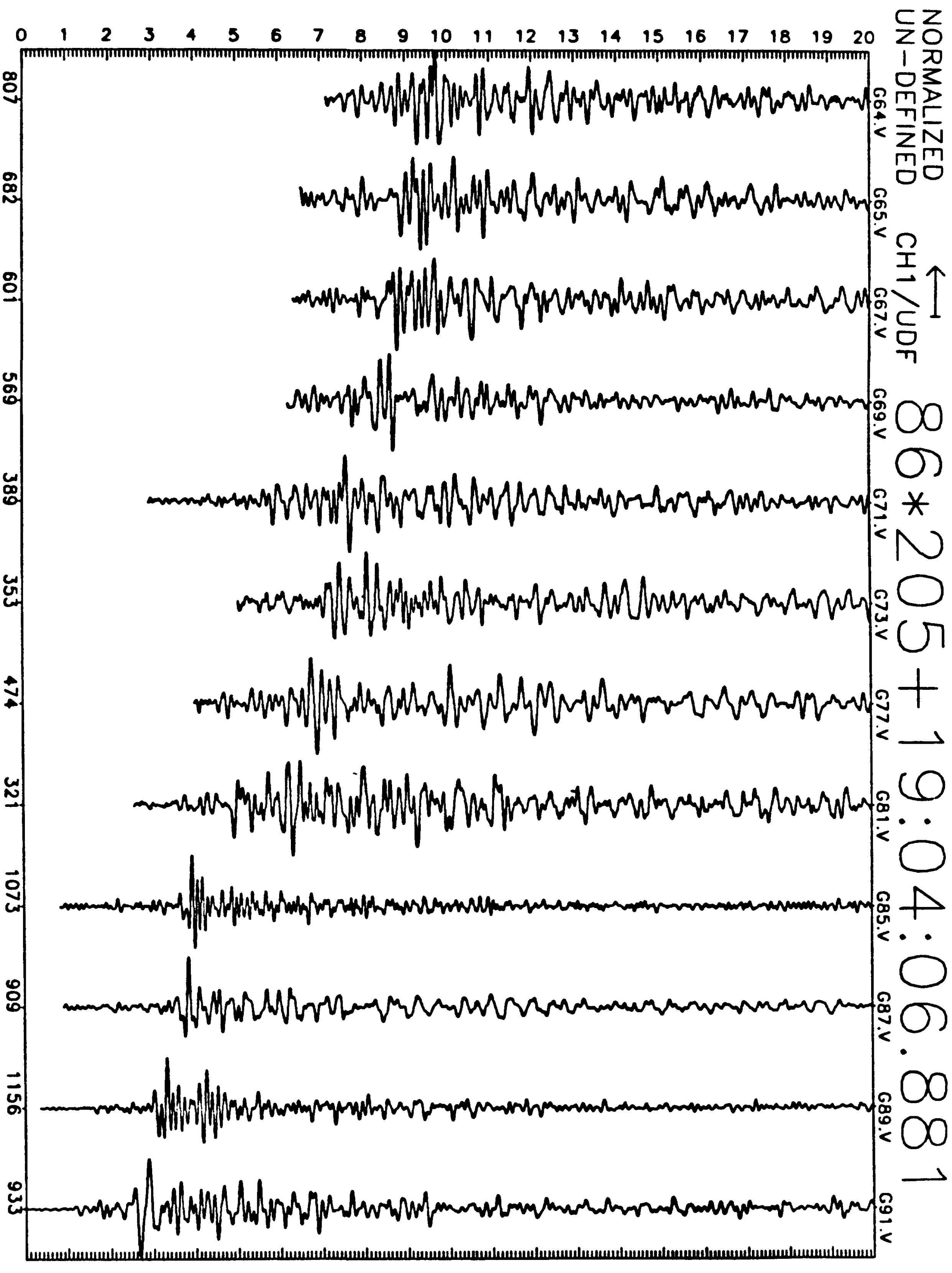

Figure D17(a): Earthquake record section for 20 seconds of vertical motion recorded at GEOS stations. Origin time for record section, station ID, and maximum digital counts (6×10^{-7} cm/sec/digital count) are indicated along abscissa.

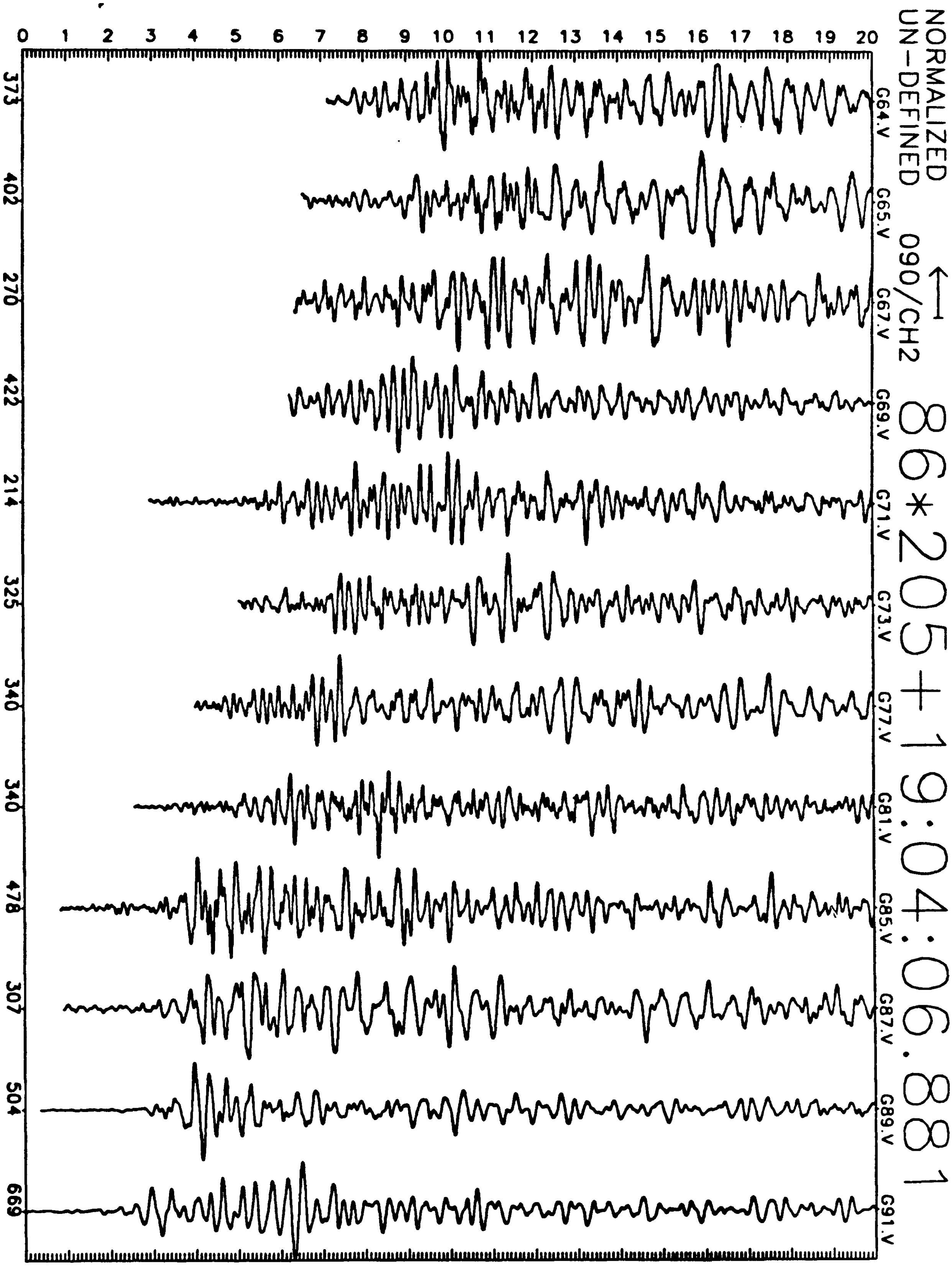

Figure D17(b): Earthquake record section for 20 seconds of N16E motion recorded at GEOS stations. Origin time for record section, station ID, and maximum digital counts (6×10^{-7} cm/sec/digital count) are indicated along abscissa.

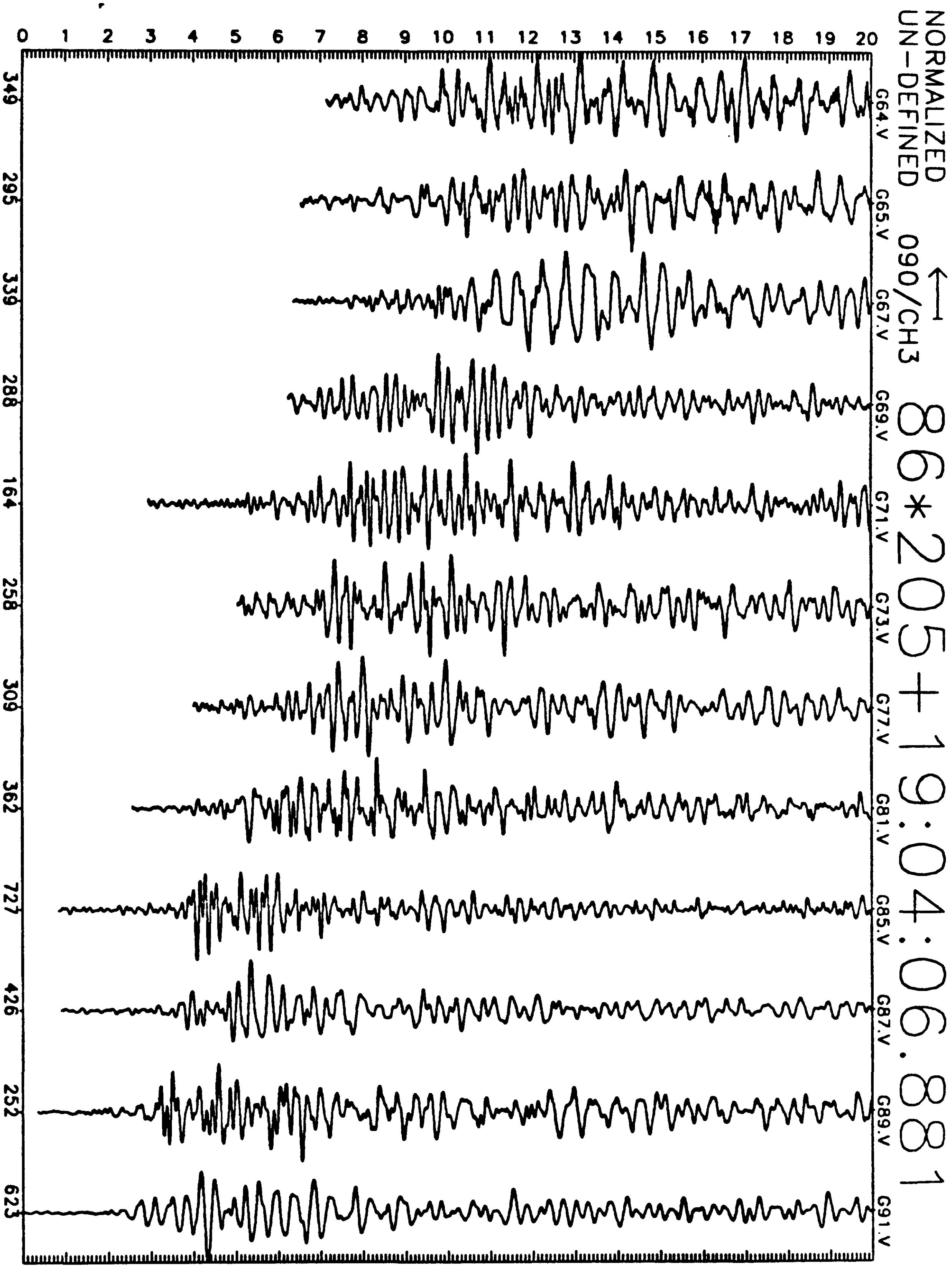

Figure D17(c): Earthquake record section for 20 seconds of N106E motion recorded at GEOS stations. Origin time for record section, station ID, and maximum digital counts (6×10^{-7} cm/sec/digital count) are indicated along abscissa.

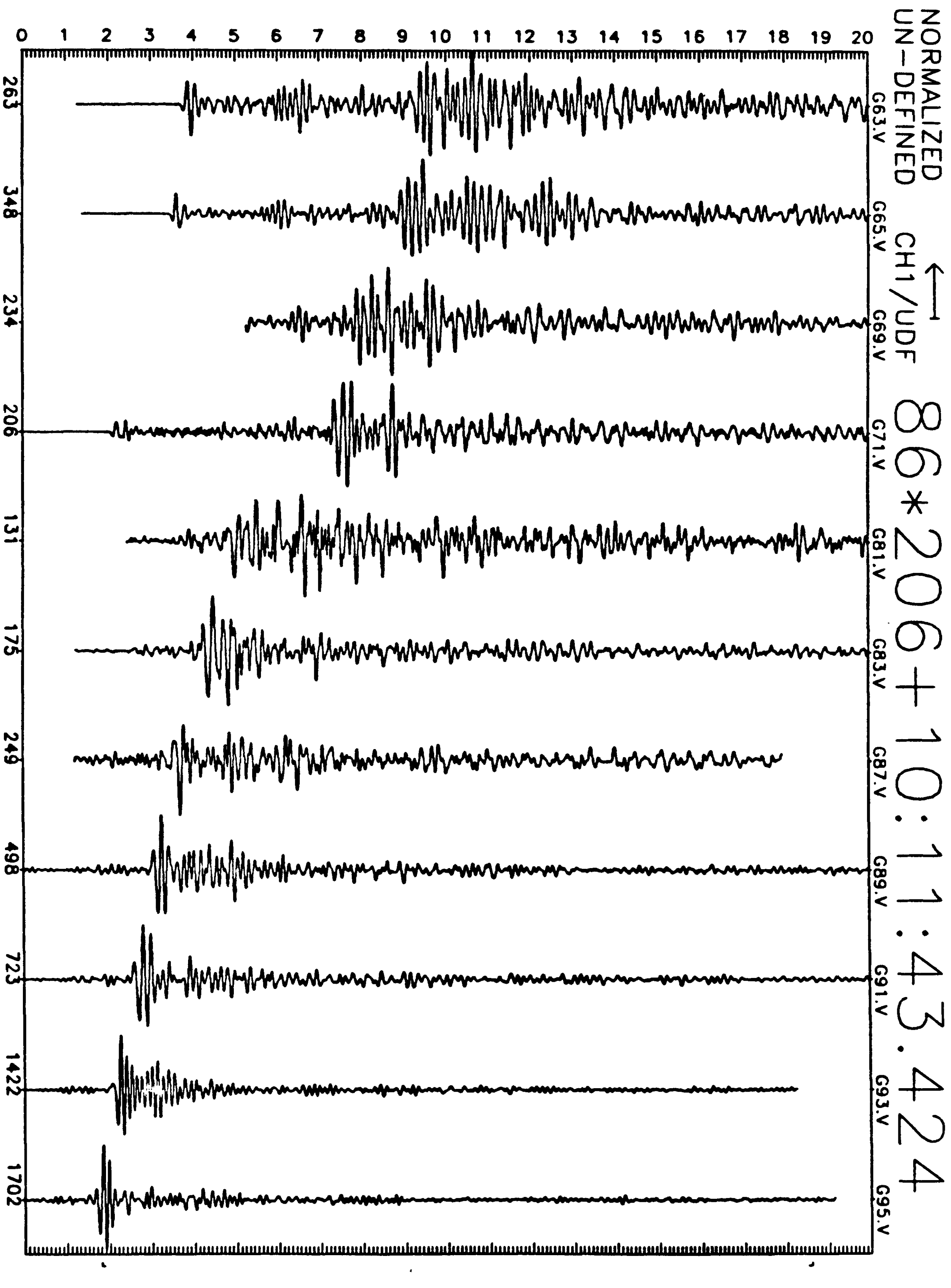

Figure D18(a): Earthquake record section for 20 seconds of vertical motion recorded at GEOS stations. Origin time for record section, station ID, and maximum digital counts (6×10^{-7} cm/sec/digital count) are indicated along abscissa.

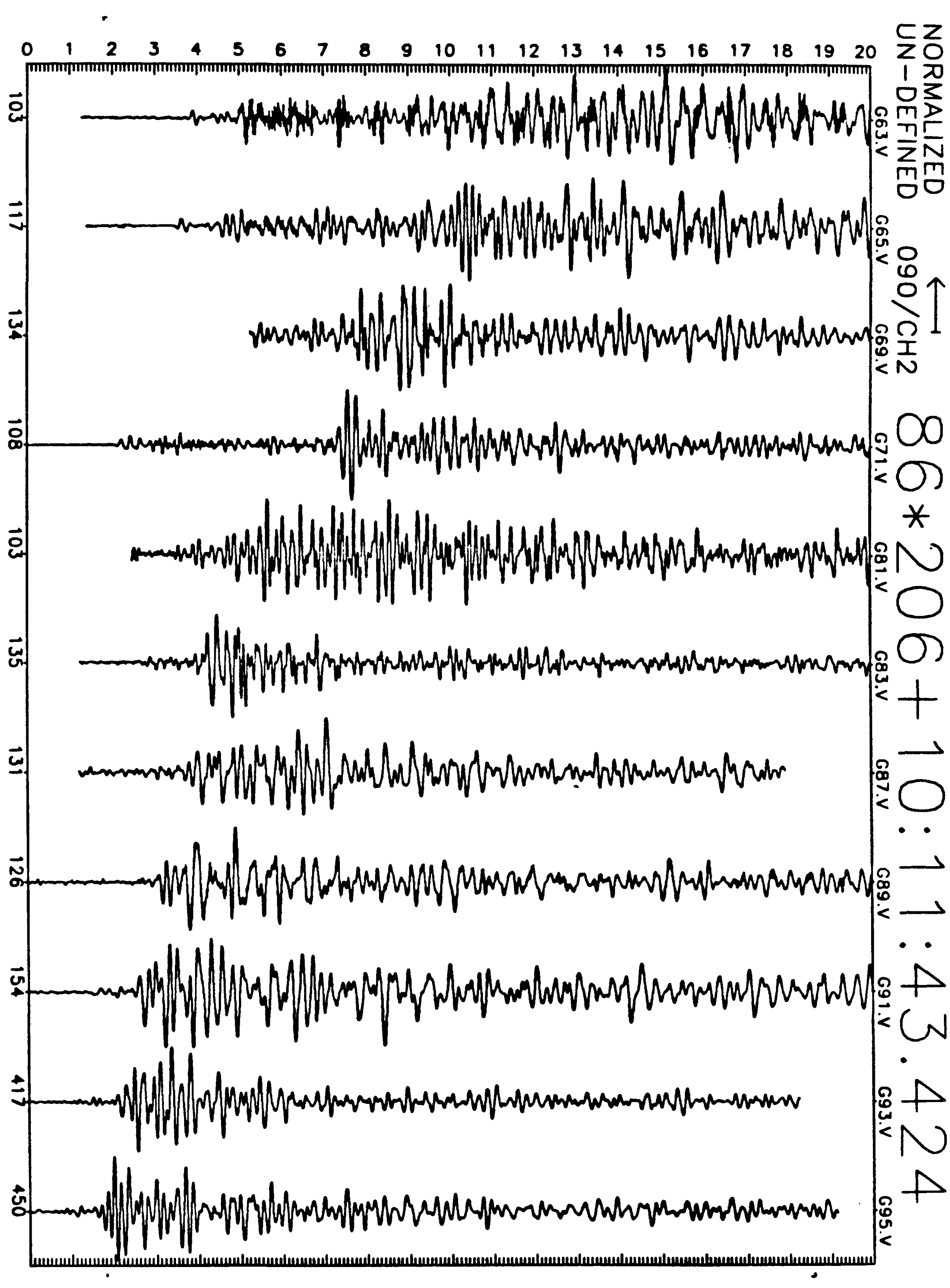

Figure D18(b): Earthquake record section for 20 seconds of N16E motion recorded at GEOS stations. Origin time for record section, station ID, and maximum digital counts (6×10^{-7} cm/sec/digital count) are indicated along abscissa.

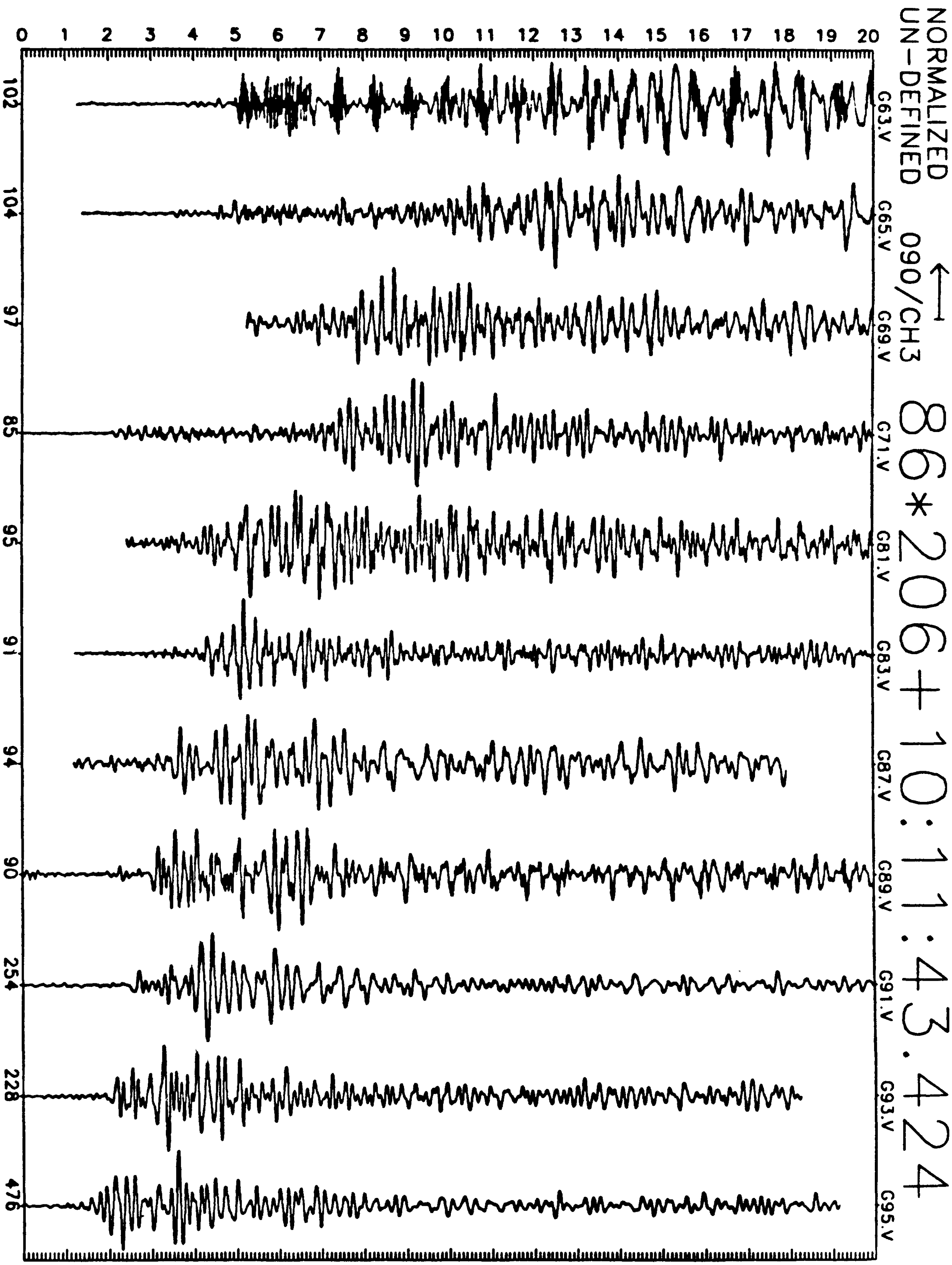

Figure D18(c): Earthquake record section for 20 seconds of N106E motion recorded at GEOS stations. Origin time for record section, station ID, and maximum digital counts (6×10^{-7} cm/sec/digital count) are indicated along abscissa.

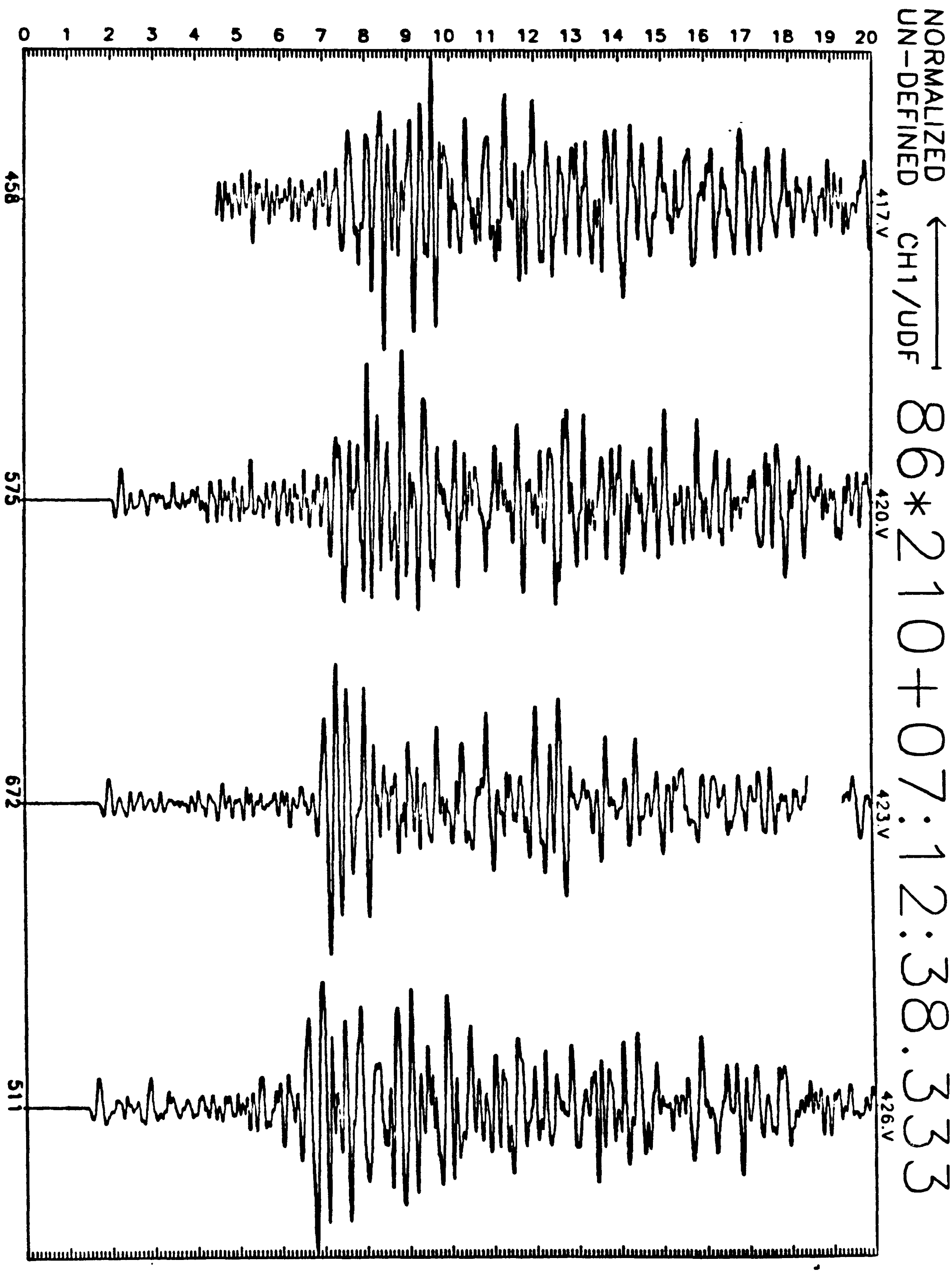

Figure D19(a): Earthquake record section for 20 seconds of vertical motion recorded at GEOS stations. Origin time for record section, station ID, and maximum digital counts (6×10^{-7} cm/sec/digital count) are indicated along abscissa.

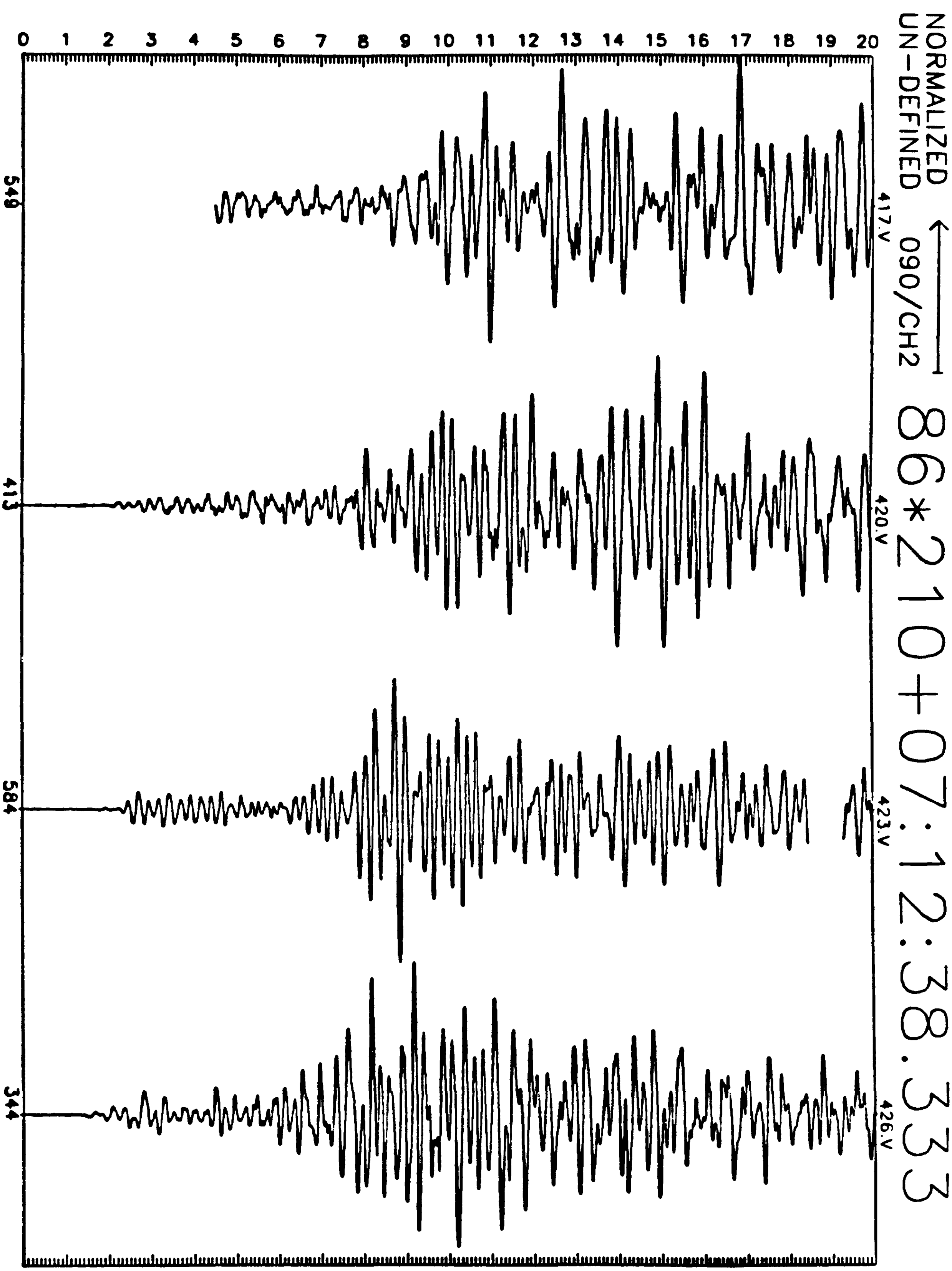

Figure D19(b): Earthquake record section for 20 seconds of N305E motion recorded at GEOS stations. Origin time for record section, station ID, and maximum digital counts (6×10^{-7} cm/sec/digital count) are indicated along abscissa.

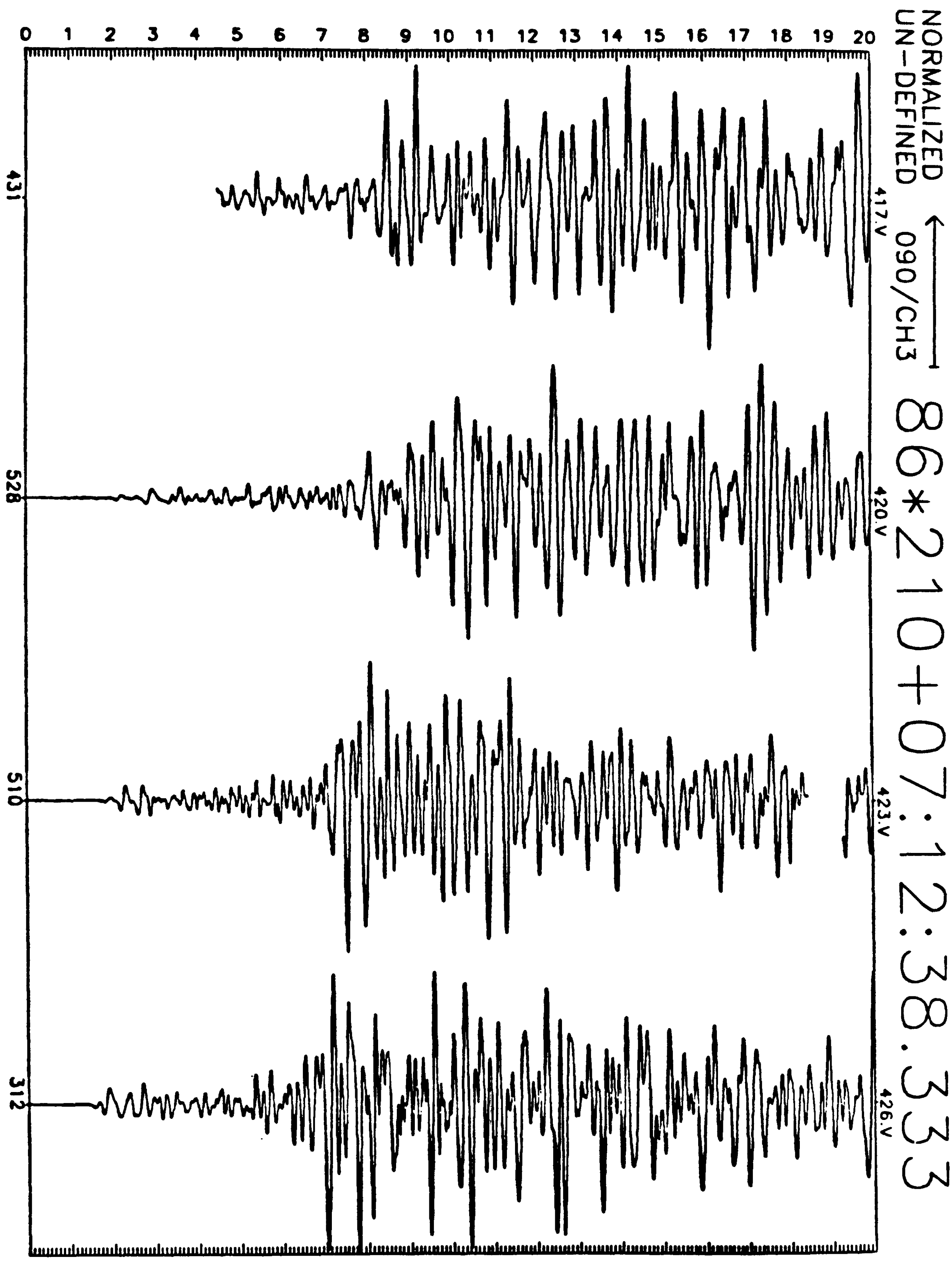

Figure D19(c): Earthquake record section for 20 seconds of N35E motion recorded at GEOS stations. Origin time for record section, station ID, and maximum digital counts (6×10^{-7} cm/sec/digital count) are indicated along abscissa.

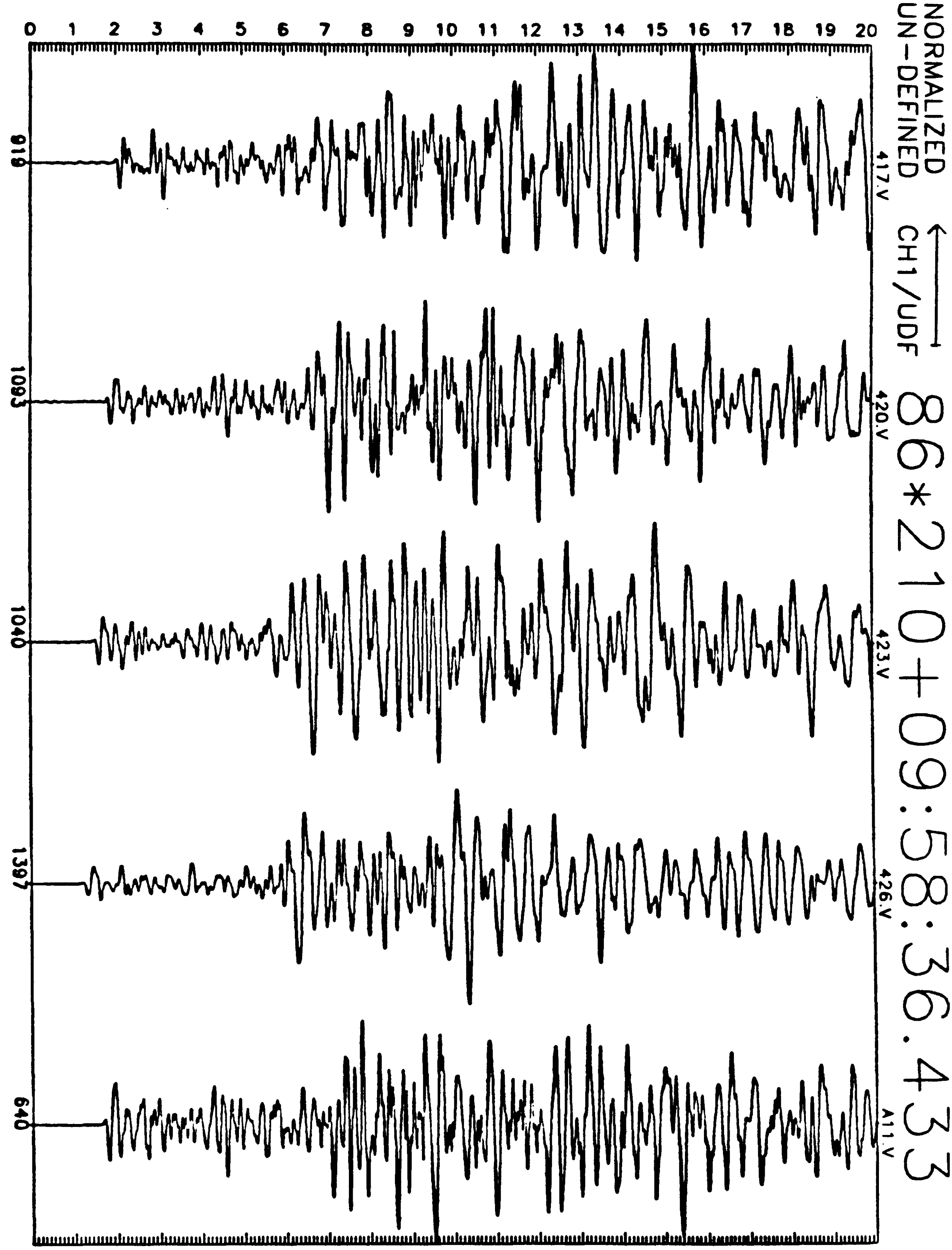

Figure D20(a): Earthquake record section for 20 seconds of vertical motion recorded at GEOS stations. Origin time for record section, station ID, and maximum digital counts (6×10^{-7} cm/sec/digital count) are indicated along abscissa.

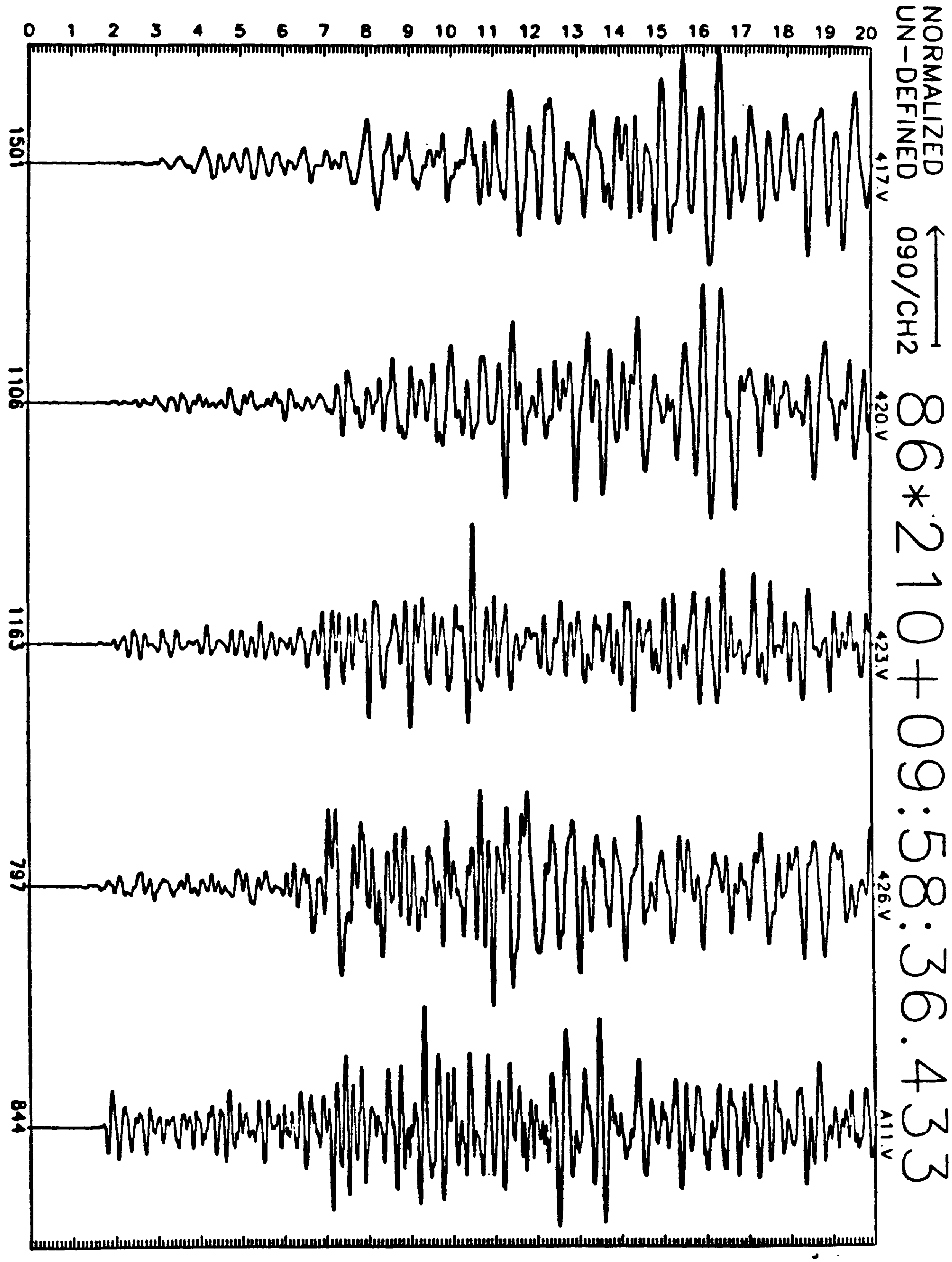

Figure D20(b): Earthquake record section for 20 seconds of N305E motion recorded at GEOS stations. Origin time for record section, station ID, and maximum digital counts (6×10^{-7} cm/sec/digital count) are indicated along abscissa.

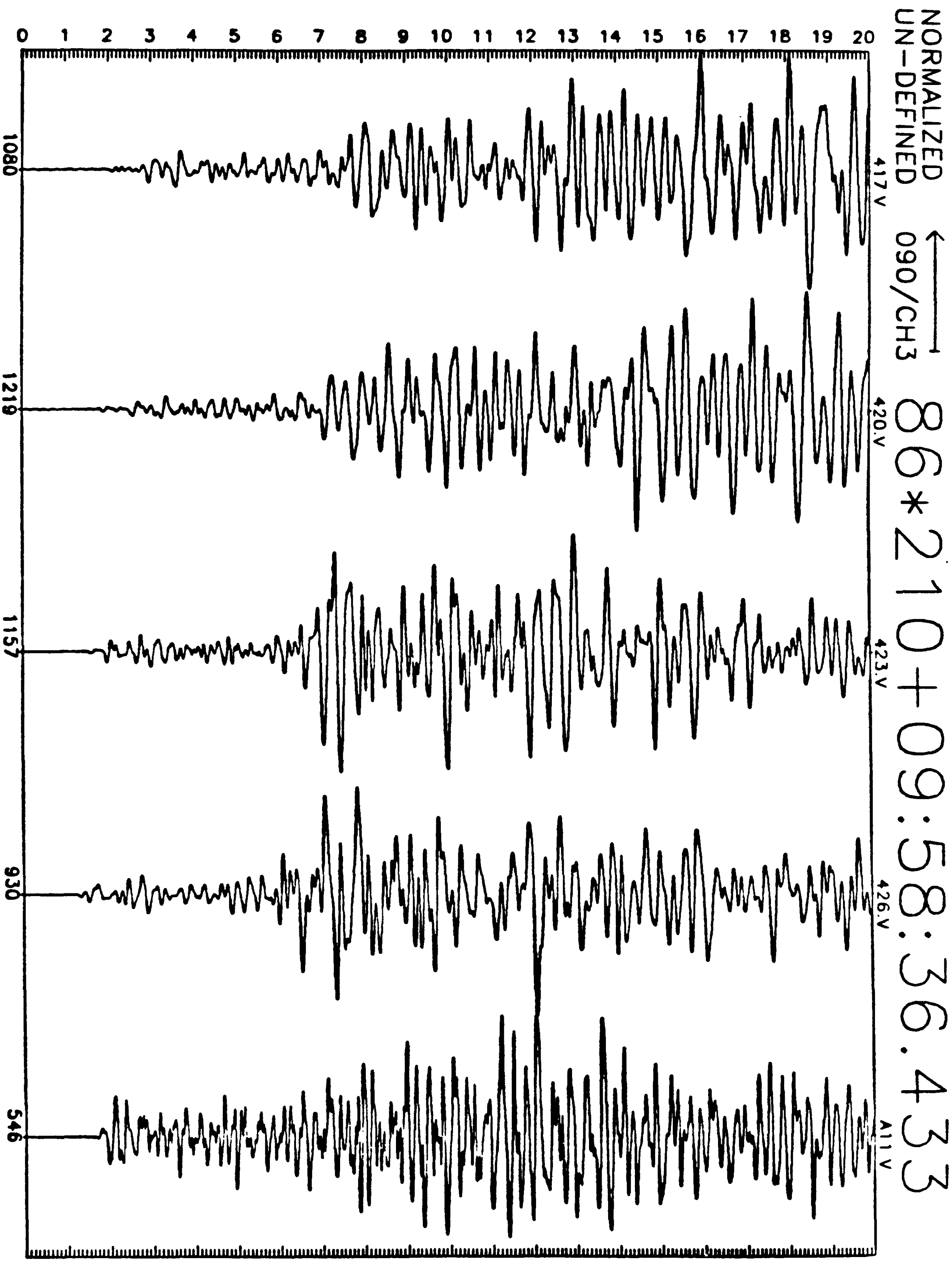

Figure D20(c): Earthquake record section for 20 seconds of N35E motion recorded at GEOS stations. Origin time for record section, station ID, and maximum digital counts (6×10^{-7} cm/sec/digital count) are indicated along abscissa.

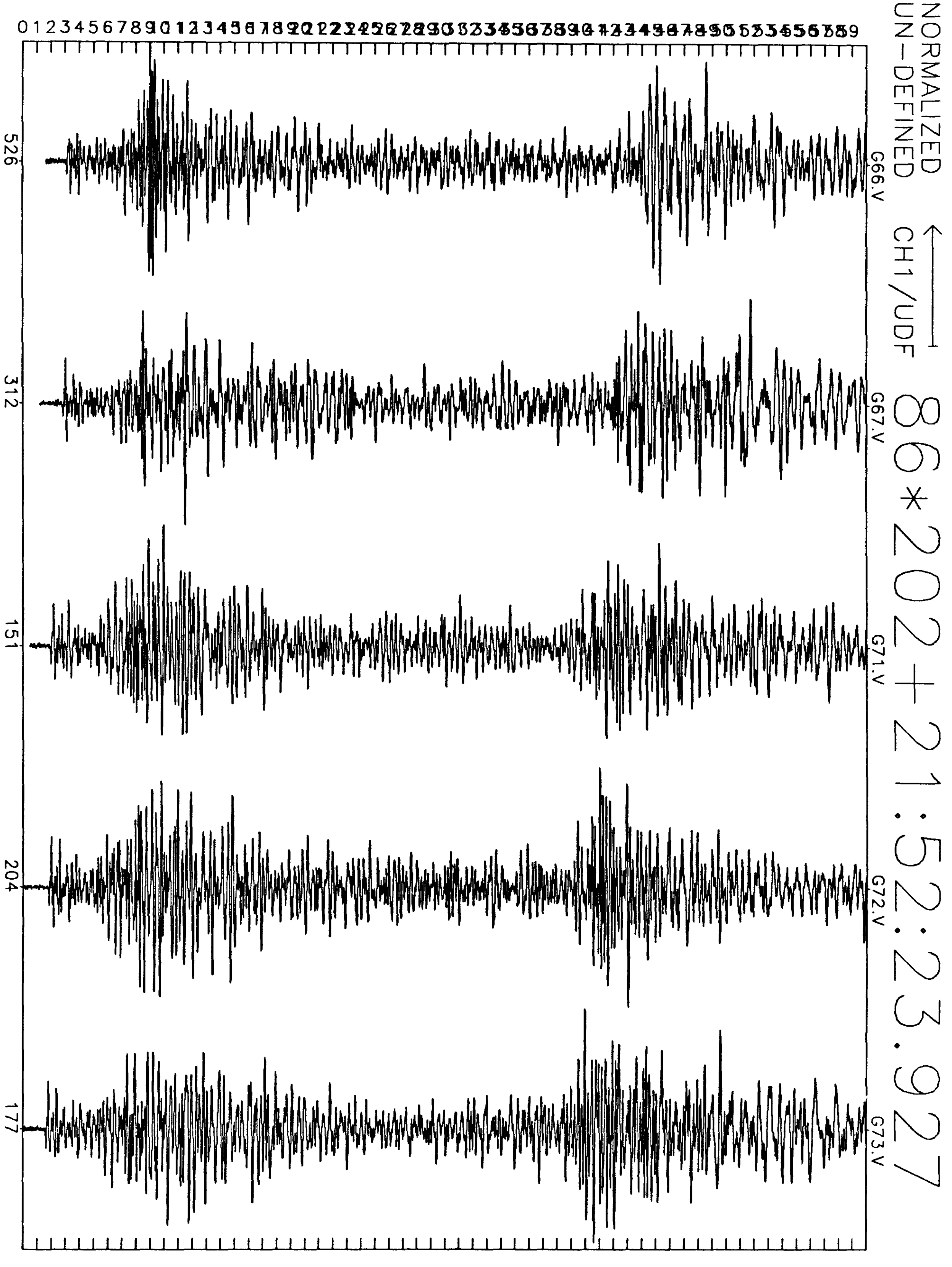

Figure E1(a): Earthquake record section for 60 seconds of vertical motion recorded at GEOS stations. Origin time for record section, station ID, and maximum digital counts (6×10^{-7} cm/sec/digital count) are indicated along abscissa.

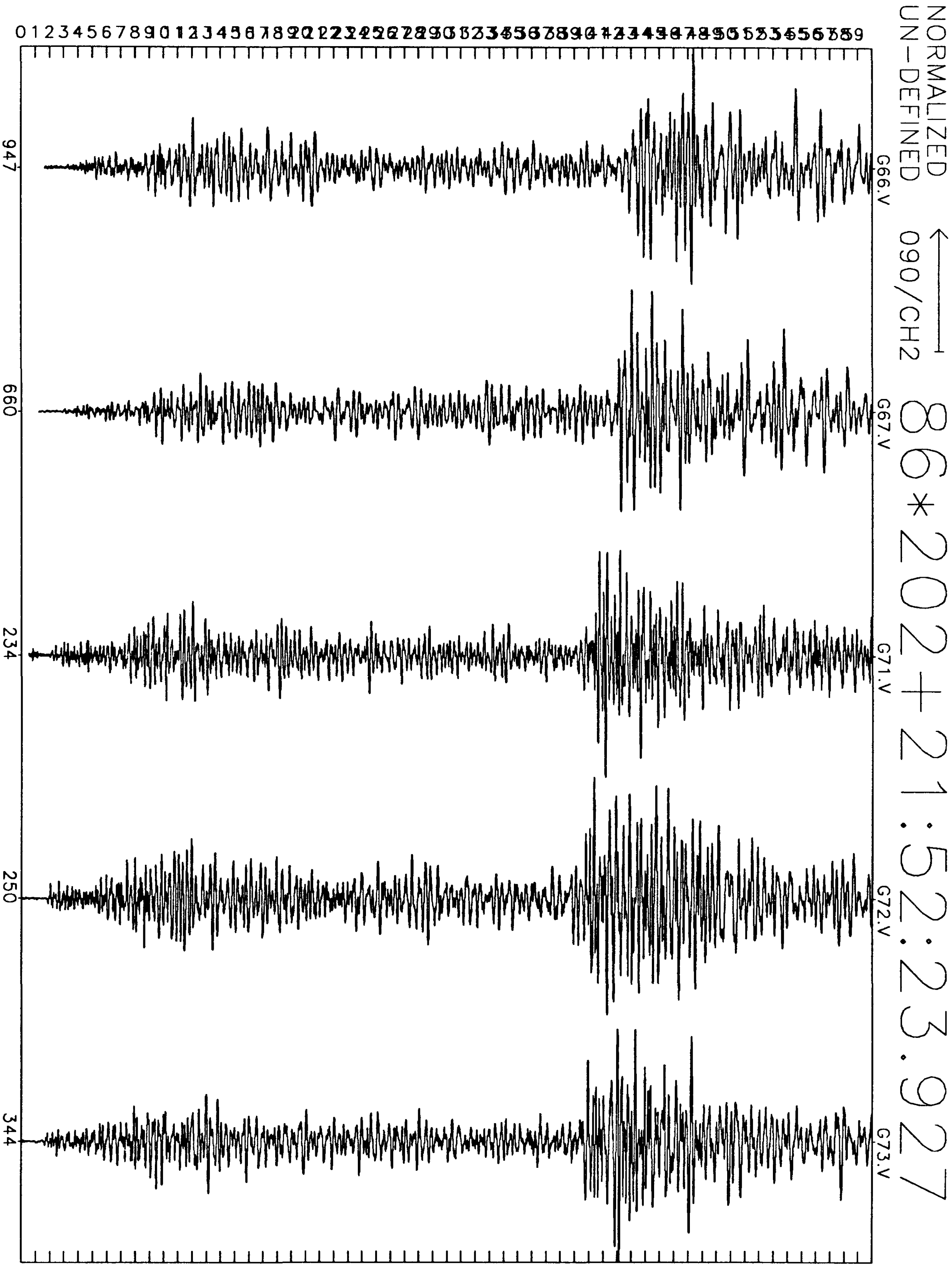

Figure E1(b): Earthquake record section for 60 seconds of N16E motion recorded at GEOS stations. Origin time for record section, station ID, and maximum digital counts (6×10^{-7} cm/sec/digital count) are indicated along abscissa.

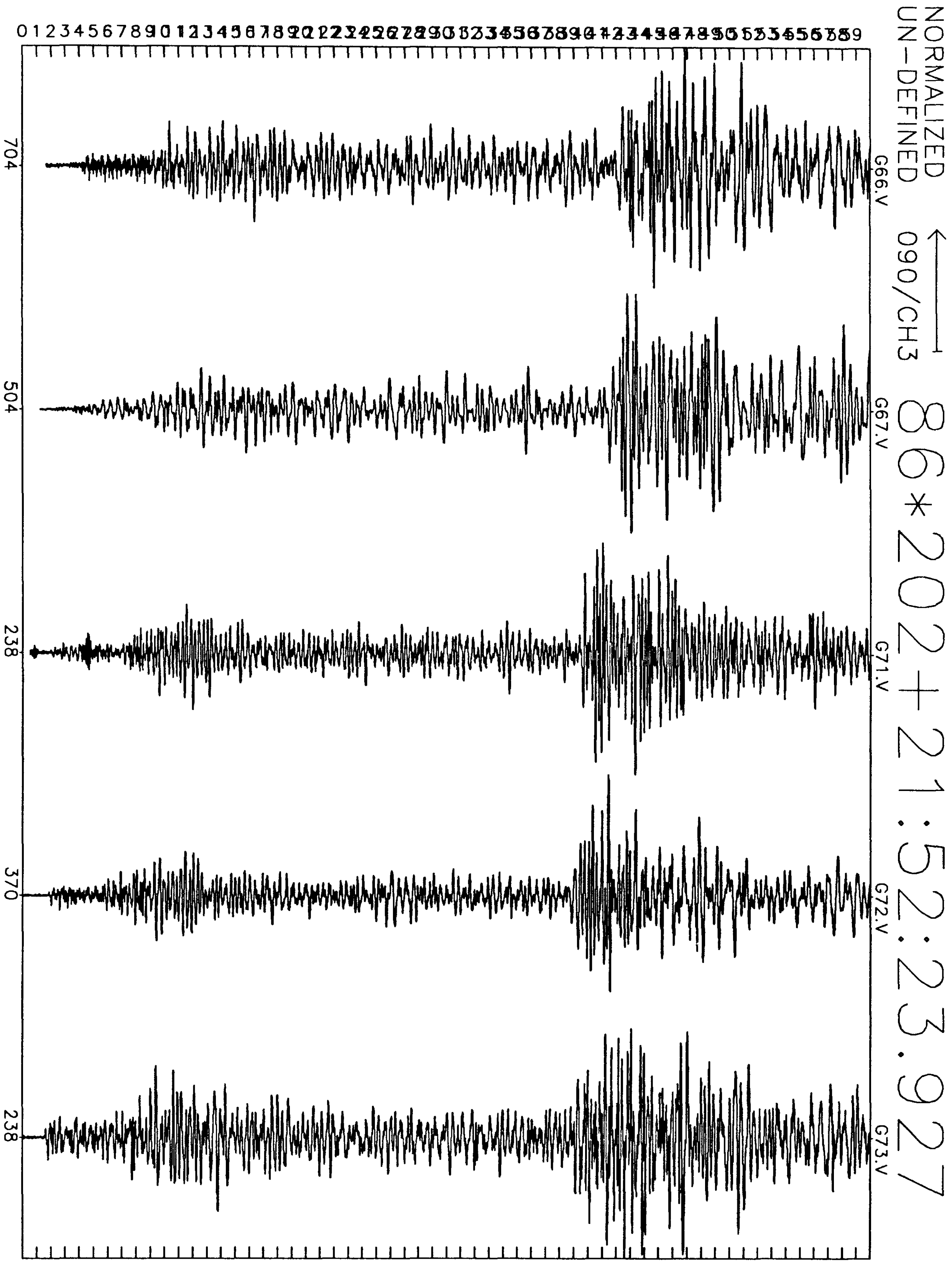

Figure E1(c): Earthquake record section for 60 seconds of N106E motion recorded at GEOS stations. Origin time for record section, station ID, and maximum digital counts (6×10^{-7} cm/sec/digital count) are indicated along abscissa.

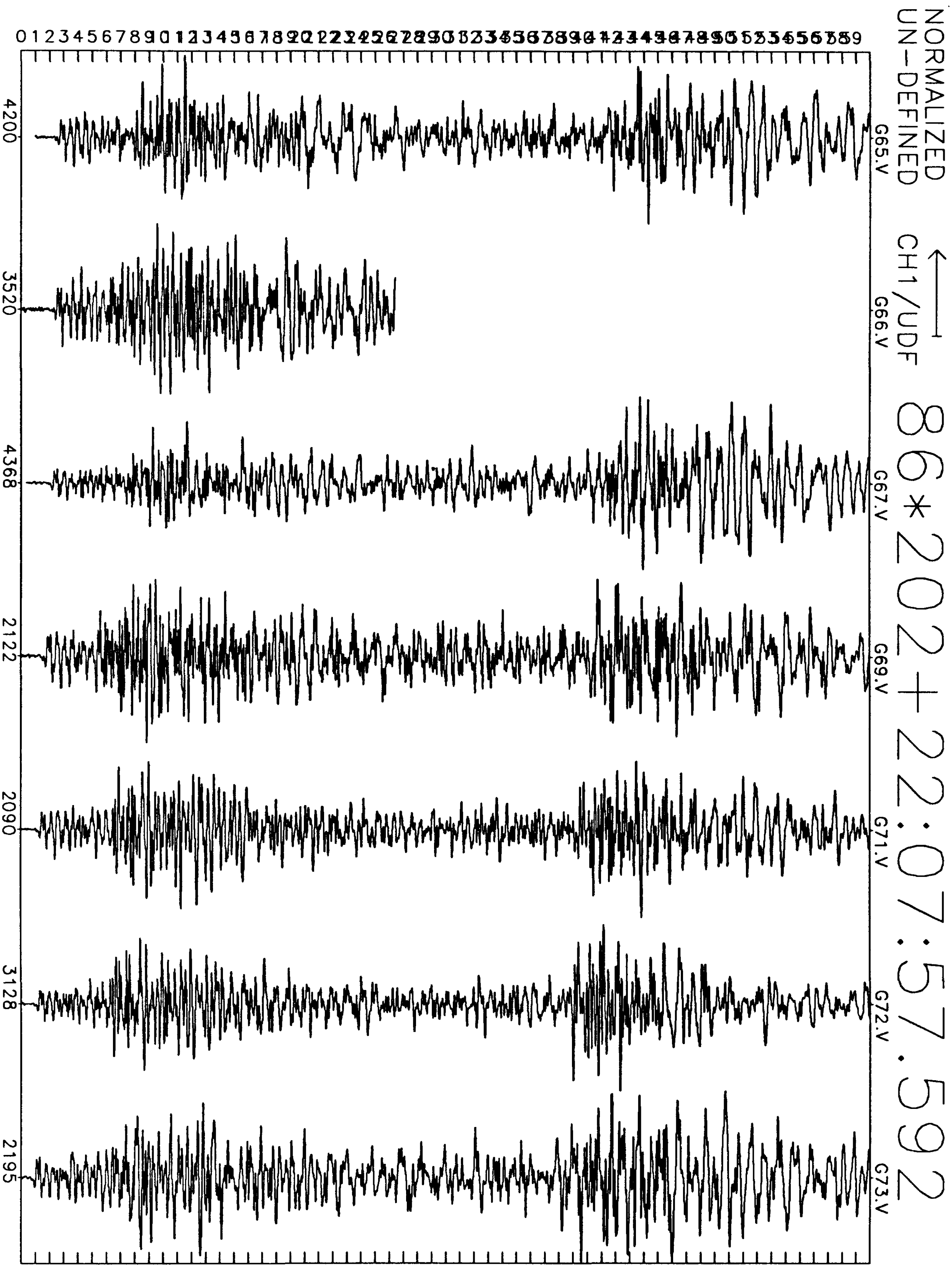

Figure E2(a): Earthquake record section for 60 seconds of vertical motion recorded at GEOS stations. Origin time for record section, station ID, and maximum digital counts (6×10^{-7} cm/sec/digital count) are indicated along abscissa.

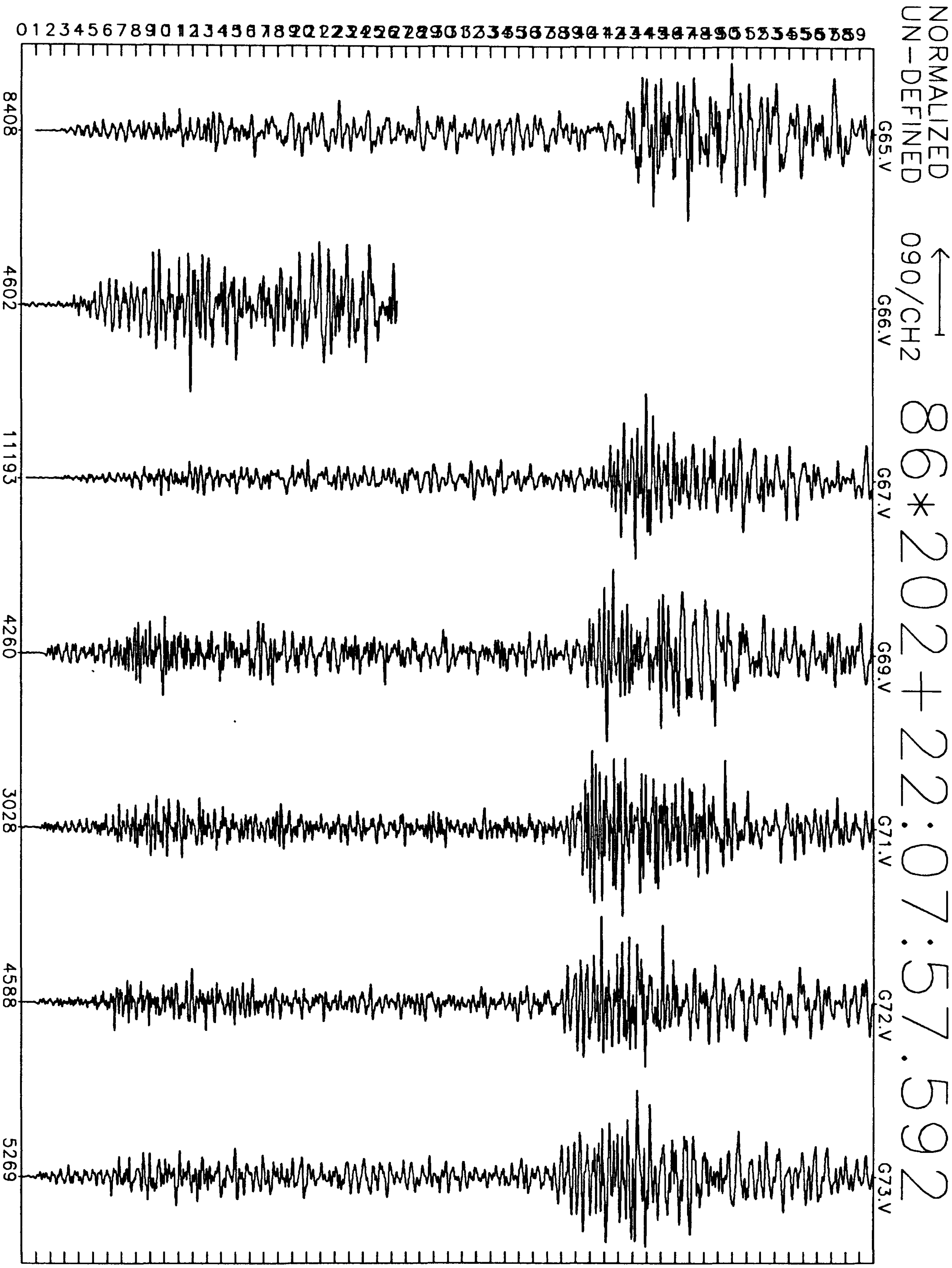

Figure E2(b): Earthquake record section for 60 seconds of N16E motion recorded at GEOS stations. Origin time for record section, station ID, and maximum digital counts (6×10^{-7} cm/sec/digital count) are indicated along abscissa.

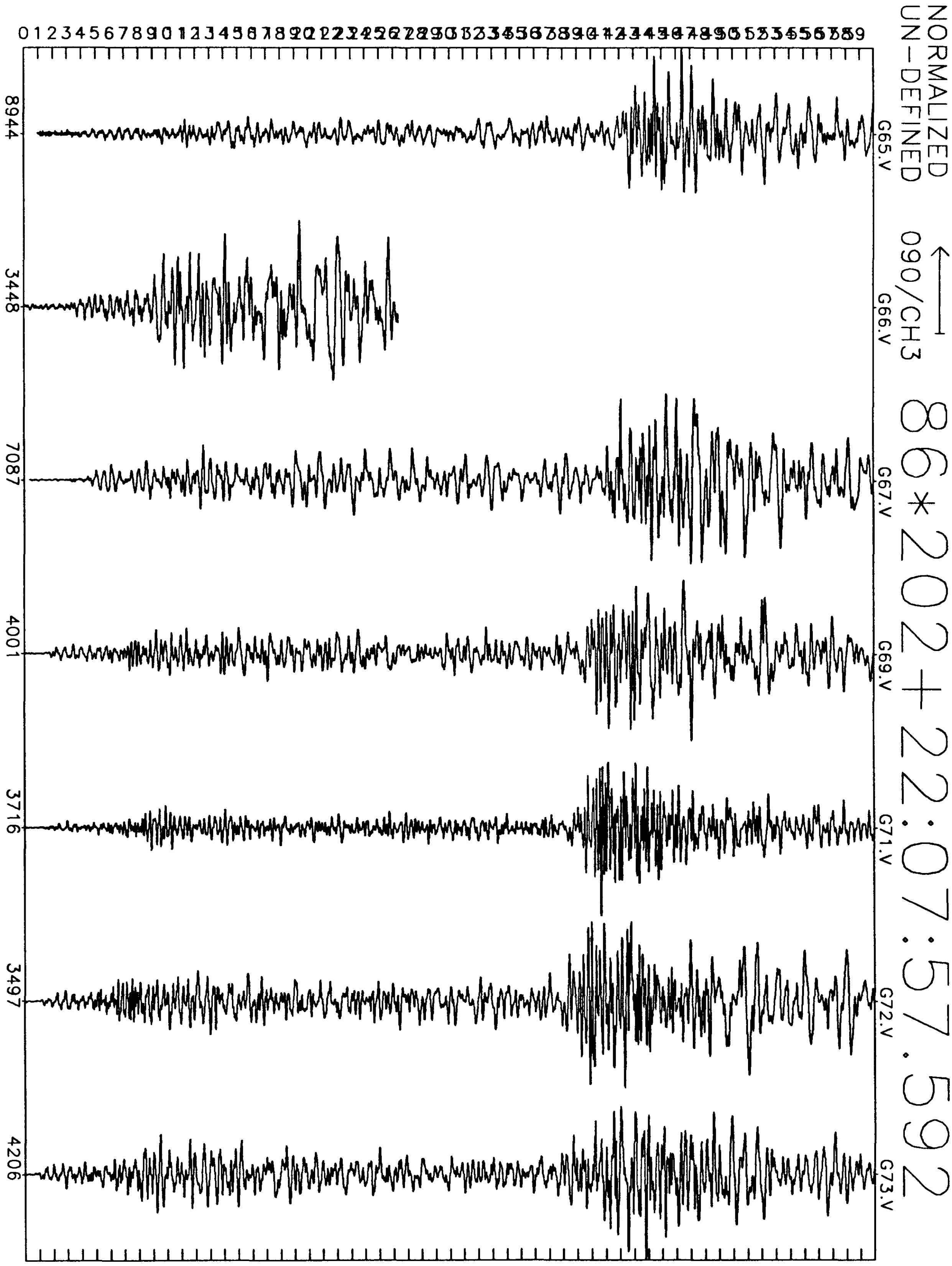

Figure E2(c): Earthquake record section for 60 seconds of N106E motion recorded at GEOS stations. Origin time for record section, station ID, and maximum digital counts (6×10^{-7} cm/sec/digital count) are indicated along abscissa.

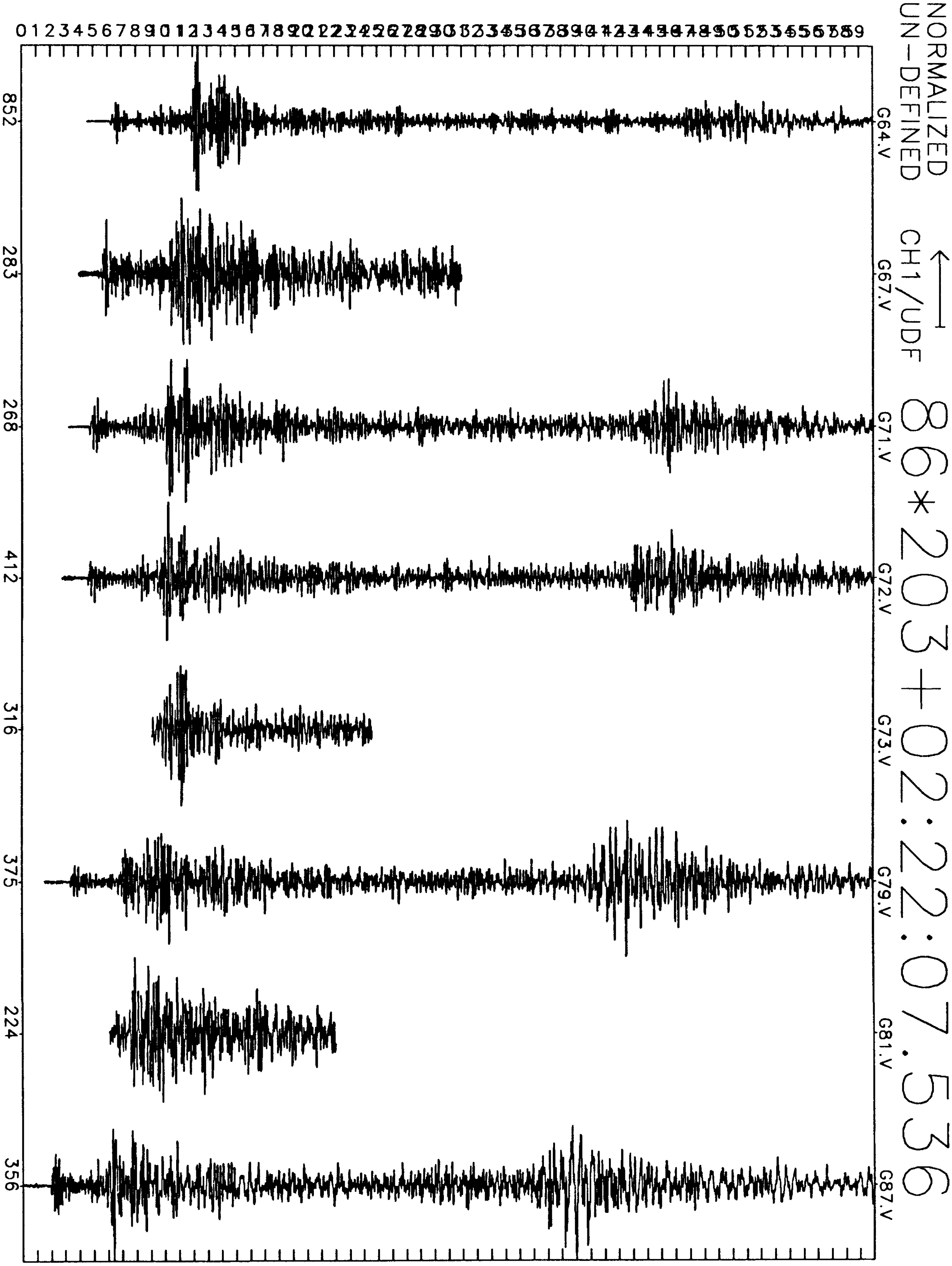

Figure E3(a): Earthquake record section for 60 seconds of vertical motion recorded at GEOS stations. Origin time for record section, station ID, and maximum digital counts (6×10^{-7} cm/sec/digital count) are indicated along abscissa.

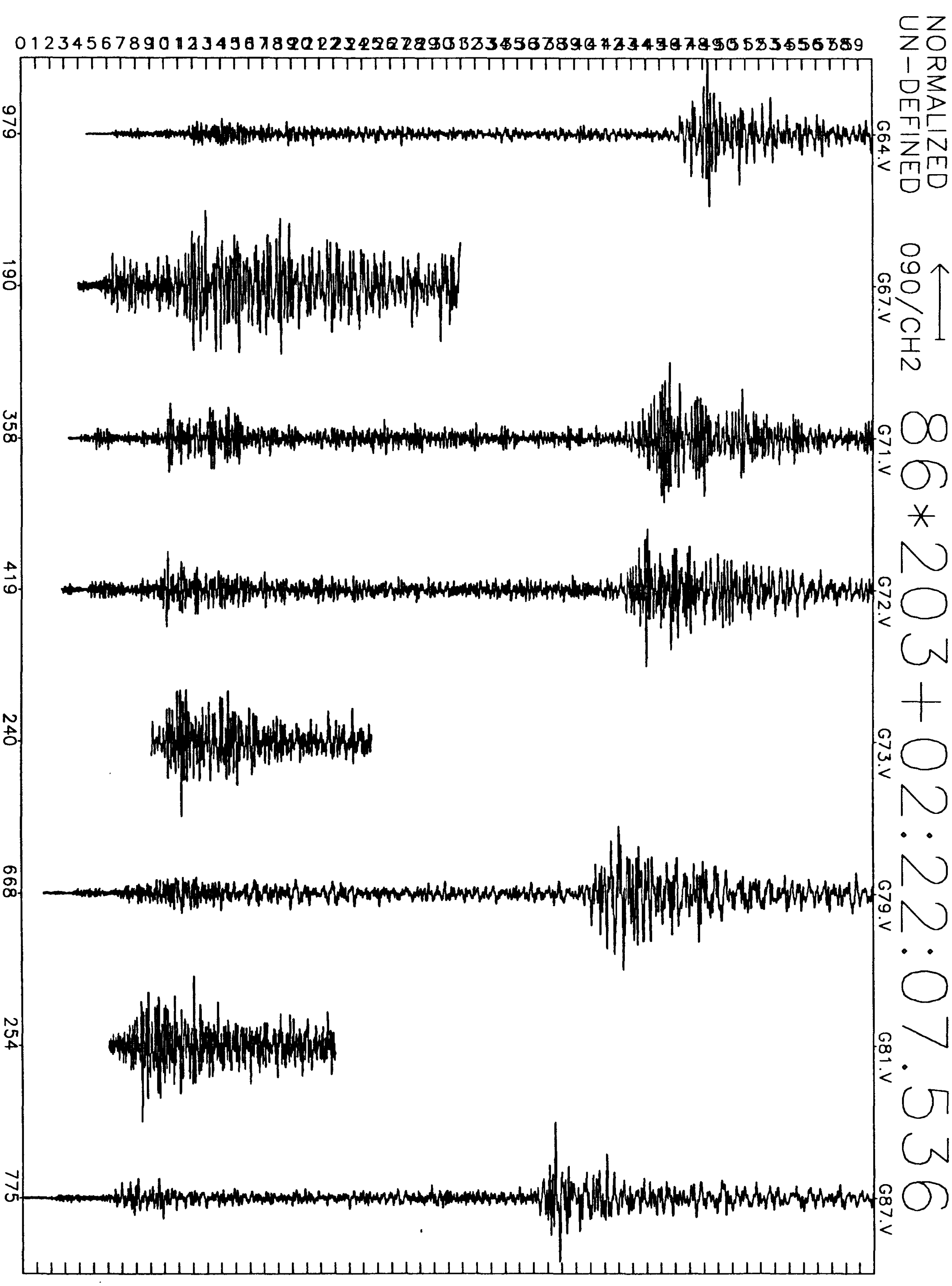

Figure E3(b): Earthquake record section for 60 seconds of N16E motion recorded at GEOS stations. Origin time for record section, station ID, and maximum digital counts (6×10^{-7} cm/sec/digital count) are indicated along abscissa.

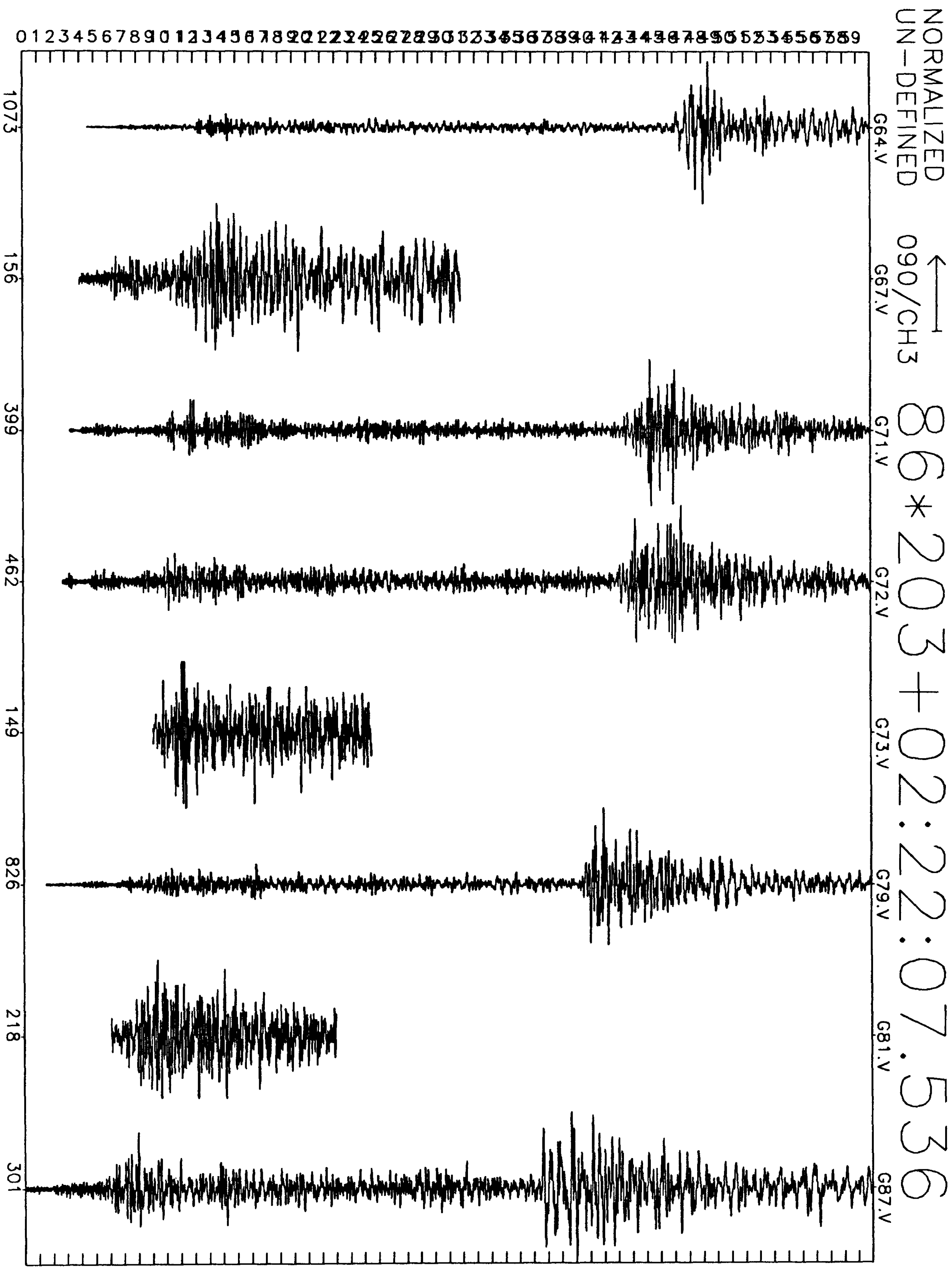

Figure E3(c): Earthquake record section for 60 seconds of N106E motion recorded at GEOS stations. Origin time for record section, station ID, and maximum digital counts (6×10^{-7} cm/sec/digital count) are indicated along abscissa.

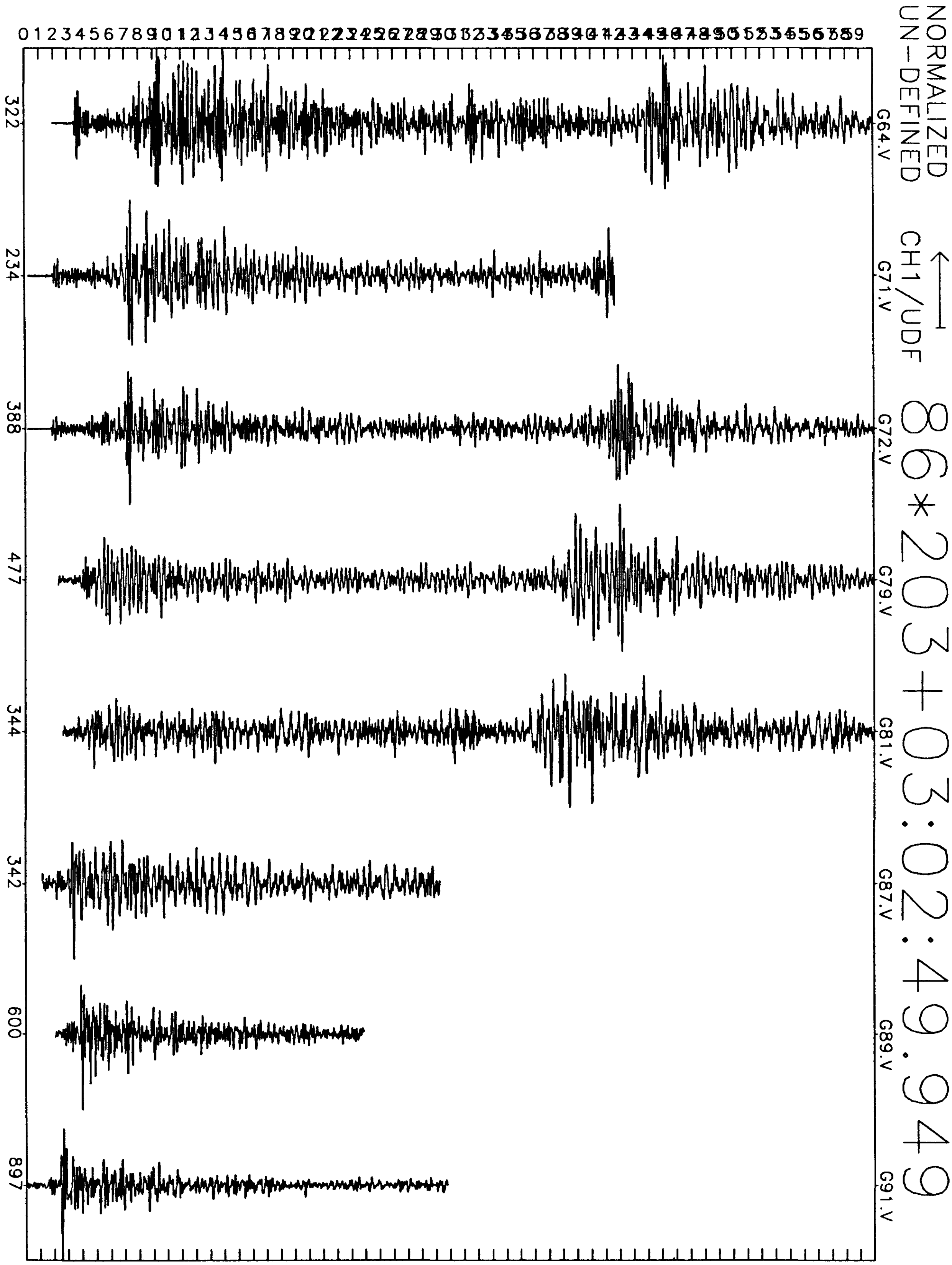

Figure E4(a): Earthquake record section for 60 seconds of vertical motion recorded at GEOS stations. Origin time for record section, station ID, and maximum digital counts (6×10^{-7} cm/sec/digital count) are indicated along abscissa.

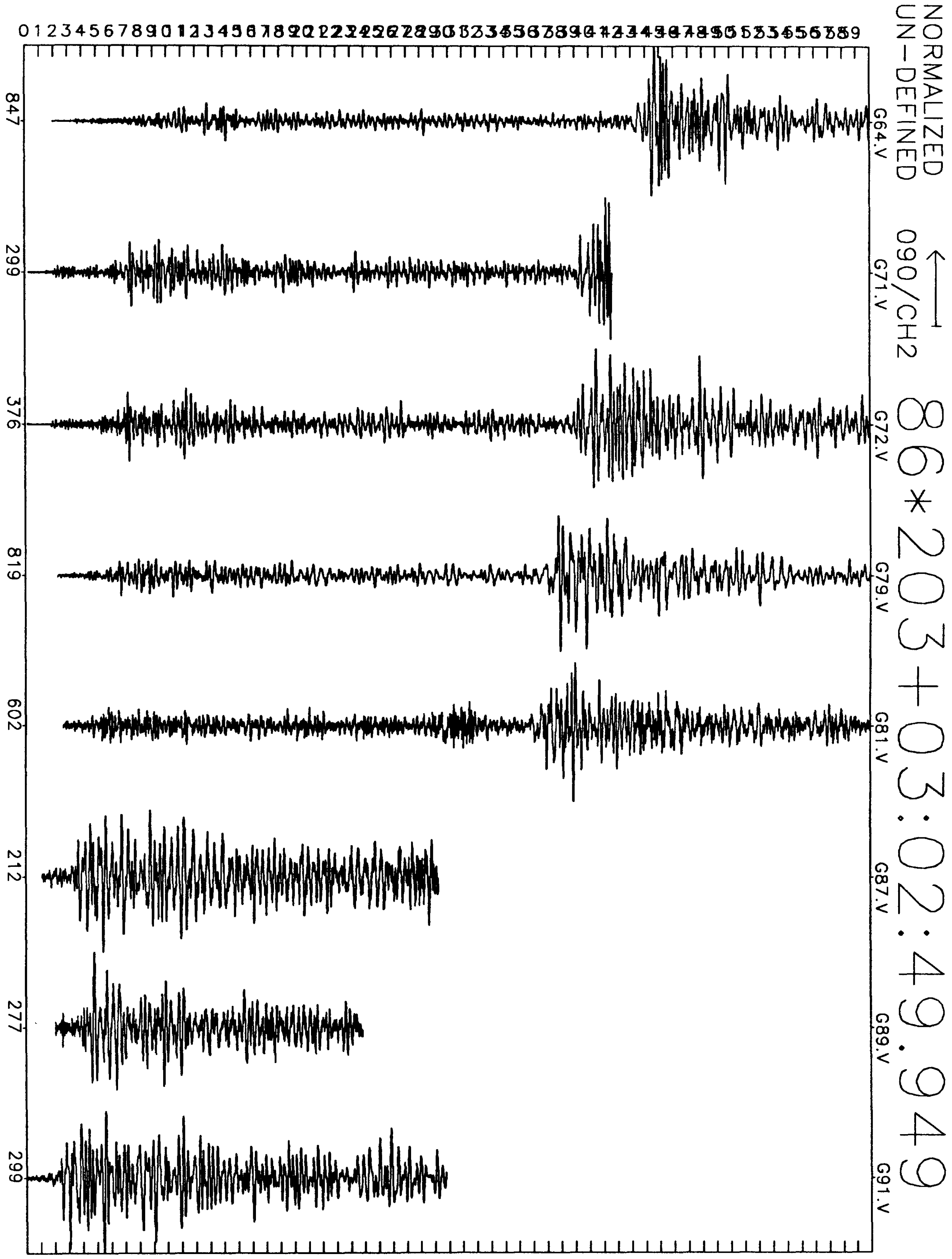

Figure E4(b): Earthquake record section for 60 seconds of N16E motion recorded at GEOS stations. Origin time for record section, station ID, and maximum digital counts (6×10^{-7} cm/sec/digital count) are indicated along abscissa.

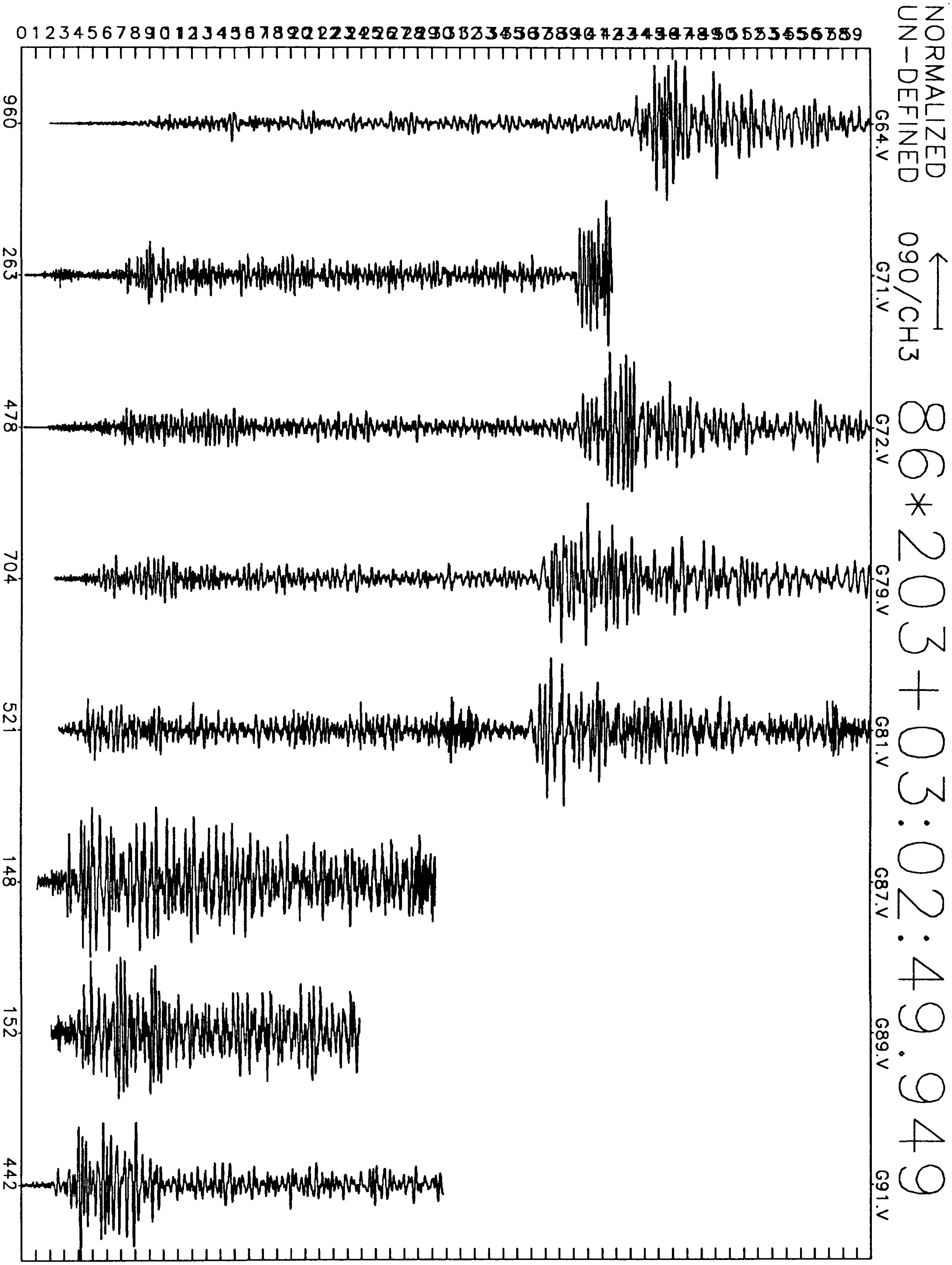

Figure E4(c): Earthquake record section for 60 seconds of N106E motion recorded at GEOS stations. Origin time for record section, station ID, and maximum digital counts (6×10^{-7} cm/sec/digital count) are indicated along abscissa.

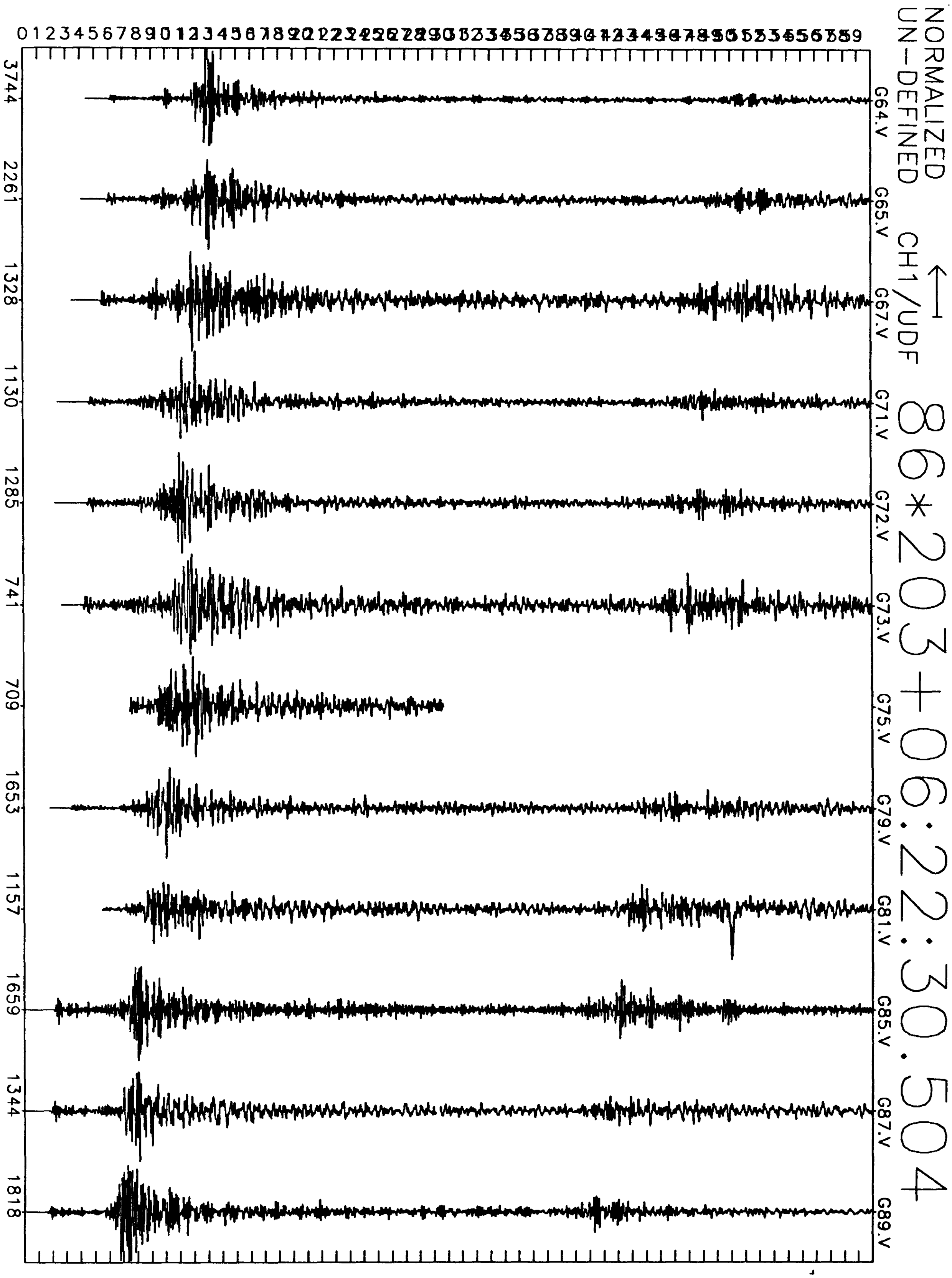

Figure E5(a): Earthquake record section for 60 seconds of vertical motion recorded at GEOS stations. Origin time for record section, station ID, and maximum digital counts (6×10^{-7} cm/sec/digital count) are indicated along abscissa.

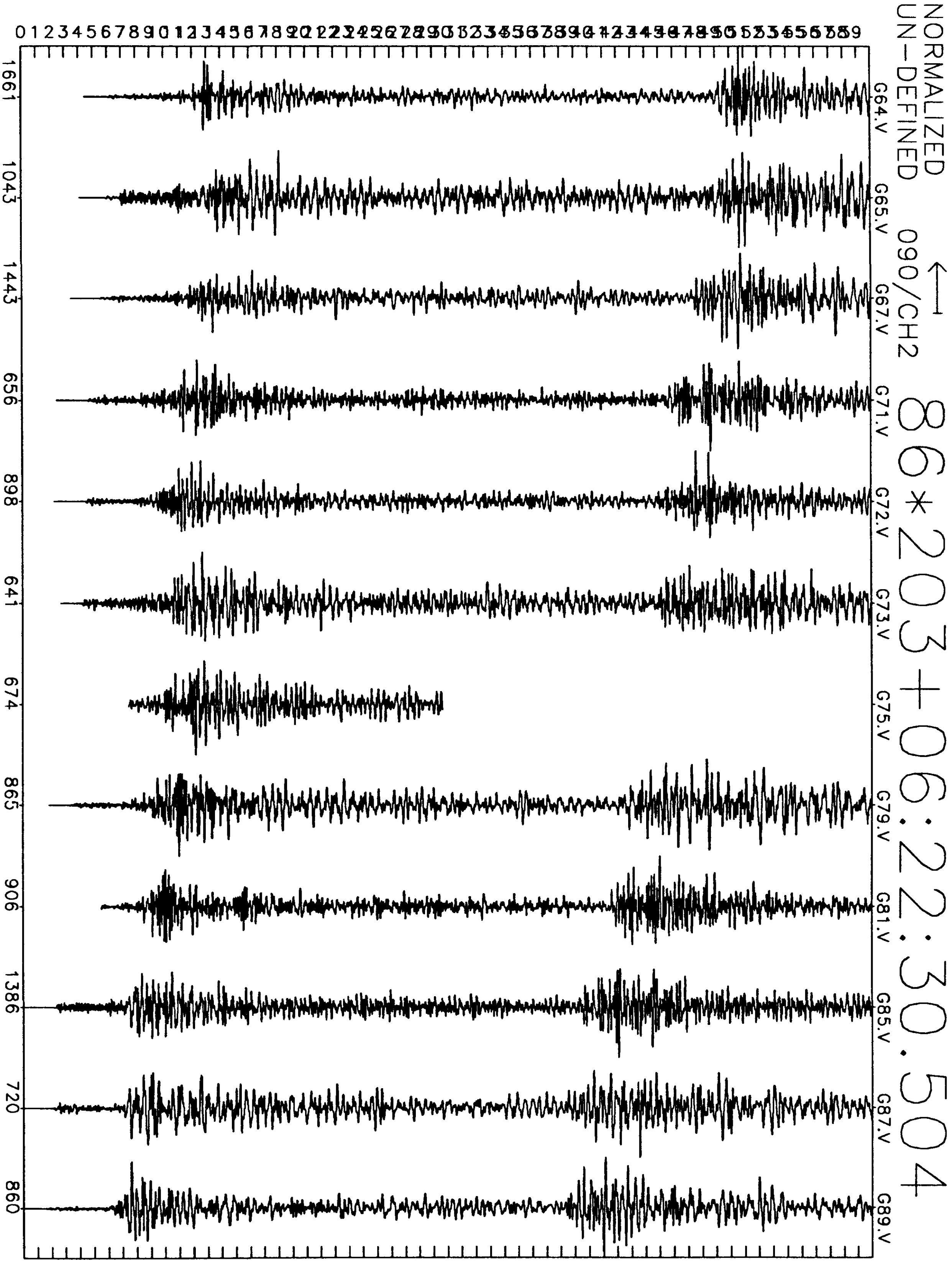

Figure E5(b): Earthquake record section for 60 seconds of N16E motion recorded at GEOS stations. Origin time for record section, station ID, and maximum digital counts (6×10^{-7} cm/sec/digital count) are indicated along abscissa.

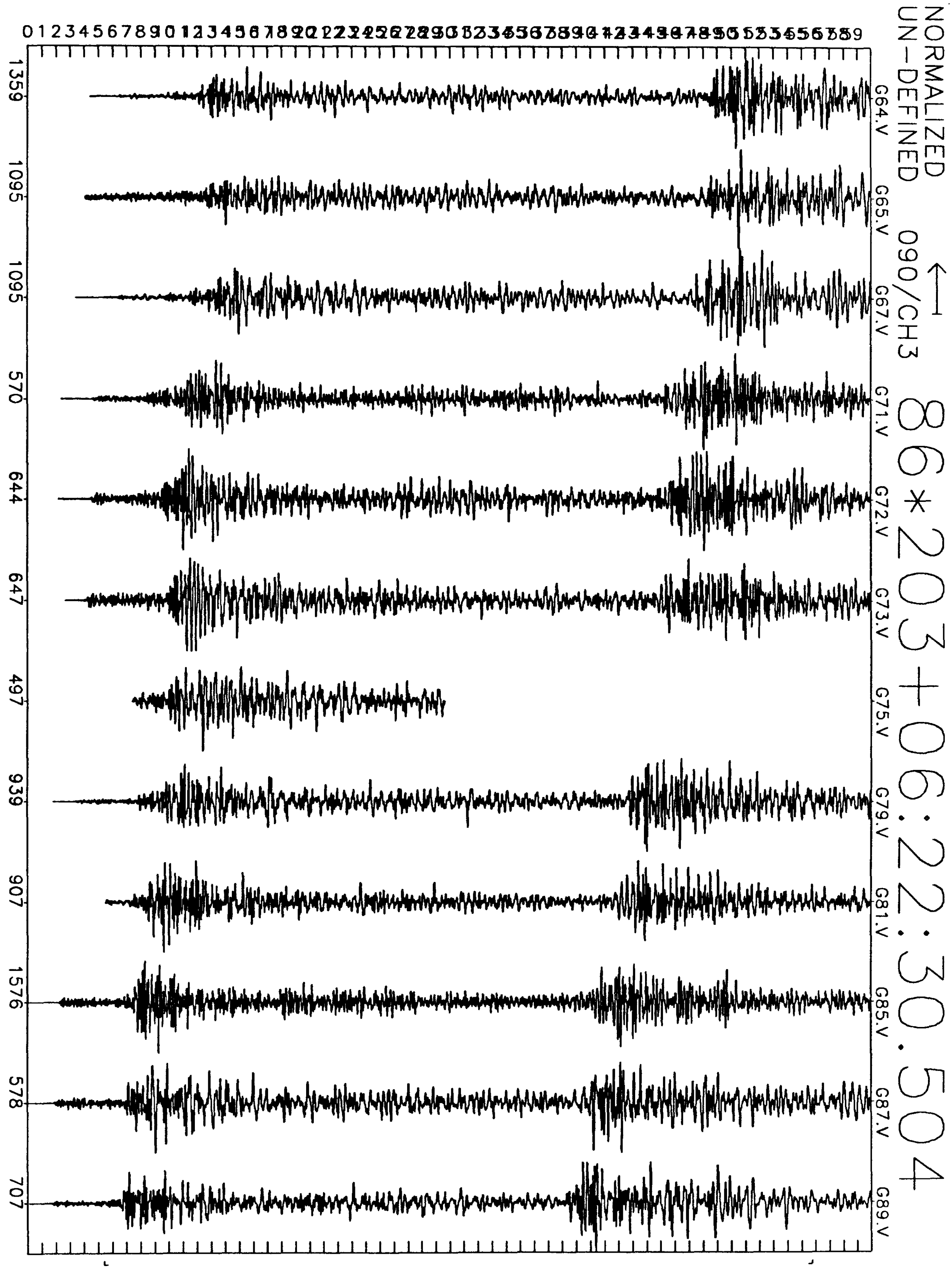

Figure E5(c): Earthquake record section for 60 seconds of N106E motion recorded at GEOS stations. Origin time for record section, station ID, and maximum digital counts (6×10^{-7} m/sec/digital count) are indicated along abscissa.

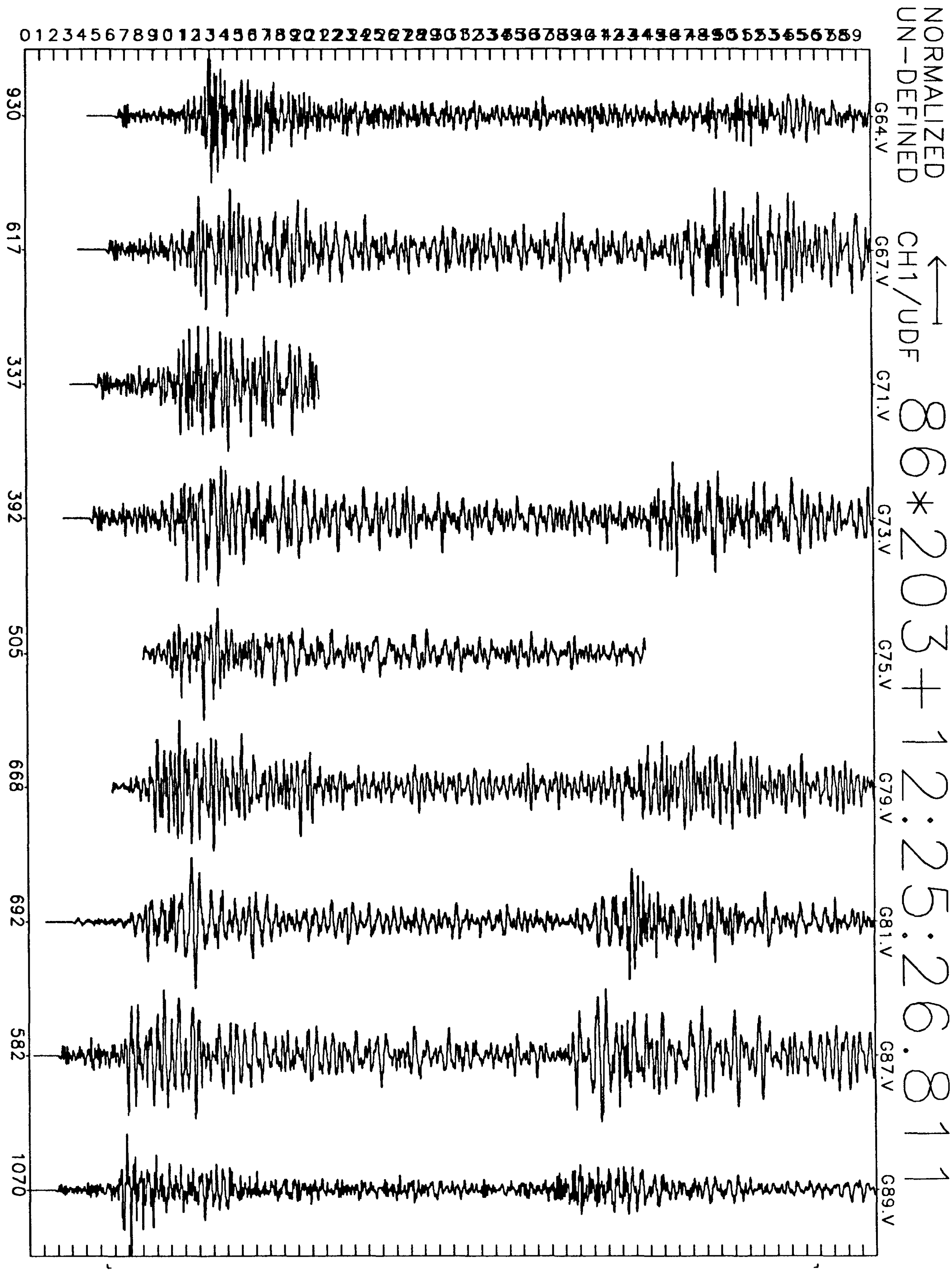

Figure E6(a): Earthquake record section for 60 seconds of vertical motion recorded at GEOS stations. Origin time for record section, station ID, and maximum digital counts (6 × 10^{-7} cm/sec/digital count) are indicated along abscissa.

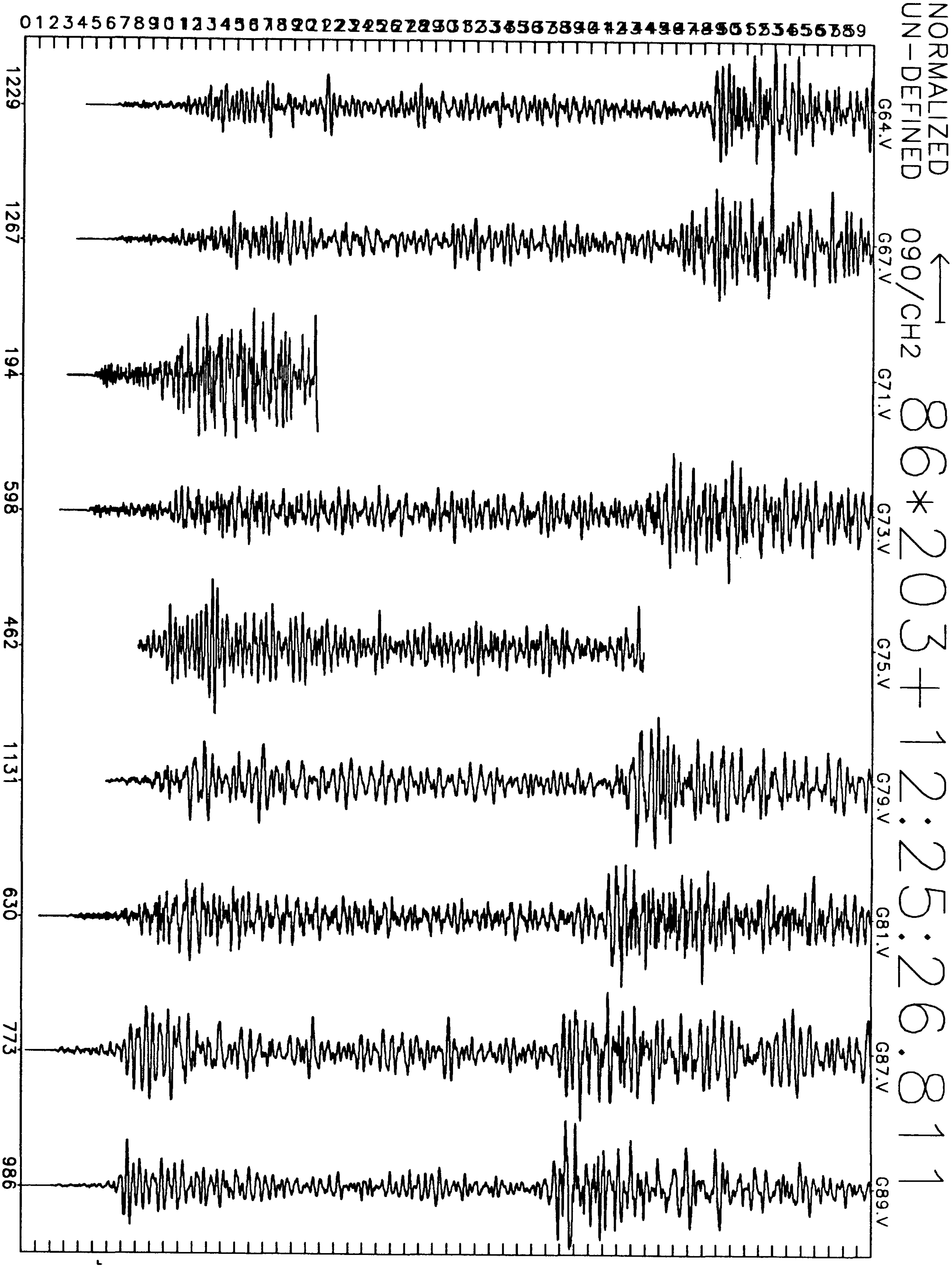

Figure E6(b): Earthquake record section for 60 seconds of N16E motion recorded at GEOS stations. Origin time for record section, station ID, and maximum digital counts (6 × 10^{-7} cm/sec/digital count) are indicated along abscissa.

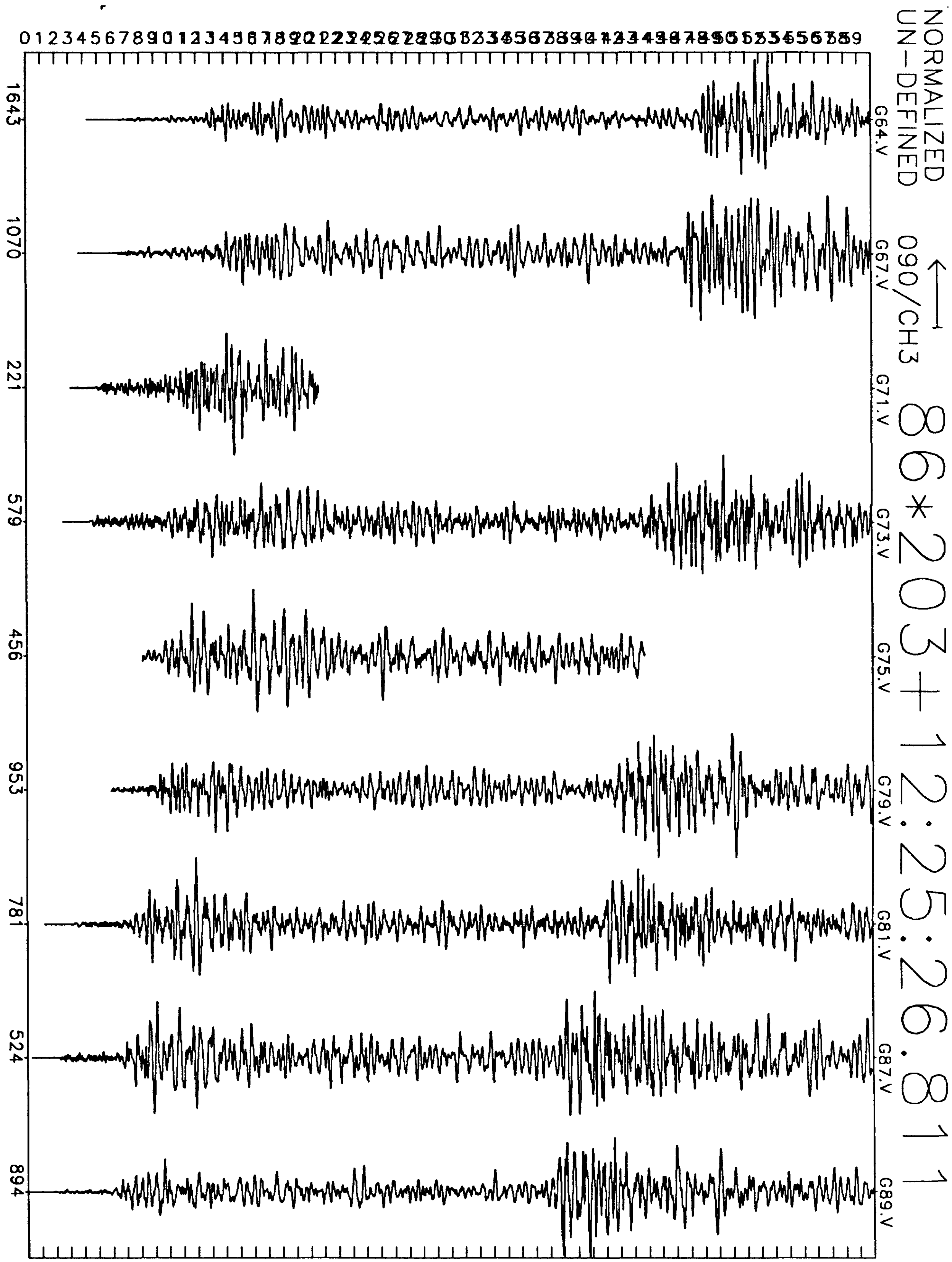

Figure E6(c): Earthquake record section for 60 seconds of N106E motion recorded at GEOS stations. Origin time for record section, station ID, and maximum digital counts (6×10^{-7} cm/sec/digital count) are indicated along abscissa.

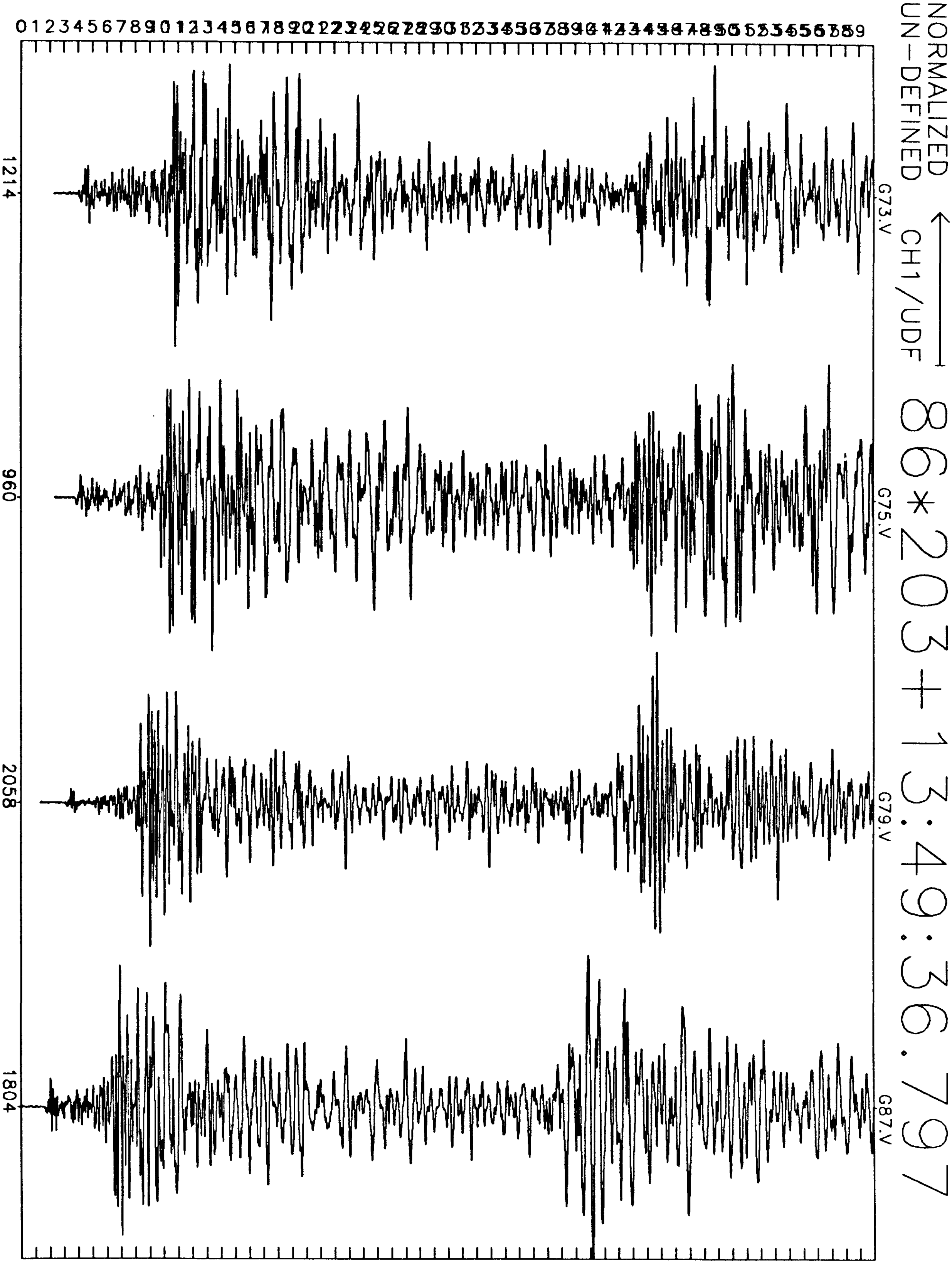

Figure E7(a): Earthquake record section for 60 seconds of vertical motion recorded at GEOS stations. Origin time for record section, station ID, and maximum digital counts (6×10^{-7} cm/sec/digital count) are indicated along abscissa.

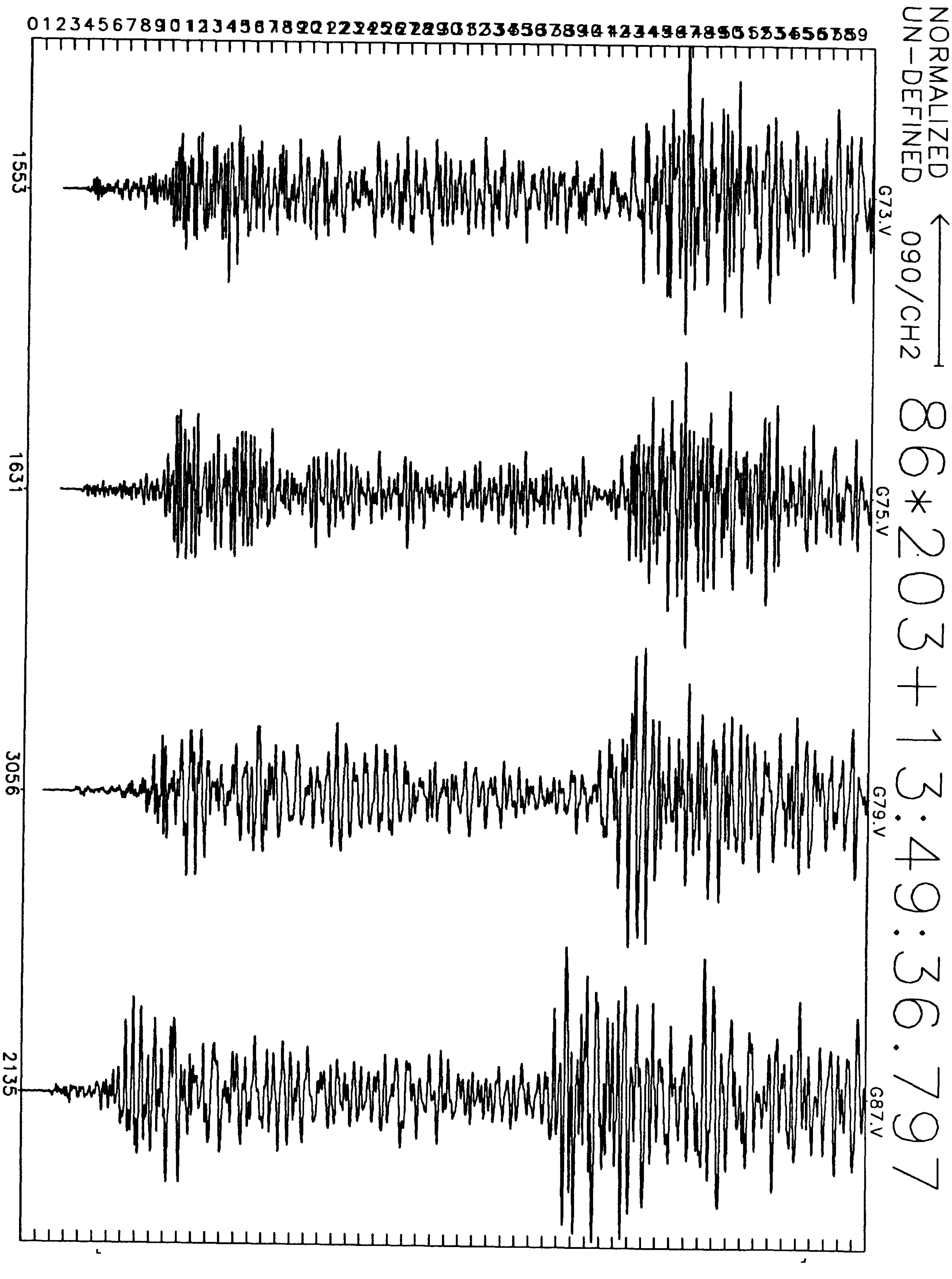

Figure E7(b): Earthquake record section for 60 seconds of N16E motion recorded at GEOS stations. Origin time for record section, station ID, and maximum digital counts (6×10^{-7} cm/sec/digital count) are indicated along abscissa.

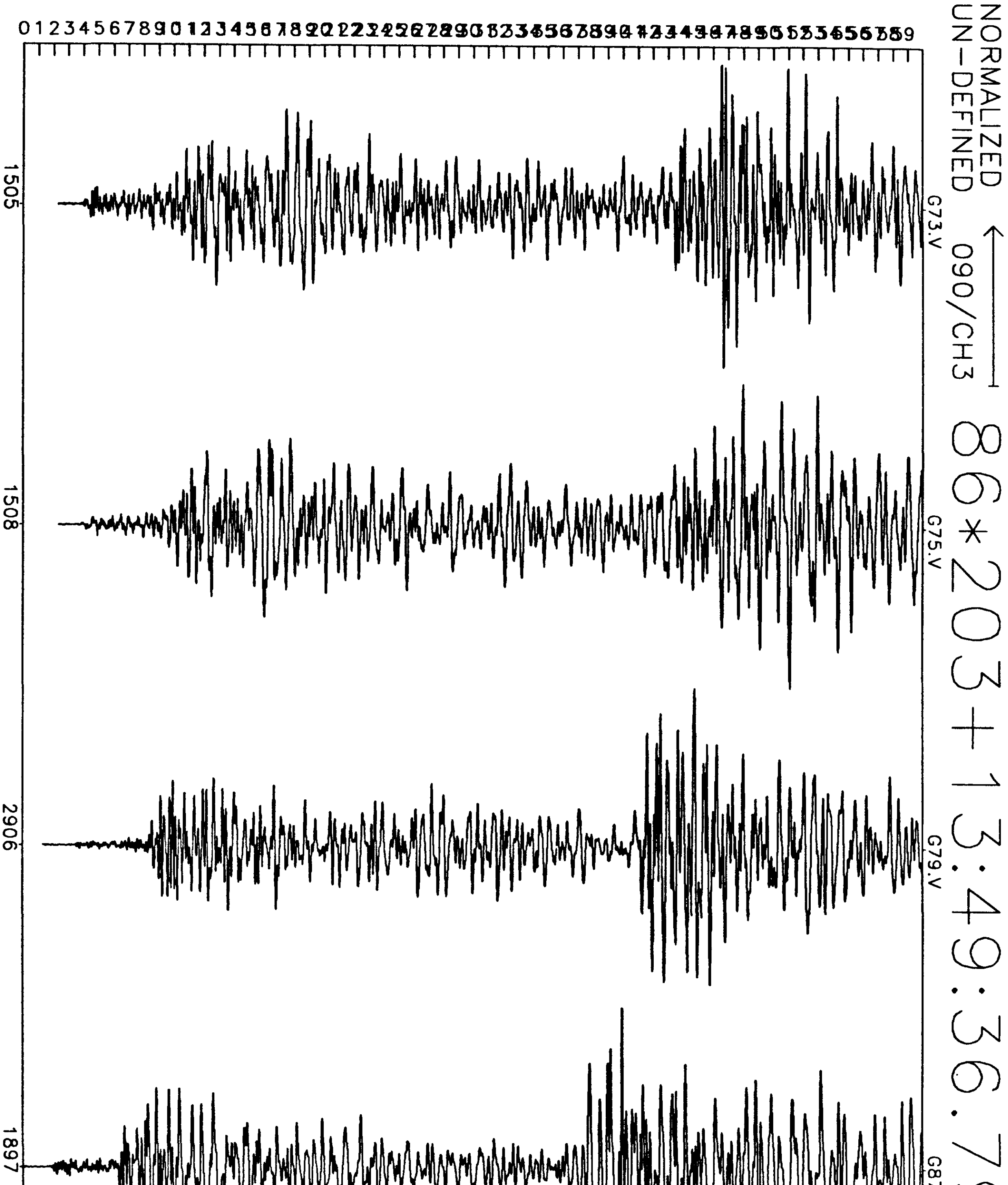

Figure E7(c): Earthquake record section for 60 seconds of N106E motion recorded at GEOS stations. Origin time for record section, station ID, and maximum digital counts (6×10^{-7} cm/sec/digital count) are indicated along abscissa.

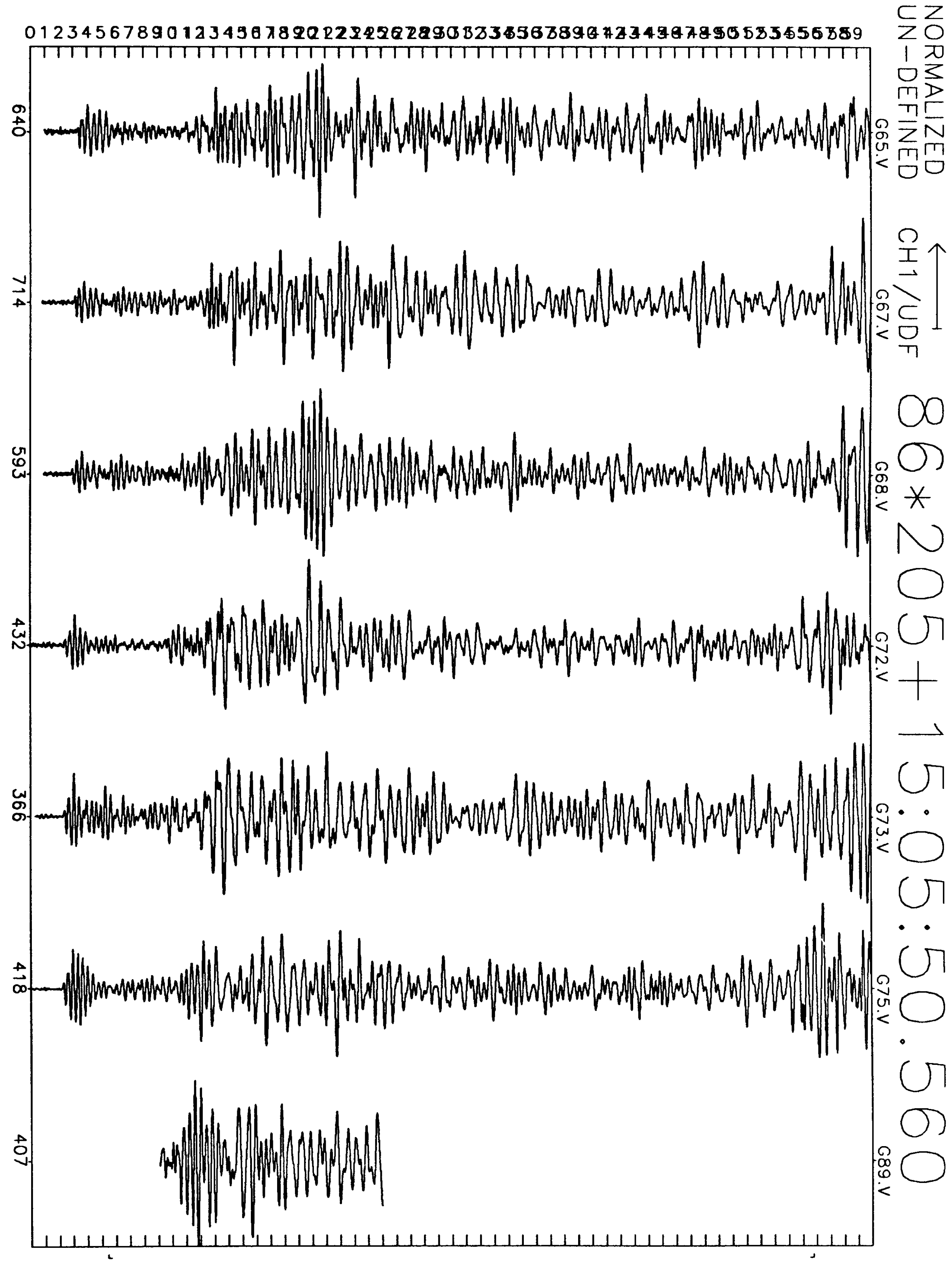

Figure E8(a): Earthquake record section for 60 seconds of vertical motion recorded at GEOS stations. Origin time for record section, station ID, and maximum digital counts (6×10^{-7} cm/sec/digital count) are indicated along abscissa.

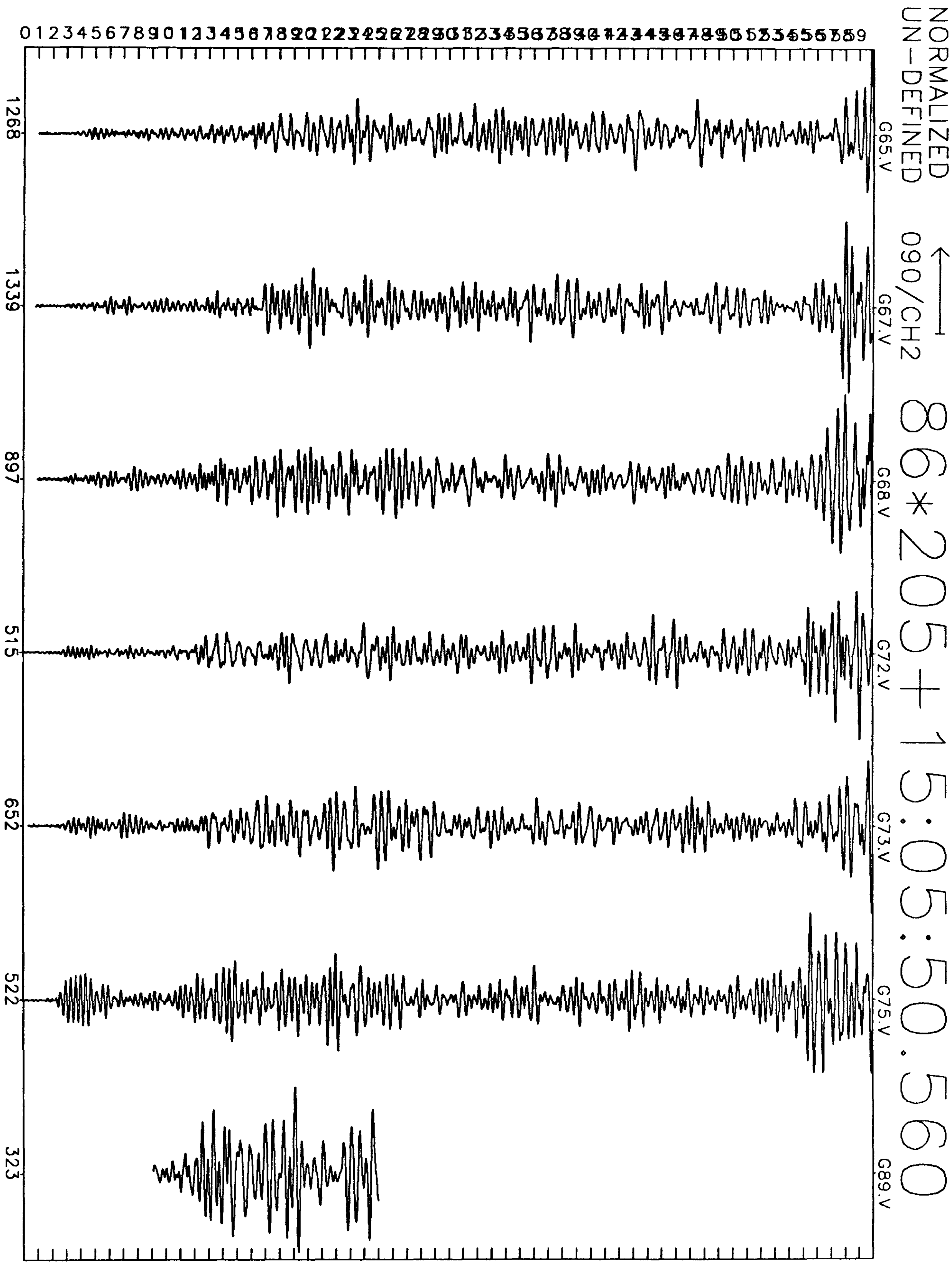

Figure E8(b): Earthquake record section for 60 seconds of N16E motion recorded at GEOS stations. Origin time for record section, station ID, and maximum digital counts (6×10^{-7} cm/sec/digital count) are indicated along abscissa.

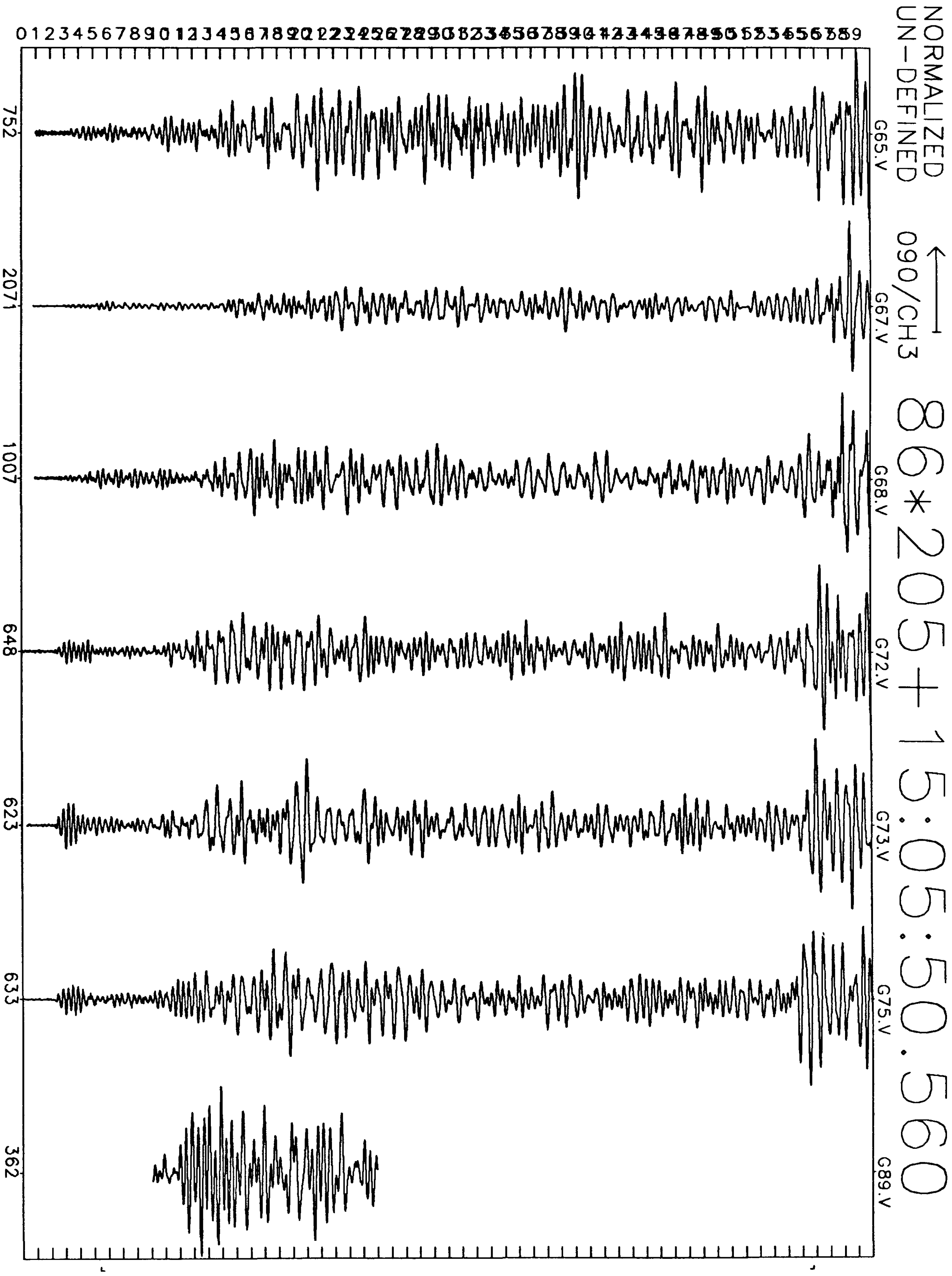

Figure E8(c): Earthquake record section for 60 seconds of N106E motion recorded at GEOS stations. Origin time for record section, station ID, and maximum digital counts (6×10^{-7} cm/sec/digital count) are indicated along abscissa.

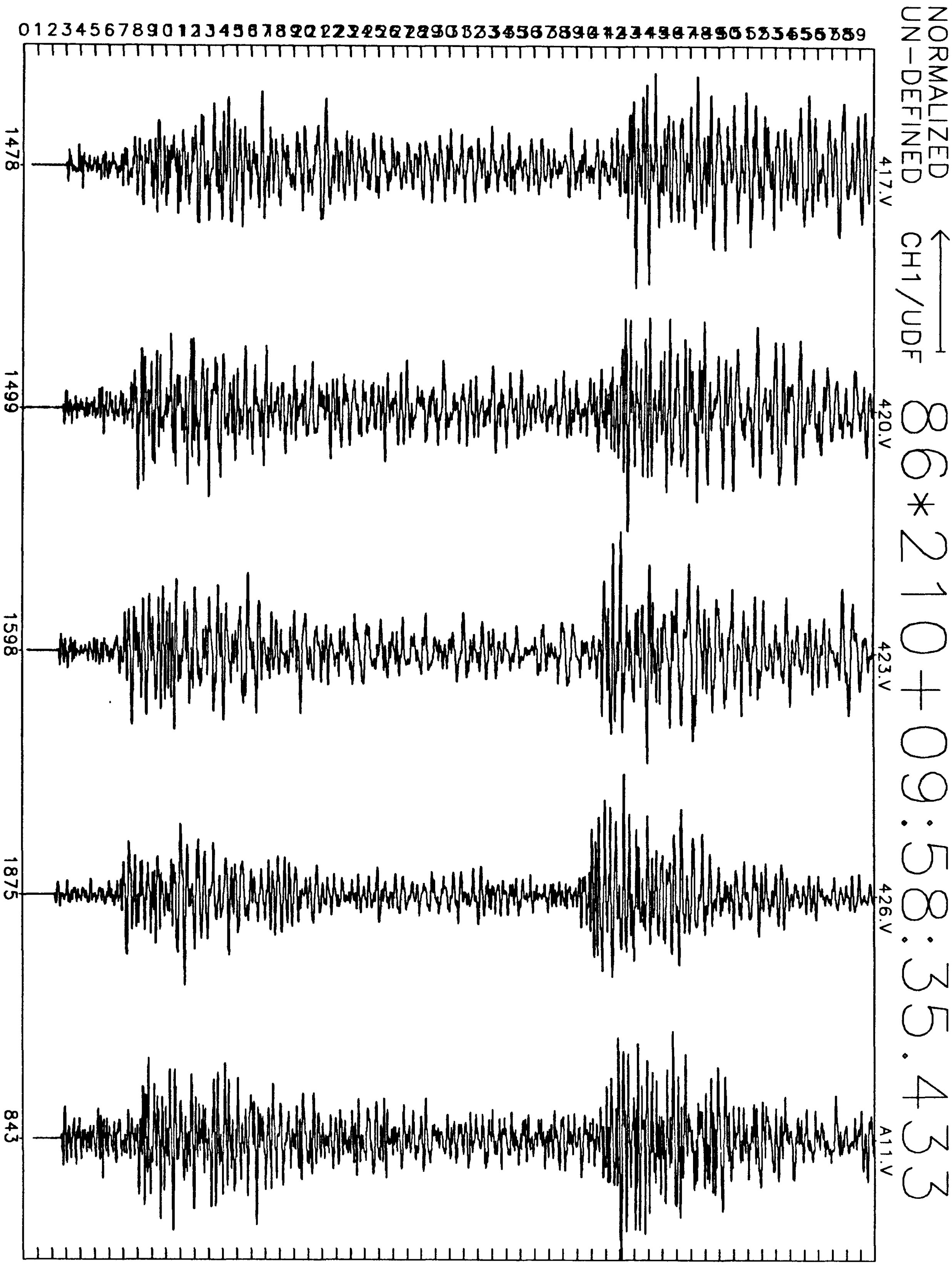

Figure E9(a): Earthquake record section for 60 seconds of vertical motion recorded at GEOS stations. Origin time for record section, station ID, and maximum digital counts (6×10^{-7} cm/sec/digital count) are indicated along abscissa.

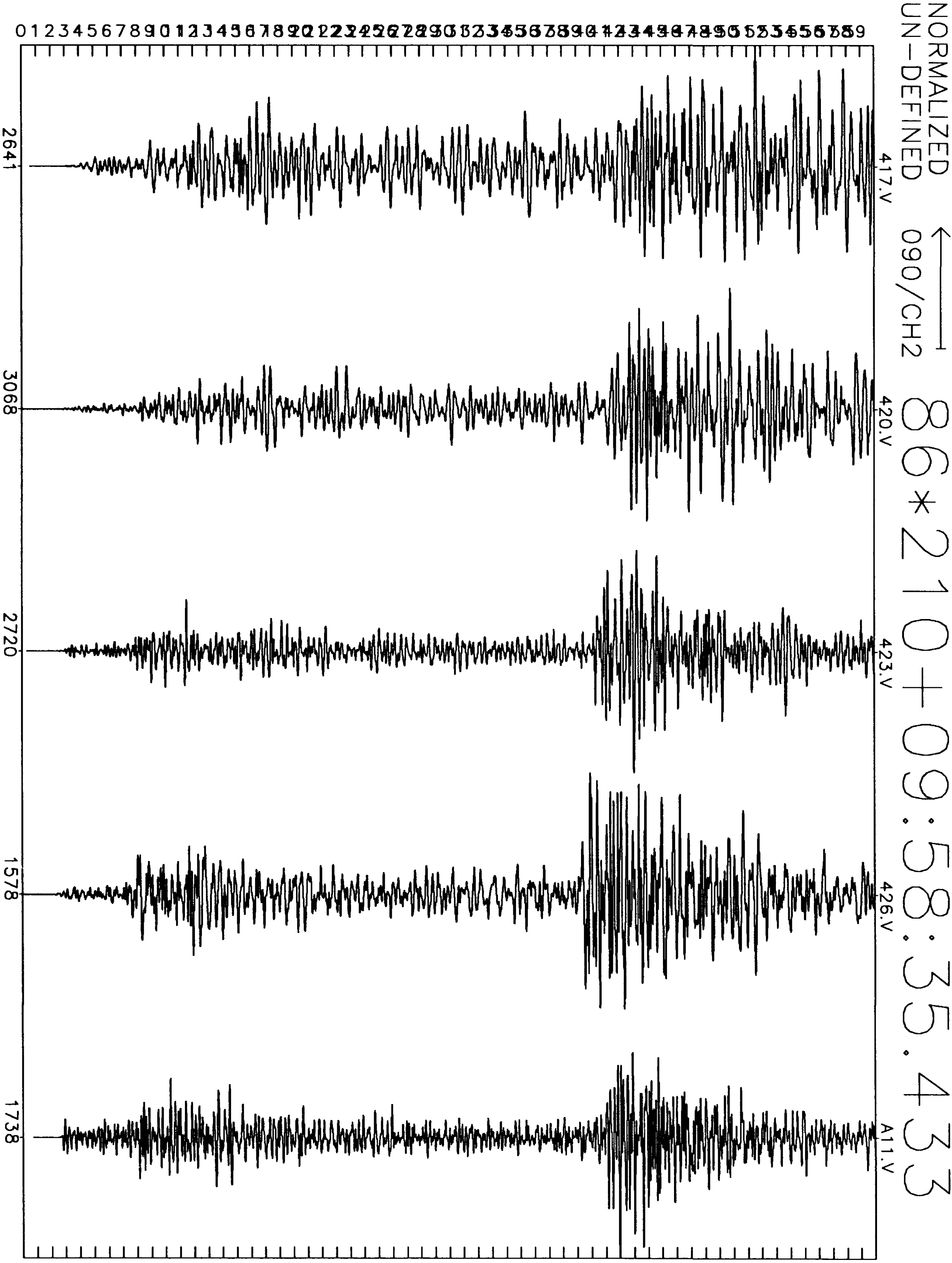

Figure E9(b): Earthquake record section for 60 seconds of N305E motion recorded at GEOS stations. Origin time for record section, station ID, and maximum digital counts (6 × 10^{-7} cm/sec/digital count) are indicated along abscissa.

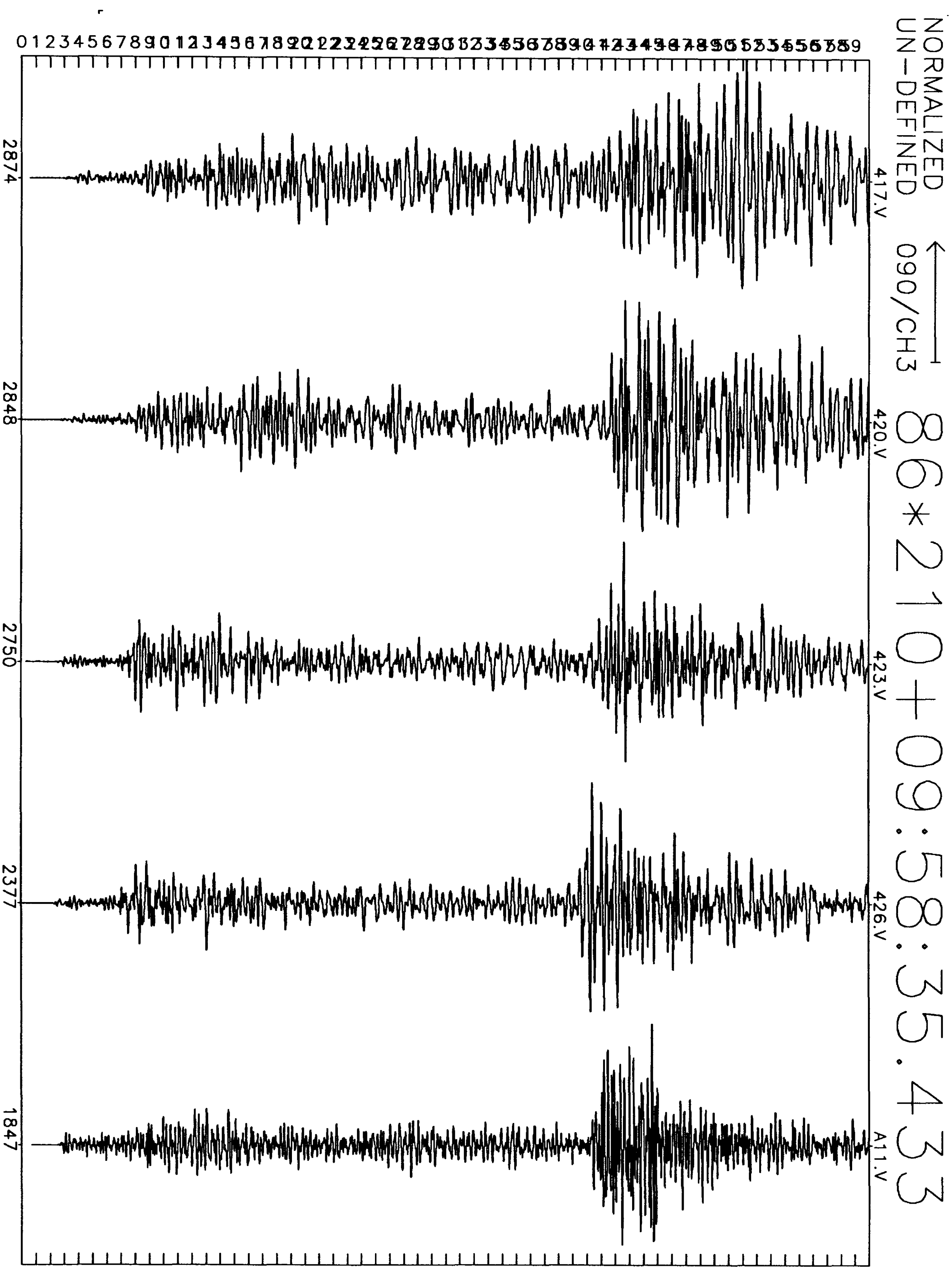

Figure E9(c): Earthquake record section for 60 seconds of N35E motion recorded at GEOS stations. Origin time for record section, station ID, and maximum digital counts (6×10^{-7} cm/sec/digital count) are indicated along abscissa.

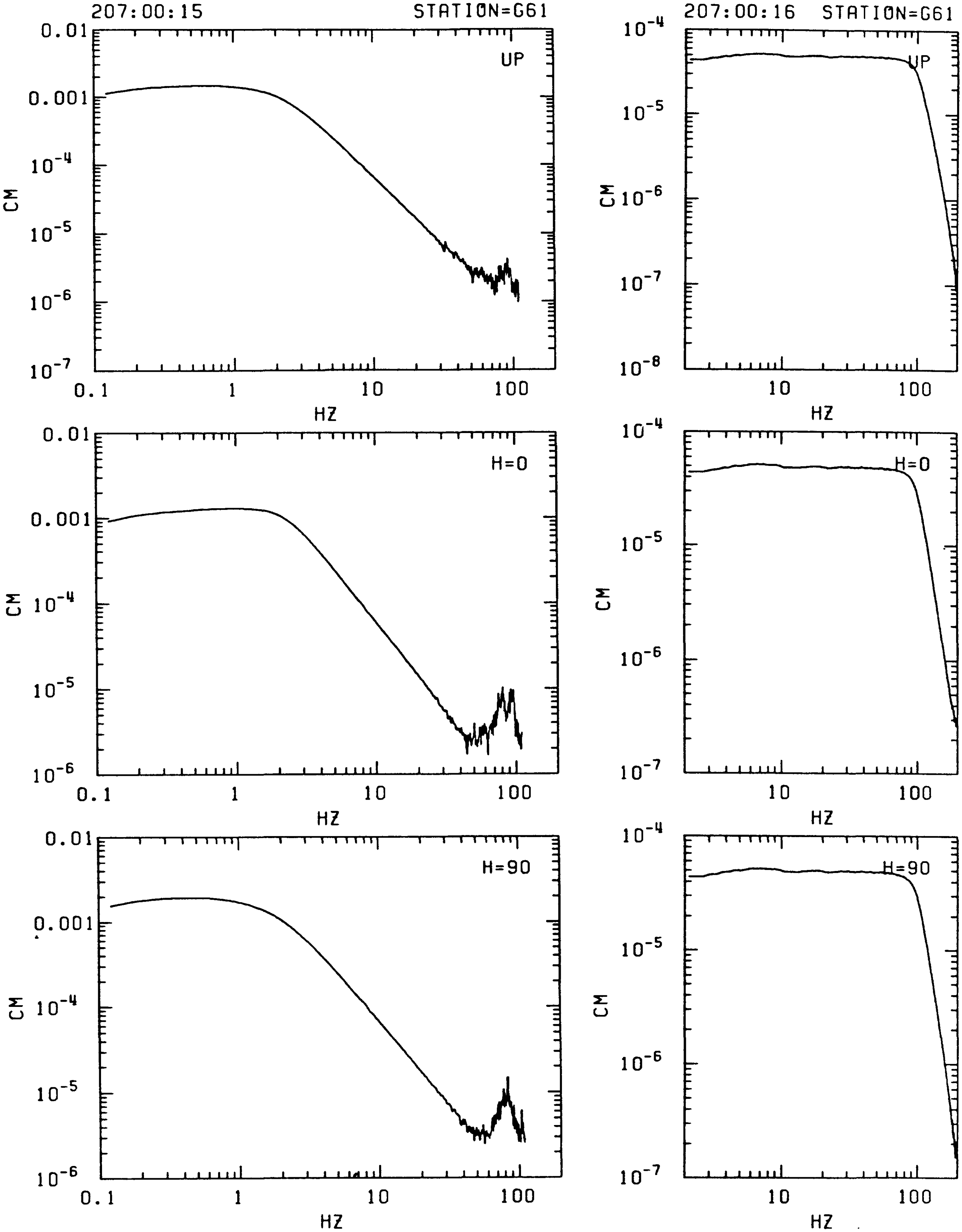

Figure F1: Amplitude response curves computed from in-situ recordings of step function in ground acceleration (left column; seismometer mass release from rest due to applied DC voltage) and delta function in voltage applied to recorder input (right column) for channels corresponding to vertical, radial and transverse components of motion recorded at station indicated at top. (See text for interpretation.)

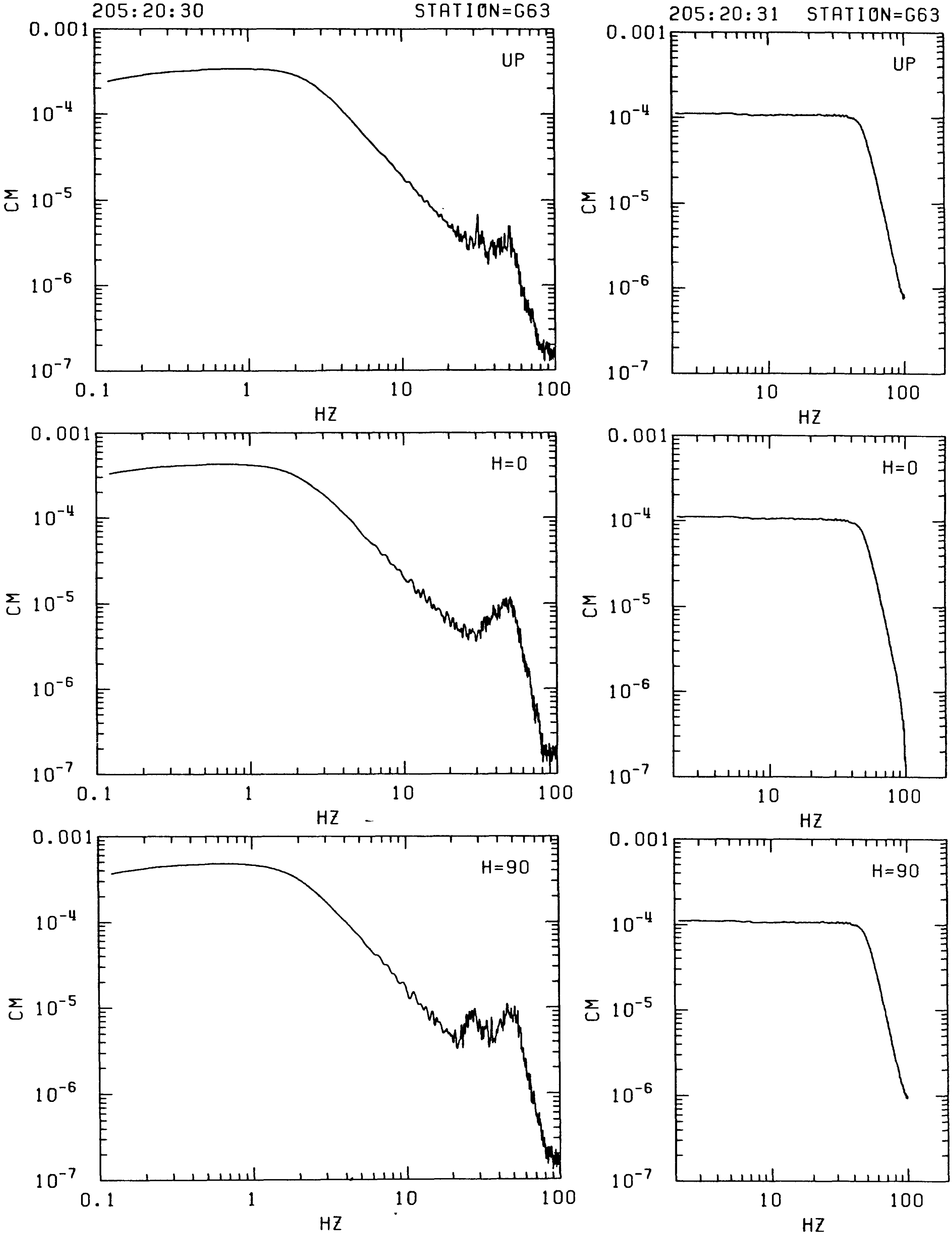

Figure F2: Amplitude response curves computed from in-situ recordings of step function in ground acceleration (left column; seismometer mass release from rest due to applied DC voltage) and delta function in voltage applied to recorder input (right column) for channels corresponding to vertical, radial and transverse components of motion recorded at station indicated at top. (See text for interpretation.)

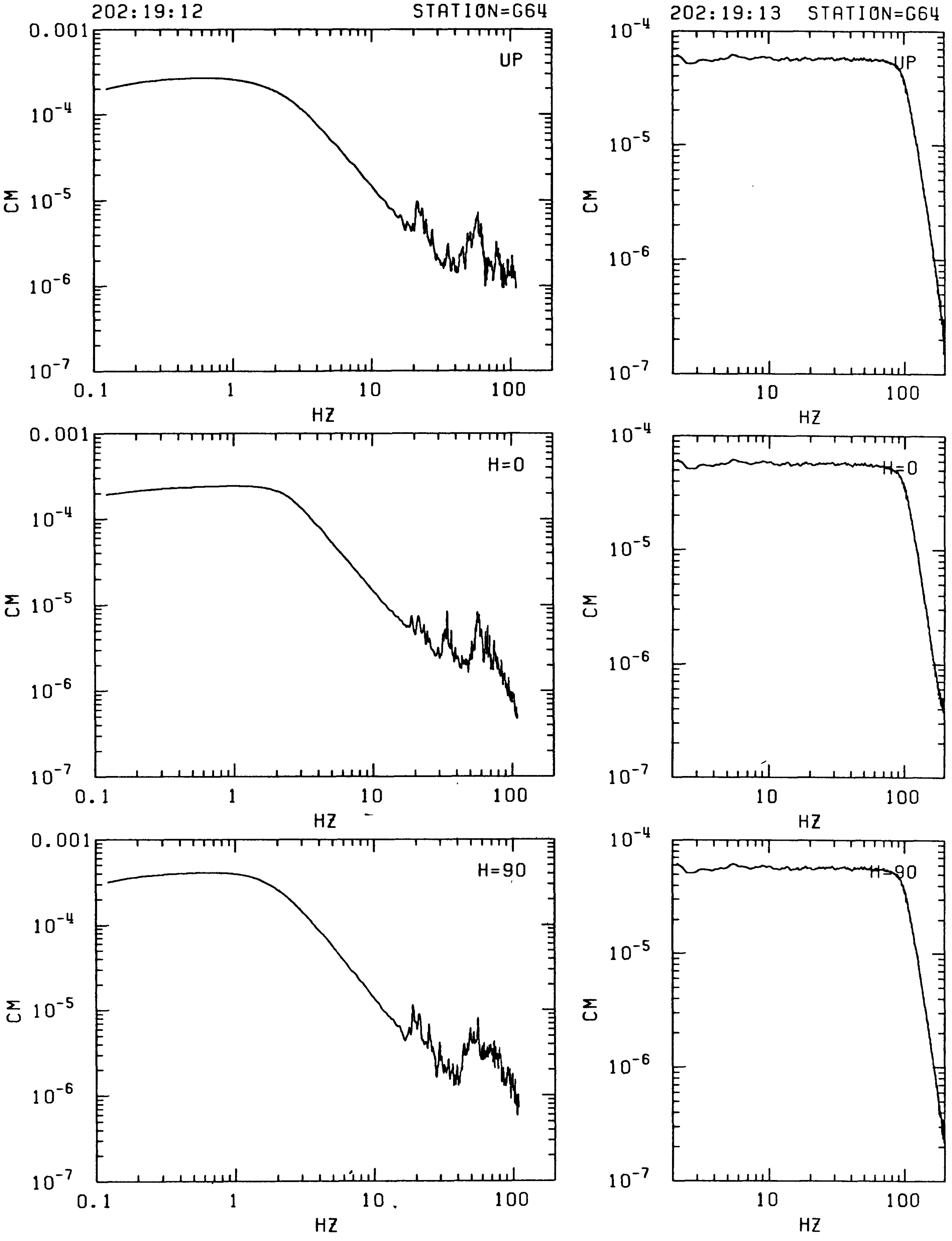

Figure F3: Amplitude response curves computed from in-situ recordings of step function in ground acceleration (left column; seismometer mass release from rest due to applied DC voltage) and delta function in voltage applied to recorder input (right column) for channels corresponding to vertical, radial and transverse components of motion recorded at station indicated at top. (See text for interpretation.)

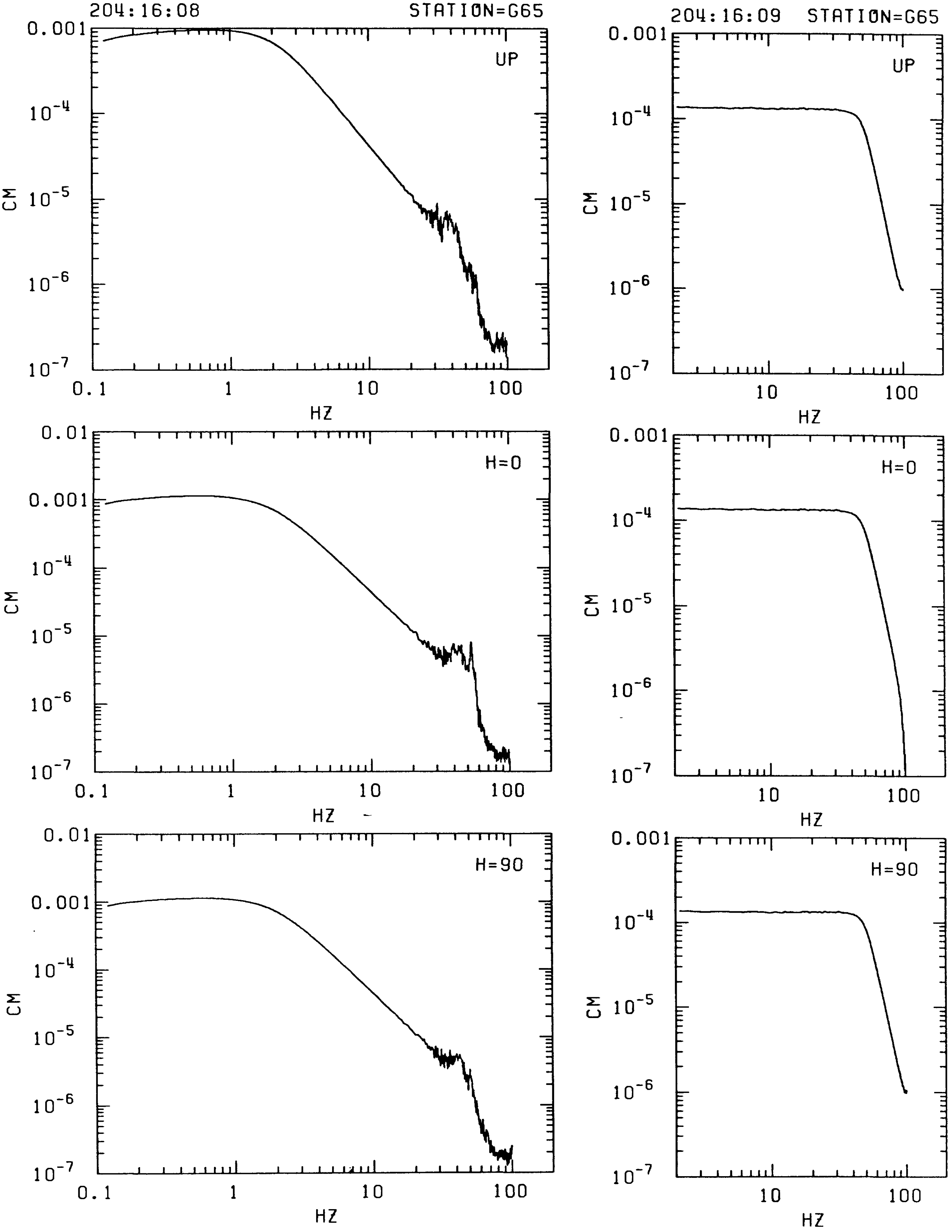

Figure F4: Amplitude response curves computed from in-situ recordings of step function in ground acceleration (left column; seismometer mass release from rest due to applied DC voltage) and delta function in voltage applied to recorder input (right column) for channels corresponding to vertical, radial and transverse components of motion recorded at station indicated at top. (See text for interpretation.)

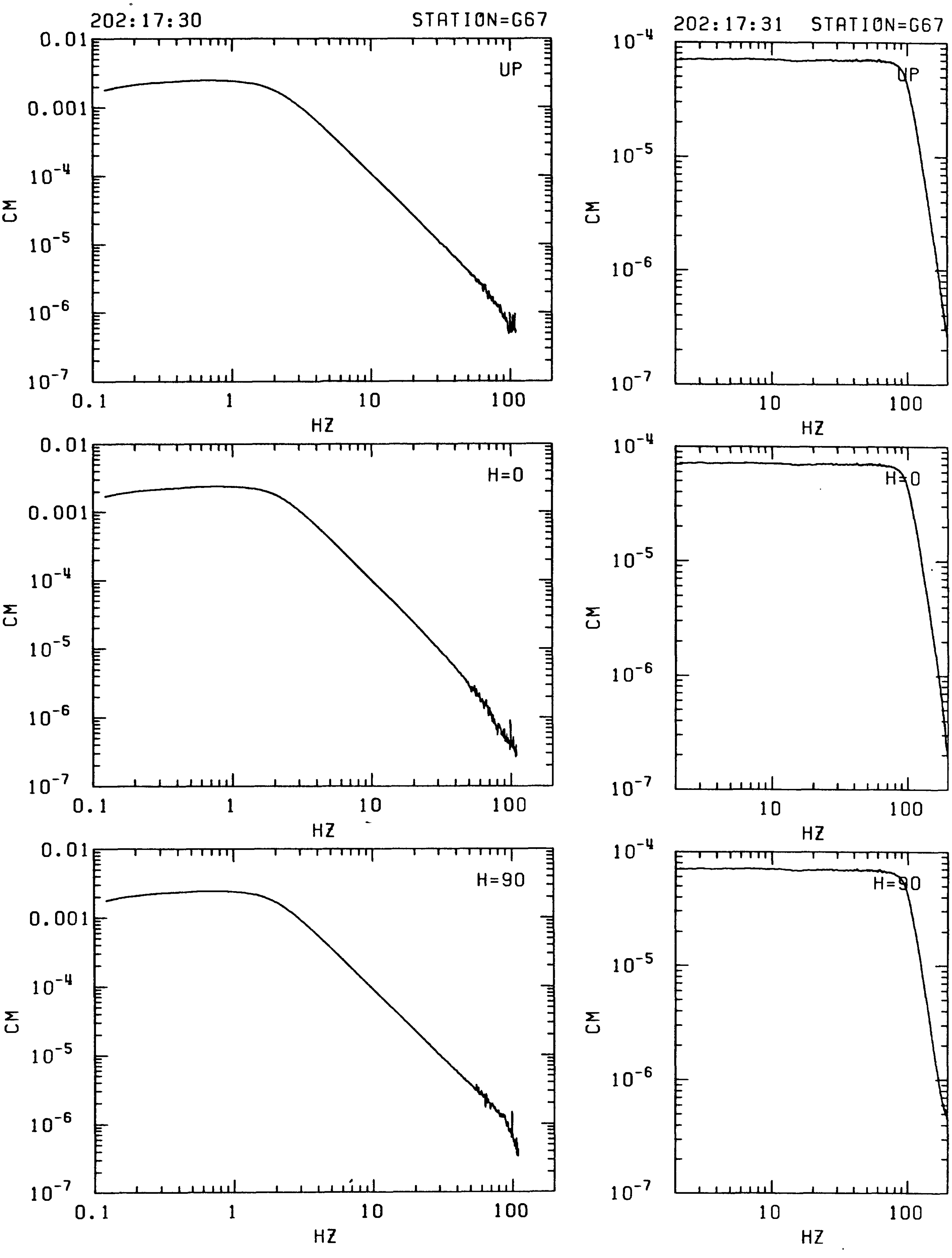

Figure F5: Amplitude response curves computed from in-situ recordings of step function in ground acceleration (left column; seismometer mass release from rest due to applied DC voltage) and delta function in voltage applied to recorder input (right column) for channels corresponding to vertical, radial and transverse components of motion recorded at station indicated at top. (See text for interpretation.)

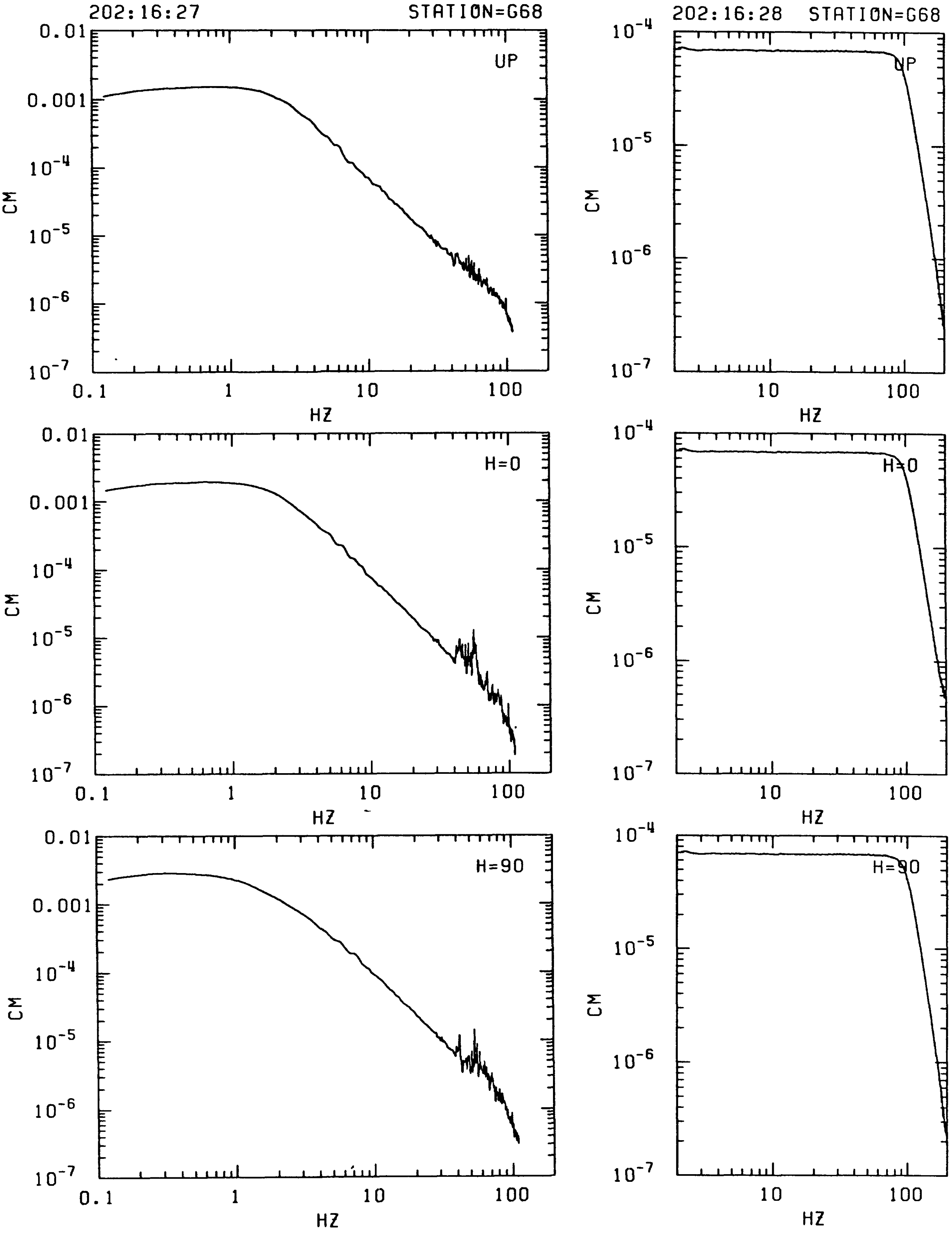

Figure F6: Amplitude response curves computed from in-situ recordings of step function in ground acceleration (left column; seismometer mass release from rest due to applied DC voltage) and delta function in voltage applied to recorder input (right column) for channels corresponding to vertical, radial and transverse components of motion recorded at station indicated at top. (See text for interpretation.)

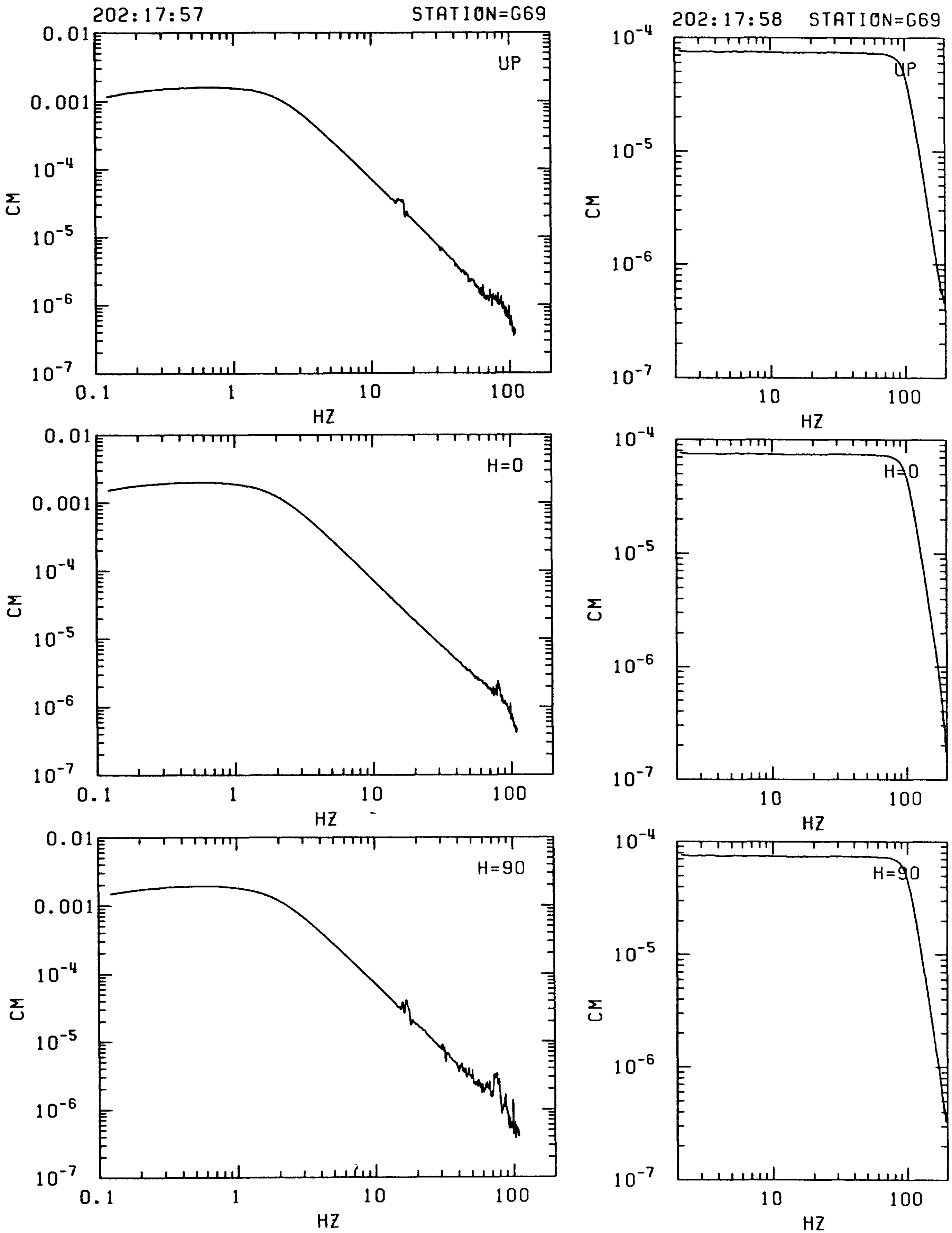

Figure F7: Amplitude response curves computed from in-situ recordings of step function in ground acceleration (left column; seismometer mass release from rest due to applied DC voltage) and delta function in voltage applied to recorder input (right column) for channels corresponding to vertical, radial and transverse components of motion recorded at station indicated at top. (See text for interpretation.)

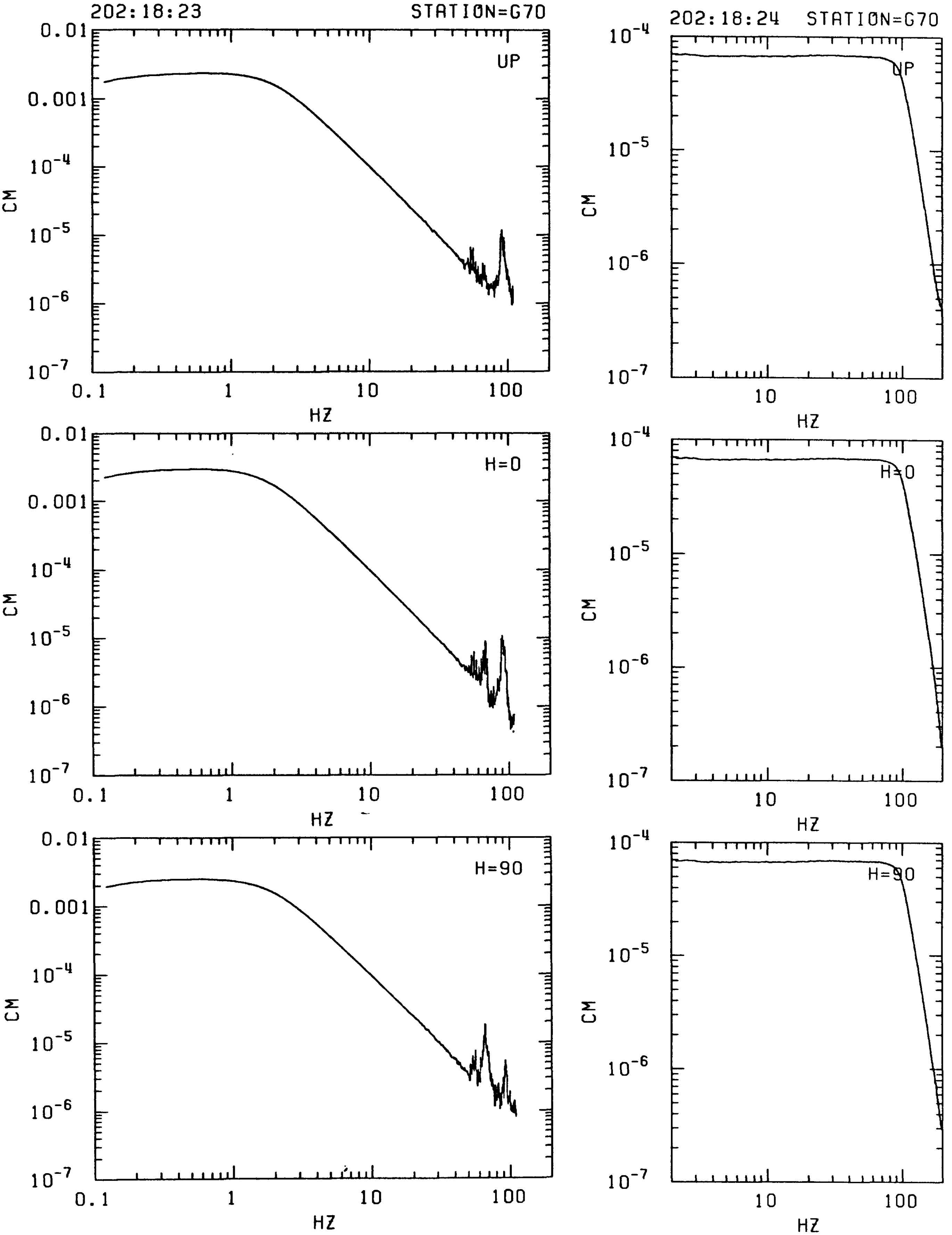

Figure F8: Amplitude response curves computed from in-situ recordings of step function in ground acceleration (left column; seismometer mass release from rest due to applied DC voltage) and delta function in voltage applied to recorder input (right column) for channels corresponding to vertical, radial and transverse components of motion recorded at station indicated at top. (See text for interpretation.)

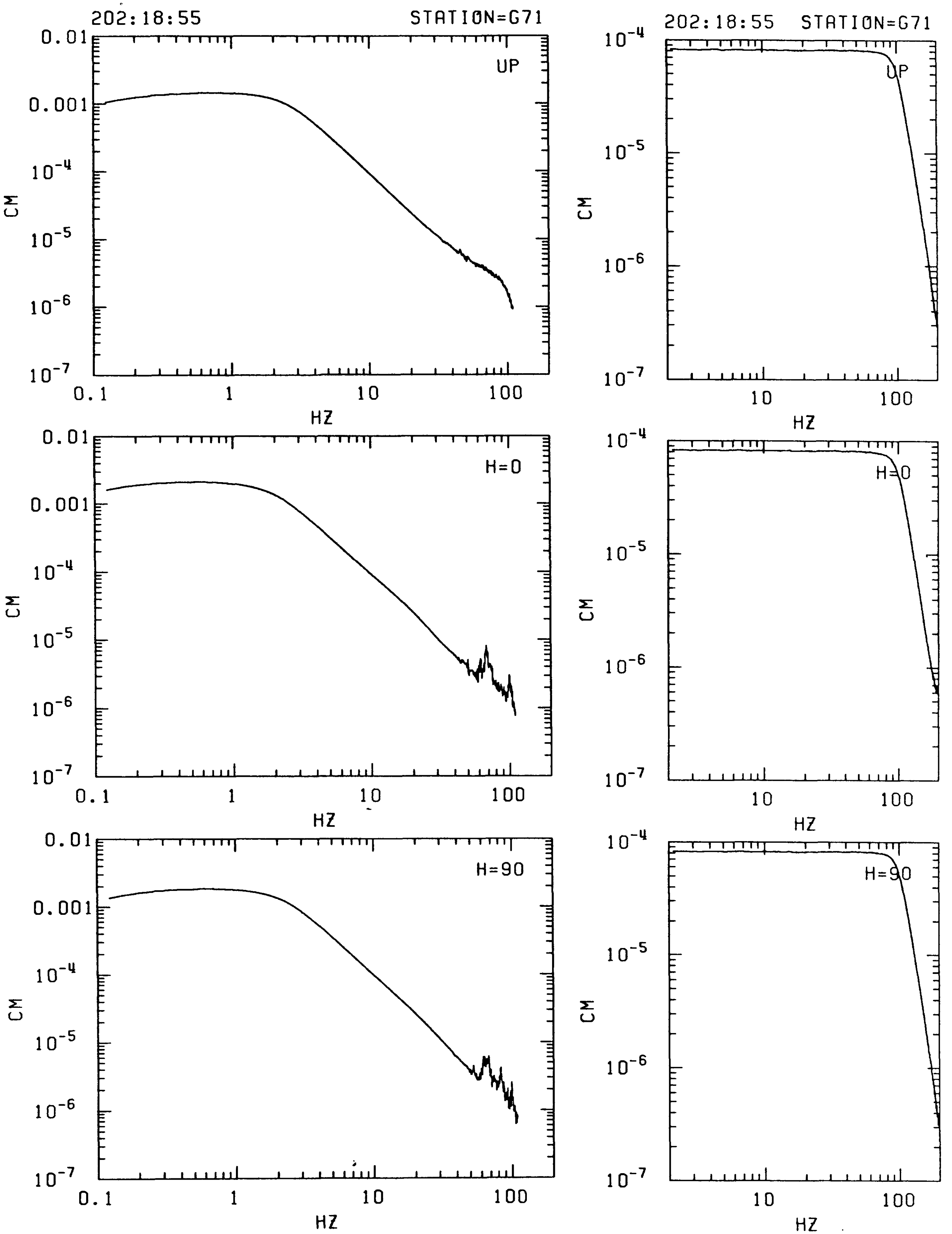

Figure F9: Amplitude response curves computed from in-situ recordings of step function in ground acceleration (left column; seismometer mass release from rest due to applied DC voltage) and delta function in voltage applied to recorder input (right column) for channels corresponding to vertical, radial and transverse components of motion recorded at station indicated at top. (See text for interpretation.)

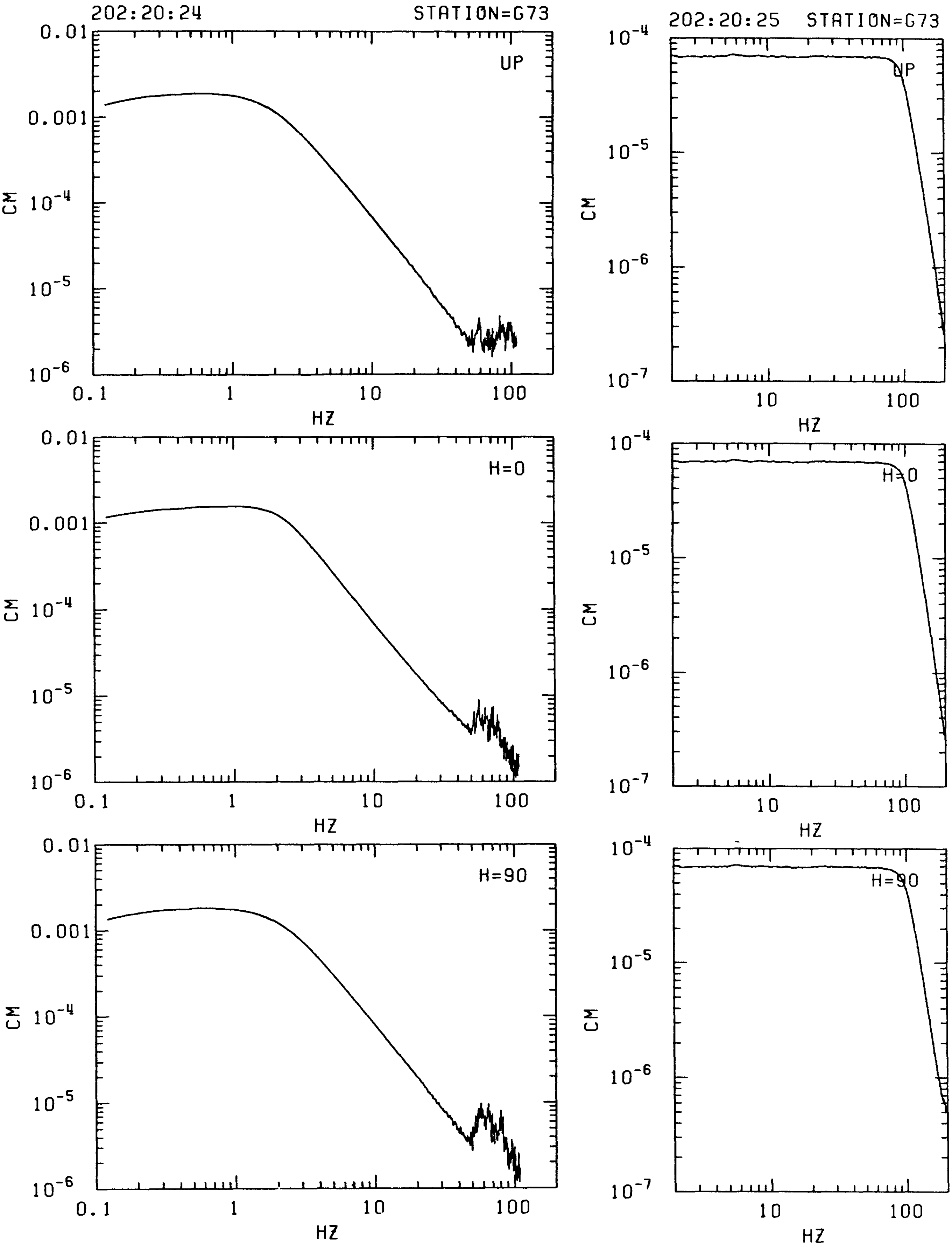

Figure F10: Amplitude response curves computed from in-situ recordings of step function in ground acceleration (left column; seismometer mass release from rest due to applied DC voltage) and delta function in voltage applied to recorder input (right column) for channels corresponding to vertical, radial and transverse components of motion recorded at station indicated at top. (See text for interpretation.)

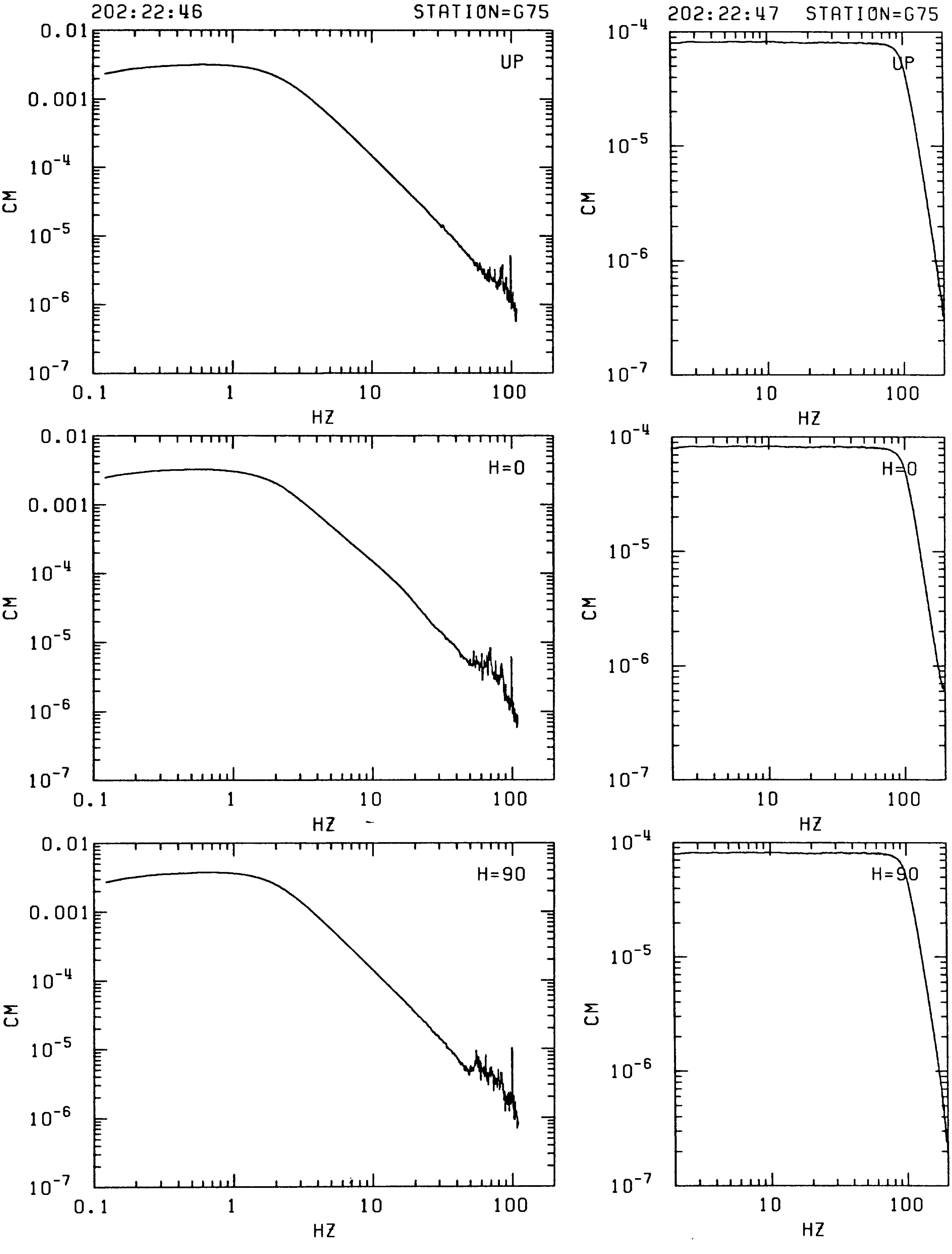

Figure F11: Amplitude response curves computed from in-situ recordings of step function in ground acceleration (left column; seismometer mass release from rest due to applied DC voltage) and delta function in voltage applied to recorder input (right column) for channels corresponding to vertical, radial and transverse components of motion recorded at station indicated at top. (See text for interpretation.)

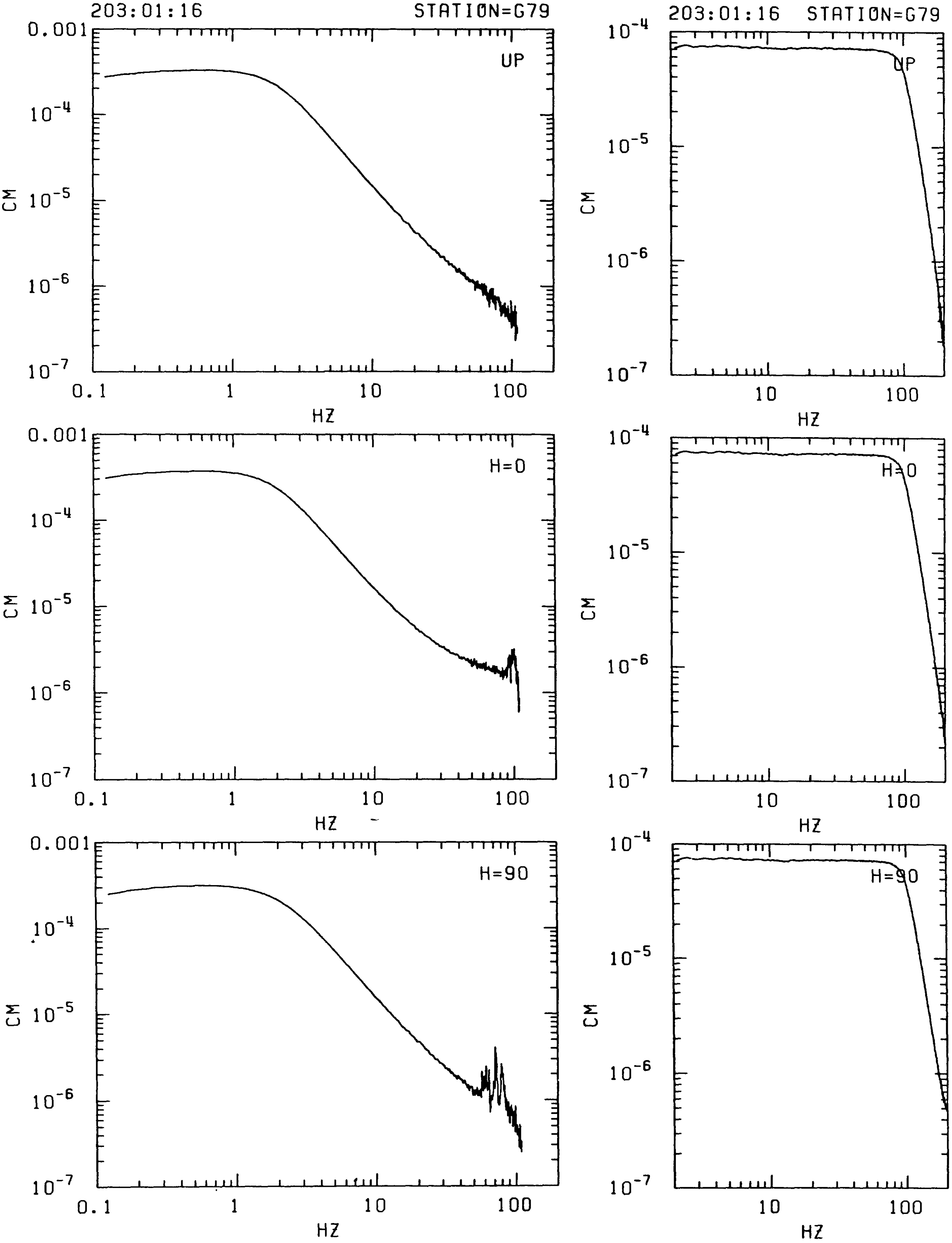

Figure F12: Amplitude response curves computed from in-situ recordings of step function in ground acceleration (left column; seismometer mass release from rest due to applied DC voltage) and delta function in voltage applied to recorder input (right column) for channels corresponding to vertical, radial and transverse components of motion recorded at station indicated at top. (See text for interpretation.)

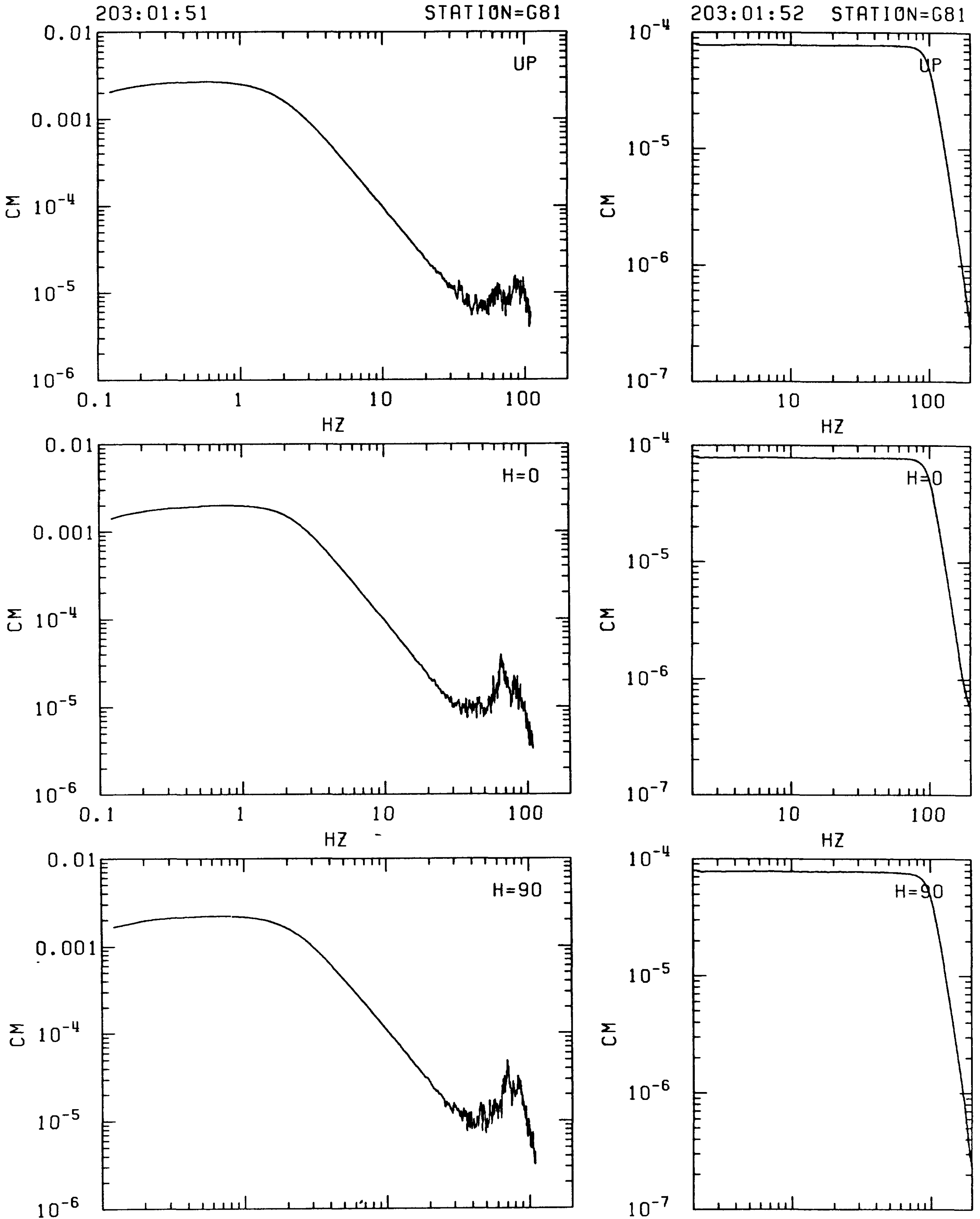

Figure F13: Amplitude response curves computed from in-situ recordings of step function in ground acceleration (left column; seismometer mass release from rest due to applied DC voltage) and delta function in voltage applied to recorder input (right column) for channels corresponding to vertical, radial and transverse components of motion recorded at station indicated at top. (See text for interpretation.)

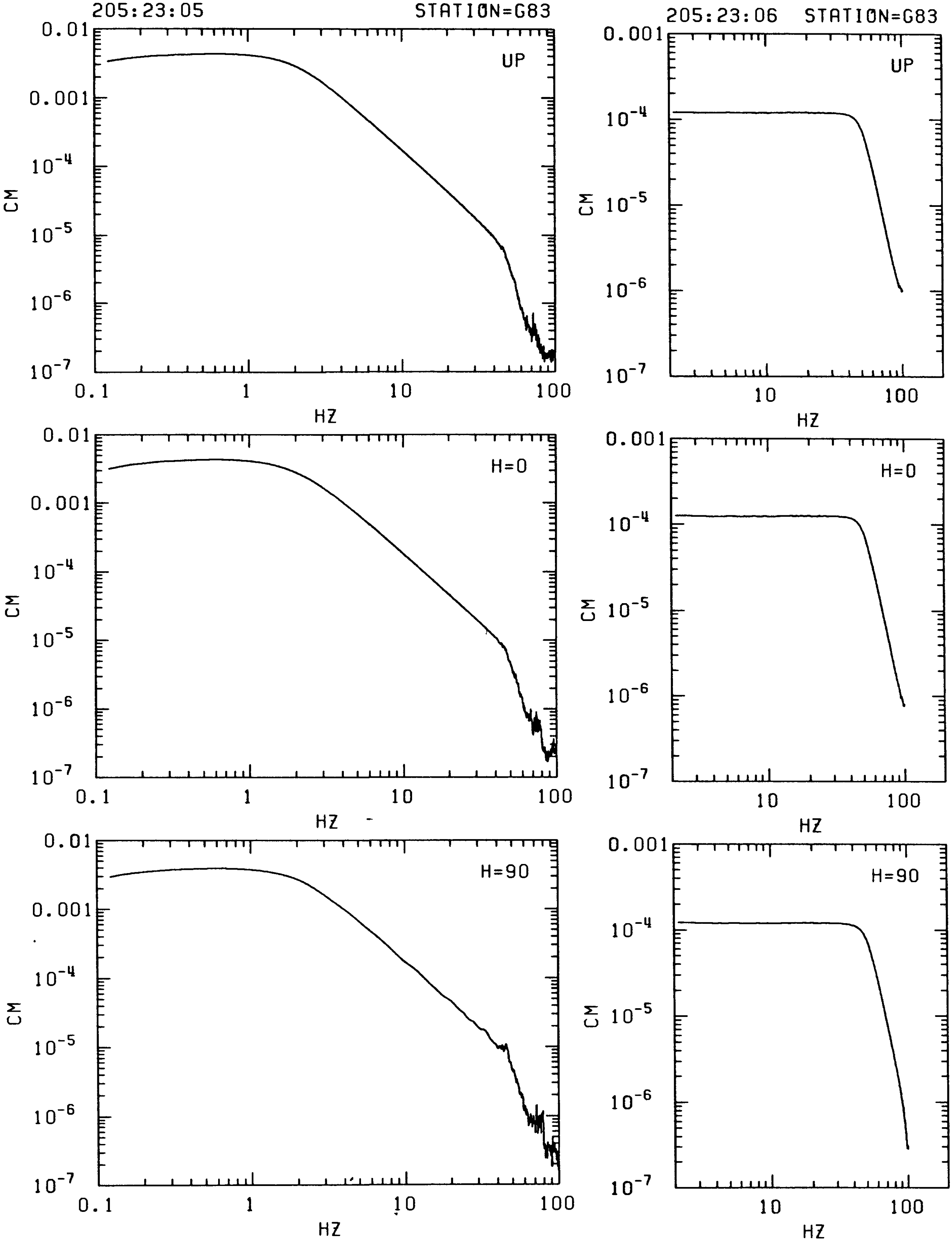

Figure F14: Amplitude response curves computed from in-situ recordings of step function in ground acceleration (left column; seismometer mass release from rest due to applied DC voltage) and delta function in voltage applied to recorder input (right column) for channels corresponding to vertical, radial and transverse components of motion recorded at station indicated at top. (See text for interpretation.)

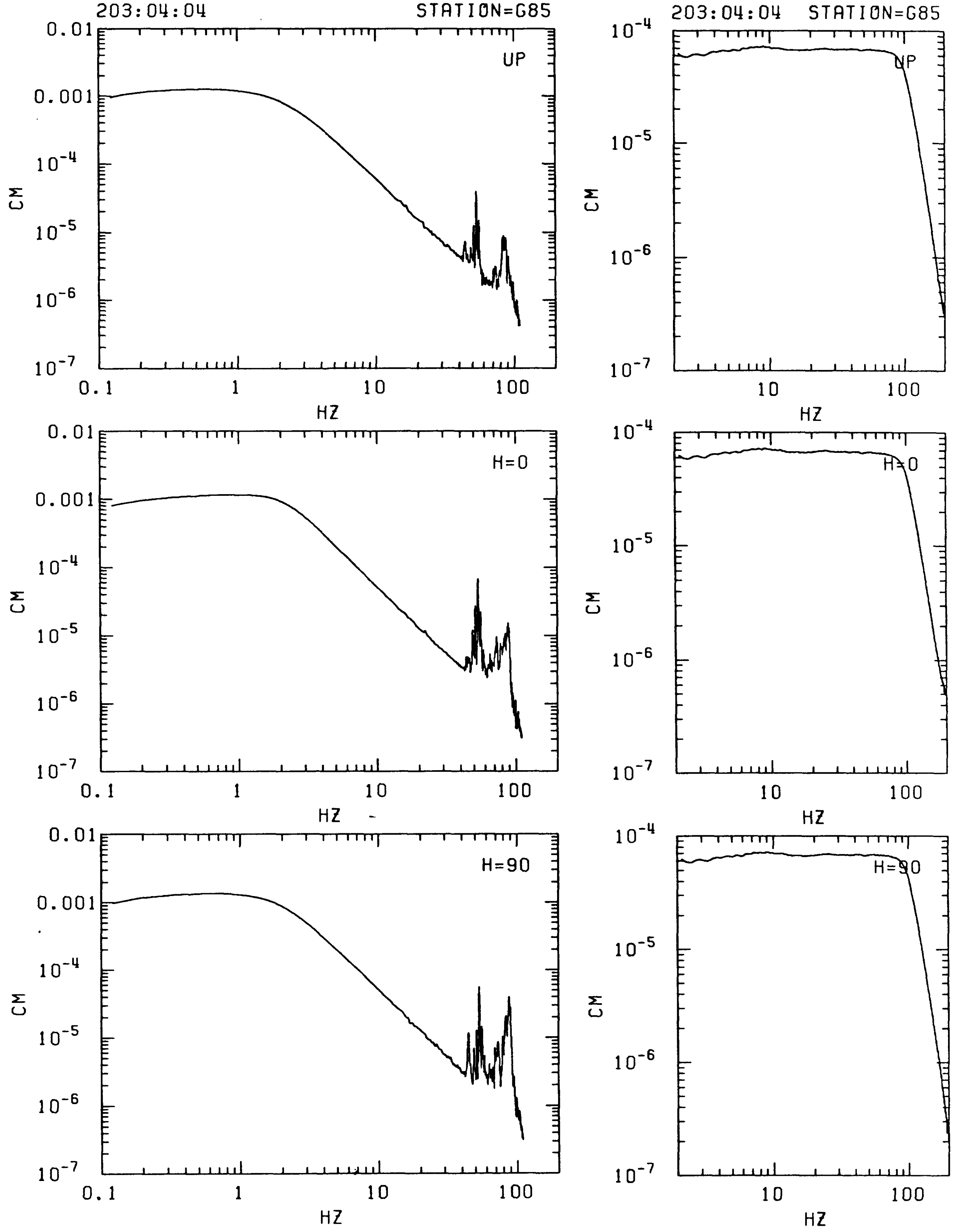

Figure F15: Amplitude response curves computed from in-situ recordings of step function in ground acceleration (left column; seismometer mass release from rest due to applied DC voltage) and delta function in voltage applied to recorder input (right column) for channels corresponding to vertical, radial and transverse components of motion recorded at station indicated at top. (See text for interpretation.)

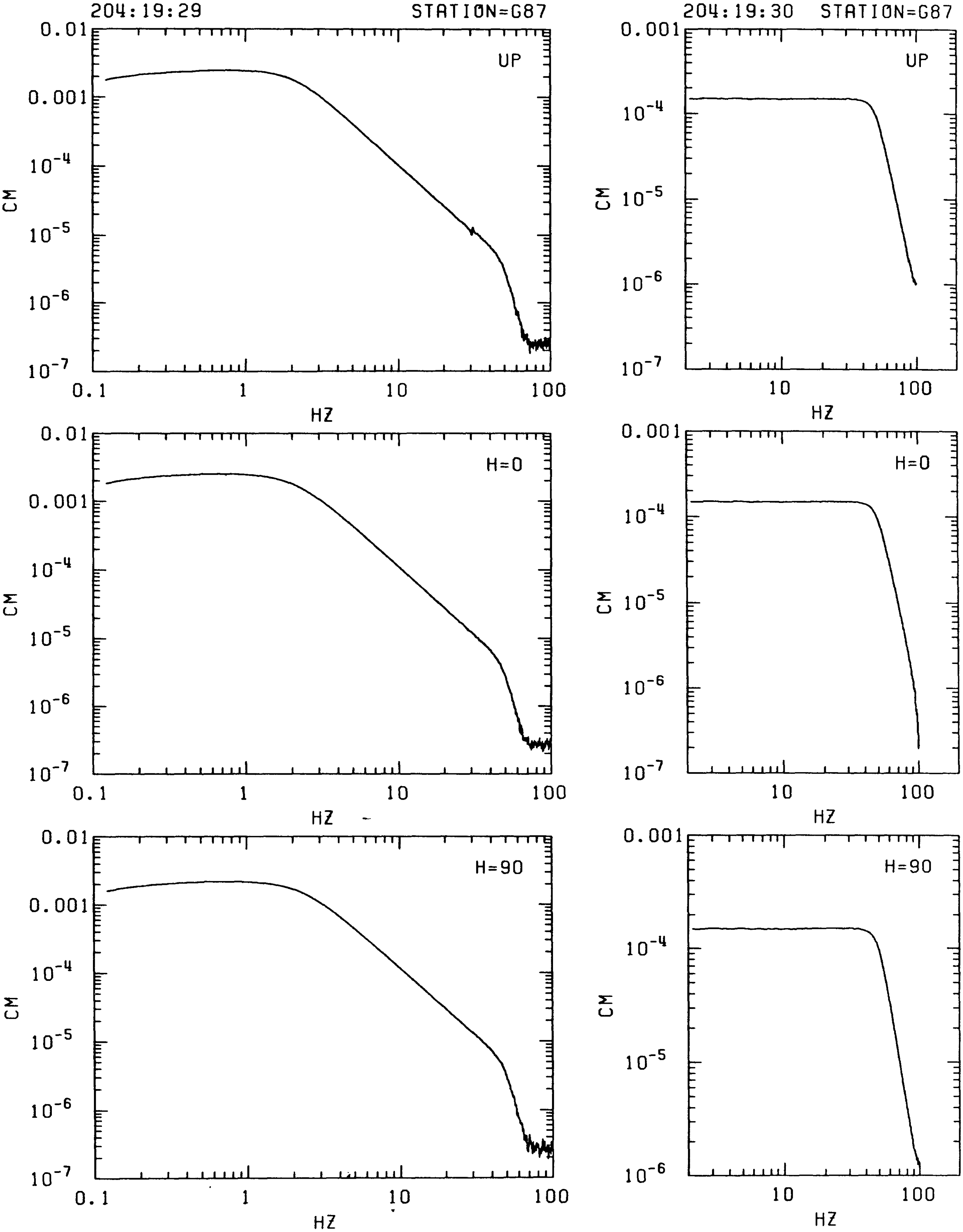

Figure F16: Amplitude response curves computed from in-situ recordings of step function in ground acceleration (left column; seismometer mass release from rest due to applied DC voltage) and delta function in voltage applied to recorder input (right column) for channels corresponding to vertical, radial and transverse components of motion recorded at station indicated at top. (See text for interpretation.)

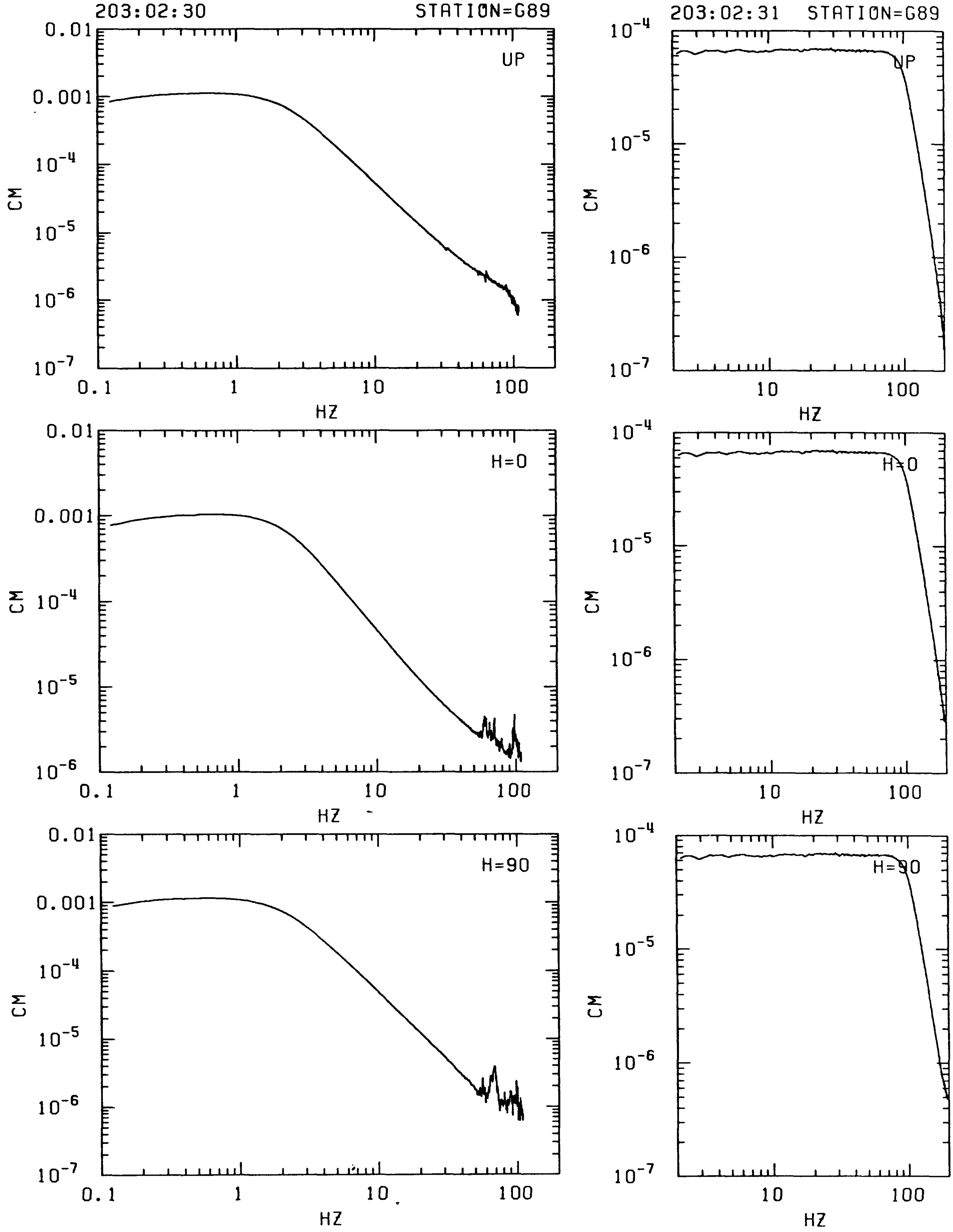

Figure F17: Amplitude response curves computed from in-situ recordings of step function in ground acceleration (left column; seismometer mass release from rest due to applied DC voltage) and delta function in voltage applied to recorder input (right column) for channels corresponding to vertical, radial and transverse components of motion recorded at station indicated at top. (See text for interpretation.)

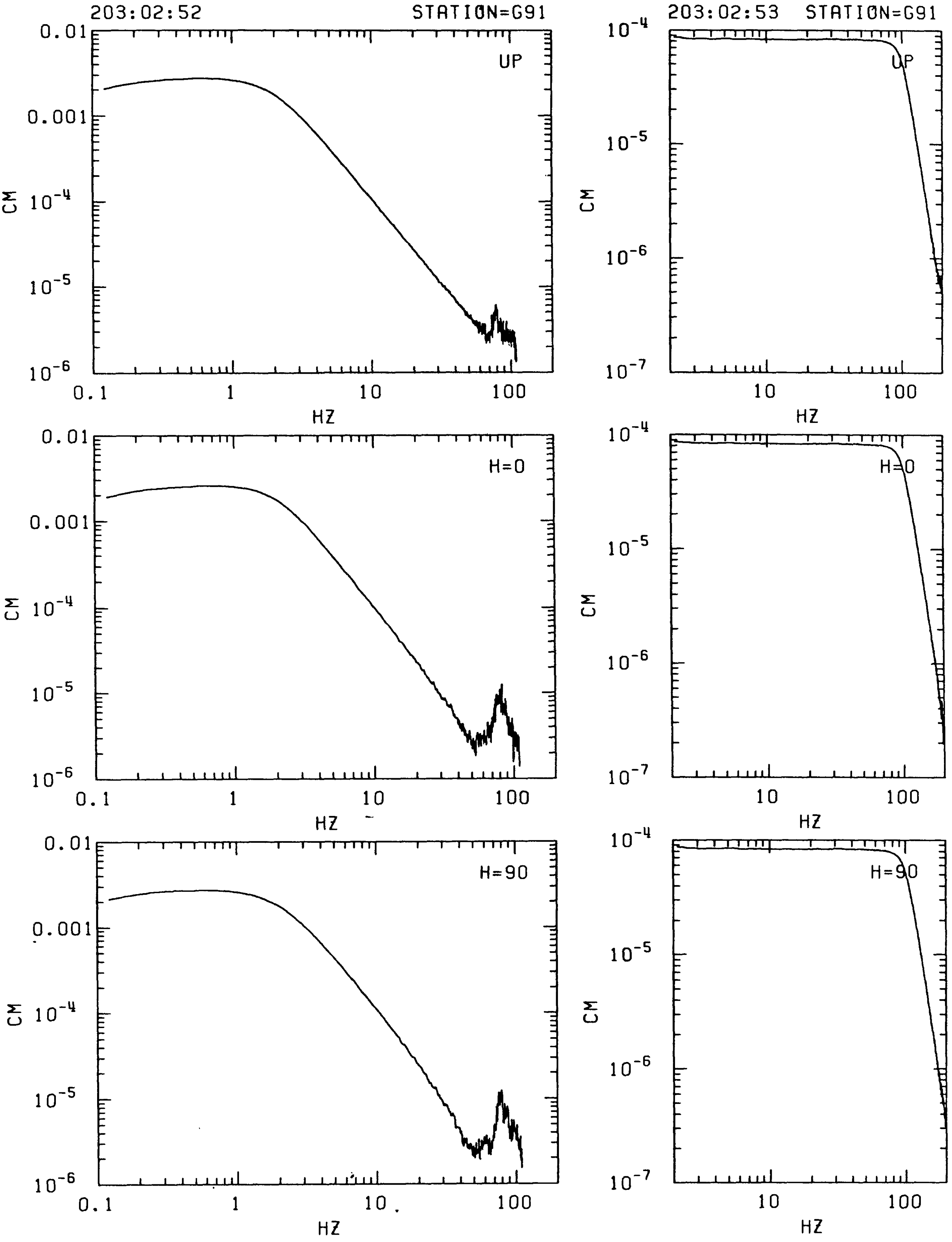

Figure F18: Amplitude response curves computed from in-situ recordings of step function in ground acceleration (left column; seismometer mass release from rest due to applied DC voltage) and delta function in voltage applied to recorder input (right column) for channels corresponding to vertical, radial and transverse components of motion recorded at station indicated at top. (See text for interpretation.)

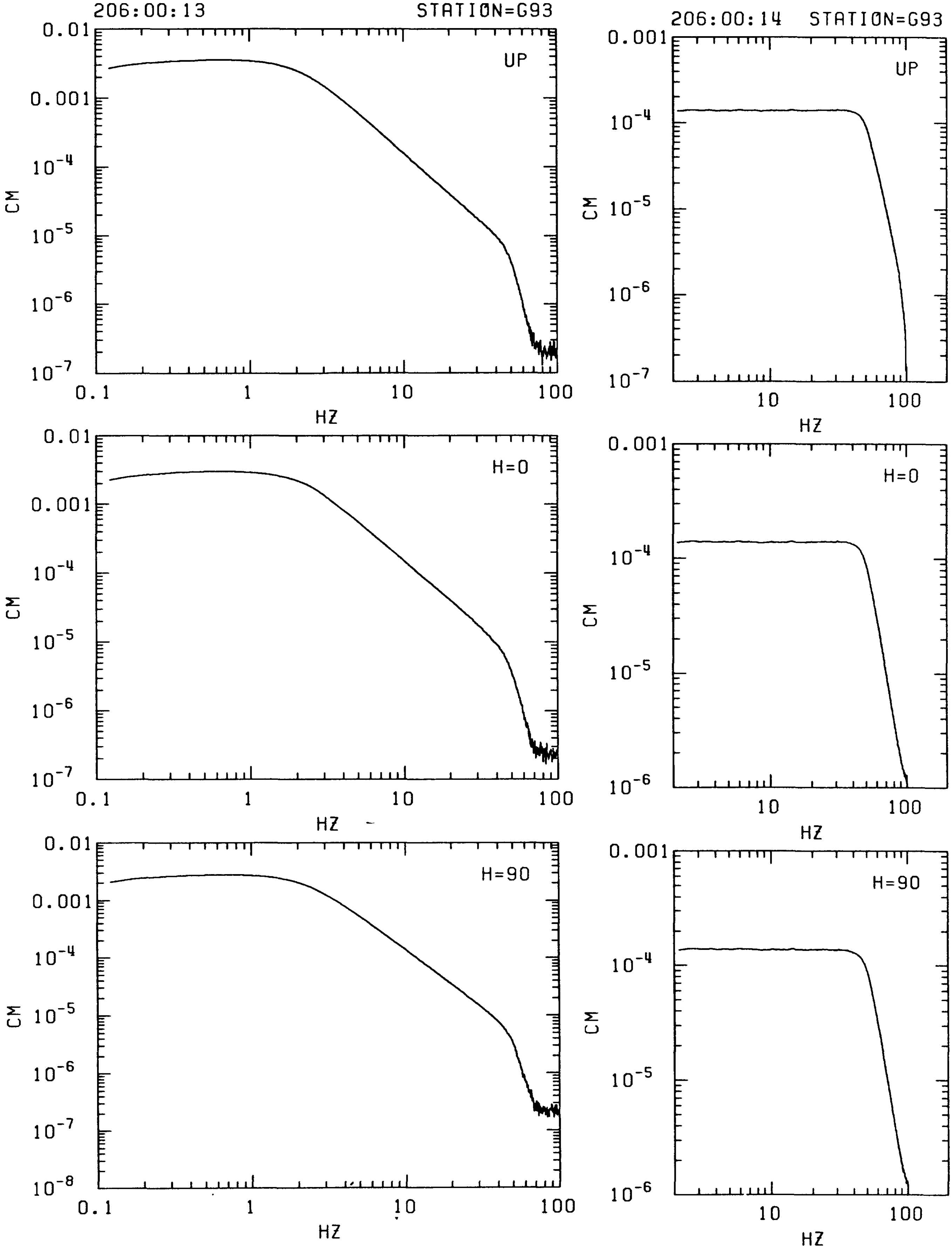

Figure F19: Amplitude response curves computed from in-situ recordings of step function in ground acceleration (left column; seismometer mass release from rest due to applied DC voltage) and delta function in voltage applied to recorder input (right column) for channels corresponding to vertical, radial and transverse components of motion recorded at station indicated at top. (See text for interpretation.)

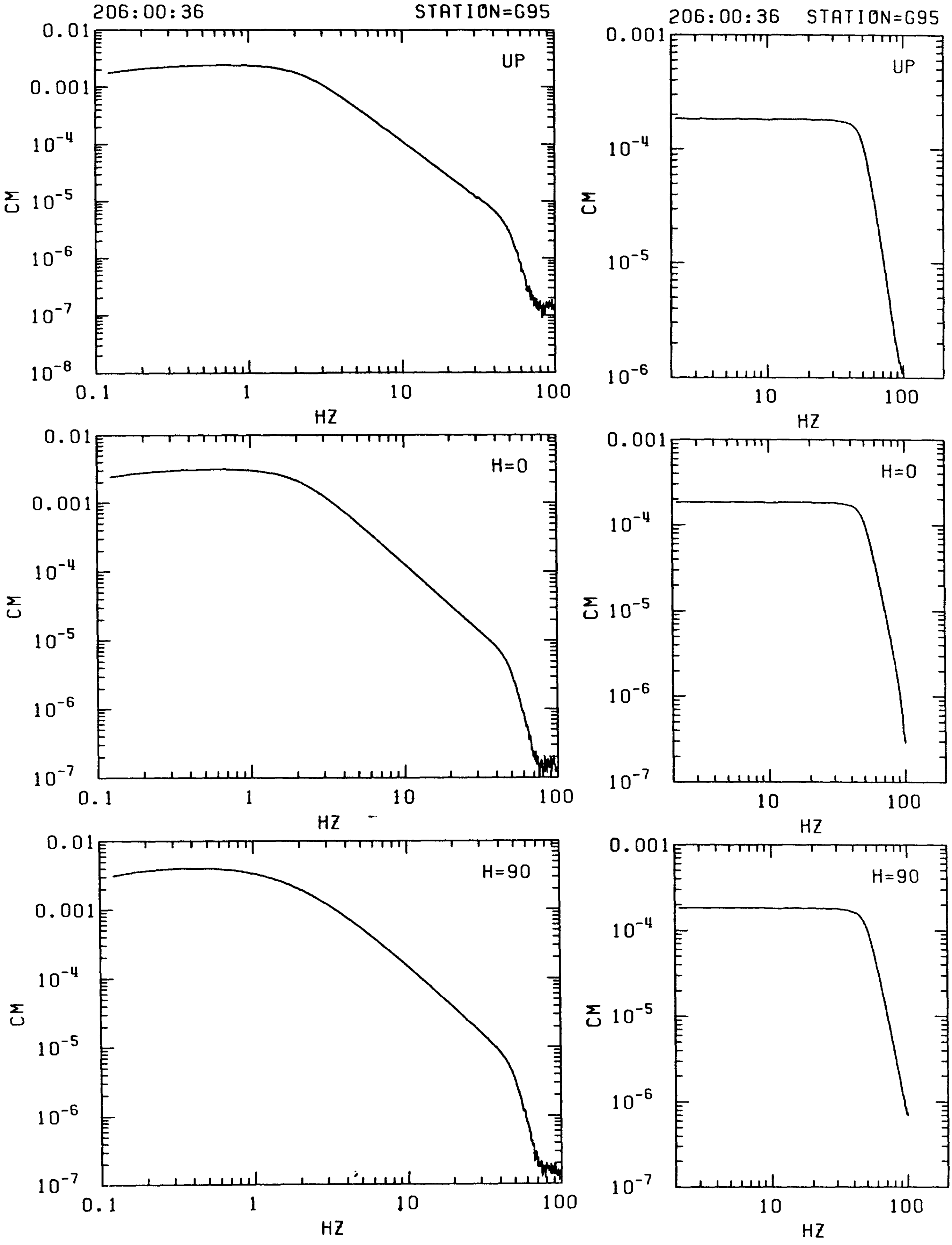

Figure F20: Amplitude response curves computed from in-situ recordings of step function in ground acceleration (left column; seismometer mass release from rest due to applied DC voltage) and delta function in voltage applied to recorder input (right column) for channels corresponding to vertical, radial and transverse components of motion recorded at station indicated at top. (See text for interpretation.)

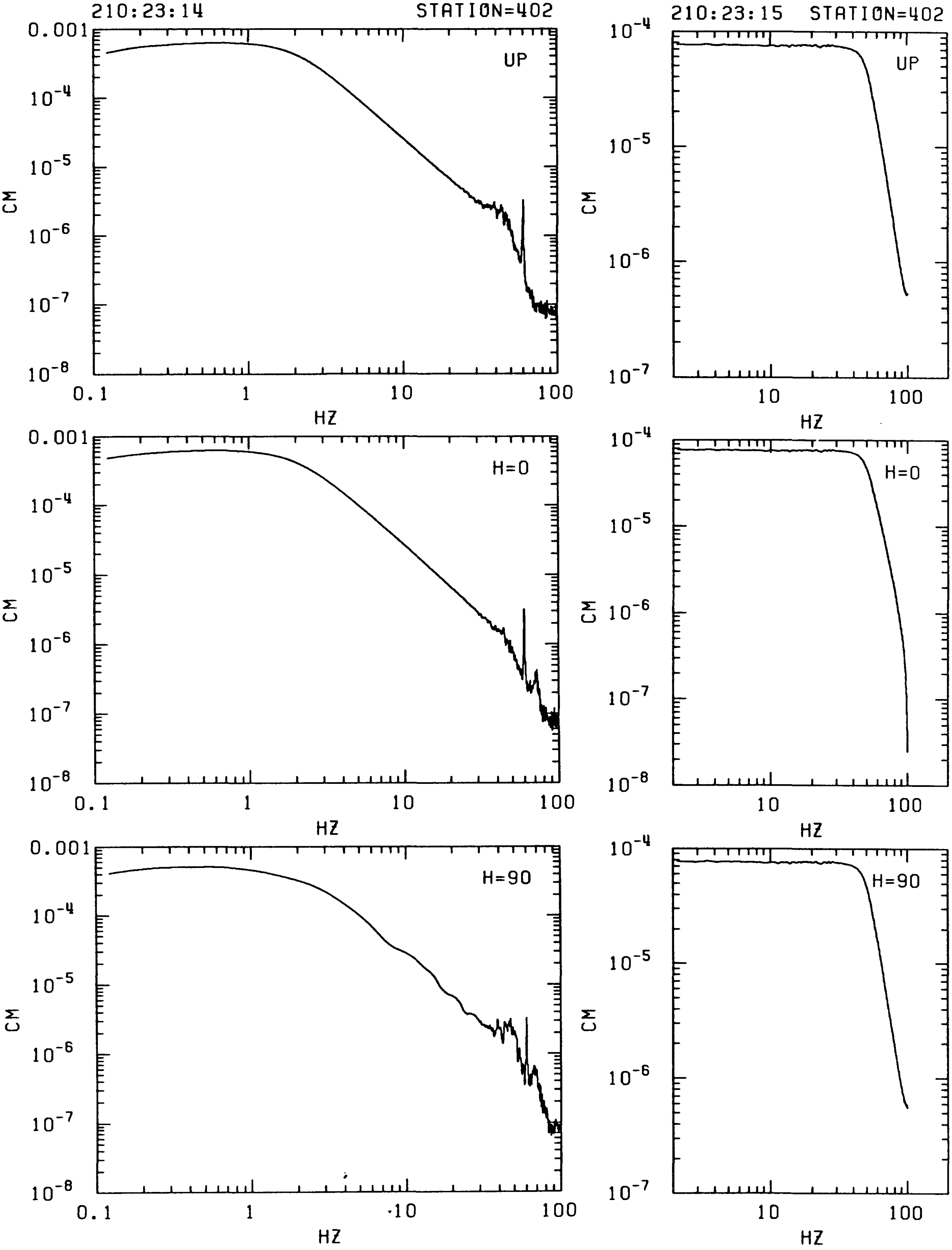

Figure F21: Amplitude response curves computed from in-situ recordings of step function in ground acceleration (left column; seismometer mass release from rest due to applied DC voltage) and delta function in voltage applied to recorder input (right column) for channels corresponding to vertical, radial and transverse components of motion recorded at station indicated at top. (See text for interpretation.)

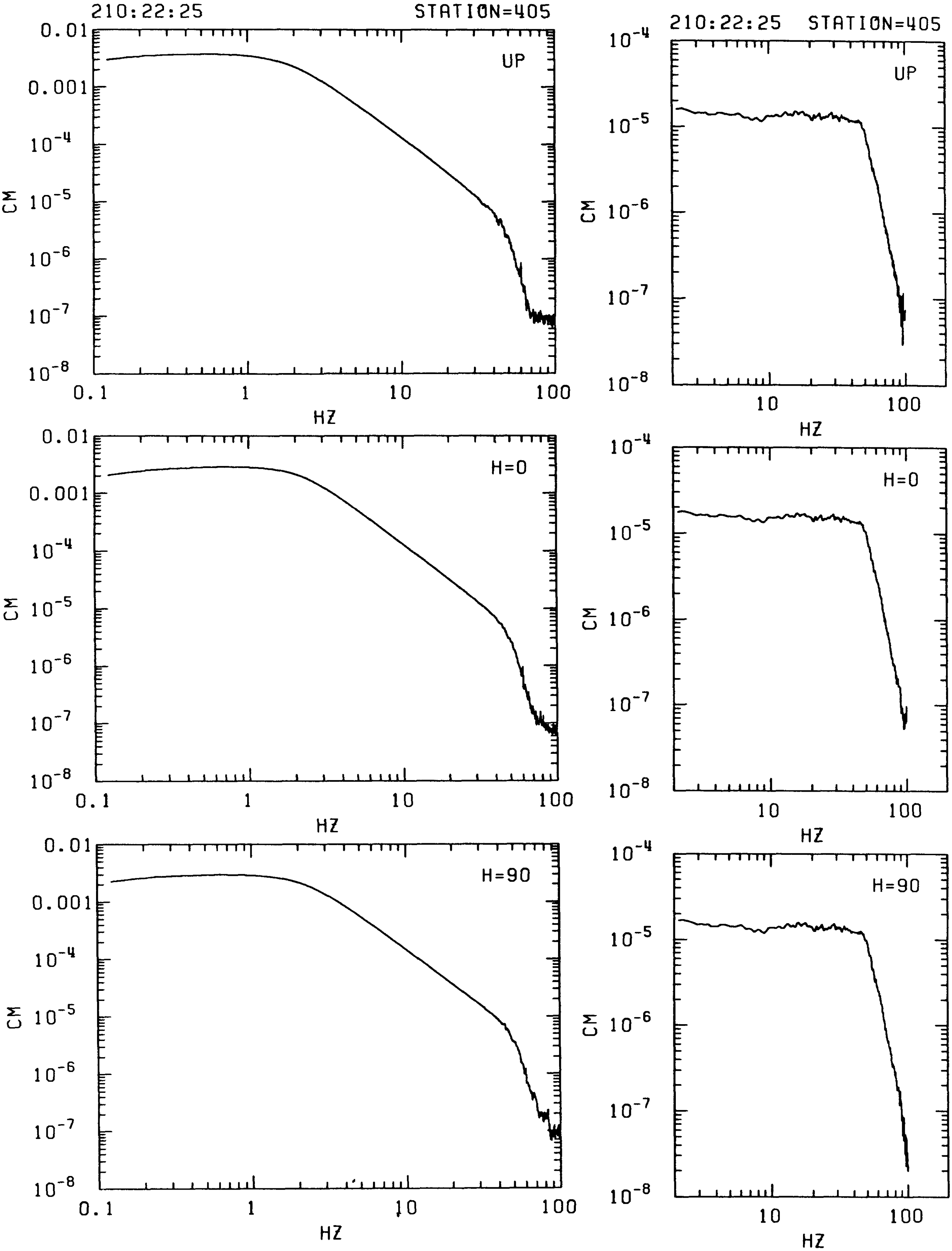

Figure F22: Amplitude response curves computed from in-situ recordings of step function in ground acceleration (left column; seismometer mass release from rest due to applied DC voltage) and delta function in voltage applied to recorder input (right column) for channels corresponding to vertical, radial and transverse components of motion recorded at station indicated at top. (See text for interpretation.)

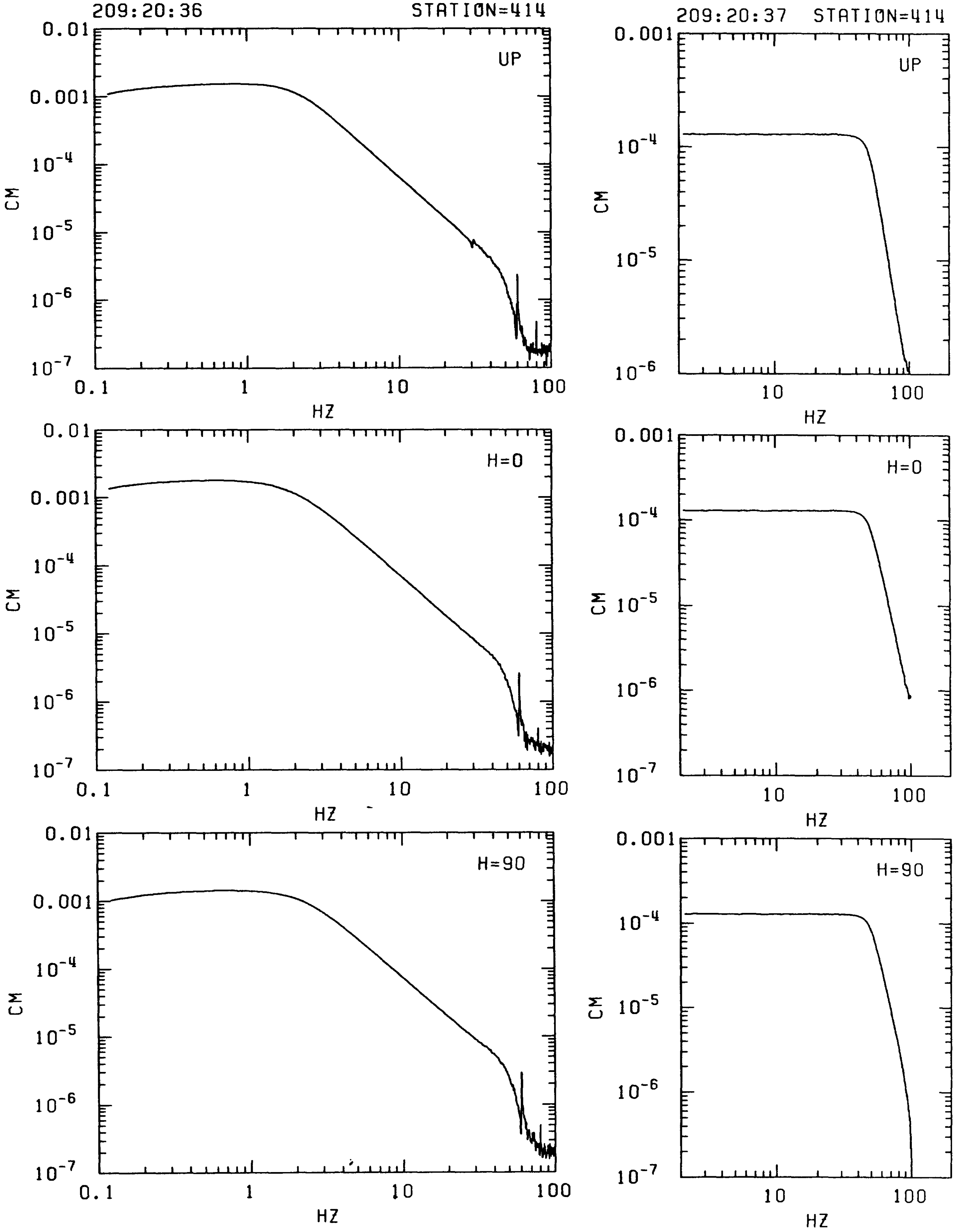

Figure F23: Amplitude response curves computed from in-situ recordings of step function in ground acceleration (left column; seismometer mass release from rest due to applied DC voltage) and delta function in voltage applied to recorder input (right column) for channels corresponding to vertical, radial and transverse components of motion recorded at station indicated at top. (See text for interpretation.)

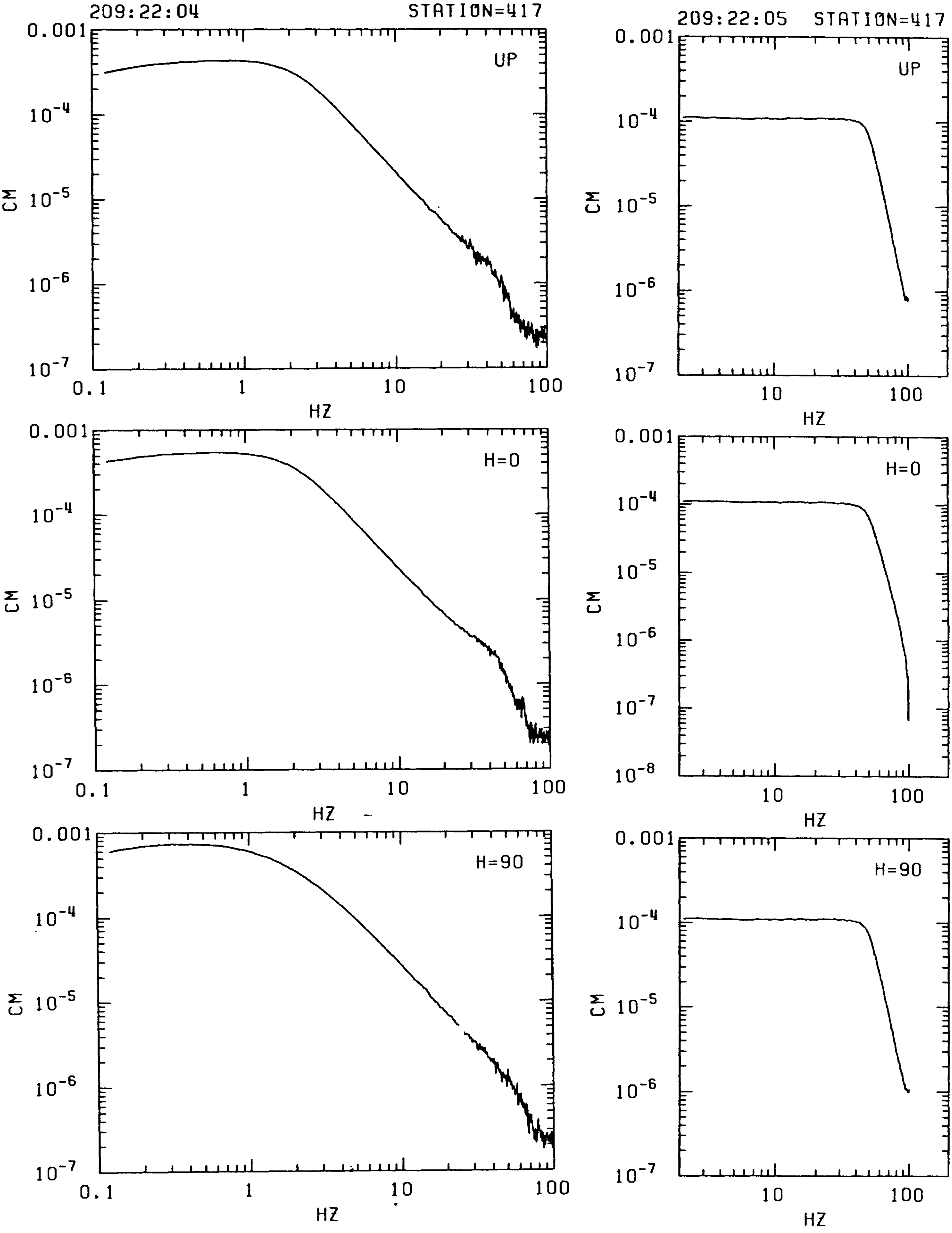

Figure F24: Amplitude response curves computed from in-situ recordings of step function in ground acceleration (left column; seismometer mass release from rest due to applied DC voltage) and delta function in voltage applied to recorder input (right column) for channels corresponding to vertical, radial and transverse components of motion recorded at station indicated at top. (See text for interpretation.)

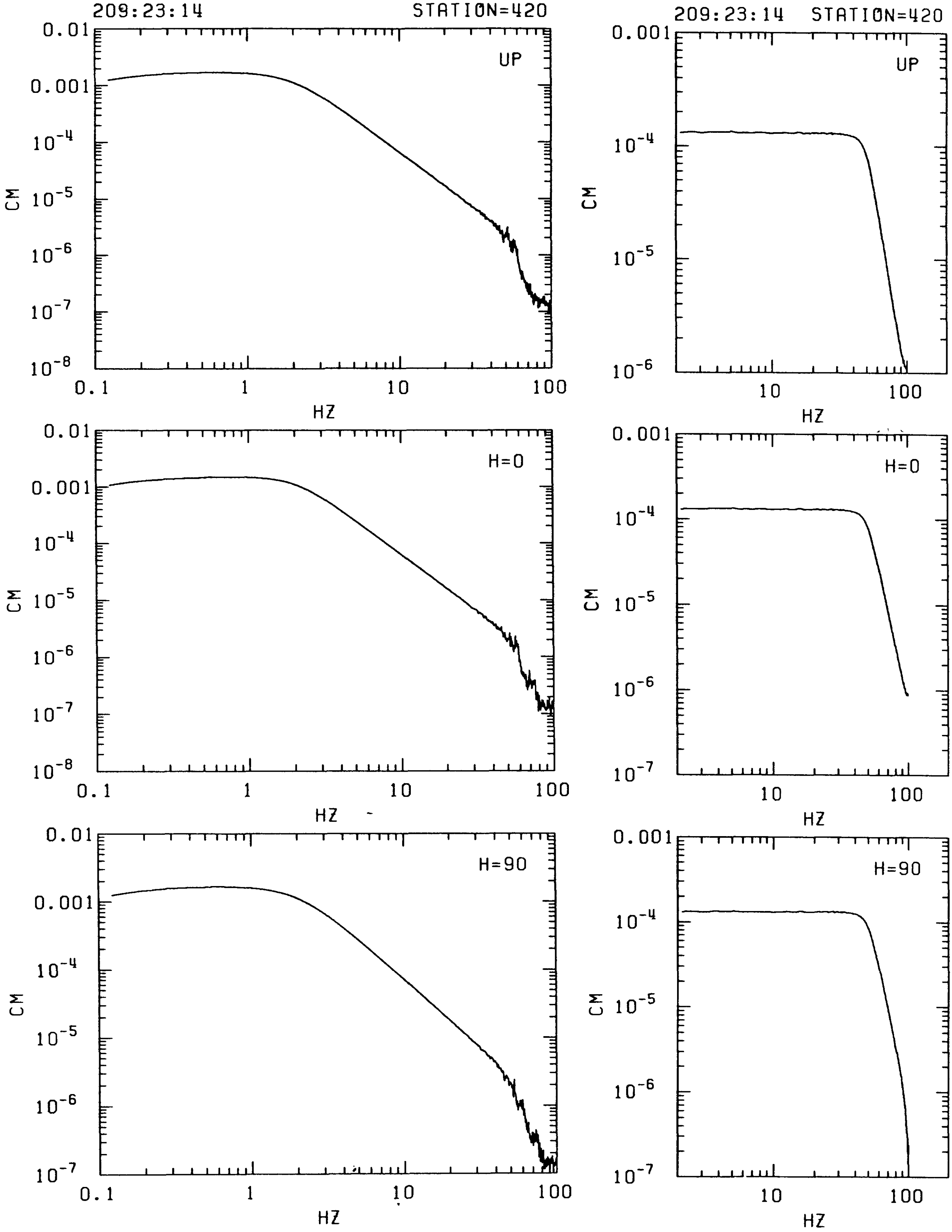

Figure F25: Amplitude response curves computed from in-situ recordings of step function in ground acceleration (left column; seismometer mass release from rest due to applied DC voltage) and delta function in voltage applied to recorder input (right column) for channels corresponding to vertical, radial and transverse components of motion recorded at station indicated at top. (See text for interpretation.)

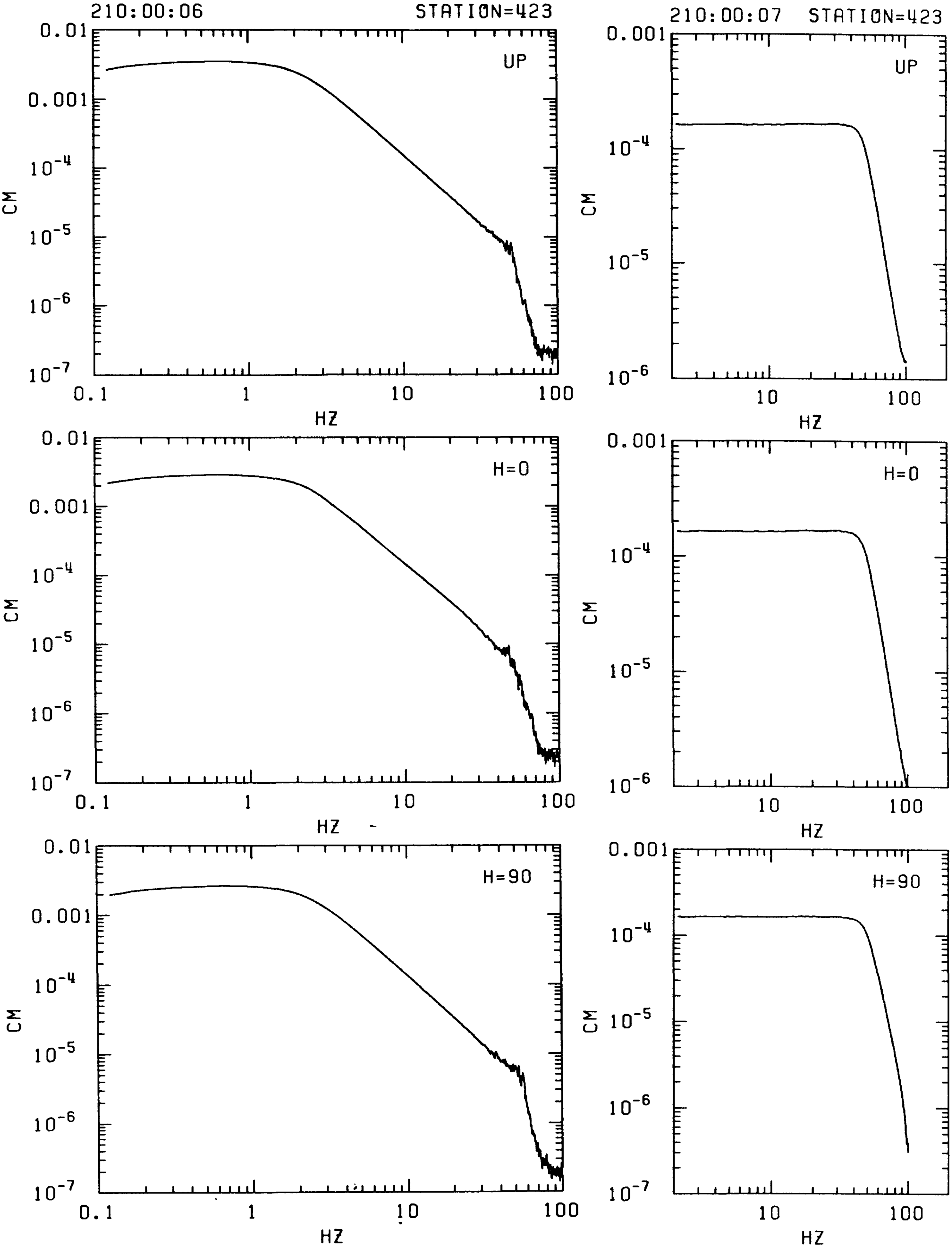

Figure F26: Amplitude response curves computed from in-situ recordings of step function in ground acceleration (left column; seismometer mass release from rest due to applied DC voltage) and delta function in voltage applied to recorder input (right column) for channels corresponding to vertical, radial and transverse components of motion recorded at station indicated at top. (See text for interpretation.)

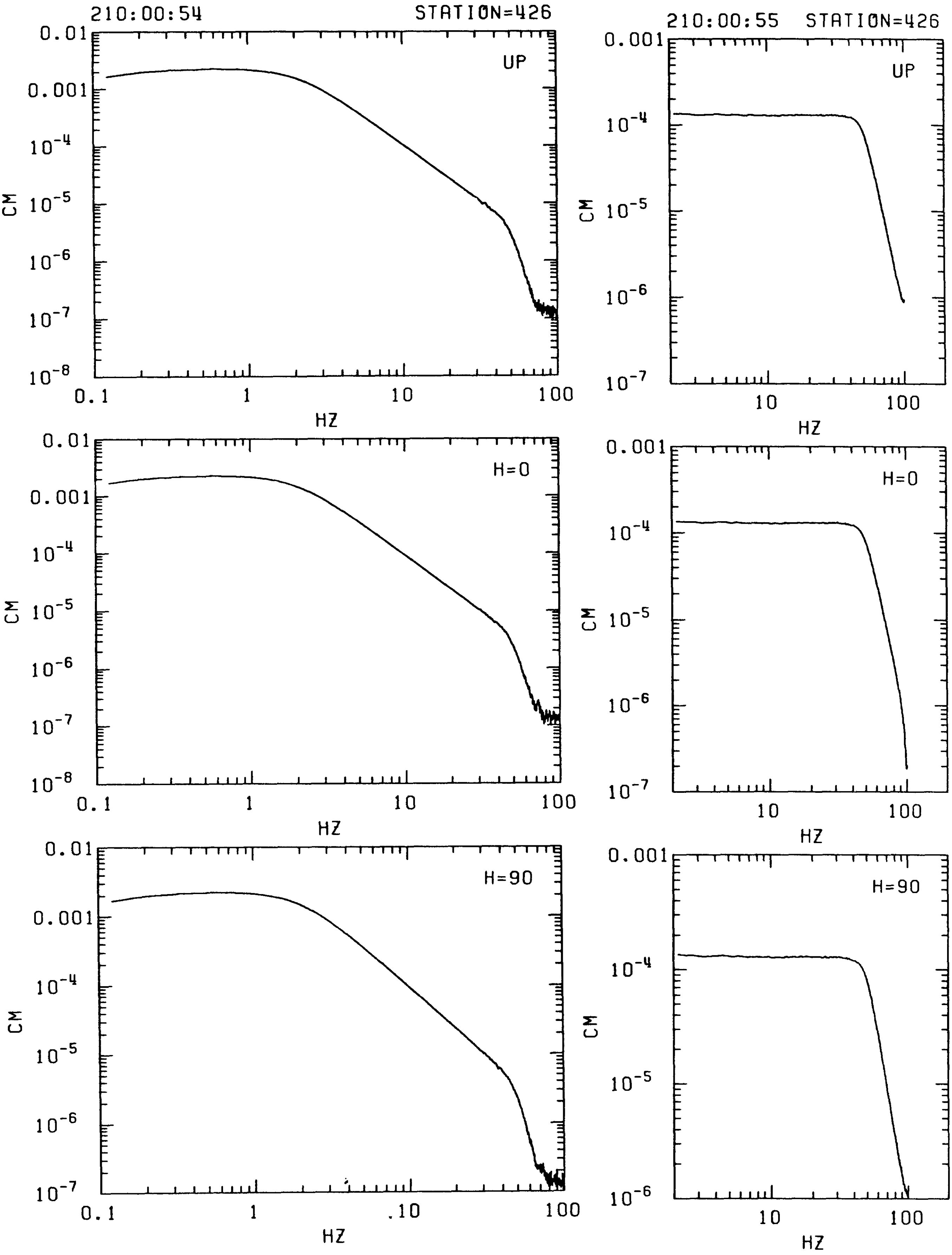

Figure F27: Amplitude response curves computed from in-situ recordings of step function in ground acceleration (left column; seismometer mass release from rest due to applied DC voltage) and delta function in voltage applied to recorder input (right column) for channels corresponding to vertical, radial and transverse components of motion recorded at station indicated at top. (See text for interpretation.)

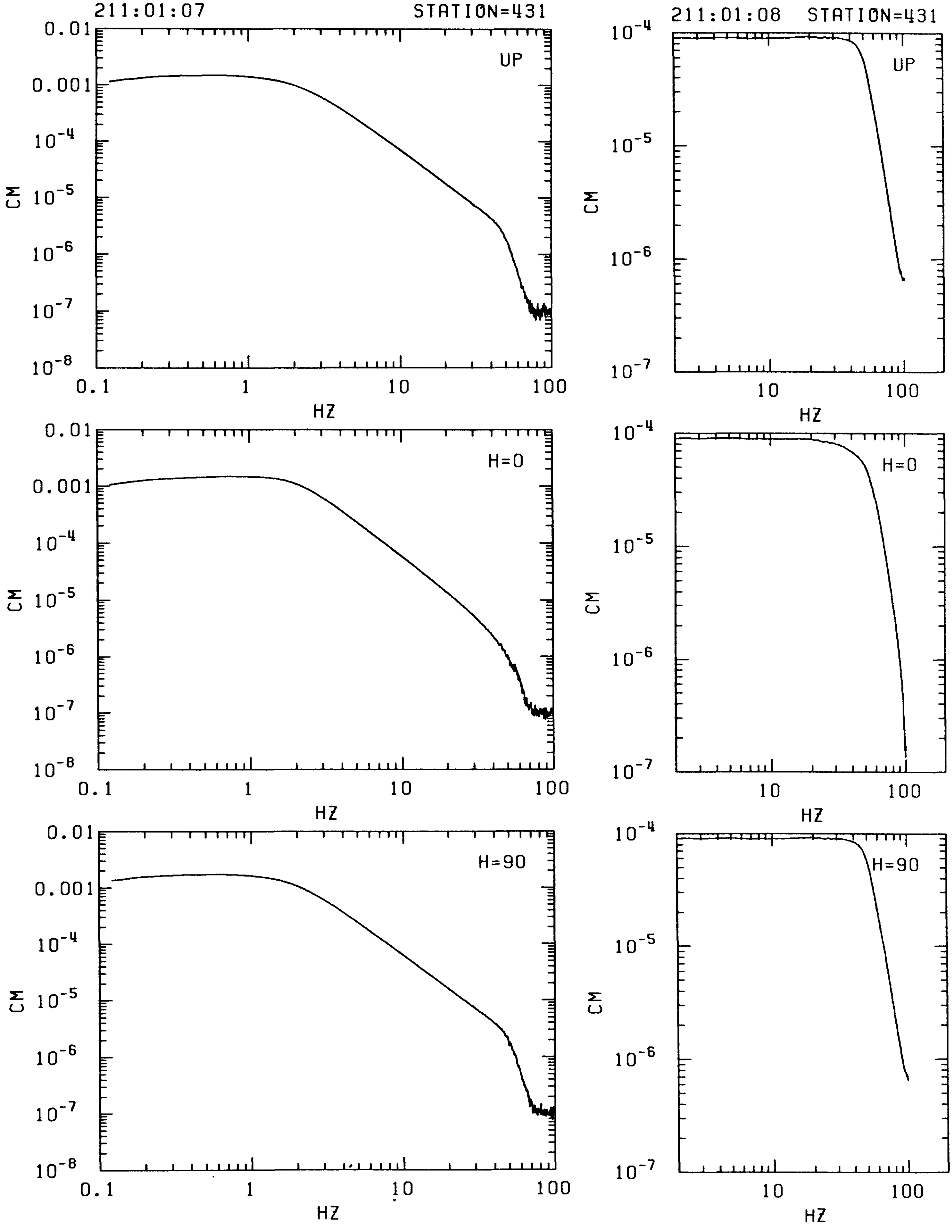

Figure F28: Amplitude response curves computed from in-situ recordings of step function in ground acceleration (left column; seismometer mass release from rest due to applied DC voltage) and delta function in voltage applied to recorder input (right column) for channels corresponding to vertical, radial and transverse components of motion recorded at station indicated at top. (See text for interpretation.)

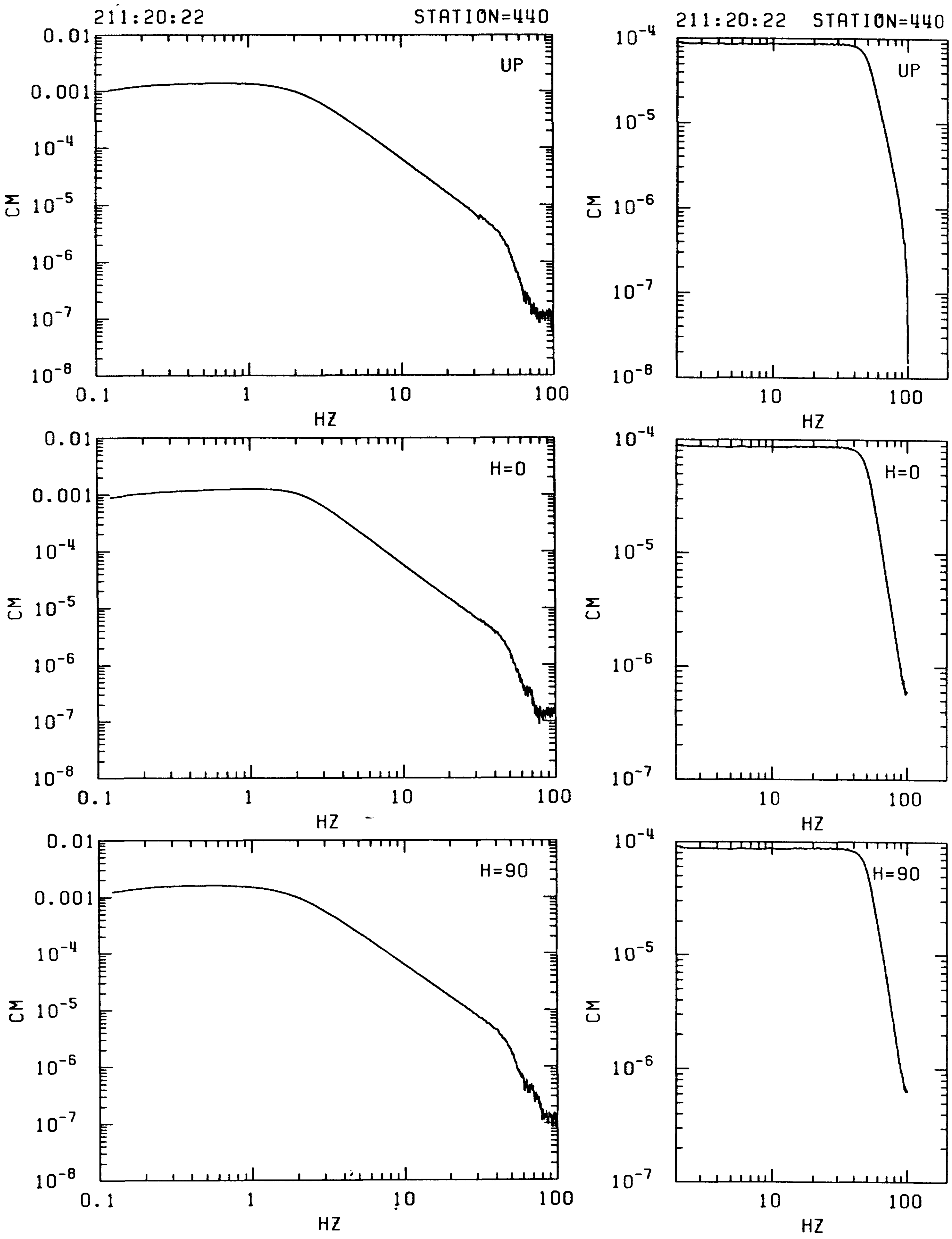

Figure F29: Amplitude response curves computed from in-situ recordings of step function in ground acceleration (left column; seismometer mass release from rest due to applied DC voltage) and delta function in voltage applied to recorder input (right column) for channels corresponding to vertical, radial and transverse components of motion recorded at station indicated at top. (See text for interpretation.)

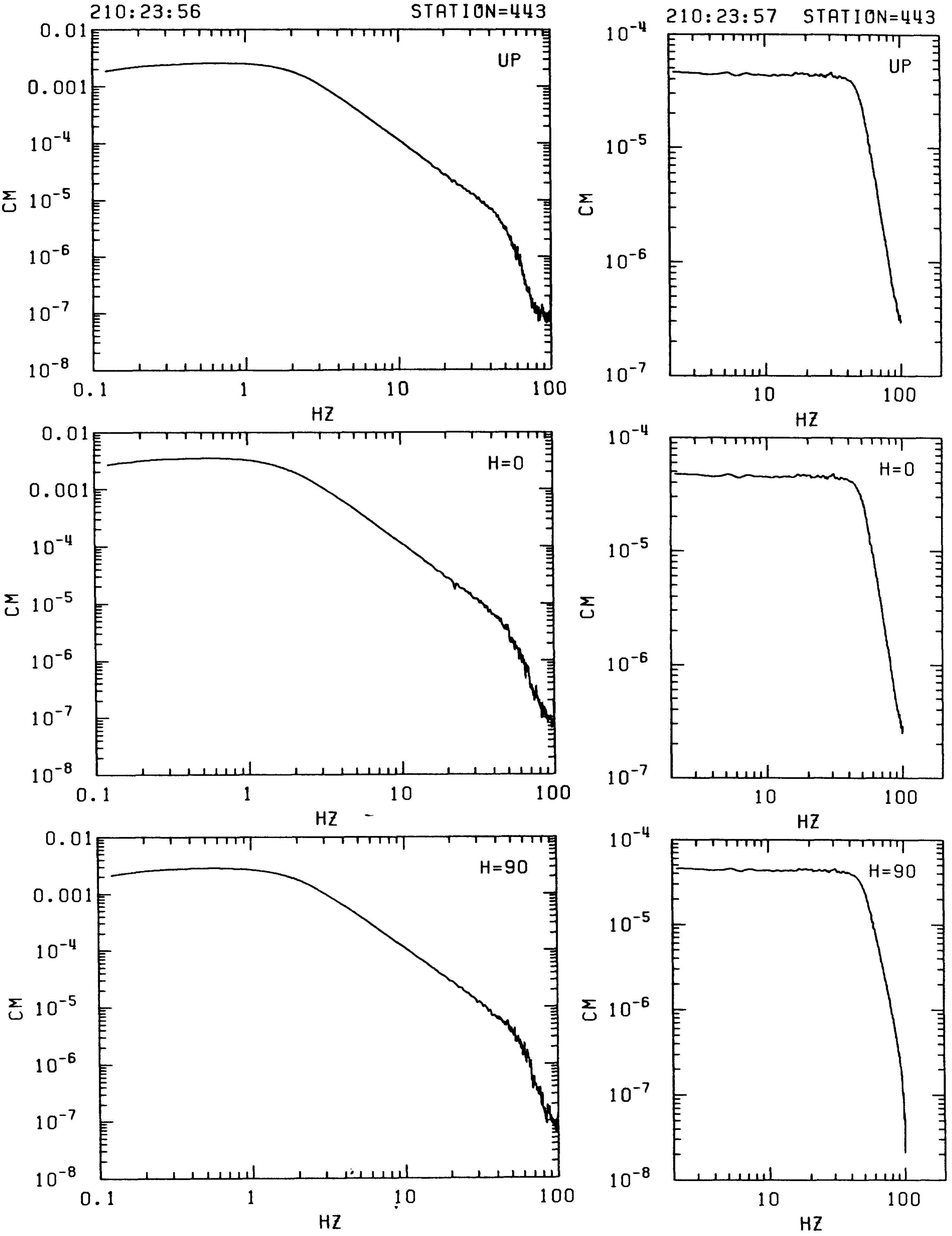

Figure F30: Amplitude response curves computed from in-situ recordings of step function in ground acceleration (left column; seismometer mass release from rest due to applied DC voltage) and delta function in voltage applied to recorder input (right column) for channels corresponding to vertical, radial and transverse components of motion recorded at station indicated at top. (See text for interpretation.)

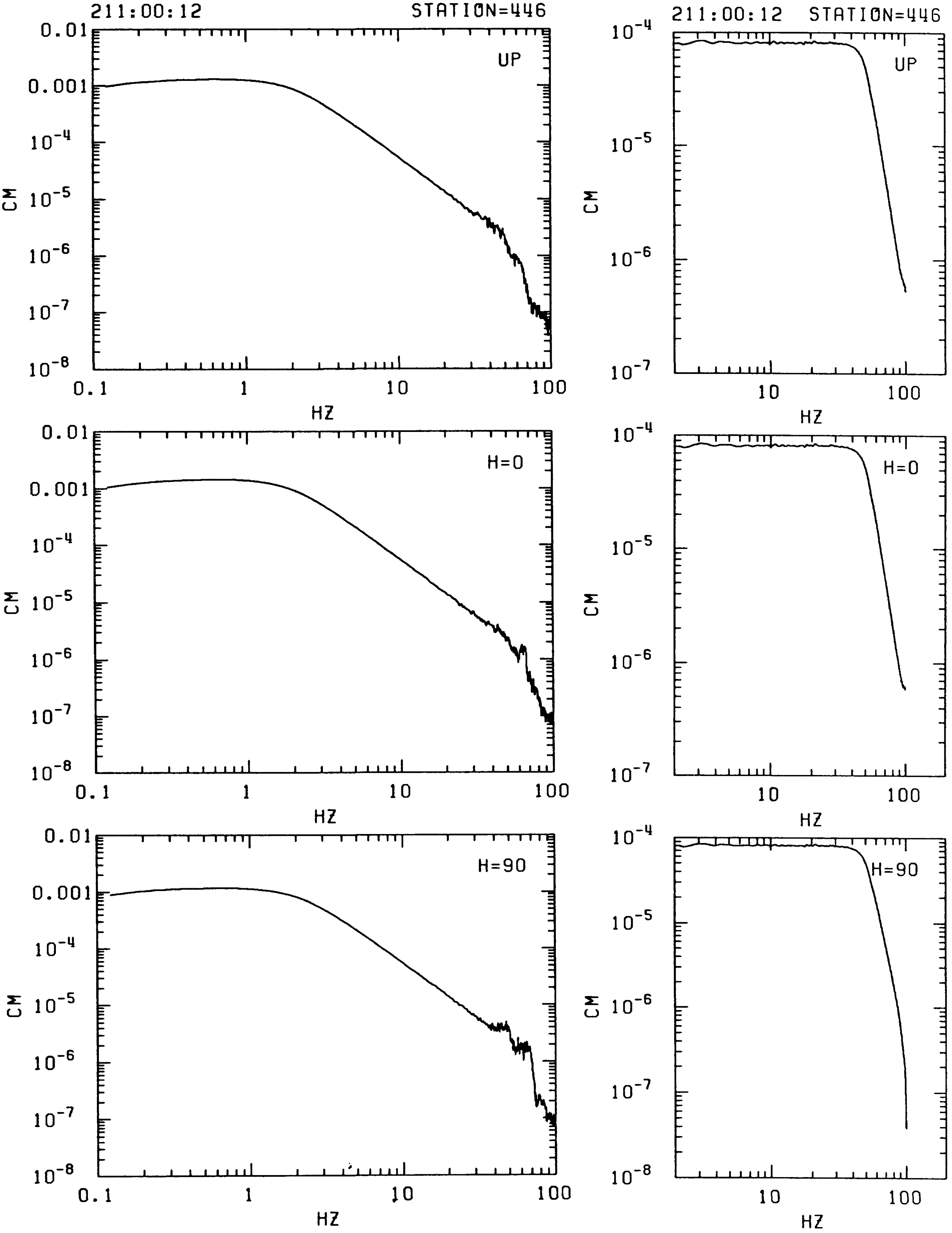

Figure F31: Amplitude response curves computed from in-situ recordings of step function in ground acceleration (left column; seismometer mass release from rest due to applied DC voltage) and delta function in voltage applied to recorder input (right column) for channels corresponding to vertical, radial and transverse components of motion recorded at station indicated at top. (See text for interpretation.)

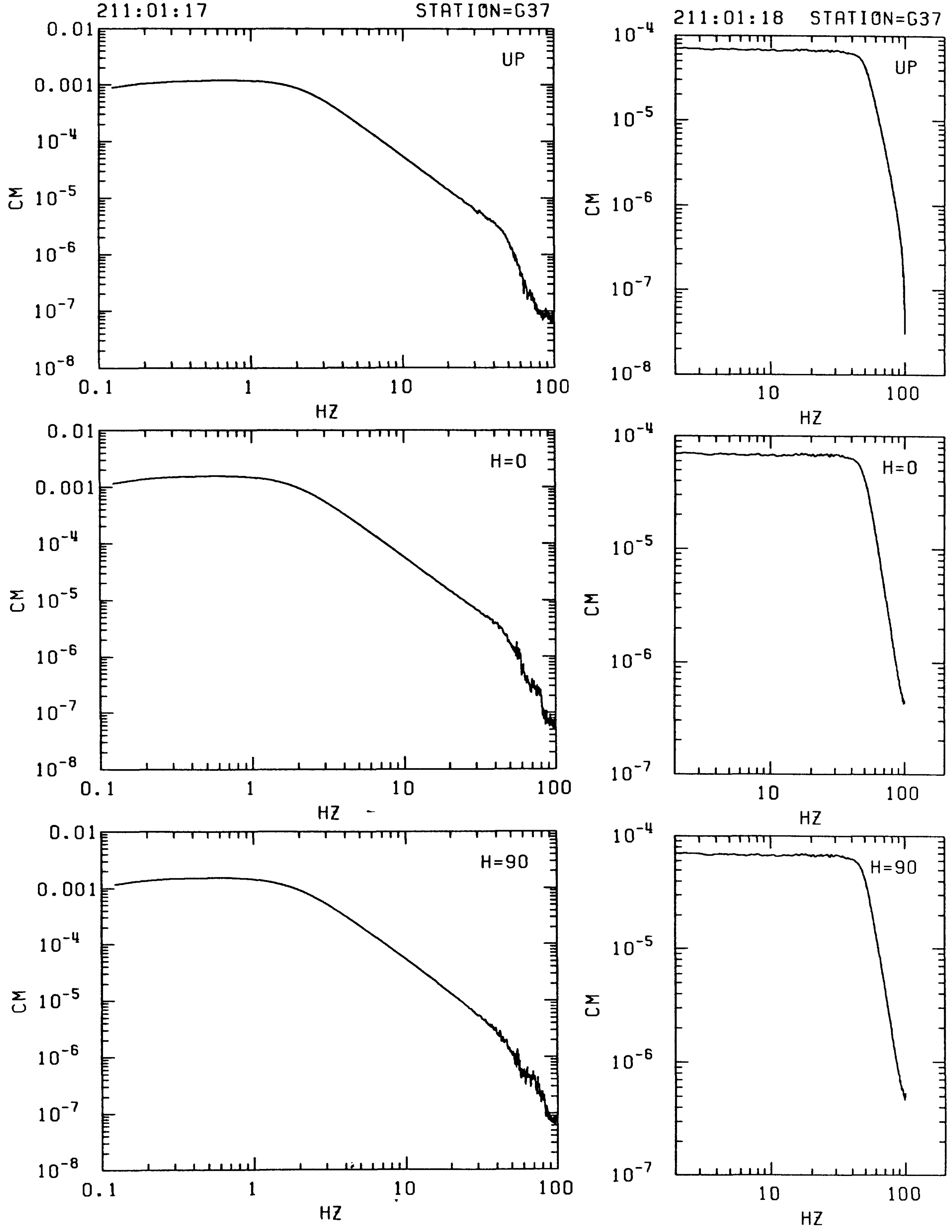

Figure F32: Amplitude response curves computed from in-situ recordings of step function in ground acceleration (left column; seismometer mass release from rest due to applied DC voltage) and delta function in voltage applied to recorder input (right column) for channels corresponding to vertical, radial and transverse components of motion recorded at station indicated at top. (See text for interpretation.)

GPO 788-002/79175